Cilt 6 Sayı 1 Haziran 2025
Volume 6 Number 1 June 2025

ISSN: 2717-8811(Online)

JOURNAL

Materials and Mechatronics:A

2025

JMMA

JOURNAL

Materials

and

Mechatronics: A

e-ISSN: 2717-8811

Cilt: 6 Sayı: 1 Haziran 2025

Volume:6 Number: 1 June 2025

2025

JOURNAL of
MATERIALS and MECHATRONICS:A

JOURNAL of
MATERIALS and MECHATRONICS:A

JOURNAL of
MATERIALS and MECHATRONICS:A

JOURNAL of
MATERIALS and MECHATRONICS:A

JOURNAL of
MATERIALS and MECHATRONICS:A

JOURNAL of
MATERIALS and MECHATRONICS:A

JOURNAL of
MATERIALS and MECHATRONICS:A

JOURNAL of
MATERIALS and MECHATRONICS:A

JOURNAL of
MATERIALS and MECHATRONICS:A

e-ISSN 2717-8811
JournalMM, 2025, 6(1), 1-14
https://doi.org/10.55546/jmm.1571384

Araştırma Makalesi / Research Article

Extraction of Clinical Entities from Chest Radiology Reports Using NLP Methods

Uçman ERGUN[1], Sedanur ORCIN[2*], Sezin BARIN[3]

[1] Afyon Kocatepe University, Faculty of Engineering, Department of Biomedical Engineering, Afyonkarahisar, Türkiye, ORCID ID: https://orcid.org/0000-0002-9218-2192, uergun@aku.edu.tr
[2*] Afyon Kocatepe University, Faculty of Engineering, Department of Biomedical Engineering, Afyonkarahisar, Türkiye, ORCID ID: https://orcid.org/0009-0007-4345-4984, orcinsedanur@gmail.com
[3] Afyon Kocatepe University, Faculty of Engineering, Department of Biomedical Engineering. Afyonkarahisar, Türkiye, ORCID ID: https://orcid.org/0000-0002-0394-2779, sbarin@aku.edu.tr

Geliş/ Received: 21.10.2024**;** **Revize/Revised:** 06.12.2024 **Kabul / Accepted:** 20.12.2024

ABSTRACT: Radiology reports are essential for clinical decision-making and diagnosis, containing complex and detailed information. However, their unstructured nature makes efficient processing and analysis challenging, increasing the workload of healthcare professionals and slowing down clinical workflows. Natural Language Processing (NLP) techniques provide effective solutions by extracting meaningful information from such texts, reducing expert workload, and expediting decision-making processes. This study focuses on Named Entity Recognition (NER) in chest radiology reports using the RadGraph dataset, annotated with four tag types. The objective is to compare the performance of two NLP models—BERT (Bidirectional Encoder Representations from Transformers) and LSTM (Long Short-Term Memory) —to identify the most suitable approach for clinical data. Various training parameters, including learning rate, optimization algorithm, and input size, were optimized to enhance model performance. To address the class imbalance in the dataset, data augmentation techniques were applied, and both models were fine-tuned. The results revealed that BERT, leveraging its attention mechanism, demonstrated superior performance in identifying complex terms and entities, outperforming LSTM in accuracy, precision, recall, and F1 score. While LSTM effectively captured long-term dependencies, it required longer training times. This research highlights the potential of NLP in automating the extraction of clinical entities from radiology reports. It provides valuable insights for optimizing models and developing clinical decision support systems, ultimately aiming to enhance the efficiency of healthcare workflows.

Keywords: Deep learning, Natural language processing, Named entity recognition, Radiological report, BERT

*Sorumlu yazar / Corresponding author: orcinsedanur@gmail.com
Bu makaleye atıf yapmak için /To cite this article

Ergün, U., Orcin, S., Barın S. (2024). Extraction of Clinical Entities from Chest Radiology Reports Using NLP Methods. Journal of Materials and Mechatronics: A (JournalMM), 6(1), 1-14.

1. INTRODUCTION

In recent years, artificial intelligence technologies have revolutionized many areas of life and attracted attention with innovative solutions. NLP technologies, one of the most prominent of these developments, are gaining more and more importance, especially in the healthcare sector. The complex expressions and findings often encountered in radiology reports can make it difficult to interpret the reports correctly, especially for inexperienced physicians, and can lead to misdiagnoses (Yamashita et al., 2022; Nishio et al., 2024). At this point, integrating NLP methods can play a critical role in overcoming these challenges. Integration of NLP into the healthcare system can provide significant improvements in diagnosis and treatment processes by offering various advantages to both physicians and patients.

This study focuses on the automatic, accurate and efficient labeling of important findings and comments in radiology reports using NLP techniques. The study examines how effective NER techniques in these reports are and how these techniques perform with different models. The hypothesis of the study is that by integrating BERT and LSTM models with NER techniques, critical information in radiology reports can be accurately and quickly labeled and the most effective method can be determined by comparing the performance of these models.

As a result of the literature review, the RadGraph dataset was studied (RadGraph Dataset, 2021). When the dataset was analyzed, it was seen that there was an unbalanced distribution between the number of tags ("ANAT-DP=5366", "OBS-DP=5046", "OBS-U=584", and "OBS-DA=1389"). To overcome this problem, the dataset was expanded. In the data preprocessing stage, the data were processed according to the needs of the selected dataset in order to present the data more consistently and to improve the performance of the model (M. Wang and Hu, 2021; Uskaner Hepsağ et al., 2023). After 2019, most of the NLP studies focus on deep learning architectures (Nag et al., 2024; C. Pereira et al., 2024). In this context, both RNN (Recurrent Neural Network) based LSTM model and Transformer architecture-based BERT model are considered in our study (Uskaner Hepsağ et al., 2023; Rani et al., 2024). Different training parameters were tested on the models and the most successful performing parameters were determined (Yan et al., 2022).

As a result, when this study was completed, significant progress was made in the automatic analysis of radiology reports and the extraction of important findings. By comparing BERT and LSTM models, it became possible to determine the most appropriate NLP methods for supporting the diagnosis and treatment processes of physicians.

2. MATERIALS AND METHODS

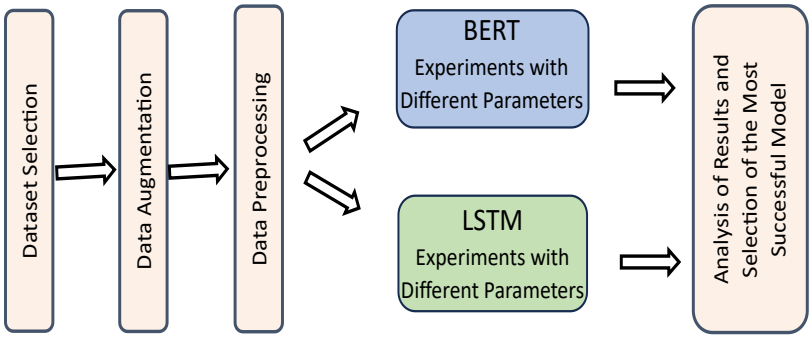

Figure 1. Workflow applied in the study

The study focuses on NER, which aims to speed up the evaluation of radiology reports by physicians and reduce errors in diagnoses. The steps planned in the study process were implemented as shown in the workflow diagram in Figure 1.

2.1 Dataset Selection

The study was conducted with the Radgraph (RadGraph Dataset, 2021) dataset, which includes the MIMIC-CXR and CheXpert datasets offered in the PhysioNET Database. In order to access the dataset, it was requested to complete the trainings prepared by the dataset providers and to achieve a 90% success rate in the exams. This process consisting of 2 sections and 16 modules was completed and the dataset was accessed. The RadGraph dataset was created by tagging chest radiology reports from the MIMIC-CXR and CheXpert datasets. The MIMIC-CXR dataset was created in collaboration with Massachusetts General Hospital and MIT Laboratory for Computational Physiology and de-identified personal health information (PHI) in accordance with HIPAA requirements. The CheXpert dataset was developed by Stanford University and was similarly de-identified in accordance with HIPAA requirements, and PHI was replaced with fake PHI using automated and manual methods. During the development of the RadGraph dataset, the MIMIC-CXR and CheXpert datasets were used to identify radiology reports entity names and relationships. In the tagging process, three radiologists tagged the reports according to the schema developed by Dr. Curt Langlotz on the Datasaur.ai platform. As a training set, 425 MIMIC-CXR reports were used, 75 reports were used for development and 50 MIMIC-CXR and 50 CheXpert reports were used for testing. The dataset used includes four entities—ANAT-DP (Anatomical Descriptor Present), OBS-DP (Observation Descriptor Present), OBS-DA (Observation Descriptor Absent), and OBS-U (Observation Descriptor Uncertain)—as well as three relationship types, aimed at structuring clinical information in radiology reports. Four entity labels were used in the study.

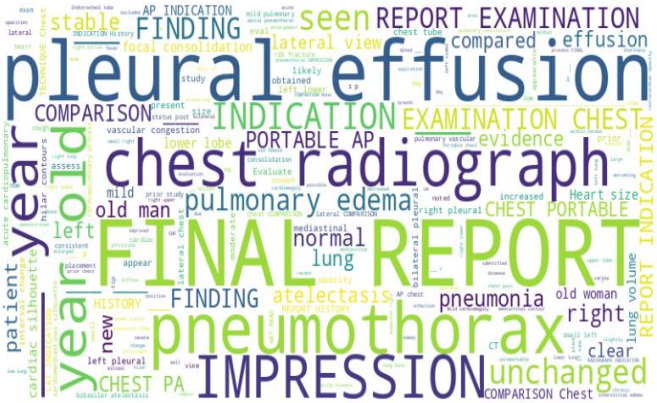

Figure 2. Commonly used words from the RadGraph dataset

2.2 Model Selection and Parameter Settings

The analysis of radiological reports has become the focus of deep learning methods today. The literature in this field reveals that RNN and Transformer deep learning architectures are increasingly used for processing radiology reports (Sun et al., 2023). These methods are of great importance for understanding the complexity of text data, extracting the information they contain, and effectively classifying reports. Deep learning techniques offer powerful tools for obtaining valuable insights from radiology reports (C. Pereira et al., 2024).

RNN is a deep learning model for processing sequential data. Especially when used in areas such as time series data and natural language processing, it takes into account the sequential structure of the data and associates the information from previous steps with the current steps. Because of this feature, it provides successful results in language processing problems (Zhang et al., 2018).

The "Transformer" architecture is a deep learning model based on the attention mechanism developed by Google in 2017 and presented in the paper "All You Need is Attention" (Vaswani et al., 2017). Traditionally used sequential processing structures such as RNN or Long Short-Term Memory (LSTM) are replaced by attention-based mechanisms in the Transformer architecture. Attention-based mechanisms are particularly notable for their "Multi-Head Attention" structure. This structure ensures that attention-oriented vectors are generated for each input token. The input tokens and vectors are combined to create an output. The importance of each token in the text relative to other tokens is determined and the contextual relations of the text are modeled more effectively (Brasoveanu & Andonie, 2020). The Transformer model has revolutionized the field of natural language processing and has achieved the best results in many tasks (Rahali and Akhloufi, 2023).

This study focuses on deep learning architectures such as the LSTM model based on RNN architecture and the BERT model based on "Transformer" architecture. The features of the models used in the study are given below.

2.2.1 LSTM (Long short-term memory)

LSTM is a special kind of RNN family and is designed to solve the problem of long-term dependency over time. It works using specialized memory units called cells. These cells can control information through input, output and forget gates. Thanks to these structures, LSTM can more effectively learn long-term dependencies and relationships in extensive texts (M. Tarwani and Edem, 2017). In this study, the performance of the LSTM model will be evaluated using an English-language dataset in the medical field. The model scheme presented in Figure 3 forms the basis of the study and the input representation is integrated into the architecture of the model (Uskaner Hepsağ et al., 2023).

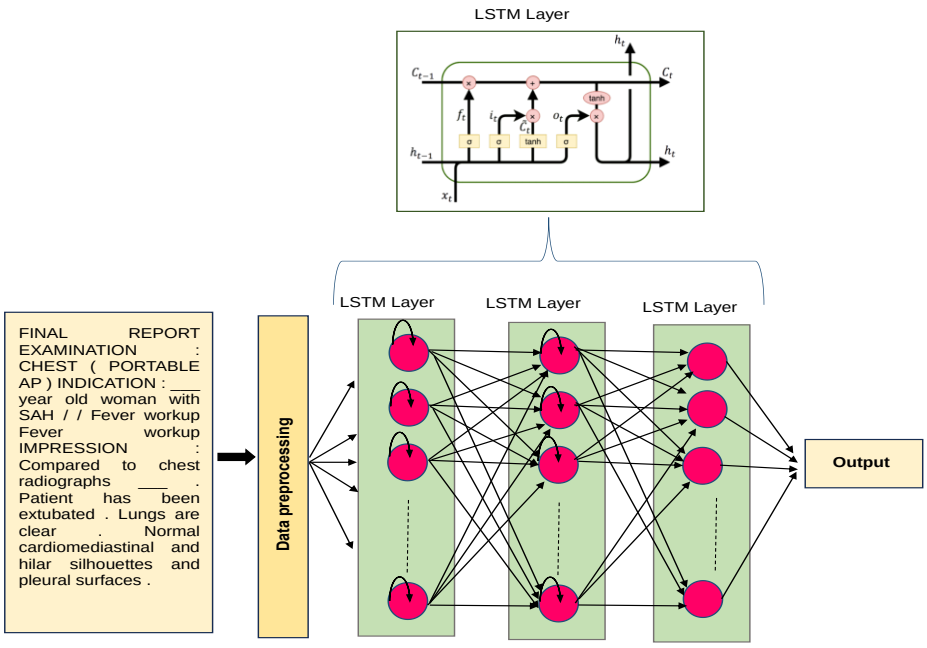

Figure 3. Schematic of the LSTM model used in the study

At the core of the LSTM architecture are the “Cell State” and various gates. “Cell State” is the channel through which information is carried in memory. The gates decide which information is important. The Forget Gate makes decisions about previous knowledge (ht) and current knowledge (xt). Sigmoid activation determines which information to forget. Input Gate updates the cell state. Sigmoid operation decides which information to update. Tanh activation organizes the data. The information to be updated is determined by multiplying the results. Output Gate determines the input of the next cell (ht+1). It is also used for prediction. The sigmoid operation helps to determine the input, while the tanh operation determines the state of the current information. Using these mechanisms, LSTM can effectively learn long-term dependencies and process complex language structure. Therefore, it is frequently used in the field of natural language processing, especially in tasks such as text prediction, translation, sentiment analysis, Entity Name Extraction (Rahman et al., 2021).

2.2.2 BERT (Bidirectional encoder representations from transformers)

BERT is a deep learning model based on the Transformer architecture developed by Google, which is an important milestone in the field of natural language processing (Vaswani et al., 2017). It is based on the masked language model. Some words in the text are subjected to random masking to improve the model's ability to understand the context. Its main architecture is a bidirectional transformer encoder. When processing a text by a given language model, allows to learn the context of each word with the influence of both preceding and following words. It provides a more powerful model that can use a wider context to determine the meaning of a word in a text. BERT is pre-trained on a large training dataset. In the training phase, a large amount of text data is used to improve the model's overall language understanding capability (Turchin et al., 2023). Figure 4 shows the schematic of the BERT model used in this study (Uskaner Hepsağ et al., 2023).

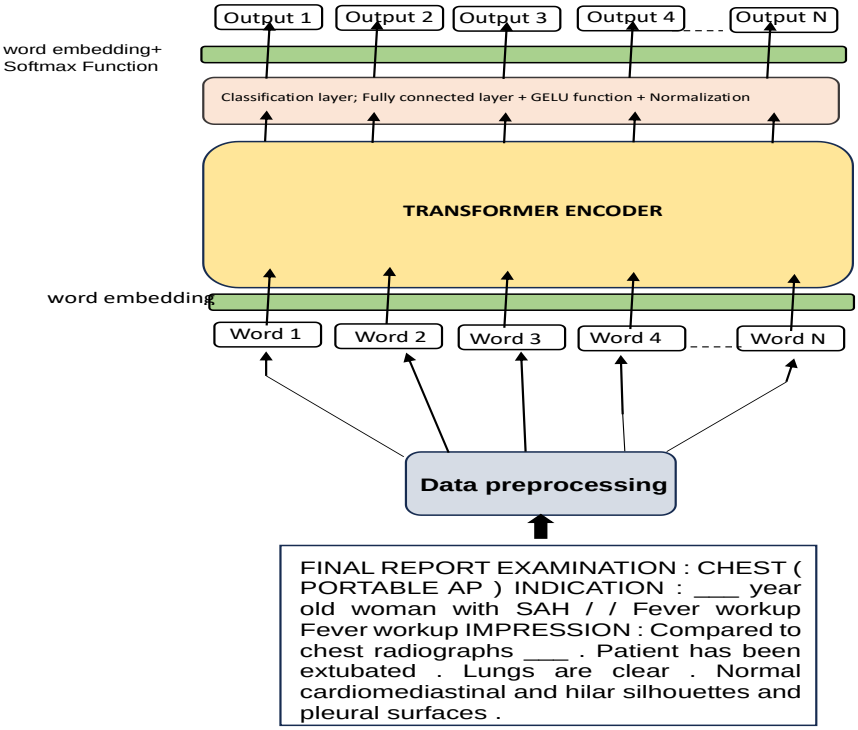

Figure 4. Schematic of the BERT model used in the study

In the diagram, the input layer receives the text of the radiological report and creates a basic structure to operate on this text. The word embedding process converts the words into numeric values to better capture the semantic relations of the text and enable the model to process the words in a more meaningful way. The encoder block processes the words in the text and extracts their features. The parallel attention mechanism determines the importance of each word and feature, allowing the model to give more weight to important words. In this way, the model can focus more on critical information in the text for more effective entity name extraction.

2.3 Data Augmentation

In this study, a BERT-based data augmentation technique was applied to increase the representation of classes with low tag counts (Abuzayed et al., 2021; Liu et al., 2022). To address the tag imbalances in the dataset, several steps were taken to reach the target number of tags for each class. First, the amount of boosting required to reach the targeted number was calculated by considering the current number of each tag. As presented in Table 1, sentences with a small number of tags in the raw dataset were extracted from the dataset and certain words in these sentences were masked. This was done by preserving the context of the sentence. The BERT model was used to predict the masked words. The BERT model performed possible word predictions based on the context of the masked word and the most likely word predictions were selected. These predicted words were used to replace the missing words in the masked sentences and new sentences were generated. Finally, the new sentences generated in this way and the corresponding tags were added to the dataset. As a result of this process, the number of tags in the augmented dataset presented in Table 1 was reached. Because of this approach, the number of labels with a small number of tags increased, allowing the model to learn them better.

The use of the BERT model played a critical role in gaining a deeper understanding of the language context and making accurate word predictions. This data augmentation method can be considered as an effective strategy to improve the performance of the model in class imbalanced datasets, especially in the field of natural language processing (NLP).

Table 1. Raw- Augmented dataset tag counts

Tag	Raw Data Set	Augmented Data Set
ANAT-DP	5366	5366
OBS-DP	5046	5046
OBS-DA	1389	6041
OBS-U	584	3904

2.3 Evaluation Metrics

The performances of the LSTM and BERT-based models used in this study are compared through the evaluation metrics presented in Table 2.

Table 2. Evaluation Metrics

Metric	Formula	Description
Accuracy	Accuracy=Correct Predictions/ Total Predictions	Represents the proportion of correctly identified entities out of the total extracted entities. This metric measures the overall success of the model.
Precision	Precision= True Positives / True Positives + False Positives	Indicates how many of the entities identified by the model are correct. High precision reflects the model's ability to make accurate predictions.

Table 2. Evaluation Metrics (continued)

Metric	Formula	Description
Recall	Recall= True Positives/ True Positives + False Negatives	Shows how well the model can identify actual entities present in the reports. High recall indicates that the model is capable of capturing most of the true entities.
F1 Score	F1 Score=2×Precision+Recall/ Precision × Recall	The harmonic means of precision and recall, the F1 score balances these two metrics, particularly in cases where the dataset has imbalanced labels. This metric assesses whether the model performs well in both precision and recall.

3. RESULTS AND DISCUSSION

3.1 Results

This study was performed on the Google Colab Pro+ platform using the A100 GPU. Various hyperparameter combinations were examined on LSTM and BERT models. The parameters that provide the highest performance were optimized. With these parameters, data augmentation methods were applied and model training and testing were performed on the enriched data set obtained at the end of this process. The experimental studies aimed to maximize the performance of the models and provide the highest accuracy rate on medical data.

3.1.1 Determination of the optimization algorithm

In the first stage, the performance of ADAM (Adaptive Moment Estimation) and SGD (Stochastic Gradient Descent) optimization algorithms were evaluated in detail using LSTM and BERT models on the RadGraph dataset. In the training process, early stopping technique was applied and training was performed for a total of 50 epochs. The impact of both algorithms is compared in terms of performance metrics such as model accuracy, loss and processing time. The test results and the success levels of the optimization algorithms are presented in Table 3.

Table 3. Performance results of different optimization algorithms in BERT and LSTM models

	BERT		**LSTM**	
	ADAM	SGD	ADAM	SGD
Accuracy (%)	89.25	90.10	78.21	79
Precision (%)	87.10	87.96	75.36	76.21
Recall (%)	88.40	88.75	76.45	77.14
F1 Score (%)	87.75	88.35	75.90	76.67

As a result of the analysis of the test results, no significant performance difference was found between the ADAM and SGD optimization algorithms. At the same time, the SGD algorithm resulted in longer training times. Therefore, in order to minimize the computational cost, the studies were continued with the ADAM optimization algorithm.

3.1.2 Determining the learning rate

Within the scope of the study, the learning rates presented in Table 4 were tested with the ADAM optimization algorithm. As a result of the experiments, the learning rate providing the highest performance was determined and presented in Table 5.

Table 4. Learning rates used in the study

Literature	Learning Rate
Houlsby et al., 2019	1×10^{-4}
Lamproudis et al.,2021	1×10^{-5}
Choi et al., 2020	2×10^{-5}

As a result of the examination of the test results, it was determined that the learning rate providing the highest success was 1×10^{-5} in the BERT model and 1×10^{-4} in the LSTM model. In line with these findings, the studies were continued on the learning rates that provided the highest success.

Table 5. Performance results of different learning rates in BERT and LSTM models.

	BERT			**LSTM**		
	2×10^{-5}	**1×10^{-5}**	**1×10^{-4}**	**2×10^{-5}**	**1×10^{-5}**	**1×10^{-4}**
Accuracy (%)	89.25	90.24	90.10	78.21	79.56	79.74
Precision (%)	87.10	89.34	88.80	75.36	78.12	78.99
Recall (%)	88.40	88.98	88.98	76.45	78.96	79.90
F1 Score (%)	87.75	89.16	88.89	75.90	78.54	79.44

3.1.3 Determining the learning rate

The effects of different input sizes (64, 128, 256) on the performance of the models were investigated. In the training process, the optimization algorithm, learning rate and epoch parameters determined in the previous steps were used. The results obtained are presented in Table 6 to evaluate the effects of input sizes on model performance.

Table 6. Effect of different input sizes on model performance in BERT and LSTM models

	BERT			**LSTM**		
	64	**128**	**256**	**64**	**128**	**256**
Accuracy (%)	85.69	90.24	90.84	76.52	79.74	80.11
Precision (%)	89.42	89.34	89.97	77.75	78.99	79.45
Recall (%)	85.63	88.98	90.26	76.69	79.90	79.68
F1 Score (%)	87.48	89.16	90.11	77.22	79.44	79.56

3.1.4 Model performance evaluation on augmented data set

As a result of the training performed with the RadGraph dataset using the parameter values specified in the previous work packages, the optimum hyperparameters were determined. In line with these optimum parameters, the model training was performed on the new data set created by the data augmentation process applied to the RadGraph data set. The training results are presented in Table 7.

Table 7 Performance results of LSTM and BERT models on the augmented dataset

	BERT	**LSTM**
Accuracy (%)	95.48	85.26
Precision (%)	94.23	83.57
Recall (%)	96.69	84.88
F1 Score (%)	95.44	84.22

According to the training results, as observed in the RadGraph dataset, the BERT model achieved a higher success rate compared to the LSTM model. While the F1 score of the BERT model was 95.44, the F1 score of the LSTM model was 84.22.

Figure 5(a) and (b) show the confusion matrices of the LSTM and BERT models, respectively. When the confusion matrices are analyzed, it is seen that the BERT model misclassifies medical entities such as ANAT-DP, OBS-DP, OBS-DA, and OBS-U much less than the LSTM model. It is observed that the BERT model recognizes common entities such as ANAT-DP and OBS-DP with high accuracy. On the other hand, the LSTM model has higher error rates, especially in the rarer OBS-DA and OBS-U classes. This is evident in the LSTM confusion matrix in Figure 5, where the false positive and false negative rates are more pronounced.

One of the main reasons why the BERT model is more successful is its transformer-based structure. BERT is better able to model long-distance dependencies between words in the text, and thanks to its bidirectional language model, it produces more accurate results by taking into account both the preceding and following context. Especially in datasets where contextual information is critical, such as medical reports, the high performance of the BERT model makes it more advantageous than the LSTM.

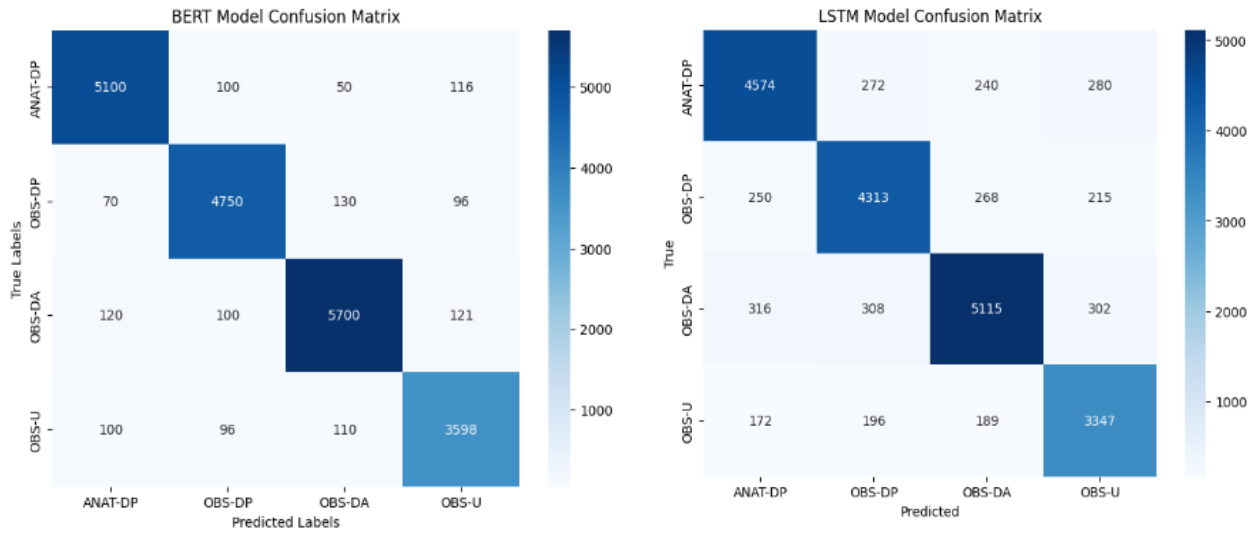

(a) (b)

Figure 5. (a) Confusion matrix of BERT model, (b) Confusion matrix of LSTM model

Figures 6(a) and (b) show the loss function plots of the LSTM and BERT models respectively during the training process. It is observed that the loss curve of the LSTM model is wavy and slow. This wavy structure indicates that the LSTM model experiences instability in the learning process and has difficulty in optimizing the parameters of the model. The sequential processing structure of the LSTM can cause gradient loss in long sentences and complex contextual relations. This slows down the learning process of the model, especially for long and complex texts such as the one used in this dataset, and causes it to face more noise. In contrast, the loss curve of the BERT model was smoother and faster. Due to the advantages of the attention mechanisms, the BERT model learned contextual information more effectively at each step and reduced errors faster. This steady reduction suggests that the model generalizes the dataset better and produces more optimized results at each

learning step. Moreover, this regular structure in BERT's training process enabled it to achieve higher performance in less time and significantly reduce training loss.

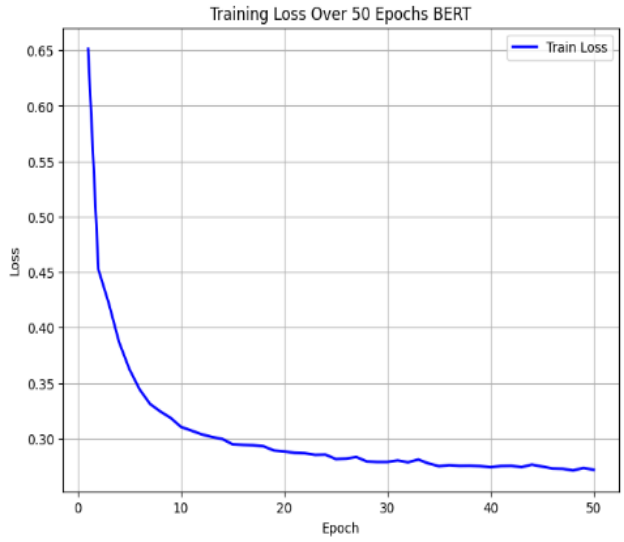

(a)

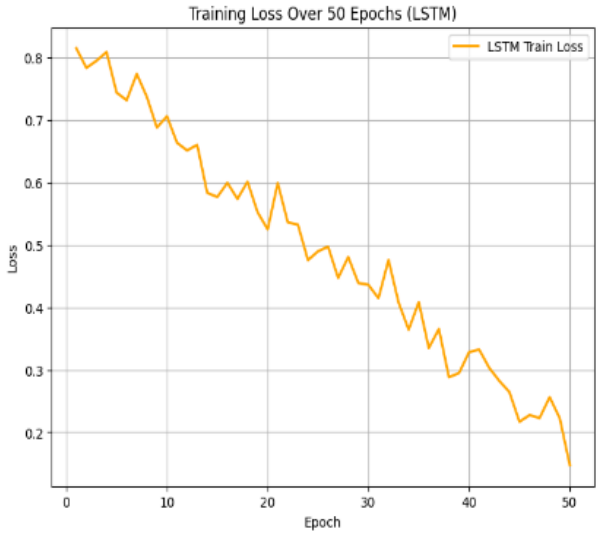

(b)

In this study, while comparing the performance of BERT and LSTM models on the augmented RadGraph dataset, the basic metrics of precision, recall, accuracy and F1 score are taken into account. The results show that the BERT model outperforms the LSTM model in all of these metrics. The higher precision of the BERT model indicates that the model increases the number of true positive classifications and decreases the number of false positive predictions. This is particularly evident for the ANAT-DP and OBS-DP tags. The fact that the BERT model classifies entities in medical reports more carefully and accurately provides a significant advantage in preventing misdiagnosis. In terms of recall, the BERT model was also more successful than the LSTM. The BERT model successfully identified a large proportion of positive examples that should be labeled correctly. Especially in medical texts, the recall rate is critical to prevent false negatives. Since false negatives can have serious consequences, for example if a disease is missed, this superiority in recall rate shows that the BERT model offers a significant advantage for medical data analysis.

Finally, the F1 score measures the overall performance of the model by balancing both metrics, precision and recall. The BERT model has a high F1 score of 95.44%, indicating that the overall performance of the model is consistent and reliable. These results show that the BERT model is more effective than the LSTM in the task of named entity recognition in medical texts and provides more accurate results with fewer errors.

3.2 Discussion

The studies conducted in literature were examined and compared with the developed model as shown in Table 8.

Table 8. Comparison of this study with other studies in the literature

Study	Dataset	Dataset Privacy	Method	Results (F1 score)
Thurkal et al. (2023)	Chest X-Ray	Private	BERT	78.97
Jain et al. (2021)	RadGraph	Public	PubMed BERT	0.86

Table 8. Comparison of this study with other studies in the literatüre (continued)

Study	Dataset	Dataset Privacy	Method	Results (F1 score)
López-Úbeda et al. (2020)	Chest CT	Private	LSTM	75.77
Yuan et al. (2019)	Chest X-Ray	Public	CNN and LSTM	CNN 0.90 LSTM 0.90
Banerjee et al. (2019)	Chest CT	Private	RNN	0.77
Cornegruta et al. (2016)	Chest X-Ray	Private	BiLSTM	0.90
Proposed Method	Augmented RadGraph	Public	LSTM and BERT	LSTM 0.84 BERT 0.95

When the table presented above is examined, it is seen that Thurkal et al. on a special dataset of chest X-ray radiology reports, an F1 score of 78.97 was reported using the BERT model (Thurkal et al., 2023). In another study with the RadGraph dataset, Jain et al. utilized the PubMed BERT model and obtained an F1 score of 0.86 (Jain et al., 2021). López-Úbeda et al. analyzed chest CT radiology reports with the LSTM model and achieved an F1 score of 75.77 (López-Úbeda et al., 2020). In the study by Yuan et al. in 2019, both CNN and LSTM models were tested on Chest X-Ray reports and an F1 score of 0.90 was recorded in both models (Yuan et al., 2019). Banerjee et al. reported an F1 score of 0.77 in their study with the RNN model on Chest CT reports (Banerjee et al., 2019). In 2019, Cornegruta et al. obtained a successful result with an F1 score of 0.90 using BiLSTM model on private Chest X-Ray radiology reports (Cornegruta et al., 2016).

In this study, unlike other studies in the literature, a comprehensive parameter optimization is performed on both BERT and LSTM models. These parameters are applied to the publicly available RadGraph dataset. The unbalanced label distribution in the RadGraph dataset was balanced with data augmentation techniques to improve the performance of the model. A comparison was made between the BERT and LSTM models using this newly created balanced dataset, and the results showed that the BERT model not only outperformed the LSTM model with a 95% success rate, but also outperformed other studies in the literature (Tokgoz et al.,2021; Yang et al.,2019).

4. CONCLUSIONS

In this study, BERT and LSTM models are studied using the publicly available RadGraph dataset of chest radiology reports. In the first stage, different optimization algorithms were tested for both models and it was determined that the ADAM algorithm gave the best results for both models. Then, various experiments were performed on the learning rate parameter and optimization was performed to determine the optimal value. In addition, as a result of the comparisons made on the maximum length parameter, a value of 256 was selected as the most appropriate parameter. After determining the parameters, improvements were made to the dataset in order to minimize the label imbalance in the dataset. The data augmentation process enabled the model to learn rare classes better and thus increased the overall performance rate. At this stage, labels with a small number of instances were increased to homogenize the overall distribution in the dataset. The regularized dataset was tested in BERT and LSTM models in line with the specified parameters. The comparison results showed that the BERT model performed better than the LSTM model, with an F1 score of 95% for the BERT model and 84% for the LSTM model. In the future, this study is planned to be optimized with different parameters to further improve the F1 score. In addition, the results obtained have the

potential to be integrated with Hospital Information Management Systems (HIMS) to provide support to specialist physicians.

5. ACKNOWLEDGEMENTS

This study was supported by the Scientific and Technological Research Council of Türkiye (TÜBİTAK) within the scope of the 2210-C National Graduate Scholarship Program.

6. CONFLICT OF INTEREST

Authors approve that to the best of their knowledge, there is not any conflict of interest or common interest with an institution/organization or a person that may affect the review process of the paper.

7. AUTHOR CONTRIBUTION

Uçman ERGÜN contributed to the Determining the concept and/or design process of the research. Sezin BARIN and Uçman ERGÜN contributed to the Management of the concept and/or design process of the research. Sedanur ORCİN contributed to the Data Collection. Sedanur ORCİN and Sezin BARIN contributed to the Data analysis and interpretation of the results. Uçman ERGÜN and Sedanur ORCİN contributed to the Preparation of the manuscript. Sezin BARIN contributed to the Critical analysis of the intellectual content. Uçman ERGÜN, Sedanur ORCİN, and Sezin BARIN contributed to the Final approval and full responsibility.

8. REFERENCES

Abuzayed A., Al-Khalifa H., Sarcasm and sentiment detection in Arabic tweets using BERT-based models and data augmentation. In Proceedings of the sixth Arabic natural language processing workshop 312-317, 2021.

Banerjee I., Ling Y., Chen M. C., Hasan S. A., Langlotz C. P., Moradzadeh N., Chapman B., Amrhein T., Mong D., Rubin D. L., Farri O., Lungren M. P., Comparative effectiveness of convolutional neural network (CNN) and recurrent neural network (RNN) architectures for radiology text report classification. Artificial Intelligence in Medicine 97, 79–88, 2019. https://doi.org/10.1016/j.artmed.2018.11.004

Brasoveanu A. M. P., Andonie R., Visualizing Transformers for NLP: A Brief Survey, 24th International Conference Information Visualisation (IV), Melbourne/Australia, September 07-11, 2020, pp: 270–279. https://doi.org/10.1109/IV51561.2020.00051

Choi H., Kim J., Joe S., Gwon Y., Evaluation of bert and albert sentence embedding performance on downstream nlp tasks, In 2020 25th International conference on pattern recognition (ICPR), Milan/Italy, January 10-15, 2021, pp: 5482-5487. 10.1109/ICPR48806.2021.9412102

Cornegruta S., Bakewell R., Withey S., Montana G., Modelling radiological language with bidirectional long short-term memory networks. arXiv preprint arXiv:1609.08409, 2016.

Houlsby N., Giurgiu A., Jastrzebski S., Morrone B., De Laroussilhe Q., Gesmundo A., Gelly S., Parameter-efficient transfer learning for NLP. 36th International Conference on Machine Learning, Long Beach/California, 2019, pp: 2790-2799. https://doi.org/10.1007/978-3-030-77211-6_12

Jain S., Agrawal A., Saporta A., Truon S. Q., Duong D. N., Bui T., Rajpurkar P., Radgraph: Extracting clinical entities and relations from radiology reports. arXiv preprint arXiv:2106.14463, 2021.

Lamproudis A., Henriksson A., Dalianis H., Developing a clinical language model for Swedish: continued pretraining of generic BERT with in-domain data, In International Conference Recent Advances in Natural Language Processing (RANLP'21), Shoumen, September 1-3, 2021, pp: 790-797, 2021.

Liu J., Chen Y., Xu J., Low-Resource NER by Data Augmentation with Prompting, Thirty-First International Joint Conference on Artificial Intelligence, July 23-29, 2022, pp: 4252-4258.

López-Úbeda P., Díaz-Galiano M. C., Martín-Noguerol T., Luna A., Ureña-López L. A., Martín-Valdivia M. T., COVID-19 detection in radiological text reports integrating entity recognition. Computers in Biology and Medicine 127, 104066, 2020. https://doi.org/10.1016/j.compbiomed.2020.104066

López-Úbeda P., Martín-Noguerol T., Luna A., Automatic classification and prioritisation of actionable BI-RADS categories using natural language processing models. Clinical Radiology 79(1), e1-e7, 2024. https://doi.org/10.1016/j.crad.2023.09.009

Nag P. K., Bhagat A., Priya R. V., Khare D. kumar. Emotional Intelligence Through Artificial Intelligence: NLP and Deep Learning in the Analysis of Healthcare Texts, arXiv preprint arXiv: 2403.09762, 2024. http://arxiv.org/abs/2403.09762

Nishio M., Matsunaga T., Matsuo H., Nogami M., Kurata Y., Fujimoto K., Sugiyama O., Akashi T., Aoki S., Murakami T., Fully automatic summarization of radiology reports using natural language processing with large language models. Informatics in Medicine Unlocked 46, 101465, 2024. https://doi.org/10.1016/j.imu.2024.101465

Pereira S. C., Mendonça A. M., Campilho A., Sousa P., Lopes C. T., Automated image label extraction from radiology reports—A review. Artificial Intelligence in Medicine 149, 102814, 2024. https://doi.org/10.1016/j.artmed.2024.102814

RadGraph Dataset. Last Access Date: 13 Haziran 2024 from https://physionet.org/content/radgraph/1.0.0/

Rahali A., Akhloufi M. A., End-to-End Transformer-Based Models in Textual-Based NLP. AI, 4(1), 54–110, 2023. https://doi.org/10.3390/ai4010004

Rahman M. H., Islam M. S., Jowel M. M. U., Hasan M. M., Latif S., Classification of Book Review Sentiment in Bangla Language Using NLP, Machine Learning and LSTM, 12th International Conference on Computing Communication and Networking Technologies (ICCCNT), Kharagpur/India, July 06-08, 2021, IEEE- 51525. https://doi.org/10.1109/ICCCNT51525.2021.9580116

Rani S., Jain A., Kumar A., Yang G., CCheXR-Attention: Clinical concept extraction and chest x-ray reports classification using modified Mogrifier and bidirectional LSTM with multihead attention. International Journal of Imaging Systems and Technology, 34(1), 1-15, 2024. https://doi.org/10.1002/ima.23025

Sun Z., Lin M., Zhu Q., Xie Q., Wang F., Lu Z., Peng Y., A scoping review on multimodal deeplearning in biomedical images and texts. Journal of Biomedical Informatics 146, 104482, 2023. https://doi.org/10.1016/j.jbi.2023.104482

Tarwani K. M., Edem S., Survey on Recurrent Neural Network in Natural Language Processing. International Journal of Engineering Trends and Technology 48(6), 301-304, 2017. https://doi.org/10.14445/22315381/IJETT-V48P253

Thukral A., Dhiman S., Meher R., Bedi P., Knowledge graph enrichment from clinical narratives using NLP, NER, and biomedical ontologies for healthcare applications. International Journal of Information Technology, 15(1), 53-65, 2023.

Tokgoz M., Turhan F., Bolucu N., Can B., Tuning language representation models for classification of Turkish news, 2021 International symposium on electrical, electronics and information engineering, 2021, pp: 402-407.

Turchin A., Masharsky S., Zitnik M., Comparison of BERT implementations for natural language processing of narrative medical documents. Informatics in Medicine Unlocked 36, 101139, 2023. https://doi.org/10.1016/j.imu.2022.101139

Uskaner Hepsağ P., Özel S. A., Dalcı K., Yazıcı A., Using BERT models for breast cancer diagnosis from Turkish radiology reports. Language Resources and Evaluation, 58, 981-1012 2024. https://doi.org/10.1007/s10579-023-09669-w

Vaswani A., Shazeer N., Parmar N., Uszkoreit J., Jones L., Gomez A. N., Kaiser L., Polosukhin I. Attention Is All You Need, arXiv preprint arXiv: 1706.03762, 2017. http://arxiv.org/abs/1706.03762

Wang M., Hu F., The application of nltk library for python natural language processing in corpus research. Theory and Practice in Language Studies 11(9), 1041-1049, 2021. https://doi.org/10.17507/tpls.1109.09

Yamashita R., Bird K., Cheung P. Y. C., Decker J. H., Flory M. N., Goff D., Morimoto L. N., Shon A., Wentland A. L., Rubin D. L., Desser T. S., Automated Identification and Measurement Extraction of Pancreatic Cystic Lesions from Free-Text Radiology Reports Using Natural Language Processing. Radiology: Artificial Intelligence 4(2), e210092, 2022.

Yan A., McAuley J., Lu X., Du J., Chang E. Y., Gentili A., Hsu C. N., RadBERT: Adapting Transformer-based Language Models to Radiology. Radiology: Artificial Intelligence 4(4), e210258, 2022. https://doi.org/10.1148/ryai.210258

Yang Z., Dai Z., Yang Y., Carbonell J., Salakhutdinov R. R., Le Q. V., Xlnet: Generalized autoregressive pretraining for language understanding. Advances in Neural Information Processing Systems, 32, 10, 2019.

Yuan J., Liao H., Luo R., Luo J., Automatic Radiology Report Generation Based on Multi-view Image Fusion and Medical Concept Enrichment. Lecture Notes in Computer Science (Including Subseries Lecture Notes in Artificial Intelligence and Lecture Notes in Bioinformatics), 11769 LNCS, 721-729, 2019. https://doi.org/10.1007/978-3-030-32226-7_80

Zhang X., Chen M. H., Qin Y., NLP-QA Framework Based on LSTM-RNN, 2nd International Conference on Data Science and Business Analytics (ICDSBA), Changsha/China, September 21-23, 2018, 307-311, 2018. https://doi.org/10.1109/ICDSBA.2018.00065

JOURNAL of
MATERIALS and MECHATRONICS:A

e-ISSN 2717-8811
JournalMM, 2025, 6(1), 15-31
https://doi.org/10.55546/jmm.1606483

Araştırma Makalesi / Research Article

Makine Öğrenmesi ile 6082 Alüminyum Alaşımının Yorulma Ömrü Tahmini

Resul ÜNAL[1*], Recai KUŞ[2], Mustafa ACARER[3]

[1*] Kilis 7 Aralık Üniversitesi, Makine ve Metal Teknolojileri Bölümü, Kilis, Türkiye,
ORCID ID: https://orcid.org/0000-0002-7597-9490, resulunal@kilis.edu.tr
[2] Selçuk Üniversitesi, Teknoloji Fakültesi, Makine Mühendisliği Bölümü, Konya, Türkiye,
ORCID ID: https://orcid.org/0000-0002-7705-7924, recaikus@gmail.com
[3] Selçuk Üniversitesi, Teknoloji Fakültesi, Metalurji ve Malzeme Mühendisliği Bölümü, Konya, Türkiye,
ORCID ID: https://orcid.org/0000-0003-2876-4881, macarer@selcuk.edu.tr

Geliş/ Received: 24.12.2024**;** **Revize/Revised:** 02.01.2025 **Kabul / Accepted:** 13.01.2025

ÖZET: Alüminyum alaşımlar endüstride oldukça sık tercih edilen malzemelerdendir. Alüminyumun en önemli özelliklerinden biri yoğunluklarının düşük olmasıdır. Bu sayede otomotiv sektörü de dahil olmak üzere birçok sektörde önemli bir mühendislik malzemesi olarak yerini almıştır. Otomotiv sektöründe kullanılan alüminyum alaşımlardan bir tanesi de 6082 serisi alüminyum alaşımıdır. Tekrarlı yüklere maruz kalan makine parçalarında zamanla mikro çatlaklar oluşarak birikir ve bu çatlaklar ani kırılmalara sebep olur. Malzemelerde yorulma olarak bilinen bu olgunun anlaşılması ve yorulma deneylerinin yapılarak kırılma çevrim sayılarının belirlenmesi büyük önem taşır. Bu çalışmada 6082 alüminyum alaşımının yorulma testleri sırasında DCPD (Direct Current Potential Drop) tekniğiyle numune üzerinden akım ve gerilim değerleri toplanırken, uygulanan kuvvet ve meydana gelen deplasman verileri de eş zamanlı olarak kaydedilmiştir. Daha sonra bu veriler karar ağacı, ekstra ağaçlar, rastgele orman, XGBoost (Aşırı Gradyan Arttırma) ve KNN (K-En Yakın Komşu) olmak üzere 5 farklı makine öğrenmesi algoritmasına girdi olarak verilmiş ve çevrim sayıları tahmin edilmiştir. Test edilen modeller arasında R-kare (R^2) ve ortalama mutlak yüzde hata (MAPE) değerleri baz alındığında en iyi performansı karar ağacı ve ekstra ağaçlar makine öğrenmesi modelleri göstermiştir.

Anahtar Kelimeler: Yorulma, DCPD, 6082 Alüminyum alaşımı, Makine öğrenmesi, Tahmin

*Sorumlu yazar / Corresponding author: resulunal@kilis.edu.tr
Bu makaleye atıf yapmak için /To cite this article

Ünal, R., Kuş, R., Acarer, M. (2025). Makine Öğrenmesi ile 6082 Alüminyum Alaşımının Yorulma Ömrü Tahmini. Journal of Materials and Mechatronics: A (JournalMM), 6(1), 15-31.

Fatigue Life Prediction of 6082 Aluminum Alloy with Machine Learning

ABSTRACT: Aluminum alloys are one of the most preferred materials in industry. One of the most important properties of aluminum is its low density. In this way, it has taken its place as an important engineering material in many sectors, including the automotive sector. One of the aluminum alloys used in the automotive industry is the 6082 series aluminum alloy. Machine parts subjected to repetitive loads develop and accumulate micro cracks over time and these cracks cause sudden breakage. It is of great importance to understand this phenomenon known as fatigue in materials and to determine the number of fracture cycles by performing fatigue tests. In this study, during the fatigue tests of 6082 aluminum alloy, current and voltage values were collected from the specimen using DCPD (Direct Current Potential Drop) technique, while the applied force and displacement data were recorded simultaneously. These data were then given as input to 5 different machine learning algorithms: decision tree, extra trees, random forest, XGBoost (eXtreme Gradient Boosting) and KNN (K-Nearest Neighbor) and the number of cycles were estimated. Among the tested models, the decision tree and extra trees machine learning model performed the best based on R-square (R^2) and mean absolute percentage error (MAPE) values.

Keywords: Fatigue, DCPD, 6082 Aluminum alloy, Machine learning, Prediction

1. GİRİŞ

Alüminyum alaşımlar gelişmiş mekanik özelliklerinden dolayı çeşitli sektörlerde yaygın kullanıma sahiptirler (Sagar ve ark., 2023). Örneğin, havacılık sektöründe alüminyum alaşımlar büyük ölçüde kullanılırlar (Malek ve ark., 2020). Bununla birlikte Avrupa'daki otomobillerde kullanılan alüminyum içeriğinin 2022'de 205 kg iken, 2026'da 237 kg'a (+%15.6) ve 2030'da araç başına 256 kg'a (+%24.9) çıkacağı öngörülmektedir (European Aluminium, 2023).

Al-Si-Mg-Mn alaşımları, 200 MPa'nın üzerinde yüksek bir akma dayanımına sahiptir (Cai ve ark., 2020). 6xxx serisi alaşımlar, sahip oldukları ekstrüde edilebilirlik özelliği ile metal tasarım şekillerinin, karmaşık mimari formların ve tek şekillerin üretilmesine olanak tanırlar. 6082 Al alaşımının ana uygulamaları açısından otomotiv sektörü benzersiz bir sektördür (Kumar ve ark., 2024). Alüminyumun tasarım ve boyutlandırma süreçleri çelik için kullanılanlara benzer olsa da önemli fiziksel farklılıklar vardır (Gitter, 2006). Alüminyum gibi bazı metallerin tek eksenli gerilim altında sınırlı uzamalara sahip olduğu ve kırılmadan önce düşük uzama nedeniyle çekme testlerinin doğruluğunu olumsuz etkilediği bildirilmiştir (Olguner ve Bozdana, 2020).

Metallerin yorulma kırılması endüstride sık karşılaşılır ve bu sebeple, tasarım yorulma ömrü ilgi çeken bir araştırma konusu olmuştur (He ve ark., 2021). Genelde, alüminyum malzemelerin yorulma ömürleri, güvenilirliğini değerlendirmek için farklı üretim ortamlarında ölçülür (Lian ve ark., 2022). Çeliklerde gözlemlenen çatlak büyüme hızı ile çatlak uzunluğu arasındaki doğrusallığın, alüminyum 6082-T6 alaşımında da geçerli olduğu doğrulanmıştır (Jíša ve ark., 2010). Bu alaşımının yorulma ömrü tahmini için literatürdeki bir çalışmada önerilen yaklaşımın, değişken genlikli yüklemelerde, yorulma ömrü tahminine uygulanabilir olduğu ifade edilmiştir (Guo ve ark., 2022). 6082 alaşımının farklı varyantlarıyla yapılan bir çalışmada saflık arttıkça yorulma özelliklerinin iyileştiği de bildirilmiştir (Sarkar ve ark., 2024).

Maliyetleri azaltma çabası tasarım sürecine de uygulanmalı ve güvenilir malzeme verileri elde etmek, pahalı deneysel çalışmalar gerektirmemelidir (Karolczuk ve ark., 2022). Ayrıca, bazı fiziksel

temeller kullanılmasına rağmen seçilen gerilme/gerinim büyüklükleri ve malzeme parametreleri, deneysel sonuçlara en iyi uyumu elde etmek için keyfi şekilde formüle edilmiş parametrik fonksiyonlarla ilişkilendirilir (Karolczuk ve ark., 2022). Bu sebeplerle farklı yapay zekâ modellerinin, örneğin sinir ağı modellerinin, çekme dayanımının modellenmesi gibi (Yılmaz ve ark., 2016), malzemelerin mekanik özelliklerinin tahmin edilmesinde kullanmak oldukça elverişlidir. Sinir ağı modelleri, yorulma ile ilgili yapılan çalışmalarda da önemli bir etki oluşturmuş ve bu etkinin yapay zekâ alanındaki son gelişmelerle birlikte hızla artması beklenmektedir (Chen ve Liu, 2022). Alüminyum alaşımlarda korozyona bağlı yorulma çatlak büyüme oranının artırımlı öğrenme stratejine dayalı tahmini (Peng ve ark., 2024), yapay sinir ağı modelinin lamine kompozitlerin yorulma ömrünün tahmini (Mirzaei ve ark., 2024), yapay sinir ağları ve destek vektör regresyon modelleri uygulanarak yorulma ömrü tahmini (Li ve ark., 2024) gibi literatürde yorulma ömrünün tahminiyle ilgili birçok çalışma mevcuttur. Karmaşık bir doğaya sahip olan yorulma olgusunun tahmini için makine öğrenmesi modellerinin iyi performans göstermesi beklendiğinden, bu çalışmada yorulma deneylerinden elde edilen verilerle yapılacak tahminlerde makine öğrenmesi modelleri kullanıldı.

Literatürdeki bazı çalışmalarda da (Silva ve Pinho, 2002; Doré ve Maddox, 2013; Arunachalam ve Fawaz, 2016; Funk ve Bär, 2019;) olduğu gibi, çatlak yayılımı ve büyümesini ölçmek için kullanılan yöntemlerden biri de DCPD yöntemidir. DCPD yöntemi bir numunenin tüm kesitinden geçen homojen bir doğru akımın, numunedeki çatlakların neden olduğu potansiyel düşüşün meydana gelmesini temel alarak çalışır (Černý, 2004). DCPD yönteminde, yorulma çatlağının bulunduğu numuneden sabit bir elektrik akımı geçirilir ve elektrik potansiyel düşüşü ölçülür (Vecchiato ve ark., 2021). İki potansiyel arasındaki fark ve oran, çatlak ilerleme davranışındaki farklılıkları tanımlamak için yararlı parametrelerdir (Funk ve Bär, 2019). Yapılan bir çalışmada araştırmacılar, 6082-T6 alüminyum alaşımından üretilen tek kenarlı çentik gerilimi (SENT) numunesi ile yorulma deneylerinde özel bir DCPD yöntemi kullanmışlar ve bu tekniğin çok kısa çatlaklara sahip alüminyum alaşımlarına uygulanabilir olduğunu kanıtlamışlardır (Mann ve ark., 2007).

Literatürde T6 ısıl işlemi görmüş 6082 alüminyum alaşımı için DCPD yöntemiyle toplanan verilerin yanında, aksiyal deplasman ve aksiyal kuvvet verilerinin de kullanıldığı ve bu veriler kullanılarak geliştirilen makine öğrenmesi modelleri ile çevrim sayılarının tahmin edildiği bir çalışmaya rastlamadık. Bu çalışmada, T6 ısıl işlemi görmüş 6082 alüminyum alaşımı için, DCPD yöntemi ile topladığımız verilerle birlikte eş zamanlı toplanan kuvvet ve deplasman verileri, veri ön işleme yapılarak birleştirilip, makine öğrenmesi algoritmalarına girdi olarak verildi. Geliştirilen 5 farklı makine öğrenmesi modeliyle numunelerin çevrim sayıları tahmin edildi. Bu modellerin 6082 serisi alüminyum alaşımlarının yorulma testlerindeki çevrim sayılarını tahmin etme performansı gösterildi.

2. MATERYAL VE YÖNTEM

Yaptığımız yorulma deneylerinde, kimyasal bileşim sınırları Çizelge 1.'de verilen 6082 serisi alüminyum alaşımı kullanıldı.

Çizelge 1. 6082 Alüminyum alaşımını kimyasal bileşimi (Ağırlıkça %) (ASTM, 2021).

								Diğer Elementler		
Si	**Fe**	**Cu**	**Mn**	**Mg**	**Cr**	**Zn**	**Ti**	**Herbiri**	**Toplam**	**Alüminyum**
0.7-1.3	0.5	0.1	0.40-1	0.6-1.2	0.25	0.2	0.1	0.05	0.15	Kalan

Deney numuneleri ASTM E466 standardına göre hazırlandı. Hazırlanan numune şekli ve ölçüleri Şekil 1.'de verilmiştir. Numunenin en ince kesiti 6 mm'dir.

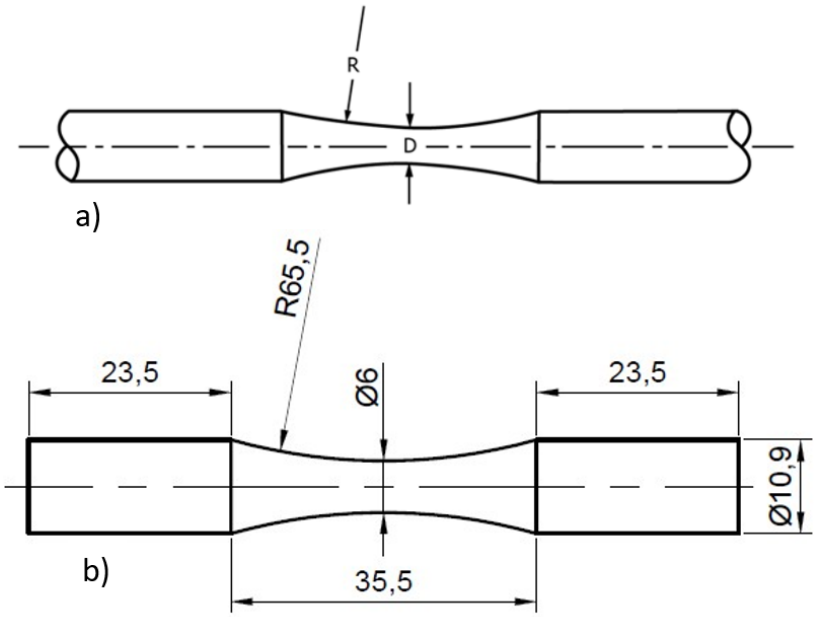

Şekil 1. a) Test numunesi şekli (ASTM, 2002) b) Üretilen test numunesi ölçüleri

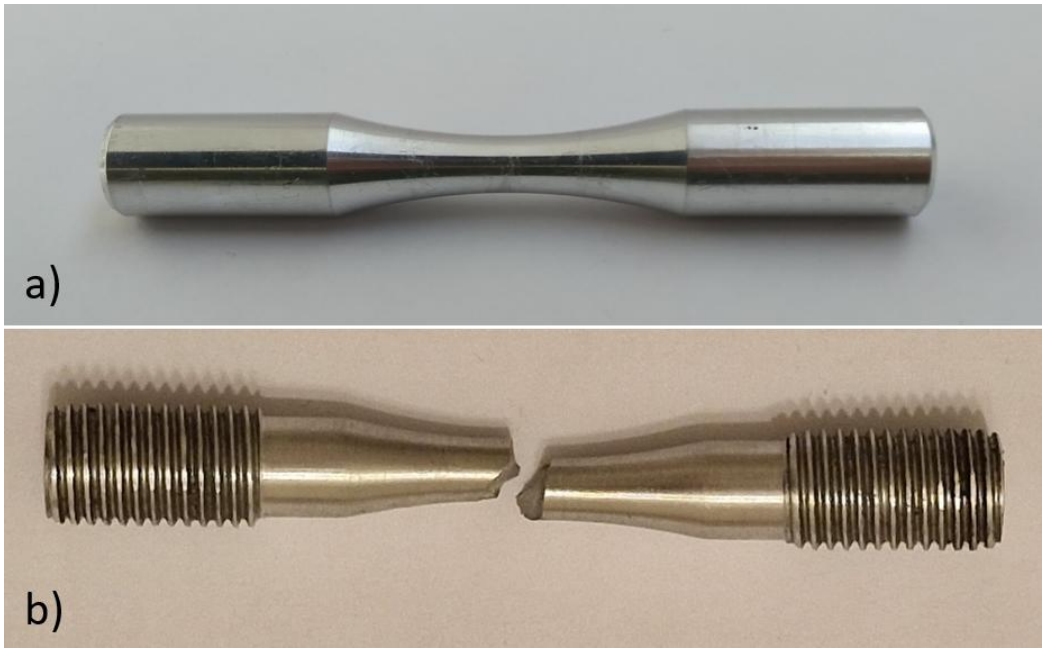

Şekil 2. a) Üretilen test numunesi b) Deney sonrası kırılmış test numunesi

Şekil 2a.'da üretilen test numunesi ve Şekil 2b'de yapılan deneyler sonucunda kırılan numune görülmektedir.

DCPD yöntemiyle akım ve gerilim değerlerinin ölçülebilmesi için, test problarının numune üzerinde durmasını kolaylaştıracak bir aparat tasarımı yapıldı. Tasarlanan aparatta numuneye uygun şekilde yerleştirilebilen 4 adet prob bulunmaktadır. Aparat tasarımında, literatürde bulunan bir çalışmada (Vecchiato ve ark., 2021) kullanılan aparattan esinlenildi. İletkenliğin yüksek olması için bakır çubuklar kullanılarak aparata yerleştirildi. Elektriksel ölçümler için Şekil 4.'de görülen Keithley 2634B cihazı kullanıldı.

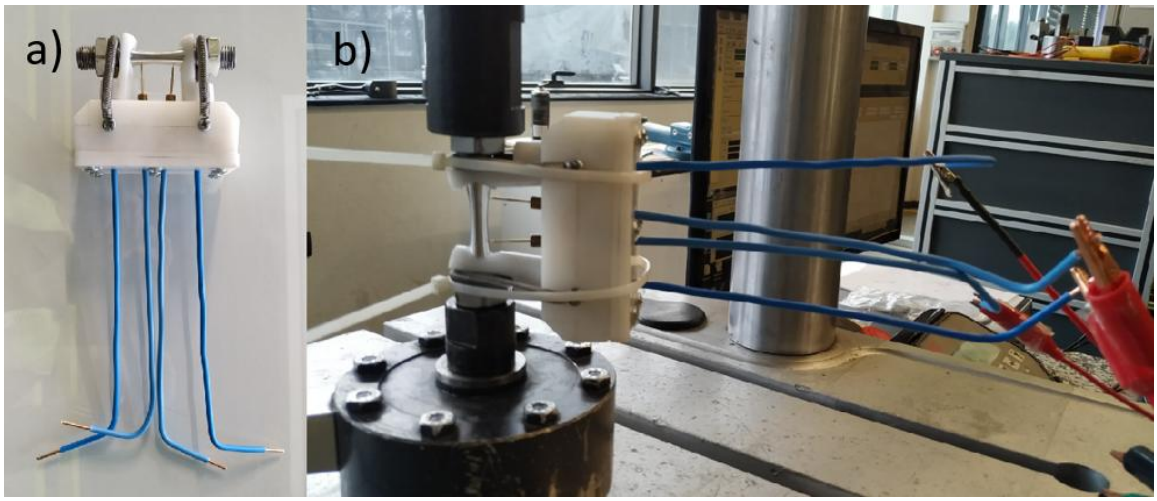

Şekil 3. a) Tasarlanan aparat b) Deney düzeneğine montajı yapılan aparat

Şekil 3a'da numuneye bağlı aparat, Şekil 3b'de ise yorulma deney cihazına bağlı numune görülmektedir. Yorulma deneyleri MTS Landmark masaüstü yorulma test cihazı kullanılarak yapıldı. Bu test cihazı maksimum 100 Hz ve 15 kN yükte çalışabilir. Bazı deneysel çalışmalarda 6082 serisi alüminyum alaşımın akma dayanımı yaklaşık olarak 300 MPa bulunmuştur. (Birol ve ark., 2016).

Şekil 4. Keithley 2634B Sourcemeter cihazı.

Deneyler sabit kuvvet uygulanarak gerilme aralığı R=-1 yükleme durumunda yapıldı. Uygulanan kuvvet ve gerilim değerleri Çizelge 2'de verilmiştir.

Çizelge 2. Numunelere uygulanan kuvvet, gerilim ve yorulma kırılmasının gerçekleştiği çevrim değerleri

Numune	Kuvvet (N)	Gerilim (MPa)	Çevrim
Numune 1	5500	195	38035
Numune 2	6000	212	45828
Numune 3	6500	230	9547

Çizelge 2 incelenecek olursa Numune 2'ye uygulanan kuvvet Numune 1'e uygulanan kuvvetten fazla olmasına karşı yorulma kırılmasının gerçekleştiği çevrim sayısının daha fazla olduğu görülmektedir. Bu iki değer birbirine oldukça yakındır. Numune 1'in kırılma çevrim sayısı yaklaşık

olarak $4x10^4$ iken, Numune 2'nin kırılma çevrim sayısı $4.5x10^4$ çevrimdir. Numune 3 ise yaklaşık 10^4 çevrimde kırılmıştır. Çizelge 3 incelenirse, numunelere uygulanan gerilim değerlerinin hepsi akma dayanımına yakındır.

Çizelge 3. 6082-T6 Alüminyum alaşımının mekanik özellikleri (ASTM, 2021)

Malzeme	Minimum Çekme Dayanımı (Mpa)	Minimum Akma Dayanımı (Mpa)	Uzama (%)
6082-T6	310	260	6 - 8

Paris-Erdoğan modelinden (Paris ve Erdogan, 1963) de bilindiği üzere, çatlak gelişimi çevrim başına çatlak büyümesi üzerinden düşünülecek olursa, minimum ve maksimum gerilim yığılma faktörleri arasındaki farkla ilişkilendirildiğinde, yorulma kırılmasının 3 temel aşamadan gerçekleştiği söylenebilir. İkinci aşama lineer bir davranış sergilese de ilk ve son aşama daha belirsizdir. Özellikle son aşamada çatlak hızla ilerleyerek kırılma gerçekleşir. Bu aşamalar dikkate alındığında yorulma ömrü, malzemelerin mikroyapılarına oldukça bağlıdır. Literatürde bulunan bir çalışmada (Winter ve ark., 2020), ortalama gerilim duyarlılığının, kabul görmüş bir görüşe göre, yalnızca çekme dayanımından değil, aynı zamanda malzemenin mikro yapısal ve mekanik özelliklerinin yanında işleme geçmişinden de etkilendiği ve basınç yüklemesinin yüksek çevrimli yorulma rejiminde, çekme kadar önemli olduğu bildirilmiştir. İfade edildiği gibi mikroyapı kusurları yorulma ömrü üzerinde önemli bir etkiye sahiptir ve çatlakların ilerleme hızını etkiler. Malzemeler aynı olsa dahi mikro yapıdaki farklılıklar, kullanılan makine elemanlarının yorulma ömrünün tahmin edilmesi güçleştirmektedir. Buradaki mikroyapı farklılıklarından kasıt, mikroyapıda bulunan kusurların türü ve sayısı, yeni oluşan veya daha önceden mevcut olan mikro çatlakların büyüklüğü, sayısı ve ilerleme doğrultusu gibi her numuneye özel farklı parametrelerdir. Yaptığımız deneylerde de buna benzer sonuçlar elde edilmiştir. Numune 1'e göre Numune 2'ye uygulanan kuvvetin artmasına karşı çevrim sayısı da bir miktar artmıştır. Bu durumun sebebinin, her numune için bahsedilen mikroyapı farklılıklarının olduğu düşünülmektedir.

DCPD yöntemi yorulma için tercih edilen yaygın deneysel yöntemlerden biridir (Pokharel ve ark., 2023). DCPD yönteminin temel çalışma prensibinde, numuneye sabit bir akım verilerek çatlak boyunca potansiyel farkın ölçülmesi yatar, uzayan çatlak boyu numunedeki elektriksel direnci artırarak ölçülen potansiyel düşüşün artmasına neden olur (Doremus ve ark., 2015).

Hazırlanan numunelere Şekil 5'te gösterilen 3-4 noktaları arasından, Şekil 4'te görülen Keithley 2634B Sourcemeter cihazı kullanılarak sabit 1 amper akım verildi. Deneyler yapılırken 1-2 ve 3-4 noktaları arasındaki akım ve gerilim değerleri DCPD yöntemiyle anlık olarak saniyede 30 veri kaydedildi. Ayrıca deney sırasında uygulanan kuvvet ve deplasman verileri de eş zamanlı olarak saniyede 30 veri alınarak toplandı. Toplanan bu veriler daha sonra birleştirilerek makine öğrenmesi algoritmalarıyla çevrim sayılarının tahmini için kullanıldı.

Verilerin ön işlemesi için Python programından faydalanıldı. Ham veriler programda farklı veri setleri olarak alındı ve daha sonra tek veri setindeki sütunlar yan yana gelecek şekilde birleştirildi. Eksik değerler bir sonraki satırda bulunan değerler kullanılarak doldurulduu. Oluşan yeni veri seti makine öğrenmesi algoritmalarında kullanıldı.

Toplamda 3 numune için 92895 satır ve 5 özellik bulunan veri seti, makine öğrenmesi modellerini eğitmek için kullanıldı. Bağımlı değişken olarak yorulma deneylerinden elde edilen çevrim sayıları seçildi. Bu değişken sıfırdan kırılmanın gerçekleştiği çevrim sayısına kadar artmaktadır. Bağımsız değişkenler ise aksiyal deplasman, aksiyal kuvvet ve numunelerden ölçülen

elektriksel gerilim değerleridir. Veri setinde bulunan değişkenlerin minimum ve maksimum değerleri Çizelge 4'te verilmektedir.

Çizelge 4. Veri setindeki bağımlı ve bağımsız değişkenlerin minimum ve maksimum değerleri

	Deplasman (mm)		**Kuvvet (N)**		**1-2 Arası Gerillim (V)**		**3-4 Arası Gerillim (V)**		**Çevrim Sayısı**	
	Min.	**Mak.**	**Min.**	**Mak.**	**Min.**	**Mak.**	**Min.**	**Mak.**	**Min.**	**Mak.**
Numune 1	-0.17	8.51	-5536	5539	-0.001931	0.000098	0.34964	0.384992	0	38035
Numune 2	-0.16	6.7	-6036	6048	-0.001888	0.000226	0.35045	0.355692	0	45828
Numune 3	-0.19	3.43	-6526	6532	-0.001888	0.000184	0.34967	0.352607	0	9547

Deneyler sırasında numune üzerine probların temas ettiği noktalar ve bu noktalar arası mesafeler Şekil 5' te gösterilmektedir.

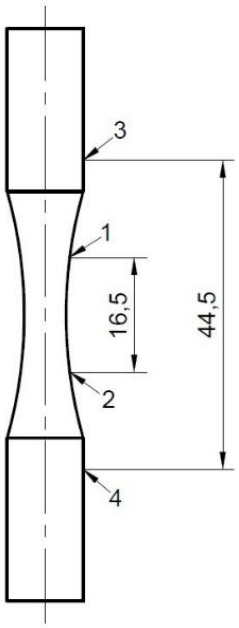

Şekil 5. Probların numune üzerindeki temas noktalarının mesafeleri

Her bir numune için toplanan veriler %80 ve %20 oranında eğitim ve test verisi olmak üzere rastgele ayrıldı. Eğitim verileri kullanılarak eğitilen farklı makine öğrenmesi modelleriyle, numunelerin eğitim ve test verileri üzerinde çevrim sayılarının tahminleri yapıldı. Karar ağacı, ekstra ağaçlar, rastgele orman, XGBoost (Aşırı Gradyan Arttırma) ve KNN (K-En Yakın Komşu) olmak üzere 5 farklı makine öğrenmesi algoritması kullanıldı ve eğitilen modeller test verileri kullanılarak test edildi. Hiperparametrelerin en iyi kombinasyonunu bulmak için ızgara arama tekniğiyle her bir model için belirlenen en iyi parametreler kullanılarak modeller eğitildi ve numunelerin çevrim sayıları tahmin edildi. Izgara arama yöntemiyle belirlenen en iyi hiperparametreler Çizelge 5'de verilmiştir.

Çizelge 5. Sırasıyla tüm numuneler için ızgara arama yöntemiyle belirlenerek makine öğrenmesi modellerinde kullanılan en iyi hiperparametreler

Karar Ağacı	**max_depth**	**min_samples_leaf**	**min_samples_split**		
	None-None-20	1	5-2-2		
Ekstra Ağaçlar	**max_depth**	**max_features**	**min_samples_leaf**	**min_samples_split**	**n_estimators**
	None-None-30	sqrt - sqrt - log2	1	2	200-200-100
Rastgele Orman	**max_depth**	**max_features**	**min_samples_leaf**	**min_samples_split**	**n_estimators**
	None-None-30	sqrt-log2-sqrt	1	2	200
	algorithm	**leaf_size**	**n_neighbors**	**p**	**weights**
KNN	auto	10	9-7-5	1	distance
	colsample_bytree	**learning_rate**	**max_depth**	**n_estimators**	**subsample**
XGBoost	1	0.2	7	200	0.6-0.8-1.0

Model performansları R-kare (R^2) ve ortalama mutlak yüzde hata (MAPE) metrikleriyle ölçülmüştür.

R^2 değeri Denklem 1. (Elmousalami, 2020) ile hesaplanabilir.

$$R^2 = 1 - \frac{\sum_{i=1}^{n}(y_i - \hat{y}_i)^2}{\sum_{i=1}^{n}(y_i - \bar{y})^2} \quad (1)$$

Burada;

y_i: Gerçek değeri,

$\hat{y}_i$: Tahmin edilen değeri,

$\bar{y}$: Gerçek değerlerin ortalamasını ifade etmektedir.

MAPE değerini hesaplamak için Denklem 2. (Elmousalami, 2020) kullanılabilir.

$$MAPE = \frac{1}{n}\sum_{i=1}^{n}\frac{|y_i - \hat{y}_i|}{\hat{y}_i}\ x\ 100 \quad (2)$$

Burada;

y_i:Gerçek değeri,

$\hat{y}_i$:Tahmin edilen değeri

n: veri kümesindeki toplam örnek sayısını, ifade etmektedir

Elde edilen bulgular çizelge ve grafiklerle sunulmuştur.

3. BULGULAR VE TARTIŞMA

3.1 Bulgular

Numunelerin Şekil 5'te gösterilen 1-2 noktaları arasından alınan gerilim değerlerinin 1. dereceden eğilim grafiği Şekil 6'da verilmiştir. Bütün numunelerdeki ölçülen elektriksel gerilim değerleri çevrim sayısı arttıkça artmaktadır. Numune içindeki çatlak miktarı arttığından, numuneden akımın geçmesi zorlaşmış ve ölçülen gerilim değeri de akımın sabit tutulması sebebiyle artma eğilimi göstermiştir.

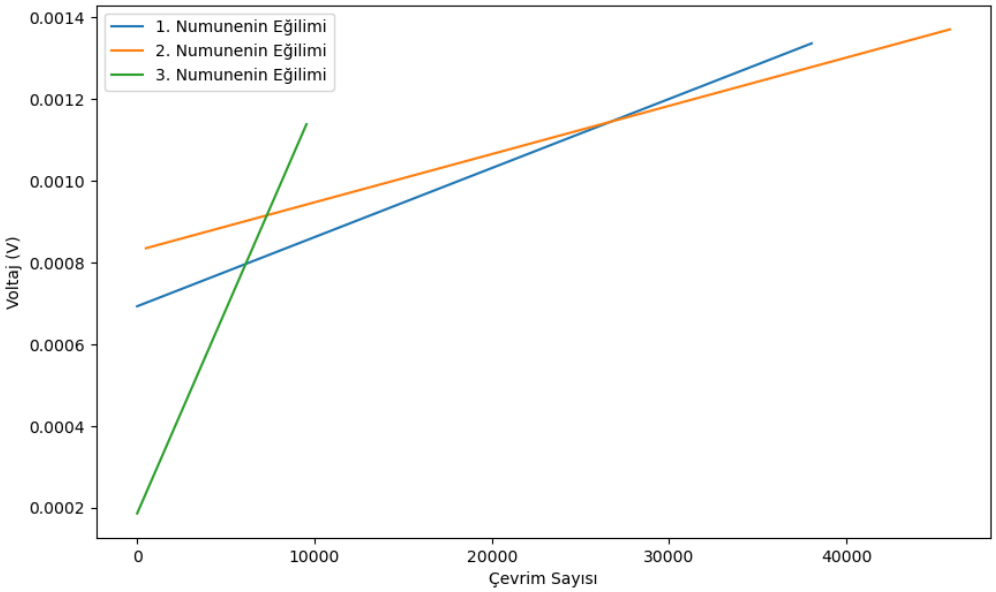

Şekil 6. Numune üzerindeki 1-2 noktaları arasından ölçülen gerilim değerlerinin 1. dereceden eğilim grafiği

Her numunenin eğitim verilerindeki tahminlerine bağlı olarak hesaplanan R^2 hata ve MAPE değerleri Çizelge 6'da sunulmuştur.

Çizelge 6. Makine öğrenmesi modellerinin eğitim verileri üzerindeki performansları

Numune	Karar Ağacı		Ekstra Ağaçlar		Rastgele Orman		XGBoost		KNN	
	R^2	MAPE	R^2	MAPE	R^2	MAPE	R^2	MAPE	R^2	MAPE
Numune 1	1.00	0.00	1.00	0.00	1.00	0.06	1.00	1.64	1.00	0.00
Numune 2	1.00	0.00	1.00	0.00	1.00	0.06	0.99	0.38	1.00	0.00
Numune 3	1.00	0.01	1.00	0.00	1.00	0.07	1.00	0.26	1.00	0.00

Test verilerindeki tahminler sonucunda hesaplanan R^2 hata ve MAPE ise Çizelge 7'de gösterilmektedir.

Çizelge 7. Makine öğrenmesi modellerinin test verileri üzerindeki performansları

Numune	Karar Ağacı		Ekstra Ağaçlar		Rastgele Orman		XGBoost		KNN	
	R^2	MAPE	R^2	MAPE	R^2	MAPE	R^2	MAPE	R^2	MAPE
Numune 1	0.99	0.05	0.99	0.04	0.99	0.08	0.99	0.55	0.95	1.10
Numune 2	0.99	0.08	0.99	0.07	0.99	0.17	0.99	0.66	0.85	1.61
Numune 3	0.98	0.06	0.99	0.04	0.99	0.08	0.99	0.17	0.51	1.55

Çizelge 7'de bulunan değerler tüm numuneler için değerlendirildiğinde KNN modeli hariç tüm modellerin yüksek bir R^2 değerine sahip olduğu görülebilir. R^2 değerinin 1'e yakın olması modellerin veri seti üzerinde iyi uyum sağladığını göstermektedir. Hata değerlendirmeleri için kullanılan MAPE değerleri ise tüm numuneler için karar ağacı ve ekstra ağaçlar modellerinde 0.1'in altındadır. En iyi MAPE değerlerine sahip olan bu iki model için eğitim ve test verileri kullanılarak elde edilen tahmin ve gerçek değer nokta grafikleri Şekil 7 ve Şekil 8'de verilmiştir.

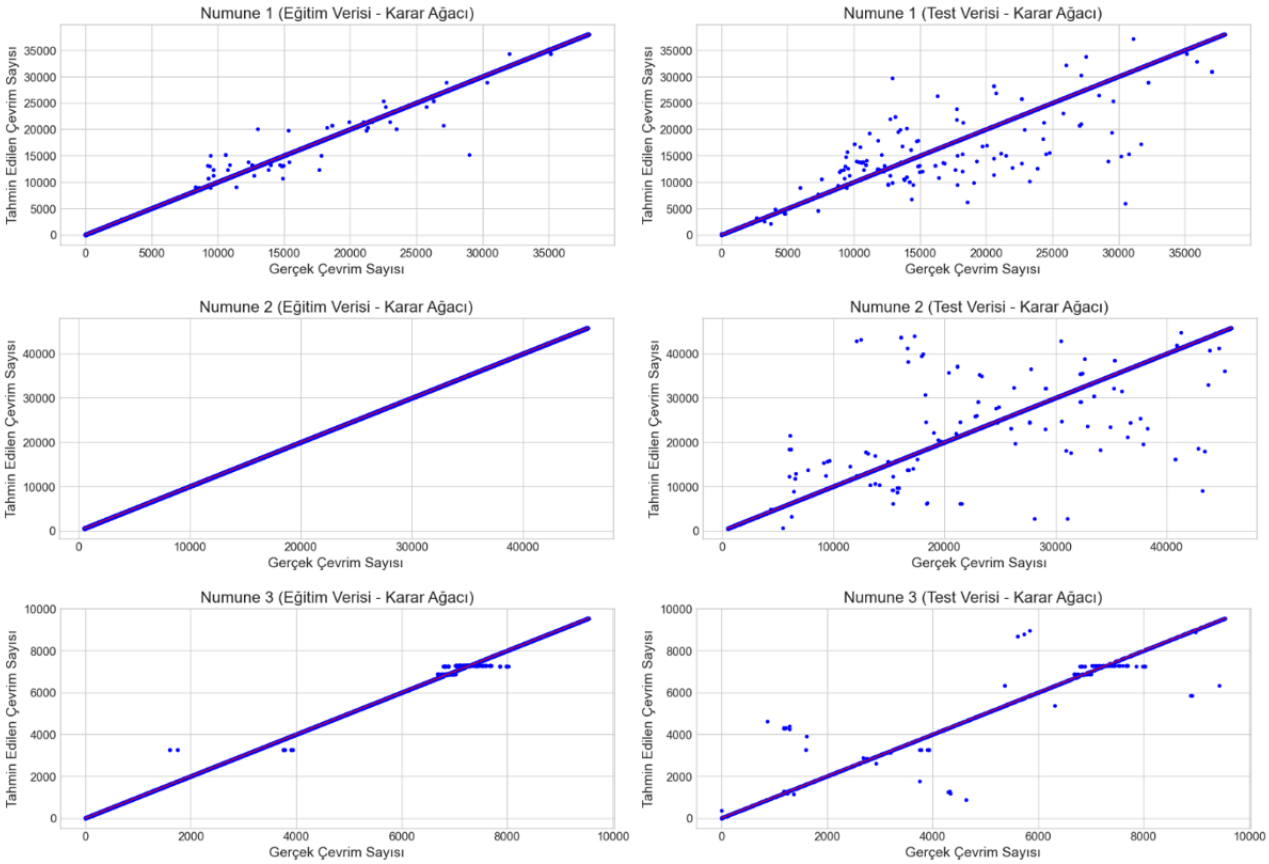

Şekil 7. Sıralanmış gerçek ve tahmin edilen değerler için karar ağacı modelinin nokta grafiği

Şekil 7'de gerçek ve karar ağacı modeli ile tahmin edilen değerler görülmektedir. Model daha önce görmediği test verilerinde bazı büyük hatalar yapmasına karşılık, modelin genel performansı oldukça iyidir. Nitekim Çizelge 7'deki R^2 ve MAPE değerleri bunu desteklemektedir. Ayrıca eğitim verisi üzerinde de Numune 1 ve Numune 2 için bazı değerleri hatalı tahmin ettiği de görülmektedir. Eğitim verileri üzerindeki performansı test verilerine göre daha başarılıdır.

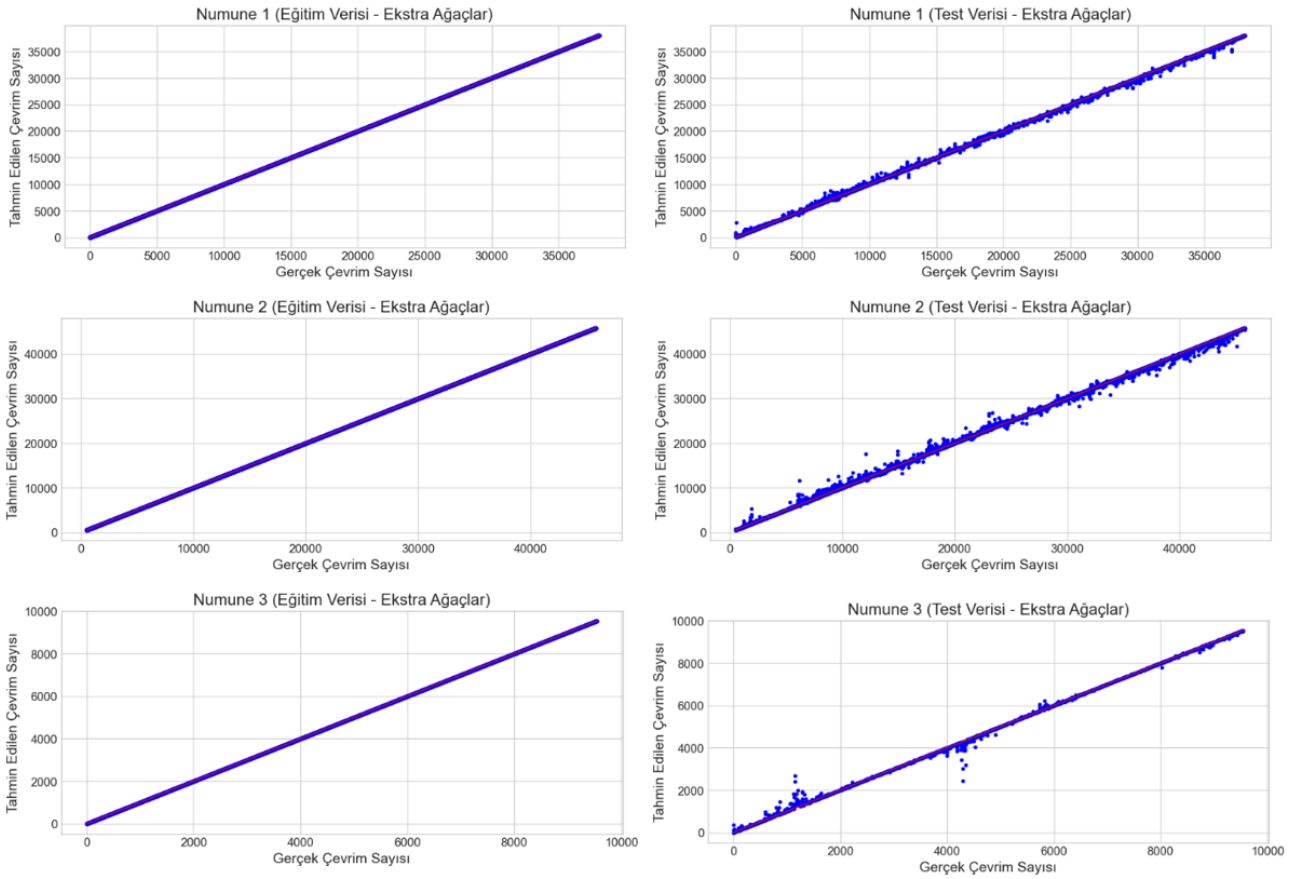

Şekil 8. Sıralanmış gerçek ve tahmin edilen değerler için ekstra ağaçlar modelinin nokta grafiği

Şekil 8'de ise gerçek ve ekstra ağaçlar modeli ile tahmin edilen değerler görülmektedir. Ekstra ağaçlar modeli test veri setinde, karar ağacı modeline göre daha küçük hatalar yapsa da hata sayısı karar ağacı modeline göre biraz daha fazladır. Eğitim veri setinde ise karar ağacı modeline göre daha başarılıdır.

Karar ağacı ve ekstra ağaçlar makine öğrenmesi modelleri, numunelerin çevrim sayılarını tahmin etmede R^2 ve MAPE metrikleriyle değerlendirildiğinde, birbirlerine yakın performans gösterdiler. MAPE değerleri tüm numuneler için 0.1 değerinden daha küçüktür. Bu ise her iki modelin de yüksek bir doğruluk oranı yakaladığını ve yapılan hataların kabul edilebilir aralıkta olduğunu göstermektedir. MAPE değerleriyle birlikte değerlendirildiğinde, her iki modelin de R^2 değerlerinin 0,97'nin üzerinde olması modellerin iyi performans sergilediklerinin göstergesidir. Rastgele orman algoritması kullanılarak geliştirilen model ise Numune 2 için yapılan tahminde MAPE değeri 0.1'in üzerine çıkmıştır. Bu değer biraz büyük görünse de kabul edilebilir hata sınırları içerisindedir. Rastgele orman modeli de karar ağacı ve ekstra ağaçlar modeline yakın performans sergilemiştir. Diğer makine öğrenmesi modellerinde de R^2 değerleri yüksektir. Bu sonuçlar modelin veriye iyi uyum sağladığını gösterse de MAPE değerlerinin karar ağacı, ekstra ağaçlar ve rastgele orman modellerine göre yüksek olması, modelin tahminlerde yaptığı hata sayılarının veya değerlerinin yüksek olmasının bir sonucudur. Veri ölçeklemesi yaparak ya da ızgara arama parametreleri genişletilerek diğer modellerden de daha iyi sonuçlar elde edilebilir.

3.2 Tartışma

Yapılan bir araştırmada (Doré ve Maddox, 2013), 6082 T651 alüminyum alaşımında çatlak büyümesi hızlanmasının temel olarak, düşük yükün ardından etkin çatlak ucu ortalama gerilimindeki artıştan kaynaklandığı ileri sürülmektedir. Yorulma çatlağı büyüme davranışı genellikle mikro

yapının içsel morfolojisi ve malzemede bulunan faz sayısından etkilendiği gösterilen başka bir çalışmada (Ojo ve ark., 2022) ise, enerji biriktirme eklemeli üretim yöntemiyle üretilen Ti–6Al–4V alaşımları için, iki farklı yönelimli yorulma çatlağı büyüme özelliklerinde önemli anizotropi gösterdiği ve kıvrımlı çatlak yollarına sahip numunelerin, pürüzsüz çatlak yolları gösteren numunelere kıyasla daha düşük yorulma çatlağı büyüme oranlarına sahip olduğu ifade edilmiştir.

Laboratuvar ortamında yaygın olarak kullanılan çatlak büyümesi izleme tekniklerinden biride, doğru akım potansiyel düşüşü (DCPD) tekniğidir (Ni ve ark., 2024). Yüksek çözünürlüklü bir DC potansiyel düşüşü ölçümüyle, bir çatlağın çok erken tespit edilebileceği, ancak ilk çatlağın gerçek şeklini ve yerini görüntülemenin mümkün olmadığı söylenen bir çalışmada (Funk ve Bär, 2019), tek kenarı çentikli (SEN) numuneleri üzerinde iki bağımsız potansiyel probu ile yapılan yorulma çatlağı yayılma deneylerinin, ölçülen potansiyel değerlerinde belirgin farklılıklar gösterdiği belirtilmiştir. Ayrıca literatürdeki bir diğer çalışmada (Vavouliotis ve ark., 2011) ise, yorulma yüklemesine maruz izotropik karbon elyaf takviyeli laminatların elektrik direnci tepkisinin doğrudan hasar birikimiyle bağlantılı olduğu söylenmiştir. Biz de yaptığımız çalışmada yorulma tahmini için makine öğrenmesi modeline girdi olarak kullanılacak verileri DCPD yöntemi ile topladık. Literatürdeki tüm bu çalışmaları destekleyici nitelikte, yaptığımız çalışmada numunelerin gerilim değerlerinin, Şekil 6'da bulunan eğilim çizgilerinden de görüleceği üzere, çevrim sayısına paralel bir değişim içinde olduğunu gösterdik.

Yapılan bir çalışmada (Pokharel ve ark., 2023) araştırmacılar DCPD yöntemiyle topladıkları verileri, LSTM (uzun kısa süreli bellekli) mimarisinde kullanarak ve Inconel 718 (IN718) süper alaşımının düşük çevrimli yorulma yüklemelerindeki önceki çatlak sıçramalarına dayanarak gelecekteki çatlak olaylarını tahmin edebildiklerini, modelin daha fazla deney yapılmadan tüm ara koşulları üretebileceğini ve bunun da daha iyi hasar modelleri üretmek için bir araç sağlayacağını ifade etmişlerdir. Diğer bir çalışmada (Lian ve ark., 2022) da sadece bileşim ve temperleme girdileri kullanılarak Al alaşımlarının yorulma dayanımının tahmini için güvenilir bir model sunulmuştur. Farklı bir çalışmada (Abdullatef ve ark., 2023) ise çeşitli makine öğrenmesi teknikleriyle saf burulma yüklemesi altında yüksek mukavemetli 2090-T83 alüminyum alaşımının yorulma ömrü tahmininde, geleneksel yaklaşımlara kıyasla, sinir ağı ve nöro-bulanık modellerin daha iyi sonuçlar ürettiği, güçlendirme yinelemeleri tekniği kullanılarak eğitilen sinir ağı modellerinin en iyi performansı sağladığı ifade edilmiştir. Yapay sinir ağının (ANN) Monte-Carlo yöntemi (MCM) ile ilişkilendirildiği diğer bir çalışmada (Song ve ark., 2022) araştırmacılar, kalıntı yorulma ömrü tahmin modeli oluşturmuşlar ve oluşturulan modelin kullanılarak kalıntı yorulma ömrünü %3,264 bağıl hata oranıyla tahmin ettiklerini belirtmişlerdir. Farklı bir çalışmada (Guo ve ark., 2023) demir alaşımlarının yorulma ömürlerinin tahmini için Bayes optimizasyon algoritması ile optimize edilmiş rastgele orman regresyonu kullanımının, doğrusal regresyon, yapay sinir ağı, karar ağacı regresyonu ve destek vektör regresyonu ile karşılaştırıldığında üstün performans ve doğruluk gösterdiğini belirtilmiştir. 17-4 PH paslanmaz çeliklerin yorulma ömrü ve çatlak büyüme oranını analiz etmek için, KNN, karar ağacı, rastgele ormanlar ve aşırı gradyan artırma algoritmaları kullanılan diğer bir çalışmada (Kalita ve ark., 2024) ise hiper parametreleri optimize ettikten sonra eğitilen modellerin, görülmemiş verileri, eğitilen veriler kadar iyi tahmin ettiği ve en iyi performansı XGB modelinin gösterdiği söylenmiştir. Östenitik paslanmaz çeliklerin yorulma ömrü tahminleri için 4 makine öğrenmesi ve 1 yapay sinir ağı modeli geliştirilen literatürdeki farklı bir çalışmada (Bhardwaj ve Shukla, 2024), yapay sinir ağı modelinin klasik modellere ve makine öğrenimi modellerine göre tahmin doğruluğunu artırdığı ifade edilmiştir. Yapılan diğer bir çalışmada (Çavdar ve ark., 2024) ise AISI H11 sıcak iş takım çeliğinin kutu borlama tekniğiyle borlanmasında işlem sıcaklığı ve süresinin

kaplama kalınlığı, yüzey pürüzlülüğü, sertliği ve korozyon oranına etkisini makine öğrenmesi yöntemleriyle modelleyerek, kaplama kalınlığı ve korozyon oranı için SVR, yüzey pürüzlülüğü ve mikrosertlik için RF algoritmalarının en iyi sonuçları verdiği ifade edilmiştir.

Yaptığımız çalışmada en iyi performansı karar ağacı ve ekstra ağaçlar modelleri gösterirken, en kötü performansı KNN modeli gösterdi. Literatürde bulunan çalışmalardaki modellerin performanslarıyla ilgili temel farklılık, yapılan çalışmalardaki toplanan veri yapılarının farklı olması ve modellerin farklı verilerde, farklı doğruluk oranlarını vermesinden kaynaklandığı düşünülmektedir. Deney verilerinin ve seçilen hiperparametrelerin optimizasyonu yapılarak geliştirilen diğer makine öğrenmesi algoritmalarının da yüksek doğruluk ve düşük MAPE değerlerine sahip tahminler yapması sağlanabilir. Yaptığımız çalışma, bahsedilen çalışmalarda da gösterildiği gibi, geliştirilen makine öğrenmesi modellerinin yorulma çevrim sayılarının tahmin edilmesinde başarılı araçlar olarak kullanılabileceğini desteklemektedir.

Makine öğrenmesi algoritmalarının iyi bir genelleme yaparak, doğru performans göstermesinin en önemli etkenlerinden biri de hiperparametre ayarlarının iyi seçilmiş olmasıdır. Hiperparametre ayarları her problem ve veri setine göre değişkenlik gösterir. Karar ağaçlarında bulunan bir karar ağacı, karar düğümleri, dallar ve ağacın daha fazla ayrılamayacağı yaprak düğümlerinden oluşur (Efeoğlu, 2022). Ekstra Ağaçlar algoritması, klasik yukarıdan aşağıya prosedüre göre budanmamış karar veya regresyon ağaçlarından oluşan bir topluluk oluşturur. Diğer ağaç tabanlı topluluk yöntemleriyle arasındaki iki ana fark, düğümleri tamamen rastgele seçerek düğümleri bölmesi ve ağaçları büyütmek için tüm öğrenme örneğini kullanmasıdır (Geurts ve ark., 2006). Karar ağacı ve ekstra ağaçlar algoritmaları doğrusal olmayan ilişkilerde daha iyi sonuç verebilirler. Rastgele ormanlar, her ağacın ormandaki tüm ağaçlar için bağımsız olarak ve aynı dağılımla örneklenen rastgele bir vektörün değerlerine bağlı olduğu ağaç öngörücülerinin bir kombinasyonudur ve ağaç sınıflandırıcılarından oluşan bir ormanın genelleme hatası, ormandaki bireysel ağaçların gücüne ve bunlar arasındaki korelasyona bağlıdır (Breiman, 2001). Rastgele ormanda rastgele seçime bağlı olarak model çeşitliliği artarken, aşırı uyumun azaltılması hedeflenir. Çok fazla çeşitlilik olması ise bazı veri yapılarında çeşitliliğin birbirini dengelemesi ile doğruluk oranının azalmasına neden olur. Yaptığımız çalışmada rastgele orman modeli, karar ağacı ve ekstra ağaçlar modellerine yakın performans sergilese de Numune 2 için MAPE değeri 0.1'in üzerine çıkmıştır. XGBoost (eXtreme Gradient Boosting), esnek ve taşınabilir, optimum dağıtılmış karar gradyan arttırma kitaplığıdır (Chen ve ark., 2020). Birçok zayıf öğreniciyi bir araya getirerek güçlü bir tahmin modeli oluşturmaya ve her adımda modelin hatalarını düzeltmeye çalışır. Bu durum modelin daha karmaşık hale gelmesine sebep olarak doğruluk oranını düşürebilir. KNN algoritması, sınıflandırma ve regresyon için parametrik olmayan bir yöntemdir. Giriş, her alandaki en yakın k örnekten oluşur. Verilen N eğitim vektörü için, k-en yakın komşu algoritması k sayıda en yakın komşuyu tanımlar (Pandey ve Jain, 2017). Bu çalışma kapsamında en kötü tahmini KNN modeli yapmıştır. Bunun sebebinin, bahsedildiği gibi KNN algoritmasının komşu verileri dikkate almasına bağlı olarak, veri setinin büyüklüğü nedeni ile kötü performans gösterdiği düşünülmektedir.

4. SONUÇ

Bu çalışmada 6082 alüminyum alaşımının yorulma deneyleri yapıldı. Deneyler sırasında DCPD yöntemi kullanılarak değişen potansiyel fark verileri toplandı. Ayrıca gerçek zamanlı olarak, deneyler sırasında deplasman ve kuvvet verileri de eş zamanlı olarak kaydedildi. Daha sonra karar ağacı, ekstra ağaçlar, rastgele orman, XGBoost (eXtreme Gradient Boosting) ve KNN (K-En Yakın Komşu) olmak

üzere 5 farklı makine öğrenmesi algoritmasına bu veriler girdi olarak verildi ve eğitilen modellerle numunelerin çevrim sayıları tahmin edildi.

Tahminlerde karar ağacı ve ekstra ağaçlar algoritmaları ile geliştirilen modeller, tüm numuneler için MAPE değerleri 0.1'in altında kalarak en iyi performansı gösterdi. Rastgele orman algoritması kullanılarak geliştirilen model ise Numune 2 için hesaplanan MAPE değerinin 0.1'in üzerinde olmasına rağmen karar ağacı ve ekstra ağaçlar modellerine benzer performans gösterdi. Çizelge 7'de verilen değerler incelendiğinde, XGBoost modeli kullanılarak yapılan tahminlerde R^2 değerleri istenildiği gibi 1'e yakındır. Fakat, MAPE değerlerinin beklenenden yüksek olduğu görülmektedir. Bu sonuçlar, XGBoost modelinin verilere iyi uyum sağladığını göstersede, bazı değerler için gerçek ve tahmin edilen değerler arasındaki farkın, dolayısıyla da hata oranının yüksek olduğunu ifade eder. KNN algoritması kullanılarak geliştirilen model en kötü performansı gösterdi. Numune 1 için MAPE değeri istenen gibi 1'e yakın olsa da diğer numuneler 0.9 değerinden küçüktür. Ayrıca MAPE değerleri de 1'in üzerindedir. KNN modeli diğer modellere göre en çok hata yapan modeldir.

5. TEŞEKKÜR

Yazarlar Selçuk Üniversitesi Bilimsel Araştırma Projeleri Koordinatörlüğüne maddi desteklerinden dolayı teşekkür ederler. Ayrıca yazarlar bu çalışmada gerçekleştirilen yorulma deneylerindeki katkılarından ve yardımlarından dolayı AYD ARGE ekibine teşekkür ederler.

6. ÇIKAR ÇATIŞMASI

Yazarlar, bilinen herhangi bir çıkar çatışması veya herhangi bir kurum/kuruluş ya da kişi ile ortak çıkar bulunmadığını onaylamaktadırlar.

7. YAZAR KATKISI

Resul ÜNAL çalışmanın kavramsal ve tasarım süreçlerinin belirlenmesi, veri toplama, veri analizi ve yorumlama, makale taslağının oluşturulması, fikirsel içeriğin eleştirel incelemesi, son onay ve tam sorumluluk kısımlarında katkıda bulunmuştur. Recai KUŞ çalışmanın kavramsal ve tasarım süreçlerinin yönetimi, makale taslağının oluşturulması, son onay ve tam sorumluluk kısımlarında katkıda bulunmuştur. Mustafa ACARER çalışmanın kavramsal ve tasarım süreçlerinin belirlenmesi, fikirsel içeriğin eleştirel incelemesi, son onay ve tam sorumluluk kısımlarında katkıda bulunmuştur.

8. KAYNAKLAR

Abdullatef M. S., Alzubaidi F. N., Al-Tamimi A., Mahmood Y. A., Fatigue Life Estimation of High Strength 2090-T83 Aluminum Alloy Under Pure Torsion Loading Using Various Machine Learning Techniques, Fluid Dynamics and Materials Processing, 19(8), 2083–2107, 2023.

Arunachalam S., Fawaz S., Test Method for Corrosion Pit-To-Fatigue Crack Transition From A Corner of Hole in 7075-T651 Aluminum Alloy, International Journal of Fatigue, 91, 50–58, 2016.

ASTM, Specification for Aluminum and Aluminum-Alloy Extruded Bars, Rods, Wire, Profiles, and Tubes, Test, 2021.

ASTM, Standard Practice for Conducting Force Controlled Constant Amplitude Axial Fatigue Tests of Metallic Materials, Test, 03, 4–8, 2002.

Bhardwaj H. K., Shukla M., Low-Cycle Fatigue Life Prediction of Austenitic Stainless Steel Alloys: A Data-Driven Approach with Identification of Key Features, International Journal of Fatigue, 187, 108454, 2024.

Birol Y., Gokcil E., Ali M., Akdi S., A Processing of High Strength EN AW 6082 Forgings Without a Solution Heat Treatment, Materials Science & Engineering:A, 674, 25–32, 2016.

Breiman L., Random forests, Machine Learning, 45(1), 5–32, 2001.

Cai Q., Mendis C. L., Chang I. T. H., Fan Z., Microstructure Evolution and Mechanical Properties of New Die-Cast Al-Si-Mg-Mn Alloys, Materials & Design, 187, 108394, 2020.

Černý I., The use of DCPD Method for Measurement of Growth of Cracks in Large Components at Normal and Elevated Temperatures, Engineering Fracture Mechanics, 71(4–6), 837–848, 2004.

Chen J., Liu Y., Fatigue Modeling Using Neural Networks: A Comprehensive Review, Fatigue and Fracture of Engineering Materials and Structures, 45(4), 945–979, 2022.

Chen J., Zhao F., Sun Y., Yin Y., Improved XGBoost Model Based On Genetic Algorithm, International Journal of Computer Applications in Technology, 62(3), 240, 2020.

Çavdar F., Günen A., Sert M., Borlanmış AISI H11 Takım Çeliğinin Kaplama Özellikleri ve Korozyon Oranının Makine Öğrenmesi Temelli Modellenmesi, Çukurova Üniversitesi Mühendislik Fakültesi Dergisi, 39(3), 625–638, 2024.

Doré M. J., Maddox S. J., Accelerated Fatigue Crack Growth in 6082 T651 Aluminium Alloy Subjected to Periodic Underloads, Procedia Engineering, 66, 313–322, 2013.

Doremus L., Nadot Y., Henaff G., Mary C., Pierret S., Calibration of The Potential Drop Method for Monitoring Small Crack Growth from Surface Anomalies - Crack Front Marking Technique and Finite Element Simulations, International Journal of Fatigue, 70, 178–185, 2015.

Efeoğlu E., Kablosuz Sinyal Gücünü Kullanarak İç Mekan Kullanıcı Lokalizasyonu için Karar Ağacı Algoritmalarının Karşılaştırılması, Acta Infologica, 163 - 173, 2022.

Elmousalami H. H., Artificial Intelligence and Parametric Construction Cost Estimate Modeling: State-of-the-Art Review, Journal of Construction Engineering and Management, 146(1) 2020.

European Aluminium, Aluminium Usage in Cars Surges As Automotive Industry Shifts Towards Electrification, (May) www.european-aluminium.eu.

Funk M., Bär J., DCPD Based Detection of the Transition from Short to Long Crack Propagation in Fatigue Experiments on The Aluminum Alloy 7475 T761, Procedia Structural Integrity, 17, 183–189, 2019.

Geurts P., Ernst D., Wehenkel L., Extremely Randomized Trees. Machine Learning, 63(1), 3–42, 2006.

Gitter R., Aluminium Materials for Structural Engineering – Essential Properties and Selection of Materials, Structural Engineering International, 16(4), 294–300, 2006.

Guo J., Zan X., Wang L., Lei L., Ou C., Bai S., A Random Forest Regression with Bayesian Optimization-Based Method for Fatigue Strength Prediction of Ferrous Alloys, Engineering Fracture Mechanics, 293, 109714, 2023.

Guo Y. B., Liu K. G., Lan Z. Y., Du X. K., Fatigue Life Prediction and System Development for 6082-T6 Aluminum Alloy Under Variable Amplitude Loading, International Conference on Advanced Sensing and Smart Manufacturing (ASSM 2022), SPIE 2022.

He L., Wang Z. L., Akebono H., Sugeta A., Machine Learning-Based Predictions of Fatigue Life and Fatigue Limit for Steels, Journal of Materials Science & Technology, 90, 9–19, 2021.

Jíša D., Liškutín P., Kruml T., Polák J., Small Fatigue Crack Growth in Aluminium Alloy EN-AW 6082/T6, International Journal of Fatigue, 32(12), 1913–1920, 2010.

Kalita B., Abhiraaj R. C., Jayaganthan R., Fatigue Life and Crack Growth Rate Prediction of Additively Manufactured 17-4 PH Stainless Steel Using Machine Learning, Procedia Structural Integrity, 56, 105–110, 2024.

Karolczuk A., Skibicki D., Pejkowski Ł., Gaussian Process for Machine Learning-Based Fatigue Life Prediction Model Under Multiaxial Stress–Strain Conditions, Materials, 15(21) 2022.

Kumar V., Singh I. V., Mishra B. K., Jayaganthan R., Crack Growth Behavior of 6082 Al Alloys Under Mixed Mode-I Loading, In: Kumar A., Kumar Singla Y., Maughan M.R. (Ed.), Fracture Behavior of Nanocomposites and Reinforced Laminate Structures (pp. 207–237), Springer Nature Switzerland: Cham 2024.

Li S., Zhu Q., Lu Z., Yan H., Zhu C., Li P., Fatigue Life Prediction of AA2524 Thin Plate Strengthened using Compound Laser Heating and Laser Shot Peening Method. Theoretical and Applied Fracture Mechanics, 129, 104178, 2024.

Lian Z., Li M., Lu W., Fatigue Life Prediction of Aluminum Alloy Via Knowledge-Based Machine Learning, International Journal of Fatigue, 157, 106716, 2022.

Malek B., Mabru C., Chaussumier M., Fatigue Behavior of 2618-T851 Aluminum Alloy under Uniaxial And Multiaxial Loadings, International Journal of Fatigue, 131, 105322, 2020.

Mann T., Härkegård G., Stärk K., Short Fatigue Crack Growth in Aluminium Alloy 6082-T6, International Journal of Fatigue, 29(9–11), 1820–1826, 2007.

Mirzaei A. H., Haghi P., Shokrieh M. M., Prediction of Fatigue Life of Laminated Composites by Integrating Artificial Neural Network Model and Non-Dominated Sorting Genetic Algorithm, International Journal of Fatigue, 188, 108528, 2024.

Ni C., Xue H., Wang S., Yang F., Zhao K., Effect of Deformation on Crack Extension Measurement for Compact Tension Specimen with the DCPD Technique, Proceedings of the Institution of Mechanical Engineers, Part C: Journal of Mechanical Engineering Science, 238(5), 1618–1628, 2024.

Ojo S. A., Shrestha S., Manigandan K., Morscher G. N., Gyekenyesi A. L., Scott-Emuakpor O. E., Application of Small Geometry Specimens to Determine the Fatigue Crack Growth Anisotropy of Ti–6Al–4V Additively Manufactured for Repair, Results in Materials, 15 2022.

Olguner S., Bozdana A. T., Prediction of Lankford Coefficients for AA1050 and AA5754 Aluminum Sheets Using Uniaxial Tensile Tests and Cup Drawing Experiments, Lecture Notes in Mechanical Engineering, 438–446, 2020.

Pandey A., Jain A., Comparative Analysis of KNN Algorithm using Various Normalization Techniques, International Journal of Computer Network and Information Security, 9(11), 36–42, 2017.

Paris P., Erdogan F., A Critical Analysis of Crack Propagation Laws, Journal of Basic Engineering, 85(4), 528–533, 1963.

Peng Y., Zhang Y., Zhang L., Yao L., Guo X., Prediction of Corrosion Fatigue Crack Growth Rate in Aluminum Alloys Based on İncremental Learning Strategy, International Journal of Fatigue, 187, 108481, 2024.

Pokharel A., Keesler-Evans J., Tempke R., Musho T., A Machine Learning Model for Predicting Progressive Crack Extension Based on Experimental Data Obtained Using DCPD Measurement Technique, Journal of Materials Research and Technology, 24, 5687–5701, 2023.

Sagar S., Singh N. K., Maurya N. S., Compressıon, Flexure and Wear Behavıours of Aluminium 6082-T6 Alloy, U.P.B. Scientific Bulletin, Series D: Mechanical Engineering, 85(3), 193–204, 2023.

Sarkar A., Aktunali M., Marthe Arbo S., Holmestad J., Mario Viespoli L., Nyhus B., Ringen G., Razavi N., A Study on the Influence Of Impurity Content on Fatigue Endurance In A 6082 Al-Alloy, International Journal of Fatigue, 186, 108406, 2024.

Silva F. S., Pinho A. C. M., The Effect of Temperature on Crack Behavior In An 7175 Aluminum Alloy Under Mode I + Steady Mode III, European Structural Integrity Society, 29(C), 247–256, 2002.

Song M., Liu J., Chen H., Hu Y., Shi Z., Yin H., Xia J., Berto F., Li R., Effects and Optimization of Biomimetic Laser Shock Peening on Residual Fatigue Life İmprovement of Aluminum Alloy Used In Aircraft Skin. Theoretical and Applied Fracture Mechanics, 117, 103155, 2022.

Vavouliotis A., Paipetis A., Kostopoulos V., On the Fatigue Life Prediction of CFRP Laminates using The Electrical Resistance Change Method, Composites Science and Technology, 71(5), 630–642, 2011.

Vecchiato L., Campagnolo A., Meneghetti G., Numerical Calibration and Experimental Validation of The Direct Current Potential Drop (DCPD) Method for Fracture Mechanics Fatigue Testing of Single-Edge-Crack Round Bars, International Journal of Fatigue, 150(February) 2021.

Winter L., Hockauf K., Winter S., Lampke T., Equal-Channel Angular Pressing Influencing the Mean Stress Sensitivity In The High Cycle Fatigue Regime of the 6082 Aluminum Alloy, Materials Science and Engineering: A, 795, 140014, 2020.

Yılmaz N. F., Çakır M. V., Yılmaz M., Saplama Kaynak Bağlantılarının Çekme Dayanımının ANFIS ile Modellenmesi, Çukurova Üniversitesi Mühendislik-Mimarlık Fakültesi Dergisi, 31(ÖS1), 79–88, 2016.

JOURNAL of
MATERIALS and MECHATRONICS:A

e-ISSN 2717-8811
JournalMM, 2025, 6(1), 32-48
https://doi.org/10.55546/jmm.1590391

Araştırma Makalesi / Research Article

Comprehensive Design and Testing of a BLDC Motor for Direct Drive EV Applications

Mücahit SOYASLAN[1*], Mohamad BAZAZIAN[2], Osman ELDOĞAN[3]

[1*] Sakarya University of Applied Sciences, Faculty of Technology, Department of Mechatronics Engineering, Sakarya, Türkiye, ORCID ID: https://orcid.org/0000-0001-6658-5169, msoyaslan@subu.edu.tr
[2] Sakarya University of Applied Sciences, Faculty of Technology, Department of Mechatronics Engineering, Sakarya, Türkiye, ORCID ID: https://orcid.org/0000-0003-2881-958X, mohamad.bazazian@ogr.sakarya.edu.tr
[3] Sakarya University of Applied Sciences, Faculty of Technology, Department of Mechatronics Engineering, Sakarya, Türkiye, ORCID ID: https://orcid.org/0000-0001-9236-8985, eldogan@subu.edu.tr

Geliş/ Received: 24.11.2024**;** **Revize/Revised:** 24.12.2024 **Kabul / Accepted:** 14.01.2025

ABSTRACT: This paper proposes a 2 kW in-wheel brushless direct current (BLDC) motor design for a light electric vehicle (EV). The EV is designed for a predefined route in electric vehicle races. The BLDC motor was directly mounted into the vehicle's wheel rim. Initially, dynamic model of EV was calculated according to vehicle characteristics. The motor's slot/pole ratio was selected as 36/32. The designs for the stator, rotor, and magnets were subsequently developed based on the motor's boundary dimensions, aiming for low cogging torque and high efficiency. To achieve this, the distance between stator tooth tips was optimized. The design was validated through 2D finite element analyses, followed by the motor's production. Performance tests conducted with the experimental setup confirmed that the design matches the experimental results.

Keywords: Electric vehicle, BLDC motor, Electric motor design, Outer rotor, EV dynamic model

*Sorumlu yazar / Corresponding author: msoyaslan@subu.edu.tr
Bu makaleye atıf yapmak için /To cite this article

Soyaslan, M., Bazazian, M., Eldoğan, O. (2025). Comprehensive Design and Testing of a BLDC Motor for Direct Drive EV Applications. Journal of Materials and Mechatronics: A (JournalMM), 6(1), 32-48.

1. INTRODUCTION

Electric vehicles (EVs) have begun to replace internal combustion vehicles in today's world. Various companies engaged in this sector focus on designing high efficiency EVs. Various battery packs and electric motors are used in these vehicles. Permanent Magnet Synchronous Motors (PMSMs) typically find application in larger electric or hybrid vehicles, whereas BLDC motors are favoured for smaller light EVs. Light EVs are typically scooters, small cars or cargo bikes with a carrying capacity of 50-100 kg and a speed of 25-50 km/h (Soyaslan, 2023).

BLDC motors used in light EVs can be classified into two types based on their structure: radial flux and axial flux. The studies conducted compare radial and axial flux motors in terms of efficiency, cost, and volume. Radial flux motors are further classified into two types: internal and outer rotor designs. While internal rotor motors are utilized in certain applications to transfer motion, outer rotor designs also referred to as in-wheel motors are the preferred choice for direct wheel drive applications. In outer rotor EV designs, parameters such as slot/pole ratio, axial length, winding structures, magnet type, and thickness are generally optimized (Cabuk et al., 2019; Chawrasia et al., 2020; Cagıslar et al., 2020; Akar et al., 2021; Aliyadin et al., 2022; Ozupak, 2022; Tosun and Serteller, 2022; Soyaslan, 2023).

Rotor and stator designs and the effects of single or double rotors and stators on performance have been investigated (Zuki et al. 2020; Lee et al, 2020; Vadde and Sachin, 2021; Hussain et al. 2021). Studies have been carried out to minimize cogging torque and torque fluctuation for more vibration-free and comfortable motors. In these studies, various pole embraces (ratio of magnetic pole arc to pole pitch), skewing stator or rotor laminations technique, and various magnet shapes, and various control techniques were used (Ocak et al., 2016; Soyaslan et al., 2019; Minh et al., 2021; Rupam and Marwaha, 2021; Anuja and Doss, 2021; Anuja et al., 2022; Ozupak and Cinar, 2023).

In this paper, 2 kW outer rotor BLDC motor with 36/32 slot-pole was designed for a light EV. Distance between stator tooth tips (B_{s0}) was optimized for minimizing cogging torque. Parametric optimization method was used for achieving the optimum B_{s0} value. This study aims to reduce cogging torque by focusing on the distance between stator tooth tips, demonstrating that cogging torque minimization is possible without the need for the complex operations used in previous studies. The current density and magnetic flux density (B) values were kept below 4-5 A/mm^2 and 1.6 Tesla, respectively. In addition, stator slot fill factor value was selected below 50% for a more suitable winding. The motor design was validated after analytical and electromagnetic analyses. Prototype motor was produced and tested in the test setup and EV, confirming that the analysis results aligned with the test outcomes.

2. MATERIALS AND METHODS

2.1 Dynamic Model of EV

The EV's characteristics for racetrack conditions with low angle of slope were computed. Table 1 summarizes the vehicle parameters used based on track conditions. Racetrack view can be seen from Figure 1. The track is 1.950 km long, 10-12 meters wide and designed to turn clockwise. The total number of bends on the track is 9, 4 on the right and 5 on the left, and the highest longitudinal slope on the track is 1%. The selection of parameters, including slope angle and acceleration values, is based on typical driving conditions in electric vehicle races. The goal is to achieve the desired acceleration values, power output, and high motor efficiency based on the maximum slope angle on the race track and vehicle dynamics.

Table 1. EV characteristics.

Parameter	Value
Total mass, M (kg)	210
Rolling resistance coefficient, C_{rr}	0.007
Air density, ρ (kg/m^3)	1.2
Drag coefficient, C_d	0.3427
Frontal area, A (m^2)	1.29
Velocity of vehicle, V (m/s)	12.5
Acceleration, a (m/s^2)	0.12
Tire radius, r (m)	0.2921
Surface slope angle, θ (°)	1.2
Gravity acceleration, g (m/s^2)	9.81

Figure 1. EV racetrack view

The dynamic model of the vehicle is shown in Figure 2. The maximum torque requirement for an EV arises during full-load conditions on an inclined road, particularly when accelerating from zero speed to its nominal speed. The torque calculations for the BLDC motor are based on the torque required to achieve this acceleration, considering the maximum incline values of the race track. According to EV's dynamic model, traction force F_t and BLDC motor's output torque T_m was calculated. Three different forces acting on the vehicle in the opposite direction of movement are expressed in (1-3) (Soyaslan, 2023; Krasopoulos et al., 2017). These forces are aerodynamic resistance F_{ar}, rolling resistance F_{rr} and weight component of EV along sloped surface F_{ws}. F_{ar} force is calculated at the nominal speed of the vehicle which is taken 45 km/h (12.5 m/s). Tire radius is 23 inch, rotational speed and angular velocity are 408.6 rpm and 42.8 rad/s respectively. According to Newton's second law for the dynamic model of the EV, F_t was calculated with (4) as 124.2 N. Consequently, the required torque value (T_m) for the vehicle to move at the desired nominal speed has been calculated from (5) as 36.28 Nm, and the power value (P_{out}) has been calculated from (6) as 1552 W. Since the slope angles of different tracks are greater and the acceleration can be bigger, the output power value P_{out} has been updated to 2000 W and the rotational speed (N) to 526.42 rpm to achieve the desired speeds. Thus, the designed motor will be able to provide the desired torque even on high slope angle roads and with bigger acceleration values.

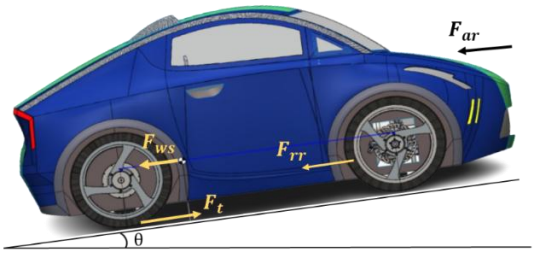

Figure 2. Dynamic model of the EV

$$F_{ar} = \frac{1}{2}\rho A C_d V^2 \tag{1}$$

$$F_{rr} = C_{rr} mg\cos(\theta) \tag{2}$$

$$F_{ws} = mg\sin(\theta) \tag{3}$$

$$M.a = F_t - F_{ar} - F_{rr} - F_{ws} \tag{4}$$

$$T_m = F_t r \tag{5}$$

$$P_{out} = T_m \omega \tag{6}$$

2.2 Outer Rotor BLDC Motor Design

The output torque expression for motor basic sizing is used as given in (7). Here, *k* is a constant, *D* is the air gap diameter, and *L* is the motor length. The region where rotational force is generated in motors is the air gap zone, where the interaction between the stator and rotor occurs. For inner rotor motors, the rotor diameter is generally used for *D* in the equation, while for outer rotor motors, the air gap diameter (D_{ag}) or stator outer diameter (D_{so}) is employed. In analytical motor calculations, the rotational speed in revolutions per second (*rps*, *n*) and the power per revolution (P_s) are obtained using (8) and (9), respectively. The air gap flux density (B_g) and specific electric loading (*ac*) values are selected from the graph in Figure 3 (Tosun and Serteller, 2022; Gürdal, 2001). The pole embrace value (α_m), representing the ratio of the magnetic pole arc to the pole pitch, is taken as 0.7. The average air gap flux density (B_{av}) and the motor output coefficient (C_o) are calculated using (10) and (11).

$$T_m = kD^2L \tag{7}$$

$$n = \frac{N}{60} \tag{8}$$

$$P_s = \frac{P_{out}}{n} \tag{9}$$

$$B_{av} = B_g\, \alpha_m \tag{10}$$

$$C_o = \pi^2 B_{av}\, ac\, 10^{-3} \tag{11}$$

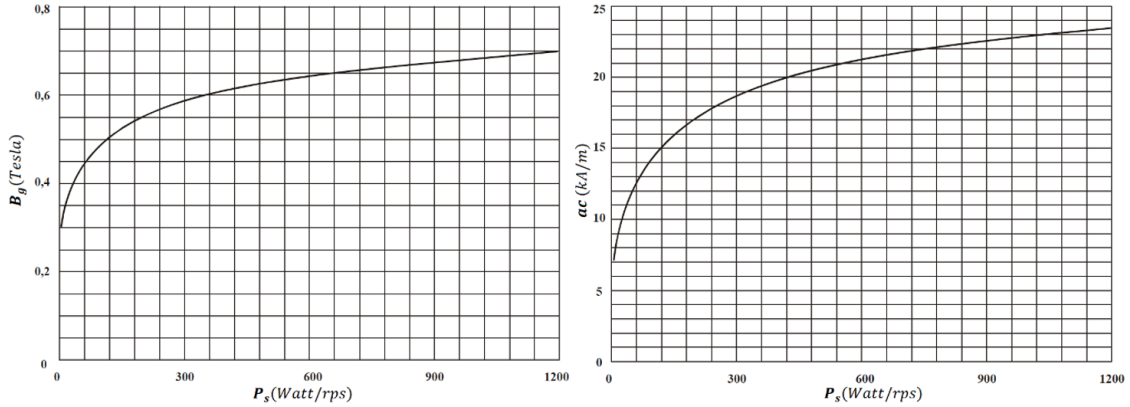

a) b)

Figure 3. a) Power per round per second-Air gap flux density graph, b) Power per round per second-Specific electrical loading graph.

The volume of the motor's active components is closely related to $D_{ag}{}^2L$, and the rated torque is proportional to *Pout*/*n*. Therefore, the size-to-power relationship for an outer rotor BLDC motor is expressed using (12). According to this equation, the product of the motor stator diameter and length is determined. Subsequently, the motor's axial length to pole-pitch ratio (L/τ) must be defined. Various studies have examined this topic, selecting different ratios based on motor dimensions and power requirements. The pole-pitch ratio (τ) is calculated using (13), where *Np* represents the total number of poles. For surface-mounted brushless motors, τ values are typically chosen between 1 and 3 to minimize manufacturing costs (Murali et al., 2020). In this study, experiments with different τ values were conducted, ultimately deciding on τ = 3. The motor parameters derived from the given equations and selections are presented in Table 2. Based on these values, D_{ag} is calculated as 225.23 mm, and L as 66.33 mm. However, due to mechanical constraints and the requirement for EV installation, the axial length L was updated to 55 mm. The air gap thickness was set to 1 mm, considering manufacturing tolerances, and D_{so} was selected as 224 mm.

$$D_{ag}^2 L = \frac{P_{out} * 10^{-3}}{C_o n} \tag{12}$$

$$\tau = \frac{D_{ag}}{N_p} \tag{13}$$

Table 2. BLDC motor parameters

Parameter	**Value**
Output power, P_{out} (Watt)	2000
Pole number, N_p	32
Slot number, N_s	36
Round per minute, N (rpm)	526.42
Round per second, n (rps)	8.773
Power per round per second, P_s (watt/rps)	227.954
Airgap flux density, B_g (Tesla)	0.57
Specific electrical loading, ac (kA/m)	17200
Magnetic pole arc to pole pitch ratio, α_m	0.7
Average airgap flux density, B_{av} (Tesla)	0.399
Output coefficient value, C_o	67.733
Motor axial length to pole pitch ratio, L/τ	3

2.3 Dimensions and Cogging Torque Optimization

Fundamental sizing calculations were performed based on calculated values. After the basic sizing, parameter selections were refined through parametric testing. The stator slot dimensions were chosen to ensure sufficient space for windings and optimal flux flow. To reduce saturation in corner regions, radii were applied to the stator tooth tips. Excessively thick stator teeth narrow the slot area, reducing winding space, while overly thin teeth lead to saturation in the silicon steel. Therefore, the stator tooth width was selected to optimize magnetic flux density. The rotor core thickness was set to 11.25 mm, and the magnet thickness to 3.5 mm, aiming for the optimal thickness to produce the required torque. The magnets were embedded in slots created within the rotor using the wire erosion method, with a slot depth of 1.25 mm for secure magnet installation. The motor cross-sectional variables are shown in Figure 4, with their dimensions detailed in Table 3.

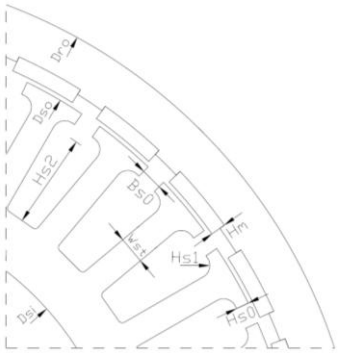

Figure 4. Dimensions of BLDC Motor

Table 3. BLDC motor dimension values

Motor Paremeter	Value
Stator outer diamater, D_{so}	224 mm
Stator inner diameter, D_{si}	145 mm
Rotor outer diamater, D_{ro}	253 mm
Stack length, L	55 mm
Magnet height, H_m	3.5 mm
Stator tooth width, W_{st}	6.3 mm
Tooth tip gap, B_{s0}	5 mm
Tooth tip height, H_{s0}	3 mm
Tooth tip Radius, H_{s1}	3 mm
Slot height, H_{s2}	21 mm

The reduction of cogging torque is essential to improve the efficiency and to reduce permanent magnet requirements of electric motors (Smolka and Nowacka, 2022; Jhankal, 2023). In the context of vibration and noise reduction, cogging torque has been identified as a significant factor affecting the smooth rotation of the rotor and the life of electric motors (Soyaslan et al., 2019, Kim et al., 2006). To minimize cogging torque and torque fluctuations in external rotor BLDC motors, various effective methods have been proposed in the literature. Adjusting the punching layout and applying placement irregularities in rotor magnets were used to reduce the cogging torque (Anuja and Doss, 2021; Leitner et al., 2019). Asymmetric magnets, step skewing and shifting angles have been experimentally applied to reduce harmonics of cogging torque (Doss et al., 2016; Avsar et al., 2024a). Optimizing BLDC motors by utilizing a skew angle on the stator or rotor core, along with enlarging the air gap, has shown significant reductions in cogging torque (Mandasari, 2023). Skewing the rotor and

implementing a Halbach magnet array on the permanent magnet surface has been suggested to eliminate torque ripples and reduce cogging torque in permanent magnet BLDC motors (Minh et al., 2021). Additionally, adjusting slot and tooth widths, employing permanent magnet skewing, creating auxiliary teeth, using slot-less armatures, and incorporating notches in the rotor structure have been identified as effective methods to minimize cogging torque magnitude (Karthick et al., 2021). Furthermore, the reduction of cogging torque is crucial in direct-drive systems where there are no gears to minimize or absorb the cogging torque (Sarac, 2019). These methods play a crucial role in enhancing motor efficiency, reducing noise, and improving overall performance in a wide range of applications. In this study, stator tooth tip gap (B_{s0}) was selected as an optimization parameter for reducing the cogging torque. The objective function for the optimization was defined as the cogging torque, which the optimization sought to minimize. Parametric optimization method was used between 4-6 mm with 0.1 mm step. The parametric optimization results indicated that a B_{s0} value of 5 mm yielded one of the lowest cogging torque values. The optimized result is depicted in Figure 5.

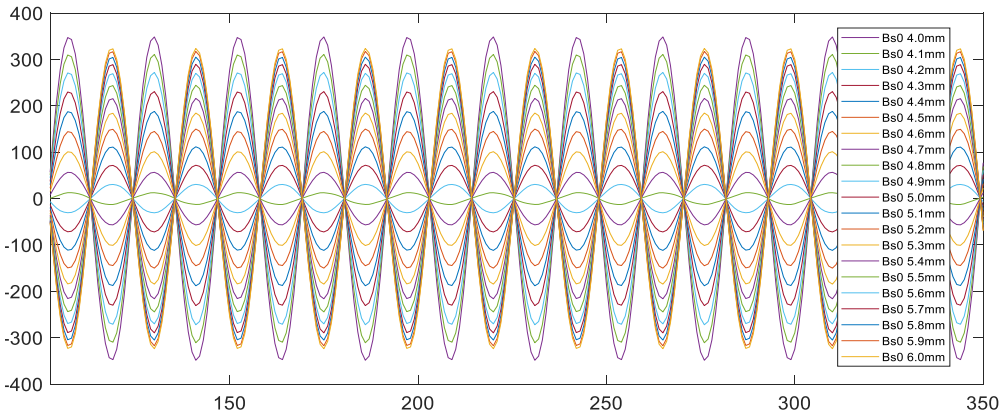

Figure 5. Cogging torque values regarding to B_{so} value

3. RESULTS AND DISCUSSION

3.1 Analyses Results

Electromagnetic analysis was conducted based on the specified stator and rotor dimensions. The winding scheme and hall effect sensors placement, derived using the Winding Scheme Calculator tool, are presented in Figure 6 (Niessen, 2019). A double-layer concentrated winding technique was applied to achieve high power density (Soyaslan, 2020).

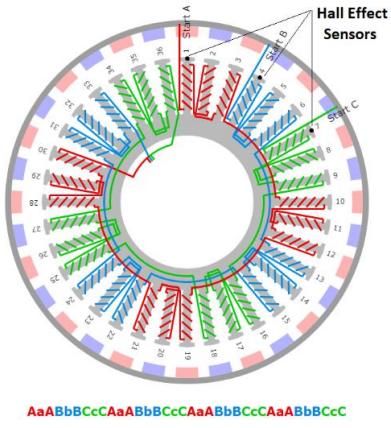

Figure 6. BLDC motor 36/32 Slot-Pole combination winding scheme

The electromagnetic transient analysis results obtained using Ansys Maxwell software are presented in Figures 7–9. Magnetic vector potential was used to determine the distribution and intensity of the magnetic field. A uniform distribution of this potential indicates an efficient magnetic circuit, while imbalances can reduce motor efficiency. Figure 7 demonstrates a uniform flux line distribution. Magnetic flux density (B) indicates the efficiency of the magnetic materials in the motor's magnetic circuits. Excessively high B values suggest the material is approaching magnetic saturation, increasing iron losses, while low B values indicate underutilization, reducing power efficiency. Operating in the knee region of the $B-H$ curve ensures optimal motor performance (Avsar et al., 2024b). As seen in Figure 8, the magnetic flux densities lie in the knee region of the B-H curve of the utilized steel material, indicating maximum efficiency without saturation. The current densities in the windings are shown in Figure 9, with an average current density of 3.7 A/mm^2 and a maximum of 4.41 A/mm^2, demonstrating that the motor operates within safe limits even under high loads.

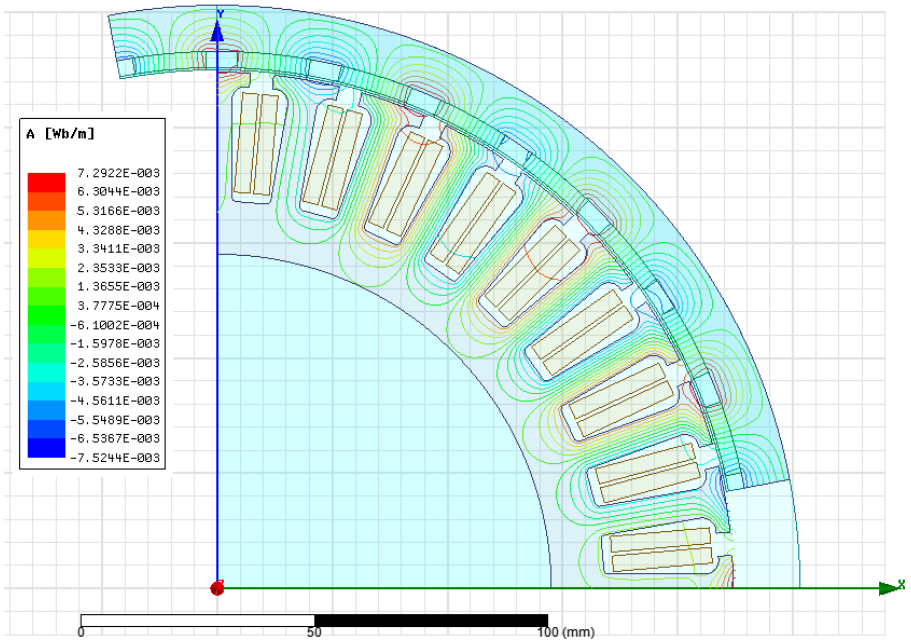

Figure 7. Magnetic vector potential (A:Wb/m)

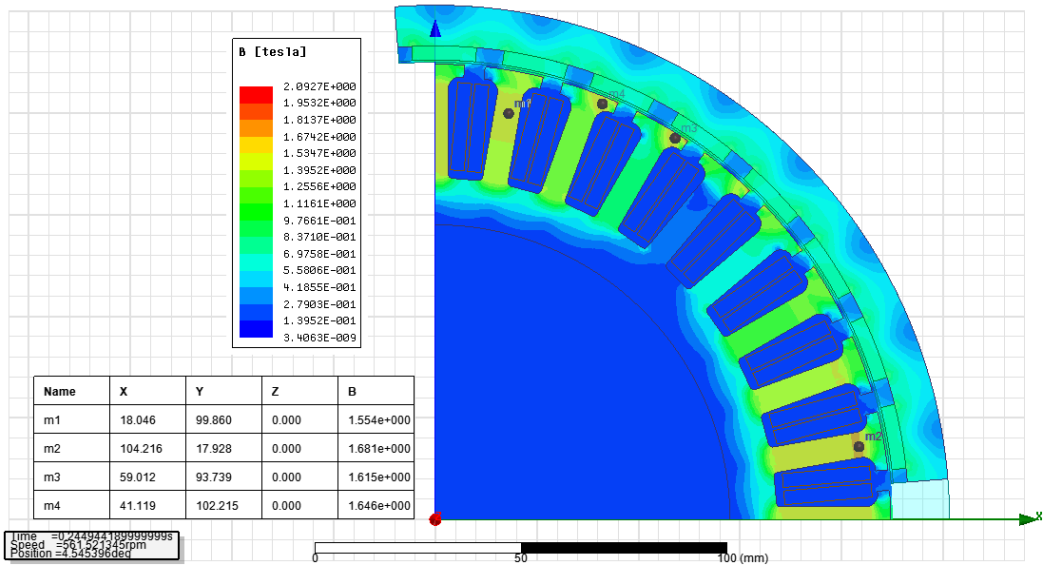

Figure 8. Magnetic flux density (B:Tesla)

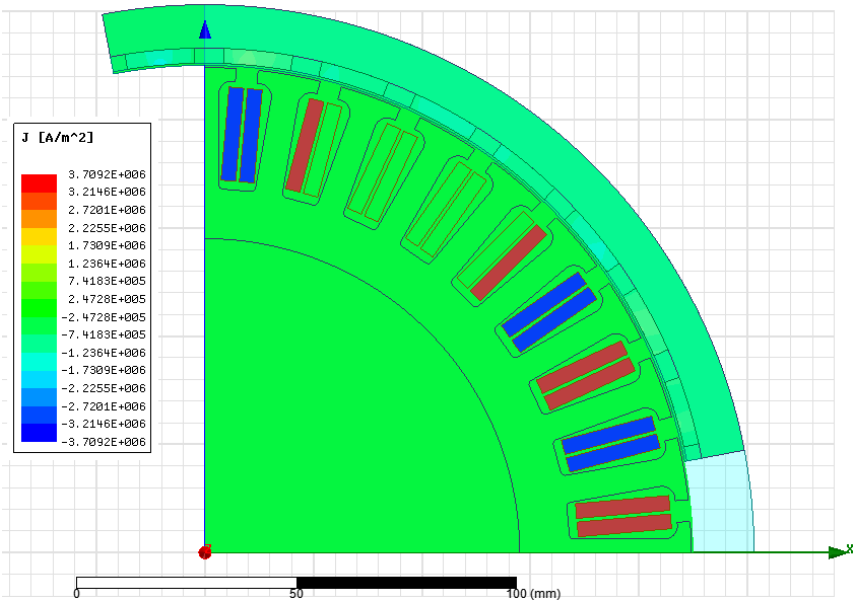

Figure 9. Electric current density (J:A/m^2)

Figure 10 shows the motor's RMS current as 31.9 A, while Figure 11 indicates a nominal efficiency of 90.5%. The output torque graph in Figure 12 reveals a torque ripple of ±4.3 Nm, equivalent to 11.83% of the nominal output torque of 36.35 Nm, which is within acceptable limits for BLDC motors.

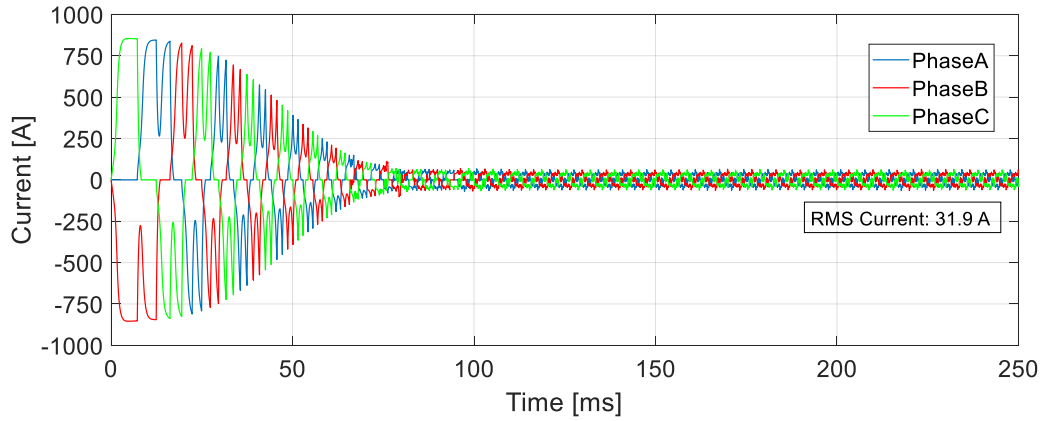

Figure 10. Time-current graph

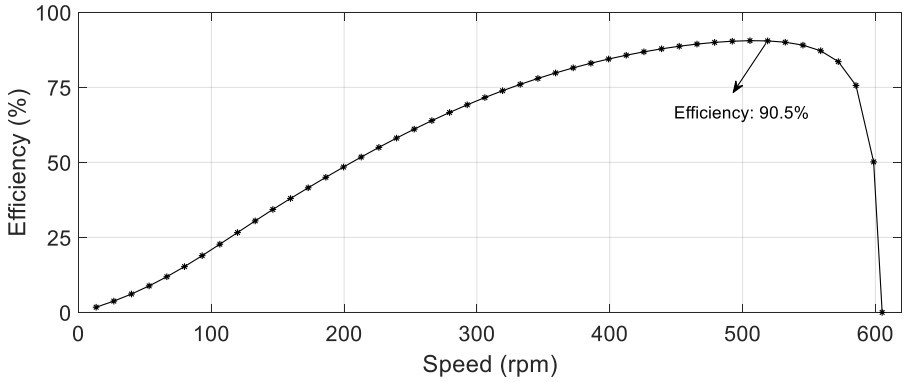

Figure 11. Speed-efficiency graph

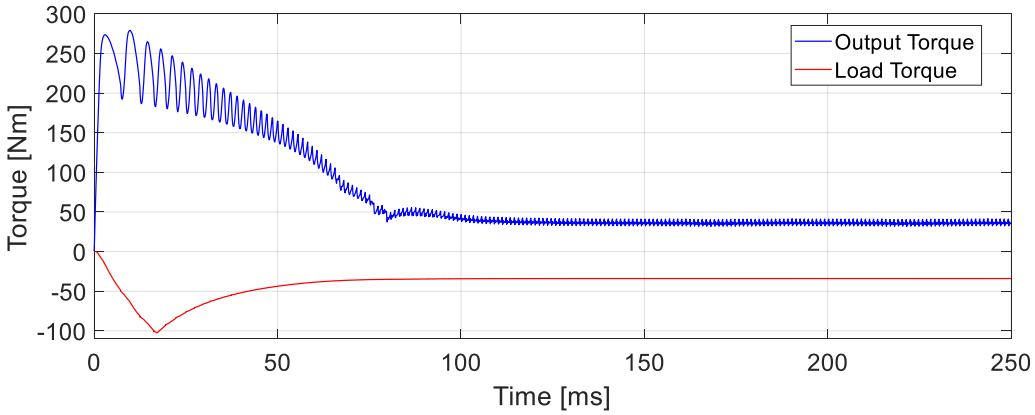

Figure 12. Time-torque graph

In electric motors, windings experience the highest temperatures. Since the magnets are not in direct contact with the windings and rotate with the rotor, their temperatures remain lower than the stator windings. Thus, the maximum winding temperature reflects the motor's maximum internal temperature (Soyaslan, 2020).

Thermal analyses were conducted by linking Ansys Maxwell and Ansys Workbench (Bazazian, 2022). Results obtained from the Ansys Maxwell 2D module were transferred to the Steady-State Thermal module in Ansys Workbench. Thermal properties of materials were defined, contact surfaces specified, and heat generation data and mesh structures imported from Maxwell. The ambient temperature was set to 40°C for the analysis. At full load, the motor reached a steady-state temperature, with results shown in Figure 13. Maximum temperatures of 65.79°C for the windings and 51.75°C for the magnets indicate safe thermal operation.

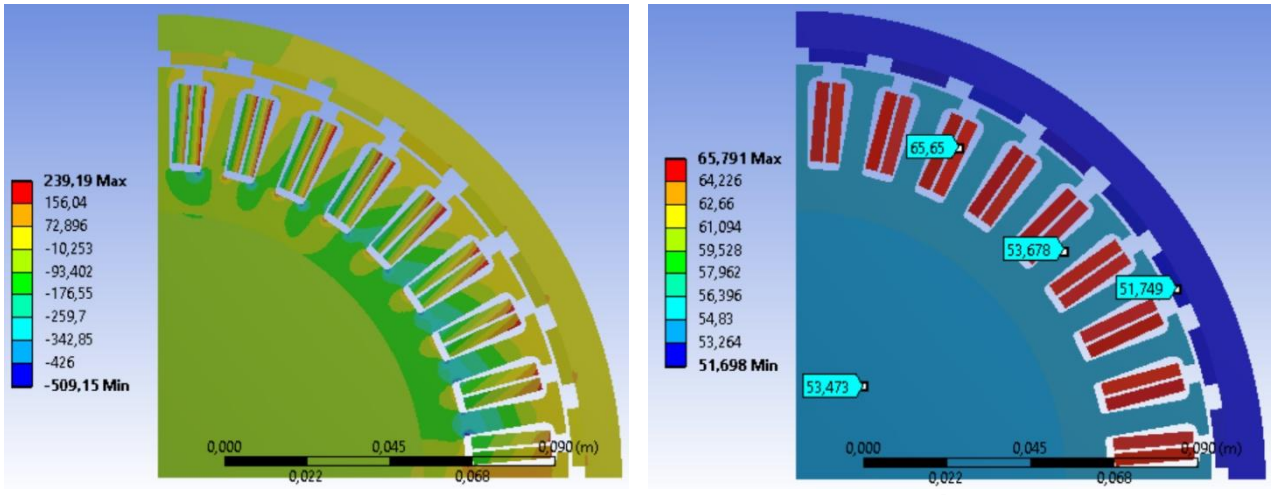

a) b)

Figure 13. a) Directional heat flux, b) Temperature distribution

3.1 Production and Test Results

Following the electromagnetic and thermal validations, the 3D design and technical drawing for direct wheel drive were created, as shown in Figure 14. An aluminum hub was used between the motor shaft and stator core. Slots for the magnets were machined into the rotor via wire erosion, ensuring consistent spacing between magnets. The motor's nameplate values are provided in Table 4, and production images of the motor components are displayed in Figure 15.

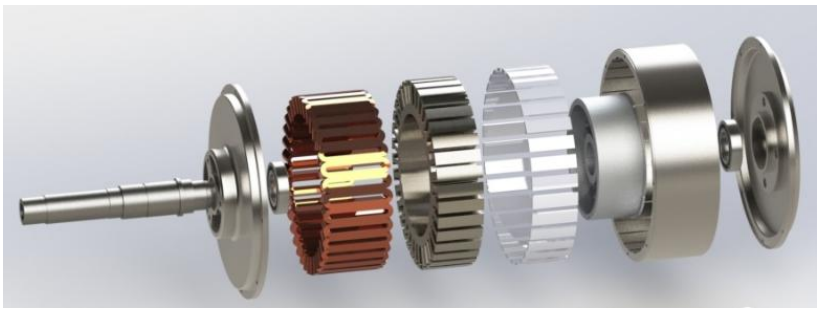

a)

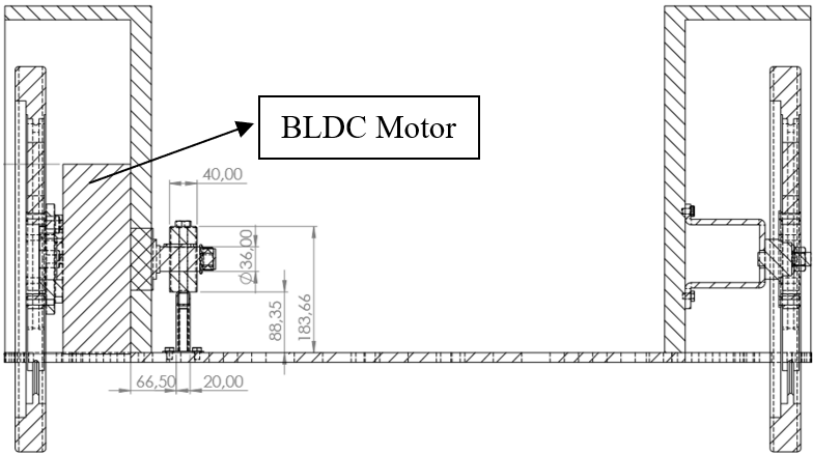

b)

Figure 14. a) 3D model of the BLDC motor, b) Placement of the motor on the EV

Table 4. BLDC motor nameplate values

Parameter	**Value**
Power (kW)	2
Voltage (V)	72
Efficiency (%)	90.5
Rated torque (Nm)	36.35
Rated speed (rpm)	561.5
Rated rms current (A)	31.9
Slot number	36
Pole number	32
Winding type	Double layer, Y
Magnet type	N40SH
Magnet thickness (mm)	3.5
Stator material	M350-50A
Output diameter (mm)	253
Stack length (mm)	55

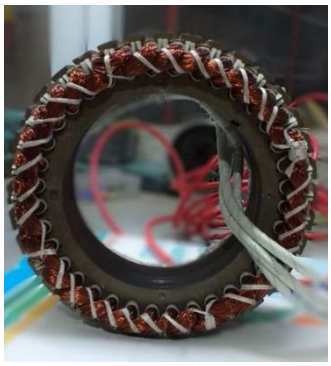

Figure 15. Production of the motor parts

After manufacturing the motor, load tests were conducted on the test bench shown in Figure 16. The test results were compared with the analysis results, demonstrating agreement in Figure 17. Finally, the motor mounted on the electric vehicle is shown in Figure 18. Track tests confirmed the vehicle's operation at expected current values based on road slope. The test results showed that the nominal efficiency value matched the analysis results and was found to be 91%. Also it has been observed that the motor remained within its thermal limits under full load conditions. The differences between the test results and the analysis results stem from the sensitivity of the experimental setup. The small deviations in the obtained results are evaluated within the defined acceptable tolerance ranges.

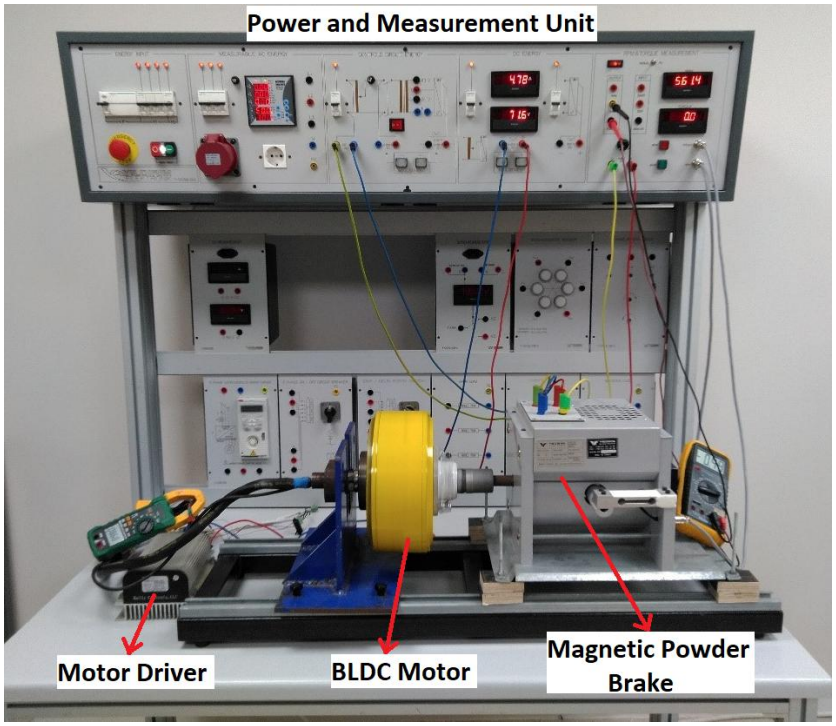

Figure 16. Motor loading tests

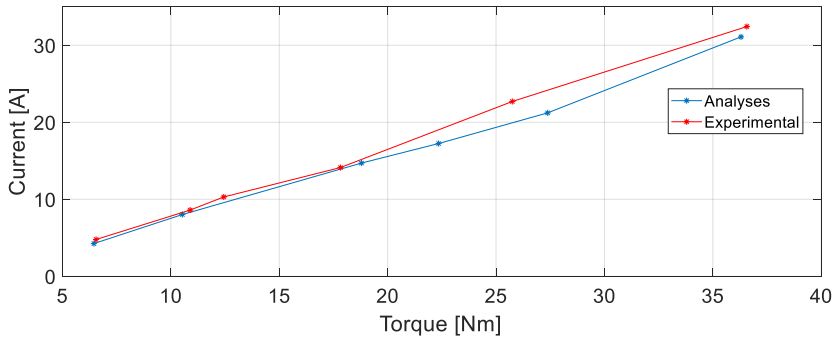

Figure 17. Comparison of analysis and test results

Figure 18. EV with BLDC motor mounted

4. CONCLUSIONS

This study presented the design, production, and validation of a 2 kW outer rotor BLDC motor specifically developed for light electric vehicle applications. The motor was integrated into the vehicle's wheel rim, optimizing weight distribution and improving system efficiency. A dynamic model of the vehicle was constructed to determine the required motor specifications, taking into account the vehicle's characteristics and predefined racetrack conditions. The motor was designed with a 36/32 slot-pole ratio, and the stator tooth tip gap was optimized to minimize cogging torque and improve overall motor performance. Analytical and 2D finite element analyses validated the design, demonstrating that the average magnetic flux density and current density values were kept within safe operational limits. Additionally, parametric optimization yielded an optimal stator tooth tip gap of 5 mm, effectively reducing cogging torque. Thermal analysis confirmed the motor’s capability to operate within acceptable temperature ranges, with maximum stator winding temperatures of 65.79 °C and magnet temperatures of 51.75 °C under full load conditions.

Experimental tests of the prototype motor corroborated the analytical and simulation results, achieving a peak efficiency of 90.5% and a rated torque of 36.35 Nm. Torque ripple and temperature performance were within acceptable limits, ensuring reliability and smooth operation. The study highlights the importance of integrating electromagnetic, mechanical, and thermal optimization techniques in motor design to enhance efficiency and performance in light electric vehicle applications. Future work could explore advanced control strategies and alternative cooling solutions to further optimize the performance of outer rotor BLDC motors in similar applications. With

advanced control techniques, motor operation can be made more efficient and quieter. These techniques optimize the motor's torque and speed in real-time, minimizing unwanted vibrations and acoustic noise. Additionally, cooling systems can reduce the motor sizes, and current densities can be improved. These advancements enhance the motor's thermal management, allowing it to operate safely at higher current densities while maintaining optimal temperatures, thus enabling more compact and powerful motor designs for high-performance applications such as electric vehicles. This research contributes to the development of compact, high-efficiency motor solutions, paving the way for innovative designs in the electric vehicle industry.

5. ACKNOWLEDGEMENTS

The authors would like to thank to Sakarya University of Applied Sciences, SUBU-TETRA Electromobile Team and its members for their support.

6. CONFLICT OF INTEREST

Authors approve that to the best of their knowledge, there is not any conflict of interest or common interest with an institution/organization or a person that may affect the review process of the paper.

7. AUTHOR CONTRIBUTION

Mücahit SOYASLAN contributed to the Determining the concept and/or design process of the research. Mücahit SOYASLAN contributed to the Management of the concept and/or design process of the research. Mohamad BAZAZIAN contributed to the Data Collection. Mücahit SOYASLAN, Mohamad BAZAZIAN, and Osman ELDOĞAN contributed to the Data analysis and interpretation of the results. Mücahit SOYASLAN contributed to the Preparation of the manuscript. Mohamad BAZAZIAN and Osman ELDOĞAN contributed to the Critical analysis of the intellectual content. Mücahit SOYASLAN, Mohamad BAZAZIAN, and Osman ELDOĞAN contributed to the Final approval and full responsibility.

8. REFERENCES

Akar M., Eker M., Akın F., BLDC motor design and application for light electric vehicle. Afyon Kocatepe University, Journal of Science and Engineering 21.2, 326-336, 2021.

Aliyadin A. Z., Purwadi A., Hidayat S., Performance Analysis and Design of 250 Watt Outer Rotor BLDC Motor for Urban Electric Bicycles, 2022 7th International Conference on Electric Vehicular Technology (ICEVT), Bali, Indonesia, 2022, pp. 195-199, doi: 10.1109/ICEVT55516.2022.9925011.

Anuja T.A., Doss M.A.N., Reduction of Cogging Torque in Surface Mounted Permanent Magnet Brushless DC Motor by Adapting Rotor Magnetic Displacement. Energies 14 (10), 2861, 2021. https://doi.org/10.3390/en14102861.

Anuja T.A., Doss M.A.N., Senthilkumar R., Rajesh K.S., Brindha R., Modification of Pole Pitch and Pole Arc in Rotor Magnets for Cogging Torque Reduction in BLDC Motor, IEEE Access, vol. 10, pp. 116709-116722, 2022. doi: 10.1109/ACCESS.2022.3217233.

Avsar Y., Fenercioglu A., Soyaslan M., Design Optimization of PM Synchronous Motor: Rail Mounted Belt Drive Elevator Systems, IEEE Transactions on Industry Applications, vol. 60, no. 1, pp. 301-311, Jan.-Feb. 2024b. doi: 10.1109/TIA.2023.3311781.

Avsar, Y., Soyaslan, M., & Fenercioglu, A. PMSM Design for Elevators: Determination of the Basic Topology Affecting Performance. The Eurasia Proceedings of Science Technology Engineering and Mathematics, 28, 342-351, 2024a. https://doi.org/10.55549/epstem.1523527

Bazazian, M., Design of an outer rotor brushless dc motor used in electric vehicles, Master Thesis. Dept. of Mechatronics Eng., Sakarya University of Applied Sciences, Graduate Education Institute, Sakarya, 2022.

Cabuk, A. S., Saglam, S., & Ustün, Ö., Investigation on efficiency of in-wheel BLDC motors for different winding structures. Journal of the Faculty of Engineering and Architecture of Gazi University, 34(4), 1975-1985, 2019.

Cagıslar A. S., İn S., Tiryaki H., Effects of Magnet Type and Thickness on Outer Rotor Brushless Direct Current Motor Designed by Calculating the Required Motor Power for an Electric Vehicle Prototype. Erzincan University Journal of Science and Technology 13(3), 1025-1041, 2020. https://doi.org/10.18185/erzifbed.707837.

Chawrasia S.K., Das A., Chanda C.K., Banerjee S., Design, analysis and comparative study of Hub motor for an electric bike. Michael Faraday IET International Summit 2020a MFIIS, pp. 242–247, 2020. https://doi.org/10.1049/icp.2021.1179.

Doss M., Mohanraj K., Vakesan K., Karthik K., Reduction of Cogging Torque by Adapting Bifurcated Stator Slots and Minimization of Harmonics and Torque Ripple in Brushless DC Motor, International Journal of Power Electronics and Drive Systems (IJPEDS), 7(3), 781, 2016. https://doi.org/10.11591/ijpeds.v7.i3.pp781-789.

Gürdal O., Elektrik Makinalarının Tasarımı, Atlas Yayın Dağıtım, İstanbul, 2001.

Hussain M., Ulasyar A., Sheh Zad H., Khattak A., Nisar S., Imran K., Design and Analysis of a Dual Rotor Multiphase Brushless DC Motor for its Application in Electric Vehicles, Eng. Technol. Appl. Sci. Res., vol. 11, no. 6, pp. 7846–7852, Dec. 2021.

Jhankal T., Design and Cogging Torque Reduction of Radial Flux Brushless DC Motors with Varied Permanent Magnet Pole Shapes for Electric Vehicle Application, Transactions on Energy Systems and Engineering Applications, 4(2), 1-13, 2023. https://doi.org/10.32397/tesea.vol4.n2.535.

Karthick K., Ravivarman S., Samikannu R., Vinoth K., Sasikumar B., Analysis of the Impact of Magnetic Materials on Cogging Torque in Brushless DC Motor, Advances in Materials Science and Engineering, 2021, 1-10. https://doi.org/10.1155/2021/5954967.

Kim Y., Yang B., Kim C., Noise Source Identification of Small Fan-BLDC Motor System for Refrigerators," International Journal of Rotating Machinery, 2006(1). https://doi.org/10.1155/ijrm/2006/63214.

Krasopoulos C.T., Beniakar M.E., Kladas A.G., Velocity and Torque Limit Profile Optimization of Electric Vehicle Including Limited Overload, IEEE Transactions on Industry Applications, vol. 53, no. 4, pp. 3907-3916, July-Aug. 2017, doi: 10.1109/TIA.2017.2680405.

Lee B.-C., Song C.-H., Kim D.-H., Kim K.-C., Study on Process Derivation and Characteristic Analysis for BLDC Motor Design Using Dual Rotor Structure with High Torque Density. Energies 2020, 13, 6745. https://doi.org/10.3390/en13246745.

Leitner S., Gruebler H., Muetze A., Cogging Torque Minimization and Performance of the Sub-fractional hp BLDC Claw-pole Motor, IEEE Transactions on Industry Applications, 55(5), 4653-4664, 2019. https://doi.org/10.1109/tia.2019.2923569.

Mandasari D., Design and Optimization of Brushless DC Motor for Electric Boat Thruster, Evergreen, 10(3), 1928-1937, 2023. https://doi.org/10.5109/7151773.

Minh D., Quoc V., Huy P., Efficiency Improvement of Permanent Magnet BLDC Motors for Electric Vehicles," Engineering Technology & Applied Science Research, 11(5), 7615-7618, 2021. https://doi.org/10.48084/etasr.4367.

Murali, N., Ushakumari, S., Mini, V. P., & Varghesee, A. T., Sizing and Performance Analysis of an Electric Motor in an E-rickshaw. IEEE International Conference on Power Systems Technology (POWERCON) (pp. 1-6), Sep., 2020.

Murat N., Ushakumari S., Mini V.P., Varghesee A.T., Sizing and Performance Analysis of an Electric Motor in an E-rickshaw, 2020 IEEE International Conference on Power Systems Technology (POWERCON), pp. 1-6, Sept. 2020.

Niessen F., Winding Scheme Calculator, Erişim: 31 Ekim 2019, http://www.bavaria-direct.co.za/scheme/calculator/.

Ocak C., Tarimer I., Dalcali A., Uygun D., Investigation effects of narrowing rotor pole embrace to efficiency and cogging torque at PM BLDC motor. TEM Journal 5(1), 25, 2016.

Ozupak Y. Efficiency analysis of BLDC motor for variable magnetic field. MANAS Journal of Engineering,10(1):105-109, 2022. doi:10.51354/mjen.1097668

Ozupak, Y., & Çınar, M. Design and Co-Analysis of A Permanent Magnet Brushless DC Motor By Using Clonal Selection Principle Based Wound Healing Algorithm and Ansys-Maxwell. Gazi University Journal of Science Part A: Engineering and Innovation, 10(4), 499-510, 2023. https://doi.org/10.54287/gujsa.1371904

Rupam, S. Marwaha, Mitigation of Cogging Torque for the Optimal Design of BLDC Motor, IEEE 2nd International Conference On Electrical Power and Energy Systems (ICEPES), Bhopal, India, pp. 1-5, 2021, doi: 10.1109/ICEPES52894.2021.9699544.

Smółka, K. and Firych-Nowacka, A., Comparison of the design of 3-pole bldc actuators/motors with a rotor based on a single permanent magnet. Sensors, 22(10), 3759, 2022. https://doi.org/10.3390/s22103759

Soyaslan M., Avşar Y., Fenercioğlu A., Eldoğan O., Cogging Torque Reduction in External Rotor PM Synchronous Motors by Optimum Pole Embrace, 3rd International Symposium on Multidisciplinary Studies and Innovative Technologies (ISMSIT), Ankara, Turkey, 2019, pp. 1-4, doi: 10.1109/ISMSIT.2019.8932915.

Soyaslan M., Design of an External Rotor Permanent Magnet Synchronous Motor for Elevator Traction Systems, PhD Thesis, Dept. of Mechatronics Eng., Sakarya University, Institute of Natural Sciences, Sakarya, 2020.

Soyaslan, M., External Rotor BLDC Motor Design for a Light Electric Vehicle: 24 Slot/22 Pole Combination, 18th Conference on Electrical Machines, Drives and Power Systems (ELMA), Varna, Bulgaria, pp. 1-4, 2023, doi: 10.1109/ELMA58392.2023.10202463

Tosun, O., Serteller, N.F.O., The Design of the Outer-Rotor Brushless DC Motor and an Investigation of Motor Axial-Length-to-Pole-Pitch Ratio. Sustainability 2022, 14, 12743. https://doi.org/10.3390/su141912743.

Vadde A., Sachin S., Influence of Rotor Design in BLDC Motor for Two-Wheeler Electric Vehicle, 1st International Conference on Power Electronics and Energy (ICPEE), Bhubaneswar, India, 2021, pp. 1-6, doi: 10.1109/ICPEE50452.2021.9358520.

Zuki, N. A. M., Othman, R. N. F. K. R., Ahmad, S. R. C., & Shukor, F. A. A., Consideration of various constants in double stator permanent magnet brushless DC motor, International Journal of Applied Electromagnetics and Mechanics 63.1, 1-17, 2020.

JOURNAL of
MATERIALS and MECHATRONICS:A

e-ISSN 2717-8811
JournalMM, 2025, 6(1), 49-67
https://doi.org/10.55546/jmm.1619158

Araştırma Makalesi / Research Article

Numerical Investigation of the Flow Characteristics of Slurry Manure in a Digestion Tank

Emre Aşkın ELİBOL*

* Giresun University, Faculty of Engineering, Department of Mechanical Engineering, Giresun, Türkiye,
ORCID ID: https://orcid.org/0000-0001-8573-6065, emre.elibol@giresun.edu.tr

Geliş/ Received: 13.01.2025; **Revize/Revised:** 10.02.2025 **Kabul / Accepted:** 20.02.2025

ABSTRACT: Animal manure, agricultural wastes and sewage sludge are the most widely used organic wastes in biogas production. In our country, manure from animals such as cattle, sheep and chickens is an important source for biogas production. The mixing process in the digestion tank of the reactors used for biogas production significantly affects the biogas production efficiency. In recent years, it is known that the geometric structure of the digestion tank where the mixing process is carried out also affects this efficiency. In the mixing process, the most commonly used mixing type is mechanical mixing with the help of an propeller/impeller. Due to the high cost and time-consuming aspect of experimental studies, in recent years, the flow characteristics inside the digestion tank have been studied with the help of computational fluid dynamics software. In this context, velocity, turbulent eddy dissipation rate and turbulent kinetic energy distributions in the velocity range 50-175 rpm were investigated in a 60° slope digestion tank with a 6-flat-bladed impeller and the potential effects on biogas production were interpreted. The working fluid in the tank is considered by modeling dairy cattle manure as a non-Newtonian fluid. The results show that the velocity, turbulent kinetic energy and turbulent eddy dissipation rate distributions are generally more effective in the impeller region and at the impeller blade tips. In addition, as the impeller angular velocity increased from 50 rpm to 175 rpm, the amount of volume in the tank with velocity values higher than 0.1 m/s increased from 0.000323 m^3 to 0.00262 m^3.

Keywords: Biogas, Digester tank, Mechanical mixing, Renewable energy, CFD

*Sorumlu yazar / Corresponding author: emre.elibol@giresun.edu.tr
Bu makaleye atıf yapmak için /To cite this article

Elibol, E. A. (2025). Numerical Investigation of the Flow Characteristics of Slurry Manure in a Digestion Tank. Journal of Materials and Mechatronics: A (JournalMM), 6(1), 49-67.

1. INTRODUCTION

Anaerobically digesting organic waste is an economical solution for the sustainable use of energy. The mixing process is an important operation that homogenizes the anaerobic bacteria, nutrients, and temperature inside the reactor digestion tank in order to improve biogas production. Among the most common mixing methods are gas mixing, mechanical mixing, and mechanical pumping; among these, it is known that mechanical mixing is the most efficient method (Wu, 2009). The mechanical mixing process is generally carried out in a closed cylindrical tank, commonly referred to as a digester, which has a large diameter-to-height ratio. To obtain a highly efficient mixing process on an industrial scale, testing different mixing regimes in the digester to understand the physical properties of the mixing is quite costly economically. Therefore, in the study of the mixing performance of full-scale anaerobic digestion tanks, utilizing computational fluid dynamics (CFD) software is considered a highly suitable approach in terms of both cost-effectiveness and time savings (Sadino-Riquelme et al., 2018). Moreover, visualizing the flow model of the mixing process carried out in a biogas reactor using CFD software can provide researchers with information about flow behavior (Wang et al., 2018). In the future, considering the increasing energy demand and consequently the demand for biogas as a renewable energy source, it is expected that interest in the mixing process technology occurring within the reactor digestion tank will also increase. Moreover, CFD has the capability to assist in the design of the reactor digestion tank and optimal impeller/mixer designs before the actual reactor manufacturing. In this sense, it is obvious that CFD softwares will continue to be a useful tool in the development of mixing technologies. To date, studies numerically examining the effects of a broad variety of impeller types, both with and without buffles, on mechanical mixing in the reactor digestion tank have been summarized in Table 1.

Table 1. Literature studies investigating flow characteristics in a reactor digestion tank

Study	Impeller type	Working fluid	Tank geometry	Buffle	Angular velocity	The parameter being examined	Main findings
(Wu, 2012)	Lightning A310 (3-pitched-bladed)	Non-Newtonian (cattle manure slurry)	Cylindrical	None	500 rpm	Effects of different sliding mesh methods on velocity distribution in Large Eddy Simulation.	Smagorinsky–Lilly, wall-adapting local eddy viscosity and kinetic energy transfer models have shown similar flow field results.
(Wu, 2011)	Lightning A310 (3-pitched-bladed) PMSL 3LS39 (3-pitched-bladed)	Non-Newtonian (cattle manure slurry)	Cylindrical	Exists	250-500 rpm	The effect of 6 different turbulence models on the flow coefficient.	In the cases where the total solid content (TS) = 7.5% and TS = 12%, the standard k-ε, RNG k-ε, and realizable k-ε models yielded higher mixing flow coefficients compared to the other models.
(Wu, 2010)	2-spiral-bladed	Non-Newtonian (cattle manure slurry)	Bulb-shaped Cylindrical	None	400-750 rpm	The difference has compared various turbulence models in different TSs in terms of mixing intensity levels.	It has been stated that the mixing density level (W/m^3) of the bulb-shaped tank geometry is more efficient compared to the cylindrical one.
(Wu, 2009)	2-spiral-bladed	Newtonian (water) Non-Newtonian (cattle manure slurry)	Cylindrical	None	216-410 rpm	The effect of the impeller's position inside the tank on the velocity distribution.	In the case of TS ≤ 5.4%, a homogeneous velocity distribution was observed for all examined cases.

Tablo 1. Literature studies investigating flow characteristics in a reactor digestion tank (continued)

Study	Impeller type	Working fluid	Tank geometry	Buffle	Angular velocity	The parameter being examined	Main findings
(Abu-Farah et al., 2010)	Rushton (6-flat-bladed)	Newtonian (Cyclohexane/water mixture)	Cylindrical	None	350-750 rpm	The effect of different impeller angular velocities on velocity distribution.	-It has been observed that the standard k-ε turbulence model is quite close to the experimental dispersion behavior. -It has been determined that the minimum impeller velocity for complete dispersion is approximately 550 rpm.
(Bridgeman, 2012)	2 pieces of 2-flat-bladed	Non-Newtonian (sewage slurry)	Cylindrical	None	20-200 rpm	-The effect of TS content on dead zone volume. -The effect of different impeller angular velocities on the velocity gradient.	-They have observed that as TS increases, the volume of the dead zone inside the tank also increases. -Even with the increase in impeller velocity from 100 rpm to 200 rpm, very little change has been observed in the turbulence characteristics of the flow field (1/s).
(Shen et al., 2013)	1 pieces of 2-pitched-bladed 2 pieces of 2-pitched-bladed 3 pieces of 2-pitched-bladed	Non-Newtonian (rice straw slurry)	Cylindrical	None	20-160 rpm	The effects of different impeller designs and numbers on the velocity and turbulence kinetic energy (TKE) distribution within the tank have been examined at different angular velocities.	-They stated that 3 pieces of 2-pitched-bladed impeller at 80 rpm provided better results in terms of the affected volume ratio in the tank. -They observed that the TKE increased from 0.014 m^2/s^2 to 0.02 m^2/s^2 as the angular velocity increased from 120 rpm to 160 rpm.
(Sindall et al., 2013)	4-flat-bladed	Non-Newtonian (sewage slurry)	Cylindrical	Exists (4 pieces)	50-200 rpm	Effects of angular velocity on the velocity gradient.	It has been stated that within the examined angular velocity range, the velocity gradient is less than 10 s^{-1} in 20%-85% of the tank.

Tablo 1. Literature studies investigating flow characteristics in a reactor digestion tank (continued)

Study	Impeller type	Working fluid	Tank geometry	Buffle	Angular velocity	The parameter being examined	Main findings
(Rasool et al., 2017)	Chemineer S-4 (4-bladed) 4-pitched-bladed Spiral-bladed	Newtonian (water)	Cylindrical	Exists (4 pieces)	60-135 rpm	The effect of the impeller type and angular velocity on the velocity distribution.	The pitched-bladed impeller has created a smaller weak mixing zone compared to the Chemineer impeller.
(Cao et al., 2018)	2 pieces of 3-pitched-bladed	Non-Newtonian (mud slurry)	Cylindrical Oval	None	10-40 rpm	The effect of tank geometry and angular velocity on velocity distribution and dead zone volume.	-In TS = 4% and 40 rpm conditions, they observed that the dead zone volume was smaller. -The results of both tank geometries are similar in terms of velocity distribution.
(Oates et al., 2020)	2 pieces of 3-pitched-bladed in addition to 1 pieces of 2-pitched-bladed Spiral-bladed	Non-Newtonian (water-glycerin mixture)	Cylindrical	None	2.5-12 rpm	The effects of different impeller designs and TSs on the velocity distribution and the affected volume ratio of the tank have been examined.	-The affected volume ratio of the tank is highest at 60%-98% (TS = 2.5%) when using a spiral-bladed impeller; it is highest at 12%-67% (TK = 5.4%) when using the other configuration.
(Servati and Hajinezhad, 2020)	4-flat-bladed	Non-Newtonian (mud slurry)	Cylindrical	Exists (4 pieces)	50-200 rpm	The effect of angular velocity on velocity, TKE, turbulence intensity, and velocity gradient distribution.	-The dead zone volume has been determined to be 10% within the examined angular velocity range. -The turbulence intensity distribution is similar at all angular velocities. - The turbulence intensity is less than 10%-20% in areas close to the tank walls; 20%-30% in the rotating part, and 10% in the other part.

Tablo 1. Literature studies investigating flow characteristics in a reactor digestion tank (continued)

Study	Impeller type	Working fluid	Tank geometry	Buffle	Angular velocity	The parameter being examined	Main findings
(Hoseini et al., 2021)	Rushton (6-flat-bladed) 6-V shape-bladed 6-U shape-bladed	Newtonian (water)	Cylindrical	Exists (4 pieces)	201-401 rpm	The effect of different impeller designs and angular velocities on the distribution of velocity, TKE, and turbulence eddy dissipation rate (TED).	-The highest TKE value was obtained in the Rushton impeller. - The highest TED ratio value was obtained for the 6-U shape-bladed impeller. -The highest radial velocity value was obtained in the Rushton impeller.
(Thakur et al., 2023)	1 pieces of 2-flat-bladed 2 pieces of 4-flat-bladed	Non-Newtonian (sewage slurry)	Cylindrical	None	50-600 rpm	The effect of different designs, different TSs, and different angular velocities on the dead zone volume and velocity distribution.	-They have observed that the volume of the dead zone decreases with the increase in angular velocity. -When using 2 pieces of 4-flat-bladed impeller, the maximum velocity value increases.
(Celik et al., 2024)	Rushton (6-flat-bladed)	Newtonian (water)	Cylindrical	None	25-100 rpm	The effect of tank geometry and impeller angular velocity on the distribution of velocity, TKE, TED ratio, and dead zone volume.	-In the case of using a 60° slope tank, they observed that the dead zone volume decreased and the maximum velocity, TKE, and TED ratio increased.

For biogas production, animal (cattle, sheep, poultry, slaughterhouse waste, etc.), plant, household, and industrial wastes are commonly used. These wastes are mixed with water to form a slurry and then transferred to the reactor digestion tank. Here, during the mechanical mixing process of the slurry, the slurry waste is broken down by bacteria present in an anaerobic environment, resulting in a mixture of methane, carbon dioxide, and other gases known as biogas. Since the slurry in question behaves like a non-Newtonian fluid, its thermophysical and rheological properties must be accurately defined in the computational domain generated by CFD. Otherwise, using the input parameters (impeller angular velocity, impeller geometry, tank geometry, etc.) in the simulation, the results obtained from the simulations cannot be expected in practice. However, of course, by defining a Newtonian fluid like water in the reactor digestion tank, it can be determined which type of impeller or which tank geometry is more effective with CFD. As seen in Table 1, some researchers have numerically examined the flow behavior inside the reactor slurry tank, modeling the working fluid as Newtonian, while others have modeled it as a non-Newtonian fluid. Although a very wide range of impeller angular velocities is generally adopted in the literature, simulations have mostly been conducted for the traditional 90° slope (cylindrical) tank geometry. However, in a very recent study (Celik et al., 2024), it is stated that the dead zone volume decreases when using a 60° slope tank geometry compared to using a traditional 90° slope (cylindrical) tank geometry. Additionally, no study has been found that addresses dairy cattle manure as the working fluid in terms of thermo-physical and rheological properties. The modeling of the working fluid in the reactor tank as a real manure slurry is another unique aspect of the current study, especially providing an insight for researchers working in the field of biogas.

In order to address the lack of literature on the subject, in this study, dairy cattle manure was modelled as a non-Newtonian fluid in a 60° slope and 4 buffles reactor digestion tank with a 6-flat-bladed Rushton impeller and the flow behaviour inside the tank at different impeller angular velocities was numerically investigated (with ANSYS Fluent software) in terms of velocity distribution, TKE and TED rate.

2. MATERIALS AND METHODS

2.1 Physical Model and Computational Domain

The geometric dimensions and schematic view of the reactor digestion tank and the 6-flat-bladed impeller inside it are shown in Figure 1. There are four buffles with the same geometric dimensions on the tank wall. The impeller is mounted accurately in the center of the tank. The 3D view of the computational domain consisting of the tank and impeller is shown in Figure 2. The choice to set the impeller's angular velocity at 175 rpm or below is due to the possible danger that increased velocities might harm microbiological organisms in practical terms, hence negatively affecting biogas production.

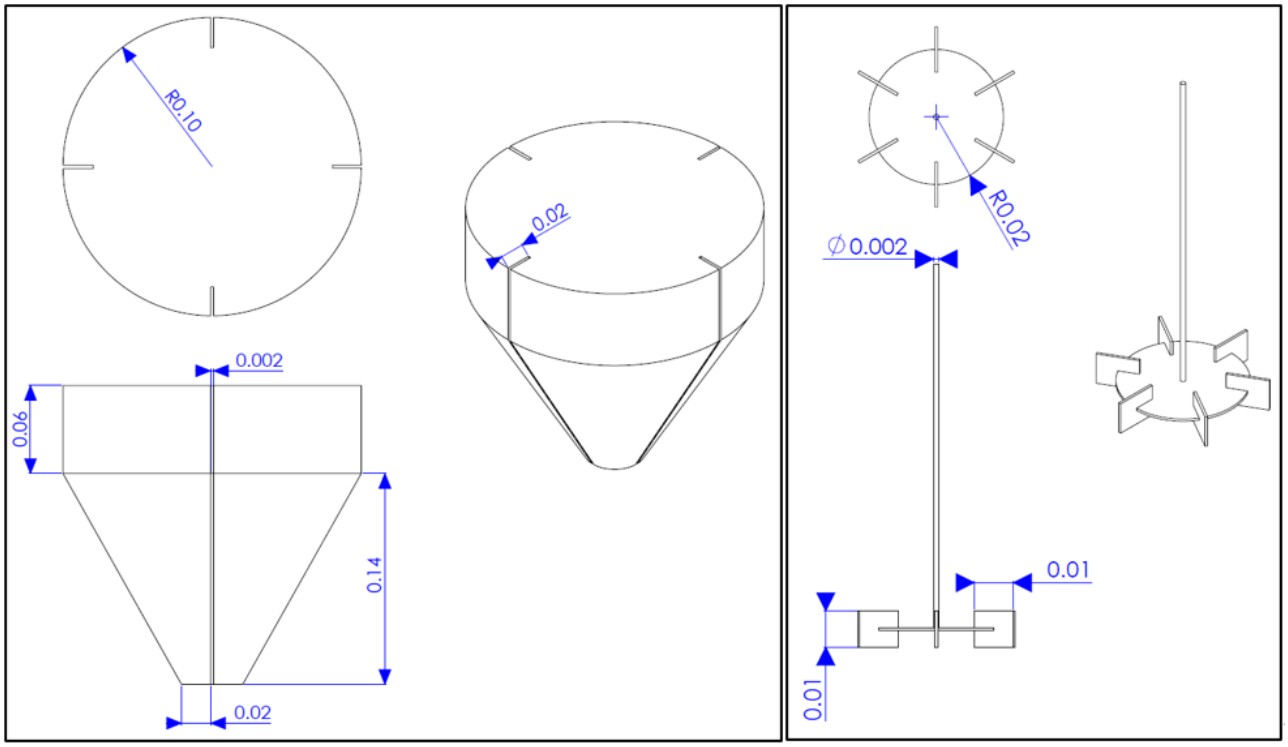

Figure 1. Geometric dimensions and schematic view of the tank and impeller

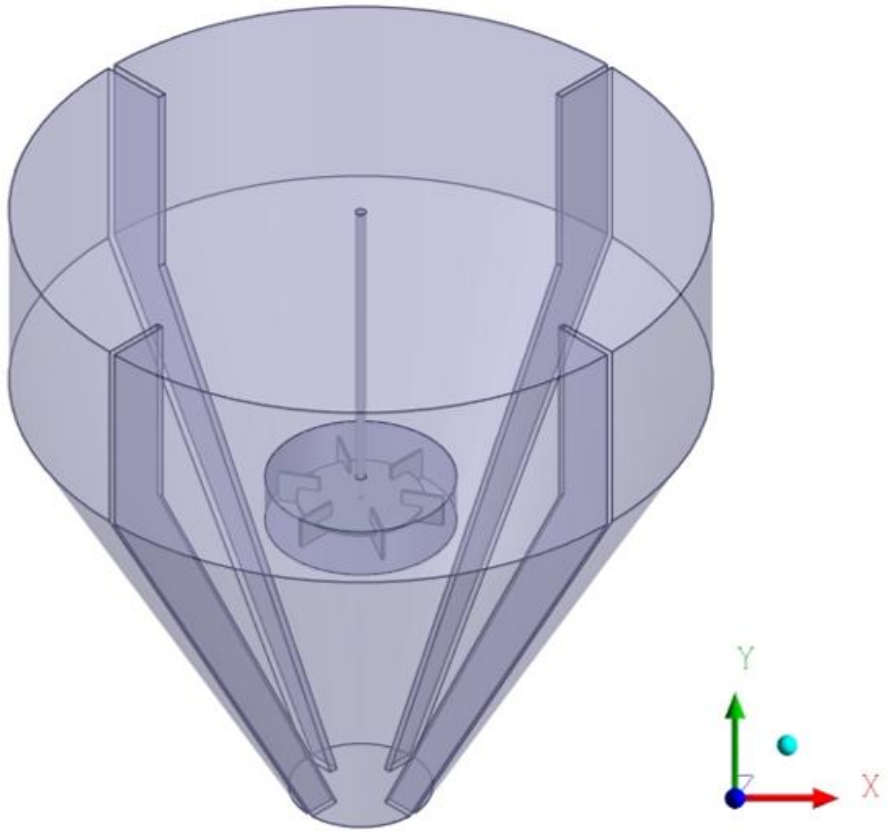

Figure 2. 3D view of the computational domain consisting of tank and impeller

2.2 Thermo-physical and Rheological Properties of Dairy Cattle Manure

The rheological and thermo-physical properties of the working fluid were calculated at T = 298 K and TS = 12%. Within the parameters of total solids ranging from 2.5% to 12% and temperatures stretching from 20°C to 60°C, dairy cattle manure exhibits characteristics of a pseudoplastic fluid. Given these parameters, it's possible to derive the consistency coefficient (K) and the behavior index through the following calculations (Achkari-Begdouri and Goodrich, 1992):

$$K = \left(8.722e^{(4830/T)+0.58319(TS)}\right) \times 10^{-10} \tag{1}$$

$$n = 0.6894 + 0.0046831(T - 273) - 0.042813(TS) \tag{2}$$

Here, the temperature, T, is in Kelvin and TS is in percent.

For the range of 10% to 50% of TS, the density of dairy cattle manure can be calculated as follows (Wang et al., 2019):

$$\rho = 0.0367(TS)^3 - 2.38(TS)^2 + 14.6(TS) + 1000 \tag{3}$$

2.3 Governing Equations

Since it was assumed that the temperature inside the reactor digestion tank is constant, the energy conservation equation was not taken into account. Additionally, it has been assumed that the flow inside the tank is steady. In this way, the continuity equation in the rotating reference frame of the reactor tank can be expressed as follows:

$$\nabla \cdot \vec{V} = 0 \tag{4}$$

With the same assumptions, the momentum equations (Mousavi et al., 2019) for the stationary part of the reactor tank (inertial reference frame) and the rotating part (rotating reference frame) are respectively shown in Equation 5 and Equation 6:

$$\rho\nabla\left(\vec{V}\vec{V}\right) = -\nabla p + \nabla \cdot \tau + \rho\vec{g} \tag{5}$$

$$\rho\nabla\left(\vec{V}\vec{V}\right) = -\nabla p + \nabla \cdot \tau + \rho\vec{g} + \vec{F} \tag{6}$$

The expression on the left side of Equation 5 and Equation 6 denotes the convective (local) acceleration. The initial, subsequent, and tertiary terms on the right side of both equations denote the pressure gradient, internal stress forces (viscous effects), and external body forces (attributable to gravitational influence), respectively. The fourth term of Equation 6, denoted as F, represents the force arising from the rotating reference frame (the added/body forces acting on the fluid).

The shear stress, τ, in Equation 5 and Equation 6 can be expressed as follows:

$$\tau = \mu_{eff}\left[\left(\nabla\vec{V} + \nabla\vec{V}^T\right) - \frac{2}{3}\nabla\vec{V}I\right] \tag{7}$$

2.4 Turbulence Model

The standard k-ε turbulence model was used to describe the turbulent flow inside the reactor tank. The turbulent kinetic energy (k) equation and turbulent eddy dissipation rate (ε) equation (Launder and Spalding, 1972; Versteeg and Malalasekera, 2007) for the standard k-ε turbulence model are as follows, respectively:

$$\rho\nabla\left(\vec{V}k\right) = \nabla\left(\frac{\mu_T}{\sigma_k}\nabla k\right) + G_k - \rho\varepsilon \tag{8}$$

$$\rho\nabla\left(\vec{V}\varepsilon\right) = \nabla\left(\frac{\mu_T}{\sigma_\varepsilon}\nabla\varepsilon\right) + \frac{\varepsilon}{k}(C_{1\varepsilon}G_k - C_{2\varepsilon}\rho\varepsilon) \tag{9}$$

Here, G_k is the turbulence due to shear (which can also be caused by mean velocity gradients), σ_k is the turbulence Prandtl number for k. σ_ε is the turbulence Prandtl number for ε, and $C_{1\varepsilon}$ and $C_{2\varepsilon}$ are the associated constants. The values of turbulence related constants $C_{1\varepsilon}$, $C_{2\varepsilon}$, σ_k and σ_ε in the standard k-ε turbulent model are 1.44, 1.92, 1.0 and 1.3, respectively. Also, μ_T is the eddy viscosity and can be expressed as:

$$\mu_T = \rho C_\mu \frac{k^2}{\varepsilon} \tag{10}$$

Here, C_μ equals to 0.09.

In the computational domain, a non-slip boundary condition was applied on the outer and lower surfaces of the tank. Furthermore, the rotating and stationary parts were automatically connected to each other (interfaces) by means of a general connection boundary condition.

2.5 Non-Newtonian Fluid Model

Slurry fluids with TS ≥ 2.5% can be defined as non-Newtonian pseudoplastic fluids. k-ε turbulence model was originally derived for Newtonian fluids. However, it can be extended to non-Newtonian fluids with some modifications. The 'power law' model is a simplified rheological model often used to describe the non-Newtonian behaviour of fluids, especially those exhibiting shear thinning or shear thickening behaviour. There are other mathematical models for modelling non-Newtonian fluids in the literature, such as Carreau (Carreau et al., 2021). In the 'power law' model, the inherent viscosity, μ, can be determined at each point in the flow field. The model for the inherent viscosity of dairy cattle manure in slurry form, which is considered as a non-Newtonian fluid, can be expressed as follows (Wu and Chen, 2008):

$$\mu = K(\dot{\gamma})^{n-1} \tag{11}$$

Here, K is the coefficient of consistency (a measure of the average viscosity of the fluid), $\dot{\gamma}$ is the shear per unit time and n is the behaviour/power law index (a measure of the deviation of the fluid from Newtonian behaviour). In this study, n < 1, i.e. the fluid class is shear-thinning (pseudoplastics) flow.

$$\mu_{eff} = \frac{\mu}{\mu_T} \tag{12}$$

2.6 Numerical Procedure and Mesh Structure

The computational domain is comprised of two distinct components: the inner section, which encompasses the rotating space, and the outer section, which contains the fixed volume of the remaining stirred tank reactor. To delineate the inner section, the Sliding Mesh (SM) technique was employed, resulting in the partitioning of the computational domain into two distinct components. One component engages with the stirrer, whereas the other remains in a state of rest. The COUPLED algorithm, one of the pressure-velocity conjugate solution options, was used since faster convergence was desired. The second order Upwind method was used to discretize the conservation equations, while the first order Upwind method was used to discretize the turbulence model equations. The residue criteria of the equations were set to 10^{-5}.

By comparing the results obtained from different mesh numbers, the optimal number of cells for the accurate solution was determined as 8165238. A sample tetrahedral mesh structure is shown in Figure 3.

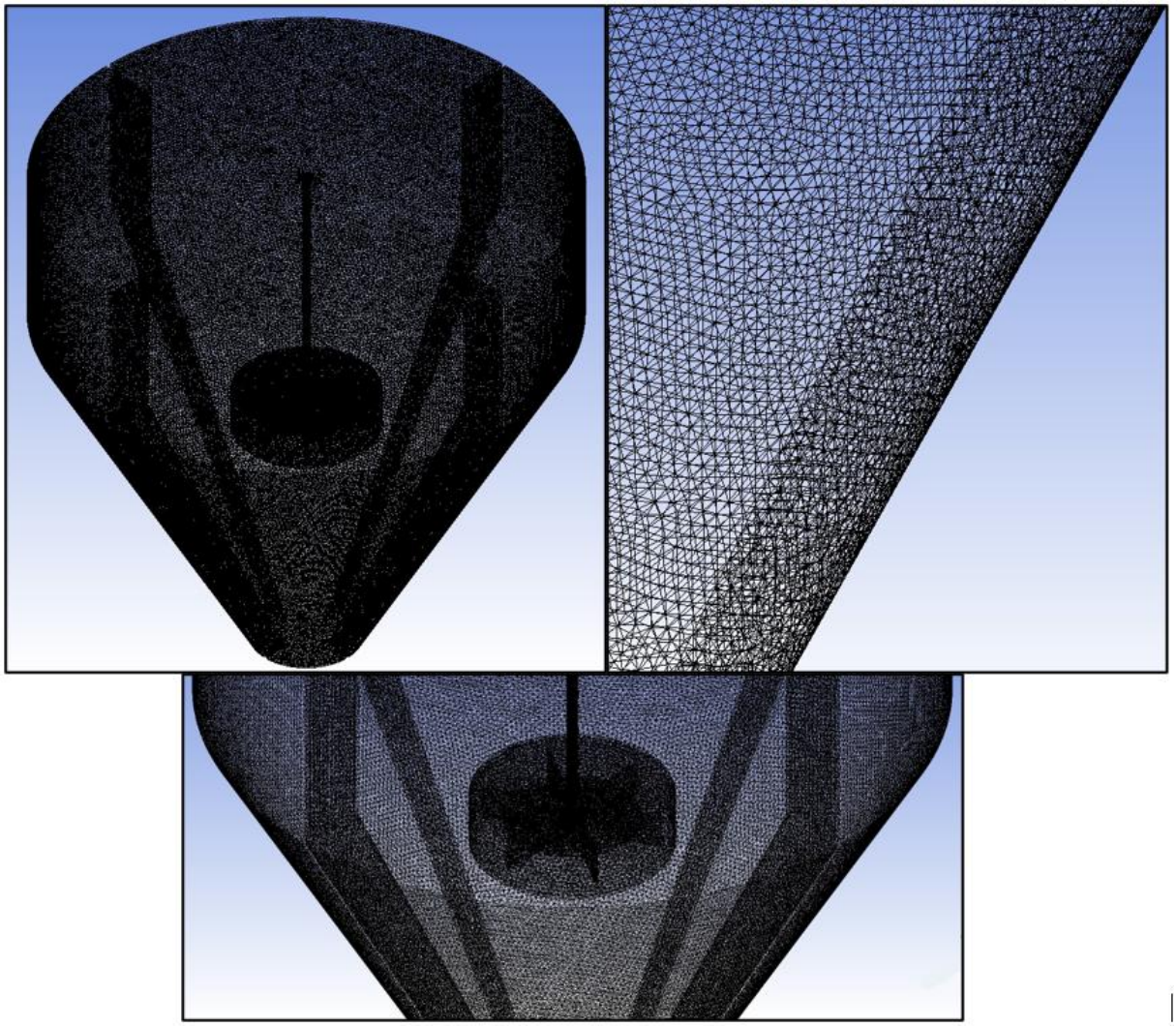

Figure 3. Mesh structure in an example solution

2.7 Model Validation

Before proceeding to the original part of the current study, the results were verified by adopting the same configurations based on the literature study (Celik et al., 2024) that was performed as a numerical. As shown in Figure 4, both studies are compared with regards to dead zone volume.

Accordingly, it is seen that the dead zone volume obtained in this study and the dead zone volume in the aforementioned literature study are very close to each other (≤ 10%).

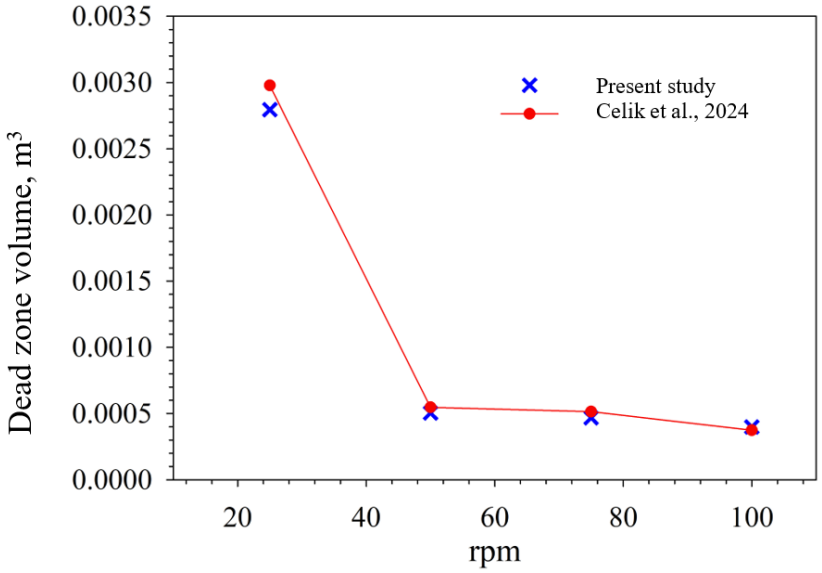

Figure 4. Variation of dead zone volume with respect to impeller angular velocity

3. RESULTS AND DISCUSSION

Figure 5 shows the velocity distribution obtained for different angular velocities of the impeller. Given that the fluid motion along the axial direction significantly influences the overall mixing within the digester tank, the axial velocity at the central vertical surface was selected to illustrate the simulation results. As expected, the maximum velocity value inside the reactor tank increases with increasing angular velocity. It can also be seen that the velocity variations in the impeller region are more effective, similar to those in the literature (Bridgeman, 2012). The maximum velocities in the selected plane are 0.608, 0.891, 1.200, 1.507, 1.818 and 2.126 m/s for 50, 75, 100, 125, 150 and 175 rpm angular velocities of the impeller, respectively. Near the bottom of the reactor digester tank, the velocity is lower, so much so that it is almost stagnant. The possible reason for this is that the non-Newtonian fluid in these areas is subjected to relatively low driving forces due to the impeller. In this case, stagnant regions are formed, resulting in a weak mixing effect in localised areas. Furthermore, the use of buffles on the tank walls has helped to reduce to some extent the low mixing zones that can occur on a tank wall without buffles (see literature studies (Hoseini et al., 2021; Celik et al., 2024)).

In order to understand whether an effective mixing is provided in the reactor tank, the velocity value of 0.1 m/s is determined as the critical velocity and the volume occupied by these regions in the reactor tank for 50 and 175 rpm values are presented in Figure 6. Accordingly, the volume with velocity values above the critical velocity for 50 rpm angular velocity is 0.000323 m^3 while this value is 0.00262 m^3 for 175 rpm angular velocity.

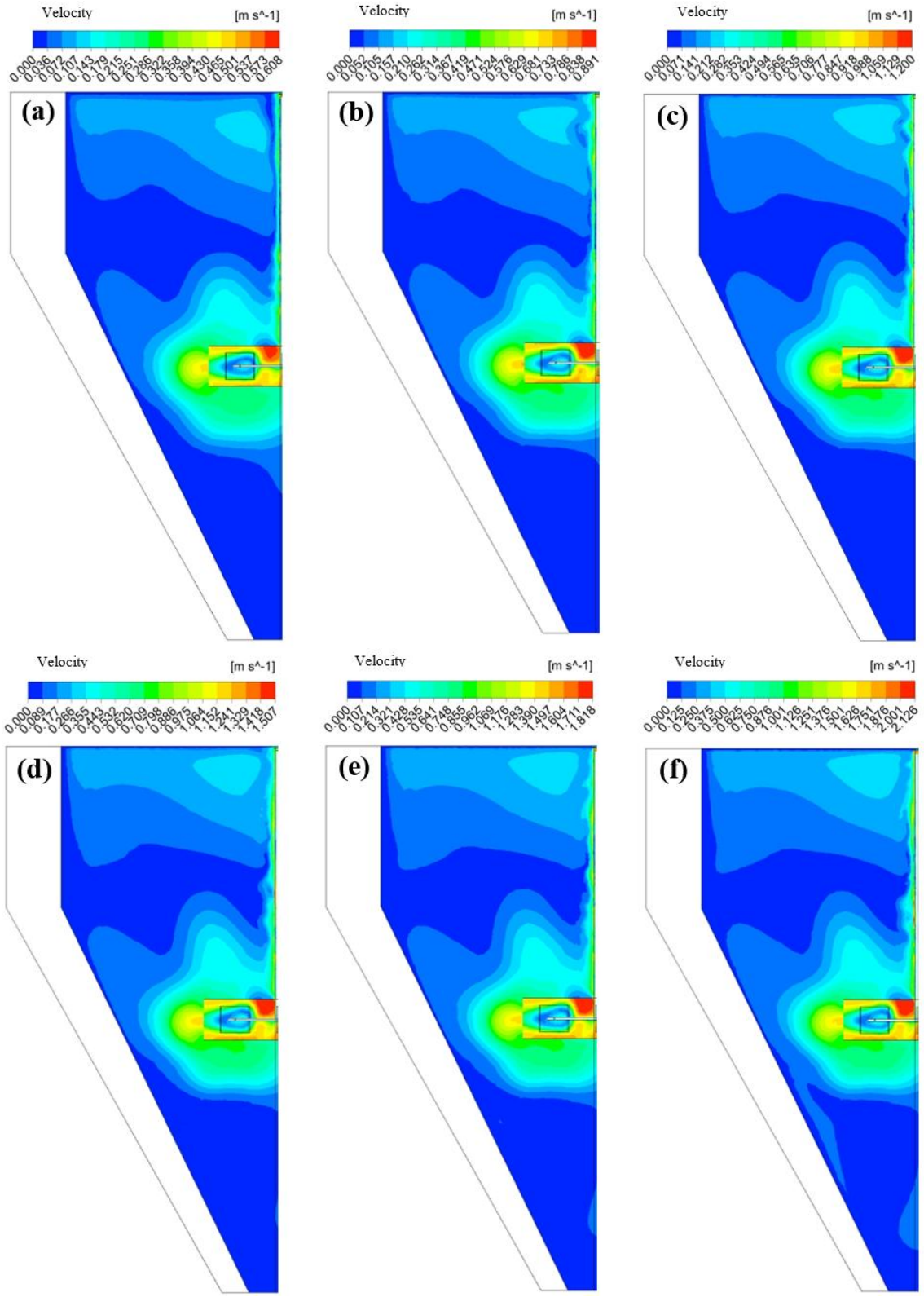

Figure 5. Side view of velocity distribution at different angular velocities: (a) 50 rpm, (b) 75 rpm, (c) 100 rpm, (d) 125 rpm, (e) 150 rpm and (f) 175 rpm

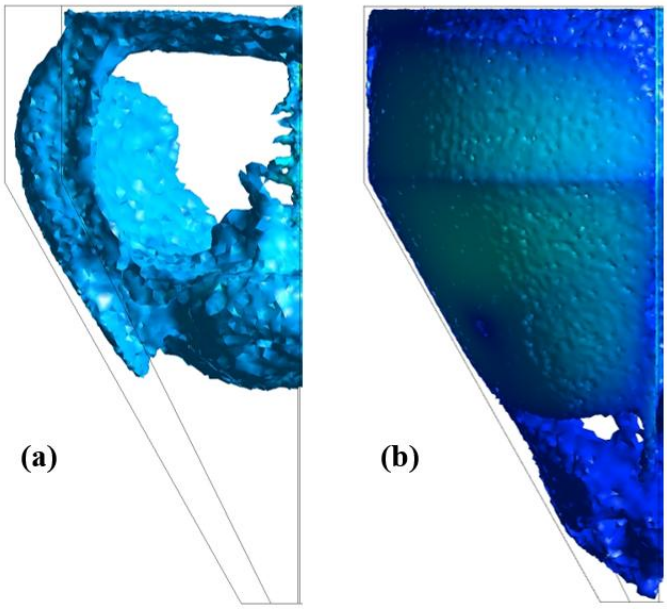

Figure 6. Side view of the volume inside the tank at different angular velocities where the velocity is higher than 0.1 m/s: (a) 50 rpm and (b) 175 rpm.

Figure 7 shows the turbulence kinetic energy distribution obtained for different angular velocities of the impeller. Similar to the velocity distribution, the TKE is more effective in the regions close to the impeller and the impeller shaft wall. In the other literature studies (Shen et al., 2013; Kong et al., 2014), it has also observed that the TKE distribution and magnitude are more intense and larger in the rotating part, i.e. close to the impeller, and become more sparse and smaller in the regions away from these regions. The maximum TKE in the selected plane is 0.063, 0.140, 0.140, 0.247, 0.382, 0.382, 0.535 and 0.715 m^2/s^2 for angular velocities of 50, 75, 100, 125, 150 and 175 rpm, respectively. The turbulence kinetic energy (TKE) equation incorporates physical terms that indicate TKE arises from the interaction of microbiological organisms within the slurry in the tank, influenced by turbulence during the mixing process. Consequently, in the analysis of flow characteristics, it is essential to consider the turbulent kinetic energy (TKE), as it directly influences the efficiency of mixing.

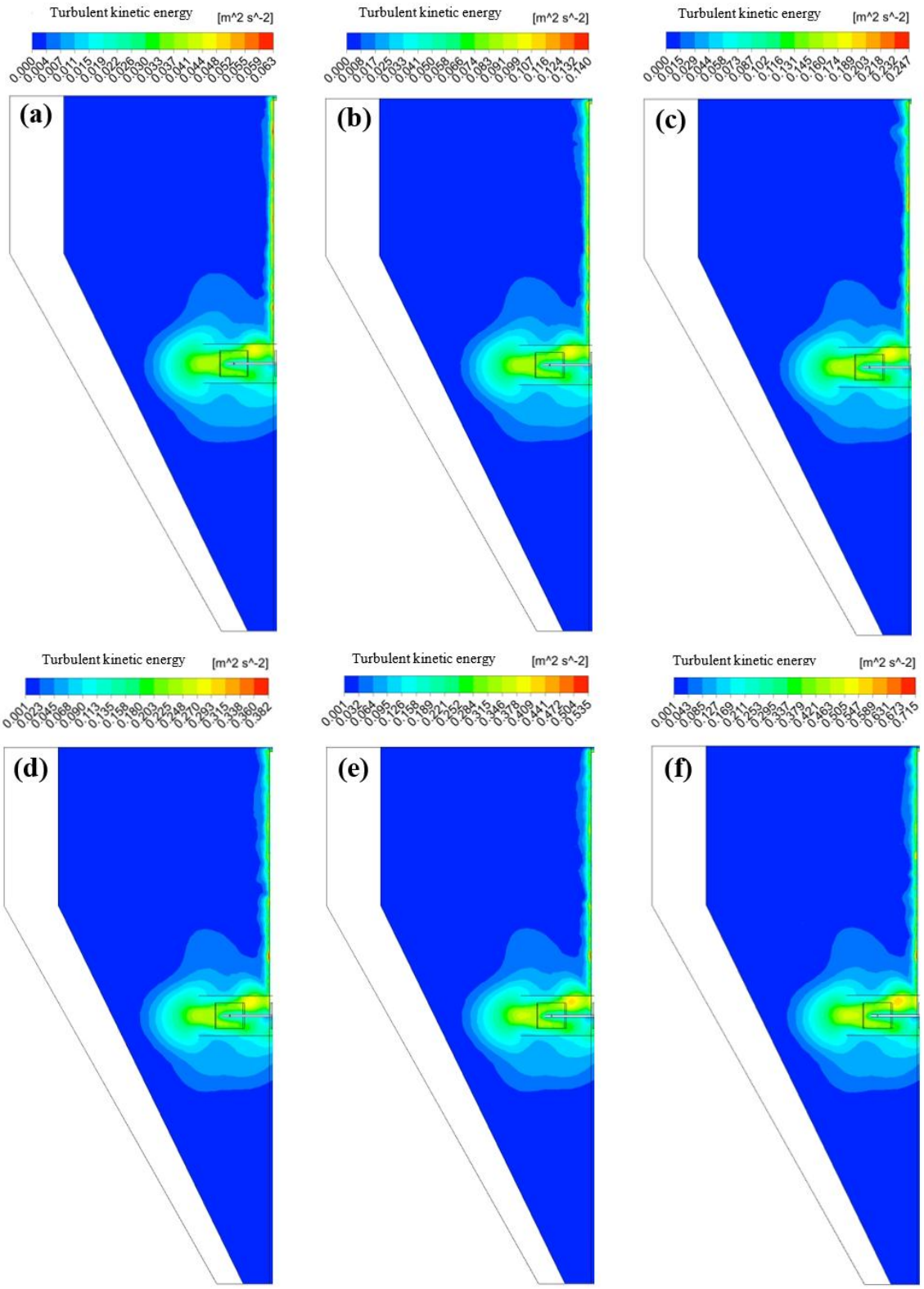

Figure 7. Side view of TKE distribution at different angular velocities: (a) 50 rpm, (b) 75 rpm, (c) 100 rpm, (d) 125 rpm, (e) 150 rpm and (f) 175 rpm.

Figure 8 shows the TED rate distribution obtained for the angular velocity range of 50-175 rpm. According to the figure, the maximum TED rate is 47.210, 112.634, 245.653, 456.622, 757.008 and 1169.555 m^2/s^3 for angular velocities of 50, 75, 100, 125, 150 and 175 rpm, respectively. The figure clearly illustrates the buffles used on the tank walls ensured that the TED rate distribution is effective in almost most regions in the considered plane. There are other studies in the literature (Fan et al.,

2015, Vilardi and Verdone, 2020) which observe that the TED rate distribution is more effective in the rotating region. Considering that a high TED rate is a measure of the rate at which TKE is converted into heat (internal energy) due to viscous losses (viscous dissipation), it can be considered that it can provide a positive effect for biogas production.

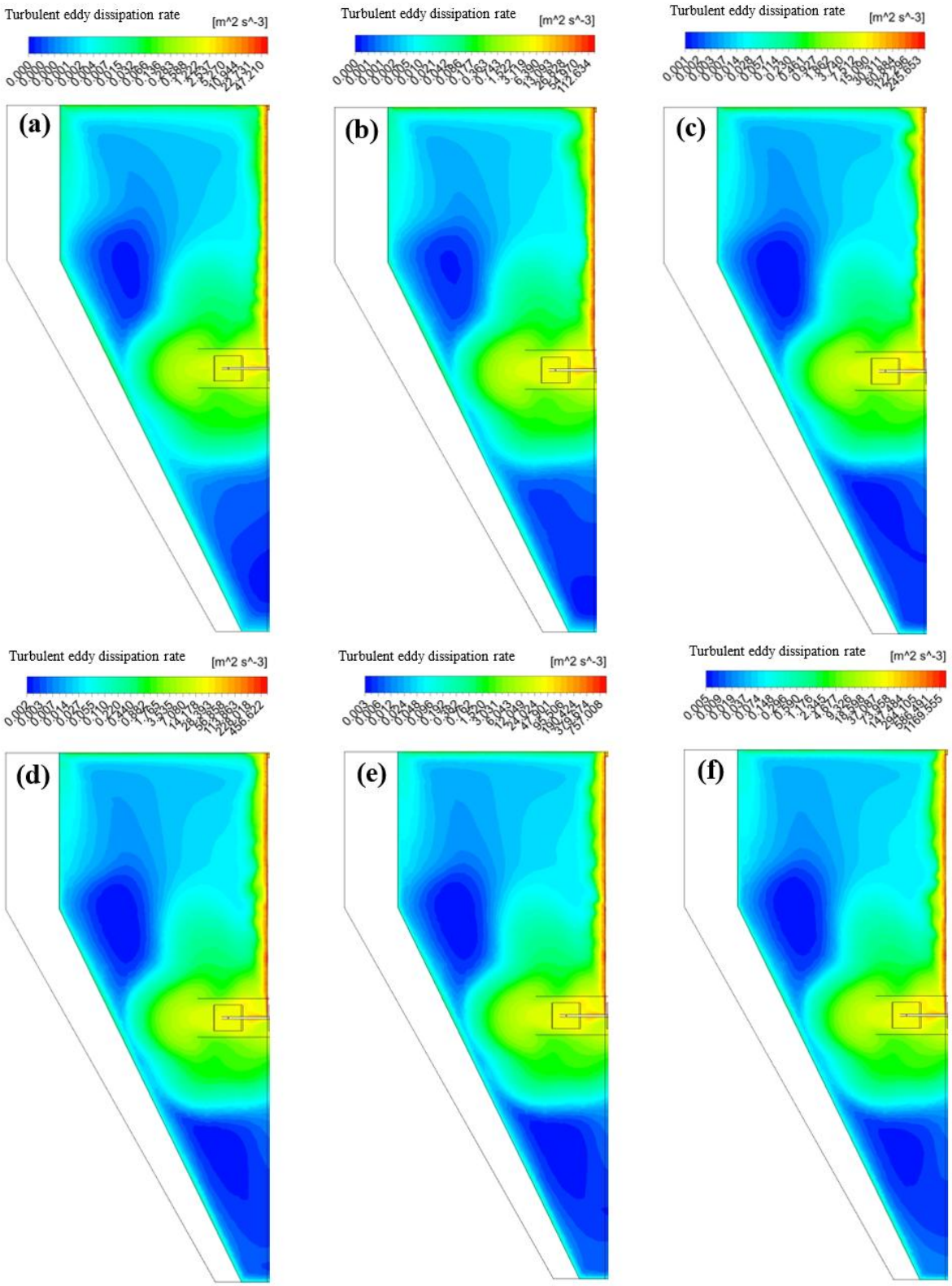

Figure 8. Side view of TED rate distribution at different angular velocities: (a) 50 rpm, (b) 75 rpm, (c) 100 rpm, (d) 125 rpm, (e) 150 rpm and (f) 175 rpm.

4. CONCLUSIONS

In this study, dairy cattle manure was modelled as a non-Newtonian fluid in a biogas reactor digester tank with a 60° slope and 4 buffles, and the flow behaviour in the tank at different angular velocities of a 6-flat-bladed Rushton impeller was numerically investigated. The thermo-physical and rheological properties of dairy manure were considered at 298 K and TS = 12%. The results were presented in terms of velocity, TKE and TED rate distributions. Some important findings obtained from the study can be listed as follows:

- It was observed that the velocity distribution was not effective in the lower parts of the impeller zone in the digester tank. For more effective mixing process in the lower parts, the impeller angular velocity should be selected higher than 175 rpm.
- By increasing the impeller angular velocity from 50 rpm to 175 rpm, the amount of volume in the tank with velocities higher than the critical velocity value of 0.1 m/s increased by approximately 710%, i.e. the dead zone volume was greatly reduced, resulting in a more effective mechanical mixing process in the tank. The volume with velocity values above the critical velocity for 50 rpm angular velocity is 0.000323 m^3 while this value is 0.00262 m^3 for 175 rpm angular velocity.
- Considering the results of the studies carried out in the literature for the reactor digester tank without an buffle, the use of buffles provided a more effective TKE and TED rate distribution near the tank walls.

Viscosity-induced losses, which significantly affect the turbulence behaviour in non-Newtonian fluids, can cause local temperature increase especially at high impeller angular velocities. Moreover, these local temperature changes may affect the thermo-physical and rheological properties of the fertiliser slurry. Therefore, the limitations of the present study can be eliminated by considering the energy equation in future studies.

5. ACKNOWLEDGEMENTS

This study did not benefit from any support.

6. CONFLICT OF INTEREST

Author approves that to the best of their knowledge, there is not any conflict of interest or common interest with an institution/organization or a person that may affect the review process of the paper.

7. AUTHOR CONTRIBUTION

Emre Aşkın ELİBOl has the full responsibility of the paper about determining the concept of the research, data collection, data analysis and interpretation of the results, preparation of the manuscript and critical analysis of the intellectual content with the final approval.

8. REFERENCES

Abu-Farah L., Al-Qaessi F., Schönbucher A., Cyclohexane/water dispersion behaviour in a stirred batch vessel experimentally and with CFD simulation. Procedia computer science 1(1), 655-664, 2010.

Achkari-Begdouri A., Goodrich P. R., Rheological properties of Moroccan dairy cattle manure. Bioresource technology 40(2), 149-156, 1992.

Bridgeman J., Computational fluid dynamics modelling of sewage sludge mixing in an anaerobic digester. Advances in Engineering Software 44(1), 54-62, 2012.

Cao X., Jiang K., Ding H., Yang P., Zhao Z., Xu G., Simulation and Analysis of Flow Field in Sludge Anaerobic Digestion Reactor based on Computational Fluid Dynamics. International Journal of Chemical Reactor Engineering 16(3), 2018.

Carreau P. J., De Kee D. C., Chhabra R. P., Rheology of polymeric systems: principles and applications, Carl Hanser Verlag GmbH Co KG, 2021.

Celik A. F., Elibol E. A., Turgut O., Senol H., Sillanpää M., Interpretation of possible biogas production capacity by investigating the effects of anaerobic digester tank geometry and angular velocity on flow characteristics. Environmental Science and Pollution Research: 1-15, 2024.

Fan W. B., Li W. G., Gong X. J., Zhang X. R., Evaluation of the effect of a hydraulic impeller in a flocculation basin on hydrodynamic behavior using computational fluid dynamics. Desalination and Water Treatment 54(4-5), 1361-1374, 2015.

Hoseini S., Najafi G., Ghobadian B., Akbarzadeh A., Impeller shape-optimization of stirred-tank reactor: CFD and fluid structure interaction analyses. Chemical Engineering Journal 413, 127497, 2021.

Kong J. Y., Wu Z. W., Hou Y., Wang X. D., Numerical simulation for solid-liquid two-phase flow in stirred vanadium leaching tank. Applied Mechanics and Materials 456, 314-319, 2014.

Launder B. E., Spalding D. B., Lectures in mathematical models of turbulence. 1972.

Mousavi S. E., Choudhury M. R., Rahaman M. S., 3-D CFD-PBM coupled modeling and experimental investigation of struvite precipitation in a batch stirred reactor. Chemical Engineering Journal 361, 690-702, 2019.

Oates A., Neuner T., Meister M., Borman D., Camargo-Valero M., Sleigh A., Fischer P., Modelling mechanically induced non-Newtonian flows to improve the energy efficiency of anaerobic digesters. Water 12(11), 2995, 2020.

Rasool A. A., Ahmad S. S., Hamad F., Effect of impeller type and rotational speed on flow behavior in fully baffled mixing tank. International Journal of Advanced Research (IJAR) 5(1), 1195-1208, 2017.

Sadino-Riquelme C., Hayes R. E., Jeison D., Donoso-Bravo A., Computational fluid dynamic (CFD) modelling in anaerobic digestion: General application and recent advances. Critical Reviews in Environmental Science and Technology 48(1), 39-76, 2018.

Servati P., Hajinezhad A., CFD simulation of anaerobic digestier to investigate sludge rheology and biogas production. Biomass Conversion and Biorefinery 10(4), 885-899, 2020.

Shen F., Tian L., Yuan H., Pang Y., Chen S., Zou D., Zhu B., Liu Y., Li X., Improving the mixing performances of rice straw anaerobic digestion for higher biogas production by computational fluid dynamics (CFD) simulation. Applied biochemistry and biotechnology 171(3), 626-642, 2013.

Sindall R., Bridgeman J., Carliell-Marquet C., Velocity gradient as a tool to characterise the link between mixing and biogas production in anaerobic waste digesters. Water science and technology 67(12), 2800-2806, 2013.

Thakur H., Verma N. K., Dhar A., Powar S., Investigation of continuous stirred tank reactors for improving the mixing in anaerobic digestion: A numerical study. Results in Engineering 19, 101317, 2023.

Versteeg H. K., Malalasekera W., An introduction to computational fluid dynamics: The finite volume method, England, Pearson, 2007.

Vilardi G., Verdone N., Production of metallic iron nanoparticles in a baffled stirred tank reactor: Optimization via computational fluid dynamics simulation. Particuology 52, 83-96, 2020.

Wang H., Aguirre-Villegas H. A., Larson R. A., Alkan-Ozkaynak A., Physical properties of dairy manure pre-and post-anaerobic digestion. Applied Sciences 9(13), 2703, 2019.

Wang J., Xue Q., Guo T., Mei Z., Long E., Wen Q., Huang W., Luo T., Huang R., A review on CFD simulating method for biogas fermentation material fluid. Renewable and Sustainable Energy Reviews 97, 64-73, 2018.

Wu B., CFD analysis of mechanical mixing in anaerobic digesters. Transactions of the ASABE 52(4), 1371-1382, 2009.

Wu B., CFD simulation of mixing in egg-shaped anaerobic digesters. Water research 44(5), 1507-1519, 2010.

Wu B., CFD investigation of turbulence models for mechanical agitation of non-Newtonian fluids in anaerobic digesters. Water research 45(5), 2082-2094, 2011.

Wu B., Large eddy simulation of mechanical mixing in anaerobic digesters. Biotechnology and Bioengineering 109(3), 804-812, 2012.

Wu B., Chen S., CFD simulation of non-Newtonian fluid flow in anaerobic digesters. Biotechnology and bioengineering 99(3), 700-711, 2008.

JOURNAL of
MATERIALS and MECHATRONICS:A

e-ISSN 2717-8811
JournalMM, 2025, 6(1), 68-82
https://doi.org/10.55546/jmm.1581662

Araştırma Makalesi / Research Article

Yapay Sinir Ağı ile Mikro Parçacık Dolgulu Kompozitlerin Tribolojik Özelliklerinin Tahmini

Hüseyin GÜRBÜZ[1*], Mehmet Emin DEMİR[2], Şehmus BADAY[3], İbrahim Halil AKCAN[4]

[1*] Batman Üniversitesi, Mühendislik Mimarlık, Makine Mühendisliği Bölümü, Batman, Türkiye,
ORCID ID: https://orcid.org/0000-0003-1391-172X, huseyin.gurbuz@batman.edu.tr
[2] Batman Üniversitesi, Beşiri Organize Sanayi MYO, Makine Bölümü, Batman, Türkiye,
ORCID ID: https://orcid.org/0000-0001-9630-6378, memin.demir@batman.edu.tr
[3] Batman Üniversitesi, Beşiri Organize Sanayi MYO, Makine Bölümü, Batman, Türkiye,
ORCID ID: https://orcid.org/0000-0003-4208-8779, sehmus.baday@batman.edu.tr
[4] Batman Üniversitesi, Mühendislik Mimarlık, Makine Mühendisliği Bölümü, Batman, Türkiye,
ORCID ID: https://orcid.org/0009-0007-8075-2323, ibrahimhalilakcan1@gmail.com

Geliş/ Received: 08.11.2024; **Revize/Revised:** 27.11.2024 **Kabul / Accepted:** 08.01.2025

ÖZET: Yapay sinir ağı (YSA), polimer kompozitlerin tribolojik performansı gibi karmaşık mühendislik problemlerini çözmek için kullanılan etkili tekniklerden biridir. Bu çalışmanın amacı bor karbür (B_4C) ve grafit (Gr) dolgulu epoksi matrisli kompozit malzemenin aşınma performansını YSA ile modellemektir. Cam elyaf takviyeli epoksi reçine içerisinde ağırlıkça %5, %10 ve %15 oranında B_4C ve Gr dolgulu kompozitler basit elle yatırma tekniği ile hazırlanmıştır. Bu kompozitlere, Taguchi'nin ortogonal dizi tasarımına göre kuru kayma koşullarında aşınma deneyleri gerçekleştirilmiştir. Deneysel veriler kullanılarak, aşınma davranışı üzerinde çeşitli kontrol faktörlerinin etkisini tahmin etmek amacıyla bir YSA modeli eğitilmiş ve test edilmiştir. Oluşturulan YSA modelinde, ağ yapısı ileri beslemeli ve geri yayılımlı, eğitim algoritması Levenberg–Marquardt, transfer fonksiyonu tansig kullanarak deneysel sonuçlar tahmin edilmiştir. Sürtünme katsayısı (COF) için eğitim, doğrulama, test ve genel regresyon katsayı değerleri sırasıyla 0,9936 – 0,99996 – 0,99807 ve 0,9911 iken, aşınma oranı için ise 0,9968 – 0,99891 – 0,83971 ve 0,93886 olarak elde edilmiştir. Aşınma oranı ve COF değerleri için oluşturulan YSA modelinden elde edilen regresyon katsayısı değerlerine göre, deneysel sonuçların yüksek doğruluk oranlarıyla tutarlı olduğu görülmüştür.

Anahtar Kelimeler: Mikro parçacık, Cam elyaf, Kompozit, Aşınma, Yapay sinir ağları

*Sorumlu yazar / Corresponding author: huseyin.gurbuz@batman.edu.tr
Bu makaleye atıf yapmak için /To cite this article

Gürbüz, H., Demir, M. E., Baday, Ş., Akcan, İ. H. (2025). Yapay Sinir Ağı ile Mikro Parçacık Dolgulu Kompozitlerin Tribolojik Özelliklerinin Tahmini. Journal of Materials and Mechatronics: A (JournalMM), 6(1), 68-82.

Prediction of Tribological Properties of Micro-Particle-Filled Composites Using Artificial Neural Network

ABSTRACT: Artificial neural network (ANN) is one of the effective techniques used to solve complex engineering problems such as tribological performance of polymer composites. The aim of this study is to model the wear performance of boron carbide (B_4C) and graphite (Gr) filled epoxy matrix composite material with ANN. Composites with 5 wt.%, 10 wt. % and 15 wt. % B_4C and Gr fillers in glass fiber reinforced epoxy resin were prepared by simple hand lay-up technique. Wear tests were performed on these composites under dry sliding conditions according to Taguchi's orthogonal array design. Using experimental data, an ANN model was trained and tested to predict the effect of various control factors on wear behavior. In the created ANN model, the network structure is feed forward and back propagation, Levenberg–Marquardt training algorithm, tansig transfer function is used to estimate experimental results. The values of the training, validation, testing and general regression coefficients for coefficient of friction (COF) were 0.9936 – 0.99996 – 0.99807 and 0.9911, respectively, while for the wear rate, they were 0.9968 – 0.99891 – 0.83971 and 0.93886. According to the regression coefficient values obtained from the ANN model created for the wear rate and COF values, the experimental results were consistent with high accuracy rates.

Keywords: Micro particle, Glass fiber, Composite, Wear, Artificial neural networks

1. GİRİŞ

Günümüz dünyasında, elyaf takviyeli polimer kompozitler (ETPK), havacılık endüstrisi, sıhhi tesisat borulama sistemleri, gemi inşası, rulmanlar, otomobil üretimi, dişli ve rüzgar türbini kanadı imalatı gibi birçok alanda geniş uygulama alanına sahiptir. Bu kompozitler, hafiflik, olağanüstü özgül dayanım/rijitlik, daha iyi korozyon direnci ve anizotropik davranış gibi üstün mekanik özelliklere sahiptir (Thakur ve Singh, 2020; Jayan ve ark., 2021). ETPK'ler ve polimer kompozitler, kuru sürtünme koşullarında metallere kıyasla daha düşük sürtünme değerlerine sahip olmaları nedeniyle büyük ilgi görmektedir (Friedrich, 2018). Polimer kompozitler, kuru sürtünme koşullarına maruz kalan birçok uygulamada kendiliğinden yağlama özellikleri sayesinde metal muadillerinin yerini almaktadır (Çetkin ve ark., 2022; Ouyang ve ark., 2022). Polimer kompozitler yapısal malzemelerde ve tasarımda geniş ölçüde kullanılmaktadır. Genellikle polimer kompozitler metal temas yüzeyi ile etkileşim halindedir. ETPK'lerde dolgu malzemelerinin kullanımı mekanik ve tribolojik özelliklerin geliştirilmesi açısından önemlidir. Dolgu maddelerinin kullanım amacı iki temel kategoriye ayrılabilir: birincisi, mekanik, termal veya tribolojik özellikleri iyileştirmek; ikincisi ise bileşenin maliyetini düşürmektir. Seramik veya metal parçacıklarından oluşan sert parçacık dolgular ve camdan yapılmış elyaf dolgular, günümüzde doğal lif kompozitlerinde aşınma direnci gibi mekanik özellikleri önemli ölçüde iyileştirmek için kullanılmaktadır (Ray, 2021). Tribolojik uygulamalarda yaygın kullanımları nedeniyle, polimer kompozitlerin tribolojik özellikleri birçok araştırmacı tarafından incelenmiştir (Demir ve ark., 2019; Negi ve ark., 2019; Kumar ve Singh, 2020; Turaka ve ark., 2021). Epoksi, yüksek mukavemeti ve modülü, düşük çekme seviyeleri ve uçuculuğu, daha iyi yapışma ve kimyasal direnç gibi özelliklerinin yanında işlenme kolaylığı nedeniyle en yaygın kullanılan matris malzemesidir (Zhao ve ark., 2016; Li ve ark., 2017; Singh ve ark., 2021). Literatür araştırmaları, cam, karbon ve kevlar gibi liflerle polimer reçinelerinin takviye edilmesinin, metal temas yüzeyi karşısında kuru sürtünme koşullarında polimerlerin aşınma direncini önemli ölçüde artırdığını ortaya

koymuştur. Kompozitlerde aşınma süreçleri, birçok çalışma değişkenini içeren karmaşık olgudur ve kompozitlerin aşınma özelliklerinin farklı çalışma koşullarından nasıl etkilendiğini anlamak esastır (Padhi ve Satapathy, 2013). Ancak, elyaf yönelimi, matris bileşimi ve uygulanan yük, kayma ortamları, sıcaklık ve kayma hızı gibi test parametreleri de tribolojik performans üzerinde önemli bir etkiye sahiptir (Findik ve ark., 2004; Chowdhury ve Helali, 2008; Agrawal ve ark., 2016). Bununla birlikte eklenen dolgu parçacıklarının şekli, boyutu, hacim fraksiyonu ve spesifik yüzey alanı da, kompozitlerin tribolojik özelliklerini büyük ölçüde etkilemektedir (Kranthi ve Satapathy 2010).

Aşınma oranı ve sürtünme katsayısı (COF) gibi tribolojik özelliklerin değerlendirilmesine yönelik araştırma çalışmaları, tekrar eden deneyler gerektirdiği için oldukça zaman almaktadır. Deney süresinden tasarruf sağlamak amacıyla, parametrik modelleme, regresyon modeli, bulanık mantık ve yapay sinir ağı (YSA) gibi çeşitli modelleme yöntemleri kullanılmaktadır (Jiang ve ark., 2007; Gyurova ve Friedrich, 2011; Chowdhury ve ark., 2019). Ancak, literatürde yer alan çalışmalar, YSA'nın diğer modelleme yöntemlerine kıyasla daha yüksek bir doğruluğa sahip olduğunu göstermektedir. YSA kullanılarak tahmin edilen değerler, hedef değerlerle güçlü bir korelasyon göstermekte ve bu sayede diğer modelleme yöntemlerine göre daha yüksek doğruluk sağlamaktadır (Shtub ve Versano, 1999; Ciurana ve ark., 2008). Hem dolgulu kompozitler ile ilgili deneysel çalışmalar ve hem de deneysel verilerin YSA yöntemi ile modellendiği birçok çalışma mevcuttur (Padhi ve Satapathy, 2013; Divya ve ark., 2023; Teli ve ark., 2023; Demir, 2024; Demir ve ark., 2024; Kose ve ark., 2024). Zhang ve arkadaşları, YSA kullanarak kısa fiber takviyeli poliamid 4,6 kompozitinin spesifik aşınma oranı ve sürtünme katsayısını tahmin etmiştir. Farklı eğitim algoritmalarının (Bayesian düzenlemesi, Levenberg-Marquardt vb.) etkisini tahmin etmek için geri yayılım yöntemiyle çok katmanlı algılayıcı kullanmışlardır. Çalışma, sınırlı sayıda ölçüm sonucuna dayanarak, YSA'nın malzeme tasarımında, parametrelerin incelenmesinde ve polimer kompozit özelliklerinin analizinde faydalı bir matematiksel araç olduğunu göstermiştir (Zhang ve ark., 2002). Kumar ve ark. AlSi10Mg – MWCNT bazlı kompozit fren balatasının aşınmasını, yük ve çalışma süresi gibi girdileri alarak tahmin etmek için YSA'yı uygulamışlardır. Ayrıca deneysel sonuçların tahmininde 0,99447'lik bir korelasyon katsayısı elde etmişlerdir (Kumar ve ark., 2021a). Kumar ve ark. bir diğer çalışmalarında ise normal kuvvet, sıcaklık ve diskin devir sayısı olmak üzere üç girdi alarak $NiSO_4$ kompozit fren balatası için bir YSA modeli geliştirmişlerdir. Kütle kaybı ve sürtünme katsayısını (COF) sırasıyla 0,99073 ve 0,98217 korelasyon katsayıları ile tahmin etmişlerdir (Kumar ve ark., 2021b). Rodrigues ve ark. silan uygulanmış B_4C'nin epoksi reçinesine eklenmesiyle mekanik özelliklerde önemli bir iyileşme sağlamışlardır. Kompozitlerin eğilme ve çekme mukavemetlerinin sırasıyla yaklaşık %24 ve %56 oranında arttığını belirlemişlerdir (Rodrigues & Broughton, 2013). Abenojar ve ark. ortalama parçacık boyutu 23 µm olan %6 oranında B_4C parçacıklarının epoksiye eklenmesinin, 7 µm parçacık içeren kompozitlere kıyasla daha düşük bir aşınma oranı sağladığını bulmuşlardır. Ancak, B_4C parçacık boyutu artırıldığında tersine bir etki yaptığını gözlemlemişlerdir. B_4C dolgusunun, cam-epoksi kompozitlere ilave edildiğinde, kompozitlerin aşınma özelliklerini iyileştirdiğini belirlemişlerdir (Abenojar ve ark., 2009).

Elyaf takviyeli kompozitlerde dolgu tipi ve dolgu oranı aşınma özellikleri üzerinde önemli bir etkiye sahiptir. Bu kompozitlerin endüstriyel uygulamalarda farklı alanlarda çalışma şartlarına bağlı olarak birbirleriyle temaslarından dolayı malzemelerde aşınma sonucu kütle kayıpları ve deformasyonlar meydana gelmekte ve böylece işlevlerini kaybetmektedirler. Ortaya çıkan bu durum kompozitlerde maliyet artırıcı bir unsur olarak karşımıza çıkmaktadır. Bu yüzden aşınma parametrelerinin ve malzeme özelliklerinin birbirleriyle olan etkileşimlerinin belirlenmesinde, zaman ve maliyet açısından farklı modelleme ve optimizasyon yöntemlerinin kullanılması önem arz

etmektedir. Bu bağlamda, bu çalışmada çeşitli parametrelerin ve bunların etkileşimlerinin etkisini incelemek ve sürtünme katsayısı ile aşınma oranını tahmin etmek amacıyla YSA yöntemi kullanılmıştır.

2. MATERYAL VE YÖNTEM

2.1 Kompozitlerin Üretimi

Bu çalışmada, farklı ağırlık yüzdelerinde dolgu tipi içeren polimer kompozitler, basit el yatırma tekniği ile üretilmiştir. Matris malzemesi olan ARC 152 epoksi reçine ve sertleştiricisi "ARC Marine" firmasından temin edilmiştir. Cam elyaf takviye malzemesi olarak düz dokuma cam elyaf, karbomid firmasından, Gr ve B_4C dolgu parçacıkları ise Ege Nanotek firmasından temin edilmiştir. Sertleştirici, epoksi reçine içine dörtte bir oranında katılmıştır. Dolgu parçacıkları öncelikle belirlenen oranlarda hassas terazide tartılarak epoksi reçine içine katılmış ve homojenliğin sağlanması amacıyla mekanik bir çubukla 15 dakika karıştırılmıştır. Matris oranı %50 oranında tutulmuştur. B_4C ve Gr dolguları için ayrı ayrı ağırlık yüzdesi, %5, 10 ve 15 olmak üzere 3 farklı oranda matris malzeme içinde karıştırıldıktan sonra 30 x 30 cm boyutlarındaki her cam elyaf katmanına sürülerek plakalar hazırlanmıştır. Ortalama 5 mm numune kalınlığı elde etmek amacıyla 13 katman cam elyaf kullanılarak dolgulu 6 tip kompozit panel üretilmiştir. Plakaların kuruması için 1 gün boyunca kürleşmeye bırakılmıştır. Aşınma testleri için 40 mm × 40 mm × 4 mm boyutlarında kompozitler kesilmiştir. Bu çalışmada laminatların üretiminde kullanılan matris, takviye ve dolgu maddelerinin özellikleri Çizelge 1'de sunulmuştur. Kompozitlerin üretim aşamaları ve aşınma test düzeneği Şekil 1'de verilmiştir.

Çizelge 1. Cam elyaf ve dolgu parçacıklarının özellikleri

	Cam Elyaf		**Gr**	**B_4C**
Ağırlık	220 gr/m^2	**Toz Boyutu**	30 mikron	30 mikron
Kopma Uzaması	%2,50	**Yoğunluk**	2,09-2,23 g/cm^3	2,52 g/cm^3
Çekme Mukavemeti	1300 MPa	**Saflık**	% 99,9	% 96
Elastisite Modülü	65 GPa	**Sertlik**	0,32 GPa	44 GPa

Kompozitlerin Üretim Aşaması Aşınma Test Cihazı

Şekil 1. Kompozitlerin üretilmesi ve aşınma deney düzeneği (Gürbüz ve ark., 2024)

2.2 Aşınma Testi

Dolgulu kompozitlerin aşınma testleri için değişken yük, kayma hızı, dolgu oranı gibi tüm deney kombinasyonlarının birbiri ile etkileşiminin araştırılması gerekmektedir. Bu çalışmada deney sayısının belirlenmesinde Taguchi metodu kullanılmıştır. Taguchi deneysel tasarımının

kullanılmasının amacı, aşınma testlerindeki tüm parametreleri kapsayan daha az deneyle tüm parametreler arasındaki ilişkileri belirlemektir. Aşınma deneyleri 250 m, 500 m, 750 m kayma mesafesi ve 5 N, 10 N ile 15 N yükte gerçekleştirilmiştir. Aşınma testlerindeki numuneler Turkyus marka pin on disk cihazında 300 dev/dk hızında 6 mm çaptaki çelik bilye ile aşındırılmıştır. Testler ASTM G99 standardına göre yapılmış olup, aşınma oranının belirlenmesinde kullanılan formül Eşitlik 1'de verilmiştir.

$$AH = 2 * \pi * R[r^2 * sin - 1(a/2 * r) - (a/4) * (4 * r^2 - a^2]^{1/2} \quad (1)$$

Burada R: iz çapını, AH: aşınma oranını, r: bilye çapını ve a: ise iz genişliğini ifade etmektedir.

2.3 Taguchi Modelleme

Bu çalışmada deney sayısını düşürerek hem finansal hem de zaman açısından kazançlı olmak için deney tasarım yöntemlerinden biri olan Taguchi metodu kullanılmıştır. Taguchi metodunda giriş parametreleri olarak dolgu malzemesi, katkı oranı, kuvvet ve kayma mesafesi iken çıkış parametreleri olarak aşınma oranı ve sürtünme katsayısı seçilmiştir. Giriş parametrelerin çıkış parametreleri üzerindeki etkisini belirlemek için üç faktörlü karışık seviye tasarımı kullanılmıştır. Deney sayısı, L18 (2^1–3^3) düzeni Taguchi mixed (karışık) tasarım olarak seçilmiştir. Aşınma oranı ve sürtünme katsayısı deneyleri için giriş parametreleri ve seviyeleri Çizelge 2'te verilmiştir.

Çizelge 2. Aşınma deneyleri için giriş parametreleri ve seviyeleri

Seviyeler	Dolgu malzemesi	Kayma mesafesi (m)	Kuvvet (N)	Dolgu oranları (%)
1	B_4C	250	5	5
2	Gr	500	10	10
3		750	15	15

2.4 YSA Analizi

YSA, girdilerin çıktılar üzerindeki etkisini tahmin etmek için veri tabanı eğitimi içeren bir tekniktir. İyi tasarlanmış bir YSA'yı eğitmek için belirli bir miktarda deneysel sonuca ihtiyaç duyulmaktadır. YSA, çözülmesi güç olan denklemleri öğrendikten sonra çok sayıda deney yapmaya gerek kalmadan sonuçları tahmin edilebilmektedir. YSA, nöron adı verilen birçok çapraz bağlı basit işlem biriminden oluşan bir sistemdir. Ağ, seri bağlı üç kısımdan oluşur. Bunlar giriş katmanı, gizli katman ve çıkış katmanıdır. YSA'da giriş katmanı işlenmemiş verileri kabul eder, gizli katmanda bu veriler işlenir ve çıkış katmanı aracılığıyla sonuçlar dışa aktarılır (Pati, 2019). Aşınma oranı ve COF değerinin tahmin etmek amacıyla, dört nöronlu bir giriş katmanı (dolgu tipi, dolgu içeriği, uygulanan yük ve kayma mesafesi), 10-8-3 nöronlu üç gizli katmanlı ve iki nöronlu bir çıkış katmanı (aşınma oranı ve COF) ile YSA modeli oluşturulmuştur. Oluşturulan YSA modeli Şekil 2'de gösterilmiştir. Gizli katmandaki nöron sayısının belirlenmesi, ortalama kare hata kriterine dayalı olarak deneme-yanılma yöntemiyle yapılmıştır. YSA'yı geliştirmek ve giriş parametrelerine bağlı olarak çıkış parametrelerini tahmin etmek amacıyla, COF için 18 veri kümesi ve aşınma oranı için 18 veri kümesinden oluşan deneysel bir veri tabanı kullanılmış, Çizelge 5 ve Çizelge 6'da gösterilmiştir. Oluşturulan YSA modelinde, deneysel verilerin, %70'ni eğitim ve %15'ini test verileri ve geriye kalan %15'ini doğrulama verileri olarak seçilmiş ve MATLAB programına yüklenmiştir. Bu çalışmada, COF ve aşınma oranlarını tahmin etmek için ileri beslemeli geri yayılımlı ağ tipi (Feed-Forward Back Propagation Network), Levenberg–Marquardt eğitim algoritması ve tansig transfer

fonksiyonu uygulanmıştır. YSA modelinde verilerin tahmininde kullanılan genel formül Eşitlik 2'de verilmiştir.

$$NETi = \sum_{j=1}^{n} w_{ij} + w_{bi} \tag{2}$$

Burada; satır numarasını "i", deney sayısını "n", sütün numarasını "j", nöronların ağırlığını "w" ve ağırlığa ait dengelemeyi "w_b" ifade etmektedir. Kullanılan transfer fonksiyonu Eşitlik 3'te verilmiştir.

$$tansig(n) = \frac{2}{(1 + e^{-2NETi})} - 1 \tag{3}$$

YSA modellemesi için MATLAB yazılım paketi kullanılmıştır. Tahmini hata miktarının hesaplanmasında Eşitlik 4'deki formül kullanılmıştır.

$$\text{Tahmini hata} = (\text{Deneysel veri} - \text{YSA verisi}) \tag{4}$$

Deney parametrelerinin 0-1 arasında olması YSA modelinin daha doğru sonuçlar vermesini sağlamaktadır. Bu amaçla deney parametrelerinin minimize edilmesinde kullanılan formül Eşitlik 5'te verilmiştir.

$$\bar{x} = \frac{(x - x_{min})}{(x_{max} - x_{min})} \tag{5}$$

Bu eşitlikte $\bar{x}$ normalize edilmiş veriyi, X_{min} en düşük veriyi, X_{max} en büyük veriyi ve X ise ölçülen veriyi ifade etmektedir. Regresyon katsayısının hesaplanmasında kullanılan formül Eşitlik 6'te verilmiştir.

$$R^2 = 1 - \frac{\sum_{i=1}^{n}(Z_{gerçek} - Z_{tahmini})^2}{\sum_{i=1}^{n}(Z_{gerçek} - Z_{ortalama})^2} \tag{6}$$

Eşitlik 6'da $Z_{gerçek}$ gerçek veriyi, $Z_{tahmini}$ tahmin edilen veriyi, $Z_{ortalama}$ verilerin ortalamasını, R^2 regresyon katsayısını ve n ise toplam gözlem sayısını ifade etmektedir.

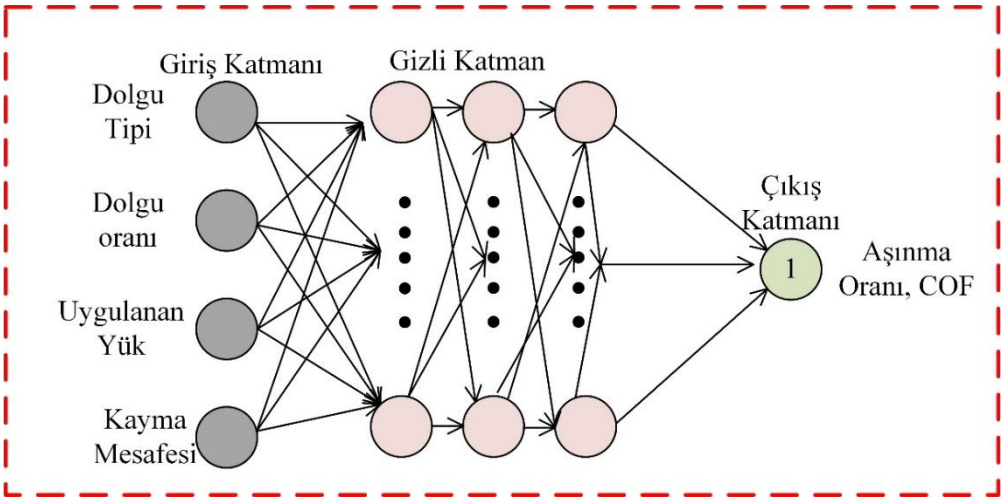

Şekil 2. Deneysel verilerin YSA modeli

3. BULGULAR VE TARTIŞMA

Aşınma ve COF için Levenberg–Marquardt eğitim algoritması sürecinden elde edilen değerler Çizelge 3 ve Çizelge 4'te verilmiştir. COF için eğitim algoritması 12. döngüde, aşınma oranı için ise 7. döngüde tamamlanmıştır. Mu değeri, Levenberg-Marquardt algoritmasının eğitim sürecinde ayarlanan bir parametre olarak kullanılmaktadır. Bu parametre başlangıçta 0,001 olarak belirlenmiş ve eğitim süreci ilerledikçe 1e-07 değerine kadar düşmüştür. Burada Mu değerinin başlangıçtan itibaren belirgin şekilde azaldığı gözlenmiştir.

Çizelge 3. COF için Levenberg–Marquardt eğitim algoritması süreci

Eğitim İşlemi	Başlangıç Değeri	Durma Değeri	Hedef Değer
Döngü	0	12	1000
Geçen Süre	-	00:00:00	-
Performans	0,152	7,96e-21	-
Gradient	0,352	9,23e-12	1e-07
Mu	0,001	1e-07	1e+10
Doğrulama	0	3	6

Çizelge 4. Aşınma oranı için Levenberg–Marquardt algoritması eğitim prosesi

Eğitim İşlemi	Başlangıç	Durma Değeri	Hedef Değer
Döngü	0	7	1000
Geçen Süre	0	00:00:00	-
Performans	157	1,16E-18	0
Gradient	385	1,44E-08	1e-07
Mu	0,001	0,00001	1e+10
Doğrulama	0	3	6

COF ve aşınma oranları için oluşturulan YSA'dan elde edilen hata histogram grafikleri Şekil 3a ve Şekil 3b'de sunulmuştur. Deneysel verilerin hata histogramını gösteren Şekil 3a ve Şekil 3b'deki veri kümelerinin çoğunun sıfır hata çizgisine yakın olan -0,00293 ve -0,1512'lik bir hataya sahip olduğu ortaya çıkmıştır. COF ve aşınma oranı için elde edilen genel veri kümelerinin hata miktarlarının sırasıyla 0,07'den ve 4,6'dan az olduğu gözlenmiştir ve bu da tüm deneyler için

minimum bir hata olduğunu kanıtlamaktadır. Bu nedenle, deneysel veriler için geliştirilen YSA modelinin tutarlı ve doğru olduğu kabul edilebilir.

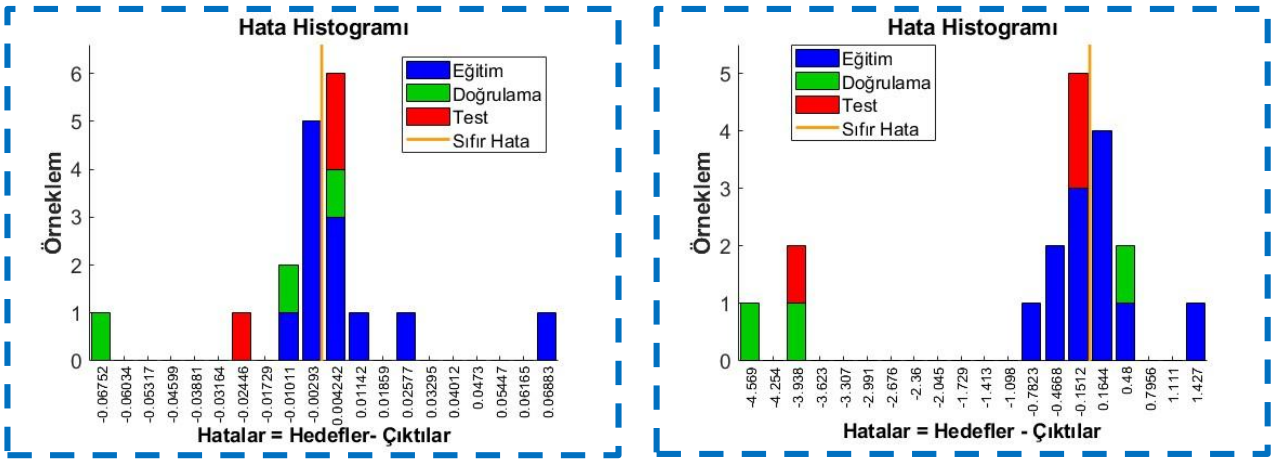

a) b)

Şekil 3. Hata histogramı: a) COF, b) Aşınma oranı

COF ve aşınma oranına ait deneysel verilerin performans grafikleri Şekil 4'te verilmiştir. Şekil 4'te verilen doğrulama performans grafiği, YSA modelinin doğruluğunu özetlemekte ve verilerin bütünlüğünü değerlendirmek için kullanılmaktadır. Şekil 4a'daki modelin 12. döngüye kadar eğitildiği, en iyi performans değerinin 9. döngüde elde edildiği ve 9. döngüdeki ortalama kare hata değerinin 0,0017084 olduğu belirlenmiştir. 9. döngüden sonra gerçek değerler ve tahmini değerler arasındaki hata oranı artığından dolayı program bu döngüde sonlanmıştır. Bu, ortalama kare hata değerinin sıfıra yakın olması YSA modelinin çok iyi eğitildiğini ve dolayısıyla geliştirilen modelin hedef değerlere çok yakın değerleri tahmin edebileceğini göstermektedir. Şekil 4b'de ise aşınma oranı için modelin 7. döngüye kadar eğitildiği ve en iyi performansın 4. döngüde elde edildiği ve 4. döngü ortalama kare hata değerinin 12,9078 olduğu tespit edilmiştir. Şekil 4a ve Şekil 4b'de verilen COF ve aşınma oranlarına ait eğitim hata değerlerinin artan döngü sayısıyla azaldığı gözlenmiştir.

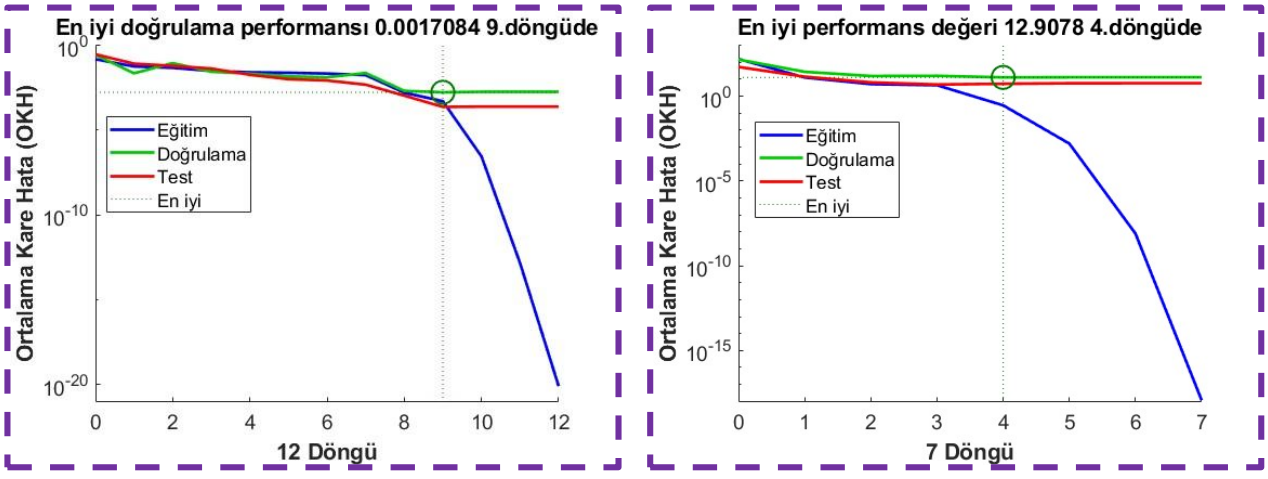

a) b)

Şekil 4. Performans grafiği: a) COF, b) Aşınma oranı

Dolgulu cam elyaf takviyeli kompozitlerin COF ve aşınma oranlarına ait deneysel veriler eğitildikten sonra elde edilen regresyon grafikleri Şekil 5a ve Şekil 5b'de verilmiştir. Şekil 5'teki

COF ve aşınma oranı için verilen grafikler eğitim, doğrulama, test ve genel regresyon grafiklerini içermektedir. Şekil 5a ve Şekil 5b'deki grafiklerde görülen 45 derecelik açıya sahip çizginin etrafında yer alan hedef ve çıktıların birbirine yakın değerlerde olması istenmektedir.

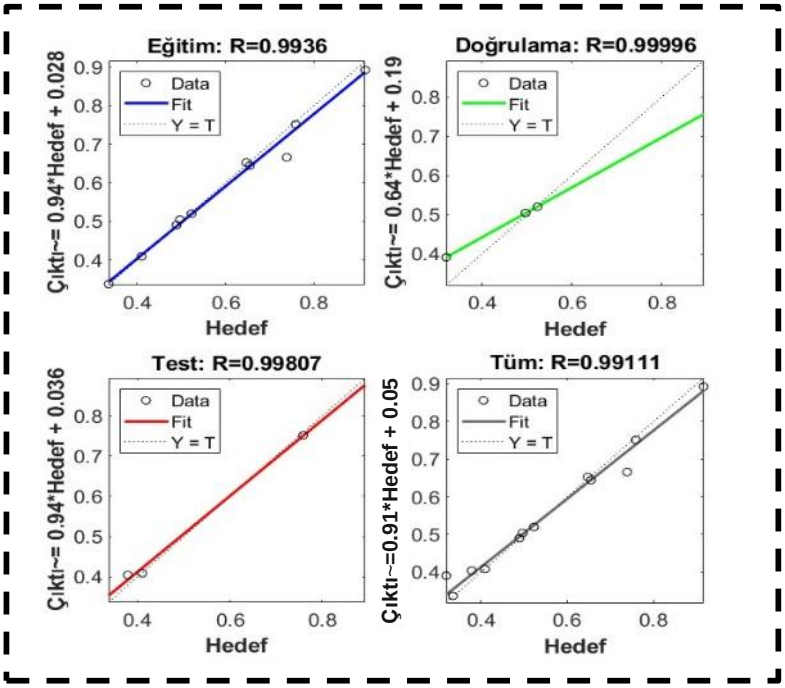

a)

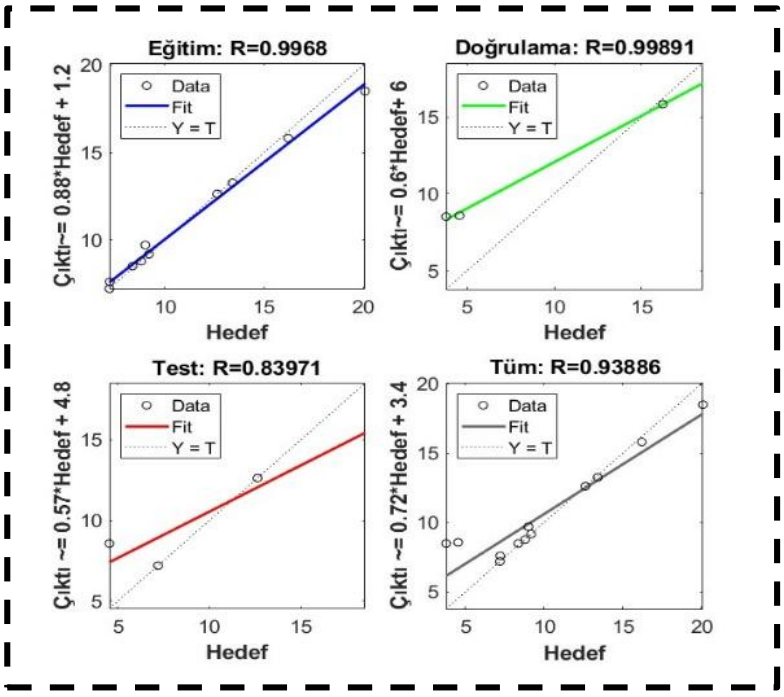

b)

Şekil 5. Regresyon grafikleri: a) COF b) Aşınma oranı

COF için eğitim, doğrulama, test ve genel regresyon katsayı değerleri sırasıyla 0,9936 – 0,99996 – 0,99807 ve 0,99111 olarak elde edilmiştir. Aşınma oranında ise eğitim, doğrulama, test ve genel regresyon katsayı değerleri sırasıyla 0,9968 – 0,99891 – 0,83971 ve 0,93886 olarak ortaya çıkmıştır. Hem COF hem de aşınma oranı için elde edilen regresyon değerlerinin 1'e çok yakın elde

edilmesi, ağın iyi eğitildiğini, güvenilir olduğunu ve deneysel veriler ile arasında güçlü bir korelasyon olduğunu kanıtlamaktadır. Bu sonuçlar, geliştirilen ağ modelinin deney sonuçlarından çok az sapmayla aşınma oranını ve COF değerini tahmin etmedeki etkinliğini doğrulamaktadır. Şekil 5b'de yer alan test regresyon katsayı değeri diğerlerine göre daha düşük çıkmıştır. Bunun nedeni olarak deneysel verilerin alınması sırasındaki hata payından kaynaklandığı düşünülmektedir. COF ve aşınma oranı için hedef, çıktı ve hata değerleri Şekil 6'da verilmiştir. Şekil 6a'da COF değerlerinin tahmin edilmesinde en fazla sapma miktarı 9. ve 10. deney verilerinde meydana gelmiştir. Genel olarak COF değerlerinin tahmin edilmesinde sapma miktarlarının çok düşük olduğu gözlenmiş, hedef ve çıktı değerlerinin birbiriyle örtüştüğü Şekil 6a'daki grafikten anlaşılmaktadır. Şekil 6b'deki aşınma oranı değerlerinin tahmininde 1, 4 ve 7. deney verilerinin diğer deney verilerine göre sapma miktarının biraz daha fazla çıktığı tespit edilmiştir. COF deneysel verilerinin tahmini, aşınma oranı verilerinin tahminine göre daha başarılı olduğu Şekil 6a ve Şekil 6b' deki çıktı ve hedef grafiklerinden anlaşılmaktadır.

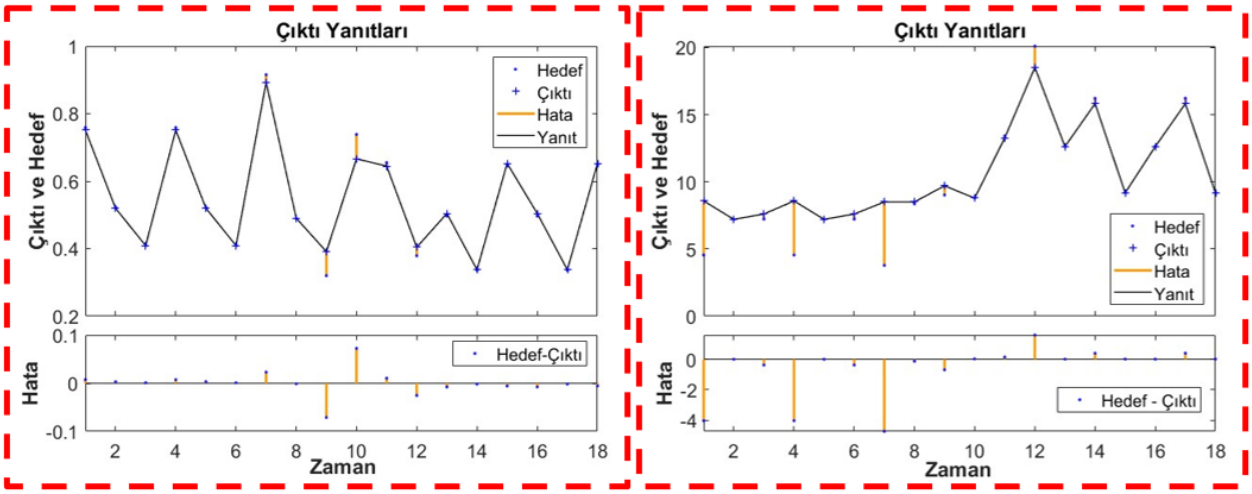

a) b)

Şekil 6. Çıktı ve hedef grafikleri: a) COF, b) Aşınma oranı

Farklı parametrelere bağlı olarak elde edilen COF ve aşınma oranı için deneysel veriler, tahmin değerleri ve sapma miktarları Çizelge 5 ve Çizelge 6'da verilmiştir. Çizelge 5'teki değerler incelendiğinde YSA analizi ile elde edilen tahmini COF değerlerinin deneysel veriler ile oldukça örtüştüğü görülmektedir. En düşük ve en yüksek sapma değerleri sırasıyla 0,00009 ve 0,072 olarak elde edilmiştir. Aşınma oranları için verilen Çizelge 6' daki değerler incelendiğinde tahmin değerleri ile deneysel değerlerin birbirine genel olarak yakın olduğu tespit edilmiştir. En yüksek sapma miktarı 7. deney verisinde (4,72707) ve en düşük sapma değeri ise 2. deney verisinde (0,00147) ortaya çıkmıştır. COF ve aşınma oranı tahminlerindeki sapma miktarlarını sıfıra yakın elde edilmesi deneysel veriler için uygulanan YSA modelinin geçerliliğini göstermektedir.

Çizelge 5. Farklı parametrelere bağlı gerçek ve tahmini COF değerleri

Katkı	Dolgu oranı (%)	Kuvvet	Mesafe	Gerçek COF	Tahmini COF	Sapma
Gr	5	5	250	0,758695327	0,76613	0,0070
Gr	10	10	500	0,522985143	0,52609	0,0030
Gr	15	15	750	0,410057631	0,41098	0,00009
Gr	5	5	250	0,758695321	0,76613	0,00700
Gr	10	10	500	0,522985143	0,52609	0,0030

Çizelge 5. Farklı parametrelere bağlı gerçek ve tahmini COF değerleri (devamı)

Katkı	Dolgu oranı (%)	Kuvvet	Mesafe	Gerçek COF	Tahmini COF	Sapma
Gr	15	15	750	0,410000004	0,41098	0,0009
Gr	5	5	500	0,915565003	0,93852	0,0229
Gr	10	10	750	0,489149649	0,48796	-0,0010
Gr	15	15	250	0,320000000	0,24889	-0,0710
B_4C	5	5	750	0,738546406	0,8109	0,0720
B_4C	10	10	250	0,655046567	0,66538	0,0100
B_4C	15	15	500	0,378975930	0,35354	-0,0250
B_4C	5	10	750	0,496672426	0,48895	-0,0070
B_4C	10	15	250	0,335832063	0,33411	-0,0010
B_4C	15	5	500	0,647040914	0,641314	-0,0050
B_4C	5	10	750	0,496672426	0,48895	-0,0070
B_4C	10	15	250	0,335832063	0,33411	-0,0010
B_4C	15	5	500	0,647040914	0,64131	-0,0050

Çizelge 6. Farklı parametrelere bağlı gerçek ve tahmini aşınma oranı değerleri

Katkı	Dolgu oranı (%)	Kuvvet	Mesafe	Gerçek Aşınma Oranı	Tahmini Aşınma Oranı	Sapma
Gr	5	5	250	4,550992	0,523157	-4,02784
Gr	10	10	500	7,205745	7,204267	-0,00147
Gr	15	15	750	7,223641	6,842672	-0,38097
Gr	5	5	250	4,550992	0,523157	-4,02784
Gr	10	10	500	7,205745	7,204267	-0,00148
Gr	15	15	750	7,223643	6,842672	-0,38097
Gr	5	5	500	3,777776	-0,94929	-4,72707
Gr	10	10	750	8,372175	8,240603	-0,13157
Gr	15	15	250	9,013273	8,319442	-0,69383
B_4C	5	5	750	8,808456	8,829651	0,021196
B_4C	10	10	250	13,41386	13,55868	0,144815
B_4C	15	15	500	20,09887	21,68337	1,584496
B_4C	5	10	750	12,63095	12,63568	0,004729
B_4C	10	15	250	16,21653	16,60995	0,393425
B_4C	15	5	500	9,193006	9,202908	0,009902
B_4C	5	10	750	12,63095	12,63568	0,004729
B_4C	10	15	250	16,21653	16,60995	0,393425
B_4C	15	5	500	9,193006	9,202908	0,009902

Çizelge 5'te dolgu tiplerinin etkisi incelendiğinde, Gr dolgulu cam elyaflı kompozitlerin sürtünme katsayılarının B_4C dolgulu cam elyaflı kompozitlere nazaran daha düşük olduğu anlaşılmaktadır. Bu durumun aşınma sırasında B_4C parçacıklarının matris içinden çıkarak çelik pin ile malzeme arasında sıkışıp sürtünme katsayısının artışına neden olduğu düşünülmektedir. Dolgu oranının etkisine bakıldığında ise artan dolgu oranlarında hem Gr hem de B_4C dolgulu kompozitlerin sürtünme katsayılarının düştüğü gözlemlenmiştir. Gr parçacıklarının yağlayıcı özelliği ve B_4C parçacıklarının yüksek sertliği Gr ve B_4C dolgulu kompozitlerin sürtünme katsayılarının artan dolgu oranlarında düşmesini sağlamıştır. Çizelge 6'daki aşınma oranları incelendiğinde, B_4C dolgusunun Gr dolgusuna kıyasla aşınma oranını daha çok arttırdığı anlaşılmaktadır. Literatür incelendiğinde Gr'nin katı yağlayıcı özelliğe sahip olmasından ötürü aşınmaya karşı olan direnci arttırdığı

bilinmektedir (Bheemappa ve ark., 2007; Sudheer ve ark., 2014). Uygulanan yükün aşınma oranı üzerindeki etkisi incelendiğinde yük artışının aşınma oranını belirgin ölçüde arttırdığı anlaşılmaktadır. Elde edilen sonuçlar literatür çalışmalarıyla paralellik arz etmektedir (Kim ve ark., 2012; Arun ve Kumar Singh, 2017).

4. SONUÇ

Mikro parçacık dolgulu cam elyaf takviyeli kompozitlerde farklı dolgu parçacıklarının ve aşınma parametrelerinin COF ve aşınma oranı üzerindeki etkisi YSA ile incelenmiş ve elde edilen sonuçlar aşağıda maddeler halinde verilmiştir.

- Geliştirilen ağ modelindeki hata histogramına göre veri kümelerinin çoğunun sıfır hata çizgisine yakın olan -0,00293 ve -0,1512'lik bir hataya sahip olduğu görülmüştür.
- Oluşturulan YSA modelinden elde edilen COF için regresyon katsayı değerleri; eğitim, doğrulama, test ve genel olmak üzere sırasıyla 0,9936 – 0,99996 – 0,99807 ve 0,99111 değerlerinde elde edilmiştir. Aşınma oranı için regresyon katsayı değerleri ise eğitim, doğrulama, test ve genel olmak üzere sırasıyla 0,9968 – 0,99891 – 0,83971 ve 0,93886 olarak ortaya çıkmıştır.
- YSA analizi ile elde edilen tahmin sonuçlarına göre en düşük ve en yüksek COF ve aşınma oranlarının sapma değerleri sırasıyla 0,00009 – 0,072 ve 0,00147 – 4,72707 olarak elde edilmiştir. Aşınma oranı ve COF değerlerinin tahmini sapma miktarlarının sıfıra yakın olarak elde edilmesi oluşturulan YSA modelinin geçerli olduğunu göstermiştir.
- YSA modelinin aşınma oranı ve COF değerlerini tahmin etmede oldukça yüksek doğruluk oranlarına sahip olduğu görülmüştür.

İlave edilen hem Gr hem de B_4C dolgu tipide kompozitlerin aşınma dirençlerini arttırdığı tespit edilmiştir.

5. TEŞEKKÜR

Bu çalışma, Batman Üniversitesi Bilimsel Araştırma Projeleri Koordinasyon Birimi tarafından "BTÜBAP-2021-YL-020" kodlu proje ile desteklenmiştir.

6. ÇIKAR ÇATIŞMASI

Yazarlar, bilinen herhangi bir çıkar çatışması veya herhangi bir kurum/kuruluş ya da kişi ile ortak çıkar bulunmadığını onaylamaktadırlar.

7. YAZAR KATKISI

Hüseyin GÜRBÜZ, Mehmet Emin DEMİR, Şehmus BADAY ve İbrahim Halil AKCAN çalışmanın kavramsal ve tasarım süreçlerinin belirlenmesi, çalışmanın kavramsal ve tasarım süreçlerinin yönetimi, veri toplama, veri analizi ve yorumlama, makale taslağının oluşturulması, fikirsel içeriğin eleştirel incelemesi, son onay ve tam sorumluluk kısımlarında katkıda bulunmuştur.

8. KAYNAKLAR

Abenojar J., Martínez M. A., Velasco F., Pascual-Sánchez V., Martín-Martínez J. M., Effect of Boron Carbide Filler on the Curing and Mechanical Properties of an Epoxy Resin. The Journal of Adhesion 85, 216-238, 2009.

Agrawal S., Singh K. K., Sarkar P. K., A comparative study of wear and friction characteristics of glass fibre reinforced epoxy resin, sliding under dry, oil-lubricated and inert gas environments. Tribology International 96, 217-224, 2016.

Arun A., Kumar Singh K., Friction and Wear Behaviour of Glass Fibre Reinforced Polymer Composite (GFRP) under Dry and Oil Lubricated Environmental Conditions. Materials Today: Proceedings 4, 7285-7292, 2017.

Chowdhury M. A., Helali M., The effect of amplitude of vibration on the coefficient of friction for different materials. Tribology International 41, 307-314, 2008.

Chowdhury M. A., Shuvho B. A., Debnath U. K., Nuruzzaman D. M., Prediction and Optimization of Erosion Rate of Carbon Fiber–Reinforced Ebonite Using Fuzzy Logic. Journal of Testing and Evaluation 47, 1244-1258, 2019.

Ciurana J., Quintana G., Garcia-Romeu M. L., Estimating the cost of vertical high-speed machining centres, a comparison between multiple regression analysis and the neural networks approach. International Journal of Production Economics 115, 171-178, 2008.

Çetkin E., Demir M. E., Ergün R. K., The effect of different fillers, loads, and sliding distance on adhesive wear in woven e-glass fabric composites. Proceedings of the Institution of Mechanical Engineers, Part E: Journal of Process Mechanical Engineering:095440892211368, 2022.

Demir M. E., Cetkin E., Ergün R. K., Denizhan O., Tribological and mechanical properties of nanofilled glass fiber reinforced composites and analyzing the tribological behavior using artificial neural networks. Polymer Composites 45, 4233-4249, 2024.

Demir M. E., Çelik Y. H., Kilickap E., Effect of matrix material and orientation angle on tensile and tribological behavior of jute reinforced composites. Materials Testing, 61(8), 806-812, 2019.

Demir M. E., Investigation of The Abrasive Wear Behavior of GFRC And CFRC with Different Parameters Using Taguchi And Artificial Neural Networks Method. Politeknik Dergisi 28(1), 215-228, 2024.

Divya G. S., Keshavamurthy R., Siddaraju C., Murthy K. V. S., Investigation on Sliding Wear Properties of Nano Metallic Particle Reinforced Hybrid Composites Through Design of Experiments and ANN. Journal of The Institution of Engineers (India): Series D 105(3), 1551-1562, 2023.

Findik F., Yilmaz R., Köksal T., Investigation of mechanical and physical properties of several industrial rubbers. Materials & Design 25, 269-276, 2004.

Friedrich K., Polymer composites for tribological applications. Advanced Industrial and Engineering Polymer Research 1, 3-39, 2018.

Gürbüz H., Akcan İ. H., Baday Ş., Demir M. E., Investigation of Drilling Performances, Tribological and Mechanical Behaviors of GFRC Filled with B4C and Gr. Arabian Journal for Science and Engineering 1-18, 2024.

Gyurova L. A., Friedrich K., Artificial neural networks for predicting sliding friction and wear properties of polyphenylene sulfide composites. Tribology International 44, 603-609, 2011.

Jayan J. S., Appukuttan S., Wilson R., Joseph K., George G., Oksman K., An introduction to fiber reinforced composite materials. Woodhead Publishing Series in Composites Science and

Engineering. (ed by K Joseph, K Oksman, G George, R Wilson & SBT-FRC Appukuttan) Woodhead Publishing, pp 1–24, 2021.

Jiang Z., Zhang Z., Friedrich K., Prediction on wear properties of polymer composites with artificial neural networks. Composites Science and Technology 67, 168-176, 2007.

Kim S. S., Shin M. W., Jang H., Tribological properties of short glass fiber reinforced polyamide 12 sliding on medium carbon steel. Wear 274, 34-42, 2012.

Kose H., Bayar I., Ergün R. K., Experimental optimization of CuO and MgO hybrid nanoparticle reinforcement ratios to enhance fatigue life of GFRP composites. Polymer Composites 45, 11125-11137, 2024.

Kranthi G., Satapathy A., Evaluation and prediction of wear response of pine wood dust filled epoxy composites using neural computation. Computational Materials Science 49, 609-614, 2010.

Kumar S., Priyadarshan, Ghosh S. K., Statistical and artificial neural network technique for prediction of performance in AlSi10Mg-MWCNT based composite materials. Materials Chemistry and Physics 273, 125136, 2021a.

Kumar S., Priyadarshan, Ghosh S. K., Statistical and computational analysis of an environment-friendly MWCNT/NiSO4 composite materials. Journal of Manufacturing Processes 66, 11-26, 2021b.

Kumar S., Singh K. K., Tribological behaviour of fibre-reinforced thermoset polymer composites: A review. Proceedings of the Institution of Mechanical Engineers, Part L: Journal of Materials: Design and Applications 234, 1439-1449, 2020.

Li Y., Zhang H., Porwal H., Huang Z., Bilotti E., Peijs T., Mechanical, electrical and thermal properties of in-situ exfoliated graphene/epoxy nanocomposites. Composites Part A: Applied Science and Manufacturing 95, 229-236, 2017.

Negi A. S., Katiyar J. K., Kumar S., Kumar N., Patel V. K., Physicomechanical and abrasive wear properties of hemp/Kevlar/carbon reinforced hybrid epoxy composites. Materials Research Express 6, 115304, 2019.

Ouyang J. H., Li Y. F., Zhang Y. Z., Wang Y. M., Wang Y. J., High-Temperature Solid Lubricants and Self-Lubricating Composites: A Critical Review. Lubricants 10(8), 177, 2022.

Padhi P. K., Satapathy A., Analysis of Sliding Wear Characteristics of BFS Filled Composites Using an Experimental Design Approach Integrated with ANN. Tribology Transactions 56, 789-796, 2013.

Pati P. R., Prediction and wear performance of red brick dust filled glass–epoxy composites using neural networks. International Journal of Plastics Technology 23, 253-260, 2019.

Ray S., Parametric Optimization and Prediction of Abrasion Wear Behavior of Marble-Particle-Filled Glass–Epoxy Composites Using Taguchi Design Integrated with Neural Network. JOM 73, 2050-2059, 2021.

Rodrigues D. D., Broughton J. G., Silane surface modification of boron carbide in epoxy composites. International Journal of Adhesion and Adhesives 46, 62-73, 2013.

Shtub A., Versano R., Estimating the cost of steel pipe bending, a comparison between neural networks and regression analysis. International Journal of Production Economics 62, 201-207, 1999.

Singh K. K, Ansari M. T. A., Azam M. S., Fatigue life and damage evolution in woven GFRP angle ply laminates. International Journal of Fatigue 142, 105964, 2021.

Subbaya K. M., Suresha B., Rajendra N., Varadarajan Y. S., Taguchi approach for characterization of three-body abrasive wear of carbon-epoxy composite with and without SiC filler. Composite Interfaces 19, 297-311, 2012.

Sudheer M., Hemanth K., Raju K., Bhat T., Enhanced Mechanical and Wear Performance of Epoxy/glass Composites with PTW/Graphite Hybrid Fillers. Procedia Materials Science 6, 975-987, 2014.

Suresha B., Chandramohan G., Sadananda Rao P. R., Sampathkumaran P., Seetharamu S., Influence of SiC filler on mechanical and tribological behavior of glass fabric reinforced epoxy composite systems. Journal of Reinforced Plastics and Composites 26(6), 565-578, 2007.

Teli G., Mahakur V. K., Paul R. Bhowmik S., Investigation of Dry Sliding Tribological Behaviour of Epoxy Composites Filled with Hemp Particulates Using Artificial Neural Networks. Arabian Journal for Science and Engineering 48, 3989-4001, 2023.

Thakur R. K. Singh K. K., Abrasive waterjet machining of fiber-reinforced composites: a state-of-the-art review. Journal of the Brazilian Society of Mechanical Sciences and Engineering 42, 381, 2020.

Turaka S., Reddy K. V. K., Sahu R. K., Katıyar J. K., Mechanical properties of MWCNTs and graphene nanoparticles modified glass fibre-reinforced polymer nanocomposite. Bulletin of Materials Science 44, 194, 2021.

Zhang Z., Friedrich K. Velten K., Prediction on tribological properties of short fibre composites using artificial neural networks. Wear 252, 668-675, 2002.

Zhao F., Li G., Österle W., Häusler I., Zhang G., Wang T., Wang Q., Tribology International Tribological investigations of glass fi ber reinforced epoxy composites under oil lubrication conditions. Tribiology International 103, 208-217, 2016.

JOURNAL of
MATERIALS and MECHATRONICS:A

e-ISSN 2717-8811
JournalMM, 2025, 6(1), 83-102
https://doi.org/10.55546/jmm.1610751

Araştırma Makalesi / Research Article

Thermomechanical Buckling Behavior of FGM Sandwich Nanoplate with Honeycomb Core Based on NSGT

Adem Fatih OZALP*

* Karabuk University, Faculty of Engineering, Department of Mechanical Engineering, Karabuk, Türkiye,
ORCID ID: https://orcid.org/0000-0001-8873-4663, ademfatihozalp@kbu.edu.tr

Geliş/ Received: 31.12.2024**;** **Revize/Revised:** 16.02.2025 **Kabul / Accepted:** 27.02.2025

ABSTRACT: This study investigates the nondimensional buckling behavior of a functionally graded material (FGM) sandwich nanoplate. The analysis consider variations in material gradation parameter, length ratio, thickness ratio, incline angle, nonlocal parameter and size parameter. Higher-order shear deformation theory (HSDT), Nonlocal strain gradient theory (NSGT), Hamilton's principle, and the Navier solution with simply supported boundary conditions are employed to derive and solve the governing equations of motion. The effects of nonlocal elasticity, strain gradient elasticity, dimension change of the core layer on the thermomechanical buckling behavior of the sandwich nanoplate have been examined in a broad framework. It is observed that the thickness ratio and incline angle in the core layer are effective on the thermomechanical buckling behavior of the sandwich nanoplate whereas length ratio change has a neglectable results. Material gradation parameter changes buckling behavior significantly. The research provides critical conclusions for the design of FG nanoplates in advanced thermal and mechanical applications, emphasizing the adjustability of buckling behavior via material and structural modifications.

Keywords: Sandwich nanoplate, Honeycomb, Ti-6Al-4V, Al_2O_3, Thermomechanical buckling

*Sorumlu yazar / Corresponding author: ademfatihozalp@kbu.edu.tr
Bu makaleye atıf yapmak için /To cite this article

Ozalp, A. F. (2025). Thermomechanical Buckling Behavior of FGM Sandwich Nanoplate with Honeycomb Core Based on NSGT. Journal of Materials and Mechatronics: A (JournalMM), 6(1), 83-102.

1. INTRODUCTION

FGMs are abundantly studied by researchers for their significant and unique resistance to environmental conditions. FGMs are researched in many different structure types such as plate, beam, hollow pipe, sphere or as shell to these specific structure types (Abuteir and Boutagouga, 2022; Akgöz and Civalek, 2014; Chen et al., 2022; Ozalp and Esen, 2025). These models are used as helpful for the production of dental applications, space technology, smart nanoelectromechanical systems, nanosensors, and invisibility technology.

FGMs are not just produced as one material as they are produced of generally metal and ceramic materials in terms of different volumes along the thickness. This characteristic of FGMs features a distinct and specific response to environmental conditions compared to composites. Also FGMs can be used with different structure types such as a plate with pure metal foam core between two FGM surface layers (Al-Waily et al., 2022). Additionally, honeycomb can be used instead of foam core and supply different results for different conditions.

Because of its cellular design, honeycomb structures have special mechanical qualities that enable effective distribution of load and energy absorption. Geometric setup, material anisotropy, and temperature fluctuations all affect these structures' thermal buckling response. For instance, the angle parameter of honeycomb cell will have the largest load capacity. This can be seen in the nanobeam's lowest level of displacement and its highest level of critical buckling stress. Different results are obtained with auxetic honeycomb structures compared to materials with positive Poisson's ratios. These structures have variable stiffness and negative Poisson's ratios, which are affected by their geometric features (Van Lieu et al., 2024).

FGMs are made with different properties that can be changed to lower stress levels and make them more resistant to heat. A lot of research has been conducted on the thermal buckling of cylindrical shells with FGM coatings. This studies show how defective cylinder shells react to thermal stress (Dang et al., 2024; Wang et al., 2016). The results show that the difference in the material's properties has a big effect on the critical buckling temperature. This shows that FGMs can make honeycomb structures more resistant to heat. The addition of auxetic materials to honeycomb constructions is very helpful in situations where high energy absorption and structural resilience are needed.

One important feature of honeycomb structures is how they change when they are hit. Experiments are conducted to assess the damage patterns that happen when high-speed impact hit honeycomb sandwich structures with FGM face plates (Arslan and Gunes, 2018). The test results showed that changing the FGM face plates' material makeup changed the types of damage they could take, how much energy they could absorb, and how well they could withstand impacts. There was also energy absorption from the honeycomb core through plastic buckling of the cell walls and lateral crushing deformations.

Spaceship bus designs should make designs more flexible and lighter without sacrificing functionality. To keep the needed rigidity while minimizing mass, a spacecraft structure needs to be very efficient. Because they are light, stiff, and strong in bending, honeycomb sandwich shapes are being used more and more in industry (Boudjemai et al., 2013).

Modern computing methods, like finite element analysis (FEA), have led to more about how honeycomb FGM plates react to temperature changes. The study of how new re-entrant circular auxetic honeycombs react to dynamic crushing shows how accurate numerical models can be at predicting what complex structures will behave under different loading conditions. Results show that

design factors might make honeycomb-FGM structures work better in terms of heat and force (Qi et al., 2022).

Biological tissues, including bone, wood, and sponge, demonstrate hierarchical cellular structures that are lightweight and exhibit enhanced energy absorption properties. A study on bio-inspired hierarchical honeycombs demonstrates the ability of these materials to exhibit improved reliability and energy absorption characteristics (Yin et al., 2018). Plates also can be utilized in many areas at nanoscale such as nanocardboard could be used as a structural element for scanning probe cantilevers, microflyer or interstellar lightsail wings, and other microscopic and macroscopic systems (Lin et al., 2018)

Mentioned literature reveals that the examination of FG surface plates with honeycomb core sandwich structures affected by temperature forms a relatively unexplored research area. Recent studies have concentrated on these structures because of the remarkable mechanical and thermal properties associated with honeycomb configurations. Honeycomb structures, due to their metamaterial characteristics, have the potential for novel applications in various fields. This study examines the thermomechanical buckling properties of composite nanoplates, consisting of a honeycomb core layer and FG metal/ceramic surface layers. This research provides a comprehensive analysis of the thermomechanical buckling response of sandwich nanoplates, with findings presented in detail. The investigation's results demonstrated that the buckling response of the sandwich nanoplate can be substantially altered to meet defined conditions and requirements. The findings of this study will contribute to important application areas, such as aerospace and submarine vehicles, which need protection against ultrasonic and mechanical waves in both standard and high temperature conditions. The results obtained are expected to be relevant for radar stealth applications and for the protection of nanoelectromechanical systems operating in high noise and vibration environments.

2. FG NANOPLATE SANDWICH STRUCTURE

Figure 1 presents a schematic representation of the sandwich nanoplate under investigation, while Figure 2 depicts core layer structure comprised of honeycomb. The sandwich structure consists of a honeycomb core layer (Ti-6Al-4V) between top and bottom FGM layers (Ti-6Al-4V; Al_2O_3).

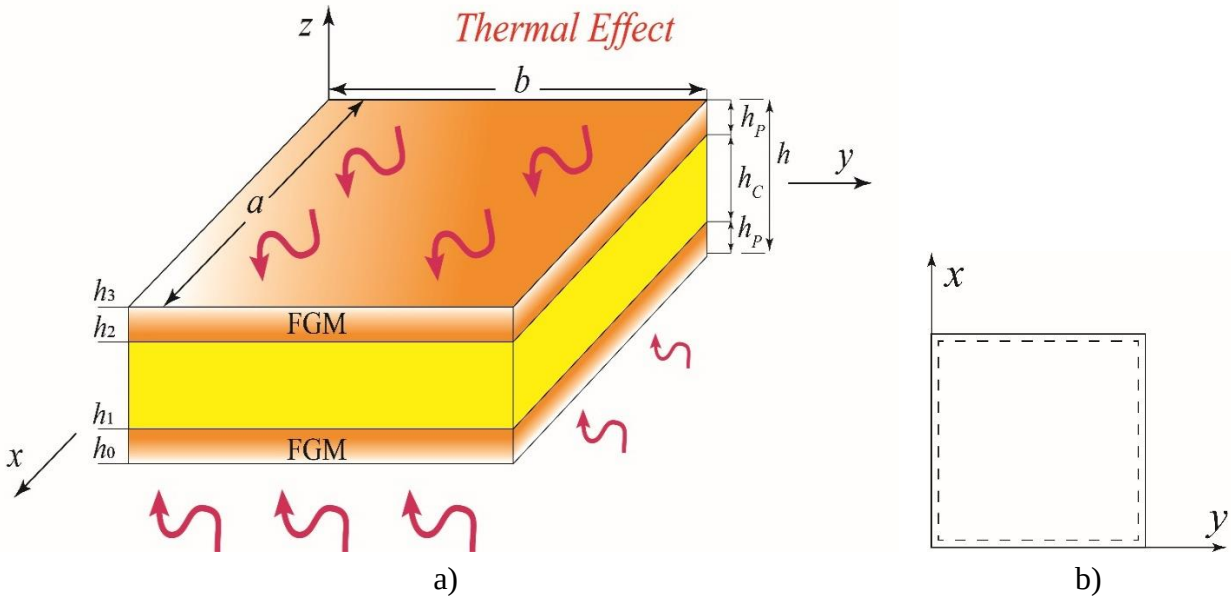

Figure 1. (a) Top and bottom FGM plates with honeycomb core (b) SSSS plate boundary conditions

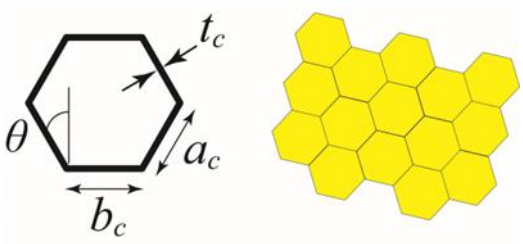

Figure 2. Honeycomb core layer and dimension symbols

2.1 Core Layer

Gibson formula (Gibson, 2003) is used to find the properties of honeycomb layer changing with structural dimensions as follows:

$$E_{11} = \frac{E_c {\zeta_3}^3 \cos\theta}{(\zeta_1 + \sin\theta)\sin^2\theta}\left[1 - {\zeta_3}^2 \cot^2\theta\right] \tag{1}$$

$$E_{22} = \frac{E_c {\zeta_3}^3 (\zeta_1 + \sin\theta)}{\cos^3\theta}\left[1 - {\zeta_3}^2 (\zeta_1 \sec^2\theta + \tan^2\theta)\right] \tag{2}$$

$$E_{33} = \frac{E_c \zeta_3 (2 + \zeta_1)}{2(\zeta_1 + \sin\theta)\cos\theta} \tag{3}$$

$$v_{12} = \frac{\cos^2\theta}{(\zeta_1 + \sin\theta)\sin\theta}\left[1 - {\zeta_3}^2 \csc^2\theta\right] \tag{4}$$

$$G_{12} = \frac{E_c {\zeta_3}^3 (\zeta_1 + \sin\theta)}{{\zeta_1}^2 (1 + 2\zeta_1)\cos\theta} \tag{5}$$

$$G_{13} = \frac{G_c \zeta_3 \cos\theta}{\zeta_1 + \sin\theta} \tag{6}$$

$$G_{23} = \frac{G_c \zeta_3}{2\cos\theta}\left[\frac{\zeta_1 + \sin\theta}{(1 + 2\zeta_1)\cos\theta} + \frac{\zeta_1 + 2\sin^2\theta}{2(\zeta_1 + \sin\theta)}\right] \tag{7}$$

$$\rho^c = \frac{\rho_{TiAlV} \zeta_3 (\zeta_1 + 2)}{2\cos\theta(\zeta_1 + \sin\theta)} \tag{8}$$

$$\alpha^c = \frac{\alpha_{TiAlV} \zeta_3 (\zeta_1 + 2)}{2\cos\theta(\zeta_1 + \sin\theta)} \tag{9}$$

$$\psi^c = \frac{\psi_{TiAlV} \zeta_3 (\zeta_1 + 2)}{2\cos\theta(\zeta_1 + \sin\theta)} \tag{10}$$

$$\zeta_1 = \frac{b_c}{a_c} \tag{11}$$

$$\zeta_3 = \frac{t_c}{a_c} \tag{12}$$

$G_{ij,ik,jk}$, v_{ij}, $E_{ii,jj}$ and ρ denote Shear moduli, Poisson's ratio, Elastic modulus, and density, respectively, for the hexagonal core. ψ denotes the thermal conductivity coefficient while α is thermal expansion coefficient. Coefficient subscript c stands for the honeycomb material (eg., E_c as Elastic moduli). For other honeycomb coefficients, a_c, b_c, and t_c denote inclined lengths, vertical length and thickness of the cell rib respectively, while θ represents the inclination degree. ζ_1 denotes length ratio and ζ_3 represents thickness ratio (Figure 1, 2).

2.2 FGM Face Layers

Numerous distribution functions have been proposed in the literature for the simulation of FGM structures (Touloukian, 1967). This research examines the applied Voigt model (Markworth et al., 1995).

Top layer:

$$P(z) = [P_m - P_c]V_c + P_m, \qquad V_c = \left(\frac{z}{h} + \frac{1}{2}\right)^p, \qquad V_c + V_m = 1, \qquad h_2 < z < h_3 \tag{13a}$$

Bottom layer:

$$P(z) = [P_c - P_m]V_m + P_c, \qquad V_m = \left(\frac{z}{h} + \frac{1}{2}\right)^p, \qquad V_c + V_m = 1, \qquad h_0 < z < h_1 \tag{13b}$$

Each layer can have a different P(z) which symbolizes effective material parameter and it changes along the z-direction. P_c stands for the properties of ceramic constituent and P_m denotes metal property characteristics. The volume fraction of the ceramic material is represented by V_c and V_m correspond to ceramic and metal material, also the power distribution, denoted as p, ranges from zero to infinity. In the condition of p=∞, the layer completely contains metal, but at p=0, it purely contains ceramic (Equation 13a, 13b). From h_0 to h_1 are the boundaries of bottom plate thickness and from h_2 to h_3 is defined as top plate thickness boundaries. For the core plate thickness boundaries range from h_1 to h_2.

The calculation of temperature dependent material coefficients can be conducted using a nonlinear temperature function (Table 1), as accounting for the temperature effect is crucial for precise predictions of the structure's behavior (Markworth et al., 1995).

$$P_i = P_0\,(P_{-1}T^{-1} + 1 + P_1T + P_2T^2 + P_3T^3) \tag{14}$$

The characteristics of each material are determined by its P_i (i=0,1,2,3) values, corresponding to various temperature (T) values.

2.3 The Temperature Effect

To find uniform, linear and nonlinear temperature rise in the equation, FG nanoplate temperature is raised to its final temperature in the condition of initial temperature is T_0=300K and plate is stress-free.

$$\Delta T = T - T_0 \tag{15}$$

Based on the assumption that the temperature increases linearly (LTR) from T_t to T_b across the thicknesses, the temperature of a horizontal surface that extends in the z-axis with the temperatures of its bottom and upper surfaces, T_b and T_t, respectively, can be computed as follows (Kiani and Eslami, 2013):

$$T(z) = T_b + (T_t - T_b)\left(\frac{h + 2z}{2h}\right) \tag{16}$$

Table 1. Temperature dependent coefficients of the FG sandwich plate (Reddy and Chin, 1998)

Material	Property	P_{-1}	P_0	P_1	P_2	P_3
Ti-6Al-4V	E(Pa)	0	122.56x10^{9}	-4.586x10^{-4}	0	0
	v	0	0.2884	1.121x10^{-4}	0	0
	$\alpha(\mathrm{K}^{-1})$	0	7.5788x10^{-6}	6.638x10^{-4}	-3.147x10^{-6}	0
	ψ(W/mK)	0	1.000	1.704x10^{-2}	0	0
	$\rho(\mathrm{kg/m^3})$	0	4420	0	0	0
Al_2O_3	E(Pa)	0	349.55 x10^{9}	-3.853 x10^{-4}	4.027 x10^{-7}	-1.673 x10^{-10}
	v	0	0.26	0	0	0
	$\alpha(\mathrm{K}^{-1})$	0	6.8269 x10^{-6}	1.838 x10^{-4}	0	0
	ψ(W/mK)	-1123.6	-14.087	-6.227 x10^{-3}	0	0
	$\rho(\mathrm{kg/m^3})$	0	3750	0	0	0

The one-dimensional heat transfer problem can be analyzed under conditions of a nonlinear temperature increase (NLTR) across the thickness of the nanoplates, utilizing defined temperature boundary limits to determine the upper and lower surface temperatures (T_b and T_t) of the plate (Ozalp and Esen, 2024).

$$-\frac{d}{dz}\left(\psi(z)\frac{dT}{dz}\right) = 0, \qquad T\left(\frac{h}{2}\right) = T_t, \quad T\left(-\frac{h}{2}\right) = T_b \tag{17}$$

ψ represents the thermal conductivity coefficient. The temperature at any position along the thickness of the *z*-axis, given a specific boundary condition, can be determined as follows:

$$T(z) = T_b + (T_t - T_b)\frac{\int_{-\frac{h}{2}}^{z}\frac{1}{\psi(z,T)}dz}{\int_{-\frac{h}{2}}^{\frac{h}{2}}\frac{1}{\psi(z,T)}d(z)} \tag{18}$$

2.4 Application of Nonlocal Strain Gradient Elasticity

The calculations for shear and normal stresses at any particular position can be performed using σ_{xx}^{t} and σ_{xz}^{t} the total stress in the *xz* and *xy* directions as follows (Arani, 2017):

$$\begin{aligned}\sigma_{xx}^{t} &= \sigma_{xx}^{c} - \nabla^2\sigma_{xx}^{h}\\ \sigma_{xz}^{t} &= \sigma_{xz}^{c} - \nabla^2\sigma_{xz}^{h}\end{aligned} \tag{19}$$

Where:

$$\sigma_{xx}^{c} = \int_{V} E(z)\alpha_0(\boldsymbol{x}', \boldsymbol{x}, e_0 a)\varepsilon'_{xx}(\boldsymbol{x}')dV' \tag{20a}$$

$$\sigma_{xx}^{h} = l_m^2 \int_{V} E(z)\alpha_1(\boldsymbol{x}', \boldsymbol{x}, e_1 a)\nabla\varepsilon'_{xx}(\boldsymbol{x}')dV' \tag{20b}$$

$$\sigma_{xz}^{c} = \int_{V} G(z)\alpha_0(\boldsymbol{x}', \boldsymbol{x}, e_0 a)\varepsilon'_{xz}(\boldsymbol{x}')dV' \tag{20c}$$

$$\sigma_{xz}^{h} = l_m^2 \int_{V} G(z)\alpha_1(\boldsymbol{x}', \boldsymbol{x}, e_1 a)\nabla\varepsilon'_{xz}(\boldsymbol{x}')dV' \tag{20d}$$

Here, σ^c and σ^h represent the normal and shear stresses of higher-order and classical types, with ∇ utilized as the Laplacian operator. Additionally, the size parameter l_m quantifies the impact of size at the nanoscale. The functions $\alpha_0\ (\boldsymbol{x}', \boldsymbol{x}, e_0 a)$ and $\alpha_1\ (\boldsymbol{x}', \boldsymbol{x}, e_1 a)$ denote the nonlocal weakening functions associated with the strains ε'_{xx} and ε'_{xz}. Additionally, V signifies volume. The nonlocality coefficients are represented as e_0 and e_1 (Arani and Jalaei, 2017). Assuming $e_0 = e_1$, and utilizing a linear differential operator, we can derive the next equation pertaining to the Nonlocal Strain Gradient Theory (NSGT) (Lim et al., 2015):

$$\left[1 - (e_0 a)^2 \nabla^2\right]\sigma_{xx}^{t} = [1 - l_m^2\nabla^2]E(z)\varepsilon_{xx} \tag{21a}$$

$$\left[1 - (e_0 a)^2 \nabla^2\right]\sigma_{xz}^{t} = [1 - l_m^2\nabla^2]G(z)\varepsilon_{xz} \tag{21b}$$

where ε_{xx} denotes normal strain, γ_{xz} signifies the shear strain, and σ^t represents the total stress:

$$\sigma_{xx}^{t} - (e_0 a)^2 \frac{\partial^2 \sigma_{xx}^{t}}{\partial x^2} = \left[\varepsilon_{xx} - l_m^2 \frac{\partial^2 \varepsilon_{xx}}{\partial x^2}\right] E(z) \tag{22a}$$

$$\sigma_{xz}^{t} - (e_0 a)^2 \frac{\partial^2 \sigma_{xz}^{t}}{\partial x^2} = \left[\gamma_{xz} - l_m^2 \frac{\partial^2 \gamma_{xz}}{\partial x^2}\right] G(z) \tag{22b}$$

2.5 Displacement Fields and Strains

The HSDT (Shimpi, 2002) is developed based on the subsequent assumptions:

$$u_1(x, y, z, t) = u(x, y, t) - z\frac{\partial w_b}{\partial x} - f(z)\frac{\partial w_s}{\partial x} \tag{23a}$$

$$u_2(x, y, z, t) = v(x, y, t) - z\frac{\partial w_b}{\partial y} - f(z)\frac{\partial w_s}{\partial y} \tag{23b}$$

$$u_3(x, y, z, t) = w_b(x, y, t) + w_s(x, y, t) \tag{23c}$$

Here, $f(z) = -z/4 + 5z^3/3h^2$. The displacements along the coordinate directions (x, y, z) are represented by u_1, u_2, u_3. The variables u and v indicate the displacements of a point on the midplane along the x and y directions. For the transverse displacement, w_s is shear component and w_b is bending component. The variable h signifies the thickness length. The HSDT, as stated earlier, neglects the effect of the thickness stretching considering a uniform transverse displacement throughout the thickness. The displacement field in equation (23c) is altered by integrating

supplementary variables addressing the thickness stretching that signifies the transverse displacement.

$$u_3(x,y,z,t) = w_b(x,y,t) + w_s(x,y,t) + g(z)w_z(x,y,t) \tag{24}$$

The displacement function w_z denotes an unspecified function that accounts for the influence of thickness stretching. The shape function $g(z)$ is established in accordance with the stress-free boundary conditions at the upper and lower surfaces of the nanoplate. Utilizing the same methods described by Reddy, the form function $g(z)$ is derived as (Reddy, 1984):

$$g(z) = 1 - f'(z) = \frac{5}{4}\left(1 - \frac{4z^2}{h^2}\right) \tag{25}$$

The linear strains associated with the newly established displacement field in equations (23, 24) are as follows:

$$\varepsilon_{xx} = \frac{\partial u}{\partial x} - z\frac{\partial^2 w_b}{\partial x^2} - f(z)\frac{\partial^2 w_s}{\partial x^2} \tag{26a}$$

$$\varepsilon_{yy} = \frac{\partial v}{\partial y} - z\frac{\partial^2 w_b}{\partial y^2} - f(z)\frac{\partial^2 w_s}{\partial y^2} \tag{26b}$$

$$\varepsilon_z = g'(z)w_z \tag{26c}$$

$$\gamma_{xy} = \frac{\partial u}{\partial y} + \frac{\partial v}{\partial x} - 2z\frac{\partial^2 w_b}{\partial x\,\partial y} - 2f(z)\frac{\partial^2 w_s}{\partial x\,\partial y} \tag{26d}$$

$$\gamma_{xz} = g(z)\left(\frac{\partial w_s}{\partial x} + \frac{\partial w_z}{\partial x}\right) \tag{26e}$$

$$\gamma_{yz} = g(z)\left(\frac{\partial w_s}{\partial y} + \frac{\partial w_z}{\partial y}\right) \tag{26f}$$

The tensions develop due to constitutive interactions.

$$\begin{bmatrix}\sigma_x\\ \sigma_y\\ \sigma_z\\ \sigma_{xy}\\ \sigma_{xz}\\ \sigma_{yz}\end{bmatrix} = \frac{1}{E(z)}\begin{bmatrix}1 & -v & -v & 0 & 0 & 0\\ -v & 1 & -v & 0 & 0 & 0\\ -v & -v & 1 & 0 & 0 & 0\\ 0 & 0 & 0 & 2(1+v) & 0 & 0\\ 0 & 0 & 0 & 0 & 2(1+v) & 0\\ 0 & 0 & 0 & 0 & 0 & 2(1+v)\end{bmatrix}\begin{bmatrix}\varepsilon_{xx}\\ \varepsilon_{yy}\\ \varepsilon_{zz}\\ \gamma_{xy}\\ \gamma_{xz}\\ \gamma_{yz}\end{bmatrix} + \alpha\Delta T\begin{bmatrix}1\\1\\1\\0\\0\\0\end{bmatrix} \tag{27}$$

C_{ijkl} represents the three-dimensional elastic constants.

$$\varepsilon_{ij} = \frac{(1+v)}{E(z)}\sigma_{ij} - \frac{v}{E(z)}\sigma_{kk}\gamma_{ij} + \alpha\Delta T\gamma_{ij} \tag{28a}$$

$$\sigma_{ij} = \frac{E(z)}{1+v}\left\{\varepsilon_{ij} + \frac{v}{(1-2v)}\right\} - \frac{E\alpha\Delta T}{1-2v}\gamma_{ij} \tag{28b}$$

$$\sigma_{ij} = C_{ijkl}(\varepsilon_{kl} - \alpha\Delta T\delta_{kl}) \text{ and } \varepsilon_{ij} = S_{ijkl}\sigma_{kl} - \alpha\Delta T\gamma_{ij} \tag{28c}$$

$$C_{ijkl} = \frac{E(z)}{2(1+v)}(\gamma_{il}\gamma_{jk} + \gamma_{ik}\gamma_{jl}) + \frac{vE(z)}{(1-2v)(1+v)}\gamma_{ij}\gamma_{kl} \tag{28d}$$

$$S_{ijkl} = \frac{(1+v)}{2E(z)}(\gamma_{il}\gamma_{jk} + \gamma_{ik}\gamma_{jl}) - \frac{v}{E(z)}\gamma_{ij}\gamma_{kl} \tag{28e}$$

In the absence of the thickness stretching effect (i.e., ε_z=0), Equation (27) is modified for constitutive relations as follows:

$$\begin{bmatrix}\sigma_x\\ \sigma_y\\ \sigma_{xy}\\ \sigma_{yz}\\ \sigma_{xz}\end{bmatrix} = \frac{E}{1-v^2}\begin{bmatrix}1 & v & 0 & 0 & 0\\ v & 1 & 0 & 0 & 0\\ 0 & 0 & \frac{(1-v)}{2} & 0 & 0\\ 0 & 0 & 0 & \frac{(1-v)}{2} & 0\\ 0 & 0 & 0 & 0 & \frac{(1-v)}{2}\end{bmatrix}\begin{bmatrix}\varepsilon_x\\ \varepsilon_y\\ \gamma_{xy}\\ \gamma_{yz}\\ \gamma_{xz}\end{bmatrix} + \frac{E\alpha\Delta T}{1-2v}\begin{bmatrix}1\\1\\1\\0\\0\\0\end{bmatrix} \tag{29}$$

Given the negligible influence of Poisson's ratio on the response of FG plates (Kitipornchai et al., 2006; Yang et al., 2005), it is assumed to be constant for simplicity. This study suggests that elastic moduli exhibits variation throughout the nanoplate thickness, following a power-law distribution based on the volume fraction of the constituents.

The mathematical expression for the strain energy of the nanoplate is as follows:

$$U = \frac{1}{2}\int_A \left(\sum_{n=1}^{3}\int_{h_{n-1}}^{h_n}\left(\sigma_x\varepsilon_x + \sigma_y\varepsilon_y + \sigma_z\varepsilon_z + \sigma_{xy}\gamma_{xy} + \sigma_{xz}\gamma_{xz} + \sigma_{yz}\gamma_{yz}\right)dz\right)dA \tag{30}$$

The area is denoted by A. By replacing equation (26) into equation (27) and subsequently applying the results in equation (30) allows for the reformulation of the strain energy expression as:

$$U = \frac{1}{2}\int_A \begin{pmatrix} N_x\frac{\partial u}{\partial x} - M_x^b\frac{\partial^2 w_b}{\partial x^2} - M_x^s\frac{\partial^2 w_s}{\partial x^2} + N_y\frac{\partial v}{\partial y} - M_y^b\frac{\partial^2 w_b}{\partial y^2} - M_y^s\frac{\partial^2 w_s}{\partial y^2} + R_z w_z \\ +N_{xy}\left(\frac{\partial u}{\partial y} + \frac{\partial v}{\partial x}\right) - 2M_{xy}^b\frac{\partial^2 w_b}{\partial x\,\partial y} - 2M_{xy}^s\frac{\partial^2 w_s}{\partial x\,\partial y} + Q_x\left(\frac{\partial w_b}{\partial x} + \frac{\partial w_z}{\partial x}\right) + Q_y\left(\frac{\partial w_s}{\partial y} + \frac{\partial w_z}{\partial y}\right) \end{pmatrix} dA \tag{31}$$

Here *N*, *M*, *Q*, and *R* represent the specified stress resultants.

$$\left(N_x, N_y, N_{xy}\right) = \sum_{n=1}^{3}\int_{h_{n-1}}^{h_n}\left(\sigma_x, \sigma_y, \sigma_{xy}\right)dz \tag{32a}$$

$$\left(M_x^b, M_y^b, M_{xy}^b\right) = \sum_{n=1}^{3}\int_{h_{n-1}}^{h_n}\left(\sigma_x, \sigma_y, \sigma_{xy}\right)dz \tag{32b}$$

$$\left(M_x^s, M_y^s, M_{xy}^s\right) = \sum_{n=1}^{3}\int_{h_{n-1}}^{h_n}\left(\sigma_x, \sigma_y, \sigma_{xy}\right)f(z)dz \tag{32c}$$

$$\left(Q_x, Q_y\right) = \sum_{n=1}^{3} \int_{h_{n-1}}^{h_n} \left(\sigma_{xz}, \sigma_{yz}\right) g(z) dz \tag{32d}$$

$$R_z = \sum_{n=1}^{3} \int_{h_{n-1}}^{h_n} \sigma_z g'(z) dz \tag{32e}$$

Replacing equation (25) into equation (26) and subsequently incorporating the resulting values into equation (32) allows for the representation of stress resultants in the form of displacement components (u, v, w_b, w_s, w_z).

$$N_x = A_{11}\frac{\partial u}{\partial x} + A_{12}\frac{\partial v}{\partial y} - B_{11}\frac{\partial^2 w_b}{\partial x^2} - B_{12}\frac{\partial^2 w_b}{\partial y^2} - B_{11}^s\frac{\partial^2 w_s}{\partial x^2} - B_{12}^s\frac{\partial^2 w_s}{\partial y^2} + X_{13}w_z \tag{33a}$$

$$N_y = A_{12}\frac{\partial u}{\partial x} + A_{22}\frac{\partial v}{\partial y} - B_{12}\frac{\partial^2 w_b}{\partial x^2} - B_{22}\frac{\partial^2 w_b}{\partial y^2} - B_{12}^s\frac{\partial^2 w_s}{\partial x^2} - B_{22}^s\frac{\partial^2 w_s}{\partial y^2} + X_{23}w_z \tag{33b}$$

$$N_{xy} = A_{66}\left(\frac{\partial u}{\partial y} + \frac{\partial v}{\partial x}\right) - 2B_{66}\frac{\partial^2 w_b}{\partial x\,\partial y} - 2B_{66}^s\frac{\partial^2 w_s}{\partial x\,\partial y} \tag{33c}$$

$$M_x^b = B_{11}\frac{\partial u}{\partial x} + B_{12}\frac{\partial v}{\partial y} - D_{11}\frac{\partial^2 w_b}{\partial x^2} - D_{12}\frac{\partial^2 w_b}{\partial y^2} - D_{11}^s\frac{\partial^2 w_s}{\partial x^2} \tag{33d}$$

$$M_y^b = B_{12}\frac{\partial u}{\partial x} + B_{22}\frac{\partial v}{\partial y} - D_{12}\frac{\partial^2 w_b}{\partial x^2} - D_{22}\frac{\partial^2 w_b}{\partial y^2} - D_{12}^s\frac{\partial^2 w_s}{\partial x^2} - D_{22}^s\frac{\partial^2 w_s}{\partial y^2} + Y_{23}w_z \tag{33e}$$

$$R_z = \sum_{n=1}^{3} \int_{h_{n-1}}^{h_n} \sigma_z g'(z) dz \tag{33f}$$

$$M_x^s = B_{11}^s\frac{\partial u}{\partial x} + B_{12}^s\frac{\partial v}{\partial y} - D_{11}^s\frac{\partial^2 w_b}{\partial x^2} - D_{12}^s\frac{\partial^2 w_b}{\partial y^2} - H_{11}^s\frac{\partial^2 w_s}{\partial x^2} - H_{12}^s\frac{\partial^2 w_s}{\partial y^2} + Y_{13}^s w_z \tag{33g}$$

$$M_y^s = B_{12}^s\frac{\partial u}{\partial x} + B_{22}^s\frac{\partial v}{\partial y} - D_{12}^s\frac{\partial^2 w_b}{\partial x^2} - D_{22}^s\frac{\partial^2 w_b}{\partial y^2} - H_{12}^s\frac{\partial^2 w_s}{\partial x^2} - H_{22}^s\frac{\partial^2 w_s}{\partial y^2} + Y_{23}^s w_z \tag{33h}$$

$$M_{xy}^s = B_{66}^s\left(\frac{\partial u}{\partial y} + \frac{\partial v}{\partial x}\right) - 2D_{66}^s\frac{\partial^2 w_b}{\partial x\,\partial y} - 2H_{66}^s\frac{\partial^2 w_s}{\partial x\,\partial y} \tag{33i}$$

$$R_z = X_{13}\frac{\partial u}{\partial x} + X_{23}\frac{\partial v}{\partial y} - Y_{13}\frac{\partial^2 w_b}{\partial x^2} - Y_{23}\frac{\partial^2 w_b}{\partial y^2} - Y_{13}^s\frac{\partial^2 w_s}{\partial x^2} - Y_{23}^s\frac{\partial^2 w_s}{\partial y^2} + Z_{33}w_z \tag{33j}$$

$$Q_x = A_{55}^s\left(\frac{\partial w_s}{\partial x} + \frac{\partial w_z}{\partial x}\right), \quad Q_y = A_{44}^s\left(\frac{\partial w_s}{\partial y} + \frac{\partial w_z}{\partial y}\right) \tag{33k}$$

Where

$$\left(A_{ij}, A_{ij}^s, B_{ij}, B_{ij}^s, D_{ij}, D_{ij}^s, H_{ij}^s\right) = \sum_{n=1}^{3} \int_{h_{n-1}}^{h_n} (1, g^2, z, f, z^2, fz, f^2) C_{ij} dz \tag{34}$$

$$\left(X_{ij}, Y_{ij}, Y_{ij}^s, Z_{ij}\right) = \sum_{n=1}^{3} \int_{h_{n-1}}^{h_n} (g', g'z, g'f, g'^2) C_{ij} dz \tag{35}$$

The effects of transverse loads q which are externally applied can be expressed as follows:

$$V = -\int_A q(w_b + w_s + gw_z)\, dA \tag{36}$$

The expression for kinetic energy is:

$$K = \frac{1}{2}\int_A \left(\sum_{n=1}^{3}\int_{h_{n-1}}^{h_n} \rho(\dot{u}_1^2 + \dot{u}_2^2 + \dot{u}_3^2)dz\right) dA \tag{37}$$

The axial force due to temperature variation is specified for both directions.

$$N_{xx}^T = \mathrm{b}\sum_{n=1}^{3}\int_{h_{n-1}}^{h_n} (Q_{11})\, \alpha^{(n)}(z)T(z)dz \tag{38a}$$

$$N_{yy}^T = \mathrm{a}\sum_{n=1}^{3}\int_{h_{n-1}}^{h_n} (Q_{11})\, \alpha^{(n)}(z)T(z)dz \tag{38b}$$

From the mid-plane distance (z) at a particular layer (n); the variable $\alpha^{(n)}$ denotes coefficient of thermal expansion of the FG sandwich plate. Q_{11} represents the honeycomb core elastic moduli. The external potential energy of thermal loads and in-plane mechanical loads are N_{ox} and N_{oy}:

$$V = \int_\Omega \left[(-N_{ox} - N_{xx}^T)\left(w_{b,xx} + w_{s,xx}\right) + \left(-N_{oy} - N_{yy}^T\right)\left(w_{b,yy} + w_{s,yy}\right)\right] d\Omega \tag{39}$$

Where $w_{b,xx} = \frac{\partial^2 w_b}{\partial x^2}$, $w_{b,yy} = \frac{\partial^2 w_b}{\partial y^2}$, $w_{s,xx} = \frac{\partial^2 w_s}{\partial x^2}$, $w_{s,yy} = \frac{\partial^2 w_s}{\partial y^2}$

Here, Hamilton's principle is applied to determine the equations of motion. The following is an analytical expression for the principle:

$$\int_0^T \delta(U + V - K)\, dt = 0 \tag{40}$$

The variational operator is δ. Replacing the formulas for U, V, and K from equations (23, 24, 37, 39) into equation (40), integrating, and collecting the coefficients of (δu, δv, δw_b, δw_s, δw_z) yields the subsequent motion equations as:

$$\delta u: \frac{\partial N_x}{\partial x} + \frac{\partial N_{xy}}{\partial y} = I_0\ddot{u} - I_1\frac{\partial \ddot{w}_b}{\partial x} - J_1\frac{\partial \ddot{w}_s}{\partial x} \tag{41a}$$

$$\delta v: \frac{\partial N_{xy}}{\partial x} + \frac{\partial N_y}{\partial y} = I_0\ddot{v} - I_1\frac{\partial \ddot{w}_b}{\partial y} - J_1\frac{\partial \ddot{w}_s}{\partial y} \tag{41b}$$

$$\begin{aligned}\delta w_b: \frac{\partial^2 M_x^b}{\partial x^2} + 2\frac{\partial^2 M_{xy}^b}{\partial x\,\partial y} + \frac{\partial^2 M_y^b}{\partial y^2} - q + (N_{xx}^T + N_{ox})\left(w_{b,xx} + w_{s,xx}\right) \\ + \left(N_{yy}^T + N_{oy}\right)\left(w_{b,yy} + w_{s,yy}\right) \\ = I_0(\ddot{w}_b + \ddot{w}_s) + J_0\ddot{w}_z + I_1\left(\frac{\partial \ddot{u}}{\partial x} + \frac{\partial \ddot{v}}{\partial y}\right) - I_2\nabla^2\ddot{w}_b - J_2\nabla^2\ddot{w}_s\end{aligned} \tag{41c}$$

$$\begin{aligned}\delta w_s: \frac{\partial^2 M_x^s}{\partial x^2} + 2\frac{\partial^2 M_{xy}^s}{\partial x\,\partial y} + \frac{\partial^2 M_y^s}{\partial y^2} + \frac{\partial Q_{xz}}{\partial x} + \frac{\partial Q_{yz}}{\partial y} - q + (N_{xx}^T + N_{ox})w_{0,xx} \\ + \left(N_{yy}^T + N_{oy}\right)\left(w_{b,yy} + w_{s,yy}\right)\end{aligned} \tag{41d}$$

$$\begin{aligned}\delta w_z: \frac{\partial Q_{xz}}{\partial x} + \frac{\partial Q_{yz}}{\partial y} - R_z - gq + (N_{xx}^T + N_{ox})\left(w_{b,xx} + w_{s,xx}\right) + \left(N_{yy}^T + N_{oy}\right)\left(w_{b,yy} + w_{s,yy}\right) \\ = J_0(\ddot{w}_b + \ddot{w}_s) + K_0\ddot{w}_z\end{aligned} \tag{41e}$$

The following is the definition of the mass moments of inertia, which are denoted by I_i, J_i, K_i.

$$(I_0, I_1, I_2) = \sum_{n=1}^{3}\int_{h_{n-1}}^{h_n}(1, z, z^2)\rho dz \tag{42a}$$

$$(J_0, J_1, J_2) = \sum_{n=1}^{3}\int_{h_{n-1}}^{h_n}(g, f, fz)\rho dz \tag{42b}$$

$$(K_0, K_1, K_2) = \sum_{n=1}^{3}\int_{h_{n-1}}^{h_n}(g, f, fz)\rho dz \tag{42c}$$

Using HSDT, the motion equations are generated by equation (41) if the influence of thickness stretching effect is ignored (w_z=0) (Thai and Choi, 2011; Thai; Thai and Choi, 2012; Thai, et al., 2012).

Replacing equation (27) into equation (32) allows for the expression of the motion equations in forms of displacements (u, v, w_b, w_s, w_z).

$$\mathfrak{B} = \left(1 - (l_m)^2\,\nabla^2\right) \tag{43a}$$

$$\mathfrak{D} = \left(1 - (e_0 a)^2\,\nabla^2\right) \tag{43b}$$

$$\begin{aligned}\mathfrak{B}\Bigg(A_{11}\frac{\partial^2 u}{\partial x^2} + A_{66}\frac{\partial^2 u}{\partial y^2} + (A_{12} + A_{66})\frac{\partial^2 v}{\partial x\,\partial y} - B_{11}\frac{\partial^3 w_b}{\partial x^3} - (B_{12} + 2B_{66})\frac{\partial^3 w_b}{\partial x\,\partial y^2} \\ -B_{11}^s\frac{\partial^3 w_s}{\partial x^3} - (B_{12}^s + 2B_{66}^s)\frac{\partial^3 w_s}{\partial x\,\partial y^2} + X_{13}\frac{\partial w_z}{\partial x}\Bigg) \\ = \mathfrak{D}\left(I_0\ddot{u} - I_1\frac{\partial \ddot{w}_b}{\partial x} - J_1\frac{\partial \ddot{w}_s}{\partial x}\right)\end{aligned} \tag{43c}$$

$$\mathfrak{B}\begin{pmatrix} A_{22}\dfrac{\partial^2 v}{\partial y^2} + A_{66}\dfrac{\partial^2 v}{\partial x^2} + (A_{12} + A_{66})\dfrac{\partial^2 u}{\partial x\,\partial y} - B_{22}\dfrac{\partial^3 w_b}{\partial y^3} \\ -(B_{12} + 2B_{66})\dfrac{\partial^3 w_b}{\partial x^2\,\partial y} + B_{22}\dfrac{\partial^3 v_s}{\partial y^3} - (B_{12}^s + 2B_{66}^s)\dfrac{\partial^3 w_b}{\partial x^2\,\partial y} + X_{13}\dfrac{\partial w_z}{\partial y}\end{pmatrix} \tag{43d}$$

$$= \mathfrak{D}\left(I_0\ddot{v} - I_1\frac{\partial\ddot{w}_b}{\partial y} - J_1\frac{\partial\ddot{w}_s}{\partial y}\right)$$

$$\mathfrak{B}\begin{pmatrix} B_{11}\dfrac{\partial^3 u}{\partial x^3} + (B_{12}+2B_{66})\left(\dfrac{\partial^3 u}{\partial x\,\partial y^2} + \dfrac{\partial^3 v}{\partial x^2\,\partial y}\right) + B_{22}\dfrac{\partial^3 v}{\partial y^3} - D_{11}\dfrac{\partial^4 w_b}{\partial x^4} \\ -D_{22}\dfrac{\partial^4 w_b}{\partial y^4} - 2(D_{12}+2D_{66})\dfrac{\partial^4 w_b}{\partial x^2\,\partial y^2} - D_{11}^s\dfrac{\partial^4 w_s}{\partial x^4} - D_{22}^s\dfrac{\partial^4 w_s}{\partial y^4} \\ -2(D_{12}^s+2D_{66}^s)\dfrac{\partial^4 w_s}{\partial x^2\,\partial y^2} + Y_{13}\dfrac{\partial^2 w_z}{\partial x^2} + Y_{23}\dfrac{\partial^2 w_z}{\partial y^2} + q \end{pmatrix} \tag{43e}$$

$$= \mathfrak{D}\begin{pmatrix} -I_2\nabla^2\ddot{w}_b - J_2\nabla^2\ddot{w}_s + I_0(\ddot{w}_b+\ddot{w}_s) + J_0\ddot{w}_z - I_1\left(\dfrac{\partial\ddot{w}}{\partial x} + \dfrac{\partial\ddot{v}}{\partial y}\right) \\ -q + (N_{xx}^T + N_{ox})\left(w_{b,xx}+w_{s,xx}\right) + \left(N_{yy}^T + N_{oy}\right)\left(w_{b,yy}+w_{s,yy}\right) \end{pmatrix}$$

$$\mathfrak{B}\begin{pmatrix} B_{11}^s\dfrac{\partial^3 u}{\partial x^3} + (B_{12}^s+2B_{66}^s)\left(\dfrac{\partial^3 u}{\partial x\,\partial y^2} + \dfrac{\partial^3 v}{\partial x^2\,\partial y}\right) + B_{22}^s\dfrac{\partial^3 v}{\partial y^3} - D_{11}^s\dfrac{\partial^4 w_b}{\partial x^4} \\ -D_{22}^s\dfrac{\partial^4 w_b}{\partial y^4} - 2(D_{12}^s+2D_{66}^s)\dfrac{\partial^4 w_b}{\partial x^2\,\partial y^2} - H_{11}^s\dfrac{\partial^4 w_s}{\partial x^4} \\ -H_{22}^s\dfrac{\partial^4 w_s}{\partial y^4} - 2(H_{12}^s+2H_{66}^s)\dfrac{\partial^4 w_s}{\partial x^2\,\partial y^2} + A_{55}^s\dfrac{\partial^2 w_s}{\partial x^2} + A_{44}^s\dfrac{\partial^2 w_s}{\partial y^2} \\ +(Y_{13}^s + A_{55}^s)\dfrac{\partial^2 w_z}{\partial x^2} + (Y_{23}^s + A_{44}^s)\dfrac{\partial^2 w_z}{\partial y^2} + q \end{pmatrix} \tag{43f}$$

$$= \mathfrak{D}\begin{pmatrix} I_0(\ddot{w}_b+\ddot{w}_s) - J_0\ddot{w}_z + J_1\left(\dfrac{\partial\ddot{w}_s}{\partial x} + \dfrac{\partial\ddot{v}_s}{\partial y}\right) - J_2\ddot{w}_b\nabla^2 - K_2\ddot{w}_s\nabla^2 - q \\ +(N_{xx}^T + N_{ox})\left(w_{b,xx}+w_{s,xx}\right) + \left(N_{yy}^T + N_{oy}\right)\left(w_{b,yy}+w_{s,yy}\right) \end{pmatrix}$$

$$\mathfrak{B}\begin{pmatrix} -X_{13}\dfrac{\partial u}{\partial x} - X_{23}\dfrac{\partial v}{\partial y} + Y_{13}\dfrac{\partial^2 w_b}{\partial x^2} + Y_{23}\dfrac{\partial^2 w_b}{\partial y^2} + (Y_{13}^s + A_{55}^s)\dfrac{\partial^2 w_s}{\partial x^2} \\ +(Y_{23}^s + A_{44}^s)\dfrac{\partial^2 w_s}{\partial y^2} + A_{55}^s\dfrac{\partial^2 w_z}{\partial x^2} + A_{44}^s\dfrac{\partial^2 w_z}{\partial y^2} - Z_{33}w_z \end{pmatrix} \tag{43g}$$

$$= \mathfrak{D}\begin{pmatrix} J_0(\ddot{w}_b+\ddot{w}_s) + (N_{xx}^T + N_{ox})\left(w_{b,xx}+w_{s,xx}\right) \\ +K_0\ddot{w}_z + \left(N_{yy}^T + N_{oy}\right)\left(w_{b,yy}+w_{s,yy}\right) \end{pmatrix}$$

2.6 Closed-Form Solutions

The Navier method is used to get the analytical solutions to equation (43) for simply supported plates. The Navier approach states as follows:

$$u(x,y,t) = \sum_{m=1}^{\infty}\sum_{n=1}^{\infty} U_{mn}e^{i\omega t}\cos\alpha x\sin\beta y \tag{44a}$$

$$v(x,y,t) = \sum_{m=1}^{\infty}\sum_{n=1}^{\infty} V_{mn}e^{i\omega t}\sin\alpha x\cos\beta y \tag{44b}$$

$$w_b(x,y,t) = \sum_{m=1}^{\infty}\sum_{n=1}^{\infty} W_{bmn} e^{i\omega t} \sin\alpha x \sin\beta y \tag{44c}$$

$$w_s(x,y,t) = \sum_{m=1}^{\infty}\sum_{n=1}^{\infty} W_{smn} e^{i\omega t} \sin\alpha x \sin\beta y \tag{44d}$$

$$w_z(x,y,t) = \sum_{m=1}^{\infty}\sum_{n=1}^{\infty} W_{zmn} e^{i\omega t} \sin\alpha x \sin\beta y \tag{44e}$$

Here, $i=\sqrt{-1},\ \alpha = m\pi/a,\ \beta = n\pi/b.$ The coefficients are denoted as $(U_{mn}, V_{mn}, W_{bmn}, W_{smn}, W_{zmn})$. In this context, ω denotes the angular frequency. A modification in the double-Fourier sine series is used to represent the transverse load q.

$$q(x,y) = \sum_{m=1}^{\infty}\sum_{n=1}^{\infty} Q_{mn} \sin\alpha x \sin\beta y \tag{45}$$

The following lists the coefficients Q_{mn} for a number of sample loads:

$$\begin{aligned} Q_{mn} &= \frac{4}{ab}\int_0^a \int_0^b q(x,y)\sin\alpha x \sin\beta y \, dxdy \\ &= \begin{cases} q_0 & \text{for sinusoidally distributed load} \\ \dfrac{16q_0}{mn\pi^2} & \text{for uniformly distributed load} \end{cases} \end{aligned} \tag{46}$$

The uniform distributed load is denoted as q_0. The closed-form solutions can be obtained by replacing equation (43), with equations (44, 45).

When the thickness stretching effect is eliminated (i.e., ε_z =0), the precise HSDT solutions are given as (Thai and Choi, 2011; Thai; Thai and Choi, 2012; Thai, et al., 2012).:

$$\left(\begin{bmatrix} k_{11} & k_{12} & k_{13} & k_{14} & k_{15} \\ k_{12} & k_{22} & k_{23} & k_{24} & k_{25} \\ k_{13} & k_{23} & k_{33} & k_{34} & k_{35} \\ k_{14} & k_{24} & k_{34} & k_{44} & k_{45} \\ k_{15} & k_{25} & k_{35} & k_{45} & k_{55} \end{bmatrix} - \omega^2 \begin{bmatrix} m_{11} & 0 & m_{13} & m_{14} & 0 \\ 0 & m_{22} & m_{23} & m_{24} & 0 \\ m_{13} & m_{23} & m_{33} & m_{34} & m_{35} \\ m_{14} & m_{24} & m_{34} & m_{44} & m_{45} \\ 0 & 0 & m_{35} & m_{45} & m_{55} \end{bmatrix}\right) \begin{bmatrix} U_{mn} \\ V_{mn} \\ W_{bmn} \\ W_{smn} \\ W_{zmn} \end{bmatrix} = \begin{bmatrix} 0 \\ 0 \\ Q_{mn} \\ Q_{mn} \\ 0 \end{bmatrix} \tag{47}$$

Where

$$k_{11} = A\left(\alpha^2 + \frac{1-v}{2}\beta^2\right)c_2, \qquad k_{12} = \frac{1+v}{2}A\alpha\beta c_2 \tag{48a}$$

$$k_{22} = A\left(\frac{1-v}{2}\alpha^2 + \beta^2\right)c_2, \quad k_{13} = -B\alpha(\alpha^2+\beta^2)c_2 \tag{48b}$$

$$k_{13} = -B\alpha(\alpha^2+\beta^2)c_2, \qquad k_{14} = -B^s\alpha(\alpha^2+\beta^2)c_2 \tag{48c}$$

$$k_{14} = -B^s\alpha(\alpha^2+\beta^2)c_2, \qquad k_{23} = -B\beta(\alpha^2+\beta^2)c_2 \tag{48d}$$

$$k_{24} = -B^s\beta(\alpha^2+\beta^2)c_2, \qquad k_{33} = D(\alpha^2+\beta^2)^2c_2 + \epsilon \tag{48e}$$

$$k_{34} = D^s(\alpha^2+\beta^2)^2c_2 + \epsilon, \qquad k_{44} = \left(H(\alpha^2+\beta^2)^2 + A^s(\alpha^2+\beta^2)\right)c_2 + \epsilon \tag{48f}$$

$$m_{11} = m_{22} = I_0 c_1, \qquad m_{13} = m_{14} = -\alpha I_1 c_1 \tag{48g}$$

$$m_{23} = m_{24} = -\beta I_1 c_1, m_{33} = I_0 + I_2(\alpha^2 + \beta^2)c_1 \tag{48h}$$

$$m_{34} = I_0 + J_2(\alpha^2 + \beta^2)c_1, \qquad m_{44} = I_0 + K_2(\alpha^2 + \beta^2)c_1 \tag{48i}$$

$$\epsilon = \left(-q + (N_{xx}^T + N_{ox})\alpha^2 + \left(N_{yy}^T + N_{oy}\right)\beta^2\right)c_1 \tag{48j}$$

$$c_1 = \left(1 + (e_0 a)^2\right)(\alpha^2 + \beta^2), c_2 = \left(1 + (l_m)^2\right)(\alpha^2 + \beta^2) \tag{48k}$$

$$(A, B, B^s, D, D^s, H) = \sum_{n=1}^{3} \int_{h_{n-1}}^{h_n} (1, z, f, z^2, zf, f^2) \frac{E(z)}{1 - v^2} dz \tag{48l}$$

$$A^s = \sum_{n=1}^{3} \int_{h_{n-1}}^{h_n} \frac{g^2 E(z)}{2(1 + v)} dz \tag{48m}$$

The following is a condensed version of equation (49) for the buckling solution:

$$\begin{bmatrix} k_{11} & k_{12} & k_{13} & k_{14} & k_{15} \\ k_{12} & k_{22} & k_{23} & k_{24} & k_{25} \\ k_{13} & k_{23} & k_{33} & k_{34} & k_{35} \\ k_{14} & k_{24} & k_{34} & k_{44} & k_{45} \\ k_{15} & k_{25} & k_{35} & k_{45} & k_{55} \end{bmatrix} \begin{bmatrix} U_{mn} \\ V_{mn} \\ W_{bmn} \\ W_{smn} \\ W_{zmn} \end{bmatrix} = \begin{bmatrix} 0 \\ 0 \\ 0 \\ 0 \\ 0 \end{bmatrix} \tag{49a}$$

$$(\mathbf{K})\mathbf{d} = 0$$

With

$$\mathbf{d} = \begin{bmatrix} U_{mn} \\ V_{mn} \\ W_{bmn} \\ W_{smn} \\ W_{zmn} \end{bmatrix} \tag{49b}$$

The stiffness matrix **K** incorporates all thermal and external loads as specified in equation (48). By setting the determinant of **K** to zero, one can derive the critical buckling loads. When the **K** matrix equals zero, the thermal force terms are moved to the right, and the terms on the left are divided by the coefficients of the force terms to determine the critical buckling load $N_{cr}^T(m, n)$ as presented in equation (52).

$$(\mathbf{K})\mathbf{d} = 0 \tag{50}$$

$$N_{cr}^T(m, n) = \frac{\det(\mathbf{K}) - \Psi N^T}{\Psi} \tag{51}$$

Under the assumption that the determinant of the **K**=0, the entire set of coefficients for the thermal force of magnitude N^T in the equation is represented by the symbol Ψ.

The dimensionless buckling load of the modes (*m*, *n*) is represented by the following equation:

$$\lambda_{cr}(m,n) = \frac{12(1-v_c^2)N_{cr}a^2}{E_c h^3} \tag{52}$$

The critical buckling load is denoted by λ_{cr} and E_c is the ceramic material's elasticity moduli.

3. NUMERICAL RESULTS

A sandwich plate with the dimensions of a=b=L=500 nm, FG face-layers comprised of Ti-6Al-4V and Al_2O_3 with Ti-6Al-4V honeycomb is studied for the present study. The nondimensional buckling response λ_1 is observed according to applied thermal environment with the change of p, ζ_1, ζ_3, θ, $e_0 a$, l_m parameters.

It is observed that p rise in FG face plates drops down the buckling load λ_1 in Figure 3a. At p=0, 1, 2, 10, buckling temperatures are 2161 K, 2131 K, 2106 K, 2006 K respectively. Furthermore, at fixed temperature analysis with respect to p raise, p=0 shows higher buckling load results. p rise slopes down the dimensionless buckling load as it is seen in Figure 3b. Thermal expansion ratio directly affects the result as it is fully ceramic at p=0.

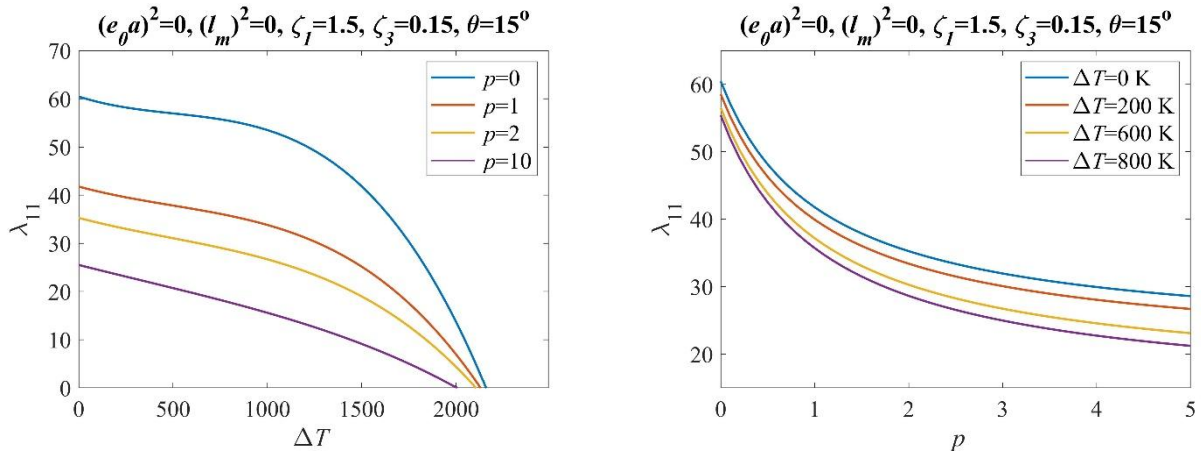

a) b)

Figure 3. Relationship between the dimensionless buckling load and (a) temperature rise for different values of p (0, 1, 2, 10), (b) material grading index p of face-plates (0-5) for different values of temperature rise (ΔT=0, 50, 100, 125 K); h_c=0.2h, h_p=0.4h, h=L/10

Increase in length ratio (ζ_1) doesn't affect the response of buckling load very much (Figure 4a), however thickness ratio rise (ζ_3) and especially incline angle (θ) rise directly change the λ_1 response (Figure 4b and 4c). After an intersection point, buckling load curve starts sloping down with increase of ζ_3. Before intersection point larger ζ_3 values cause higher buckling load. Unlike ζ_3, θ rise drops down the λ_1 response and after intersection point, λ_1 response rises together with θ rise.

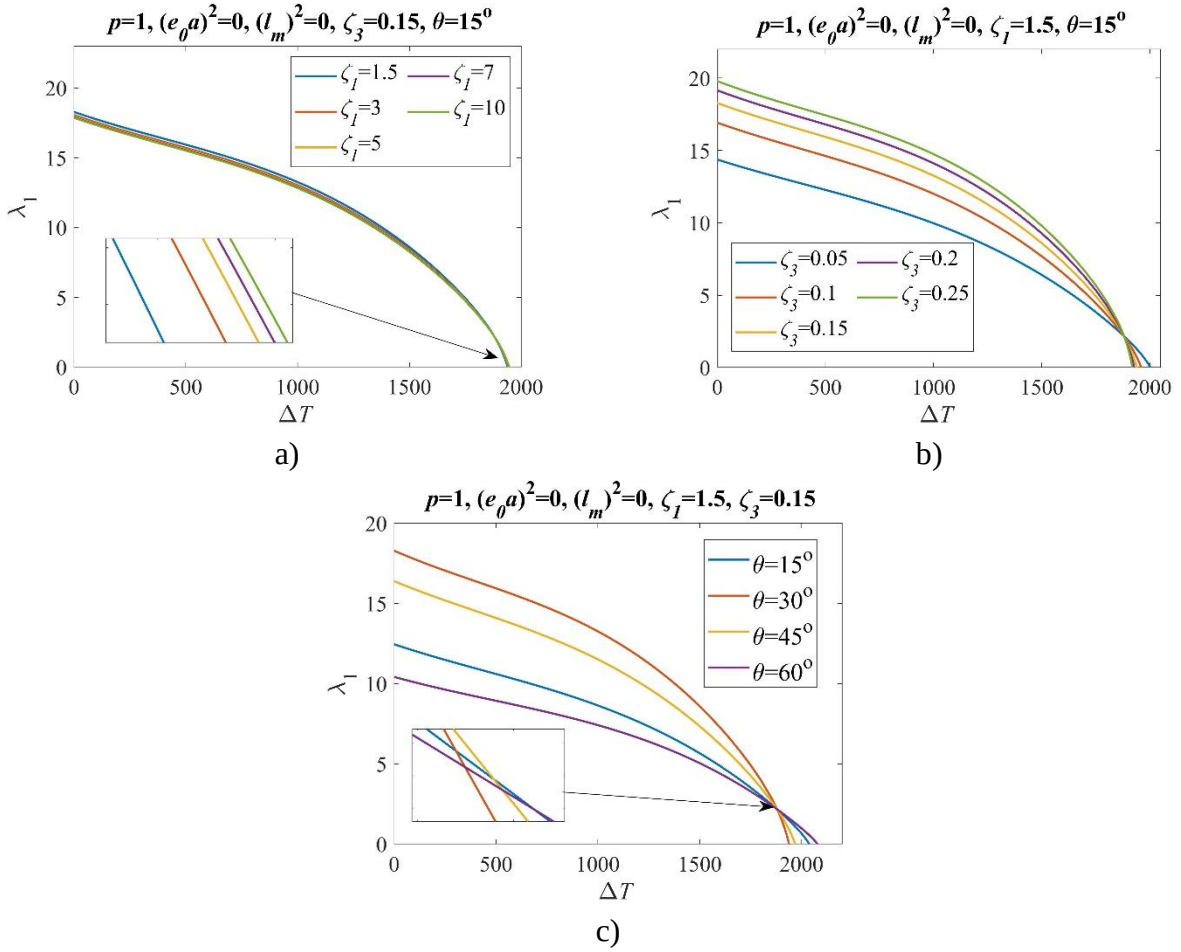

Figure 3. Relationship between the dimensionless buckling load and temperature rise for different values of (a) ζ_1=(1.5, 3, 5, 7, 10), (b) ζ_3=(0.05, 0.1, 0.15, 0.2, 0.25) (c) θ=(15°, 30°, 45°, 60°) ; h_c=0.8h, h_p=0.1h, h=L/10

At p=1 which is %50 Ti-6Al-4V and %50 Al_2O_3 constituent FG face layers, sandwich plate buckling load decreases with nonlocal parameter (e_0a) rise due to softening effect (Figure 5a). Unlike e_0a, size parameter (l_m) shows opposite results and l_m increases the λ_1 due to hardening effect. For $(e_0a)^2$=0, 1, 2, 4 nm^2 nondimensional buckling loads are 23.93, 19.98, 17.18, 13.37 at 1500 K, respectively. Additionally, for $(l_m)^2$=0, 1, 2, 4 nm^2 nondimensional buckling loads are 23.93, 28.65, 33.31, 42.81 at 1500 K respectively

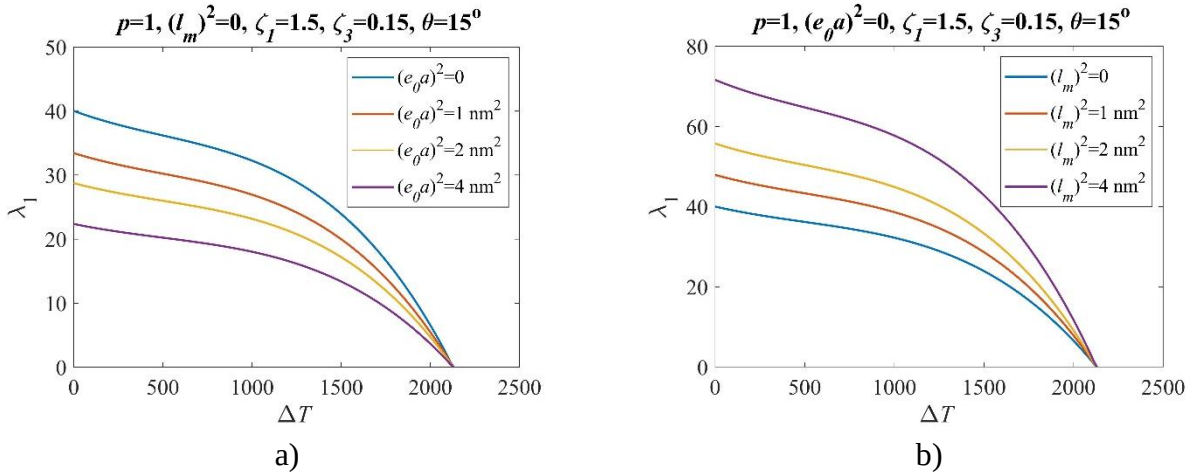

Figure 4. Relationship between the dimensionless buckling load and temperature rise for different values of (a) $(e_0a)^2$= (0, 1, 2, 4 nm^2), (b) $(l_m)^2$= (0, 1, 2, 4 nm^2); h_c=0.3h, h_p=0.35h, h=L/10.

4. CONCLUSIONS

A FGM sandwich nanoplate with honeycomb core layer and FG surface plates is analyzed in thermal environment to observe dimensionless buckling load according to changing parameters as p, ζ_1, ζ_3, θ, e_0a, l_m. For the solution higher-order shear deformation theory is considered. Using the Hamilton principle, the equations of motion of the plate are derived and written in terms of the displacement components. Assuming simply supported boundary conditions, the Navier solution is considered for the displacement components and rotation using the time harmonic function and harmonic solution along the plate length.

In summary, the results demonstrate that the structural stability of FGM sandwich nanoplates is highly sensitive to material gradation, geometric parameters, and nonlocal effects. The ceramic-rich composition (lower p values) enhances buckling resistance, while variations in thickness ratio (ζ_3) and incline angle (θ) exhibit nonlinear trends, with critical intersection points dictating their influence on structural performance. Additionally, the softening effect associated with the nonlocal parameter (e_0a) reduces buckling strength, whereas the hardening effect linked to the size parameter (l_m) improves it. These findings contribute to the optimization and design of advanced nanostructures for applications requiring superior thermal and mechanical performance in fields such as nanosensors, aerospace technology, and dental applications.

5. ACKNOWLEDGEMENTS

This study did not receive funding support from any institution or organization.

6. CONFLICT OF INTEREST

Author approves that to the best of their knowledge, there is not any conflict of interest or common interest with an institution/organization or a person that may affect the review process of the paper.

7. AUTHOR CONTRIBUTION

Adem Fatih OZALP has the full responsibility of the paper about determining the concept of the research, data collection, data analysis and interpretation of the results, preparation of the manuscript and critical analysis of the intellectual content with the final approval.

8. REFERENCES

Abuteir B. W., Boutagouga D., Free-vibration response of functionally graded porous shell structures in thermal environments with temperature-dependent material properties. Acta Mechanica 233(11), 4877-4901, 2022.

Akgöz B., Civalek Ö., Shear deformation beam models for functionally graded microbeams with new shear correction factors. Composite Structures 112, 214-225, 2014.

Al-Waily M., Raad H., Njim E. K., Free Vibration Analysis of Sandwich Plate-Reinforced Foam Core Adopting Micro Aluminum Powder. Physics and Chemistry of Solid State 23(4), 659-668, 2022.

Arani A. G., Jalaei M. H., Investigation of the longitudinal magnetic field effect on dynamic response of viscoelastic graphene sheet based on sinusoidal shear deformation theory. Physica B: Condensed Matter 506, 94-104, 2017.

Arslan K., Gunes R., Experimental Damage Evaluation of Honeycomb Sandwich Structures With Al/B4c FGM Face Plates Under High Velocity Impact Loads. Composite Structures 202, 304-312, 2018.

Boudjemai A., Bouanane M. H., Mankour A., Salem H., Hocine R., Amri R., Thermo-mechanical design of honeycomb panel with fully-potted inserts used for spacecraft design. 2013 6th International Conference on Recent Advances in Space Technologies (RAST), 39–46, Istanbul, Turkey: IEEE, 2013.

Chen X., Zhao J. L., She G. L., Jing Y., Luo J., Pu H. Y., On wave propagation of functionally graded CNT strengthened fluid-conveying pipe in thermal environment. European Physical Journal Plus 137(10), 2022.

Dang X. H., Nguyen V. L., Tran M. T., Tran B. D., Nguyen V. L., Nonlinear Dynamic Analysis of Auxetic-FGM Sandwich Plates Resting on a Kerr Elastic Substrate Under Blast Loading. Proceedings of the Institution of Mechanical Engineers Part C Journal of Mechanical Engineering Science 238(14), 6831-6846, 2024.

Gibson L. J., Cellular Solids. MRS Bulletin 28(4), 270-274, 2003.

Kiani Y., Eslami M. R., An exact solution for thermal buckling of annular FGM plates on an elastic medium. Composites Part B: Engineering 45(1), 101-110, 2013.

Kitipornchai S., Yang J., Liew K. M., Random vibration of the functionally graded laminates in thermal environments. Computer Methods in Applied Mechanics and Engineering 195(9-12), 1075-1095, 2006.

Lim C. W., Zhang G., Reddy J. N., A higher-order nonlocal elasticity and strain gradient theory and its applications in wave propagation. Journal of the Mechanics and Physics of Solids 78, 298-313, 2015.

Lin C., Nicaise S. M., Lilley D. E., Cortes J., Jiao P., Singh J., Bargatin I., Nanocardboard as a nanoscale analog of hollow sandwich plates. Nature Communications 9(1), 4442, 2018.

Markworth A. J., Ramesh K. S., Parks W. P., Modelling studies applied to functionally graded materials. Journal of Materials Science 30(9), 2183-2193, 1995.

Ozalp A. F., Esen I., Magnetic field effects on the thermomechanical vibration behavior of functionally graded biocompatible material sandwich nanobeams. Mechanics of Advanced Materials and Structures 32(3), 459-477, 2024.

Ozalp A. F., Esen I., Thermal buckling response of foam core smart sandwich nanoplates with electro-elastic and magneto-strictive layers. Acta Mechanica 236, 469-497, 2025.

Qi C., Jiang F., Yang S., Remennikov A., Chen S., Ding C., Dynamic Crushing Response of Novel Re-Entrant Circular Auxetic Honeycombs: Numerical Simulation and Theoretical Analysis. Aerospace Science and Technology 124, 107548, 2022.

Reddy J. N., A Simple Higher-Order Theory for Laminated Composite Plates. Journal of Applied Mechanics 51(4), 745-752, 1984.

Reddy J. N., Chin C. D., THERMOMECHANICAL ANALYSIS OF FUNCTIONALLY GRADED CYLINDERS AND PLATES. Journal of Thermal Stresses 21(6), 593-626, 1998.

Shimpi R. P., Refined Plate Theory and Its Variants. AIAA Journal 40(1), 137-146, 2002.

Thai H. T., Choi D. H., A refined plate theory for functionally graded plates resting on elastic foundation. Composites Science and Technology 71(16), 1850-1858, 2011.

Thai H. T., Choi D. H., A refined shear deformation theory for free vibration of functionally graded plates on elastic foundation. Composites Part B: Engineering 43(5), 2335-2347, 2012.

Thai H. T., Park T., Choi D. H., An efficient shear deformation theory for vibration of functionally graded plates. Archive of Applied Mechanics 83(1), 137-149, 2012.

Touloukian Y., Thermophysical properties of high temperature solid materials, Volume 3: Ferrous alloys. Macmillan: New York, 1967.

Van Lieu P., Zenkour A. M., Luu G. T., Static bending and buckling of FG sandwich nanobeams with auxetic honeycomb core. European Journal of Mechanics-A/Solids 103, 105181, 2024.

Wang Z. W., Zhang Q., Xia L. Z., Wu J. T., Liu P. Q., Thermomechanical Analysis of Pressure Vessels with Functionally Graded Material Coating. Journal of Pressure Vessel Technology 138(1), 011205, 2016.

Yang J., Liew K. M., Kitipornchai S., Stochastic analysis of compositionally graded plates with system randomness under static loading. International Journal of Mechanical Sciences 47(10), 1519-1541, 2005.

Yin H., Huang X., Scarpa F., Wen G., Chen Y., Zhang C., In-Plane Crashworthiness of Bio-Inspired Hierarchical Honeycombs. Composite Structures 192, 516-527, 2018.

JOURNAL of
MATERIALS and MECHATRONICS:A

e-ISSN 2717-8811
JournalMM, 2025, 6(1), 103-120
https://doi.org/10.55546/jmm.1591526

Araştırma Makalesi / Research Article

Investigation of Mechanical Properties of Auxetic Core Layered Smart Sandwich Plate Under Biaxial Compression Loads

Mustafa BUĞDAY[1,2*]

[1*] Karabuk University, Department of Mechanical Engineering, Karabuk, Türkiye
[2*] Karabuk University, Eskipazar Vocational School Rail Systems Machining Program, Karabuk, Türkiye,
ORCID ID: https://orcid.org/0000-0003-4413-509X, mustafabugday@karabuk.edu.tr

Geliş/ Received: 26.11.2024**;** **Revize/Revised:** 14.02.2025 **Kabul / Accepted:** 27.02.2025

ABSTRACT: This study uses high-order sharing deformation theory to model auxetic core layer smart sandwich plates and examines their mechanical properties. The outer layers of the smart plate consist of electro-elastic $BaTiO_3$ (Barium Titanate) and magnetostrictive $CoFe_2O_4$ (Cobalt Ferrite) materials. The auxetic core layer consists of a metallic material (Nickel) with varying auxetic cell parameters. Three fundamental parametric characteristics of the auxetic core cell are modeled: wall thickness parameter, length parameter, and inclination angle. The equations of motion are derived from Hamilton's principle and resolved using the Navier method. The findings of this study will facilitate the optimal design of smart electromechanical systems intended for operation in high-temperature environments.

Keywords: Auxetic Structure, Smart Sandwich Plate, Magneto Strictive Material, Electro Elastic Material

*Sorumlu yazar / Corresponding author: mustafabugday@karabuk.edu.tr
Bu makaleye atıf yapmak için /To cite this article

Buğday, M. (2025). Investigation of Mechanical Properties of Auxetic Core Layered Smart Sandwich Plate Under Biaxial Compression Loads. Journal of Materials and Mechatronics: A (JournalMM), 6(1), 103-120.

1. INTRODUCTION

Magneto-electro-elastic (MEE) materials are a unique class of smart materials that exhibit piezoelectric and piezomagnetic properties in a layered configuration (Mahesh et al., 2022). These materials, also known as multiferroics, have gained significant attention due to their ability to effectively couple different phases, making them valuable in various industries (Moshtagh et al., 2019). The magnetoelectric coupling effects in MEE materials have led to their widespread use in engineering applications such as sensors, actuators, robotics, structural health monitoring, vibration control, and medical instruments (Park and Han, 2018). Researchers have explored the development of multiphase magneto-electro-elastic (MMEE) materials by varying the volume fractions of different components like $BaTiO_3$ and $CoFe_2O_4$ (Mahesh and Kattimani, 2019). The study of magneto-electro-elastic nanoplates has shown that surface effects play a crucial role in the propagation of anti-plane shear waves in these materials (Wu et al., 2015). Moreover, polymer-based magneto-electro-elastic composites have emerged as promising materials with macro-scale magneto-electric coupling achieved through homogenization techniques (Miehe and Vallicotti, 2015). The mechanical behavior of magneto-electro-elastic structures has been a subject of intense research, with studies focusing on areas such as buckling analysis, free vibration analysis, and crack propagation in these materials (Aboudi, 2001; Pan and Han, 2005; Zhou et al., 2018). Investigations into the effects of imperfections like cracks and dislocations on the magneto-electro-elastic properties of solids have been conducted to understand their structural stability (Wang and Kuna, 2015). Additionally, the study of functionally graded magneto-electro-elastic materials has revealed insights into their fracture mechanical behaviors and stress analysis (Bagheri et al., 2017; Ma et al., 2007).

Auxetic materials are a unique class of materials that exhibit a negative Poisson's ratio, meaning they expand laterally when stretched longitudinally and contract laterally when compressed longitudinally (Aktaş and Güvenç, 2024; Wright et al., 2012). These materials have garnered significant interest due to their unconventional properties, such as improved toughness, resilience, shear resistance, impact resistance, and shape fitting ability (Shukla and Behera, 2023). Auxetic materials include a variety of forms such as auxetic polymers, fibers, yarns, fabrics, and composites (Kamrul et al., 2022; Zulifqar and Hu, 2019). They have been applied in diverse fields including civil engineering, architecture, sports clothing, and high-performance equipment (Xu et al., 2020). Research on auxetic materials has led to the development of auxetic textiles, which have shown promise in various applications due to their adaptability and structural variability (Gao and Chen, 2024). Additionally, auxetic structures have been explored for their mechanical properties, with improvements noted in shear, impact, and bending resistance (Peliński et al., 2020). The creation of ultra-light auxetic meta-materials with enhanced stiffness and strength has been highlighted as a practical advancement in the field (Rayneau-Kirkhope, 2018).

The thermomechanical behavior of smart plate systems is an increasingly critical area of research, as highlighted in previous studies. This study is unique in that it focuses on modeling advanced sandwich plates featuring Auxetic core layers alongside electroelastic and magnetostrictive surface layers, which has not been widely explored. The use of high-order plate theory enables an accurate representation of the complex behavior of these plates, setting this work apart from other research in the field. The primary goal was to investigate the thermomechanical buckling behavior of these smart sandwich plates within an integrated framework that considers the synergy of the core and surface layers. Additionally, a thorough analysis of the thermomechanical properties of the piezomagnetic materials used in the surface plates was performed, contributing to the development of a highly precise and robust model. This work offers groundbreaking insights that are directly

applicable to cutting-edge aerospace and space applications, where metamaterial properties and thermal performance are paramount. Furthermore, the findings hold promise for advancing electromechanical smart systems and provide valuable solutions for vibration and impact damping in high-temperature environments, distinguishing it from other conventional studies in the field.

2. MATHEMATICAL FORMULATION

As depicted in Figure 1, the rectangular plate is supposed to be thick, composed of metal auxetic core and piezo magnetic materials, with dimensions of length *a*, breadth *b*, and thickness *h*. It is situated between two piezo-electromagnetic patches with thicknesses of h_p.

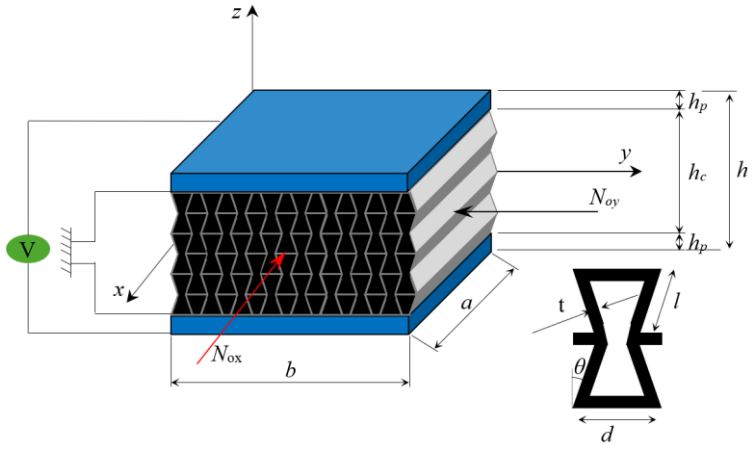

Figure 1. The schematic view of the smart sandwich plate and auxetic cell

The origin is situated in the middle plane, at the center of the plate, and the Cartesian coordinate system is used for this problem. The following is the assumption underlying the current formulation (Ersoy et al., 2018):

1. The three layers of the sandwich plate are perfectly connected to one another, preventing any slippage at their interfaces.
2. The properties of the top and bottom piezo-electromagnetic layers are identical and homogeneous.

2.1 Auxetic Core Properties

The core layer of the proposed sandwich plate is composed of an auxetic material with a negative Poisson's ratio, which exhibits superior mechanical properties under mechanical loads and strains. When the auxetic core structure is subjected to compressive and tensile loadings, it will expand and contract accordingly. Figure 1 displays the geometrical specifications of the auxetic unit cell used in the structure's core, such as the inclined angle (θ), rib thickness (t), vertical wall length (d), and inclined wall length (1). Nickel is the substance of the auxetic core in this investigation. As a result, the following equations (Li et al., 2022a) will connect the mass density and equivalent elastic characteristics of the auxetic core to the properties of the nickel (Li et al., 2022b; Nouraei et al., 2023):

$$E_{11}^{c} = E_{Al}\left[\frac{(\beta_1 - \sin(\theta)\beta_3^3}{[(\beta_1 \sec^2(\theta) + \tan^2(\theta))\beta_3^2 + 1]\cos^3(\theta)}\right] \tag{1}$$

$$E_{22}^{c} = E_{Al}\left[\frac{\beta_3^3}{(\beta_3^2 + \tan^2(\theta))(\cos(\theta)\beta_1 - \cos(\theta)\sin(\theta))}\right] \tag{2}$$

$$G_{12}^{c} = E_{Al}\left[\frac{\beta_3^3}{(2\beta_1^2 + \beta_1)\cos(\theta)}\right] \tag{3}$$

$$G_{13}^{c} = G_{Al}\left[\frac{2\sin^2(\theta) + \beta_1}{2(\eta_1 - \sin(\theta))} + \frac{-\sin(\theta) + \beta_1}{2\beta_1 + 1}\right]\frac{\beta_3}{2\cos(\theta)} \tag{4}$$

$$G_{23}^{c} = G_{Al}\left[\frac{\beta_3\cos(\theta)}{\beta_1 - \sin(\theta)}\right] \tag{5}$$

$$\rho^{c} = \rho_{Al}\left[\frac{(2 + \beta_1)\beta_3}{2(\beta_1 - \sin(\theta))\cos(\theta)}\right] \tag{6}$$

where $\beta_3 = t/l$ and $\beta_1 = d/l$. On the other hand, Poisson's ratio can be obtained directly(Li et al., 2022b) from the geometrical parameters of the auxetic unit cells (Li et al., 2022b; Nouraei et al., 2023). Equations (7a) and (7b) calculate the Poisson ratios of a material in the x-y and y-x directions depending on the geometric and material parameters and take into account the direction and effect of structural deformations.

$$\nu_{12}^{c} = \frac{(\sin(\theta) - \beta_1)(\sin(\theta))(1 - \beta_3^2)}{\cos^2(\theta)[\beta_3^2(\beta_1\sec^2(\theta) + \tan^2(\theta)) + 1]} \tag{7a}$$

$$\nu_{21}^{c} = \frac{(\beta_3^2 - 1)\sin(\theta)}{(\beta_1 - \sin(\theta))(\beta_3^2 + \tan^2(\theta))} \tag{7b}$$

Figure 1 is shown to examine the impact of the cell inclination angle (θ) on the Poisson's ratio of the auxetic core, with β_3=0.0138571 and β_1 varying between 1 and 4. It is simple to infer from this picture that positive values of lead to negative Poisson's ratios, which is an indication of the auxetic core. This figure also shows that when β_1 drops, greater values of Poisson's ratio are obtained.

Determining the temperature-dependent features is essential for accurately forecasting the behaviour of the structure. Therefore, the coefficients of thermal conductivity ψ_{ef}, Poisson's ratio v_{ef},, thermal expansion κef, and effective modulus of elasticity E_{ef}, may all be explained by a nonlinear temperature function (Abdelmola and Carlsson, 2019).

$$P = P_0(P_{-1}T^{-1} + 1 + P_1T + P_2T^2 + P_3T^3) \tag{8}$$

The P_0, P_{-1}, P_1, P_2 and P_3 values of each material with temperature T orders (-1, 0, 1, 2, and 3) define P, which in this case stands for the temperature-dependent characteristics of constituents. Moreover, according to the effective material properties, temperature variations have very little effect on the mass density $\rho(z)$, which is solely a function of z.

2.2 The types of The Temperature Increase

Equations for uniform (UTI), nonlinear (NLTI), and linear (LTI) variations in temperature are available for each thickness of the sandwich nanoplate.

If it is assumed that the temperature rises linearly (LTI) from the bottom surface T_b to the top surface T_t along the thickness, the temperature of a plane extending along the z-axis can be found using the following the equation (Kiani and Eslami, 2013):

$$T(z) = T_b + (T_t - T_b)\left(\frac{h + 2z}{2h}\right) \tag{9}$$

In the event of nonlinear temperature increase (NLTI) through the thickness, the temperatures of the sandwich nanoplate's top T_t and bottom T_b surfaces can be determined using equation 9 (Zhang, 2014).

$$-\frac{d}{dz}\left(\kappa(z)\frac{dT}{dz}\right) = 0, \qquad T\left(\frac{h}{2}\right) = T_t, \quad T\left(-\frac{h}{2}\right) = T_b \tag{10}$$

The temperature of the entire FGM sandwich nanoplate, whose initial temperature rises consistently from T_0 to T, may be calculated at a uniform temperature increase (UTI) using the following equation:

$$\Delta T = T - T_0 \tag{11}$$

$$T(z) = T_b + \frac{(T_t - T_b)}{\int_{-\frac{h}{2}}^{\frac{h}{2}} \frac{1}{\kappa(z)} d(z)} \int_{-\frac{h}{2}}^{z} \kappa(z) dz \tag{12}$$

Here $\kappa(z)$ denotes the thermal conductivity coefficient. In this study the nonlinear temperature rise (12) is used for analysis.

2.3 Displacement Field

Because shear deformations are significant in the current plate and this system requires a high degree of precision, the displacement field is modeled using two SSDT variables, as stated in (Tornabene and Viola, 2009)

$$u(x, y, z, t) = u_0(x, y, t) - z\frac{\partial w_b(x,y,t)}{\partial x} - f(z)\frac{\partial w_s(x,y,t)}{\partial x}, \tag{13}$$

$$v(x, y, z, t) = v_0(x, y, t) - z\frac{\partial w_b(x,y,t)}{\partial y} - f(z)\frac{\partial w_s(x,y,t)}{\partial y}, \tag{14}$$

$$w(x, y, z, t) = w_b(x, y, t) + w_s(x, y, t) \tag{15}$$

where u_0 v_0, w_b, and w_s are the mid-surface components of displacement and u, v, and w are the displacement components of the plate in the directions of x, y, and z. Note that the transverse displacements resulting from shearing and bending are represented by the values w_s and w_b, respectively. The shape function, f(z), is also equal to (Yuan and Dawe, 2002):

$$f(z) = z - \frac{h}{\pi}\sin\left(\frac{\pi z}{h}\right) \tag{16}$$

The strain tensor components about the displacement field in Eq. (9, 10, 11 and, 12) are as follows:

$$\begin{aligned}
\varepsilon_{xx} &= \frac{\partial u}{\partial x} - z\frac{\partial^2 w_b}{\partial x^2} - f(z)\frac{\partial^2 w_s}{\partial x^2} \\
\varepsilon_{yy} &= \frac{\partial v}{\partial y} - z\frac{\partial^2 w_b}{\partial y^2} - f(z)\frac{\partial^2 w_s}{\partial y^2} \\
\gamma_{xy} &= \frac{\partial v}{\partial x} + \frac{\partial u}{\partial y} - 2z\frac{\partial^2 w_b}{\partial x\,\partial y} - 2f(z)\frac{\partial^2 w_s}{\partial x\,\partial y} \\
\gamma_{yz} &= g(z)\frac{\partial w_s}{\partial y}
\end{aligned} \tag{17}$$

where:

$$g(z) = 1 - f'(z) \tag{18}$$

where the normal strain component is ε_{ii} and the shear strain component is γ_{ij} (ii=xx, yy and ij=xy, yz, xz), respectively.

2.4 Stress-Strain Relations

2.4.1 Auxetic plate

The nonlocal theory defines the stress-strain relations for the porous core as follows (Yuan and Dawe, 2002):

$$[1 - \mu^2\nabla^2]\begin{Bmatrix}\sigma_{xx}\\ \sigma_{yy}\\ \sigma_{yz}\\ \sigma_{xz}\\ \sigma_{xy}\end{Bmatrix} = \begin{bmatrix} c_{11} & c_{12} & 0 & 0 & 0 \\ c_{21} & c_{22} & 0 & 0 & 0 \\ 0 & 0 & c_{44} & 0 & 0 \\ 0 & 0 & 0 & c_{55} & 0 \\ 0 & 0 & 0 & 0 & c_{66} \end{bmatrix}\begin{Bmatrix}\varepsilon_{xx}\\ \varepsilon_{yy}\\ \gamma_{yz}\\ \gamma_{xz}\\ \gamma_{xy}\end{Bmatrix} \tag{19}$$

where c_{ij} are the stiffness matrix arrays, ∇^2 is the Laplacian operator, σ_{ij} are the stress components, and $\mu=e_1\alpha$ and is the nonlocal parameter that is determined by molecular dynamics, experimental research, and molecular structural mechanics.

$$c_{11} = c_{22} = \frac{E(z)}{1-\nu^2},\ c_{12} = c_{21} = \frac{\nu E(z)}{1-\nu^2} \tag{20}$$

2.5 Solution Procedure

The motion equations are derived using Hamilton's concept. This idea is stated as follows:

$$\int_{t_1}^{t_2} (\delta U - \delta T - \delta W)\mathrm{d}t = 0 \tag{21}$$

U, *T*, and *W* stand for external work, kinetic energy, and strain energy, respectively.

For equations of motion involving plates with easily supported boundary conditions, there is an analytical solution. The displacements are regarded as functions that at least meet the different geometric boundary conditions based on Navier's solution.

$$\begin{Bmatrix} u_0 \\ v_0 \\ w_b \\ w_s \\ \phi \\ \psi \end{Bmatrix} = \sum_{m=1}^{\infty} \sum_{\mathrm{n}=1}^{\infty} \begin{Bmatrix} \bar{u}\cos\left(\frac{m\pi x}{a}\right)\sin\left(\frac{n\pi y}{b}\right) \\ \bar{v}\sin\left(\frac{m\pi x}{a}\right)\cos\left(\frac{n\pi y}{b}\right) \\ \bar{w}_b\sin\left(\frac{m\pi x}{a}\right)\sin\left(\frac{h\pi y}{b}\right) \\ \bar{w}_s\sin\left(\frac{m\pi x}{a}\right)\sin\left(\frac{n\pi y}{b}\right) \\ \bar{\phi}\sin\left(\frac{m\pi x}{a}\right)\sin\left(\frac{n\pi y}{b}\right) \\ \bar{\psi}\sin\left(\frac{m\pi x}{a}\right)\sin\left(\frac{n\pi y}{b}\right) \end{Bmatrix} \mathrm{e}^{i\omega t} \tag{22}$$

In this case, the maximum values of the displacement components, electric and magnetic potentials, and unknown coefficients are denoted by the variables $\bar{u}, \bar{v}, \bar{w}_b, \bar{w}_s, \bar{\phi}$, and $\bar{\psi}$. Natural frequency is also ω. The following relation results from inserting the suggested functions into the equations of motion:

$$([K] - \omega^2[M])\mathbf{d} = \{0\} \tag{23}$$

where:

$$\{d\} = \{\bar{u}, \bar{v}, \bar{w}_b, \bar{w}_s, \bar{\phi}, \bar{\psi}\}^T \tag{24}$$

The "Appendix" section contains an explanation of the arrays of [*K*] and [*M*] matrices. The properties of piezo magnetic materials used in this study are presented in Table 1, and the material properties of Auxetic core material Ni are shown in Table 2.

Table 1. The magnetic, piezo, electro and thermal properties of $CoFe_2O_4$ and $BaTiO_3$ (Esen and Özmen, 2024; Tocci Monaco et al., 2021)

		$CoFe_2O_4$	**$BaTiO_3$**
C_{11}	[GPa]	286	166
C_{22}		286	166
C_{33}		269.5	162
C_{12}		173	77
C_{13}		170.5	78
C_{23}		170.5	78
C_{44}		45.3	43
C_{55}		45.3	43

Table 1. The magnetic, piezo, electro and thermal properties of $CoFe_2O_4$ and $BaTiO_3$ (Esen and Özmen, 2024; Tocci Monaco et al., 2021) (continued)

		$CoFe_2O_4$	**$BaTiO_3$**
C_{66}		56.5	44.5
e_{31}	[C/m^2]	0	-4.4
e_{32}		0	-4.4
e_{33}		0	18.6
q_{31}	[N/A.m]	580.3	0
q_{32}		580.3	0
q_{33}		699.7	0
ξ_{11}	[10^{-9}C^2/N.m^2]	0.08	11.2
ξ_{22}		0.08	11.2
ξ_{33}		0.093	12.6
$\zeta_{11} = \zeta_{22} = \zeta_{33}$	[s/m]	0	0
χ_{11}	[10^{-6} N.s^2/C]	-590	5
χ_{22}		-590	5
χ_{33}		157	10
$p_{11} = p_{22}$	[10^{-7}C/m^{2}K]	0	0
p_{33}		0	-11.4
$\lambda_{11} = \lambda_{22}$	[10^{-5}Wb/m^{2}K]	0	0
λ_{33}		-36.2	0
$\alpha_1 = \alpha_2$	[10^{-6}K^{-1}]	10	15.8
ρ	[kg/m^3]	5800	5300

Table 2. Material properties of the Auxetic core layer (Esen et al., 2022)

Material	Property	P_{-1}	P_0	P_1	P_2	P_3
	ρ (kg/m^3)	0	8900	0	0	0
	E (Pa)	0	223.95x 10^9	-2.794x10^{-4}	3.998x10^{-9}	0
Nickel	υ	0	0.31	0	0	0
	α (1K^{-1})	0	9.9209x10^{-6}	8.705x10^{-4}	0	0
	ψ (W/mK)	0	58.74	-4.614x10^{-4}	6.670x10^{-7}	-1.523x10^{-10}

3. RESULTS AND DISCUSSION

3.1 Effect of The Auxetic Cell Parameters on The Mechanical Properties of The Core Layer

Since it is a value frequently used in comparable research in the literature and was thought to be a suitable parameter to guarantee the model's accuracy, the value of β_1 was set at 2. Furthermore, early analytical and experimental evaluations verified that this choice best captures the system's physical behavior (Koç et al., 2024; Yıldız and Esen, 2024).

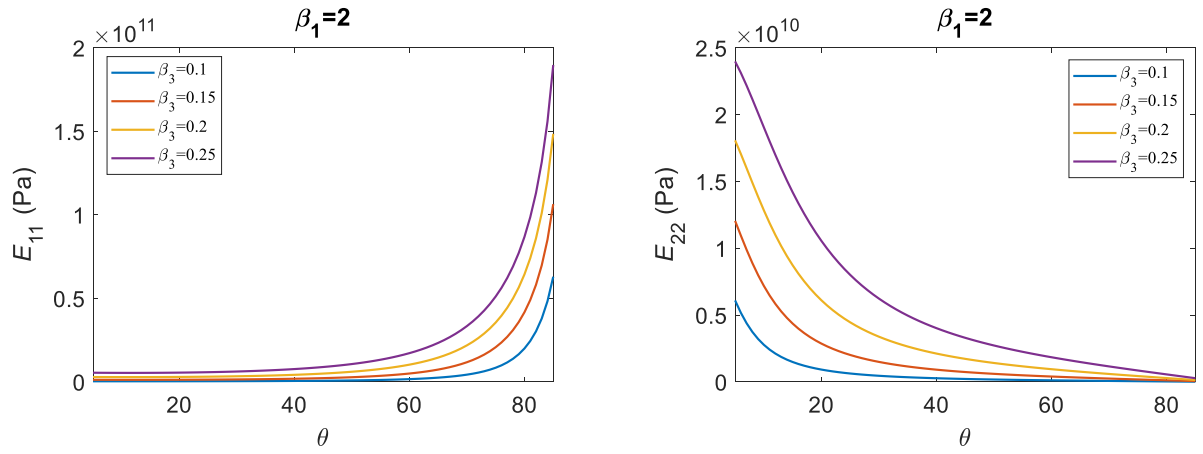

Figure 2. Variation of the Young Moduli of auxetic layer depending on the inclination angle θ for thickness ratio β_3 = 0.1, 0.15, 0.2 and, 0.25; and for length ratio β_1 = 2; a) E_{11}; b) E_{22}

In Figure 2a, the Elasticity Module E_{11} change at the θ curvature angle between 5°-85° and the thickness ratio β_3 = 0.1, 0.15, 0.20 and, 0.25 for the length ratio β_1 = 2 is presented. Figure 3b shows the change of E_{22} Elasticity Module in the y direction for the same parameters. As seen in Figure 3a, E_{11} gradually increases linearly for the inclination angle between θ = 5° and 50°. Between 50° and 70°, the increase increases rapidly non-linearly, and between 70° and 85° it increases exponentially very quickly. For β_3= 0.1, the E_{11} value at θ = 5° was calculated as 4x10^8 Pa, at θ = 50° the E_{11} value was calculated as 9x10^8 Pa, at θ = 70° the E_{11} value was calculated as 4,3x10^9 Pa and at θ = 85° the E_{11} value was calculated as 6,3x10^{10} Pa. When θ = 5° to 50°, the E_{11} value increased 23 times. When θ = increased from 50° to 70°, the E_{11} value increased 4.8 times; When θ = 70° to 85°, the E_{11} value increased 14.4 times.

As seen in Figure 2b, E_{22} decreased very rapidly between θ = 5° and 40°. At θ = 40° to 85°, the E_{22} value decreased approximately linearly. For β_3= 0.1, the E_{22} value at θ = 5° was calculated as 6x10^8 Pa, the E_{22} value at θ = 40° was calculated as 2,7x10^8 Pa, and the E_{22} value for θ = 85° was calculated as 1,8x10^7 Pa. From θ = 5° to 40°, the E_{22} value decreased by 2.2 times, and from θ = 40° to 85°, the E_{22} value decreased by 15.4 times.

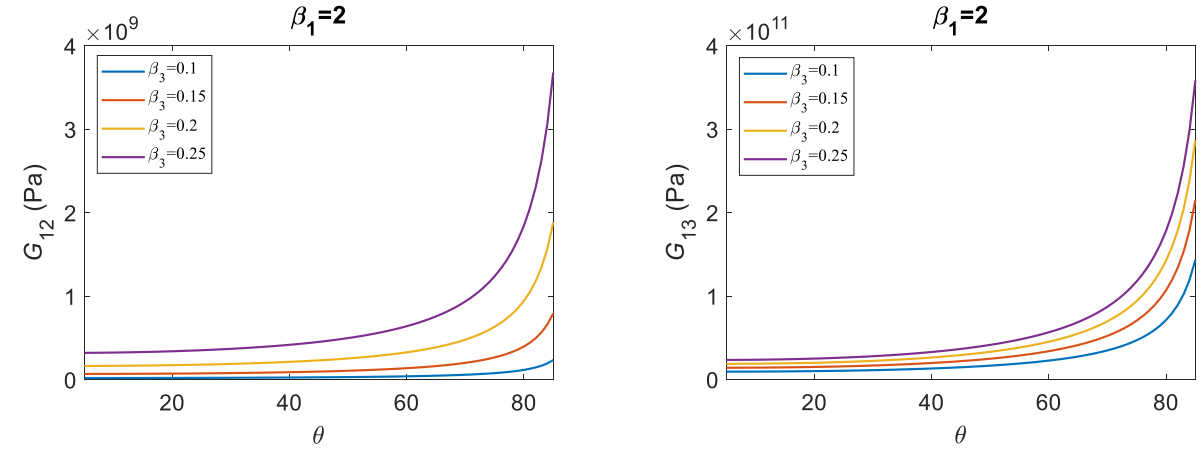

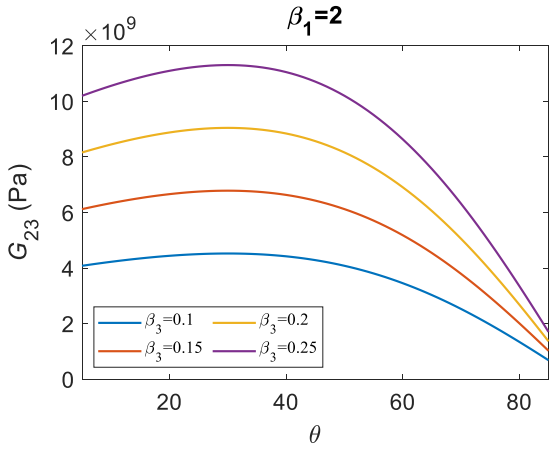

c)

Figure 3. Variation of the Shear Moduli of auxetic layer depending on the inclination angle θ for thickness ratio β_3 = 0.1, 0.15, 0.2 and, 0.25; and for length ratio β_1 = 2; a) G_{12}; b) G_{13} c) G_{23}

In Figure 3a, the Shear Modulus G_{12} change in the xy direction at the θ inclination angle between 5°-85° and the thickness ratio β_3 = 0.1, 0.15, 0.20 and, 0.25 for the length ratio β_1 = 2 is presented. In Figures 3b and 3c, Shear Modules G_{13} and G_{23} in *xz* and *yz* directions are given for the same parameters. As seen in Figure 3a, the Shear Module gradually increases linearly at the inclination angle between G_{12} θ = 5°-70°. Between 70° and 85°, it increases exponentially very quickly. For β_3= 0.1, the G_{12} value at θ = 5° was calculated as 2,1x10^7 Pa, at θ = 70° the G_{12} value was calculated as 60013700 Pa, and at θ = 85° the G_{12} value was calculated as 2x10^8 Pa. When θ = 5° to 70°, G_{12} value increased by 2.9 times. When θ = 70° to 85°, G_{12} value increased 3.9 times.

The result obtained in Figure 3b is similar to Figure 3a. G_{13} value, Shear Module gradually increases linearly at the inclination angle between θ = 5°-70°. Between 70° and 85°, it increases exponentially very quickly. For β_3= 0.1, the G_{13} value at θ = 5° was calculated as 9,4x10^9 Pa, at θ = 70° the G_{13} value was calculated as 3,5x10^{10} Pa, at θ = 85° the G_{13} value was calculated as 1,4x10^{11} Pa. When θ = 5° to 70°, G_{13} value increased by 3.7 times. When θ = 70° to 85°, G_{13} value increased 4.1 times.

In Figure 3c, G_{23} value, Shear Module increases linearly at the inclination angle between θ = 5°-30°. When θ = 30°, G_{23} value is maximum. Between 30 and 85, the Shear Modulus gradually decreases. For β_3= 0.1, the G_{23} value at θ = 5° was calculated as 4,1x10^9 Pa, at θ = 30° the G_{23} value was calculated as 4,5x10^9 Pa, and at θ = 85° the G_{23} value was calculated as 6,8x10^8 Pa. When θ = 5° to 30°, G_{23} value increased by 1.1 times. When θ = 30° to 85°, G_{23} value decreased by 6.65 times.

In Figure 4, the density (ρ) change at the thickness ratio β_3 = 0.1, 0.15, 0.20 and, 0.25 values for the θ inclination angle between 5° and 85° and the length ratio β_1 = 2 is presented. As seen in Figure 5, the density (ρ) gradually increases linearly at the inclination angle between θ = 5°-70°. Between 70° and 85°, it increases exponentially very quickly. For β_3= 0.1, the ρ value at θ = 5° was calculated as 934.106 kg/m^3, at θ = 70° the ρ value was calculated as 4908.36 kg/m^3, and at θ = 85° the ρ value was calculated as 20345.8 kg/m3. When θ = 5° to 70°, the ρ value increased by 5.25 times. When θ = 70° to 85°, the ρ value increased 4.15 times.

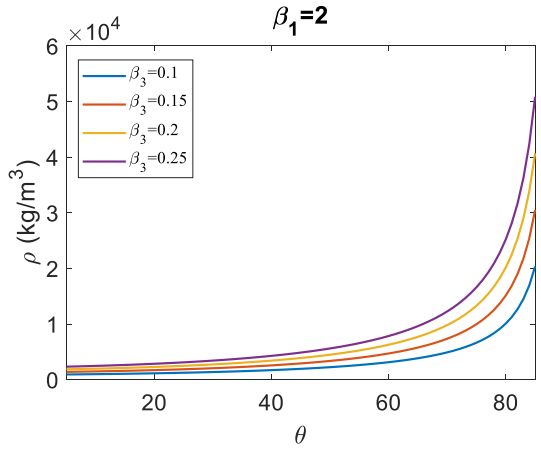

Figure 4. Variation of the density ρ of auxetic layer depending on the inclination angle θ for thickness ratio β_3 = 0.1, 0.15, 0.2 and, 0.25; and for length ratio β_1 = 2.

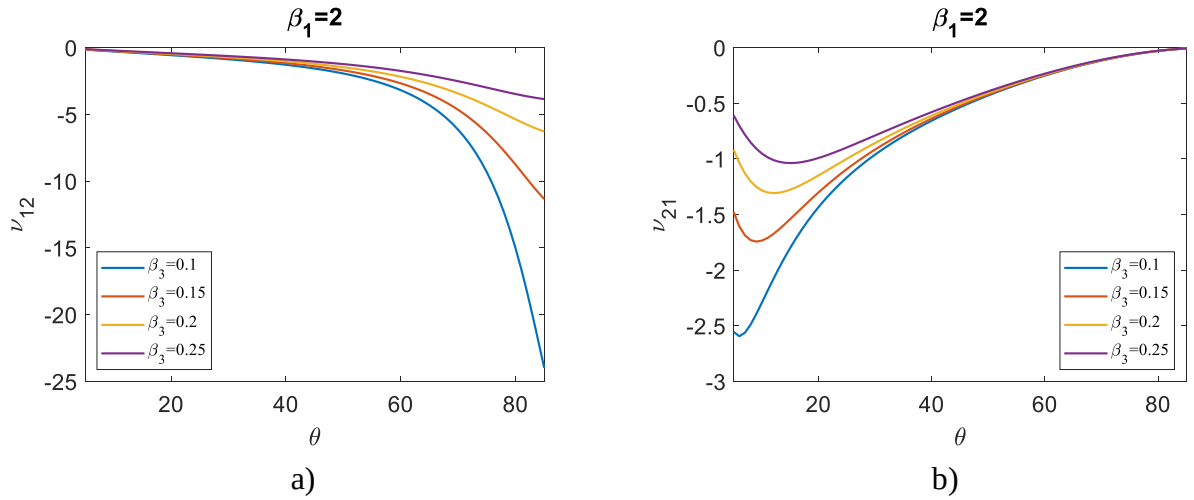

Figure 5. Variation of the Poisson ratios of auxetic layer depending on the inclination angle θ for thickness ratio β_3 = 0.1, 0.15, 0.2 and, 0.25; and for length ratio β_1 = 2; a) ν_{12}; b) ν_{21}

In Figure 5a, the variation of the Poisson ratio ν_{12} in the *xy* direction at the thickness ratio β_3 = 0.1, 0.15, 0.20 and, 0.25 for the θ inclination angle between 5° and 85° and the length ratio β_1 = 2 is presented. Figure 5b shows the Poisson ratio ν_{21} in the *yx* direction for the same parameters. As seen in Figure 5a, the Poisson ratio (ν_{12}) gradually increases linearly in the negative direction at the inclination angle between θ = 5°-60°. Between 60° and 85°, it increases exponentially and very rapidly in the negative direction. For β_3= 0.1, ν_{12} value at θ = 5° was calculated as -0.148194, ν_{12} value at θ = 60° was calculated as -3.18503, and ν_{12} value at θ = 85° was calculated as -23.9868. When θ = 5° to 60°, ν_{12} value increased 21.5 times in the negative direction. When θ = 60° to 85°, ν_{12} value increased by 7.53 times in the negative direction.

In the results obtained in Figure 5b, first a peak is seen in the negative direction and then it decreases nonlinearly towards zero as the inclination angle increases. We can list the points with peaks in the negative direction as follows: At β_3=0.1, ν21 value at θ =6° is -2.59397, at β_3=0.15, at θ =9°, ν_{21} value is -2.59397, at β_3=0.2, θ =12° ν_{21} value at -1.30753, β_3=0.25, ν_{21} value at θ =15° is -1.03767. At β_3 = 0.1, between θ = 5° and 40°, the Poisson ratio first reached its maximum value and then increased exponentially towards zero. At θ = 5°, the ν_{21} value was calculated as -2.5506, and at θ = 40°, the ν_{21} value was calculated as -0.656603. Between θ = 40°-85°, the Poisson ratio slows down and approaches zero. At θ = 85°, ν_{21} value is calculated as -0.0075197. When the θ = value

increased from 5° to 40°, the v_{21} value increased by 3.88 times. When θ = 40° to 85°, v_{21} value increased 87.3 times.

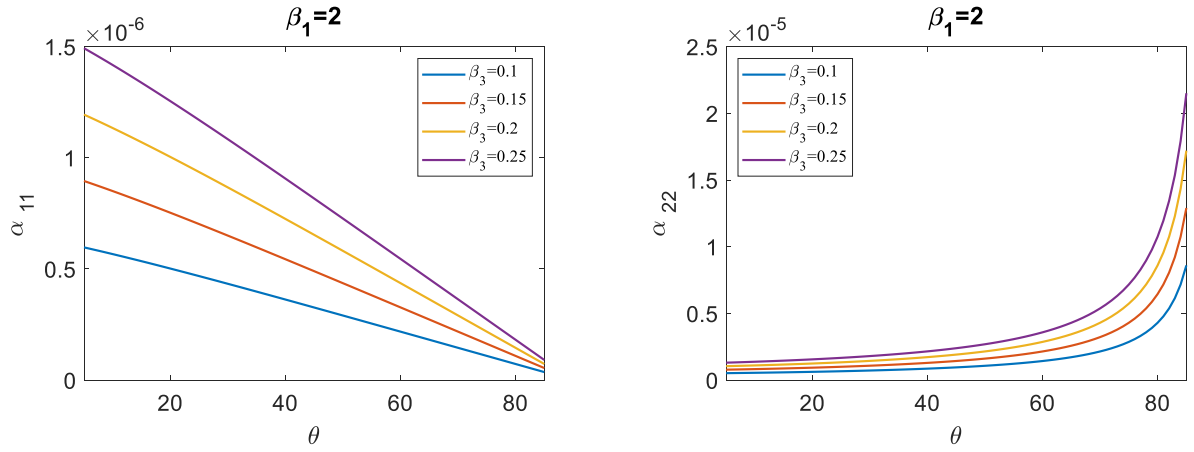

Figure 6. Variation of the Thermal expansion coefficients of auxetic layer depending on the inclination angle θ for thickness ratio β_3 = 0.1, 0.15, 0.2 and, 0.25; and for length ratio β_1 = 2; a) α_{11}; b) α_{22}

In Figure 6a, the change of thermal expansion coefficients α_{11} in the xx direction for the θ inclination angle between 5°-85° and the thickness ratio β_3 = 0.1, 0.15, 0.20 and, 0.25 for the length ratio β_1 = 2 is presented. Figure 6b shows the thermal expansion coefficients α_{22} in the *yy* direction for the same parameters. As seen in Figure 6a, thermal expansion coefficients (α_{11}) increase linearly in the negative direction at the inclination angle between α_{11} θ = 5°-85°. For β_3= 0.1, the α_{11} value at θ = 5° was calculated as 5.97x10^{-7}, and at θ = 85°, the α_{11} value was calculated as -3.64x10^{-8}. When θ = 5° to 85°, the α_{11} value increased 21.5 times in the negative direction. When θ = 60° to 85°, α_{11} value increased 16.4 times in the negative direction.

In Figure 6b, while the α_{22} value increases linearly at the inclination angle between θ = 5°-70°, it increases rapidly exponentially between θ = 70°-85°. For β_3= 0.1, the α_{22} value at θ = 5° was calculated as 5.24x10^{-7}, at θ = 70° the α_{22} value was calculated as 2.15x10^{-6}, and at θ = 85° the α_{22} value was calculated as 8.60x10^{-6}. When θ = 5° to 70°, the α_{22} value increased by 4.1 times. When θ = 70° to 85°, the α_{22} value increased 4 times.

4. CONCLUSIONS

The study examines the thermomechanical characteristics of auxetic core smart sandwich plates utilizing high-order shear deformation theory. The outer layers of the smart plate consist of electroelastic $BaTiO_3$ (Barium Titanate) and magnetostrictive $CoFe_2O_4$ (Cobalt Ferrite) materials. The mechanical properties of the core layer, encompassing elastic modulus, shear modulus, density, Poisson's ratios, and thermal expansion coefficients, are derived from the parameters of the auxetic cell, including length, thickness, and inclination angle. The results obtained are summarized as follows:

The elastic moduli in the E_{11} and E_{22} directions are significantly influenced by the length parameter β_1 and the thickness parameter β_3 of the auxetic layer cell, contingent upon the inclination angle. The elastic modulus in the E_{11} direction demonstrates exponential growth as the inclination angle θ increases, particularly beyond θ = 60°. Until θ attains 60°, the ascent velocity is comparatively

gradual. Conversely, E_{22} exhibits an exponential decline until θ attains 40°. After $\theta = 40°$, the descent rate markedly decreases.

The shear moduli in the G_{12}, G_{13}, and G_{23} directions are substantially influenced by the length parameter β1 and the thickness parameter β_3 of the auxetic layer cell, contingent upon the inclination angle. The shear modulus in the G_{12} and G_{13} axes demonstrates exponential growth as the inclination angle θ increases, particularly beyond $\theta = 60°$. The ascent rate remains comparatively gradual until θ attains 60°. Conversely, G_{23} exhibits an increase until θ attains 30°. The descent rate exhibits an exponential decline at an angle of $\theta = 40°$.

The density ρ is significantly influenced by the length parameter β_1 and the thickness parameter β_3 of the auxetic layer cell, contingent upon the inclination angle. The object's density increases proportionally with the elevation of the inclination angle θ. At an angle of $\theta = 60°$, the precipitation amount undergoes exponential growth.

The length parameter β_1 and the thickness parameter β_3 of the auxetic layer cell are significantly influenced by the Poisson ratios in the ν_{12} and ν_{21} directions, which are contingent upon the inclination angle. The Poisson ratio in the ν_{12} direction diminishes as the inclination angle θ rises. The value undergoes exponential growth after $\theta = 60°$. In contrast, ν_{21} initially declines until $\theta = 5°$, after which it exhibits exponential growth.

The thermal expansion coefficients in the α_{11} and α_{22} directions are significantly influenced by the length parameter β_1 and the thickness parameter β_3 of the auxetic layer cell, which are contingent upon the inclination angle. The thermal expansion coefficients in the α_{11} direction exhibit a linear decline with increasing inclination angle θ. Conversely, as the angle of inclination increases, α_{22} also rises, exhibiting an exponential growth pattern, particularly beyond $\theta = 60°$.

5. ACKNOWLEDGEMENTS

I am truly grateful to Prof. Dr. İsmail ESEN for his generous support, thoughtful guidance, and meaningful contributions throughout this study. His encouragement and insightful feedback made a real difference and helped shape this work into its final form.

6. CONFLICT OF INTEREST

Author approves that to the best of their knowledge, there is not any conflict of interest or common interest with an institution/organization or a person that may affect the review process of the paper.

7. AUTHOR CONTRIBUTION

Mustafa BUĞDAY has the full responsibility of the paper about determining the concept of the research, data collection, data analysis and interpretation of the results, preparation of the manuscript and critical analysis of the intellectual content with the final approval.

8. REFERENCES

Abdelmola F., Carlsson L. A., State of water in void-free and void-containing epoxy specimens. Journal of Reinforced Plastics and Composites 38(12), 556-566, 2019. https://doi.org/10.1177/0731684419833469

Aboudi J., Micromechanical analysis of fully coupled electro-magneto-thermo-elastic multiphase composites. Smart Materials and Structures 10(5), 867-877, 2001 https://doi.org/10.1088/0964-1726/10/5/303

Aktaş K. G., Güvenç M. A., Numerical and Analytical Free Vibration Analysis of Composite Plate with Auxetic Core Layer and Functionally Graded Surface Layers. ASREL 2024. https://doi.org/10.56753/ASREL.2024.2.6

Bagheri R., Ayatollahi M., Mousavi S., Stress analysis of a functionally graded magneto-electro-elastic strip with multiple moving cracks. Mathematics and Mechanics of Solids 22(3), 304-323, 2017. https://doi.org/10.1177/1081286515591303

Ersoy H., Mercan K., Civalek Ö., Frequencies of FGM shells and annular plates by the methods of discrete singular convolution and differential quadrature methods. Composite Structures 183, 7-20, 2018. https://doi.org/10.1016/j.compstruct.2016.11.051

Esen I., Abdelrhmaan A. A., Eltaher M. A., Free vibration and buckling stability of FG nanobeams exposed to magnetic and thermal fields. Engineering with Computers 38(4), 3463-3482, 2022. https://doi.org/10.1007/s00366-021-01389-5

Esen I., Özmen R., Free and forced thermomechanical vibration and buckling responses of functionally graded magneto-electro-elastic porous nanoplates. Mechanics Based Design of Structures and Machines 52(3), 1505-1542, 2024. https://doi.org/10.1080/15397734.2022.2152045

Gao Y., Chen X., Finite element analysis study of parameters influencing the Poisson's ratio of auxetic woven fabrics. Textile Research Journal 94(7-8), 886-905, 2024. https://doi.org/10.1177/00405175231221598

Kamrul H., Zulifqar A., Yang Y., Zhao S., Zhang M., Hu H., Geometrical analysis of auxetic woven fabrics based on foldable geometry. Textile Research Journal 92(3-4), 317-329, 2022. https://doi.org/10.1177/00405175211008663

Kiani Y., Eslami M. R., An exact solution for thermal buckling of annular FGM plates on an elastic medium. Composites Part B: Engineering 45(1), 101-110, 2013. https://doi.org/10.1016/j.compositesb.2012.09.034

Koç M. A., Esen İ., Eroğlu M., Thermal and Mechanical Vibration Response of Auxetic Core Sandwich Smart Nanoplate. Advanced Engineering Materials 26(20), 2024. https://doi.org/10.1002/adem.202400797

Li F., Yuan W., Zhang C., Free vibration and sound insulation of functionally graded honeycomb sandwich plates. Journal of Sandwich Structures Materials 24(1), 565-600, 2022a. https://doi.org/10.1177/10996362211020440

Li F., Yuan W., Zhang C., Free vibration and sound insulation of functionally graded honeycomb sandwich plates. Journal of Sandwich Structures Materials 24(1), 565-600, 2022b. https://doi.org/10.1177/10996362211020440

Ma L., Li J., Abdelmoula R., Wu L. Z., Mode III crack problem in a functionally graded magneto-electro-elastic strip. International Journal of Solids and Structures, 44(17), 5518-5537, 2007. https://doi.org/10.1016/j.ijsolstr.2007.01.012

Mahesh V., Kattimani S., Finite element simulation of controlled frequency response of skew multiphase magneto-electro-elastic plates. Journal of Intelligent Material Systems and Structures 30(12), 1757-1771, 2019. https://doi.org/10.1177/1045389X19843674

Mahesh V., Mahesh V., Harursampath D., Abouelregal A. E., Simulation-based assessment of coupled frequency response of magneto-electro-elastic auxetic multifunctional structures

subjected to various electromagnetic circuits. Proceedings of the Institution of Mechanical Engineers, Part L: Journal of Materials: Design and Applications 236(11), 2281-2296, 2022. https://doi.org/10.1177/14644207211021933

Miehe C., Vallicotti D., Variational Structural and Material Stability Analysis in Finite Electro-Magneto-Mechanics of Active Materials. PAMM 15(1), 7-10, 2015. https://doi.org/10.1002/pamm.201510003

Moshtagh E., Eskandari-Ghadi M., Pan E., Time-harmonic dislocations in a multilayered transversely isotropic magneto-electro-elastic half-space. Journal of Intelligent Material Systems and Structures 30(13), 1932-1950, 2019. https://doi.org/10.1177/1045389X19849286

Nouraei M., Zamani V., Civalek Ö., Vibration of smart sandwich plate with an auxetic core and dual-FG nanocomposite layers integrated with piezoceramic actuators. Composite Structures 315, 117014, 2023. https://doi.org/10.1016/j.compstruct.2023.117014

Pan E., Han F., Exact solution for functionally graded and layered magneto-electro-elastic plates. International Journal of Engineering Science 43(3-4), 321-339, 2005. https://doi.org/10.1016/j.ijengsci.2004.09.006

Park W. T., Han S. C., Buckling analysis of nano-scale magneto-electro-elastic plates using the nonlocal elasticity theory. Advances in Mechanical Engineering 10(8), 168781401879333, 2018. https://doi.org/10.1177/1687814018793335

Peliński K., Smardzewski J., Narojczyk J., Stiffness of Synclastic Wood-Based Auxetic Sandwich Panels. Physica Status Solidi (b) 257(10), 2020. https://doi.org/10.1002/pssb.201900749

Rayneau-Kirkhope D., Stiff auxetics: Hierarchy as a route to stiff, strong lattice based auxetic meta-materials. Scientific Reports 8(1), 12437, 2018. https://doi.org/10.1038/s41598-018-30822-x

Shukla S., Behera B. K., Comparative analysis of Poisson's ratio of <scp>2D</scp> woven constructions and their composites produced from different auxetic geometries. Polymer Composites 44(3), 1636-1647, 2023. https://doi.org/10.1002/pc.27193

Tocci Monaco G., Fantuzzi N., Fabbrocino F., Luciano R., Critical Temperatures for Vibrations and Buckling of Magneto-Electro-Elastic Nonlocal Strain Gradient Plates. Nanomaterials 11(1), 87, 2021. https://doi.org/10.3390/nano11010087

Tornabene F., Viola E., Free vibration analysis of functionally graded panels and shells of revolution. Meccanica 44(3), 255-281, 2009. https://doi.org/10.1007/s11012-008-9167-x

Wang Y. Z., Kuna M., General solutions of mechanical-electric-magnetic fields in magneto-electro-elastic solid containing a moving anti-plane crack and a screw dislocation. ZAMM - Journal of Applied Mathematics and Mechanics / Zeitschrift Für Angewandte Mathematik Und Mechanik 95(7), 703-713, 2015. https://doi.org/10.1002/zamm.201300279

Wright J. R., Burns M. K., James E., Sloan M. R., Evans K. E., On the design and characterisation of low-stiffness auxetic yarns and fabrics. Textile Research Journal 82(7), 645-654, 2012. https://doi.org/10.1177/0040517512436824

Wu B., Zhang C., Chen W., Zhang C., Surface effects on anti-plane shear waves propagating in magneto-electro-elastic nanoplates. Smart Materials and Structures 24(9), 095017, 2015. https://doi.org/10.1088/0964-1726/24/9/095017

Xu W., Sun Y., Lin H., Wei C., Ma P., Xia F., Preparation of soft composite reinforced with auxetic warp-knitted spacer fabric for stab resistance. Textile Research Journal 90(3-4), 323-332, 2020. https://doi.org/10.1177/0040517519866938

Yıldız T., Esen I., On the effect of the Casimir, van der Waals and electrostatic forces on the thermomechanical buckling of sandwich smart piezo magnetic nanosensor/switch plates. Microsystem Technologies, 2024 https://doi.org/10.1007/s00542-024-05813-w

Yuan W. X., Dawe D. J., Free vibration of sandwich plates with laminated faces. International Journal for Numerical Methods in Engineering 54(2), 195-217, 2002. https://doi.org/10.1002/nme.411

Zhang D. G., Thermal post-buckling and nonlinear vibration analysis of FGM beams based on physical neutral surface and high order shear deformation theory. Meccanica 49(2), 283-293, 2014. https://doi.org/10.1007/s11012-013-9793-9

Zhou L., Li M., Meng G., Zhao H., An effective cell-based smoothed finite element model for the transient responses of magneto-electro-elastic structures. Journal of Intelligent Material Systems and Structures 29(14), 3006-3022, 2018. https://doi.org/10.1177/1045389X18781258

Zulifqar A., Hu H., Geometrical analysis of bi-stretch auxetic woven fabric based on re-entrant hexagonal geometry. Textile Research Journal 89(21-22), 4476-4490, 2019. https://doi.org/10.1177/0040517519836936

Appendix

$$\{A_{ij}, B_{ij}^b, D_{ij}^b, B_{ij}^s, D_{ij}^s, H_{ij}^s\} = \int_{-\frac{h}{2}-h_p}^{-\frac{h}{2}} c_{ij}^p\{1, z, z^2, f(z), zf(z), [f(z)]^2\}\mathrm{d}z + \int_{-\frac{h}{2}}^{\frac{h}{2}} c_{ij}\{1, z, z^2, f(z), zf(z), [f(z)]^2\}\mathrm{d}z$$
$$+ \int_{\frac{h}{2}}^{\frac{h}{2}+h_p} c_{ij}^p\{1, z, z^2, f(z), zf(z), [f(z)]^2\}\mathrm{d}z,\ i,j = 1,2,6$$

$$A_{ll}^s = \int_{-\frac{h}{2}-h_p}^{-\frac{h}{2}} c_{ll}^p[g(z)]^2\ \mathrm{d}z + \int_{-\frac{h}{2}}^{\frac{h}{2}} c_{ll}[g(z)]^2\ \mathrm{d}z + \int_{\frac{h}{2}}^{\frac{h}{2}+h_p} c_{ll}^p[g(z)]^2\ \mathrm{d}z,\ l = 4,5$$

$$\{P_{11}, P_{13}, P_{15}\} = \int_{-\frac{h}{2}-h_p}^{-\frac{h}{2}} e_{31}\frac{\pi}{h_p}\sin\left(\frac{\pi\hat{z}}{h_p}\right)\{1, z, f(z)\}\mathrm{d}z + \int_{\frac{h}{2}}^{\frac{h}{2}+h_p} e_{31}\frac{\pi}{h_p}\sin\left(\frac{\pi\hat{z}}{h_p}\right)\{1, z, f(z)\}\mathrm{d}z$$

$$\{P_{12}, P_{14}, P_{16}\} = \int_{-\frac{h}{2}-h_p}^{-\frac{h}{2}} e_{32}\frac{\pi}{h_p}\sin\left(\frac{\pi\hat{z}}{h_p}\right)\{1, z, f(z)\}\mathrm{d}z + \int_{\frac{h}{2}}^{\frac{h}{2}+h_p} e_{32}\frac{\pi}{h_p}\sin\left(\frac{\pi\hat{z}}{h_p}\right)\{1, z, f(z)\}\mathrm{d}z$$

$$\{P_{17}, P_{18}\} = \int_{-\frac{h}{2}-h_p}^{-\frac{h}{2}} \cos\left(\frac{\pi\hat{z}}{h_p}\right)g(z)\{e_{15}, e_{24}\}\mathrm{d}z + \int_{\frac{h}{2}}^{\frac{h}{2}+h_p} \cos\left(\frac{\pi\hat{z}}{h_p}\right)g(z)\{e_{15}, e_{24}\}\mathrm{d}z$$

$$\{P_{20}, P_{22}\} = \int_{-\frac{h}{2}-h_p}^{-\frac{h}{2}} \cos^2\left(\frac{\pi\hat{z}}{h_p}\right)\{\kappa_{11}, \kappa_{22}\}\mathrm{d}z + \int_{\frac{h}{2}}^{\frac{h}{2}+h_p} \cos^2\left(\frac{\pi\hat{z}}{h_p}\right)\{\kappa_{11}, \kappa_{22}\}\mathrm{d}z$$

$$P_{30} = \int_{-\frac{h}{2}-h_p}^{-\frac{h}{2}} \kappa_{33}\left(\frac{\pi}{h_p}\right)^2\sin^2\left(\frac{\pi\hat{z}}{h_p}\right)\mathrm{d}z + \int_{\frac{h}{2}}^{\frac{h}{2}+h_p} \kappa_{33}\left(\frac{\pi}{h_p}\right)^2\sin^2\left(\frac{\pi\hat{z}}{h_p}\right)\mathrm{d}z$$

$$\{J_{11}, J_{13}, J_{15}\} = \int_{-\frac{h}{2}-h_p}^{-\frac{h}{2}} f_{31}\frac{\pi}{h_p}\sin\left(\frac{\pi\hat{z}}{h_p}\right)\{1, z, f(z)\}\mathrm{d}z + \int_{\frac{h}{2}}^{\frac{h}{2}+h_p} f_{31}\frac{\pi}{h_p}\sin\left(\frac{\pi\hat{z}}{h_p}\right)\{1, z, f(z)\}\mathrm{d}z$$

$$\{J_{12}, J_{14}, J_{16}\} = \int_{-\frac{h}{2}-h_p}^{-\frac{h}{2}} f_{32}\frac{\pi}{h_p}\sin\left(\frac{\pi\hat{z}}{h_p}\right)\{1, z, f(z)\}\mathrm{d}z + \int_{\frac{h}{2}}^{\frac{h}{2}+h_p} f_{32}\frac{\pi}{h_p}\sin\left(\frac{\pi\hat{z}}{h_p}\right)\{1, z, f(z)\}\mathrm{d}z$$

$$\{J_{17}, J_{18}\} = \int_{-\frac{h}{2}-h_p}^{-\frac{h}{2}} \cos\left(\frac{\pi\hat{z}}{h_p}\right)g(z)\{f_{15}, f_{24}\}\mathrm{d}z + \int_{\frac{h}{2}}^{\frac{h}{2}+h_p} \cos\left(\frac{\pi\hat{z}}{h_p}\right)g(z)\{f_{15}, f_{24}\}\mathrm{d}z$$

$$\{J_{20}, J_{22}\} = \int_{-\frac{h}{2}-h_p}^{-\frac{h}{2}} \cos^2\left(\frac{\pi\hat{z}}{h_p}\right)\{g_{11}, g_{22}\}\mathrm{d}z + \int_{\frac{h}{2}}^{\frac{h}{2}+h_p} \cos^2\left(\frac{\pi\hat{z}}{h_p}\right)\{g_{11}, g_{22}\}\mathrm{d}z$$

$$J_{30} = \int_{-\frac{h}{2}-h_p}^{-\frac{h}{2}} g_{33}\left(\frac{\pi}{h_p}\right)^2\sin^2\left(\frac{\pi\hat{z}}{h_p}\right)\mathrm{d}z + \int_{\frac{h}{2}}^{\frac{h}{2}+h_p} g_{33}\left(\frac{\pi}{h_p}\right)^2\sin^2\left(\frac{\pi\hat{z}}{h_p}\right)\mathrm{d}z$$

$$\{S_{20}, S_{22}\} = \int_{-\frac{h}{2}-h_p}^{-\frac{h}{2}} \cos^2\left(\frac{\pi\hat{z}}{h_p}\right)\{\mu_{11}, \mu_{22}\}\mathrm{d}z + \int_{\frac{h}{2}}^{\frac{h}{2}+h_p} \cos^2\left(\frac{\pi\hat{z}}{h_p}\right)\{\mu_{11}, \mu_{22}\}\mathrm{d}z$$

$$S_{30}=\int_{-\frac{h}{2}-h_p}^{-\frac{h}{2}}\mu_{33}\left(\frac{\pi}{h_p}\right)^2\sin^2\left(\frac{\pi\hat{z}}{h_p}\right)\mathrm{d}z+\int_{\frac{h}{2}}^{\frac{h}{2}+h_p}\mu_{33}\left(\frac{\pi}{h_p}\right)^2\sin^2\left(\frac{\pi\hat{z}}{h_p}\right)\mathrm{d}z$$

$$K_{11}=-\frac{m^2\pi^2}{a^2}A_{11}-\frac{n^2\pi^2}{b^2}A_{66}$$

$$K_{12}=-\frac{mn\pi^2}{ab}(A_{12}+A_{66})$$

$$K_{13}=\frac{m^3\pi^3}{a^3}B_{11}^b+\frac{mn^2\pi^3}{ab^2}\left(B_{12}^b+2B_{66}^b\right)$$

$$K_{14}=\frac{m^3\pi^3}{a^3}B_{11}^s+\frac{mn^2\pi^3}{ab^2}(B_{12}^s+2B_{66}^s)$$

$$K_{15}=\frac{m\pi}{a}P_{11}$$

$$K_{16}=\frac{m\pi}{a}J_{11}$$

$$K_{22}=-\frac{m^2\pi^2}{a^2}A_{66}-\frac{n^2\pi^2}{b^2}A_{22}$$

$$K_{23}=\frac{m^2n\pi^3}{a^2b}\left(B_{12}^b+2B_{66}^b\right)+\frac{n^3\pi^3}{b^3}B_{11}^b,$$

$$K_{24}=\frac{m^2n\pi^3}{a^2b}(B_{12}^s+2B_{66}^s)+\frac{n^3\pi^3}{b^3}B_{22}^s$$

$$K_{25}=\frac{n\pi}{b}P_{12}$$

$$K_{26}=\frac{n\pi}{b}J_{12}$$

$$K_{33}=-\frac{m^4\pi^4}{a^4}D_{11}^b-\frac{2m^2n^2\pi^4}{a^2b^2}\left(D_{12}^b+2D_{66}^b\right)-\frac{n^4\pi^4}{b^4}D_{22}^b-\left[k_1+k_2\pi^2\left(\frac{m^2}{a^2}+\frac{n^2}{b^2}\right)\right.$$
$$\left.-(N_{0x}+N_{Ex}+N_{Hx})\frac{m^2\pi^2}{a^2}-\left(N_{0y}+N_{Ey}+N_{Hy}\right)\frac{n^2\pi^2}{b^2}\right]$$

$$K_{34}=-\frac{m^4\pi^4}{a^4}D_{11}^s-\frac{2m^2n^2\pi^4}{a^2b^2}(D_{12}^s+2D_{66}^s)-\frac{n^4\pi^4}{b^4}D_{22}^s-\left[k_1+k_2\pi^2\left(\frac{m^2}{a^2}+\frac{n^2}{b^2}\right)\right.$$
$$\left.-(N_{0x}+N_{Ex}+N_{Hx})\frac{m^2\pi^2}{a^2}-\left(N_{0y}+N_{Ey}+N_{Hy}\right)\frac{n^2\pi^2}{b^2}\right]$$

$$K_{35}=-\frac{m^2\pi^2}{a^2}P_{13}-\frac{n^2\pi^2}{b^2}P_{14}$$

$$K_{36}=-\frac{m^2\pi^2}{a^2}J_{13}-\frac{n^2\pi^2}{b^2}J_{14}$$

$$K_{44}=-\frac{m^4\pi^4}{a^4}H_{11}^s-\frac{2m^2n^2\pi^4}{a^2b^2}(H_{12}^s+2H_{66}^s)-\frac{n^4\pi^4}{b^4}H_{22}^s-\frac{m^2\pi^2}{a^2}A_{55}^s-\frac{n^2\pi^2}{b^2}A_{44}^s$$
$$-\left[k_1+k_2\pi^2\left(\frac{m^2}{a^2}+\frac{n^2}{b^2}\right)-(N_{0x}+N_{Ex}+N_{Hx})\frac{m^2\pi^2}{a^2}-\left(N_{0y}+N_{Ey}+N_{Hy}\right)\frac{n^2\pi^2}{b^2}\right]$$

$$K_{45}=-\frac{m^2\pi^2}{a^2}(P_{15}-P_{17})-\frac{n^2\pi^2}{b^2}(P_{16}-P_{18})$$

$$K_{46}=-\frac{m^2\pi^2}{a^2}(J_{15}-J_{17})-\frac{n^2\pi^2}{b^2}(J_{16}-J_{18}),$$

$$K_{55}=\frac{m^2\pi^2}{a^2}P_{20}+\frac{n^2\pi^2}{b^2}P_{22}+P_{30},$$

$$K_{56}=\frac{m^2\pi^2}{a^2}J_{20}+\frac{n^2\pi^2}{b^2}J_{22}+J_{30}$$

$$K_{66}=\frac{m^2\pi^2}{a^2}S_{20}+\frac{n^2\pi^2}{b^2}S_{22}+S_{30}$$

$$M_{11}=M_{22}=-I_0$$

$$M_{12}=M_{15}=M_{25}=M_{35}=M_{45}=M_{55}=M_{56}=M_{16}=M_{26}=M_{36}=M_{46}=M_{66}=0,$$

$$M_{13}=I_1\frac{m\pi}{a}$$

$$M_{14}=I_2\frac{m\pi}{a}$$

$$M_{23}=I_1\frac{n\pi}{b}$$

$$M_{24} = I_2 \frac{n\pi}{b}\left[1 + \mu^2\pi^2\left(\frac{m^2}{a^2} + \frac{n^2}{b^2}\right)\right]$$
$$M_{33} = -\left[I_0 + I_3\pi^2\left(\frac{m^2}{a^2} + \frac{n^2}{b^2}\right)\right]$$
$$M_{34} = -\left[I_0 + I_4\pi^2\left(\frac{m^2}{a^2} + \frac{n^2}{b^2}\right)\right]$$
$$M_{44} = -\left[I_0 + I_5\pi^2\left(\frac{m^2}{a^2} + \frac{n^2}{b^2}\right)\right]$$

JOURNAL of
MATERIALS and MECHATRONICS:A

e-ISSN 2717-8811
JournalMM, 2025, 6(1), 121-134
https://doi.org/10.55546/jmm.1601100

Araştırma Makalesi / Research Article

Titreşim Spektrum Analizi ve İvme Ölçümleri ile Rulman Sağlığı Değerlendirmesi: Deneysel Bir İnceleme

Ahmet KÖKEN[1*], Sultan Seda ÜLGER[2], Abdurrahman KARABULUT[3]

[1*] Kütahya Dumlupınar Üniversitesi, Makine ve Metal Teknolojileri Bölümü, Kütahya, Türkiye,
ORCID ID: https://orcid.org/0000-0002-7047-5832, ahmet.koken@dpu.edu.tr
[2] Afyon Kocatepe Üniversitesi, Fen Bilimleri Enstitüsü, Makine Mühendisliği Anabilim Dalı, Afyonkarahisar, Türkiye
ORCID ID: https://orcid.org/0000-0003-0580-5900, s.sedaa@hotmail.com
[3] Afyon Kocatepe Üniversitesi, Teknoloji Fakültesi, Makine Mühendisliği Bölümü, Afyonkarahisar, Türkiye,
ORCID ID: https://orcid.org/0000-0002-7663-2579, akarabulut@aku.edu.tr

Geliş/ Received: 13.12.2024**;** **Revize/Revised:** 04.02.2025 **Kabul / Accepted:** 09.03.2025

ÖZET: Bu çalışma, rulman sağlığının değerlendirilmesinde ve hasar tespitinde titreşim spektrum analizleri ve ivme ölçümlerinin etkinliğini araştırmaktadır. Deneysel analizler, sağlam (A1 ve B1) ve iç bileziği hasarlı (A2 ve B2) rulmanlar üzerinde gerçekleştirilmiştir. Sağlam rulmanların titreşim spektrumlarında düşük genlikli ve belirgin olmayan pikler gözlemlenirken, hasarlı rulmanlarda karakteristik frekanslarda yüksek genlikli pikler ve ivme ölçümlerinde önemli hata sapmaları tespit edilmiştir. A2 rulmanında 15,4 Hz, 27 Hz, 48,2 Hz ve 136,9 Hz frekanslarında belirgin pikler gözlemlenmiştir. B2 rulmanında ise 80 Hz ve 160 Hz frekanslarındaki ivme ölçümleri, rulman hasarının neden olduğu önemli sapmaları ortaya koymuştur. Elde edilen bulgular, titreşim analizinin rulman arızalarının erken teşhisi için güvenilir bir yöntem olduğunu ve düzenli bakımın rulman ömrünü uzatabileceğini göstermektedir.

Anahtar Kelimeler: Titreşim analizi, Rulman sağlığı, Hasar tespiti, İvme ölçümü

*Sorumlu yazar / Corresponding author: ahmet.koken@dpu.edu.tr
Bu makaleye atıf yapmak için /To cite this article

Köken, A., Ülger, S. S., Karabulut, A. (2025). Titreşim Spektrum Analizi ve İvme Ölçümleri ile Rulman Sağlığı Değerlendirmesi: Deneysel Bir İnceleme. Journal of Materials and Mechatronics: A (JournalMM), 6(1), 121-134.

Vibration Spectrum Analysis and Acceleration Measurements for Bearing Health Assessment: An Experimental Investigation

ABSTRACT: This research explores the efficacy of vibration spectrum analysis and acceleration measurements for evaluating bearing health and detecting faults. Experimental investigations were performed on both healthy (A1 and B1) and inner race damaged (A2 and B2) bearings. The vibration spectra of healthy bearings exhibited low-amplitude and indistinct peaks, whereas damaged bearings demonstrated high-amplitude peaks at characteristic frequencies, along with significant error deviations in acceleration measurements. Notable peaks were observed in bearing A2 at frequencies of 15.4 Hz, 27 Hz, 48.2 Hz, and 136.9 Hz. Moreover, acceleration measurements at 80 Hz and 160 Hz for bearing B2 revealed substantial deviations attributable to the bearing damage. These findings suggest that vibration analysis offers a reliable approach for the early diagnosis of bearing failures, and that routine maintenance can contribute to prolonging bearing service life.

Keywords: Vibration analysis, Bearing health, Fault detection, Acceleration measurement

1. GİRİŞ

Dönen makinelerin temel bileşenlerinden biri olan rulmanların sağlık durumu, makinenin titreşim analizleri ile doğrudan ilişkilidir. Makine yataklarından ölçülen titreşim verileri, rulmanlarda meydana gelebilecek olası sorunlar hakkında kritik bilgiler sağlamaktadır. Rulmanlarda, üretim hataları, yetersiz yağlama, aşındırıcı partiküller ve nem gibi faktörler nedeniyle çeşitli arızalar ortaya çıkabilmektedir (Çimen, 2015). Bu arızaların erken tespiti ve önlenmesi amacıyla titreşim analizi yöntemi yaygın bir şekilde kullanılmaktadır. Bu yöntemde, makinelerden periyodik olarak alınan titreşim sinyalleri analiz edilerek, arızanın türü ve şiddeti belirlenmektedir. Elde edilen sonuçlara göre, makine için bakım planlaması yapılması veya arızalı parçanın değiştirilmesi gibi önlemler uygulanmaktadır. Titreşim verilerinin düzenli olarak toplanması ve analiz edilmesi, makinelerin ömrünü uzatırken, plansız duruşları ve gereksiz parça değişimlerini önlemektedir.

Mekanik sistemlerin titreşim analizinin amacı, sistem davranışlarını farklı dinamik koşullar altında elde etmektir (Çaşka ve ark., 2023; De Luca ve Book, 2016). Farklı dinamik koşullar altında sönüm oranı, artık titreşimler ve doğal frekanslar gibi sistem davranışlarını elde etmek, mekanik sistemlerde titreşim analizinin amaçlarındandır (Yavuz ve ark., 2018). Titreşim analizi, bakım stratejilerinde öngörücü bakıma geçişi sağlayarak bakım maliyetlerini önemli ölçüde azaltmaktadır. Mobley (1990) tarafından yapılan araştırmaya göre, üretim maliyetleri içerisinde bakım maliyetlerinin payı sektörlere bağlı olarak %15 ile %40 arasında değişmektedir. Gereksiz bakım faaliyetleri, toplam bakım maliyetlerinin yaklaşık üçte birini oluşturmaktadır. Bu nedenle, titreşim analizi yoluyla arızaların erken teşhisi, planlı bakım uygulamalarının yaygınlaştırılması ve bakım maliyetlerinin optimize edilmesi büyük önem taşımaktadır.

Rulmanlarda titreşim analizi yoluyla arıza tespiti, 1950'lerden bu yana mühendislik literatüründe yoğun bir şekilde incelenen bir konudur. Bu alandaki ilk çalışmalar, rulmanların titreşim özelliklerinin matematiksel olarak modellenmesi ve elde edilen verilerin çeşitli sinyal işleme teknikleri kullanılarak analiz edilmesine odaklanmıştır. Bu süreç, rulman arızalarının erken teşhisi için önemli bir veri tabanının oluşturulmasına katkı sağlamıştır. Literatürde bu konuda gerçekleştirilen çalışmalardan bazıları şu şekildedir: Darmo ve ark. (2022), burç yatak arızaları, yağ dişli pompalarında temel arıza nedenlerinden biri olarak belirtilmiştir. Burç yatak veya düz yatak iç

halkasında meydana gelen aşınma, gevşemeye neden olmakta ve bu durum dişlilerin zarar görmesine yol açmaktadır. Bu tür arızalar, dönme hızı frekansının harmonikleri ile tespit edilebilmekte olup, bu harmonikler arızanın hem belirtisi hem de nedeni olarak ifade edilmektedir. Jamaludin ve ark. (2002), akustik emisyon yöntemi kullanılarak düşük devirlerde çalışan rulmanlardaki hasarların tespitinde bu yöntemin etkinliğini ortaya koymuşlardır. Çalışmada, 1,2 dev/dk açısal hızıyla dönen bir rulmanda yuvarlanma elemanı, iç bilezik, dış bilezik hasarı, gevşek iç bilezik ve gevşek dış bilezik durumları için titreşim ölçümleri yapmışlar ve analiz etmişlerdir. Williams ve ark. (2001), rulmanların ömrünü belirlemek amacıyla sağlıklı rulmanları sabit ve değişken devirlerde hasar oluşuncaya kadar test etmişlerdir. Bu deneysel çalışma, rulmanların farklı çalışma koşullarındaki dayanımını değerlendirmeyi hedeflemişlerdir. Madar ve ark. (2022), sadece iç halka, dış halka, bilyeler ve kafeste rulman arıza sıklığını göstermekle kalmamış, aynı zamanda doğal frekans uyarımının da rulmana zarar verebileceğini ve arıza belirtilerine yol açabileceğini belirtmişlerdir. Sıvı halka kompresör için titreşim analizi ve sinyal işleme yöntemleri kullanılarak, doğal frekansların rulman arıza analizinde nasıl kullanılabileceğini ortaya koymuşlardır. Dron ve ark. (2001), bilyeli rulmanlardaki titreşim analizinde parametrik spektrum analiz yöntemini kullanmış ve hasar teşhisi için yüksek çözünürlüklü bir teknik uygulamışlardır. Bu yöntem sayesinde, rulmanlardaki hasarların daha detaylı ve doğru bir şekilde tespit edilebileceğini belirtmişlerdir. Aktürk ve ark. (2000), açısal temaslı iki rulman üzerine yataklanmış bir mil sistemi oluşturarak, rulman kaynaklı titreşimlerin oluşum mekanizmalarını incelemişlerdir. Bu çalışmada, hem sağlıklı rulmanların neden olduğu titreşim frekansları hem de rulmanlardaki üretim hatalarının titreşimlere olan etkilerini detaylı bir şekilde analiz etmişlerdir. Hemati ve ark. (2023), rulmanların statik ve dinamik yükleri tolere eden hayati bir bileşen olduğunu belirtmişlerdir. Rulmanların kalan ömrünü hesaplamak için birçok faktörün önemli olduğunu vurgulamışlardır. Oluklu arıza ve kaçak akım gibi etkenlerin rulmanların arızalanmasına neden olduğunu ifade etmişlerdir. Rulman oluklu arızası için titreşim analizi ve sinyal işleme yöntemlerini kullanarak rulman arıza analizini araştırmışlardır. Brie (2000), tek noktadan hasarlı bir rulmandaki titreşim sinyallerini matematiksel olarak modellemiştir. Rubini ve ark. (2001), normal çalışma koşullarında rulmanlardaki yorulma hasarlarının tespiti için klasik spektrum ve zarf analizi yöntemlerinin yaygın olarak kullanıldığını belirtmişlerdir. Ancak bu araştırmacılar, bu yöntemlerin her zaman yeterli olmadığını ve bazı durumlarda rulmanlardaki yorulma hasarlarının tam olarak tespit edilemeyebileceğini vurgulamışlardır. Mishra ve ark. (2022), santrifüj pompadaki bilyeli rulman arıza analizini araştırmışlardır. MATLAB yazılımını kullanarak, toplanan deneysel verilere dayalı olarak arıza analizi gerçekleştirmişlerdir. Rulman içine su girişinin, rulman ömrü üzerinde zararlı bir etkiye sahip olduğunu belirtmişlerdir. Yıldırım ve Karahan (2015), kompresör rulmanlarında gerçekleştirilen titreşim analizi sayesinde hem dış hem de iç bileziklerde oluşan hasarların tespit edildiğini ve bu analizlerin kestirimci bakım çalışmalarına veri sağladığını belirtmişlerdir. Ghazwani ve Pham (2024), bilyeli yatakların teorik frekansını hesaplamak için Hertz temasına dayalı bir matematiksel model kullanmışlardır. İğne yatağının değişken hareketi nedeniyle, iki darbe arası süreyi dikkate alarak arızalı darbe frekansını tahmin etmek için yeni bir matematiksel model önermişlerdir.

Mühendislik sistemlerinin modellenmesinde deneysel yöntemlerden gün geçtikçe daha fazla faydalanılmaktadır (Çaşka ve Dokuz, 2022). Bu araştırmada, rulman arızalarının titreşim analizi yöntemiyle belirlenmesine yönelik bir deneysel düzenek tasarlanmıştır. Referans olarak sağlıklı rulmanlardan elde edilen temel titreşim verileri, iç bilezik bilye yuvarlanma yolu hatası bulunan rulmanlardan toplanan verilerle karşılaştırılmıştır. Bu karşılaştırma sayesinde, bahsi geçen hasarın

titreşim sinyalleri üzerindeki etkileri ayrıntılı olarak incelenmiştir. Sonuçlar, grafiksel olarak sunularak kapsamlı bir değerlendirme yapılması sağlanmıştır.

1.1 Frekans Analizi

Rulmanlar, operasyon esnasında doğal yıpranma veya yapısal defektler nedeniyle karakteristik frekanslarda titreşimler üretirler. İç bilezik, dış bilezik ve yuvarlanma elemanlarındaki (bilyeler) hasarlar, rulmanın geometrik özelliklerine bağlı olarak farklı frekans bileşenlerinin ortaya çıkmasına neden olur. Bu frekans bileşenlerinin analizi, arızanın türü ve ilerleme durumu hakkında önemli bilgiler sağlamaktadır. Titreşim spektrumunda, frekans değeri arızanın tipini belirtirken, genlik değeri arızanın şiddetini yansıtır. Arıza frekansları, motorun dönme hızı ile doğrudan ilişkilidir; motor devri değiştikçe, yuvarlanma elemanlarının hasarlı bölge üzerinden geçme sıklığı da değişir ve bu durum arıza frekanslarında kaymaya yol açar. Rulmanlara ilişkin genel arıza frekansları Eşitlik 1, 2, 3 ve 4'te sunulmuştur (Aliustaoğlu ve ark., 2007).

$$Temel\ Frekans\ (TF) = \frac{f_s}{2}\left[1 - \frac{R_b}{d_m}\right] \tag{1}$$

$$Bilye\ Dönme\ Frekansı\ (BD) = \frac{f_s}{2}\frac{d_m}{R_b}\left[1 - \left[\left(\frac{R_b}{d_m}\right)^2\right]\right] \tag{2}$$

$$Dış\ Bilezik\ Frekansı = N\ (TF) \tag{3}$$

$$\text{İç}\ Bilezik\ Frekansı\ (\text{İB}) = N\ (f_s - TF) \tag{4}$$

Eşitlik 1-4 de belirtilen f_s parametresi dönme frekansını, R_b parametresi bilye çapını ve d_m parametresi ise bilye merkezleri arasındaki mesafeyi temsil etmektedir.

Rulman arıza frekansları; rulman geometrisindeki varyasyonlar, temas açısı, kayma hareketi ve mil dönme hızı gibi çeşitli faktörlerden etkilenebilir. Bu sebeple, deneysel olarak ölçülen titreşim frekansları ile teorik olarak hesaplanan frekanslar arasında küçük farklılıkların oluşması olasıdır. Hasarlı bir rulmanın titreşim spektrumunda gözlemlenen evreler, aşağıdaki şekilde tanımlanabilir (Orhan ve ark., 2003):

- Erken Evre: Spektrum analizlerinde, temel arıza frekansının kendisinden ziyade, bu frekansın harmonik bileşenleri ön plana çıkar. Bu aşamada temel arıza frekansının belirginliği düşüktür.
- Orta Evre: Arızanın ilerlemesiyle birlikte, arıza frekansının daha yoğun harmonikleri tespit edilir. Arıza frekansları, mil dönme hızı ile modülasyona uğrayarak yan bantların oluşmasına yol açar. Yan bant genliklerinin, temel frekansın genliğini aşması, arızanın kritik bir düzeye ulaştığının göstergesidir.
- Geç Evre: Spektrumda, arıza frekansının harmonik ve yan bantlarına ek olarak, temel arıza frekansı da belirgin bir şekilde ortaya çıkar.
- İleri Evre: Rulmanın sürekli bozulması, iç boşlukların artmasına sebep olur. Bu durum, rulman elemanları arasındaki çarpışmaları şiddetlendirir. Bu çarpışmalar, spektrumda geniş bantlı bir gürültü oluşumuna yol açar. Titreşim genlikleri azalabilir ve bu geniş bantlı gürültünün ayırt edilmesi güçleşebilir.

2. MATERYAL VE YÖNTEM

Bu araştırmada, rulman arızalarının titreşim analizi ile teşhisi amacıyla deneysel bir çalışma yürütülmüş ve Şekil 1'de görülen bir deney düzeneği hazırlanmıştır. Deney düzeneği, rulmanların operasyonel koşullarını simüle etmek için basit bir şaft-rulman sisteminden oluşmaktadır. Sistem, bir elektrik motoru vasıtasıyla tahrik edilen V kayışlar aracılığıyla döndürülmektedir. Rulman yatakları ve mil, rulmanların uygun şekilde konumlandırılması için tasarlanmıştır. Sistemdeki titreşimleri minimize etmek amacıyla, V kayış gerginliği optimize edilmiştir.

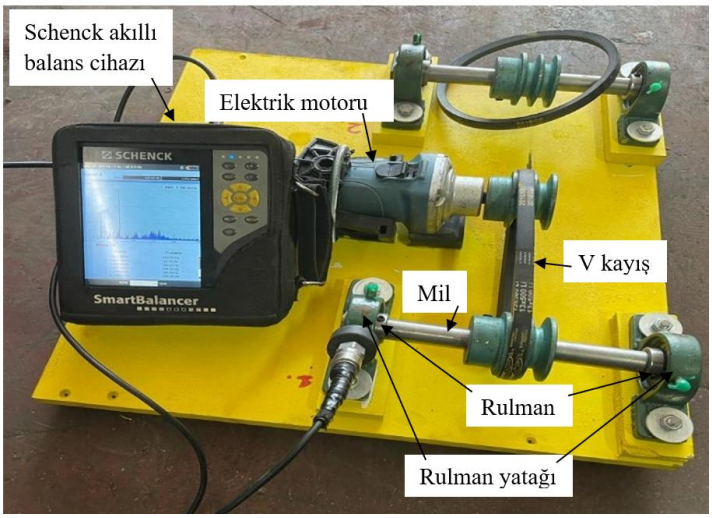

Şekil 1. Deney düzeneğinin tüm bileşenlerini gösteren genel bir görünüm

Bu deneyde, rulmanların titreşim analizlerinin gerçekleştirilmesi için Schenck akıllı balans cihazı kullanılmıştır. Elektrik motoruna bağlı mil-rulman sisteminde meydana gelen titreşimler, balans ölçer aracılığıyla ölçülerek veri toplama sistemine aktarılmıştır. Rulman yataklarına konumlandırılan titreşim sensörleri vasıtasıyla, sağlam ve hasarlı rulmanlara ait titreşim verileri karşılaştırılmıştır. Deney düzeneğinde analiz edilen UC204 tipi rulmanların geometrik özellikleri Şekil 2'de, boyutları ise Çizelge 1'de sunulmuştur.

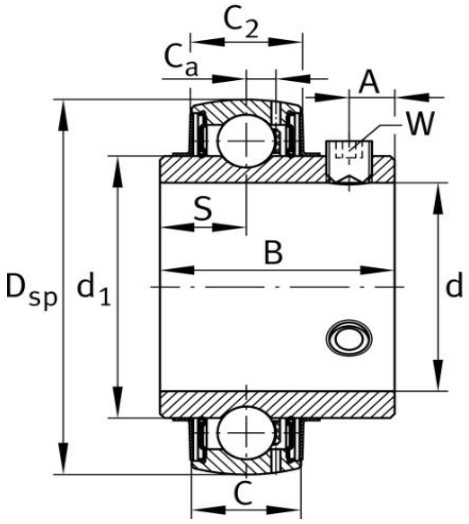

Şekil 2. UC204 test rulmanına ait geometrik özellikler

Çizelge 1. Rulman boyutları (mm)

Boyutlar	Sembol	Değer
Dış çap	D_{sp}	47
İç çap	d	20
Genişlik	B	31
Dış halka genişliği	C	17
İç halka kaburga çapı	d_1	27,56
Yuvarlanma yolu mesafesi	S	12,7
Diş mesafesi	A	5
Conta toplam genişliği	C_2	16,8
Yağlama deliğine mesafe	C_a	4,2
Düz yüzey genişliği	W	3

Bu çalışmada, rulman arızalarının erken teşhisine yönelik titreşim analizi yöntemi kullanılmıştır. Elektrik motoruna bağlı bir test düzeneğinde farklı kondisyondaki rulmanlardan elde edilen titreşim verileri, ivmeölçer ve hız transdüseri aracılığıyla kaydedilmiştir. Elde edilen verilerin frekans spektrumu analizi, rulman arızalarına özgü karakteristik frekansların belirlenmesinde kullanılmıştır. Deney sonuçlarının, titreşim sensörünün konumlandırılması ve işletme koşulları gibi faktörlerden etkilenebileceği dikkate alınmalıdır.

Rulmanların güvenilirliği ve ömrü, endüstriyel uygulamalar için kritik öneme sahiptir. Bu araştırmada, rulman arızalarının titreşim analizi ile tespitine yönelik deneysel bir inceleme yapılmıştır. Farklı hasar seviyelerindeki rulmanlardan elde edilen titreşim verileri, frekans ortamında analiz edilerek, arızanın türü ve şiddeti hakkında bilgi elde edilmiştir. Çalışma sonuçları, rulmanların güvenilirliğini artırma ve bakım stratejilerini geliştirme konusunda önemli veriler sunmaktadır.

3. BULGULAR VE TARTIŞMA

Yeni üretilen rulmanlarda bile, yüzey pürüzlülüğünden kaynaklanan hata frekansları gözlemlenmiştir. Rulman bileziğindeki mikroskobik pürüzler, düşük genlikli frekans bileşenleri oluşturarak, titreşim analizlerinde belirginleşmiştir. Bu düşük genlikli frekans bileşenleri, hasarın ilerlemesi sürecinde önemli bir gösterge olarak kullanılabilir.

3.1 Sağlam Rulman Analizleri

Sağlam (A1) rulmanının titreşim spektrumu analizine ait sonuçlar Şekil 3'te sunulmaktadır. Spektrum incelemesinde 0,5 Hz, 11,23 Hz, 26,8 Hz ve 37,3 Hz frekanslarında belirgin pikler gözlemlenmiştir. Bu piklere karşılık gelen genlik değerleri sırasıyla 0,164 mm/s, 0,027 mm/s, 0,014 mm/s ve 0,049 mm/s olarak tespit edilmiştir. 0,5 Hz'deki pik, çevresel titreşimler veya sistemin yavaş hareketleri gibi mekanik olmayan etkilerden kaynaklanabilir. Diğer frekanslardaki (11,23 Hz, 26,8 Hz ve 37,3 Hz) pikler ise rulmanın dönüş hızı veya sistemdeki diğer mekanik bileşenlerin etkileşimleri ile ilişkili olabilir. Tüm piklerin genlik değerleri oldukça düşüktür ve bu, rulmanın sağlam olduğunu ve herhangi bir ciddi hasar belirtisi göstermediğini ortaya koymaktadır. Spektrumda harmonikler veya yan bantlar gibi hasar belirtileri gözlemlenmemiştir. Bu bulgular, rulmanın düzgün çalıştığını ve sağlam durumunu koruduğunu göstermektedir. Rulmanın bu durumunu sürdürmek için düzenli bakım ve titreşim analizi önerilmektedir.

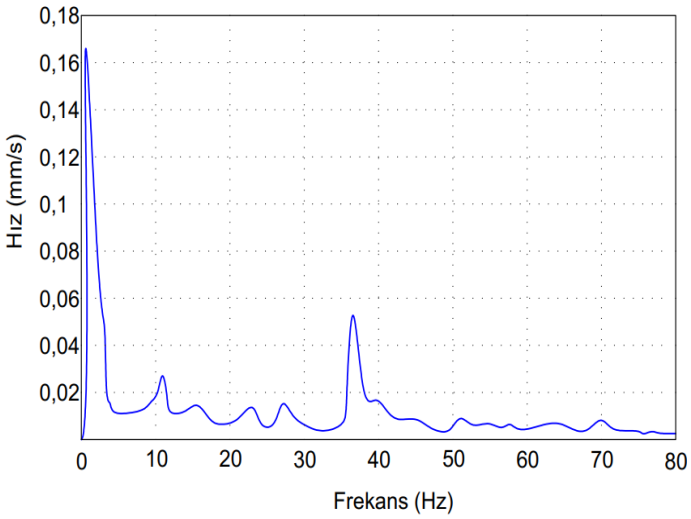

Şekil 3. Sağlam rulman (A1) titreşimleri

Sağlam (A1) rulmanının titreşim analizleri sonucunda elde edilen dış ve iç bilezik hata frekansları, Şekil 4(a)'da gösterilmekte olup, bu bulgular Şekil 4(b)'de grafiksel olarak sunulmuştur. Elde edilen ölçüm değerlerine göre, dış bilezik arıza frekansı yaklaşık 53 Hz, iç bilezik arıza frekansı ise yaklaşık 63 Hz olarak belirlenmiştir. Yeni üretilmiş rulmanlarda dahi, idealden sapmalar nedeniyle bölgesel hata karakteristikleri tespit edilebilir. Bu durum, rulman yüzeylerinin mutlak pürüzsüzlükten uzak olmasından kaynaklanmaktadır. Nitekim, Şekil 4'te sunulan sağlam bir rulmana ait titreşim verileri üzerinde yapılan analizler, rulman hata frekanslarının varlığını ortaya koymaktadır. İç ve dış bileziklerde bulunan mikroskobik yüzey kusurları, düşük genlikli frekans bileşenlerinin oluşmasına neden olmaktadır. Bu genlik değerleri, hasar gelişiminin izlenmesinde temel referans noktaları olarak değerlendirilmelidir. Bu bulgular ışığında, tamamen titreşimsiz bir mekanik sistemin varlığının teorik bir ideal olduğu söylenebilir.

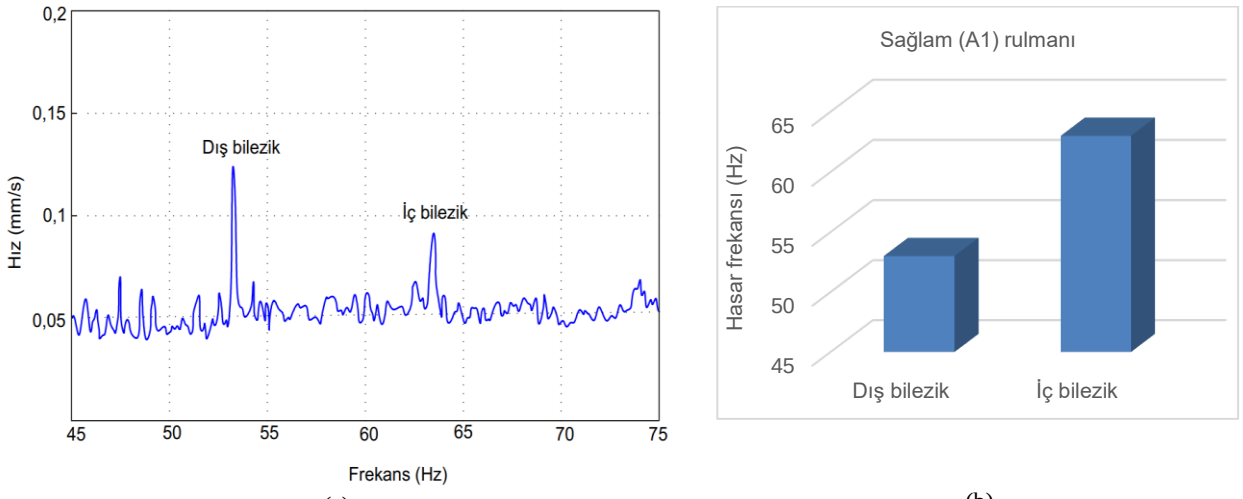

(a) (b)

Şekil 4. Sağlam (A1) rulmanı; (a) titreşim frekans spektrumu, (b) hata frekansları

Sağlam (B1) rulmanına ait titreşim spektrumu analiz sonuçları Şekil 5'te gösterilmektedir. Spektrumda 0,5 Hz, 14,7 Hz, 18,6 Hz ve 24,38 Hz frekanslarında belirgin pikler tespit edilmiştir. Bu piklerin genlik değerleri sırasıyla 0,159 mm/s, 0,027 mm/s, 0,038 mm/s ve 0,042 mm/s olarak ölçülmüştür. 0,5 Hz'deki pik, çevresel titreşimler veya sistemin yavaş hareketleri gibi mekanik olmayan etkilerden kaynaklanabilir. Diğer frekanslardaki (14,7 Hz, 18,6 Hz ve 24,38 Hz) pikler ise

rulmanın dönüş hızı veya sistemdeki diğer mekanik bileşenlerin etkileşimleri ile ilişkili olabilir. Tüm piklerin genlik değerleri oldukça düşüktür ve bu, rulmanın sağlam olduğunu ve herhangi bir ciddi hasar belirtisi göstermediğini ortaya koymaktadır. Spektrumda harmonikler veya yan bantlar gibi hasar belirtileri gözlemlenmemiştir. Bu bulgular, rulmanın düzgün çalıştığını ve sağlam durumunu koruduğunu göstermektedir. Rulmanın bu durumunu sürdürmek için düzenli bakım ve titreşim analizi önerilmektedir.

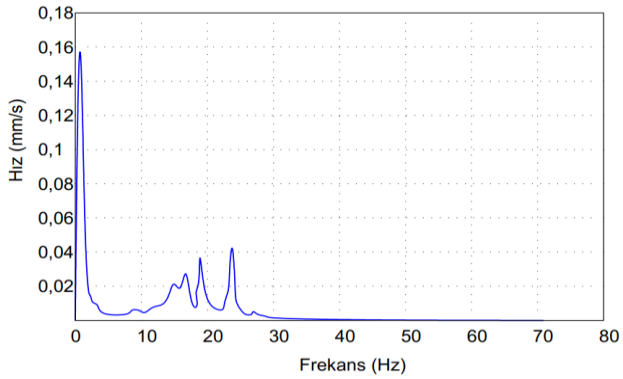

Şekil 5. Sağlam (B1) rulman titreşim spektrum analizi

Sağlam (B1) rulmanına ait dış ve iç bileziklerdeki olası arıza frekansları, titreşim analizi ile tespit edilmiş olup (Şekil 6(a)), elde edilen bu bulgular Şekil 6(b)'de grafiksel olarak ifade edilmiştir. Ölçümler sonucunda, dış bilezik hasar frekansının yaklaşık 50 Hz, iç bilezik hasar frekansının ise yaklaşık 59 Hz olduğu tespit edilmiştir. Yeni üretilen rulmanlarda dahi, ideal yüzey pürüzlülüğünden sapmalar nedeniyle bölgesel hata karakteristikleri gözlemlenebilir. Şekil 6'da sunulan titreşim analizleri, sağlam bir rulmanda bile rulman hata frekanslarının bulunduğunu göstermektedir. İç ve dış bileziklerdeki mikroskobik kusurlar, düşük genlikli frekans bileşenlerine yol açarak, hasar gelişiminin izlenmesinde referans noktası olarak kullanılabilecek veriler sunmaktadır. Bu nedenle, tamamen titreşimsiz bir mekanik sistemin varlığı, teorik bir ideal olarak kabul edilebilir.

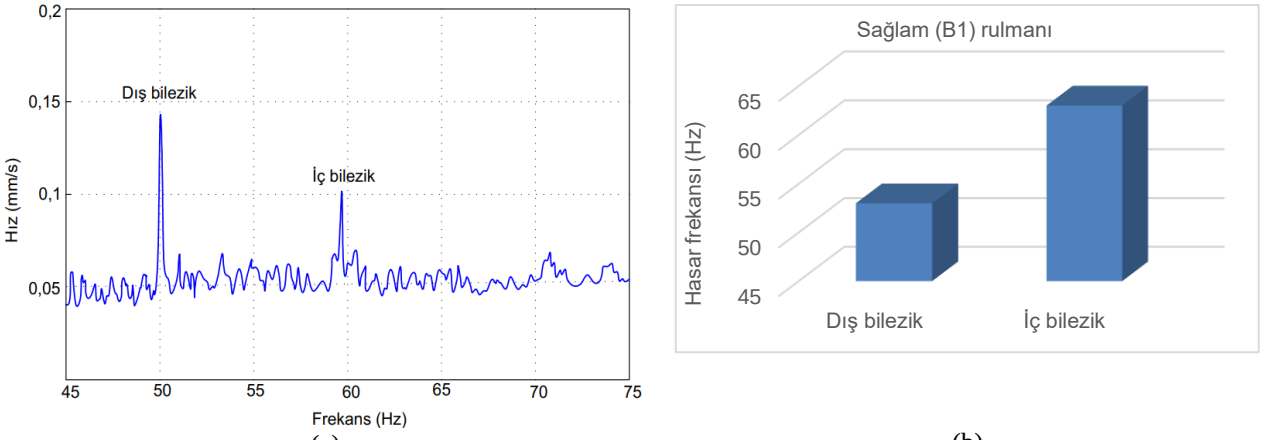

(a) (b)

Şekil 6. Sağlam (B1) rulmanı; (a) titreşim frekans spektrumu, (b) hata frekansları

Spektrum analizlerinde (Şekil 3 ve 5), düşük genlikli fakat belirgin pikler, rulman yüzeyindeki mikroskobik pürüzlülüklerin neden olduğu harmonik frekansları işaret etmektedir. Bu durum, makroskobik olarak sağlam kabul edilen rulmanlarda dahi yüzey kalitesinde idealden sapmalar olduğunu göstermektedir. Döner makinelerde sıklıkla karşılaşılan küçük seviyedeki dengesizlikler, teorik olarak titreşimsiz olması beklenen sistemlerde pratikte kaçınılmazdır. Rulman yatağında tam

kavrama sağlanamaması sonucu oluşan mekanik gevşeklik, milin dengelenmesinde yetersizlik olduğunu ortaya koymaktadır. Bu tür mekanik gevşeklikler, titreşim seviyelerini yükselterek rulmanların hizmet ömrünü kısaltma potansiyeline sahiptir.

RMS (karekök ortalama), bir sinyalin genel büyüklüğünü veya enerjisini ölçer. Titreşim analizinde, sistemin titreşim seviyesini ifade etmek için kullanılır. *RMS* değerleri Eşitlik 5 kullanılarak hesaplanabilir.

$$RMS = \sqrt{\frac{A_0^2}{2} + \sum_{i=1}^{k-1} A_i^2 + \frac{A_k^2}{2}} \tag{5}$$

Burada;

A_0 = Sinyalin sabit bileşeninin genliği,

A_i = Sinyalin *i.* harmonik bileşeninin genliği,

A_k = Sinyalin son harmonik bileşeninin genliği,

$\sum_{i=1}^{k-1} A_i^2$ = 1. harmonikten (*k-1*). harmonik bileşenine kadar olan genliklerin karelerinin toplamı.

Eğer A_k, 2. harmonikten sonraki bir bileşeni temsil ediyorsa, *k* en az 3 olmalıdır. Örneğin, eğer $A_k = A_3$ ise, $k = 3$ olur.

Spektral bir çizginin genliği "A" ile gösterilmiştir. Sağlam (A1) rulmanı için, Eşitlik 5'te, A_0 = 0,164 mm/s, A_1 = 0,027 mm/s, A_2 = 0,014 mm/s, A_k = 0,049 mm/s ve k = 3 alındığında *RMS* = 0,1288 mm/s olarak hesaplanmıştır. Bu sonuç, Şekil 7(a)'da sunulan test cihazı ölçümünde elde edilen 0,129 mm/s'lik *RMS* değeri ile uyumluluk göstermektedir.

Sağlam B1 rulmanı için, Eşitlik 5'te, A_0 = 0,159 mm/s, A_1 = 0,027 mm/s, A_2 = 0,038 mm/s, A_k = 0,042 mm/s ve k =3 alındığında, *RMS* = 0,1264 mm/s olarak hesaplanmıştır. Elde edilen bu sonuç, Şekil 7(b)'de gösterilen test cihazı ölçümünde saptanan 0,126 mm/s *RMS* değeri ile teyit edilmiştir.

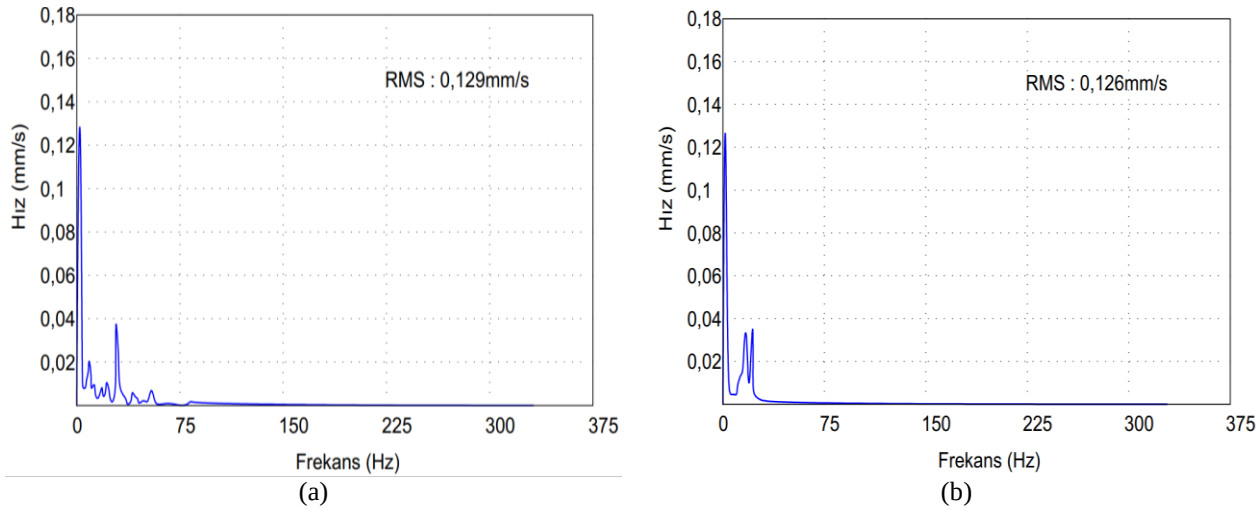

(a) (b)

Şekil 7. Sağlam rulman titreşimleri; (a) A1 rulmanı, (b) B1 rulmanı

3.2 İç Bileziği Hasarlı Rulman Analizleri

Şekil 8(a)'da iç bileziğinde hasar bulunan rulmana (A2) ait frekans spektrumu analiz sonuçları gösterilmektedir. Titreşim frekansı ve harmonikleri spektrumda 15,4 Hz, 27 Hz, 48,2 Hz ve 136,9 Hz frekanslarında titreşim yoğunluğunun arttığı belirlenmiştir. Bu frekanslardaki titreşim genlikleri ise

sırasıyla 0,186 mm/s, 0,198 mm/s, 0,178 mm/s ve 0,122 mm/s olarak ölçülmüştür. 15,4 Hz'deki pik, rulmanın karakteristik iç bilezik hasar frekansı (BPFI) olarak değerlendirilebilir ve bu frekans, ana harmonik bileşeni temsil etmektedir. 27 Hz'deki pik, 15,4 Hz'deki ana harmonik frekansın ikinci harmonik bileşeni olabilir ve bu durum, iç bilezik hasarının periyodik doğasını göstermektedir. 48,2 Hz'deki pik ise üçüncü harmonik bileşen olarak yorumlanabilir. 136,9 Hz'deki daha düşük genlikli pik (0,122 mm/s), sistemin doğal frekansı veya rezonans frekansı ile ilişkili olabilir. Bu frekans, rulman hasarı ile doğrudan ilişkili olmayan bir bileşen olarak değerlendirilebilir, ancak bu frekansta bir genlik artışı gözlemlenmesi, sistemin bu frekans civarında rezonansa girebileceğini düşündürmektedir. Spektrumda gözlemlenen frekanslar, sistemin farklı modal frekanslarına da karşılık gelebilir. Özellikle 15,4 Hz ve 27 Hz'deki yüksek genlikler, sistemin bu frekanslarda modal titreşimler ürettiğini gösterebilir. Bu modal frekanslar, rulmanın iç bileziğindeki hasarın etkisiyle daha belirgin hale gelmiş olabilir. Özellikle 15,4 Hz ve 27 Hz frekanslarındaki yüksek genlikler (0,186 mm/s ve 0,198 mm/s), rulmanın iç bileziğinde ciddi bir hasarın varlığına işaret etmektedir. Bu frekanslar, rulmanın karakteristik iç bilezik hasar frekansı (BPFI) ve bunun ikinci harmonik bileşeni ile uyumlu olabilir. 136,9 Hz'deki daha düşük genlikli pik (0,122 mm/s) ise rulman hasarı ile doğrudan ilişkili olmayan bir bileşen olarak değerlendirilebilir. Bu bulgular, rulmanın iç bileziğinde ciddi bir hasar olduğunu göstermekte olup, rulmanın durumunun daha detaylı incelenmesi ve gerekli bakım veya değişim işlemlerinin planlanması önerilmektedir.

Şekil 8(b)'de sunulan iç bileziği hasarlı rulman (B2) titreşimlerine ait spektrum analizi grafiğinde, bilye geçiş titreşim frekansı ve harmonikleri 15,9 Hz, 28,3 Hz, 49,5 Hz ve 75 Hz frekanslarında belirgin pikler saptanmıştır. Bu piklerin genlik değerleri ise sırasıyla 0,167 mm/s, 0,216 mm/s, 0,219 mm/s ve 0,122 mm/s olarak ölçülmüştür. 15,9 Hz'deki pik, rulmanın karakteristik bilye geçiş frekansı (BPFI) olarak değerlendirilebilir ve bu frekans, ana harmonik bileşeni temsil etmektedir. 28,3 Hz ve 49,5 Hz'deki pikler, 15,9 Hz'deki ana harmonik frekansın sırasıyla ikinci ve üçüncü harmonik bileşenleri olabilir ve bu durum, iç bilezik hasarının periyodik doğasını göstermektedir. 75 Hz'deki daha düşük genlikli pik (0,122 mm/s), sistemin doğal frekansı veya rezonans frekansı ile ilişkili olabilir. Bu frekans, rulman hasarı ile doğrudan ilişkili olmayan bir bileşen olarak değerlendirilebilir, ancak bu frekansta bir genlik artışı gözlemlenmesi, sistemin bu frekans civarında rezonansa girebileceğini düşündürmektedir. Spektrumda gözlemlenen frekanslar, sistemin farklı modal frekanslarına da karşılık gelebilir. Özellikle 28,3 Hz ve 49,5 Hz'deki yüksek genlikler, sistemin bu frekanslarda modal titreşimler ürettiğini gösterebilir. Bu modal frekanslar, rulmanın iç bileziğindeki hasarın etkisiyle daha belirgin hale gelmiş olabilir. Özellikle 28,3 Hz ve 49,5 Hz frekanslarındaki yüksek genlikler, rulmanın iç bileziğinde bir hasarın varlığına işaret etmektedir. Bu frekanslar, rulmanın karakteristik bilye geçiş frekansı (BPFI) ve bunun harmonik bileşenleri ile uyumlu olabilir. 75 Hz'deki daha düşük genlikli pik ise rulman hasarı ile doğrudan ilişkili olmayan bir bileşen olarak değerlendirilebilir. Bu bulgular, rulmanın iç bileziğinde ciddi bir hasar olduğunu göstermekte olup, rulmanın durumunun daha detaylı incelenmesi ve gerekli bakım veya değişim işlemlerinin planlanması önerilmektedir.

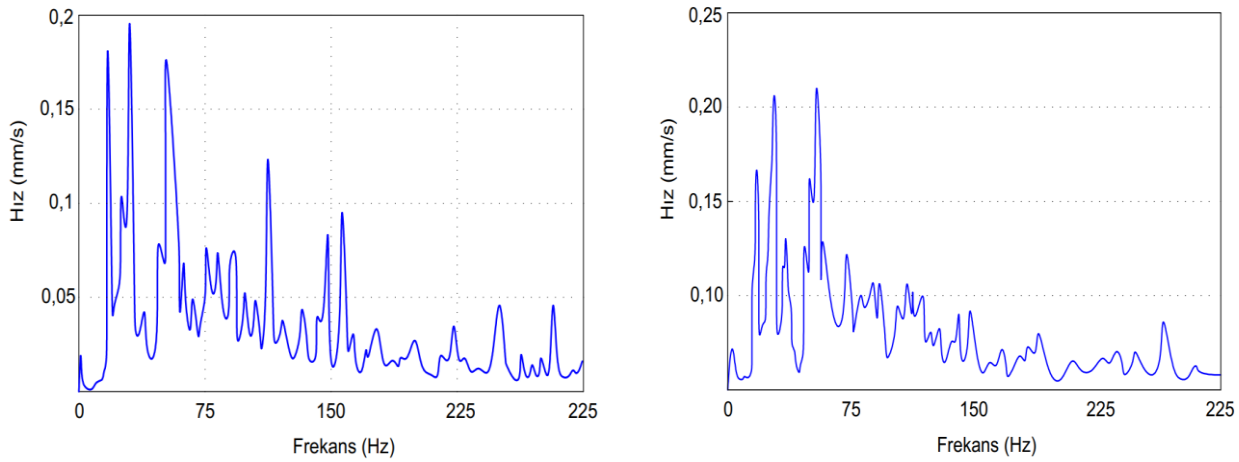

Şekil 8. İç bileziği hasarlı rulman titreşimleri; (a) A2 rulmanı, (b) B2 rulmanı

İç bileziği hasarlı (B2) rulman için 80 Hz frekansında ölçülen ivme değerleri ve hata sapmaları Şekil 9'da sunulmuştur. Uygulanan ivme değerleri ile ölçülen ivme değerleri arasındaki fark, rulman hasarının sistem üzerindeki etkisini açıkça göstermektedir. Büyük hata sapmaları, rulmanın iç bileziğindeki hasarın ciddi boyutlarda olduğunu ve sistemde önemli titreşimlere neden olduğunu işaret etmektedir. Bu sapmalar, rulmanın düzgün çalışmasını engelleyerek sistemin dinamik performansını olumsuz etkilemektedir. Bu bulgular, rulmanın acil bakım veya değişim gerektirdiğini ortaya koymaktadır. Rulmanın durumunu daha iyi değerlendirmek için, farklı frekanslarda benzer ölçümler yapılması ve zaman dalga formu analizi gibi ek yöntemlerin kullanılması önerilmektedir. Bu sayede, hasarın nedenleri daha detaylı incelenebilir ve olası arızalar önlenebilir.

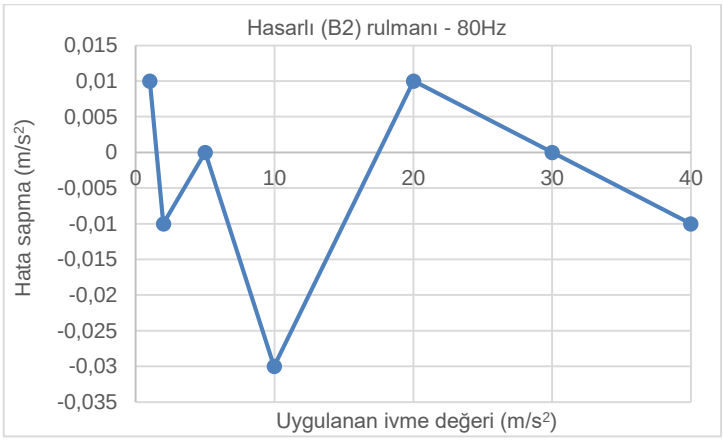

Şekil 9. İç bileziği hasarlı rulmandan (B2) 80 Hz'de ölçülen ivme değerleri

İç bileziği hasarlı (B2) rulman için 160 Hz frekansında ölçülen ivme değerleri ve hata sapmaları Şekil 10'da sunulmuştur. İç bileziği hasarlı rulman (B2) için 160 Hz'de ölçülen ivme değerleri ve büyük hata sapmaları, rulman hasarının sistem üzerinde ciddi titreşimlere ve dinamik performans kaybına neden olduğunu göstermektedir. Özellikle 160 Hz gibi yüksek frekanslarda gözlemlenen bu sapmalar, rulman hasarının mekanik sistem üzerinde yarattığı stresin bir göstergesidir. Bu bulgular, rulmanın acil bakım veya değişim gerektirdiğini ortaya koyarken, hasarın detaylı analizi için farklı frekanslarda ölçümler ve zaman dalga formu analizi gibi ileri yöntemler önerilmektedir.

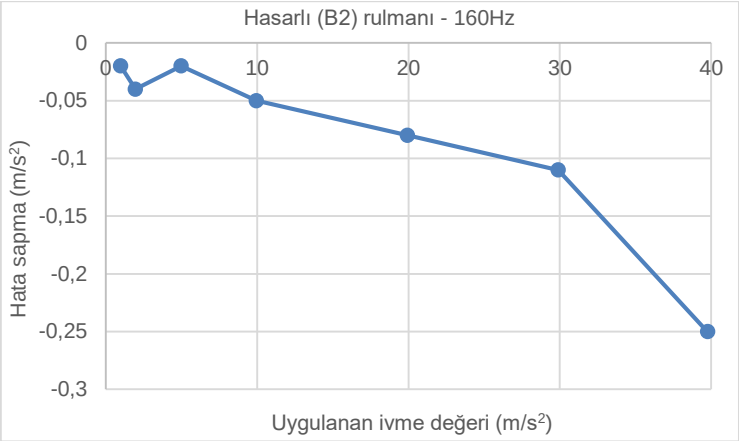

Şekil 10. İç bileziği hasarlı rulmandan (B2) 160 Hz'de ölçülen ivme değerleri

4. SONUÇ

Bu çalışmada, sağlam ve hasarlı rulmanların titreşim spektrum analizleri ve ivme ölçümleri incelenmiş, rulman sağlığının belirlenmesi ve hasar tespiti açısından önemli bulgular elde edilmiştir.

Sağlam rulmanların (A1 ve B1) titreşim spektrumlarında, düşük genlikli ve belirgin olmayan pikler gözlemlenmiştir. Örneğin, A1 rulmanında 0,5 Hz, 11,23 Hz, 26,8 Hz ve 37,3 Hz frekanslarında sırasıyla 0,164 mm/s, 0,027 mm/s, 0,014 mm/s ve 0,049 mm/s genlik değerlerinde pikler tespit edilmiştir. B1 rulmanında ise 0,5 Hz, 14,7 Hz, 18,6 Hz ve 24,38 Hz frekanslarında sırasıyla 0,159 mm/s, 0,027 mm/s, 0,038 mm/s ve 0,042 mm/s genlik değerlerinde pikler gözlemlenmiştir. Bu piklerin genlik değerleri oldukça düşüktür ve sağlam rulmanların herhangi bir ciddi hasar belirtisi göstermediğini ortaya koymaktadır.

İç bileziği hasarlı rulmanların (A2 ve B2) titreşim spektrumlarında ise karakteristik frekanslarda belirgin ve yüksek genlikli pikler gözlemlenmiştir. Örneğin, A2 rulmanında 15,4 Hz, 27 Hz, 48,2 Hz ve 136,9 Hz frekanslarında sırasıyla 0,186 mm/s, 0,198 mm/s, 0,178 mm/s ve 0,122 mm/s genlik değerlerinde pikler tespit edilmiştir. B2 rulmanında ise 80 Hz ve 160 Hz frekanslarında yapılan ivme ölçümleri, uygulanan ivme değerleri ile ölçülen ivme değerleri arasında önemli hata sapmaları olduğunu göstermiştir. Bu sapmalar, rulman hasarının sistemde ciddi titreşimlere ve dinamik bozulmalara neden olduğunu doğrulamaktadır.

Sonuç olarak, bu çalışma, titreşim analizi ve ivme ölçümlerinin rulman sağlığını değerlendirmede etkili bir yöntem olduğunu göstermiştir. Sağlam rulmanların titreşim spektrumlarında düşük genlikli pikler gözlemlenirken, hasarlı rulmanlarda karakteristik frekanslarda yüksek genlikli pikler ve önemli hata sapmaları tespit edilmiştir. Rulmanların ömrünü uzatmak ve olası arızaları önlemek için düzenli bakım ve titreşim analizi önerilmektedir. Ayrıca, benzer çalışmalarda zaman dalga formu analizi ve farklı frekanslarda ölçümler yapılarak, rulman sağlığının daha kapsamlı bir şekilde değerlendirilmesi mümkündür.

5. TEŞEKKÜR

Bu çalışmanın deneysel çalışmaları ORMEC Mühendislik tarafından desteklenmiş ve tesislerinde gerçekleştirilmiştir. Yazarlar, çalışmaya katkılarından dolayı Sn. Cem DENİZ'e içten teşekkürlerini sunar.

6. ÇIKAR ÇATIŞMASI

Yazarlar, bilinen herhangi bir çıkar çatışması veya herhangi bir kurum/kuruluş ya da kişi ile ortak çıkar bulunmadığını onaylamaktadırlar.

7. YAZAR KATKISI

Bu çalışmada Ahmet KÖKEN araştırmanın kavramsal çerçevesinin oluşturulması, metodolojik tasarımı ve makale taslağının hazırlanmasından sorumlu olmuştur; Sultan Seda ÜLGER çalışmanın kavramsal yapısının geliştirilmesi, tasarım süreçlerinin yönetimi, veri toplama ve bilimsel içeriğin eleştirel analizini gerçekleştirmiştir; Abdurrahman KARABULUT ise verilerin analizi, yorumlanması ve makalenin akademik içeriğinin bilimsel değerlendirmesini üstlenmiştir. Tüm yazarlar çalışmanın her aşamasına aktif katılım sağlamış, makalenin nihai versiyonunu incelemiş, onaylamış ve çalışmadan tam sorumluluğu paylaşmışlardır.

8. KAYNAKLAR

Aktürk N., Üzkurt İ., Yüksel Ş., Titreşim Analiziyle Rulmanların Çalışabilirlik Durumlarının Belirlenmesi, Mühendis ve Makina, TMMOB, 41(481), 28-33, 2000.

Aliustaoğlu C., Ocak H., Ertunç H. M., Rulman Titreşim Analizi ile Bölgesel Hataların İncelenmesi, TOK'07 Bildiriler Kitabı, İstanbul, 5-7 Eylül 2007.

Brie D., Modelling of the Spalled Rolling Element Bearing Vibration Signal: An Overview and Some New Results; Mechanical Systems and Signal Processing 14(3), 353-369, 2000.

Çaşka S., Dokuz M. E., Ankastre Bir Kirişin Ayrık Zamanlı Titreşim Modelinin Meta-sezgisel Optimizasyon Yöntemleri Kullanılarak Elde Edilmesi. BŞEÜ Fen Bilimleri Dergisi, 9(1), 32-41, 2022.

Çaşka S., Dokuz M. E., Aydın M., İlman M. M., Yavuz Ş., System Identification and Vibration Analysis of Rotating Beam with Lattice Structures, Int. J. of 3D Printing Tech. Dig. Ind., 7(2), 322-327, 2023.

Çimen M., Bilyeli Rulman Hasarlarının Titreşim Analizi ile Tespiti ve Gemi Makinelerinde Kestirimci Bakım Uygulaması, İstanbul Teknik Üniversitesi, Fen Bilimleri Enstitüsü, Yüksek Lisans Tezi (Basılmış), 2015.

Darmo S., Bahiuddin I., Handoko P., Rizki Priatomo H., Kuncoro M., Priyambodo S., Haryanto, Fatah Rahman N., Kanosri M., Winarno A., Failure analysis of double-row tapered roller bearing outer ring used in Coal Wagon Wheelset. Eng. Fail. Anal. 135, 106153, 2022.

De Luca A., Book W.J., Robots with Flexible Elements BT - Springer Handbook of Robotics, Springer International Publishing, Cham, pp. 243-282, 2016.

Dron J.P., Rasolofondraibe L., Bolaers F., Pavan A., High Resolution Methods in Vibratory Analysis: Application to Ball Bearing Monitoring and Production Machines, International Journal of Solids and Structures 38, 4293-4313, 2001.

Ghazwani M.H., Pham V.V., Investigating Behavior of Slider–Crank Mechanisms with Bearing Failures Using Vibration Analysis Techniques, Mathematics MDPI, 12, 544, 2024.

Hemati A., Shooshtari A., Bearing Failure Analysis Using Vibration Analysis and Natural Frequency Excitation. J. Fail. Anal. Preven. 23, 1431–1437, 2023.

Jamaludin N., Mba D., Monitoring Extremely Slow Rolling Element Bearings: Part I; NDT&E International 35(6), 349-358, 2002.

Madar E., Galiki O., Klein R., Bortman J., Nickell J., Kirsch M., A New Model for Bearing Spall Size Estimation Based on Oil Debris. Eng. Fail. Anal. 134, 106011, 2022.

Mobley R.K., An Introduction to Predictive Maintenance, Van Nostrand Reinhold, New York, 1990.

Mishra L., Kumar M., Chandrawanshi M.L., Failure Analysis of Ball Bearing in Centrifugal Pump Using Envelope and Demodulation Techniques. Mater. Today: Proc. 56, 760–767, 2022.

Orhan S., Arslan H., ve Aktürk N., Titreşim Analiziyle Rulman Arızalarının Belirlenmesi, Gazi Üniv. Müh. Mim. Fak. Der., 18(2), 39-48, 2003.

Rubini R., Meneghetti U., Application of Envelope and Wavelet Transform Analyses for Diagnosis of Incipient Faults in Ball Bearings, Mechanical Systems and Signal Processing, 15(2), 287-302, 2001.

Williams T., Ribadeneira X., Billington S., Kurfess T., Rolling Element Bearing Diagnostics in Run-To-Failure Lifetime Testing; Mechanical Systems and Signal Processing, 15(5), 979-993, 2001.

Yavuz Ş., Uyar M., Malgaca L., Karagülle H., Eşdeğer Kütle-Yay-Sönüm Elemanı Kullanılan Ankastre Kompozit Bir Kirişin Titreşim Analizi, DÜMF Fen ve Mühendislik Dergisi, 20(60), 946 – 954, 2018.

Yıldırım E., Karahan M.M.F., Titreşim Analizi ile Rulmanlarda Kestirimci Bakım, C.B.Ü. Fen Bilimleri Dergisi, 11(1), 17-23, 2015.

JOURNAL of
MATERIALS and MECHATRONICS:A

e-ISSN 2717-8811
JournalMM, 2025, 6(1), 135-149
https://doi.org/10.55546/jmm.1628129

Araştırma Makalesi / Research Article

Bazı Samaryum ve Gadolinyum İzotoplarının (n,2n) Reaksiyonlarında Teorik Modellerin Tesir Kesiti Hesaplamalarına Etkilerinin İncelenmesi

Mert ŞEKERCİ[1*], Abdullah KAPLAN[2]

[1*] Süleyman Demirel Üniversitesi, Mühendislik ve Doğa Bilimleri Fakültesi, Fizik Bölümü, Isparta, Türkiye,
ORCID ID: https://orcid.org/0000-0003-0870-0506, mertsekerci@sdu.edu.tr
[2] Süleyman Demirel Üniversitesi, Mühendislik ve Doğa Bilimleri Fakültesi, Fizik Bölümü, Isparta, Türkiye,
ORCID ID: https://orcid.org/0000-0003-2990-0187, abdullahkaplan@sdu.edu.tr

Geliş/ Received: 28.01.2025; **Revize/Revised:** 22.03.2025 **Kabul / Accepted:** 31.03.2025

ÖZET: Bu çalışmada, Samaryum ve Gadolinyum elementlerinin farklı izotopları için (n,2n) reaksiyonlarının tesir kesiti hesaplamalarında denge ve denge-öncesi nükleer reaksiyon modellerinin etkilerinin incelenmesi amaçlanmıştır. Bu kapsamda, Samaryum elementinin 144, 148, 150, 152 ve 154 kütle numaralı izotopları ile Gadolinyum elementinin 155, 156, 157, 158 ve 160 kütle numaralı izotopları için (n,2n) reaksiyonlarına ait tesir kesiti hesaplamalarında TALYS ve EMPIRE isimli kodlar kullanılmıştır. TALYS kodunun 1.8 versiyonun kullanıldığı hesaplamalarda İki Bileşenli Eksiton Model ve Hauser-Feshbach Model, EMPIRE kodunun 3.2 versiyonun kullanıldığı hesaplamalarda ise PCROSS Eksiton Model ve Hauser-Feshbach Model denge ve denge-öncesi etkilerin analiz edilebilmesi için seçilmiş olan modellerdir. Elde edilen hesaplama sonuçları, EXFOR veritabanından temin edilen deneysel verilerle karşılaştırılmış ve bulgular her bir reaksiyon için grafiksel olarak görselleştirilmiştir. Çalışmanın sonuçları bir bütün olarak değerlendirildiğinde çıktıların literatürde de mevcut olan iki durumu destekleyecek nitelikte olduğu söylenebilmektedir. Bunlardan ilki deneysel çalışmaların gerçekleştirilemediği durumlarda teorik hesaplama yöntemlerinin bilimsel araştırmalar için bir alternatif olabileceği iken diğeri ise bu tarz çalışmaların hesaplamalarda kullanılan teorik modellerin gelişimine destek sağlayabileceği öngörüsüdür.

Anahtar Kelimeler: Samaryum, Gadolinyum, Tesir kesiti, TALYS, EMPIRE, EXFOR

*Sorumlu yazar / Corresponding author: mertsekerci@sdu.edu.tr
Bu makaleye atıf yapmak için /To cite this article

Şekerci, M., Kaplan, A. (2025). Bazı Samaryum ve Gadolinyum İzotoplarının (n,2n) Reaksiyonlarında Teorik Modellerin Tesir Kesiti Hesaplamalarına Etkilerinin İncelenmesi. Journal of Materials and Mechatronics: A (JournalMM), 6(1), 135-149.

Investigation of the Effects of Some Samarium and Gadolinium Isotopes on Cross Section Calculations of Theoretical Models in (n,2n) Reactions

ABSTRACT: This study aims to investigate the effects of equilibrium and pre-equilibrium nuclear reaction models on cross-section calculations for (n,2n) reactions of different isotopes of Samarium and Gadolinium elements. In this context, cross-section calculations for (n,2n) reactions of the isotopes 144, 148, 150, 152, 154 of Samarium and 155, 156, 157, 158, 160 of Gadolinium elements were performed using the TALYS and EMPIRE codes. In the calculations performed with version 1.8 of the TALYS code, the Two-Component Exciton Model and Hauser-Feshbach Model were employed, while in the calculations using version 3.2 of the EMPIRE code, the PCROSS Exciton Model and Hauser-Feshbach Model were chosen to analyze the effects of equilibrium and pre-equilibrium mechanisms. The obtained theoretical results were examined with experimental data sourced from the EXFOR database, and the findings were visualized graphically for each reaction. When the outcomes of the study are examined as a whole, it is possible to say that the outputs support two situations that are also present in the literature. The first among them is that theoretical calculation methods can be an alternative for scientific research in situations where experimental works may not possible to be carried out, while the other is the prediction that such studies can support the development of theoretical models used in calculations.

Keywords: Samarium, Gadolinium, Crosss-section, TALYS, EMPIRE, EXFOR

1. GİRİŞ

Modern dünyada enerji ihtiyacının hızla artması yüksek verimli, uzun ömürlü ve kesintisiz sürdürülebilen enerji kaynaklarına olan talebin artmasına neden olmuştur (Şekerci, 2018). Bu gelişmeler çerçevesinde nükleer güç santralleri, enerji üretiminde bu hususlarda ön plana çıkmışlardır. Uluslararası Atom Enerjisi Ajansı'nın (IAEA) Güç Reaktörü Bilgi Sistemi (Power Reactor Information System – PRIS) verilerine göre, 15 Ocak 2025 itibariyle enerji üretimi amacıyla aktif reaktör sayısı 416 iken, 23 adet durdurulmuş operasyonel reaktör ve 62 adet yapım aşamasındaki reaktör bulunmaktadır (IAEA, 2025). Nükleer reaktörlerde, kontrollü zincirleme fisyon reaksiyonlarının güvenli ve verimli bir şekilde yürütülebilmesi için reaktör kontrol çubuklarının doğru tasarımı ise tüm süreç içerisinde oldukça yüksek önem derecesine sahip bir durumdur (DOE, 2025; IAEA, 1995; IAEA, 2000; IAEA, 2007; IAEA, 2025).

Bu noktada samaryum ve gadolinyum elementleri, yüksek nötron absorpsiyon kapasiteleri nedeniyle reaktör kontrol çubuklarında yaygın olarak kullanılmalarından dolayı ön plana çıkmaktadırlar (Ashby ve Smidman, 2010; IAEA, 1995; IAEA, 1996; IAEA, 2000; IAEA, 2007; Kalcheva ve Koonen, 2007). Bu elementlerin farklı izotoplarının nükleer reaksiyon süreçlerindeki davranışlarının detaylı incelenmesi, hem teorik model doğrulamasının sağlanması hem de pratik uygulamalarda reaktör kontrol sistemlerinin güvenliğinin ve verimliliğinin artırılması açısından büyük önem taşımaktadır.

Bu motivasyonla bu çalışmada; samaryumun 144, 148, 150, 152 ve 154, gadolinyumun ise 155, 156, 157, 158 ve 160 kütle numarası taşıyan izotoplarının (n,2n) reaksiyonları için tesir kesiti hesaplamaları gerçekleştirilmiş ve bu hesaplamalarda denge ve denge-öncesi nükleer reaksiyon modellerinin etkileri analiz edilmiştir. Tesir kesiti değeri en kolay anlaşılabilecek anlatımı ile bir nükleer reaksiyonun meydana gelme olasılığı olarak tanımlanabilir ve bu değer deneysel olarak

ölçülebileceği gibi gelişmiş teorik modellerin kullanılmasıyla da hesaplanabilir. Hesaplamaların bir araştırmacı tarafından elle yapılması durumunda karşılaşılabilecek hataların ortadan kaldırılması için ise çeşitli yazılımlar oluşturulmuştur. Bu amaçla geliştirilmiş ve literatürde pek çok çalışmada da (Aydın vd., 2013; Kaplan vd., 2016; Kaplan vd., 2017; Kaplan, 2013; Özdoğan vd., 2019; Özdoğan vd., 2023; Özdoğan vd., 2024; Şekerci vd., 2019; Üncü vd., 2023) tercih edilmiş olan kodlardan en çok bilinenleri ise TALYS (Koning vd., 2023) ve EMPIRE (Herman vd., 2007) kodlarıdır.

Bu çalışmada TALYS kodunun 1.8 versiyonunda İki Bileşenli Eksiton ve Hauser-Feshbach modelleri, EMPIRE kodunun 3.2 versiyonunda ise PCROSS Eksiton ve Hauser-Feshbach modelleri, denge ve denge-öncesi süreçlerin etkilerini analiz etmek üzere kullanılmışlardır. Bu çalışmada da kullanılan bu kodlar, yani hem TALYS hem de EMIPRE kodları, literatürde pek çok çalışmada tercih edildiği görülen ve özellikle deneysel verilerin mevcut olmadığı durumlarda araştırmacılar için son derece önemli olan öngörüleri sunabilecek yetkinlikte olan araçlardır. Bu yeteneklerini ve geniş kullanım yelpazelerini göz önünde bulundurarak yapılmış ve literatürde mevcut olan pek çok çalışmada; bu programlar ve bu programların kullanıcılarına sundukları çeşitli hesaplama modelleri ile hesaplama sonuçlarına etkisi olabilecek olan parametrelerin tesir kesiti gibi önemli değerlerin hesaplanmasındaki etkilerinin araştırılması amacıyla deneysel veriler ile teorik hesaplama sonuçlarının karşılaştırmalı olarak kıyaslandığı görülmektedir (Büyükuslu, 2025; Ozdogan vd., 2025; Yiğit vd., 2024; Küçüksucu vd., 2024; Kara vd., 2024; Yiğit, 2023; Yettou vd., 2023; Kavun vd., 2022; Büyükuslu, 2019). Bu çalışmada elde edilen teorik hesaplamaların sonuçları, EXFOR (Otuka vd., 2014) veri tabanından alınan deneysel tesir kesiti verileriyle karşılaştırılarak değerlendirilmiş ve bulgular görsel olarak analiz edilebilmek amacıyla grafiksel olarak görselleştirilmiştir. Bu grafiklerde ayrıca TENDL (Sublet vd., 2016) olarak bilinen TALYS tabanlı değerlendirilmiş nükleer veri kitaplığından alınan tesir kesiti değerlerine de yer verilmiştir. Elde edilen sonuçlar, iki temel olguyu destekler niteliktedir: Birincisi, deneysel çalışmaların mümkün olmadığı durumlarda teorik modellerin bilimsel araştırmalara önemli bir alternatif sunduğudur. İkincisi ise, bu tür teorik çalışmaların, kullanılan modellerin geliştirilmesine ve daha geniş bir uygulama alanına uyarlanmasına katkı sağlayabileceğidir.

2. MATERYAL VE YÖNTEM

Bu çalışmada; samaryumun ve gadolinyumun daha önce belirtilmiş olan kütle numaralarına sahip izotoplarının (n,2n) reaksiyonlarına ait tesir kesiti hesaplamalarında, nükleer reaksiyonların teorik analizinde yaygın olarak kullanılan TALYS ve EMPIRE kodları kullanılmıştır. Bu kodlar; denge ve denge-öncesi süreçlerin analizi için farklı teorik modelleri hesaplamalara entegre edebilme özelliklerine sahiptirler ve bu sayede nükleer reaksiyonların detaylı bir şekilde incelenmesine olanak sağlarlar. Kullanılan modellerin işleyiş mekanizmaları ve teorik yapıları, bu çalışmanın temel bileşenlerini oluşturan unsurlardandır. TALYS 1.8 kodu, geniş bir enerji aralığında nükleer reaksiyonların teorik analizini yapabilen, kapsamlı bir yazılımdır (Koning vd., 2023). Kullanıcı tanımlı girdi dosyası ile çalışan TALYS kodunda mevcut yüzlerce anahtar kelime ile bir reaksiyona ait istenilen hesaplama için farklı model ve parametrelerin tetiklendiği pek çok kombinasyonun elde edilmesi mümkündür. Bunlar arasında bu çalışmada, çalışmanın motivasyonuna uygun olarak denge ve denge-öncesi reaksiyon mekanizmalarının etkilerinin incelenebilmesi amacıyla İki Bileşenli Eksiton Model ve Hauser-Feshbach Model ayrı ayrı kullanılarak tesir kesiti hesaplamaları yapılmıştır.

Eksiton modeli, nükleer reaksiyonlarda denge-öncesi süreçlerin anlaşılmasında önemli bir yere sahiptir. Eksitonlar, reaksiyon sırasında oluşan parçacık-deşik çiftlerini ifade eder ve bu çiftlerin

sayısı, enerjinin ve momentumun sistem içinde nasıl dağıldığını belirler. İki bileşenli eksiton model, nötronlar ve protonlar için ayrı ayrı enerji ve momentum dağılımlarını ele alarak, daha hassas sonuçlar elde edilmesini sağlamayı amaçlar. Bu model, özellikle yüksek enerjili reaksiyonlarda denge-öncesi süreçlerin etkilerinin doğru bir şekilde analiz edilmesi için de oldukça kullanışlıdır (Koning vd., 2007). TALYS ile gerçekleştirilen tesir kesiti hesaplamalarında kullanılan bir diğer model ise Hauser-Feshbach Modeli'dir. Bu model, bileşik çekirdek reaksiyonlarını istatistiksel olarak analiz eden bir yaklaşıma sahiptir. Reaksiyonun denge durumunda gerçekleştiğini varsayan bu model, bileşik çekirdeğin çeşitli kanallara parçacık veya gama ışını yayınımı yapma olasılıklarını da hesaplar. Nükleer seviyelerin yoğunluğu ve geçiş olasılıkları gibi parametreleri kullanan bu model, hem düşük enerji seviyelerindeki reaksiyonların hem de daha karmaşık süreçlerin doğru bir şekilde modellenmesine olanak tanıyacak yetkinliktedir (Koning vd., 2007).

Literatürde TALYS kadar popüler olan ve kullanıcıların sıklıkla tercih ettikleri, bu çalışmada da kullanılan diğer kod ise EMPIRE kodudur. Oldukça kapsamlı bir geliştirme sürecine neticesinde araştırmacıların kullanımına sunulmuş olan EMPIRE kodunun bu çalışmada kullanılan versiyonu ise 3.2'dir. EMPIRE, modüler yapısıyla nükleer reaksiyonların teorik analizi için geniş bir uygulama alanı sunar. Bu çalışmada, EMPIRE kodunda mevcut olan PCROSS Eksiton ve Hauser-Feshbach modelleri tetiklenerek tesir kesiti hesaplamaları incelenen her bir reaksiyon için birbirlerinden bağımsız olacak şekilde tekrarlı adımlarda tamamlanmıştır. PCROSS, denge-öncesi süreçlerin modellenmesinde kullanılan bir eksiton modelidir. Bu model; eksitonların oluşum ve evrim süreçlerini izlerken, aynı zamanda kompleks parçacık yayınımını da dikkate almaktadır. Bu bağlamda model, eksitonların dinamik davranışlarını detaylı bir şekilde ele alan bir model olarak bilinir ve ayrıca bu ve diğer özellikleri sayesinde yüksek enerjili reaksiyonlarda enerjinin nasıl dağıldığını anlamak için de tercih edilir (Herman vd., 2007). Hauser-Feshbach Modeli ise bileşik çekirdek reaksiyonlarının istatistiksel analizi için temel bir araçtır. Enerji seviyelerinin yoğunluğu ve geçiş olasılıkları gibi parametreleri kullanarak farklı yayınım kanallarının olasılıklarını hesaplayan bu model, hem düşük hem de yüksek enerjili süreçlerde geniş bir uygulama alanına sahiptir (Herman vd., 2007).

Hem TALYS hem de EMPIRE kodları birçok parametre ve modelin kullanıcı tarafından tanımlanarak hesaplamaların bu parametre ve model ve parametrelerin etkileri ile gerçekleştirilmesini sağlayabilecek yetkinliktedirler. Bu çalışmanın motivasyonunda ise incelenmek üzere seçilen reaksiyonlarda TALYS ve EMPIRE kodlarındaki denge ve denge-öncesi reaksiyon modellerinin etkilerinin tesir kesiti hesaplamaları üzerine olan etkilerinin incelenmesi amaçlanmıştır. Bu motivasyona uygun olarak hesaplamalarda TALYS ve EMPIRE kodlarının mevcut seçenekler arasından kullanıcının tercihine izin verdiği pek çok parametre her iki kodun da kendi ön tanımlı varsayılan değerinde tutularak kullanılmıştır. Bu sayede kodların geniş parametre seçenekleri arasından sadece bu çalışma motivasyonuna uygun parametrelerin değiştirilmesi durumunda hesaplamaların nasıl etkileneceğinin incelenmesi sağlanabilmiştir. Çalışmanın motivasyonuna uygun olarak incelenmek üzere seçilmiş reaksiyonlarda TALYS ve EMPIRE kodları kullanılarak yapılan hesaplamalar sonucunda elde edilen tesir kesiti değerleri hem birbirleri ile hem de deneysel veriler ile karşılaştırılmıştır. Buradaki amaçlardan bir tanesi, incelenen reaksiyon özelinde denge ve denge-öncesi reaksiyon mekanizmalarına ait modellerden hangisinin deneysel veriler ile daha uyumlu sonuçlar ortaya koyduğunu anlayabilmek iken bir diğer amaç da TALYS ve EMPIRE kodları kullanılması durumunda sonuçlarda nasıl farklılaşmalar olacağını inceleyebilmektedir. Hesaplama sonuçları ve deneysel veriler arasındaki ilişkinin daha rahat gözlemlenerek yorumlanabilmesi

amacıyla her bir incelenen reaksiyon için hesaplama sonuçları ve deneysel veriler birlikte olacak şekilde grafikler oluşturulmuştur.

TALYS ve EMPIRE kodları kullanılarak yapılan hesaplamalar sonucunda her bir reaksiyon için elde edilen tesir kesiti değerleri, ilgili reaksiyona ait EXFOR'dan temin edilmiş deneysel veriler ve TALYS tabanlı değerlendirilmiş veri tabanı olan TENDL'dan alınmış hesaplama verileri ile birlikte grafikleştirilmiştir. Bu aşamadan önce hesaplama işlemlerinde dikkat edilen bir hususun burada açıklanması yerinde olacaktır. İncelenen her bir reaksiyon için EXFOR veri tabanı kontrol edilerek deneysel verilerin mevcudiyeti görüldükten sonra gerçekleştirilen hesaplama işlemlerinde kullanılan enerji değerleri, deneysel verilerdeki enerji değerleri ile aynı olacak şekilde seçilmiştir. Bu durum; TENDL veri tabanından ilgili reaksiyona ait tesir kesiti sonuçlarına erişim aşamasında da geçerli olmuştur. Bu sayede, incelenen her bir reaksiyon için doğru kıyaslama yapılabilecek uygun enerji aralığı kendiliğinden seçilmiştir. Bu durum aynı zamanda kıyaslamada bütüncül bir yapı oluşturarak okuyucuların daha rahat bir şekilde yorum yapabilmelerine olanak sağlamayı amaçlamıştır. Ayrıca bu amaca destek olacak şekilde oluşturulan tüm grafiklerde yatay eksende enerji değerleri, dikey eksende ise tesir kesiti verileri yerleşecek şekilde sistematik bir gösterim yapılmıştır.

3. BULGULAR VE TARTIŞMA

Denge ve denge-öncesi nükleer reaksiyon mekanizmalarının incelenebilmesine olanak sağlayacak yapıda geliştirilmiş olan nükleer reaksiyon modellerini içeren TALYS ve EMPIRE kodları ile ^{144,148,150,152,154}Sm ve ^{155,156,157,158,160}Gd izotopların (n,2n) reaksiyonlarında tesir kesiti hesaplama sonuçlarının EXFOR'dan temin edilmiş olan deneysel sonuçlar ve TENDL'dan edinilen hesaplama verileri ile kıyaslanmasının amaçlandığı bu çalışmada elde edilen bulgular bu bölümde gösterilmiştir. Bulguların daha kolay şekilde yorumlanabilmesi amacıyla incelenen her bir reaksiyon için x-ekseninde enerji ve y-ekseninde tesir kesiti değeri olacak şekilde bulgular grafik olarak sunulmuştur.

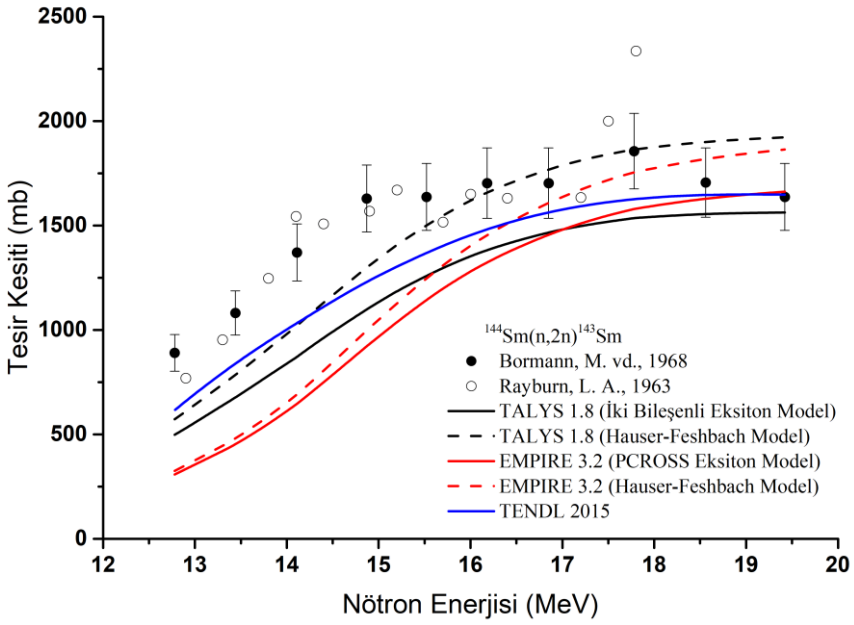

Şekil 1. ^{144}Sm(n,2n)^{143}Sm reaksiyonu için hesaplama sonuçları, deneysel veriler ve TENDL verileri

Bu çalışmada incelenen ilk reaksiyon olan $^{144}Sm(n,2n)^{143}Sm$ reaksiyonu kapsamında yapılan hesaplama işlemlerinin sonuçları ve bu sonuçların deneysel verilerle kıyaslanması Şekil 1'de gösterilmiştir. Bu reaksiyon özelinde incelenen tüm enerji aralığı göz önünde bulundurulursa modellerin kullanılması ile elde edilen hesaplama sonuçlarının birbirleri ile benzer bir dağılım sergiledikleri görülmektedir. Bunun yanı sıra, hesaplamalarda kullanılan modellerin ürettikleri sonuçlar arasında diğerlerine nazaran daha başarılı olanının 15.5 MeV'den büyük enerji değerlerinde deneysel sonuçlara daha yakın değerlerde sonuçların da elde edildiği TALYS 1.8 kodunun Hauser–Feshbach modeli olduğu görülmüştür.

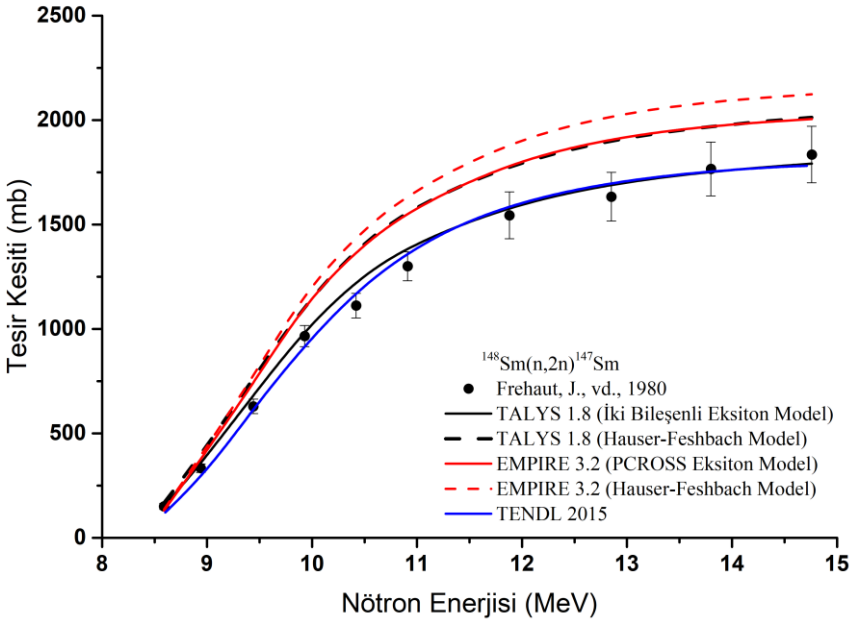

Şekil 2. $^{148}Sm(n,2n)^{147}Sm$ reaksiyonu için hesaplama sonuçları, deneysel veriler ve TENDL verileri

Literatürden temin edilmiş olan deneysel çalışmalara ait tesir kesiti verileri ile diğer modellere nazaran daha uyumlu sonuçlar veren modelin TALYS 1.8 kodunun İki Bileşenli Eksiton Modeli olan hesaplama sonuçlarının elde edildiği $^{148}Sm(n,2n)^{147}Sm$ reaksiyonuna ait grafik, Şekil 2'de sunulmuştur. Şekilden kolaylıkla görülebilen bir diğer sonuç ise, nötron gelme enerjisinin yaklaşık olarak 10.5 MeV'den büyük olduğu durumlarda TALYS İki Bileşenli Eksiton Model kullanılarak elde edilen tesir kesiti hesaplama sonuçları ile TENDL verileri arasındaki farklılığının ortadan kalkmaya başlaması ve bu değerden sonraki enerji değerlerinde neredeyse aynı tesir kesiti değerlerinde sonuçlar elde edilmiş olmasıdır.

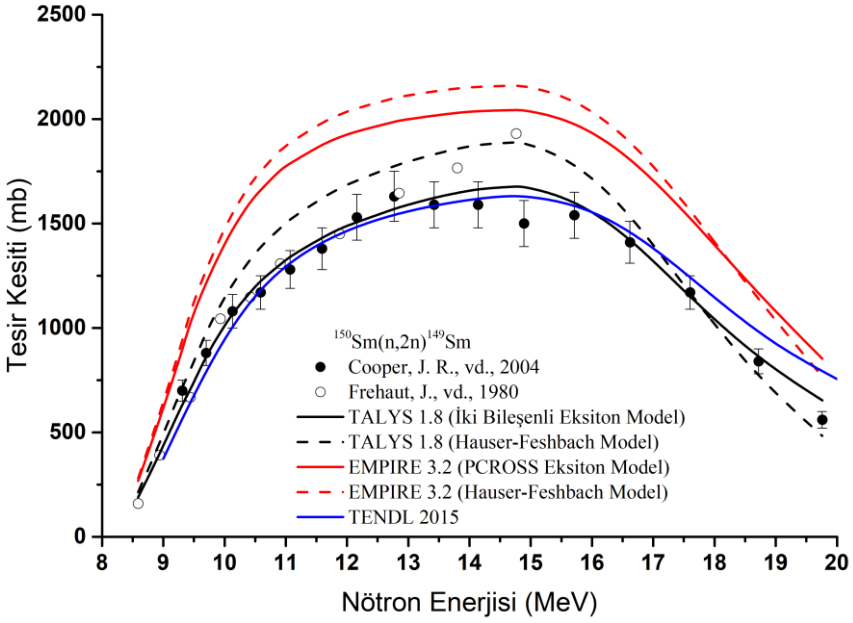

Şekil 3. $^{150}Sm(n,2n)^{149}Sm$ reaksiyonu için hesaplama sonuçları, deneysel veriler ve TENDL verileri

$^{150}Sm(n,2n)^{149}Sm$'ye ait sonuçlar Şekil 3'de gösterilmiştir. Literatürdeki deneysel veriler ile aynı olacak şekilde seçilen bu reaksiyonda incelenen enerji aralığında neredeyse tüm deneysel tesit kesiti sonuçlarını yakalayacak kadar uyumlu tesir kesiti hesaplaması yapabilen model TALYS 1.8 kodunun İki Bileşenli Eksiton Modeli olarak öne çıkmaktadır. Bu duruma ek olarak, hesaplamaların gerçekleştirildiği her iki kodda kullanılan her iki modelin de deneysel verilerinkine benzer geometrik yapılar oluşturabildiğinden rahatlıkla bahsedilebilir. Bu hususta gözden kaçmayan önemli bir durum ise; aynı enerji değerleri için EMPIRE kodu kullanılarak yapılan hesaplamalarda elde edilen sonuçların, hem deneysel verilerden hem de TALYS kodu kullanılarak elde edilen hesaplamalarda daha yüksek değerlerde tesir kesiti sonuçları vermiş olmasıdır.

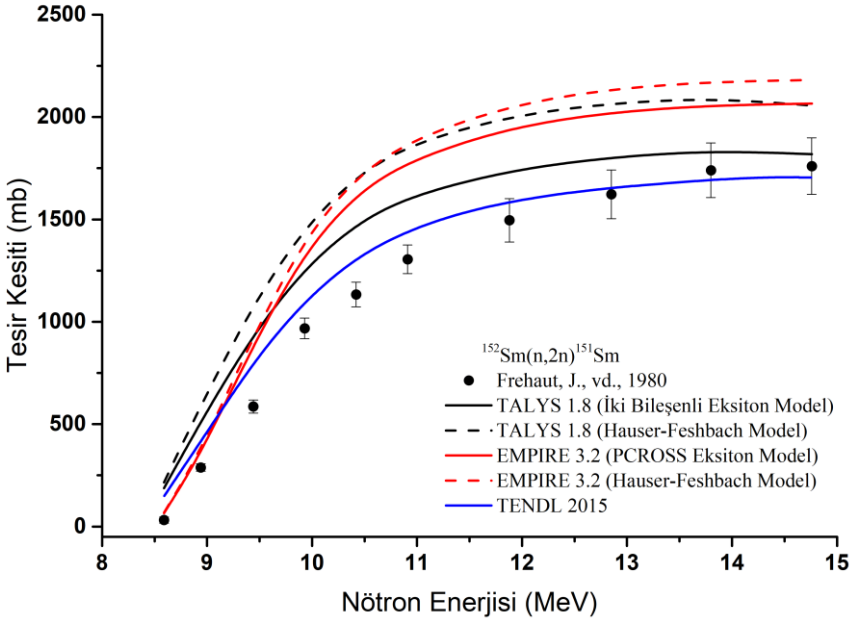

Şekil 4. $^{152}Sm(n,2n)^{151}Sm$ reaksiyonu için hesaplama sonuçları, deneysel veriler ve TENDL verileri

Şekil 4, $^{152}Sm(n,2n)^{151}Sm$ reaksiyonuna ait sonuçların gösterildiği grafiği içermektedir. Şekilden kolaylıkla anlaşılabileceği üzere deneysel veriler ile modellerin kullanıldığı hesaplama sonuçları tam olarak uyuşmamakta ancak hesaplama sonuçları deneysel verilerin oluşturdukları dağılıma benzer bir yapı sergilemektedirler. Bu bağlamda Şekil 4'ün incelenmesi ile deneysel veriler ile diğerlerine kıyasla daha uyumlu olabilecek hesaplama sonuçları üreten modelin TALYS 1.8'den İki Bileşenli Eksiton Model olduğu kanısına varılabilmektedir. $^{152}Sm(n,2n)^{151}Sm$ reaksiyonu sonuçlarının dikkat çekici bir diğer durumu ise, TENDL verilerinin deneysel verilere hem TALYS hem de EMPIRE kodu ile yapılan hesaplama sonuçlarından daha uyumlu olarak elde edilmiş olmasıdır.

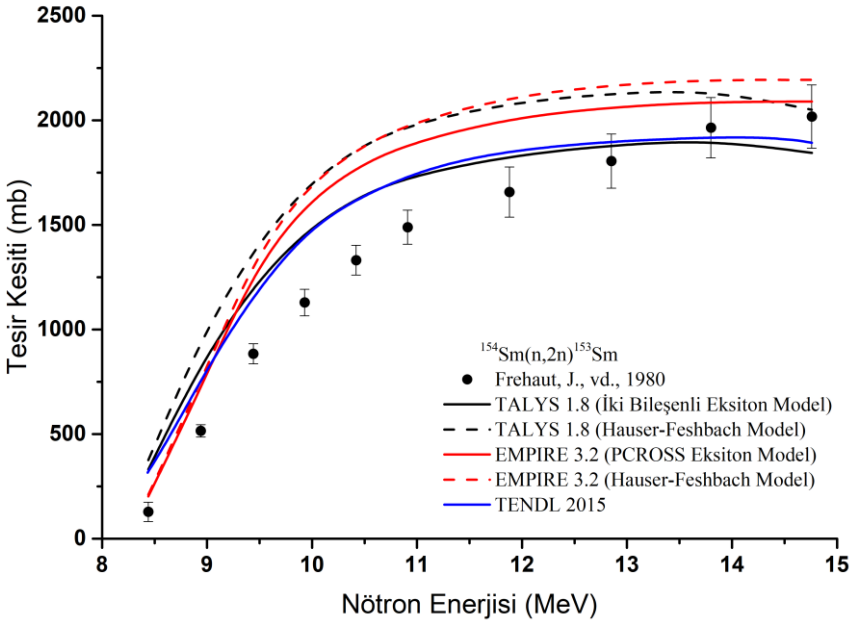

Şekil 5. $^{154}Sm(n,2n)^{153}Sm$ reaksiyonu için hesaplama sonuçları, deneysel veriler ve TENDL verileri

Şekil 5 ile $^{154}Sm(n,2n)^{153}Sm$ reaksiyonu kapsamında yapılan hesaplama sonuçları neticesinde elde edilen tesir kesiti sonuçları ile literatürde mevcut deneysel veriler birliktegrafikleştirilerek sonuçların görsel olarak analiz edilebilmesi amaçlanmıştır. Şekil 5'den kolaylıkla anlaşılabileceği gibi, hem denge hem de denge-öncesi modeller kullanılarak elde edilen hesaplama sonuçlarının incelenen aynı enerji değeri için birbirlerinden farklı değerlerde oldukları görüldüğü halde, tüm enerji aralığının bir bütün olarak değerlendirilmesi ile genel olarak deneysel veriler ile uyumlu bir yapı oluşturabildikleri söylenebilir. Bu reaksiyon için yapılan hesaplamalar sonucunda diğer modeller arasından deneysel veriler ile daha uyumlu sonuçları üreten modelin TALYS 1.8 İki Bileşenli Eksiton Model olduğu görülmektedir. Bununla birlikte bu sonuçların TENDL veriler ile de neredeyse aynı değerlerde olduğu söylenebilir.

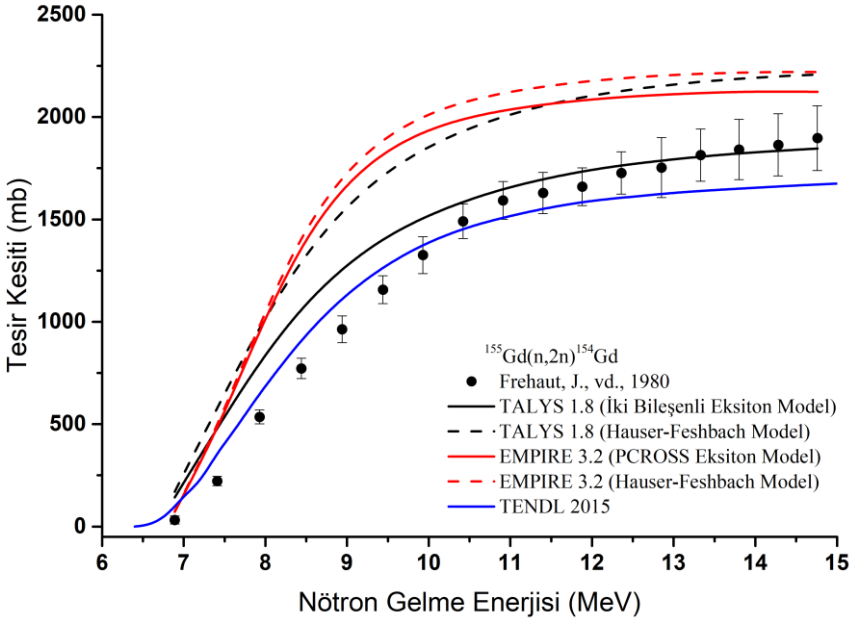

Şekil 6. ^{155}Gd(n,2n)^{154}Gd reaksiyonu için hesaplama sonuçları, deneysel veriler ve TENDL verileri

^{155}Gd izotopu için (n,2n) reaksiyonuna ait karşılaştırmalar Şekil 6 ile gösterilmiştir. Bu reaksiyon için yapılan hesaplamaların sonuçları ve deneysel verilerin kıyaslanması bir bütün olarak düşünüldüğünde; deneysel veriler ile diğerlerine oranla daha uyumlu sonuçlar üreten kod ve model olarak TALYS kodu ve İki Bileşenli Eksiton Model işaret edilebilir. Öte yandan, deneysel verilerin nötron gelme enerjisine göre göstermiş olduğu tesir kesiti hesaplamasındaki değişimin diğer modeller tarafından da benzer bir yapı oluşturacak şekilde elde edildiği görülmüş ancak, TALYS İki Bileşenli Eksiton Model tarafından üretilmiş olan hesaplama sonuçlarından daha yüksek tesir kesiti hesaplama sonuçları ürettikleri anlaşılmıştır. TALYS İki Bileşenli Eksiton Model kullanılarak elde edilen tesir kesiti hesaplama sonuçlarının özellikle 9–12 MeV aralığındaki nötron gelme enerjisi bölgesinde deneysel veriler oldukça uyumlu oldukları, 12 MeV sonrasındaki bölgede ise deneysel veriler ile neredeyse aynı sonuçlarda oldukları dikkat çekmektedir.

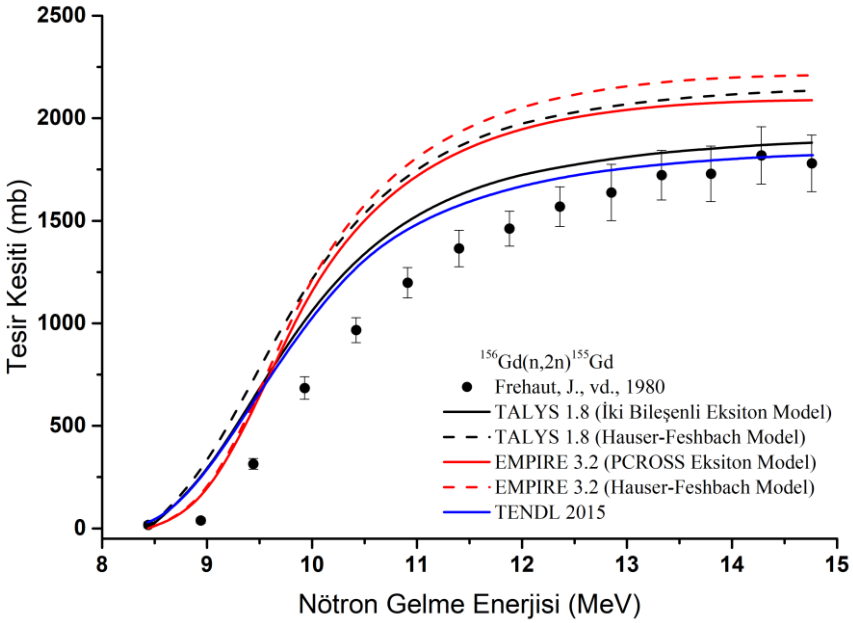

Şekil 7. ^{156}Gd(n,2n)^{155}Gd reaksiyonu için hesaplama sonuçları, deneysel veriler ve TENDL verileri

Bu çalışmada incelenmek üzere seçilmiş olan bir diğer gadolinyum izotopu olan ^{156}Gd için (n,2n) reaksiyonu tesir kesiti hesaplamalarının sonuçları Şekil 7'de gösterilmiştir. Bu reaksiyonda da maksimum nötron gelme enerjisi 15 MeV'dir ve bu reaksiyon için de literatürde mevcut deneysel veri aralığı baz alınarak hesaplamalar yapılmıştır. Bu hesaplamalar neticesinde deneysel veriler ile en uyumlu hesaplama sonuçlarının TALYS 1.8 kodunun İki Bileşenli Eksiton Model kullanılması durumunda elde edildiği görülmüştür. Öte yandan; bu reaksiyonda bu model ile eşlde edilen hesaplama sonuçlarının deneysel verileri bir önceki reaksiyon olan ^{155}Gd(n,2n)^{154}Gd reaksiyonuna göre daha az miktarda yakalayabildiği de görülmektedir. Bu duruma rağmen, tüm enerji aralığı bir bütün olarak değerlendirildiğinde modeller kullanılarak elde edilen tesir kesiti hesaplama sonuçlarının deneysel verilerin oluşturduğuna benzer bir yapı sergileyebildikleri de görülmektedir.

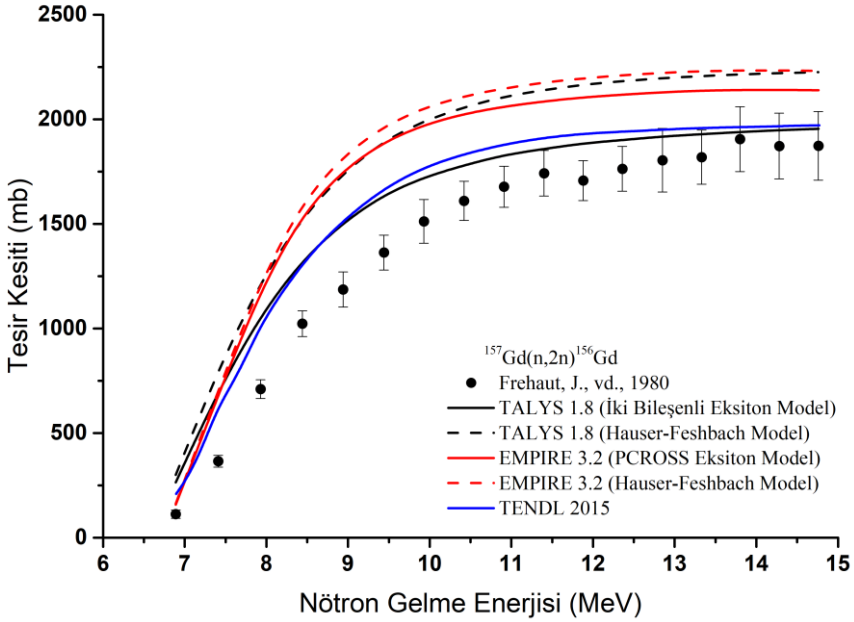

Şekil 8. ^{157}Gd(n,2n)^{156}Gd reaksiyonu için hesaplama sonuçları, deneysel veriler ve TENDL verileri

Şekil 8, ^{157}Gd(n,2n)^{156}Gd reaksiyonuna ait hesaplamaların gösterildiği şekildir. Bu reaksiyona ait hesaplamalar sonucunda, tüm modellerin ürettikleri sonuçların deneysel verilerle uyumlu bir geometrik şekil ortaya çıkarmış olduğu görülmektedir. Öte yandan tüm hesaplamalar içinde tüm enerji bölgelerinde diğer modellere kıyasla daha başarılı hesaplama sonuçları veren modelin TALYS 1.8 kodunun İki Bileşenli Eksiton Modeli olduğu da rahatlıkla Şekil 8'den görülmektedir. TENDL verilerinin de, hem deneysel veriler hem de TALYS İki Bileşenli Eksiton Model hesaplamaları ile uyum içinde olduğu görülmektedir.

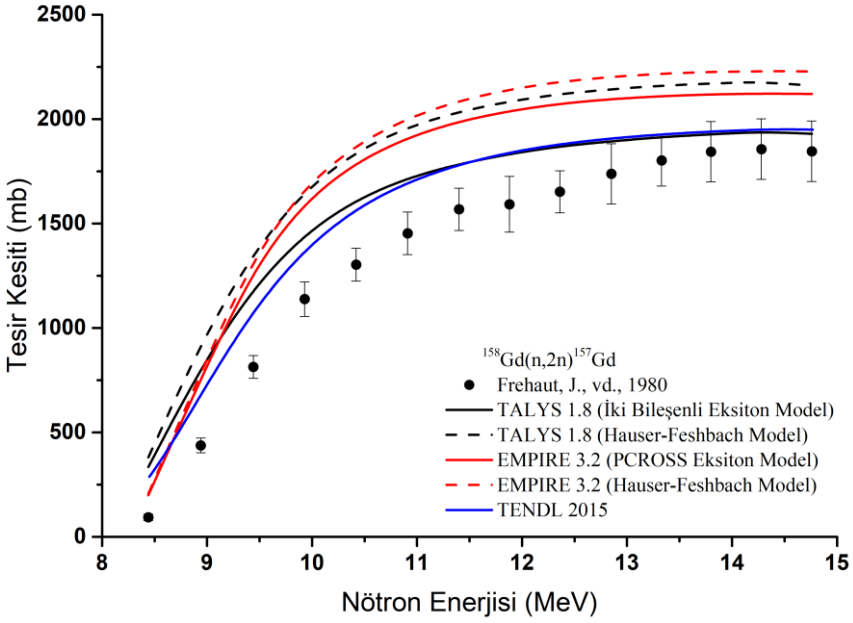

Şekil 9. ^{158}Gd(n,2n)^{157}Gd reaksiyonu için hesaplama sonuçları, deneysel veriler ve TENDL verileri

^{158}Gd(n,2n)^{157}Gd reaksiyonuna ait sonuçlar Şekil 9'da sunulmuştur. Bu çalışma kapsamında incelenmiş olup şimdiye kadar sonuçlarından bahsedilen diğer gadolinyum izotoplarına ait (n,2n) reaksiyonlarında olduğu gibi, ^{158}Gd(n,2n)^{157}Gd reaksiyonunda da deneysel veriler ile diğer modellerin kullanılması durumunda elde edilen sonuçlardan daha uyumlu hesaplama sonuçları üretebilmiş olan model TALYS kodunun İki Bileşenli Eksiton Modeli olmuştur. Diğer modellerin kullanılması ile elde edilmiş olan hesaplama sonuçlarının ise, özellikle artan enerji değerleri ile birlikte tesir kesiti sonuçlarının değişim eğilimi göz önünde bulundurulduğunda, bundan önceki gadolinyum izotopları için yapılan hesaplama sonuçlarındakine benzer bir düzende elde edildiği de açıkça görülebilmektedir.

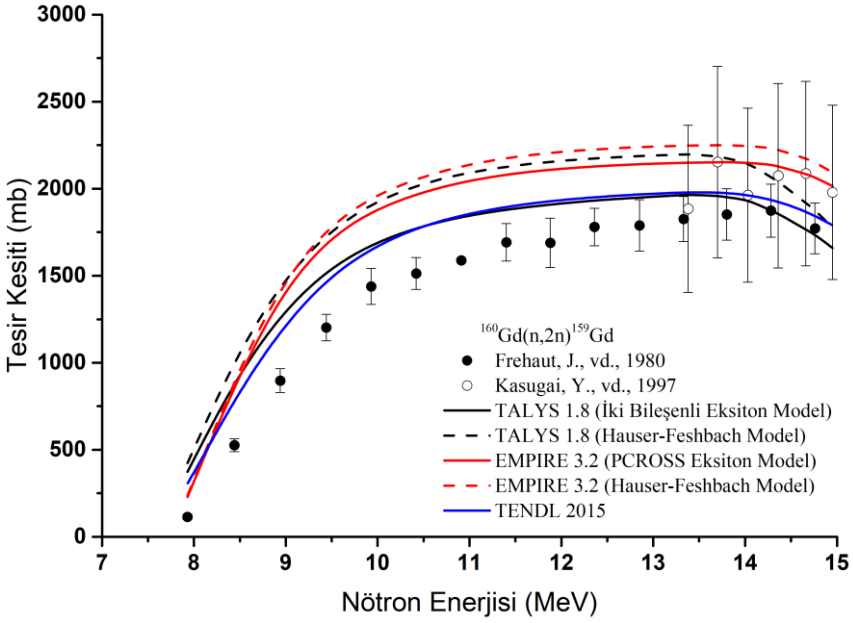

Şekil 10. ^{160}Gd(n,2n)^{159}Gd reaksiyonu için hesaplama sonuçları, deneysel veriler ve TENDL verileri

Gadolinyumun nötron girişli reaksiyonlarda incelenen son izotopu olan ^{160}Gd için gerçekleştirilen (n,2n) reaksiyonuna ait hesaplamaların deneysel veriler ile karşılaştırmaları Şekil 10'da verilmiştir. Bu reaksiyonda bu izotop için yapılan hesaplamaların sonuçlarının bir bütün olarak değerlendirilmesi ile tesir kesiti hesaplamalarının gerçekleştirildiği modeller arasında deneysel veriler ile diğerlerine göre daha uyumlu sonuçları veren modelin TALYS kodunun İki Bileşenli Eksiton Modeli olduğu rahatlıkla söylenebilir. Bu çalışmada incelenen diğer gadolinyum izotopları için yapılan (n,2n) reaksiyon hesaplamaları arasında TENDL verileri ile en uyumlu sonuçlarının bu izotop için olduğu da görülmektedir.

4. SONUÇ

Bu çalışmada, samaryum ve gadolinyum elementlerinin 144,148,150,152,154Sm ve 155,156,157,158,160Gd izotoplarına ait (n,2n) reaksiyonlarının tesir kesiti hesaplamaları, TALYS ve EMPIRE kodları kullanılarak gerçekleştirilmiştir. Bu süreçte bu kodların kullanıcılara kullanım imkânı sunduğu farklı modeller ile denge ve denge-öncesi süreçlere ait etkilerin de incelenmesi amaçlanmıştır. Teorik hesaplama sonuçları, EXFOR veri tabanından alınan deneysel veriler ve TENDL veri tabanındaki hesaplamalı metotlarla elde edilmiş tesir kesiti değerleri ile karşılaştırılarak değerlendirilmiştir.

Elde edilen bulgular, teorik modellerin kullanıldığı hesaplamalarla üretilmiş tesir kesiti değerlerinin deneysel verilerle genellikle uyumlu olacak şekilde elde edildiği sonucunu ortaya koymaktadır. Özellikle TALYS kodunun İki Bileşenli Eksiton Modeli, bu çalışmada incelenen birçok reaksiyon için deneysel verilere en yakın sonuçları sağlayan model olmuştur. Bu sonuç sayesinde bu modelin, bu çalışmada incelenen spesifik enerji aralığındaki reaksiyonlarda denge-öncesi süreçleri doğru bir şekilde temsil edebildiği yorumu yapılabilir. Benzer şekilde, Hauser-Feshbach modeli de bileşik çekirdek reaksiyonlarının analizi için güvenilir sonuçlar üretmiştir. EMPIRE kodu ile yapılan hesaplamalar da genel olarak deneysel verilerle uyumlu bir eğilim gözlemlenmiş, ancak bazı durumlarda TALYS koduna kıyasla tesir kesiti hesaplamalarının sonuçlarını daha yüksek değerlerde olacak şekilde ürettiği görülmüştür. Bu durum, farklı modellerin ve kodların teorik hesaplamalarda nasıl farklılıklar yaratabileceğini de açıkça göstermektedir.

Çalışmanın sonuçları; teorik hesaplama yöntemlerinin, deneysel çalışmaların mümkün olmadığı durumlarda nükleer reaksiyonların anlaşılmasında önemli bir alternatif sunduğunu ortaya koymaktadır. Ayrıca; bu tür çalışmaların, kullanılan modellerin geliştirilmesine ve daha geniş bir uygulama alanına uyarlanmasına katkı sağlama potansiyeline sahip olduğu da öngörülebilecek bir diğer sonuçtur. Öte yandan, özellikle nükleer reaktör kontrol çubuklarında kullanılan samaryum ve gadolinyum gibi elementlerin izotoplarının nükleer reaksiyon süreçlerindeki davranışlarının detaylı bir şekilde incelenmesi, hem teorik hem de pratik açıdan önemli sonuçlar doğurabilecek niteliktedir.

Sonuç olarak; bu çalışma, nükleer reaksiyonların teorik modelleme ve hesaplama araçları ile detaylı bir şekilde analiz edilebileceğini ve bu analizlerin deneysel verilerle desteklenerek bilimsel araştırmalara önemli katkılar sağlayabileceğini gösteren önemli bir çalışmadır. Bu tür çalışmalar, nükleer bilim ve teknoloji alanında gelecekteki araştırmalar için güçlü bir temel oluşturmakta ve enerji üretimi, medikal uygulamalar ve diğer endüstriyel alanlarda katkı sağlayabilecek çalışmalara zemin hazırlayabilecek niteliktedir.

5. TEŞEKKÜR

Bu çalışmanın bağlantılı olduğu Doktora tezi Süleyman Demirel Üniversitesi Bilimsel Araştırma Projeleri Koordinasyon Birimi tarafından 4599-D2-16 kodlu proje ile desteklenmiştir.

6. ÇIKAR ÇATIŞMASI

Yazarlar, bilinen herhangi bir çıkar çatışması veya herhangi bir kurum/kuruluş ya da kişi ile ortak çıkar bulunmadığını onaylamaktadırlar.

7. YAZAR KATKISI

Bu çalışmada Mert ŞEKERCİ çalışmanın kavramsal ve tasarım süreçlerinin belirlenmesi, çalışmanın kavramsal ve tasarım süreçlerinin yönetimi, veri toplama, veri analizi ve yorumlama, makale taslağının oluşturulması, son onay ve tam sorumluluk konusunda, Abdullah KAPLAN çalışmanın kavramsal ve tasarım süreçlerinin belirlenmesi, çalışmanın kavramsal ve tasarım süreçlerinin yönetimi, veri analizi ve yorumlama, fikirsel içeriğin eleştirel incelemesi, son onay ve tam sorumluluk konusunda katkı sağlamıştır.

8. KAYNAKLAR

Ashby M. F., Smidman M., Materials for Nuclear Power Systems, Granta Material Inspiration, Version 1.1, 20 s, 2010.

Aydın A., Sarpün İ. H., Kaplan A., Tel E., Calculations of Double Differential Deuteron Emission Cross Sections at 62 MeV Proton Induced Reactions, Journal of Fusion Energy, 32(3), 378-381, 2013.

Büyükuslu H., Dispersive optical-model potential parameters for neutron scattering on 197Au up to 200 MeV, Nuclear Physics A, 1055, 123004, 2025.

Büyükuslu H., Parametrization study for the estimation of light particles (p, d, 3He, α) induced total reaction cross sections of target mass greater than 9 within the energy range of 10–200 MeV, Radiation Physics and Chemistry, 165, 108431, 2019.

DOE, 2025. DOE Fundamentals Handbook, Nuclear Physics and Reactor Theory Volume 2 of 2, https://www.standards.doe.gov/standards-documents/1000/1019-bhdbk-1993-v2 (Erişim Tarihi: 15.01.2025).

Herman M., Capote R., Carlson B. V., Oblozinsky P., Sin M., Trkov A., Wienke H., EMPIRE: Nuclear Reaction Model Code System for Data Evaluation, Nucl. Data Sheets, 108, 2655-2715, 2007.

IAEA, 1995. Advances in Control Assembly Materials for Water Reactors, IAEATECDOC-813, http://www.iaea.org/inis/collection/NCLCollectionStore/_Public/26/077/26077302.pdf (Erişim Tarihi:20.01.2025).

IAEA, 1996. Absorber Materials, Control Rods and Designs of Shutdown Systems for Advanced Liquid Metal Fast Reactors, IAEATECDOC-884, http://www.iaea.org/inis/collection/NCLCollectionStore/_Public/27/072/27072854.pdf (Erişim Tarihi:20.01.2025).

IAEA, 2000. Control assembly materials for water reactors: Experience, performance and perspectives, IAEATECDOC-1132, http://www-pub.iaea.org/MTCD/Publications/PDF/te_1132_prn.pdf (Erişim Tarihi:20.01.2025).

IAEA, 2007. Nuclear Power Plant Design Characteristics, IAEATECDOC-1544, http://www-pub.iaea.org/MTCD/Publications/PDF/te_1544_web.pdf (Erişim Tarihi:20.01.2025).

IAEA, 2025. Power Reactor Information System (PRIS), https://www.iaea.org/pris/ (Erişim Tarihi:16.01.2025).

Kalcheva S., Koonen E., Optimized Control Rods of the BR2 Reactor, Open Report SCK-CEN-BLG-1054, SCK-CEN, 139s, 2007.

Kaplan A., Investigation of Neutron Production Cross Sections of the Structural Fusion Material 181Ta for xn Reactions up to 150 MeV Energy, Journal of Fusion Energy, 32(3), 382-388, 2013.

Kaplan A., Şekerci M., Çapalı V., Özdoğan H., Computations of a xn Reaction Cross Section for 107 109Ag Coated Materials with Possible Application in Accelerators and Nuclear Systems, Journal of Fusion Energy, 35(4), 715-723, 2016.

Kaplan A., Şekerci M., Çapalı V., Özdoğan H., Photon Induced Reaction Cross-Section Calculations of Several Structural Fusion Materials, Journal of Fusion Energy, 36(6), 213-217, 2017

Kara A., Mammadzada E., Analyzing neutron emission cross sections for 22.2 MeV proton-induced reactions on 58Ni and 52Cr, Applied Radiation and Isotopes, 206, 111242, 2024.

Kavun Y., Vashi V., Makwana R., Investigation of (d, 3n) reaction cross section using theoretical nuclear codes calculations on some nuclear materials, Applied Radiation and Isotopes, 189, 110426, 2022.

Koning A. J, Hilaire S., Goriely S., TALYS: modeling of nuclear reactions, Eur. Phys. J. A 59, 131, 2023.

Koning A. J., Hilaire S., Duijvestijn M. C. TALYS-1.0: A nuclear reaction program. Proceedings of the International Conference on Nuclear Data for Science and Technology, 211-214, 2007.

Küçüksucu S., Yiğit M., Paar N., Isotopic dependence of (n,α) reaction cross sections for Fe and Sn nuclei, Nuclear Physics A, 1041, 122779, 2024.

Otuka N., Dupont E., Semkova V., Pritychenko B., Blokhin A. I., Aikawa M., Babykina S., Bossant M., Chen, G., Dunaeva S., Forrest R. A., Fukahori T., Furutachi N., GanesanS., Ge, Z., Gritzay O.O., Herman M., Hlavač S., Katō K., Lalremruata B., Lee Y. O., Makinaga A., Matsumoto K., Mikhaylyukova M., Pikulina G., Pronyaev V. G., Saxena A., Schwerer O., Simakov S. P., Soppera N., Suzuki R., Takács S., Tao X., Taova S., Tárkányi F., Varlamov V. V., Wang J., Yang S. C., Zerkin V., Zhuang Y., Towards a more complete and accurate experimental nuclear reaction data library (EXFOR): International collaboration between nuclear reaction data centres (NRDC), Nuclear Data Sheets, 120, 272, 2014.

Ozdogan H., Uncu Y. A., Sekerci M., Kaplan A., Calculation of double differential neutron cross-sections for the 115In(a,xn) reaction, Applied Radiation and Isotopes, 219, 111713, 2025.

Özdoğan H., Şekerci M., Kaplan A., Investigation of gamma strength functions and level density models effects on photon induced reaction cross–section calculations for the fusion structural materials 46,50Ti, 51V, 58Ni and 63Cu, Applied Radiation and Isotopes, 6-10, 2019.

Özdoğan H., Üncü Y. A., Şekerci M., Kaplan A., Calculation of double differential neutron cross-sections of 56Fe and 90Zr isotopes, Applied Radiation and Isotopes, 199, 110922, 2023.

Özdoğan H., Üncü Y. A., Şekerci M., Kaplan A., Investigation of 209Bi (α,2n)211At reaction route for the production of α-emitter 211At, The European Physical Journal Plus, 139(6), 511, 2024.

Sublet J. Ch., Koning A. J., Rochman D., Fleming M., Gilbert M., TENDL-2015: Delivering Both Completeness and Robustness, Advances in Nuclear Nonproliferation Technology and Policy Conference, Sept. 25-30, Santa Fe, NM, USA, 2016.

Şekerci M., Nükleer Reaktör Kontrol Çubuklarında Kullanılan Bazı Malzemeler için Farklı Reaksiyon ve Enerjilerde Parçacık Yayınlanma Spektrumu, Durdurma Gücü, Giricilik Mesafesi ve Tesir Kesiti Hesaplamaları, Süleyman Demirel Üniversitesi, Fen Bilimleri Üniversitesi, Doktora Tezi (Basılmış), 2018.

Şekerci M., Özdoğan H., Kaplan A., Investigation on the Different Production Routes of 67Ga Radioisotope by Using Different Level Density Models, Moscow University Physics Bulletin, 74(3), 277-281, 2019.

Üncü Y. A., Özdoğan H., Şekerci M., Kaplan A., Investigation of the production routes of Palladium-103 and Iodine-125 radioisotopes, Radiation Physics and Chemistry, 2023.

Yettou L., Belgaid M., Belouadah N., Preequilibrium models for 58Ni (n, xp) and 60Ni (n, xp) reactions in neutrons at 8, 9, 9.4, 11 and 14.8 MeV using the EMPIRE and TALYS codes, Applied Radiation and Isotopes, 193, 110643, 2023.

Yiğit M., (n,2n) cross section calculations for tungsten, tantalum and osmium nuclei, Applied Radiation and Isotopes, 201, 110999, 2023.

Yiğit M., Kara A., Yilmaz A., A study on interactions of 14.7-MeV protons and 3.6-MeV alphas in ^{93}Nb target, Fusion Science and Technology, 80(2), 156-165, 2024.

JOURNAL of
MATERIALS and MECHATRONICS:A

e-ISSN 2717-8811
JournalMM, 2025, 6(1), 150-169
https://doi.org/10.55546/jmm.1660142

Araştırma Makalesi / Research Article

Comprehensive Comparative Analysis of GWO and Its Variants for Solving Mechanical Optimization Problems

Nermin ÖZCAN*

* Iskenderun Technical University, Faculty of Engineering and Natural Sciences, Department of Biomedical Engineering, Hatay, Türkiye
ORCID ID: https://orcid.org/0000-0001-5327-9090, nermin.ozcan@iste.edu.tr

Geliş/ Received: 18.03.2025; **Revize/Revised:** 22.04.2025 **Kabul / Accepted:** 06.05.2025

ABSTRACT: The intricacy of decision variables, multiple objectives, and nonlinear restrictions make it difficult to find suitable solutions for mechanical design problems. An alternative approach to these difficult challenges, the Grey Wolf Optimizer (GWO) is recognized for its ease of use, flexibility, scalability, and unique balance between exploration and exploitation. Like every stochastic approach, GWO has drawbacks, though, and numerous enhanced variants have been put up to overcome them. The GWO algorithm and its variants are examined in this investigation. It conducts an experimental comparison of the original approach and its two variations. It examines how the approaches behave with various combinations of parameters. Five mechanical design problems are used to test the algorithms' effectiveness utilizing statistical analysis and search performance. In the literature, the performance of alternative approaches is also contrasted with the ideal outcomes.

Keywords: Grey wolf optimizer, Engineering problem, Mechanical design, Meta-heuristic algorithm, Optimization

*Sorumlu yazar / Corresponding author: nermin.ozcan@iste.edu.tr
Bu makaleye atıf yapmak için /To cite this article

Özcan, N. (2025). Comprehensive Comparative Analysis of GWO and Its Variants for Solving Mechanical Optimization Problems. Journal of Materials and Mechatronics: A (JournalMM), 6(1), 150-169.

1. INTRODUCTION

Engineering design across disciplines such as machinery, mechatronics, and construction is a crucial research domain focused on attaining a precise equilibrium between technical specifications and cost efficiency. Issues in this domain encompass diverse complexities, including linear and nonlinear constraints stemming from geometric, kinematic, and material considerations, alongside challenges related to high dimensionality (Gupta et al., 2021). Traditional optimization techniques encounter challenges such as premature convergence, entrapment in local minima, and sluggish convergence rates (Ezugwu et al., 2022). The nonlinearity of the issues or constraints restricts the application of linear methods (Lee et al., 2025). These challenges hinder traditional methods from achieving optimal solutions, resulting in inadequacies in addressing real-world problems due to their restricted applicability. The growing integration of disciplines like operations research, drug discovery, and engineering design with machine learning and technological advancements heightens the significance of optimization methods and necessitates the development of more advanced techniques to address complex challenges (Özcan and Kuntalp, 2017; Çetinkaya and Taşkıran, 2022; Ayğahoğlu et al., 2023; Kababulut et al., 2023; Gürkan Kuntalp et al., 2024).

In view of the escalating intricacy of real-world optimization problems in engineering, researchers are increasingly adopting meta-heuristic algorithms sas a viable solution (Li et al., 2024). While these stochastically structured algorithms do not consistently ensure optimal solutions, they provide a resilient alternative to conventional methods for addressing complex problems marked by nonlinearity and high dimensionality (Debnath et al., 2024). Over the past thirty years, numerous meta-heuristic algorithms have been devised and utilized for optimization challenges in engineering disciplines such as mechanical precision engineering (Ransegnola et al., 2019; Cui et al., 2020), automotive sector (Millo et al., 2018; Sun et al., 2018; Xu et al., 2025), structural design optimization (Hamza et al., 2018; Jahangiri et al., 2020), and power system issues (Eke et al., 2021; Coban and Saka, 2024). Nonetheless, it is prevalent that even these sophisticated algorithms often succumb to local minima and fail to address every problem with robustness.

Traditional meta-heuristics, including genetic algorithms (GA) (Holland, 1992), particle swarm optimization (PSO) (Eberhart and Kennedy, 1995), differential evolution (DE) (Storn and Price, 2009), and ant colony optimization (ACO) (Socha and Dorigo, 2008), have been extensively utilized in the past. The NFL theorem (Wolpert and Macready, 1997) and the difficulty of addressing complex optimization problems have compelled researchers to develop novel methods, resulting in an increase of meta-heuristic algorithms to over 500 (Li et al., 2024). Recent methodologies established, including the grasshopper optimization algorithm (Saremi, Mirjalili and Lewis, 2017), salp swarm optimization (Mirjalili et al., 2017), whale optimization algorithm (Mirjalili and Lewis, 2016), pathfinder algorithm (Yapici and Cetinkaya, 2019), equilibrium optimization (Faramarzi et al., 2020), harris hawks optimization (Heidari et al., 2019), and student psychology-based optimization (Das et al., 2020), have been employed by numerous researchers and have attained contemporary popularity. Furthermore, recently proposed methodologies, including artificial circulatory system algorithm (Özcan et al., 2025), african vulture optimization algorithm (Abdollahzadeh et al., 2021), animated oat optimization algorithm (Wang et al., 2025) and enzyme action optimizer (Rodan et al., 2025), have garnered attention due to their competitive efficacy.

Exploration and exploitation constitute the two primary phases in the optimization process of meta-heuristic algorithms, and these phases directly influence the algorithm's efficacy in addressing optimization challenges (Gezici, 2023). The intricacy of the issue restricts algorithms' capacity to explore and exploit. Exploration is linked to the capacity to transcend local minima, allowing the

algorithm to conduct a global search of the search space. Exploitation denotes the capacity to conduct localized searches, enhancing the quality of solutions within particular areas. Performance is linked to a judicious equilibrium between these two phases. Proposing novel meta-heuristic algorithms and refining established algorithms is a prevalent strategy to enhance exploration and exploitation capabilities.

Grey Wolf Optimization (GWO) is a metaheuristic algorithm inspired from the hunting behavior and social structure of grey wolves (Mirjalili et al., 2014). Since its introduction, GWO has garnered considerable attention owing to its simplicity, efficiency, and capacity to address complex optimization challenges. The algorithm's capacity to equilibrate exploration and exploitation enables it to adeptly traverse the search space, rendering it an invaluable asset for practitioners in pursuit of optimal solutions. Nonetheless, akin to numerous metaheuristics, GWO exhibits limitations including sluggish convergence rate, susceptibility to local optima, and an imbalance between exploration and exploitation. Numerous adaptations of GWO have been suggested, each presenting distinct strategies to tackle these challenges and enhance the algorithm's efficacy (Faris et al., 2018).

This paper examines GWO methodologies. The primary justifications for selecting this method are: (1) its popularity, ease of implementation, and algorithmic stability, and (2) its efficacy in addressing unconstrained and discrete optimization problems in preliminary assessments. The investigation offers an extensive summary of the algorithm and its modifications. It analyzes the enhancements, contributions, and applications of the GWO method. It also undertakes an experimental procedure to execute optimization tasks in the manufacturing processes of mechanical design issues. It seeks to achieve optimal solutions to problems through parameter optimization. It contrasts the outcomes derived from the GWO algorithm with its two modifications and the optimal solutions reported in the literature.

Section II provides a thorough literature review on the implementations, evolution, and current variations of the popular optimization algorithm, which serves as the theoretical foundation of the study. Section III presents the biological motivation and mathematical modeling of the GWO algorithm, as well as technical details of R-Walk and Improved GWO modifications. Section IV provides technical details on mathematical formulations of mechanical design problems, boundary conditions, and problem specifications. Section V details experimental methods, parameter optimization strategies, and findings, including quantitative and qualitative analyses, comparative algorithm performances, and statistical significance levels. Section VI critically discusses results, presents theoretical and practical implications, and presents limitations and suggestions for future research, integrating recent literature and academic rigor.

2. RELEATED WORKS

The GWO is a swarm intelligence algorithm created by Mirjalili et al. in 2014 and is widely regarded as one of the most prominent meta-heuristic algorithms among researchers (Mirjalili et al., 2014). The algorithm's efficacy has inspired other researchers to employ this method for addressing various optimization challenges. GWO has been utilized in machine learning for diverse applications, including feature selection (Emary et al., 2016), neural network training (Altay and Varol, 2023), and clustering tasks (Zhang and Zhou, 2015). It has also been utilized in image processing (Khairuzzaman and Chaudhury, 2017), bioinformatics applications (Jayapriya and Arock, 2015), and environmental prediction models (Song et al., 2015).

Other possible uses of GWO encompass a diverse array of engineering challenges. In control engineering, it has emerged as a commonly employed algorithm for tuning the parameters of controllers, including integral (I), proportional-integral (PI), and proportional-integral-derivative (PID) controllers, as well as addressing power distribution challenges related to optimal load distribution for resource operation and planning, robotics technologies, road planning, and wireless sensor network issues (Li and Wang, 2015; Sulaiman et al., 2015; Zhang et al., 2016; Saka, 2024). Research indicates that GWO markedly enhances the efficacy of the optimized components. Furthermore, GWO surpasses other optimization methods, including GA, PSO, and DE, regarding accuracy and efficiency. Nonetheless, certain researchers have identified limitations in the implementation of GWO owing to the intricate nature of real-world optimization challenges. The GWO algorithm has been redesigned to align with the search space of intricate domains.

Researchers seeking to enhance the efficacy of the GWO can be classified into four categories based on the nature of modifications they suggest for the GWO: (1) Research endeavors aimed at enhancing the equilibrium between exploration and exploitation processes concentrated on refining GWO mechanisms. Mittal et al. investigated the potential enhancement of the exploration process in GWO by reducing the value of a through an exponential decay function rather than employing a linear modification (Mittal et al., 2016). Malik et al. employed an alternative methodology for updating individual positions. Rather than employing a simple average of the best individuals, they utilized a weighted average of the positions of alpha, beta, and gamma wolves (Malik et al., 2015). Rodríguez et al. devised a methodology utilizing weighted averages and fuzzy logic to update the positions of omega wolves (Rodríguez et al., 2017). (2) Some researchers have concentrated on examining the enhancement of GWO performance through the incorporation of novel operators, such as crossover, or by employing a local search algorithm. Kishor et al. proposed a modified version of GWO to enhance population diversity by incorporating a straightforward crossover operator between two randomly selected distinct individuals. The transition operator's function is to enhance information exchange among individuals within the swarm (Kishor and Singh, 2016). Zhou et al. proposed the optimization of the parameters of the equivalent model for the small hydro generator swarm by integrating GWO with chaotic local search (Zhou et al., 2016).

(3) In a study (Luo et al., 2016), a variant of GWO was introduced wherein individuals possess distinct coding schemes. The authors employed a complex-valued coding approach rather than the conventional real-valued coding method. In this coding, the individual's genes consist of two primary components: an imaginary component and a real component. The authors contended that this technique can augment the information capacity of the individual and enhance the diversity of the population. (4) Another study employed a modified population structure and hierarchy (Yang *et al.*, 2017). In contrast to the four distinct wolf types in the traditional GWO, the population is segmented into two autonomous subpopulations: the first is designated as the cooperative hunting group, and the second as the random scout group. The objective of the scout group is to conduct extensive exploration, whereas the objective of the cooperative hunting group is to perform intensive exploitation. The alterations were not confined to this. Given that the GWO algorithm addresses single-objective problems, multi-objective variants of GWO have been introduced in the literature to tackle multi-objective challenges (Mirjalili et al., 2016). Moreover, certain researchers have suggested various hybrid approaches by integrating GWO to leverage the strengths and capabilities of alternative optimizers (Kamboj, 2016).

Despite a great deal of investigation on GWO and its many variations, certain gaps persist in the literature. The optimization of GWO parameters is inadequately explored in the literature.

Parameter tuning is essential for all optimization algorithms when addressing real-world problems. Moreover, GWO and its subsequent versions can be evaluated under equal experimental conditions on actual problems featuring intricate and varied constraints. This should be addressed to enhance comprehension of the current version of GWO and to evaluate its merits and drawbacks in relation to other variants of GWO. Consequently, our study has thoroughly examined the GWO algorithm and its two enhanced variants across five distinct mechanistic challenges. The experimental process encompasses the examination of mean performance, statistical evaluation, and the capacity to attain the optimal solution, as well as the influence of algorithmic parameters, including population structure and iteration count, on fitness landscapes. The number of GWO modifications was limited to two in order to be able to be analyzed in detail and to avoid complexity. Popular variants defined in the same library were preferred to avoid any superiority in the coding of the algorithms.

3. GREY WOLF OPTIMIZERS

3.1 Overview of the GWO

The primary inspiration for the GWO algorithm is the leadership structure and hunting tactics of grey wolves. The following sections elaborate on these essential components:

Leadership Hierarchy: The GWO follows to a rigid hierarchical framework, governed by wolves with distinct divisions of labor. Leaders, referred to as alphas, make critical decisions for the pack regarding activities such as hunting, selecting sleeping locations, and determining waking hours. Beta wolves are subordinate members of the pack who aid the alpha in decision-making and various activities. Delta wolves oversee territorial boundaries and alert the pack to potential threats. They safeguard and ensure the security of the pack, assisting the alphas and betas in hunting and procuring sustenance for the group. The omega wolves, the lowest-ranking members of the grey wolf hierarchy, monitor the other wolves and execute their directives. In the GWO algorithm, roles identified throughout the search process are assigned to solutions.

Hunting Mechanism: The algorithm emulates the encircling, hunting, and attacking behaviors of grey wolves during a hunt. This is accomplished via mathematical models that revise the locations of the search agents (wolves) within the solution space.

(1) Encircling prey - Wolves encircle prey by modifying their positions in relation to the optimal solution identified thus far. It employs the subsequent equations to mathematically represent the encircling behavior:

$$\boldsymbol{X}(t+1) = \boldsymbol{X}(t) - \boldsymbol{A}.\boldsymbol{D} \tag{1}$$

where **X**(t+1) represents the subsequent position of the wolf, **X**(t) denotes the current position, **A** is a coefficient matrix, and **D** is a vector contingent upon the prey's location (by **X**p), computed as follows:

$$\boldsymbol{D} = |\boldsymbol{C}.\boldsymbol{X}p(t) - \boldsymbol{X}(t)| \tag{2}$$

where,

$$\boldsymbol{C} = 2.\boldsymbol{r}_2 \tag{3}$$

The random components of the aforementioned equations replicate varying step lengths and velocities of grey wolves. The equations that delineate their values are as follows:

$$\boldsymbol{A} = 2\boldsymbol{a}.\boldsymbol{r}_1 - \boldsymbol{a} \tag{4}$$

where $\boldsymbol{a}$ is a vector whose values diminish linearly from 2 to 0 throughout the execution. $\mathbf{r_1}$ is a vector generated randomly from the interval [0,1].

(2) Hunting - Grey wolves possess the capability to detect and encircle their prey. The alpha typically directs the prey. In the mathematical simulation of grey wolf hunting behavior, the alpha is regarded as possessing superior knowledge regarding the probable locations of prey. Consequently, it retains the initial three optimal solutions acquired and adjusts the positions of the remaining wolves based on this data. In this context, the subsequent formulas are employed.

$$\boldsymbol{X}(t+1) = \frac{1}{3}\boldsymbol{X_1} + \frac{1}{3}\boldsymbol{X_2} + \frac{1}{3}\boldsymbol{X_3} \tag{5}$$

where $\mathbf{X_1}$ and $\mathbf{X_2}$ and $\mathbf{X_3}$ are calculated with Eq. 6.

$$\begin{aligned} \boldsymbol{X_1} &= \boldsymbol{X}_\alpha(t) + \boldsymbol{A_1}.\boldsymbol{D}_\alpha \\ \boldsymbol{X_2} &= \boldsymbol{X}_\beta(t) + \boldsymbol{A_2}.\boldsymbol{D}_\beta \\ \boldsymbol{X_3} &= \boldsymbol{X}_\delta(t) + \boldsymbol{A_3}.\boldsymbol{D}_\delta \end{aligned} \tag{6}$$

where $\mathbf{D_\alpha}$ and $\mathbf{D_\beta}$ and $\mathbf{D_\delta}$ are calculated using Eq. 7.

$$\begin{aligned} \boldsymbol{D}_\alpha &= |\boldsymbol{C_1}.\boldsymbol{X}_\alpha - \boldsymbol{X}| \\ \boldsymbol{D}_\beta &= |\boldsymbol{C_2}.\boldsymbol{X}_\beta - \boldsymbol{X}| \\ \boldsymbol{D}_\delta &= |\boldsymbol{C_3}.\boldsymbol{X}_\delta - \boldsymbol{X}| \end{aligned} \tag{7}$$

(3) Attacking the prey - As the search advances, the algorithm transitions from exploration to exploitation, and the wolves near their target. To mathematically model the prey's approach, we reduce **a**. The variable vector A within the interval [-2**a**, 2**a**] diminishes **a** from 2 to 0 across successive iterations.

The algorithm continues to iterate until a termination condition is satisfied, enhancing its solutions with each iteration and achieving the optimal solution.

3.2 Random Walk GWO

The Random Walk GWO algorithm is derived from the conventional GWO method, which is based on the hunting behavior and social hierarchy of grey wolves (Gupta and Deep, 2019). The primary distinction between this method and classical GWO lies in the incorporation of a random walk in the algorithm's exploration strategy, with the step size derived from the Cauchy distribution. The rationale for contemplating a random step size is the infinite variance of the Cauchy distribution. This concept posits that during periods of inactivity in the exploration of the search space, the dominant wolves are inclined to investigate potential optimal solutions by making significant leaps.

The algorithm is founded on the fundamental mathematical formulations of the original GWO. Nevertheless, it offers enhancement of the random walk through Eq. 8 for the modification of the random walk.

$$\boldsymbol{b} = 2 - 2\left(\frac{t}{\max no\ of\ iterations}\right)$$
$$\text{ᵯ} = 2\mathbf{b}.\boldsymbol{r}_1 - \mathbf{b} \tag{8}$$

The wolves' expression around the prey is updated with Eq. 9.

$$\boldsymbol{X}(t+1) = \boldsymbol{X}(t) - \text{ᵯ}.\boldsymbol{D} \tag{9}$$

3.3 Improved GWO

The Improved GWO is a modification of the traditional GWO algorithm designed to refine the optimization process (Kaveh and Zakian, 2018). It refines the optimization process by calibrating the parameter settings and seeks to enhance the outcomes through the implementation of novel techniques. Moreover, Enhanced GWO incorporates supplementary internal parameters that enhance flexibility and adaptability in complex problems, accelerating the optimization process and elevating solution quality relative to classical GWO.

In the Original GWO (as per Eq. 4), $\boldsymbol{a}$ uniform linear decreasing function is established for alpha, beta, and delta wolves. In Improved GWO, distinct functions are established for each scenario based on dominance principles to augment the exploration and application of the algorithm. In Eq. 10, alpha, beta, and delta exhibit the following exponentially decreasing functions for a single parameter:

$$\boldsymbol{a}_\alpha(i) = \boldsymbol{a}_{\max}\exp\left(\left(\frac{i}{\boldsymbol{i}_{\max}}\right)^{\eta_\alpha}\ln\left(\frac{\boldsymbol{a}_{\min}}{\boldsymbol{a}_{\max}}\right)\right)$$
$$\boldsymbol{a}_\delta(i) = \boldsymbol{a}_{\max}\exp\left(\left(\frac{i}{\boldsymbol{i}_{\max}}\right)^{\eta_\delta}\ln\left(\frac{\boldsymbol{a}_{\min}}{\boldsymbol{a}_{\max}}\right)\right) \tag{10}$$
$$\boldsymbol{a}_\beta = (\boldsymbol{a}_\alpha(i) + \boldsymbol{a}_\delta(i))/2$$

where $\boldsymbol{a}_{\max}$, $\boldsymbol{a}_{\min}$, i, $\boldsymbol{i}_{\max}$, η_α and η_δ are the upper bound of $\boldsymbol{a}$, lower bound of $\boldsymbol{a}$, current iteration, maximum number of iteration, growth factor of alpha and growth factor of delta, respectively.

4. MECHANICAL DESIGN PROBLEMS

Mechanical design optimization problems encompass numerous nonlinear constraints and intricate variables associated with kinematics, geometric conditions, and material strength. Over the past three decades, optimization methods have been utilized to tackle numerous engineering problems and real-world challenges. This paper analyzes five prevalent problems to perform a comparative assessment of GWO variants and Table 1 delineates the critical informations regarding these problems.

Table 1. Summary of five mechanical optimization problems.

Problem Name	Abbr	Dimension	Constraints
Cantilever Beam Problem	CBP	5	1
Tubular Column Design	TCD	2	6
Piston Lever Design	PLD	4	4
Corrugated Bulkhead Problem	CBHD	4	6
Reinforced Concrete Beam	RCB	3	2

Figure 1 illustrates these problems graphically, with their definitions detailed in the subheadings. Various versions of the issues exist in the literature, and scholars have tailored the fitness function and limitations to align with their research objectives. In our research, we utilized the Enoppy library, which encompasses a standardized problem repository to facilitate comparisons and ensure the reproducibility of the study (Van Thieu, 2023). Mathematical expressions of the problems, including the fitness function, constraints and variable range, can be accessed from the Supplementary File.

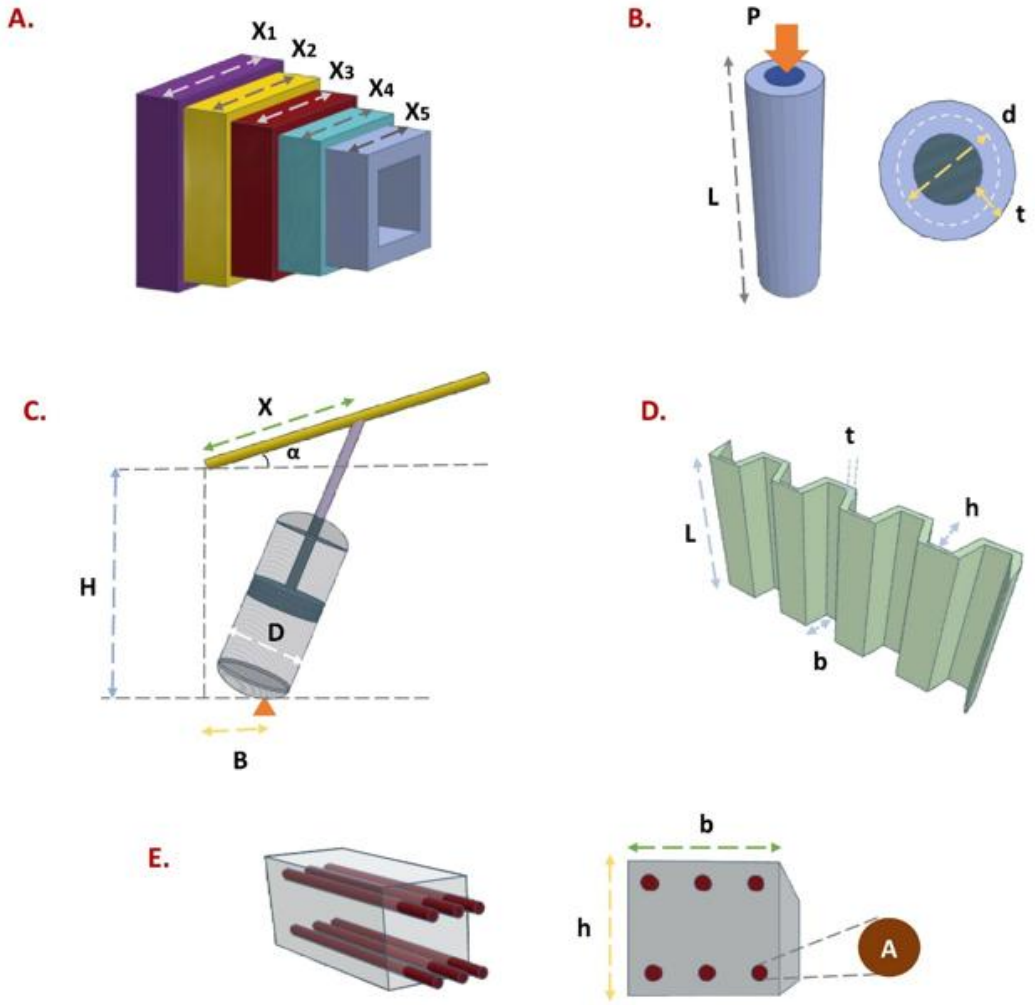

Figure 1. The demonstration of the mechanical design problems. (A) CBP, (B) TCD, (C) PLD, (D) CBHD, (E) RCB

4.1 The Cantilever Beam Design (CBP)

The cantilever is a design depicted in Figure 1.A comprises five hollow square blocks of uniform thickness. The dimensions of the blocks are represented by X_1, X_2, X_3, X_4, and X_5 for height

and width. The objective of the problem is to minimize the weight of the cantilever beam while adhering to structural requirements and to ascertain the optimal block dimensions.

4.2 The Tubular Column Design (TCD)

The tubular column depicted in Figure 1.B is a structural component comprising a hollow cylinder constructed from metal, concrete, or alternative materials. It is frequently utilized in construction to reinforce beams and other structural components, as well as in bridges and various other edifices. Tubular columns are typically more robust and efficient than solid columns due to their ability to withstand torsional, bending, and shear forces. The goal of the problem is to optimize the construction cost of the column by utilizing the variables d, representing the average diameter of the column, and t, denoting the thickness of the column.

4.3 The Piston Lever Design (PLD)

The piston lever problem holds significant relevance in engineering applications, including the automotive industry, aerospace, and mechanical engineering. The primary aim of this problem is to optimally position the piston lever components H, B, D, and X by minimizing the oil volume as α in the piston lever is increased from 0° to 45° in the design illustrated in Figure 1.C.

4.4 The Corrugated Bulkhead Design (CBHD)

The corrugated bulkheads are commonly utilized on vessels owing to their benefits, including ease of maintenance and adaptability to thermal expansion and contraction. Reducing the weight of these mechanical designs is crucial due to the current high cost of materials and constitutes the primary objective of this problem. The structural component depicted in Figure 1.D possesses four design variables: width (b), depth (h), length (L), and thickness (t) of the plate.

4.5 The Reinforced Concrete Beam Design (RCB)

The design of reinforced concrete beams is a challenge faced in civil engineering. The issue pertains to a structure depicted in Figure 1.E. Concrete beams are fortified with steel bars to enhance their resistance to internal stresses. The process is a complex optimization involving three design variables: reinforcement area (A), beam width (b), and beam depth (h).

5. EXPERIMENTAL PROCEDURE, RESULTS AND DISCUSSION

This section presents an experimental comparison of the GWO, Improved GWO, and Random Walk GWO algorithms. To assess the efficacy of each algorithm, they were implemented on five distinct mechanical design challenges: CBD, TCD, PLD, CBHD, and RCB. All experiments were performed on a PC with an Intel Core(TM) i5-12400 (2.50 GHz) processor, 512 GB SSD, 16 GB RAM, and the Windows 11 Operating System. Furthermore, the Python programming language was employed for all computations, and the Mealpy (Van Thieu and Mirjalili, 2023) and Enoppy (Van Thieu, 2023) libraries were utilized alongside the fundamental libraries. In the optimization of the fundamental parameters of the algorithms, the iteration counts were established at 100, 500, 1000, and 5000, while the population sizes were designated as 20, 50, 100, 200, and 500, respectively. All case studies were executed under equal experimental conditions. Each algorithm was executed 25 times to assess the robustness of the comparative methods in solving the problem. The experimental methodologies and the resultant findings are elaborated upon in the subsequent subsections.

5.1 Average Efficacy

Figure 2 illustrates average values derived from the application of the three optimization models to five problems. The averages are computed based on the fitness results derived from 25 iterations across all iteration and population size parameters of the problems.

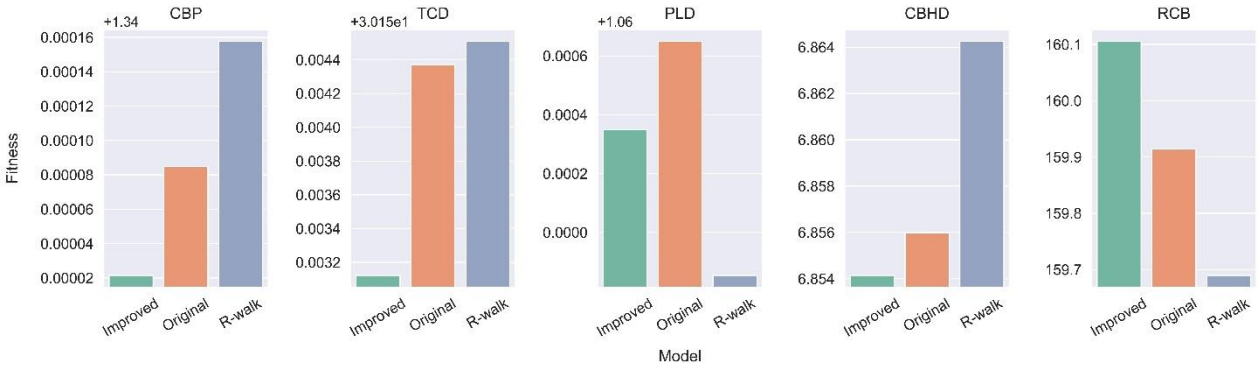

Figure 2. Average performance of optimization models in mechanical problems

Given that all optimization tasks are minimization problems, Improved GWO achieved the lowest average fitness value in addressing CBP, TCD, and CBHD problems. It demonstrates superior optimization efficacy relative to the Original method and Random Walk GWO. Conversely, in PLD and RCB issues, Random Walk GWO emerges as the most effective model. The enhanced GWO outperformed the original method in the PLD problem.

5.2 Statistical Assessments

The average performance graph offers a qualitative comparison of the methods, yet this is inadequate on its own. Statistical tests were conducted in the study to assess the superiority of the methods relative to one another and to determine if a statistically significant difference was achieved.

The results acquired for each parameter combination of the algorithms employed in the study were regarded as a single data. To ascertain the appropriate statistical test, the normality of the data distribution was initially assessed. The Shapiro-Wilk test was utilized for normality assessments owing to the limited sample size ($n<50$). The Shapiro-Wilk test results indicated that approximately 68.5% of the total data group satisfied the $p<0.05$ criterion and exhibited a non-normal distribution. The optimization method exhibiting the highest incidence of anomalies was R-walk GWO, while TCD was the most prevalent by problem type. The propensity for normal distribution heightened with an increase in population size.

In the second stage, a multiple comparison test was conducted to assess the statistical significance among the methods. ANOVA was conducted when $p >= 0.05$, while the Kruskal-Wallis test was utilized in other instances, as determined by the normality test. Analysis of the multiple comparison test results revealed that the methods satisfied the $p<0.05$ acceptance criterion in the majority of parameter combinations (77.7%), yielding statistically significant differences. Furthermore, 44.7% of the findings exhibited substantial significance ($p<0.001$). Systematic superiority was particularly evident in CBP and CBHD problems.

The results indicated systematic and quantifiable differences among the three methods. Nevertheless, comprehensive pairwise comparisons were conducted in the final stage to assess the nature of these differences among the methods. At this juncture, Dunn's test was employed due to the failure of the majority of normal distribution assumptions in data integrity. The average results derived from the data (across all problems) were Improved vs Original: 0.0092 ± 0.021, Improved vs

R-walk: 0.0004 ± 0.0021, and Original vs R-walk: 0.6821 ± 0.2974. The Improved GWO demonstrated considerable superiority ($p<0.01$) compared to the other two methods. No systematic difference exists between Original GWO and the R-walk variant ($p>0.05$). The statistical results align with the findings of Section 5.1.

5.3 Evaluation of Parameters

In optimization problems, the objective is to identify the optimal solutions with consistent stability. The average efficacy of an algorithm across a broad spectrum of problems appears to be a viable strategy; however, it is not invariably adequate. Achieving optimal solutions through efficient parameterization is essential. This section compares the results obtained from the GWO algorithm and its two variants with parameter modifications. Figure 3-7 displays the results for the CBP, TCD, PLD, CBHD, and RCB problems. Fitness results are normalised in graphical representations to ensure numerical traceability and to facilitate the observation of differences in comparisons.

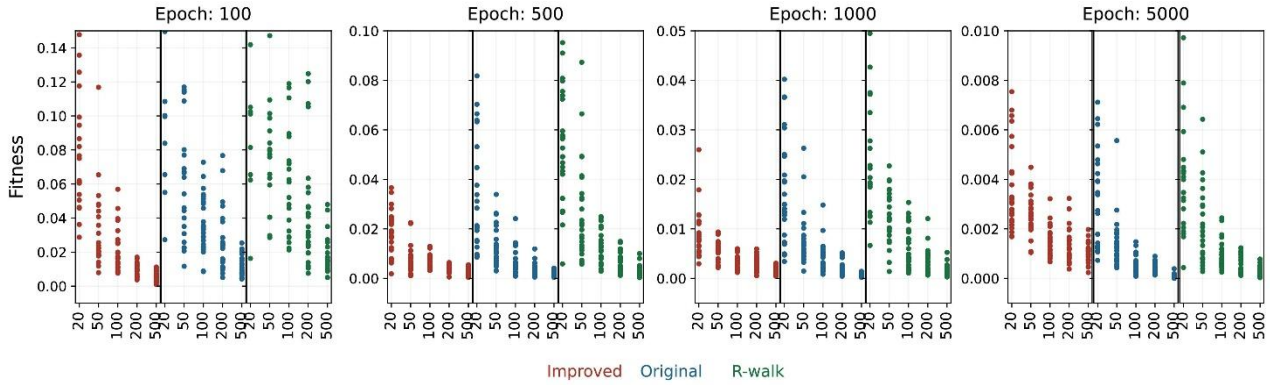

Figure 3. Fitness outcomes for all parameter combinations of GWOs on CBP

Figure 3 indicates that the improved GWO method on the CBP problem consistently yields consistent results across high iterations and population size combinations, despite minor fluctuations in performance with decreasing parameters. Stability is evident at medium to high population densities. The original model demonstrates highly stable behavior at an epoch value of 5000, sustaining competitive levels despite population size decreases. However, the R-walk variant experiences substantial performance declines when parameters drop below critical thresholds, leading to unregulated variations and discrepancies, especially at minimal population sizes.

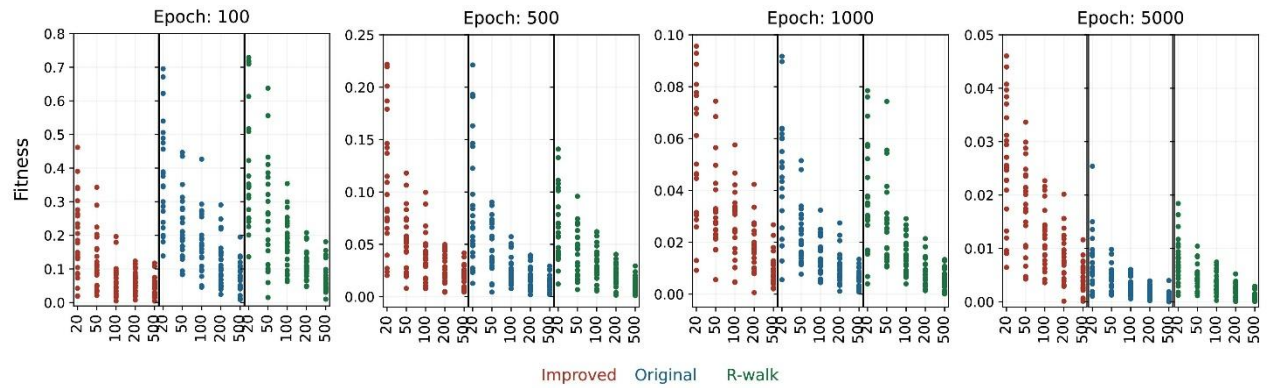

Figure 4. Fitness outcomes for all parameter combinations of GWOs on TCD

According to Figure 4, the TCD problem shows that the impact of epoch parameter is less pronounced than in the CBP problem. GWO and the R-walk variant show similar performance at elevated iteration and population sizes. The Original GWO yields the most consistent results with a population size of 500 and 5000 epochs. At 5000 iterations, they exhibit generally tolerant behavior, but minor performance declines occur as the population size diminishes. In situations with low populations, considerable fluctuations emerge, albeit in a more regulated manner than in the Improve model. The R-walk model demonstrates satisfactory performance only at elevated population and epoch values.

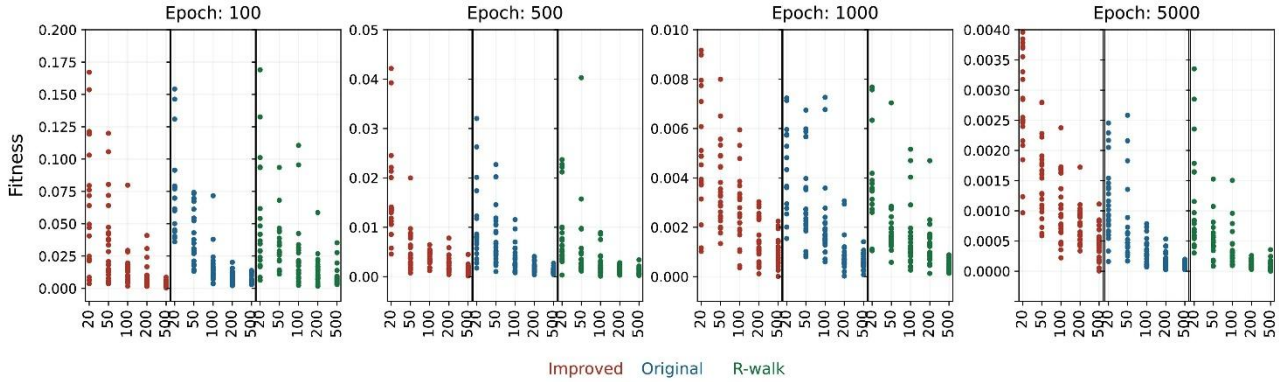

Figure 5. Fitness outcomes for all parameter combinations of GWOs on PLD

Figure 5 indicates that, generally, the performance of all models improves with population size and epochs, with the Original and R-walk models showing optimality. The R-walk model achieved lower minimum values, while the Original model had a limited spectrum of solutions, indicating greater stability reliability. The Improved model showed competitive performance at 100 and 500 epochs, but lagged behind other methods when epochs increased. The Original model's outcomes were concentrated on a limited spectrum, suggesting greater reliability.

Figure 6 illustrates that the Improved model offers optimal results for general applications, with minimal error and consistent outcomes at high epoch and population sizes. The Original model is particularly reliable in industrial-scale contexts, especially when maximum resources are used. R-walk, despite its theoretical ability to achieve minimal fitness values, is only suitable for resource-rich and regulated settings due to erratic deviations under low parameters. Prioritizing Improved or Original in resource-unrestricted contexts and incorporating additional validation measures in experimental or risk-tolerant situations is recommended.

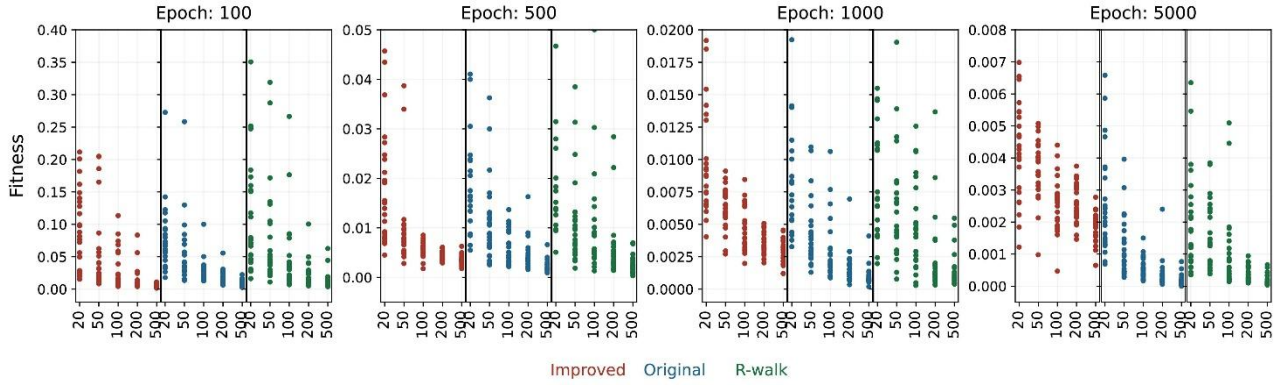

Figure 6. Fitness outcomes for all parameter combinations of GWOs on CBHD

Figure 7 demonstrates the performance of Improved, Original, and R-walk models in relation to epoch and pop_size parameters. All models yield low fitness and consistent results in high source scenarios. The Original model excels in industrial applications due to minimal variation, while the Improved model provides stability across parameters. R-walk achieves competitive measures in medium-scale configurations but poses a risk of inconsistency in low-source scenarios.

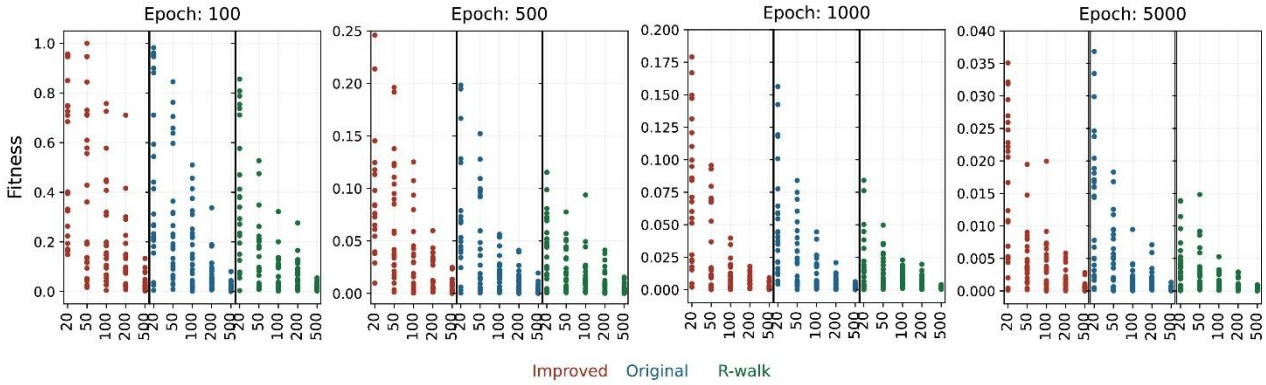

Figure 7. Fitness outcomes for all parameter combinations of GWOs on RCB

5.4 Optimal Performances and Literature Comparison

This section assesses the optimal fitness values attained by the algorithms. Table 2 presents the experimental outcomes for five engineering optimization challenges among GWOs. Furthermore, the outcomes of the top-performing models are juxtaposed with the advanced algorithms suggested in the literature to address the same issues. The results are presented in Tables 3 to 7.

Table 2. The minimum outcomes of algorithms on five mechanical problems

Problem	Improved	Original	R-walk
CBP	1.339958	1.339956	1.339957
TCD	30.149763	30.149755	30.149759
PLD	1.057401	1.057406	1.057400
CBHD	6.843375	6.843013	6.843038
RCB	159.360007	159.360037	159.360041

Table 2 illustrates notable disparities among the Improved, Original, and R-walk methodologies. The Original algorithm demonstrated better results in CBP, TCD, and CBHD problems, whereas the R-walk model scored in PLD. The enhanced algorithm demonstrated superiority in RCB. These findings indicate that the selection of algorithms tailored to specific problems is essential, with Improved being favored in particular contexts such as RCB.

Table 3. The optimal comparison of optimizers in CBP

Model	Parameters	Fitness
SRIME (Zhong et al., 2024)	Epoch:20000, Psize:100	1.3419
LLMOA (Zhong, Hussien, et al., 2025)	E:50000, Psize:100	1.3399
SHBA (Xu et al., 2024)	E:50000, Psize:100	1.3400
SNS (Bayzidi et al., 2021)	E:12000, Psize: Unknown	1.3399
L-SHACSO (Zhong, Wang, et al., 2025)	E:10000, Psize:100	1.3400
Original GWO (This Study)	E:5000, Psize:500	1.3399

Analysis of the comparisons reveals that the GWO methodologies employed in your study (Original GWO, R-walk, and Improved GWO) exhibit a notable performance. In the CBP problem, Original GWO proved its computational efficiency by achieving the same fitness value (1.3399) as LLMOA and SNS with 5 times fewer epochs (E:5000) and larger population.

Table 4. The optimal comparison of optimizers in TCD

Model	Parameters	Fitness
CCOA (Zhong, Zhang and Yu, 2024b)	E:20000, Psize:100	30.1670
SRIME (Zhong et al., 2024)	E:20000, Psize:100	30.1500
LLMOA (Zhong, Hussien, et al., 2025)	E:20000, Psize:100	30.1497
SHBA (Xu et al., 2024)	E:20000, Psize:100	30.1500
L-SHACSO (Zhong, Wang, et al., 2025)	E:10000, Psize:100	30.1488
Original GWO (This Study)	E:5000, Psize:500	30.1497

In TCD, although L-SHACSO achieves a superior result of 30.1488, Original GWO surpasses most methods in the literature (CCOA, SRIME) with a score of 30.1497, demonstrating a balanced performance.

Table 5. The optimal comparison of optimizers in PLD

Model	Parameters	Fitness
SRIME (Zhong et al., 2024)	E:40000, Psize:100	1.0574
SHBA (Xu et al., 2024)	E:40000, Psize:100	1.0570
L-SHACSO (Zhong, Wang, et al., 2025)	E:10000, Psize:100	1.0743
R-walk (This Study)	E:5000, Psize:500	1.0574

In PLD, R-walk yields an equivalent value to SRIME (1.0574) at one-eighth of the epoch cost, thereby demonstrating its adaptive search efficiency.

Table 6. The optimal comparison of optimizers in CBHD

Model	Parameters	Fitness
CVEGE (Zhong, Zhang and Yu, 2024a)	E:10000, Psize:100	6.8430
CCOA (Zhong, Zhang and Yu, 2024b)	E:20000, Psize:100	6.8485
SRIME (Zhong et al., 2024)	E:20000, Psize:100	6.8436
LLMOA (Zhong, Hussien, et al., 2025)	E:40000, Psize:100	6.8429
SNS (Bayzidi et al., 2021)	E:3125, Psize: Unknown	6.8429
L-SHACSO (Zhong, Wang, et al., 2025)	E:10000, Psize:100	6.8429
Original GWO (This Study)	E:5000, Psize:500	6.8430

Despite Original GWO in CBHD trailing LLMOA and SNS by a mere 0.0001, the fact that these methods utilize 4-8 times more epochs underscores GWO results are remarkable.

In RCB, the Improved GWO attains an equivalent fitness level as CCOA (159.3600) within one-quarter of an epoch, underscoring the algorithm's efficacy.

Table 7. The optimal comparison of optimizers in RCB

Model	Parameters	Fitness
CCOA (Zhong, Zhang and Yu, 2024b)	E:20000, Psize:100	159.3600
SRIME (Zhong et al., 2024)	E:20000, Psize:100	159.3700

Table 7. The optimal comparison of optimizers in RCB (continued)

Model	Parameters	Fitness
LLMOA (Zhong, Hussien, et al., 2025)	E:30000, Psize:100	159.4122
SHBA (Xu et al., 2024)	E:30000, Psize:100	160.3000
Improved GWO (This Study)	E:5000, Psize:100	159.3600

Overall, the parameter optimization in this study has yielded results that are competitive with existing methods in the literature, particularly regarding computational resource optimization using the low epoch-large population strategy. The slight advantage of certain methods, such as LLMOA and SNS in CBHD, necessitates a thorough examination of parameter adaptation mechanisms.

6. CONCLUSIONS

GWO is regarded as an effective algorithm for identifying the optimal solution to mechanical design problems. The intricacy of the issues, encompassing complexity, mixed variables with continuous and discrete elements, multiple objectives, and diverse nonlinear constraints associated with performance operations, manufacturing prerequisites, and kinematic conditions, prompted researchers to devise this efficient algorithm.

This article thoroughly examines the GWO algorithm and introduces various modifications of this widely-used algorithm. The present investigation not only reviews the GWO literature but also compares the original algorithm with its two variants under identical experimental conditions. The experiments encompass three models, twenty distinct combinations of fundamental parameters (four epochs, five population sizes) and five mechanical design challenges. The methods' performance is assessed based on their average efficacy, the statistically significant differences attained, stability under parameter variations, and the minimum fitness values achieved. The subsequent conclusions can be derived from the experimental analyses:

(1) The GWO modifications yielded distinct outcomes compared to the original algorithm, despite being based on the same methodology. This is statistically significant in the majority of instances.
(2) The original GWO exhibits strengths including consistency across various problem types and minimal parameter sensitivity. The substantial resource demand (5000 iterations/500 populations) constitutes a limitation of the Original GWO.
(3) In situations involving abundant resources and uncomplicated issues (e.g., RCB), the Enhanced model demonstrates effective performance. The absence of diversification in low populations increases the risk of local minima, representing a limitation of this method.
(4) The R-walk model demonstrates robust performance when employed by specialists in environments where parameters are meticulously regulated and substantial populations are feasible. Nonetheless, it may present risks when extensive and elevated parameter requirements are unmet.

These conclusions indicate that problem type, resource limitations, and performance consistency are interdependent factors in the selection of optimization algorithms. Given that energy efficiency and stability are paramount in industrial systems, even minor performance variances hold significant long-term implications. The Original model is evidently the more dependable choice regarding resource efficiency and robustness in comparison to alternative methods. The five problems examined in the investigations pertain solely to single-objective optimization. They have not undergone testing in real-time dynamic environments. These are the limitations of the study. Nonetheless, the comparative examination of the algorithms elucidates the merits and demerits of

GWO and its variations. The study can function as a reference for researchers to tackle issues across multiple engineering domains, including materials, machinery, automotive, and construction.

7. ACKNOWLEDGEMENTS

This study did not benefit from any support.

8. CONFLICT OF INTEREST

Author approves that to the best of their knowledge, there is not any conflict of interest or common interest with an institution/organization or a person that may affect the review process of the paper.

9. AUTHOR CONTRIBUTION

Nermin ÖZCAN has the full responsibility of the paper about determining the concept of the research, data collection, data analysis and interpretation of the results, preparation of the manuscript and critical analysis of the intellectual content with the final approval.

10. REFERENCES

Abdollahzadeh B., Gharehchopogh F. S., Mirjalili S., African Vultures Optimization Algorithm: A New Nature-Inspired Metaheuristic Algorithm for Global Optimization Problems, Computers and Industrial Engineering 158(5), 107408, 2021.

Altay O., Varol E., A Novel Hybrid Multilayer Perceptron Neural Network with Improved Grey Wolf Optimizer, Neural Computing and Applications, 35(1), 529–556, 2023.

Ayğahoğlu M. E., Gümüş M. S., Çakan, A., Kalyoncu M., Dimension Optimization of Polycentric Knee Mechanism using the Bees Algorithm And Genetic Algorithm, Journal of Materials and Mechatronics: A 4(1), 318–332, 2023.

Bayzidi H., Talatahari S., Saraee M., Lamarche, C. P., Social Network Search for Solving Engineering Optimization Problems, Computational Intelligence and Neuroscience 548639, 2021.

Çetinkaya M. B., Taşkıran K., Meta-Sezgisel Algoritmalara Dayalı Retinal Damar Bölütleme, Journal of Materials and Mechatronics: A 3(1), 79–90, 2022.

Coban M., Saka M., Directly Power System Harmonics Estimation using Equilibrium Optimizer, Electric Power Systems Research, 234(110565), 2024.

Cui D., Wang G., Lu Y., Sun K., Reliability Design and Optimization of The Planetary Gear by a GA Based on the DEM and Kriging Model, Reliability Engineering & System Safety 203,107074, 2020.

Das B., Mukherjee V., Das D., Student Psychology based Optimization Algorithm: A New Population based Optimization Algorithm for Solving Optimization Problems, Advances in Engineering Software 146(3), 102804, 2020.

Debnath S., Debbarma S., Nama S., Saha A. K., Dhar R., Yildiz A. R., Gandomi A. H., Centroid Opposition-Based Backtracking Search Algorithm For Global Optimization And Engineering Problems, Advances in Engineering Software 198, 103784, 2024.

Eberhart R., Kennedy J., New Optimizer using Particle Swarm Theory, Proceedings of the International Symposium on Micro Machine and Human Science 39–43, 1995.

Eke I., Saka M., Gozde H., Arya Y., Taplamacioglu M. C., Heuristic Optimization based Dynamic Weighted State Feedback Approach for 2DOF PI-Controller in Automatic Voltage Regulator, Engineering Science and Technology, an International Journal 24(4), 899–910, 2021.

Emary E., Zawbaa H. M., Hassanien A. E., Binary Grey Wolf Optimization Approaches for Feature Selection, Neurocomputing 172, 371–381, 2016.

Ezugwu A. E., Agushaka J. O., Abualigah L., Mirjalili S., Gandomi A. H., Prairie Dog Optimization Algorithm, Neural Computing and Applications 34(22), 2022.

Faramarzi A., Heidarinejad M., Stephens B., Mirjalili S., Equilibrium Optimizer: A Novel Optimization Algorithm, Knowledge-Based Systems 191, 105190, 2020.

Faris H., Aljarah I., Al-Betar M. A., Mirjalili S., Grey Wolf Optimizer: A Review ff Recent Variants and Applications, Neural Computing and Applications 30(2), 413–435, 2018.

Gezici H., Improved Tuna Swarm Optimization Algorithm for Engineering Design Problems, Journal of Materials and Mechatronics: A 4(2), 424–445, 2023.

Gupta S., Abderazek H., Yıldız B. S., Yildiz A. R., Mirjalili S., Sait, S. M., Comparison of Metaheuristic Optimization Algorithms for Solving Constrained Mechanical Design Optimization Problems, Expert Systems with Applications 183, 2021.

Gupta S., Deep K., A Novel Random Walk Grey Wolf Optimizer, Swarm and Evolutionary Computation 44, 101–112, 2019.

Gürkan Kuntalp D., Özcan N., Düzyel O., Kababulut F. Y., Kuntalp M., A Comparative Study of Metaheuristic Feature Selection Algorithms for Respiratory Disease Classification, Diagnostics 14(19), 2244, 2024.

Hamza F., Abderazek H., Lakhdar S., Ferhat D., Yıldız A. R., Optimum Design of Cam-Roller Follower Mechanism using a New Evolutionary Algorithm, The International Journal of Advanced Manufacturing Technology 99(5), 1267–1282, 2018.

Heidari A. A., Mirjalili S., Faris H., Aljarah I., Mafarja M., Chen H., Harris Hawks Optimization: Algorithm and Applications, Future Generation Computer Systems 97, 849–872, 2019.

Holland J. H., Genetic Algorithms, Scientific American 267(1), 66–72, 1992.

Jahangiri M., Hadianfard M. A., Najafgholipour M. A., Jahangiri M., Gerami M. R., Interactive Autodidactic School: A New Metaheuristic Optimization Algorithm for Solving Mathematical and Structural Design Optimization Problems, Computers & Structures 235, 2020.

Jayapriya J., Arock M., A Parallel GWO Technique for Aligning Multiple Molecular Sequences, International Conference on Advances in Computing, Communications and Informatics (ICACCI), India, 210–215, 2015.

Kababulut F. Y., Gürkan Kuntalp D., Düzyel O., Özcan N., Kuntalp M., A New Shapley-Based Feature Selection Method in a Clinical Decision Support System for the Identification of Lung Diseases, Diagnostics 13(23), 3558, 2023.

Kamboj V. K., A Novel Hybrid PSO–GWO Approach for Unit Commitment Problem, Neural Computing and Applications 27(6), 1643–1655, 2016.

Kaveh A., Zakian P., Improved GWO Algorithm for Optimal Design of Truss Structures, Engineering with Computers 34(4), 685–707, 2018.

Khairuzzaman A. K. M., Chaudhury S., Multilevel Thresholding using Grey Wolf Optimizer for Image Segmentation, Expert Systems with Applications 86, 64–76, 2017.

Kishor A., Singh P. K., Empirical Study of Grey Wolf Optimizer, Proceedings of Fifth International Conference on Soft Computing for Problem Solving, Singapore, 1037–1049, 2016.

Lee S. W., Haider A., Rahmani A. M., Arasteh B., Gharehchopogh F. S., Tang S., Liu Z., Aurangzeb K., Hosseinzadeh M., A Survey of Beluga Whale Optimization and Its Variants: Statistical Analysis, Advances, and Structural Reviewing, Computer Science Review 57, 2025.

Li G., Zhang T., Tsai C. Y., Yao L., Lu Y., Tang J., Review of the Metaheuristic Algorithms in Applications: Visual Analysis based on Bibliometrics, Expert Systems with Applications 255, 2024.

Li S. X., Wang J. S., Dynamic Modeling of Steam Condenser and Design of Pi Controller based on Grey Wolf Optimizer, Mathematical Problems in Engineering 120975, 2015.

Luo Q., Zhang S., Li Z., Zhou Y., A Novel Complex-Valued Encoding Grey Wolf Optimization Algorithm, Algorithms 9(1), 2016.

Malik M. R. S., Mohideen E. R., Ali L., Weighted Distance Grey Wolf Optimizer for Global Optimization Problems, IEEE International Conference on Computational Intelligence and Computing Research (ICCIC), India, 1–6, 2015.

Millo F., Arya P. Mallamo F., Optimization of Automotive Diesel Engine Calibration using Genetic Algorithm Techniques, Energy 158, 807–819, 2018.

Mirjalili S., Saremi S., Mirjalili S. M., Coelho L. S., Multi-Objective Grey Wolf Optimizer: A Novel Algorithm for Multi-Criterion Optimization, Expert Systems with Applications 47, 106–119, 2016.

Mirjalili S., Lewis A., The Whale Optimization Algorithm, Advances in Engineering Software 95, 51–67, 2016.

Mirjalili S., Mirjalili S. M., Lewis A., Grey Wolf Optimizer, Advances in Engineering Software 69, 46–61, 2014.

Mirjalili S., Gandomi A. H., Mirjalili S. Z., Saremi S., Faris H., Mirjalili S. M., Salp Swarm Algorithm: A Bio-Inspired Optimizer for Engineering Design Problems, Advances in Engineering Software 114, 163–191, 2017.

Mittal N., Singh U., Sohi, B. S., Modified Grey Wolf Optimizer for Global Engineering Optimization, Applied Computational Intelligence and Soft Computing, 2016(1), 2016.

Özcan N., Kuntalp M., Determining Best HRV Indices for PAF Screening using Genetic Algorithm, 10th International Conference on Electrical and Electronics Engineering (ELECO), Bursa, 2018.

Özcan N., Utku S. Berber T., Artificial Circulation System Algorithm: A Novel Bio-Inspired Algorithm, CMES - Computer Modeling in Engineering and Sciences 142(1), 635–663, 2025.

Ransegnola T., Zhao X., Vacca A., A Comparison of Helical and Spur External Gear Machines for Fluid Power Applications: Design And Optimization, Mechanism and Machine Theory 142, 2019.

Rodan A., Al-Tamimi A. K., Al-Alnemer L., Mirjalili S., Tino P., Enzyme Action Optimizer: A Novel Bio-Inspired Optimization Algorithm, The Journal of Supercomputing 81(5), 686, 2025.

Rodríguez L., Castillo O., Soria J., Melin P., Valdez F., Gonzalez C. I., Martinez G. E., Soto J., A Fuzzy Hierarchical Operator in the Grey Wolf Optimizer Algorithm, Applied Soft Computing 57, 315–328, 2017.

Saka M., Novel HVsaGwo Algorithm for Non-Linear Dynamic Weighted State Feedback With 1DOF-PID based Controllers in AVR, Engineering Science and Technology, an International Journal 59, 2024.

Saremi S., Mirjalili S., Lewis, A., Grasshopper Optimisation Algorithm: Theory and Application, Advances in Engineering Software 105, 30–47, 2017.

Socha K., Dorigo M., Ant Colony Optimization for Continuous Domains, European Journal of Operational Research 185(3), 1155–1173, 2008.

Song X., Tang L., Zhao S., Zhang X., Li L., Huang J., Cai W., Grey Wolf Optimizer for Parameter Estimation in Surface Waves, Soil Dynamics and Earthquake Engineering 75, 147–157, 2015.

Storn R., Price K., Differential Evolution - A Simple and Efficient Heuristic for Global Optimization over Continuous Spaces, Australasian Plant Pathology 38(3), 284–287, 2009.

Sulaiman M. H., Mustaffa Z., Mohamed M. R., Aliman O., Using the Gray Wolf Optimizer for Solving Optimal Reactive Power Dispatch Problem, Applied Soft Computing 32, 286–292, 2015.

Sun G., Tian J., Liu T., Yan X., Huang X., Crashworthiness Optimization of Automotive Parts with Tailor Rolled Blank, Engineering Structures 169, 201–215, 2018.

Van Thieu N, 2023., ENOPPY: A Python Library For Engineering Optimization Problems, https://github.com/thieu1995/enoppy (Accessed: 23.03.2025).

Van Thieu N., Mirjalili S., MEALPY: An Open-Source Library for Latest Meta-Heuristic Algorithms in Python, Journal of Systems Architecture 102871, 2023.

Wang R. B., Hu R. B., Geng F. D., Xu L., Chu S. C., Pan J. S., Meng Z. Y., Mirjalili S., The Animated Oat Optimization Algorithm: A Nature-Inspired Metaheuristic for Engineering Optimization and A Case Study On Wireless Sensor Networks, Knowledge-Based Systems, 113589, 2025.

Wolpert D. H., Macready W. G., No Free Lunch Theorems for Optimization, IEEE Transactions on Evolutionary Computation 1(1), 67–82, 1997.

Xu Y., Zhong R., Cao Y., Zhang C., Yu J., Symbiotic Mechanism-based Honey Badger Algorithm for Continuous Optimization, Cluster Computing 28(2), 2024.

Xu Y., Zhong R., Zhang C., Yu J., Crested Ibis Algorithm and Its Application in Human-Powered Aircraft Design, Knowledge-Based Systems 310, 2025.

Yang B., Zhang X., Yu T., Shu H., Fang Z., Grouped Grey Wolf Optimizer for Maximum Power Point Tracking of Doubly-Fed Induction Generator based Wind Turbine, Energy Conversion and Management 133, 427–443, 2017.

Yapici H., Cetinkaya N., A New Meta-Heuristic Optimizer: Pathfinder Algorithm, Applied Soft Computing Journal 78, 545–568, 2019.

Zhang S., Zhou Y., Li Z., Pan W., Grey Wolf Optimizer for Unmanned Combat Aerial Vehicle Path Planning, Advances in Engineering Software 99, 121–136, 2016.

Zhang S., Zhou Y., Grey Wolf Optimizer based on Powell Local Optimization Method for Clustering Analysis, Discrete Dynamics in Nature and Society 481360, 2015.

Zhong R., Yu J., Zhang C., Munetomo M., SRIME: A Strengthened RIME with Latin Hypercube Sampling and Embedded Distance-based Selection for Engineering Optimization Problems, Neural Computing and Applications 36(12), 2024.

Zhong R., Hussien A. G., Yu J., Munetomo M., LLMOA: A Novel Large Language Model Assisted Hyper-Heuristic Optimization Algorithm, Advanced Engineering Informatics 64, 2025.

Zhong R., Wang Z., Hussien A. G., Houssein E. H., Al-Shourbaji I., Elseify M. A., Yu J., Success History Adaptive Competitive Swarm Optimizer With Linear Population Reduction: Performance Benchmarking and Application in Eye Disease Detection, Computers in Biology and Medicine 186, 2025.

Zhong R., Zhang C., Yu J., Chaotic Vegetation Evolution: Leveraging Multiple Seeding Strategies and a Mutation Module for Global Optimization Problems, Evolutionary Intelligence 17(4), 2024.

Zhong R., Zhang C., Yu J., Cooperative Coati Optimization Algorithm with Transfer Functions for Feature Selection and Knapsack Problems, Knowledge and Information Systems, 66(11), 2024.

Zhou J., Zhu W., Zheng Y., Li C., Precise Equivalent Model of Small Hydro Generator Cluster and Its Parameter Identification using Improved Grey Wolf Optimiser, IET Generation, Transmission and Distribution 10(9), 2016.

JOURNAL of
MATERIALS and MECHATRONICS:A

e-ISSN 2717-8811
JournalMM, 2025, 6(1), 170-184
https://doi.org/10.55546/jmm.1639413

Araştırma Makalesi / Research Article

Toz Metalurjisi ile Üretilen Nano Bor Nitrür Takviyeli Alüminyum Matrisli Kompozitlerin Mekanik ve İçyapı Özelliklerinin İncelenmesi

Hıdır Sercan ÇUBUK[1*], Uğur ÇAVDAR[2]

[1*] Dokuz Eylül Üniversitesi, Fen Bilimleri Enstitüsü, Konstrüksiyon ve İmalat Doktora Programı, İzmir, Türkiye,
ORCID ID: https://orcid.org/0000-0001-6598-351X, hsercancubuk@gmail.com
[2] İzmir Demokrasi Üniversitesi, Mühendislik Fakültesi, Makine Mühendisliği Bölümü, İzmir, Türkiye,
ORCID ID: https://orcid.org/0000-0002-3434-6670, ugur.cavdar@idu.edu.tr

Geliş/ Received: 13.02.2025; **Revize/Revised:** 19.03.2025 **Kabul / Accepted:** 08.05.2025

ÖZET: Alüminyum, düşük yoğunluğu ve yüksek korozyon direnci nedeniyle mühendislik uygulamalarında yaygın olarak tercih edilen bir metaldir. Ancak, sınırlı mekanik dayanımı bazı uygulamalarda kısıtlayıcı bir faktör olmaktadır. Bu nedenle, mekanik özelliklerini iyileştirmek amacıyla seramik malzemelerle takviye edilebilmektedir. Bu çalışmada, Nano Bor Nitrür (NBN) takviyeli alüminyum matrisli kompozitler, toz metalurji yöntemi ile üretilmiş ve mekanik ile mikro yapısal özellikleri incelenmiştir. Saf Alüminyum kontrol numunesine ek olarak; kütlece %0.1, %0.5, %1, %2 ve %5 oranlarında NBN içeren toz karışımları hazırlanmış, ardından 600°C, 650°C ve 700°C sıcaklıklarında sinterlenerek toplamda 18 farklı kompozit numune elde edilmiştir. Yapılan sertlik testleri, %0.5 NBN katkılı ve 600°C'de sinterlenen numunenin en yüksek sertlik değerine ulaştığını göstermiştir. Ancak, daha yüksek katkı oranları ve sinterleme sıcaklıkları sertlikte düşüşe neden olmuştur. Taramalı elektron mikroskobuyla yapılan analizde, düşük NBN oranlarında homojen dağılım sağlandığını, ancak %2 ve üzeri katkılarda kümelenme oluştuğunu ortaya koymuştur. Yoğunluk ölçümleri, %5 NBN katkılı ve 600°C'de sinterlenen numunenin en yüksek yoğunluğa ulaştığını, ancak 700°C'de gözenek oluşumunun arttığını göstermiştir. Genel olarak, uygun NBN katkı oranı ve sinterleme sıcaklığının belirlenmesinin, NBN takviyeli alüminyum matrisli kompozitlerin mekanik özelliklerini optimize etmek için kritik bir faktör olduğu sonucuna varılmıştır.

Anahtar Kelimeler: Alüminyum, Nano, Bor nitrür, Toz metalurji, Sinterleme

*Sorumlu yazar / Corresponding author: hsercancubuk@gmail.com
Bu makaleye atıf yapmak için /To cite this article

Çubuk, H. S., Çavdar, U. (2025). Toz Metalurjisi ile Üretilen Nano Bor Nitrür Takviyeli Alüminyum Matrisli Kompozitlerin Mekanik ve İçyapı Özelliklerinin İncelenmesi. Journal of Materials and Mechatronics: A (JournalMM), 6(1), 170-184.

Investigation of Mechanical and Microstructure Properties of Nano Boron Nitride Reinforced Aluminum Matrix Composites Produced by Powder Metallurgy

ABSTRACT: Aluminum is a metal widely preferred in engineering applications due to its low density and high corrosion resistance. However, its limited mechanical strength is a limiting factor in some applications. Therefore, it can be reinforced with ceramic materials to improve its mechanical properties. In this study, Nano Boron Nitride (NBN) reinforced aluminum matrix composites were produced by powder metallurgy method and their mechanical and microstructural properties were investigated. In addition to the Pure Aluminum control sample; Powder mixtures containing 0.1%, 0.5%, 1%, 2% and 5% NBN were prepared and then sintered at 600°C, 650°C and 700°C to obtain a total of 18 different composite samples. Hardness tests showed that the sample with 0.5% NBN added and sintered at 600°C reached the highest hardness value. However, higher additive rates and sintering temperatures caused a decrease in hardness. Analysis by scanning electron microscopy revealed that homogeneous distribution was achieved at low NBN ratios, but clustering occurred at 2% and above contributions. Density measurements showed that sample with 5% NBN added and sintered at 600°C reached the highest density, but pore formation increased at 700°C. Overall, it is concluded that determining the appropriate NBN additive ratio and sintering temperature is a critical factor to optimize the mechanical properties of NBN reinforced aluminum composites.

Keywords: Aluminum, Nano, Boron nitride, Powder metallurgy, Sintering

1. GİRİŞ

Alüminyum (Al), hafifliği, yüksek mukavemet/ağırlık oranı ve yüksek korozyon direnci gibi özellikleri sayesinde dünya çapında en yaygın kullanılan metallerden biridir. Bu özellikleri sayesinde, havacılık, otomotiv, inşaat, biyoteknoloji ve ambalajlama gibi çok çeşitli mühendislik alanlarında geniş kullanım alanına sahiptir (Başer ve ark., 2022; Erçetin ve ark., 2022; Arora ve Saxena, 2023). Ancak, saf Al ’un düşük mekanik dayanımı, özellikle yüksek performans gerektiren uygulamalarda sınırlayıcı bir faktör olmaktadır. Bu yüzden Al matrisli kompozit malzemelerin geliştirilmesi halen önemli bir araştırma konusudur. Özellikle, seramik esaslı takviyeler eklenerek Al matrisinin mekanik ve fiziksel özelliklerinin iyileştirilmesi ve daha dayanıklı ve fonksiyonel malzemelerin elde edilmesi sağlanabilmektedir (Pariyar ve ark., 2021; Pandey ve ark., 2021; Thomas ve ark., 2024). Nano Bor Nitrür (NBN), altıgen (hegzagonal) kristal yapısı (h-BN) ve grafite benzer özellikleriyle Al matrisli kompozitlerde kullanılan seramik takviyelerden biridir. Yüksek sıcaklık dayanımı, kimyasal kararlılığı ve yağlayıcı özellikleri (Aydın, 2018) sayesinde geniş bir uygulama alanı bulunmaktadır. Malzemenin nano boyutta kullanımı ise yüzey alanını artırarak fiziksel ve kimyasal aktivitelerde iyileşmeler sağlamaktadır (Pandey ve ark., 2021; Moustafa ve ark., 2022; Irshad ve ark., 2023). Bu özellikler, NBN'ün Al matrisli kompozitlerde hem mekanik performansı artırmasını hem de termal iletkenliği iyileştirmesini sağlamaktadır (Lahiri ve ark., 2013).

Toz Metalurjisi (TM) yöntemi, NBN takviyeli Al matrisli kompozitlerin ekonomik ve çevresel olarak sürdürülebilir şekilde üretilmesine olanak tanımaktadır. Bu yöntem sayesinde, belirli sıcaklık ve basınç altında sinterleme yoluyla homojen takviye dağılımına sahip kompozitler elde edilebilmektedir. Homojen dağılım, kompozit malzemenin mekanik ve fiziksel özelliklerini iyileştirmede kritik rol oynamaktadır. Üretilen metal matrisli kompozitlerin yoğunluk ölçümleri, sertlik değişimleri veya mikro yapıdaki gözenek oranları gibi değişkenler sinterleme işleminin

başarısını belirlemektedir (Pillari ve ark., 2016; Erçetin ve ark., 2020; Monahar ve ark., 2021; Kumar ve Bharti, 2021; Erçetin ve ark. 2023; Thomas ve ark., 2024; Çubuk ve ark., 2025).

Literatürde, farklı NBN oranlarının ve sinterleme sıcaklıklarının Al matrisli kompozitlerin mekanik özellikleri üzerindeki etkileri araştırılmıştır (Lahiri ve ark., 2013; Nautiyal ve ark., 2016; Firestein ve ark., 2017; Ghosh ve ark., 2024). Nautiyal ve ark. (2016) yaptıkları çalışmada, %0.5 oranında h-BN takviyeli Al kompozitlerini Kıvılcım Plazma Sinterleme (SPS) yöntemiyle üreterek, bu takviyenin aşınma direncini ve sertliği artırdığını bulmuşlardır. Ayrıca, çalışmada optimum performansın daha düşük takviye oranlarında elde edildiği vurgulamışlardır. Lahiri ve ark. (2013) yaptıkları çalışmada, BNNT takviyeli Al kompozitlerinde %2 BNNT oranında maksimum mekanik dayanım elde edildiğini rapor etmiş, ancak %2'nin üzerindeki takviye oranlarında aglomerasyon nedeniyle mekanik özelliklerde kayıplar yaşandığını belirtmişlerdir. Firestein ve ark. (2017) yaptıkları çalışmada, Kıvılcım Plazma Sinterleme (SPS) yöntemiyle %0.5, %1.5, %3, %4.5, %7 ve %10 oranlarında Bor Nitrür nano parçacıkları (BNNP) ve mikro parçacıkları (BNMP) ile takviye edilmiş Al kompozitler üretmişlerdir. Ürettikleri %4.5-7 BNMP içeren numunelerde çekme mukavemetinde en yüksek değerlere ulaştığını rapor etmişlerdir. Öte yandan Ghosh ve ark. (2024) yaptıkları çalışmada ise, h-BN takviyeli Al nano kompozitlerde %3 h-BN oranında en yüksek bağıl yoğunluk elde edildiğini yayımlamışlardır. Bu çalışmaların tümü, takviye oranı ve sinterleme koşullarının mekanik performans üzerindeki kritik etkisini vurgulamaktadır (Lahiri ve ark., 2013; Nautiyal ve ark., 2016; Firestein ve ark., 2017; Ghosh ve ark., 2024).

Bu çalışmada, saf Al ve NBN takviyeli Al kompozitleri TM yöntemiyle üretilmiş, farklı sinterleme sıcaklıkları ve NBN oranlarının mekanik ve mikro yapısal özelliklere etkisi incelenmiştir. Sertlik, mikro yapı, yoğunluk ve enerji verimliliği bulguları değerlendirilmiş ve literatürle karşılaştırılmıştır. Ayrıca burada yapılan optimizasyonların ileride yapılacak farklı sinterleme yöntemlerine ve malzeme seçimine yol gösterici bir nitelik sağlayabileceği düşünülmektedir.

2. MATERYAL VE YÖNTEM

2.1 Materyal

Bu çalışmada kullanılan Al tozları, %98.85 saflığa sahiptir. Ortalama 15 µm parçacık boyutundadır ve gaz atomizasyonu yöntemiyle üretilmiştir (Nanokar Nanoteknoloji, İstanbul). NBN tozları ise %99.85 saflıkta olup, 65–75 nm boyut aralığında dağılım göstermektedir. Hegzagonal (h-BN) yapıya sahiptir ve gaz atomizasyonu yöntemi ile üretilmiştir (Nanografi Nano Teknoloji, Ankara). Çizelge 1'de saf Al tozunun bazı özellikleri, Çizelge 2'de NBN tozunun bazı özellikleri ve Şekil 1'de Al ve NBN tozlarının SEM görüntüleri verilmektedir.

Çizelge 1. Saf alüminyumun tozunun bazı özellikleri

Alüminyum Parametreleri	**Değeri veya Özelliği**				
Üretim Şekli	Gaz Atomizasyonu				
Tane Şekli	Düzensiz/ Küresel / Pul				
Tane Boyutu (µm)	15				
Yoğunluk (gr/cm^3)	1.25- 1.45				
Bileşen (%)	Al	Fe	Si	Cu	Diğer
	98.85	0.5	0.35	0.15	0.15

Çizelge 2. Nano bor nitrür tozunun bazı özellikleri

Nano Bor Nitrür Parametreleri	Değeri veya Özelliği
Malzeme Saflığı (%)	99.85
Ortalama Parçacık Boyutu (nm)	65-75
Gerçek Yoğunluk (g/cm^3)	2.25
Moleküler Ağırlık (g/mol)	24.82
Kristalite (h-BN)	Hegzagonal (h-BN)
Termal İletkenlik (W/m)	29 ila 60
Termal Genleşme (µm/m)	0.54 ila 18
Gencin Modülü (GPa)	14 ila 60
Tam Kütle (g)	25,0124

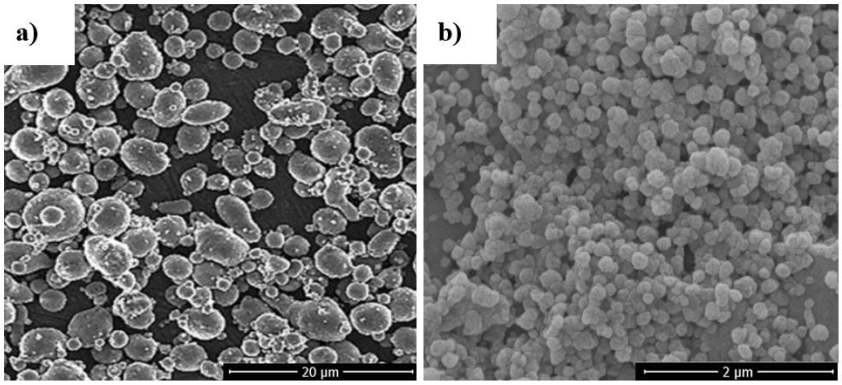

Şekil 1. Çalışmada kullanılan a) alüminyum ve b) nano bor nitrür tozlarının SEM görüntüleri

2.2 Numune Hazırlığı

Bu çalışma katkı oranlarının, sinterleme koşullarının ve sinterleme sıcaklıklarının optimizasyonuyla başlamıştır. Katkı oranlarını belirlemek amacıyla, saf Al tozundan üretilen kontrol numunelerine ek olarak, kütlece %0.1, %0.5, %1, %2 ve %5 NBN içeren metal matrisli kompozitler seçilmiştir. Katkı oranları ve sıcaklıklar, daha önce yapılmış literatür çalışmaları temel alınarak belirlenmiştir. Literatür araştırmalarındaki katkı oranlarının, %0.1–%5 aralığında optimum mekanik özelliklerin elde edilebildiğini; ancak %2'nin üzerindeki değerlerde aglomerasyon nedeniyle beklenen özellikleri olumsuz yönde değiştirebileceğini göstermektedir. (Nautiyal ve ark., 2016; Lahiri ve ark., 2013; Firestein ve ark., 2017; Antillon ve ark., 2018). Bu yüzden %5'in üzerindeki katkı oranlarının mekanik performansı artırmak yerine azaltabileceği, %0.1'in altındaki oranların ise anlamlı bir değişken sunmayacağı öngörülerek çalışma kapsamına dâhil edilmemiştir. Çalışmanın hiçbir aşamasında oksit giderme veya yüzey modifikasyonu gibi bir ön işlem uygulanmamıştır. Çünkü literatürde Al ve NBN tozlarında oluşan yüzey modifikasyonlarının bağlanmayı zayıflatarak homojen yoğunlaşmayı engelleyebileceği belirtilmektedir (Chen ve ark., 2015; Lv ve ark., 2025).

Bu kapsamda toplamda altı farklı metal matrisli kompozit tozu oluşturulmuştur. Her bir toz numunesinin hassas bir şekilde hazırlanabilmesi için Weightlab Instruments marka WSA-224T model, 0.0001 g hassasiyetli elektronik terazi kullanılmıştır. Daha sonra, tartılan Al ve Al-NBN esaslı tozlar, homojen bir dağılım elde etmek amacıyla sızdırmaz V tipi bir karıştırıcıda, 60 dakika (dak.) boyunca 40 dev/dak. hızında karıştırılmıştır. Karıştırma sonucu elde edilen homojen toz karışımları, tek eksenli ve tek tesirli bir kalıpta soğuk pres yöntemiyle şekillendirilmiştir. Bu bağlamda, "tek eksen" terimi presleme kuvvetinin yalnızca dikey yönde uygulandığını; "tek tesir" ise bu kuvvetin

yalnızca üst zımbadan iletilip alt zımbanın sabit kaldığını ifade etmektedir. Böylece presleme işlemi, eksenel ve yerçekimi yönüyle aynı doğrultuda tek yönlü olarak gerçekleştirilmiştir.

Metal matrisli kompozitlerin sıkıştırılması 20 bar basınçla, Hidropir marka pres kullanılarak uygulanmıştır. Kullanılan sıkıştırma kalıbı, alaşımlı sertleştirilmiş çelikten üretilmiş bir silindirdir. Dış çapı 56 mm ve yüksekliği 61 mm olarak tasarlanmıştır. Kalıba giren zımbanın çapı ise 16 mm olarak belirlenmiştir. Sıkıştırma sonrasında elde edilen bozuk para benzeri silindir ham numunelerin çapı 16 mm (Hata Payı - Error Range: E.R. ±0.5%) ve kalınlığı 4.96 mm (E.R. ±0.5%) olarak ölçülmüştür. Bu aşamaların her biri, numunelerin mekanik ve mikro yapısal özelliklerinin homojenliğini sağlamak amacıyla hassasiyetle yapılmaya çalışılmıştır. Şekil 2'de %5 NBN içeriğinin tartılması, metal matrisli kompozitlerinin kalıp içerisine doldurulması ve presleme sonrası elde edilen ham numuneler gösterilmektedir.

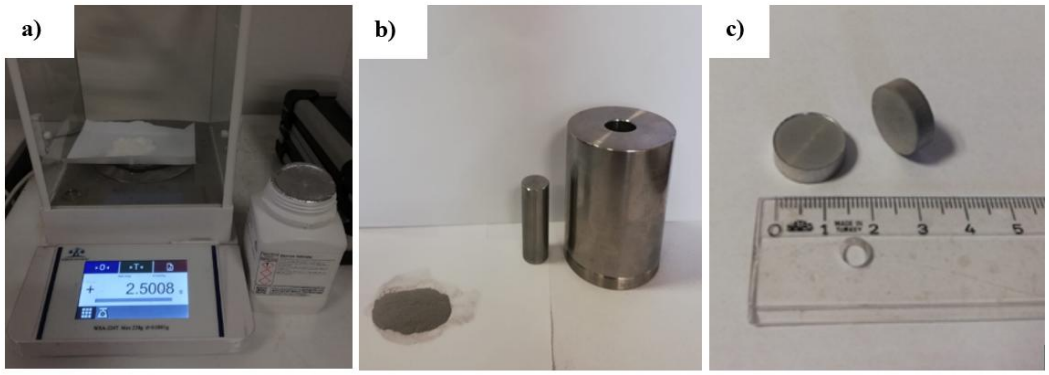

Şekil 2. a) %5 NBN içeriğinin tartılması, b) karışmış ve toz haldeki metal matrisli kompozitlerin kalıp içerisine doldurulması, c) presleme sonrası elde edilen bozuk para benzeri silindir ham numuneler

Sıkıştırma sonrası elde edilen ham numuneler, mekanik ve mikroyapısal özelliklerin değerlendirilmesi amacıyla fırın içerisine alınmış ve 600°C, 650°C ve 700°C'de atmosfer koşullarında (hava ortamında) sinterlenmiştir. Bu çalışmada fırın kullanılmasının sebebi olarak donanım erişilebilirliği ve süreç kolaylığı verilebilmektedir. Ayrıca numune hazırlamada yüksek üretim hacmine uygunluğu ve basit sinterleme koşulları bu yöntemin uygulama açısından pratikliğini artırmaktadır (Çivi ve Atik, 2025). Alternatif yöntemler arasında yer alan SPS ve İndüksiyon gibi gelişmiş yöntemler; daha hızlı sinterleme süreleri, daha yüksek bağıl yoğunluklar ve tane büyümesini sınırlayan etkileriyle ön plana çıkmaktadır. Ancak bu yöntemler donanım maliyeti ve karmaşık yapısı gibi dezavantajlara sahiptir ve araştırılması gerekir (Firestein ve ark., 2017; Nautiyal ve ark., 2016; Dudina ve ark., 2023; Erçetin ve ark, 2023; Sekar ve Panigrahi, 2024). Dolayısıyla bu çalışma kapsamında kullanılan fırın, basit sinterleme koşulları ve düşük donanım gereksinimiyle laboratuvar ölçeğinde güvenilir ve tekrarlanabilir sonuçlar sağlamak açısından uygun bulunmuş ve gelecek çalışmalarda gelişmiş sinterleme teknikleriyle karşılaştırmalı analizlerin yapılmasının ön çalışması olarak tercih edilmiştir.

İşlemin gerçekleştiği fırın, belirlenen sıcaklıklara 0.173°C/saniye ısıtma hızıyla ulaşmıştır. Ardından numuneler ilgili bekleme sıcaklıklarında fırına yerleştirilmiş ve 60 dakika süreyle hava atmosferinde sinterlendikten sonra fırın dışına alınarak normal atmosfer koşullarında soğumaya bırakılmıştır. Süreç sonunda farklı katkı oranları ve sinterleme sıcaklığı parametrelerine uygun olarak toplam 18 farklı özelliğe sahip numune üretilmiştir. Her bir numunenin ortalama ağırlığı 2.5 gram (E.R. ±0.3%) olarak ölçülmüştür. Çizelge 3'te numunelerin kütlece takviye oranı ile sıcaklıkları, Şekil 3'te ise üretilen numuneler gösterilmiştir.

Çizelge 3. Numunelerin kütlece takviye oranı ve sinterleme sıcaklıkları

Numune No.	Metal Matris	NBN Kütlece Katkı Oranı *(%)*	Sıcaklık *(°C)*
1	Saf Al	0 (Sıfır)-Kontrol Numunesi	600°C
2	Saf Al	0.1	600°C
3	Saf Al	0.5	600°C
4	Saf Al	1	600°C
5	Saf Al	2	600°C
6	Saf Al	5	600°C
7	Saf Al	0 (Sıfır)-Kontrol Numunesi	650°C
8	Saf Al	0.1	650°C
9	Saf Al	0.5	650°C
10	Saf Al	1	650°C
11	Saf Al	2	650°C
12	Saf Al	5	650°C
13	Saf Al	0 (Sıfır)-Kontrol Numunesi	700°C
14	Saf Al	0.1	700°C
15	Saf Al	0.5	700°C
16	Saf Al	1	700°C
17	Saf Al	2	700°C
18	Saf Al	5	700°C

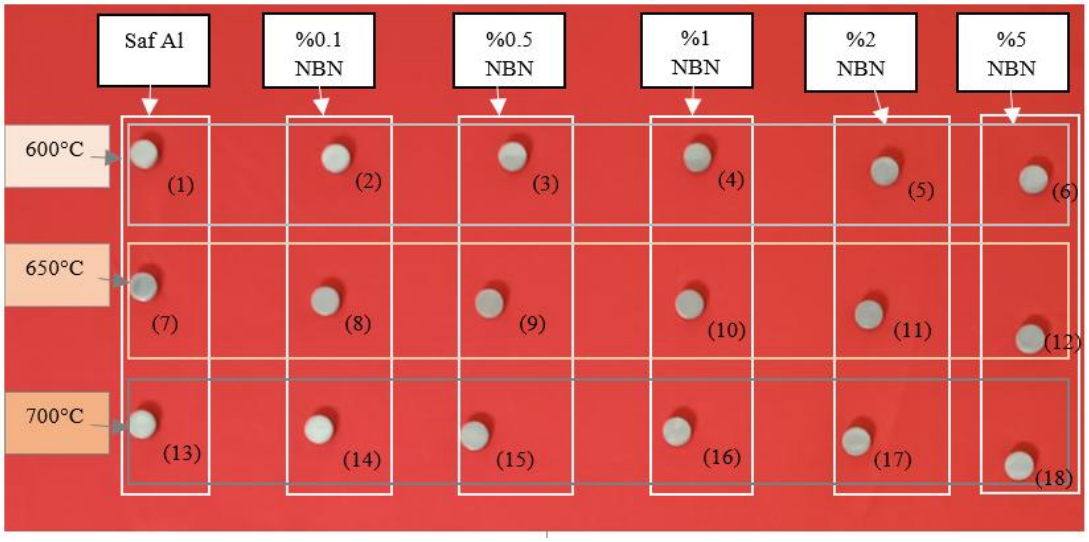

Şekil 3. Farklı katkı oranı ve sıcaklık parametreleriyle hazırlanmış numuneler

Numunelerin analiz ve değerlendirme sürecine geçilmeden önce, mekanik ve mikro yapısal testlerin gerçekleştirilebilmesi için yüzey hazırlık işlemleri uygulanmıştır. Bu kapsamda tüm numuneler 100-2500 grit aralığında silisyum karbür (SiC) zımpara kullanılarak zımparalanmış, ardından 6 µm ve 1 µm elmas süspansiyonlu çuha ile parlatılmıştır. Parlatma işleminden sonra mikro yapısal detayların daha net bir şekilde incelenebilmesi için, %1 hidroflüorik asit (HF), %1.5 hidroklorik asit (HCl), %2.5 nitrik asit (HNO_3) ve %95 saf su içeren Keller reaktifi ile 4 saniye boyunca dağlanmıştır. Süreç, mikro yapısal analizlerde tane sınırlarının ve faz dağılımının daha iyi gözlemlenmesini sağlamak amacıyla kontrollü bir şekilde yürütülmüştür.

2.3 Analiz ve Değerlendirme

Numunelerin sertlikleri Metkon Duroline-LV Vickers Hardness Tester (HV) sertlik ölçme cihazında ASTM E92 standardına uygun olarak 10 saniye (san.) süre ve 3 kgf yükte gerçekleştirilmiştir. Şekil 4'te gösterildiği üzere, her numune üzerinde dış çaptan merkeze doğru beş adet ölçüm noktası belirlenmiştir. Bu beş ölçüm noktasının her birinden, aynı konumda olmak üzere ardışık beş sertlik ölçümü yapılmış (örneğin Şekil 4'te gösterilen 3. noktadan 5 ölçüm yapılmış) ve elde edilen değerlerin aritmetik ortalaması hesaplanarak (E.R.i en aza indirmek amacıyla) ilgili noktanın ortalama sertlik değeri belirlenmiştir. Sertlik ölçümleri, kütlece farklı katkı oranları (%0.1, %0.5, %1, %2 ve %5) ve sinterleme sıcaklıklarına (600°C, 650°C, 700°C) göre değerlendirilmiştir. Şekil 4'te sertlik ölçüm noktalarının numune üzerindeki şematik konumu verilmektedir.

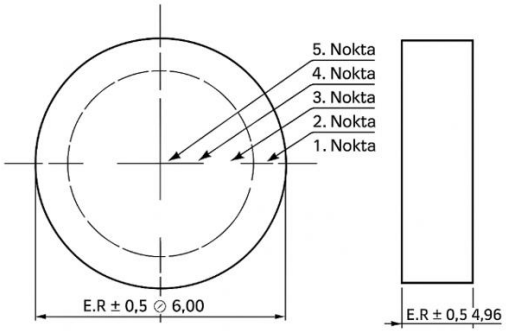

Şekil 4. Sertlik ölçüm noktalarının numune üzerindeki şematik konumu

Numunelerin mikro yapısal özellikleri ise Taramalı Elektron Mikroskobu (SEM) kullanılarak değerlendirilmiştir. SEM görüntüleme işlemi FEI marka QUANTA FEG 250 model cihaz kullanılarak yapılmıştır. SEM analizleri, NBN parçacıklarının Al matrisindeki dağılımını ve sinterleme sürecinde oluşan değişiklikleri incelemek amacıyla gerçekleştirilmiştir.

Numunelerin yoğunluk ölçümleri, ASTM B962-17 standardına uygun olarak Arşimet prensibiyle gerçekleştirilmiştir. Bu yöntemde, sinterleme işlemi sonrası elde edilen numunelerin tartı üzerindeki ve su içerisinde asılıyken kütleleri ölçülerek deneysel yoğunluklar hesaplanmıştır. Teorik yoğunluk hesaplamaları ise, Eşitlik 1 de verilen formül kullanılarak, Al ve NBN bileşenlerinin yoğunlukları (ρ_{Al} = 2.70 g/cm^3 ve ρ_{NBN} = 2.25 g/cm^3) ve kütlece yüzdeleri dikkate alınarak yapılmıştır. Deneysel ve teorik yoğunluk değerleri kullanılarak Eşitlik 2 yardımıyla bağıl yoğunluk (BD) değeri hesaplanmıştır. Aşağıda ilgili bağıntılar sunulmaktadır.

$$\rho_{teorik} = (w_{Al} \cdot \rho_{Al}) + (w_{NBN} \cdot \rho_{NBN}) \quad (1)$$

$$BD(\%) = \left(\frac{\rho_{deneysel\ yoğunluk}}{\rho_{teorik\ yoğunluk}}\right) \times 100 \quad (2)$$

Çalışmada tek bir sıkıştırma basıncı uygulandığı için homojenlik veya gözeneklilik doğrudan ölçülmemiştir. Bağıl yoğunluk değerleri ve SEM görüntüleri değerlendirilerek çıkarımlarda bulunulmuştur.

Son olarak sinterleme sırasında, fırının tükettiği enerji miktarı kWh cinsinden ENTES marka E-M serisi cihaz kullanılarak ölçülmüştür. Bu veriler, enerji tüketimini optimize etmek ve sinterleme maliyetlerini değerlendirmek için kullanılmıştır.

3. BULGULAR VE TARTIŞMA

Bu bölümde, saf Al ile kütlece %0.1, %0.5, %1, %2 ve %5 oranlarında NBN takviyesi içeren Al matrisli kompozitlerin sinterlemesi sonrasında elde edilen sertlik sonuçları, SEM görüntüleri, yoğunluk bulguları ve enerji tüketim verilerine yer verilmiştir.

3.1 Sertlik Bulguları

Elde edilen sertlik sonuçları, 600°C'de sinterlenen %0.5 NBN katkılı numunenin (3) en yüksek sertlik değeri olan 53.5 HV'e ulaştığını göstermiştir. Bu katkı oranı sertlik optimizasyonu açısından tepe noktayı oluşturmaktadır. Ancak, %0.5 NBN katkısından sonra, katkı oranındaki artışa bağlı olarak sertlik değerlerinde lineer bir azalma gözlemlenmiştir. Ayrıca, aynı kimyasal kompozisyona sahip malzemelerde sinterleme sıcaklığının 600°C'den 700°C'ye yükseltilmesi durumunda da sertlik değerlerinde bir düşüş meydana geldiği anlaşılmıştır. Bunun temel sebebi, yüksek sıcaklıkların mikro yapıda gözenek oluşumunu artırarak mekanik özellikleri olumsuz etkilemesi olabilmektedir (Şenel ve ark., 2018). Öte yandan, 700°C sinterlenen %5 NBN içeren numunede (18) sertlik değeri 28.7 HV'e kadar düşmüştür. Bu durum, yüksek katkı oranlarında NBN partiküllerinin homojen dağılım göstermekte zorlanması ve aglomerasyon eğiliminin artmasıyla açıklanabilmektedir (Aslan ve ark., 2020).

Literatürdeki benzer çalışmalarla kıyaslandığında, %0.5 Bor Nitrür (BN) katkılı Al kompozitlerinin Kıvılcım Plazma Sinterleme (SPS) yöntemiyle üretildiği ve bu katkı oranına kadar sertliğin arttığı, ancak daha yüksek oranlarda aglomerasyon nedeniyle mekanik özelliklerin düştüğü rapor edilmiştir (Nautiyal ve ark., 2016). Bu bulgu, mevcut çalışmada %0.5 NBN katkısının en yüksek sertlik değerini sağlayan katkı oranı olduğu sonucunu desteklemektedir. Başka bir çalışmada ise, BN nano parçacık (BNNT) takviyeli Al kompozitlerinde %2'den daha fazla takviye oranlarında aglomerasyon nedeniyle mekanik özelliklerde düşüş yaşandığı bildirilmiştir (Lahiri ve ark., 2013). Mevcut çalışmada %2 ve %5 NBN katkısında sertlik değerlerinde düşüşler gözlemlenmiştir. Şekil 5'te sinterleme sonucunda elde edilen sertlik bulguları verilmektedir (E.R. ± %3.24).

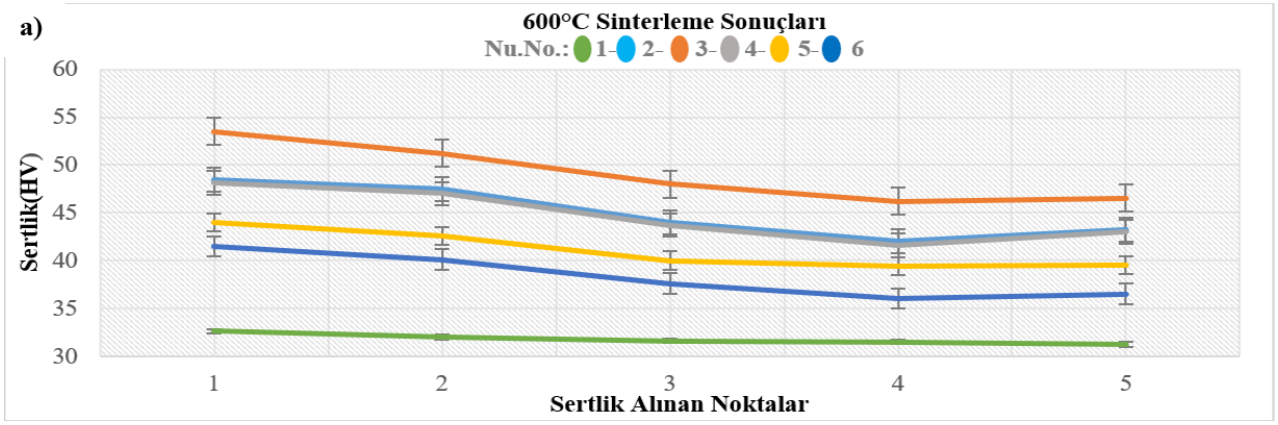

Şekil 5. a) 600°C sinterleme sonucunda numunelerde elde edilen sertlik bulguları, b) 650°C sinterleme sonucunda numunelerde elde edilen sertlik bulguları c) 700°C sinterleme sonucunda numunelerde elde edilen sertlik bulguları d) kütlece %0.5 NBN katkısında HV sertlik sonuçları e) kütlece %5 NBN katkısında HV sertlik sonuçları

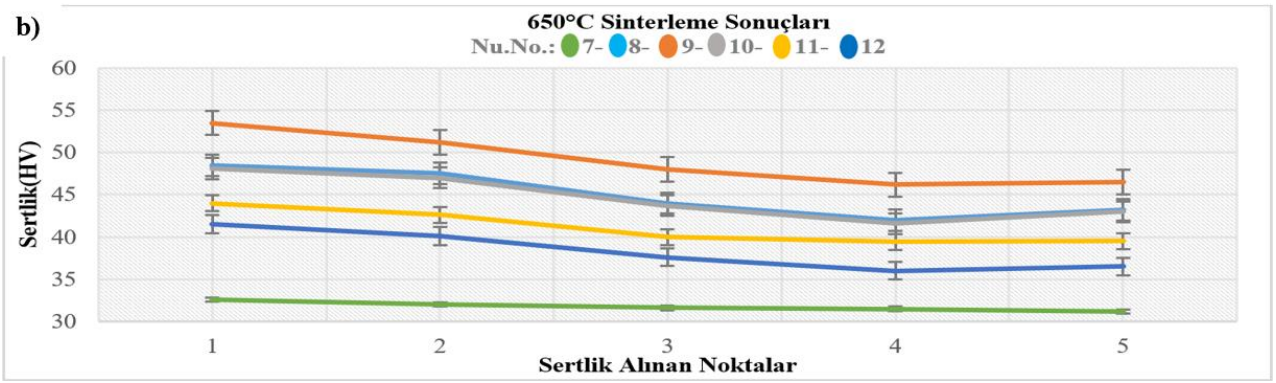

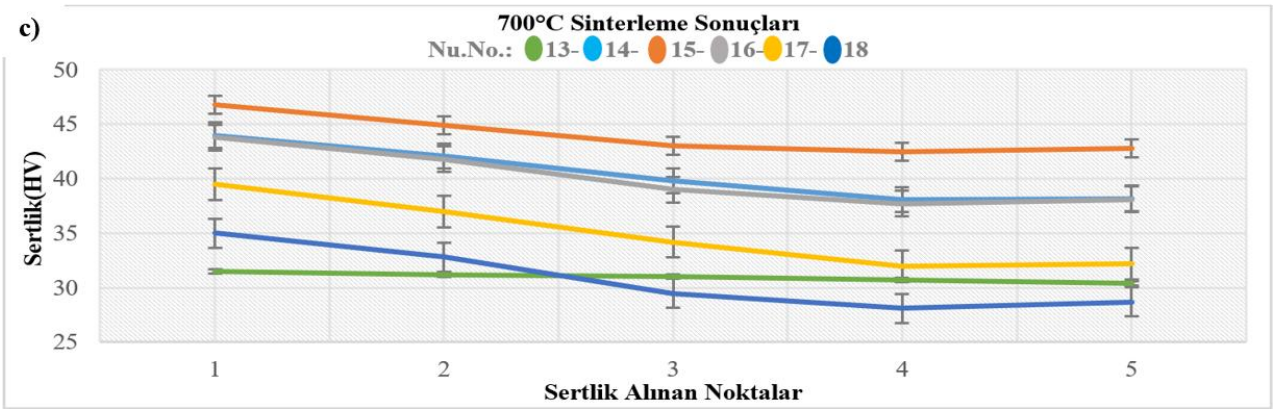

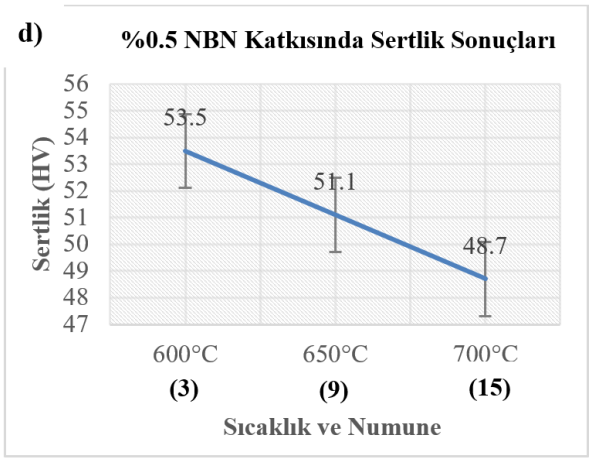

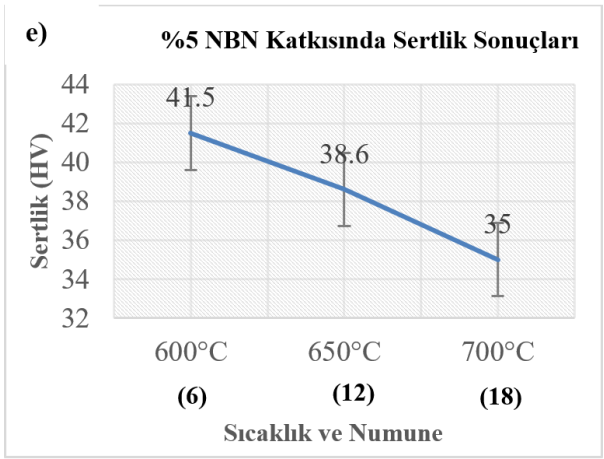

Şekil 5. a) 600°C sinterleme sonucunda numunelerde elde edilen sertlik bulguları, b) 650°C sinterleme sonucunda numunelerde elde edilen sertlik bulguları c) 700°C sinterleme sonucunda numunelerde elde edilen sertlik bulguları d) kütlece %0.5 NBN katkısında HV sertlik sonuçları e) kütlece %5 NBN katkısında HV sertlik sonuçları (devamı)

3.2 Mikro Yapı Bulguları

5 µm – 100 µm büyütme oranlarında gerçekleştirilen SEM analizleri, düşük NBN oranlarında takviyenin Al matrisinde homojen dağıldığını ve iyi bağlandığını ancak %2 ve üzeri katkı oranlarında kümelenme eğilimi gösterdiğini ortaya koymaktadır. Ayrıca, 700°C sinterleme sıcaklığında gözenek oluşumu belirgin hale gelmiştir. Bu gözenekler sinterleme işlemi sırasında oluşan gaz boşalımı ya da yetersiz yoğunlaşmadan kaynaklanmaktadır. Bu gözeneklerin dağılımı ve yoğunluğu, malzemenin mekanik özelliklerini etkileyebilecek önemli bir faktör olarak değerlendirilmiştir. Burada gözlenen bulgular, sertlik sonuçlarıyla da paralellik taşımaktadır. Çünkü aynı kimyasal kompozisyonda olup farklı sinterleme sıcaklığında işlem gören numunelerde sertlik değerinin değiştiği gözlemlenmektedir. SEM incelemelerine bakılarak, daha yüksek sıcaklıkların mikro yapıda gözeneklerin artması ve buna bağlı olarak sertlik özelliklerin olumsuz etkilendiği söylenebilmektedir.

Bu çalışmada gözlemlenen homojen dağılım ve yüksek katkı oranlarındaki kümelenme eğilimi literatürdeki sonuçlarla benzerlik göstermektedir. Bor Nitrür (BN) takviyeli Al kompozitleri ile yapılan bir çalışmada; %2 BN katkısına kadar homojen dağılım gözlemlendiği, ancak daha yüksek oranlarda BN partiküllerinin matriste kümelenerek materyaldeki mekanik özellikleri olumsuz etkilediği belirtilmiştir (Lahiri ve ark., 2013). Bu bulgu, mevcut çalışmada %5 NBN katkısında gözlemlenen kümelenme eğilimi ile örtüşmektedir. Öte yandan yüksek sinterleme sıcaklığının (>650°C) gözenek oluşumunu artırarak partiküllerin dağılımını olumsuz etkilediği raporlanmaktadır (Firestein ve ark., 2017). Benzer şekilde BN takviyeli Al kompozit üretiminde, 700°C ve üzerinde gözenekli yapıya dikkat çekilmektedir (Nautiyal ve ark., 2016). Literatürdeki bu bulgular ile mevcut çalışma değerlendirildiğinde; aynı kimyasal kompozisyondaki 600°C'de sinterlenen numunelerde (1,2,3,4,5,6) daha homojen bir mikro yapı elde edildiği görülürken, 700°C'de sinterlenen numunelerde (13,14,15,16,17,18) belirgin gözenek ve gaz boşlukları oluşumu tespit edilmiştir. Şekil 6'da bazı numunelere ait SEM görüntüleri verilmektedir.

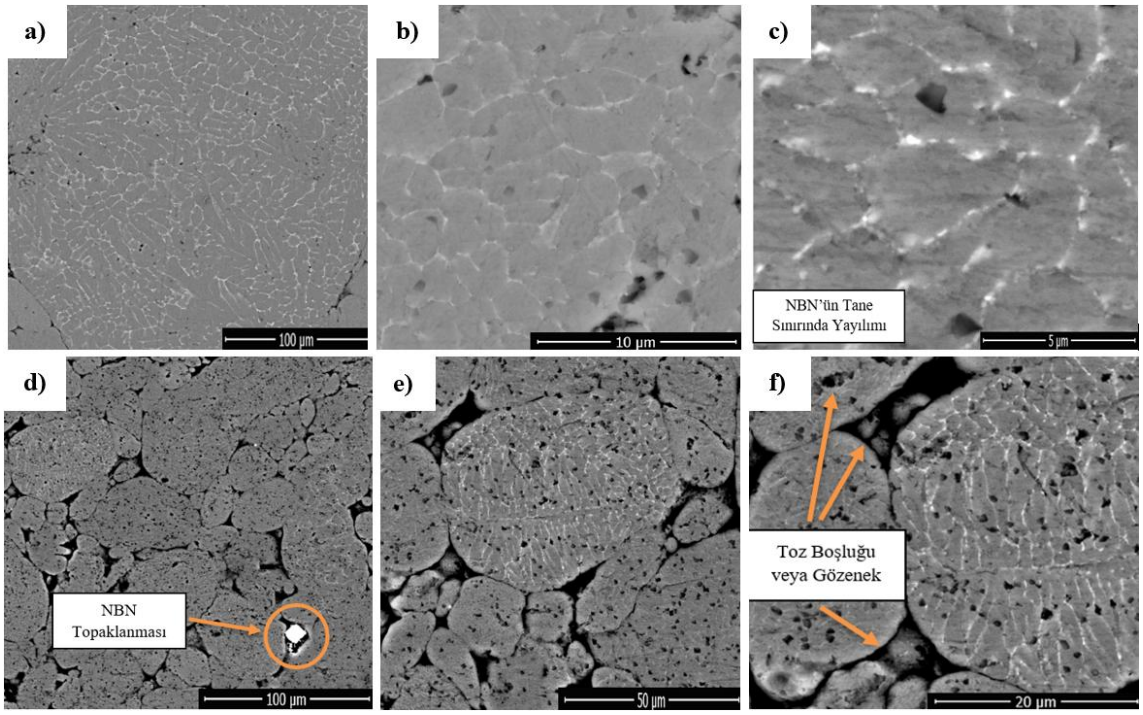

Şekil 6. a)–c) 600 °C'de %0.5 NBN katkısıyla sinterlenen numunede (3) NBN'in tane sınırında bulunması ve yayılımı, d)–f) 700 °C'de %5 NBN katkısıyla sinterlenen numunede (18) gözlenen NBN topaklanması, matris içi dağılım ve belirgin toz boşlukları/gözenek oluşumu

3.3 Yoğunluk Bulguları

Sinterleme sıcaklığı ve NBN katkı oranının yoğunluk değişimi ile bağıl yoğunluk üzerindeki yapılan değerlendirmede, tüm numunelerde sinterleme sonrası yoğunluk değişimi gözlemlenmiştir. 600 °C'de sinterlenen numunelerde görece olarak yoğunluk değişimi daha fazladır. Sinterleme sıcaklığındaki artışa bağlı olarak bazı numunelerde yoğunluk değişiminde azalmanın olduğu anlaşılmıştır. Özellikle %5 NBN katkılı numune (6) 1.399 g/cm³ ile en yüksek yoğunluk değişimi tespit edilmiştir. 700 °C'de sinterlenen %0.5 NBN katkılı numune ise (15), 0.581 g/cm³ ile en düşük yoğunluk değişimi saptanmıştır. Bu bulgu, literatürde belirtilen optimum sinterleme sıcaklıklarının (600°C) gözenek kapanmasını desteklemesiyle uyumludur (Lahiri ve ark., 2013; Nautiyal ve ark., 2016; Firestein ve ark., 2017). Ancak özellikle 700 °C'de sinterlenen numunelerde (13,14,15,16,17,18) gözenek oluşumu ve kısmi ergimeler meydana gelmiştir. Şekil 7'de, 700 °C'de

sinterlenen 15 ve 17 numaralı numunelere ait kısmi ergimeler gösterilmektedir. Bu durum, yüksek sıcaklığın etkisiyle matris içerisindeki gözeneklerin yeterince kapanmaması, malzemenin ergime sıcaklığına yaklaşması veya mikro çatlak oluşumunun artması ile açıklanabilmektedir (Özçatal ve Başpınar, 2020; Tosun ve Kurt, 2020).

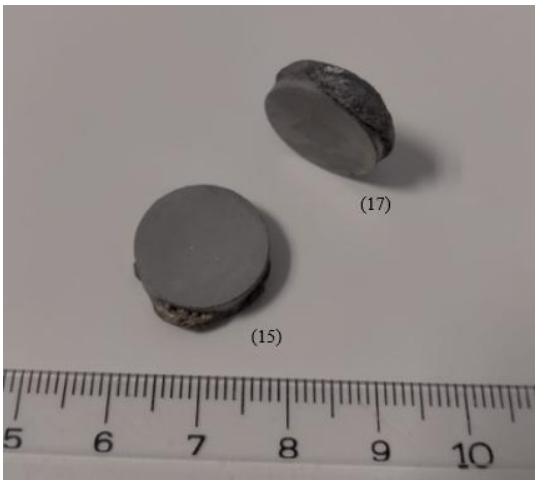

Şekil 7. 700˚C'de sinterlenen ve kısmi olarak ergiyen bazı numuneler

Bunun yanı sıra bağıl yoğunluk değerleri tüm numuneler için %94.7 ile %97.7 aralığında değişmektedir. Ölçülen en yüksek bağıl yoğunluk değeri %97.7 ile 650 °C'deki %5 NBN katkılı numuneye (12), en düşük bağıl yoğunluk değeri ise 700 °C'de NBN katkısı olmadan sinterlenen kontrol numunesine (13) aittir. Bu oranlar, sinterleme sonrası numunelerin yoğunlaşabildiğini ve gözenekliliğin azaldığını göstererek litratürle benzer sonuçları vermiştir. Örneğin Bor Nitrür takviyeli Al nanokompozitleriyle yapılan bir çalışmada; %3 katkılı Al kompozitlerinde yüksek bağıl yoğunluk (%94.11) elde edildiği görülmüştür (Ghosh ve ark., 2024). Ancak buradaki bağıl yoğunluk değerlerinde, katkı oranı veya sinterleme sıcaklığına bağlı düzenli bir artış ya da azalış eğilimi gözlenememiştir. Bunun nedeni olarak takviyenin partikül boyutu, dağılım homojenliği, aglomerasyon eğilimi, deneysel belirsizlikler veya farklı kompozisyonlarda farklı mikroyapıların oluşumu verilebilmektedir (Peng ve ark., 2016; Radhika ve Dobbidi, 2023). Çizelge 4'te çalışmada elde edilen yoğunluk bulguları (E.R. ± %3.94) gösterilmektedir.

Çizelge 4. Numunelerdeki yoğunluk bulguları

No	Sinterleme Sıcaklığı *(°C)*	NBN Katkı Oranı *(%)*	Sinterleme Süresi *(dak)*	Ham Yoğunluk *(g/cm^3)*	Sinterleme Sonrası Yoğunluk *(g/cm^3)*	Yoğunluk Değişimi *(%)*	Teorik Yoğunluk *(g/cm^3)*	Bağıl Yoğunluk (%)
1	600°C	-	60	2.550	2.575	1.145	2.700	95.370
2	600°C	0.1	60	2.552	2.584	1.253	2.699	95.719
3	600°C	0.5	60	2.568	2.600	1.246	2.697	96.376
4	600°C	1	60	2.531	2.558	1.066	2.695	94.898
5	600°C	2	60	2.560	2.589	1.132	2.691	96.209
6	600°C	5	60	2.573	2.609	1.399	2.671	97.105
7	650°C	-	60	2.551	2.569	1.024	2.700	95.148
8	650°C	0.1	60	2.554	2.584	1.174	2.699	95.719
9	650°C	0.5	60	2.551	2.575	0.940	2.697	95.449
10	650°C	1	60	2.585	2.604	0.735	2.695	96.605
11	650°C	2	60	2.562	2.589	1.053	2.691	96.209
12	650°C	5	60	2.594	2.617	0.886	2.677	97.740

Çizelge 4. Numunelerdeki yoğunluk bulguları (devamı)

No	Sinterleme Sıcaklığı *(°C)*	NBN Katkı Oranı *(%)*	Sinterleme Süresi *(dak)*	Ham Yoğunluk *(g/cm^3)*	Sinterleme Sonrası Yoğunluk *(g/cm^3)*	Yoğunluk Değişimi *(%)*	Teorik Yoğunluk *(g/cm^3)*	Bağıl Yoğunluk (%)
13	700°C	-	60	2.575	2.587	0.694	2.700	94.740
14	700°C	0.1	60	2.584	2.601	0.657	2.699	96.349
15	700°C	0.5	60	2.579	2.594	0.581	2.697	96.376
16	700°C	1	60	2.548	2.564	0.627	2.695	96.123
17	700°C	2	60	2.561	2.583	0.859	2.691	96.915
18	700°C	5	60	2.538	2.559	0.827	2.677	95.574

3.4 Enerji Kullanım Bulguları

Çalışmanın tüm aşamalarında elektrik enerjisi tüketim verileri kaydedilmiştir. Sinterleme sıcaklıklarının enerji tüketimi üzerindeki etkisini belirleyebilmek amacıyla harcanan toplam enerji miktarı, ENTES marka E-M serisi güç kalitesi ve enerji verimliliği ölçüm cihazı kullanılarak tespit edilmiştir. 600°C, 650°C ve 700°C sıcaklıklarında gerçekleştirilen sinterleme işlemlerinde sırasıyla 4894 kWh, 6387 kWh ve 7431 kWh enerji tüketimi bulunmuştur (E.R. ± %2.29). Bulgular, sinterleme sıcaklığı arttıkça enerji tüketiminin belirgin şekilde yükseldiğini göstermektedir. Özellikle, alternatif sinterleme yöntemlerinin daha düşük enerji tüketimi sağladığı ve geleneksel fırın sinterlemenin daha yüksek enerji maliyetine neden olduğu yönündeki literatür bulguları, mevcut çalışmadaki enerji sonuçlarını desteklemektedir. Bu çalışmalarda gelecekte enerji tüketiminin azaltılması için alternatif sinterleme yöntemlerinin (örneğin, mikrodalga sinterleme, indüksiyon sinterleme veya SPS) kullanılması önerilmiştir (Nautiyal ve ark., 2016; Firestein ve ark., 2017; Erçetin ve ark., 2024; Çubuk ve ark., 2025). Mevcut çalışmada tüketilen enerji miktarı Çizelge 5'te verilmektedir.

Çizelge 5. Elektrik enerjisi kullanım bulguları

Sıcaklık *(ºC)*	Ayarlanan Sinterleme Sıcaklığına Ulaşma Hızı *(°C/san.)*	Sinterleme Süresi *(dak)*	Tüketilen Toplam Enerji *(kWh)*
600 ºC	0.173	60	4894
650 ºC	0.173	60	6387
700 ºC	0.173	60	7431

4. SONUÇ

Bu çalışmada, Nano Bor Nitrür (NBN) takviyeli alüminyum matrisli kompozitler toz metalurjisi yöntemiyle üretilmiş ve mekanik ile mikroyapısal özellikleri değerlendirilmiştir. 600 °C'de sinterlenen katkısız kontrol numunesinin (1) sertliği 31.78 HV olarak ölçülürken, aynı sıcaklıkta %0.5 NBN katkısı içeren numune (3) %68.34'lük bir artışla 53.5 HV'ye ulaşarak en yüksek sertlik değerini göstermiştir. Buna karşılık, 700 °C'de sinterlenen %5 NBN katkılı numunede (18) sertlik değeri %7.30 azalarak 28.7 HV'ye düşmüştür. Bu bulgular, maximum sertlik değerinin 600 °C sinterleme sıcaklığı ve %0.5 katkı oranında elde edildiğini göstermektedir. SEM analizleri, düşük katkı oranlarında homojen dağılımın sağlandığını; ancak %2 ve üzeri oranlarda parçacık kümelenmeleri ile birlikte 700 °C'de belirgin gözenek oluşumlarının meydana geldiğini ve kısmi ergimelerin olduğunu ortaya koymuştur. Yoğunluk analizlerinde, sinterleme sonrası tüm numunelerde yoğunluk artışı gözlemlenmiştir. En yüksek değişim %5 NBN katkılı numunede (6) (1.399 g/cm³), en düşük ise %0.5 katkılı numunede (15) (0.581 g/cm³) elde edilmiştir. Bunun yanı sıra bağıl yoğunluklar %94.7–97.7 aralığında değişmiş ve literatürle uyumlu sonuçlar bulunmuştur.

Ancak katkı oranı ve sıcaklığa bağlı düzenli bir eğilim gözlenmemiştir. Bu durum, takviyenin dağılım zorlukları ve mikroyapısal farklılıklarla ilişkilendirilerek mevcut yoğunluk sonuçlarının, 600–650 °C sıcaklıkta ve %0.5–2 katkı oranınında daha uygun olduğu anlaşılmıştır. Ayrıca sinterleme sıcaklığının artışı, enerji tüketimini artırarak malzemenin yoğunluğu ve sertliği üzerinde olumsuz etkilere yol açmıştır. Genel olarak bu çalışmada yapılan mekanik ve mikroyapısal değerlendirmede, NBN takviyeli Al matrisli kompozitler için optimum katkı oranının %0.1–1 aralığında ve 600 °C sıcaklıkta olması gerektiği anlaşılmıştır. Bu değerlerin üzerindeki katkı ve sıcaklıklarda mekanik ve mikroyapısal performans olumsuz etkilenmektedir.

İleride yapılacak çalışmalarda, %0.2–%0.9 aralığındaki katkı oranlarının incelenmesi, farklı sinterleme teknikleriyle karşılaştırılması ve Al dışındaki matris malzemelerde NBN takviyesinin performansının değerlendirilmesi önerilmektedir. Ayrıca, bu kompozitlerin aşınma, korozyon ve işlenebilirlik gibi mühendislik uygulamalarındaki performanslarının test edilmesi, endüstriyel kullanım potansiyelinin belirlenmesi açısından önem taşımaktadır.

5. TEŞEKKÜR

Bu makale, İzmir Demokrasi Üniversitesi Fen Bilimleri Enstitüsü'nde Prof. Dr. Uğur ÇAVDAR danışmanlığında yürütülen ve TÜBİTAK BİDEB 2210-C Öncelikli Alanlar Yüksek Lisans Burs Programı kapsamında desteklenen (Baş. No: 1649B022215401). Hıdır Sercan Çubuk'un "Nano Bor Nitrür Takviyeli Alüminyum Tozlarının Ultra Yüksek Frekanslı İndüksiyon Sistemi ile Sinterlenmesi" başlıklı yüksek lisans tezinden üretilmiştir. Araştırmanın kapsamının genişletilmesine sağladığı destek için TÜBİTAK'a teşekkür ederiz.

6. ÇIKAR ÇATIŞMASI

Yazarlar, bilinen herhangi bir çıkar çatışması veya herhangi bir kurum/kuruluş ya da kişi ile ortak çıkar bulunmadığını onaylamaktadırlar.

7. YAZAR KATKISI

Bu makalede Uğur ÇAVDAR çalışmanın kavramsal ve tasarım süreçlerinin belirlenmesi, çalışmanın kavramsal ve tasarım süreçlerinin yönetimi, veri analizi ve yorumlama, fikirsel içeriğin eleştirel incelemesi, Hıdır Sercan ÇUBUK çalışmanın verilerinin toplanması, veri analizi ve yorumlama, makale taslağının oluşturulması, son onay ve tam sorumluluk konusunda katkı sağlamıştır.

8. KAYNAKLAR

Antillon M., Nautiyal P., Loganathan A., Boesl B., Agarwal A. Strengthening in boron nitride nanotube reinforced aluminum composites prepared by roll bonding. Advanced Engineering Materials 20(8), 1800122, 2018.

Arora G. S., Saxena K. K., A Review Study on The İnfluence of Hybridization on Mechanical Behaviour of Hybrid Mg Matrix Composites Through Powder Metallurgy, Mater Today Proceed, 2023. https://doi.org/10.1016/j. matpr.2023.02.217

Aslan M., Ergül E., Kaya A., Kurt H. İ., Yılmaz N. F., Toz Metalurjisi Yöntemiyle Üretilen Al-MgO Kompozitlerin Özelliklerine Sinterleme Sıcaklığının Etkisi, El-Cezeri 7(3), 1131-1139, 2020.

Aydın H., Nanoyapılı Hegzagonal Bor Nitrür Üretimi ve Karakterizasyonu, Fırat Üniversitesi Mühendislik Bilimleri Dergisi 30(2), 269-275, 2018.

Baser T. A., Umay E., Akıncı V., New Trends in Aluminum Die Casting Alloys For Automotive Applications, The Eurasia Proceedings of Science Technology Engineering and Mathematics 21, 79-87, 2022.

Chen Y., Chen T., Zhang S., Li P., Effect of ball milling on microstructural evolution during partial remelting of 6061 aluminum alloy prepared by cold-pressing of alloy powders, Transactions of Nonferrous Metals Society of China, 25, 2113-2121, 2015.

Çubuk, H. S., Mutlu, A., Çavdar, U., Nano bor nitrür takviyeli alüminyum tozlarının ultra yüksek frekanslı indüksiyon sistemi ile sinterlenmesi, Manufacturing Technologies and Applications, 6(1), 41-51, 2025. https://doi.org/10.52795/mateca.1588015

Çivi C., Atik E., Investigation of Induction Sinterability of Powder Metal Parts of Different Shapes and sizes. Mühendis ve Makina, 66(718), 23-38, 2025. https://doi.org/10.46399/muhendismakina.1460609

Dudina D. V., Georgarakis K., Olevsky E. A., Progress in aluminium and magnesium matrix composites obtained by spark plasma, microwave and induction sintering. International Materials Reviews 68(2), 225-246, 2023.

Ercetin A., Özgün Ö., Aslantaş K., Der O., Yalçın B., Şimşir E., Aamir M., Microstructural and mechanical behavior investigations of Nb-reinforced Mg–Sn–Al–Zn–Mn matrix magnesium composites. Metals 13(6), 1097, 2023.

Erçetin A., Aslantas K., Özgün Ö., Micro-End Milling of Biomedical TZ54 Magnesium Alloy Produced Through Powder Metallurgy, Machining Science and Technology 24(6), 924-947, 2020.

Erçetin A., Özgün Ö., Aslantaş K., Toz Metal Al2O3 Takviyeli Mg5Sn Matrisli Kompozitler: Üretim ve Karakterizasyon, Gazi Üniversitesi Mühendislik Mimarlık Fakültesi Dergisi 38(2), 1003-1012, 2022.

Firestein K. L., Corthay S., Steinman A. E., Matveev A. T., Kovalskii A. M., Sukhorukova I. V., Golberg D., Shtansky D. V., High-strength aluminum-based composites reinforced with BN, AlB2 and AlN particles fabricated via reactive spark plasma sintering of Al-BN powder mixtures. Materials Science and Engineering: A 681, 1-9, 2017.

Ghosh A., Shukla U., Sahoo N., Das B., Kar U. K., Shrivastava P., Alam S. N., Development and mechanical characterization of copper-Hexagonal boron nitride metal matrix nanocomposites using powder metallurgy route. Journal of Materials Engineering and Performance 1-17, 2024.

Irshad H. M., Farooq A., Hakeem A. S., Azeem M. Z., Ehsan M. A., Electrochemical Study of Aluminum–Cubic Boron Nitride Composites Synthesized via Spark Plasma Sintering for Engineering Applications, Journal of Alloys and Compounds 965, 171210, 2023.

Kumar N., Bharti A., Review on Powder Metallurgy: A Novel Technique For Recycling and Foaming of Aluminium-Based Materials, Powder Metallurgy and Metal Ceramics, 60, 52-59, 2021.

Lahiri D., Hadjikhani A., Zhang C., Xing T., Li L. H., Chen Y., Agarwal, A., Boron nitride nanotubes reinforced aluminum composites prepared by spark plasma sintering: Microstructure, mechanical properties and deformation behavior. Materials Science and Engineering: A 574, 149-156, 2013.

Lv W., Lv J., Liu J., Chen C., Kang, Y., Sintering dynamic evolution and enhancement mechanism of nano-Cu/boron nitride composite matrix with excellent mechanical properties from the atomic perspective. Composite Structures 354, 118756, 2025.

Manohar G., Pandey K. M., Maity S. R., Effect of Sintering Mechanisms on Mechanical Properties of AA7075/B4C Composite Fabricated by Powder Metallurgy Techniques, Ceramics International 47(11), 15147-15154, 2021.

Moustafa E. B., Mikhaylovskaya A. V., Taha M. A., Mosleh A. O., Improvement of the Microstructure and Mechanical Properties By Hybridizing The Surface of AA7075 by Hexagonal Boron Nitride With Carbide Particles Using The FSP Process, Journal of Materials Research and Technology 17, 1986-1999, 2022.

Nautiyal P., Rudolf C., Loganathan A., Zhang C., Boesl B., Agarwal, A. Directionally aligned ultra-long boron nitride nanotube induced strengthening of aluminum-based sandwich composite. Advanced Engineering Materials 18(10), 1747-1754, 2016.

Özçatal M., Başpınar M. S., SiO2 Katkısının Al2TiO5 Seramiklerinin Fiziksel Özelliklerine Etkisi, Pamukkale Üniversitesi Mühendislik Bilimleri Dergisi 26(4), 594-598, 2020.

Pandey K. K., Singh S., Choudhary S., Zhang C., Agarwal A., Li L. H., Chen Y., Keshri A. K., Microstructural and Mechanical Properties of Plasma Sprayed Boron Nitride Nanotubes Reinforced Alumina Coating, Ceramics International 47(7), 9194-9202, 2021.

Pariyar A., Perugu C. S., Toth L. S., Kailas S. V., Microstructure and Mechanical Behavior of Polymer-Derived İn-Situ Ceramic Reinforced Lightweight Aluminum Matrix Composite, Journal of Alloys and Compounds 880, 160430, 2021.

Peng X., Zhu D., Li Y., Zhou J., Lv Z., GUO P., Fabrication and property of AlN-BN composites by hot isostatic pressing. J. Inorg. Mater, 31, 535-541, 2016.

Pillari L. K., Umasankar V., Elamathi P., Chandrasekar G., Synthesis and Characterization of Nano Hexagonal Boron Nitride Powder and Evaluating The İnfluence on Aluminium Alloy Matrix, Materials Today Proceedings 3(6), 2018-2026, 2016.

Radhika E., Dobbidi P., XPS and dielectric studies of phase pure AlN-BN composite ceramics using powder bed. Materials Science and Engineering: B 297, 116783, 2023.

Sekar P., Panigrahi S. K., Understanding the corrosion and bio-corrosion behaviour of Magnesium composites–a critical review, Journal of Magnesium and Alloys, 12, 890-939, 2024.

Şenel M., Gürbüz M., Koç E., Grafen Takviyeli Alüminyum Matrisli Kompozitlerde Sinterleme Sıcaklığının Kompozitlerin Yoğunluğuna, Gözenekliliğine, Sertliğine ve Mikroyapısına Olan Etkisinin İncelenmesi, SETSCI-Conference Proceedings, Vol. 3, 2018.

Thomas S., Menachery N., Thomas L. P., N S., Kumar P. G. S., Hebbar G. S., Influence of Nano Hexagonal Boron Nitride on The Wear Properties of Aluminium Alloy, Advances in Materials and Processing Technologies 10(3), 2483-2499, 2024.

Tosun G., Kurt M., SiC Takviyeli Al-Mg Kompozitlerin Yoğunluğunun ve Mikro yapısının İncelenmesi, Niğde Ömer Halisdemir Üniversitesi Mühendislik Bilimleri Dergisi 9(1), 589-597, 2020.

JOURNAL of
MATERIALS and MECHATRONICS:A

e-ISSN 2717-8811
JournalMM, 2025, 6(1), 185-202
https://doi.org/10.55546/jmm.1646135

Araştırma Makalesi / Research Article

Üç Fazlı Şebeke Bağlantılı Fotovoltaik Eviricinin YSA Tabanlı Öngörülü Kontrolü

Süleyman YARIKKAYA[1*], Kadir VARDAR[2]

[1*] Afyon Kocatepe Üniversitesi, Mühendislik Fakültesi, Yazılım Mühendisliği Bölümü, Afyonkarahisar, Türkiye,
ORCID ID: https://orcid.org/0000-0003-1582-6588, syarikkaya@aku.edu.tr
[2] Kütahya Dumlupınar Üniversitesi, Mühendislik Fakültesi, Elektrik-Elektronik Mühendisliği, Kütahya, Türkiye,
ORCID ID: https://orcid.org/0000-0002-0197-0215, kadir.vardar@dpu.edu.tr

Geliş/ Received: 24.02.2025**;** **Revize/Revised:** 14.04.2025 **Kabul / Accepted:** 05.05.2025

ÖZET: Günümüzde sürdürülebilir enerji için yenilebilir enerji kaynaklarının kullanımı kritik bir öneme sahiptir. Yenilenebilir enerji kaynaklarından biri olan güneş enerjisinin kullanımı için yaygın olarak fotovoltaik (PV) sistemler tercih edilmektedir. PV sistemlerin kullanımının yaygınlaşmasıyla birlikte PV sistemlerin verimliliği de önem kazanmıştır. Şebeke bağlantılı sistemlerde, şebeke ile senkronizasyon çok önemlidir. Senkronizasyonu etkileyen önemli etkenlerden biri donanımsal ve yazılımsal gecikmelerdir. Evirici devrelerinde, öngörülü kontrolcüler kullanılarak sistemde oluşacak gecikmelerin etkisi azaltılabilmektedir. Bu çalışmada, öngörülü bir akım kontrolcüsü kullanılarak sistem verimliliğinin arttırılması amaçlanmıştır. Bundan dolayı, üç fazlı şebeke bağlantılı tek aşamalı PV evirici sistem kontrolünde kullanılması için öngörülü yapay sinir ağı (YSA) tabanlı bir akım kontrolcüsü önerilmektedir. Bu çalışmada ilk olarak, Matlab/Simulink ortamından 4kVA'lık üç fazlı şebeke bağlantılı bir PV evirici modellenmiştir. Benzetimde iki farklı akım kontrolcüsü kullanılmış ve elde edilen sonuçlar karşılaştırılmıştır. İlk PV evirici sistemde, akım kontrolcüsü olarak Oransal İntegratör (PI) kullanılmıştır. Daha sonra sistemde PI akım kontrolcüsü ve Referans Akım Öngörücü YSA (RefPNN) içeren bir benzetim yapısı kullanılarak PI tabanlı bir Referans Öngörülü YSA (PI-PNN) akım kontrolcüsü tasarlanmış ve eğitilmiştir. Yapılan simülasyon çalışmasından elde edilen sonuçlar karşılaştırıldığında PI-PNN'nin, PI akım kontrolcüsüne göre daha verimli olduğu tespit edilmiştir.

Anahtar Kelimeler: Yapay sinir ağları, Öngörülü akım kontrolcüsü, Şebeke bağlantılı PV evirici

*Sorumlu yazar / Corresponding author: syarikkaya@aku.edu.tr
Bu makaleye atıf yapmak için /To cite this article

Yarıkkaya, S., Vardar, K. (2025). Üç Fazlı Şebeke Bağlantılı Fotovoltaik Eviricinin YSA Tabanlı Öngörülü Kontrolü. Journal of Materials and Mechatronics: A (JournalMM), 6(1), 185-202.

ANN based Predictive Control of Three Phase Grid Connected Photovoltaic Inverter

ABSTRACT: Today, using renewable energy sources is critically essential for sustainable energy. Photovoltaic (PV) systems are widely preferred for using solar energy, one of the renewable energy sources. With the widespread use of PV systems, their efficiency has also gained importance. In grid-connected systems, synchronization with the grid is critical. One of the essential factors affecting synchronization is hardware and software delays. Inverter circuits, the effect of delays in the system can be reduced using predictive controllers. Inverter circuits, the effect of delays in the system can be reduced using predictive controllers. This study aims to increase the system efficiency using a predictive current controller. Therefore, a predictive artificial neural network (ANN) based current controller is proposed for three-phase grid-connected single-stage PV inverter system control. In this work firstly, a 4kVA three-phase grid-connected PV inverter is modeled in a Matlab/Simulink environment. Two different current controllers are used in the simulation, and the obtained results are compared. The Proportional Integrator (PI) was used as the current controller in the first PV inverter system. Then, a PI-based Reference Predictive ANN (PI-PNN) current controller was designed and trained using a simulation structure that includes a PI current controller and a Reference Predictive ANN (RefPNN) in the system. When the results obtained from the simulation study were compared, it was determined that PI-PNN was more efficient than the PI current controller.

Keywords: Artificial neural networks, Predictive current controller, Grid connected PV inverter

1. GİRİŞ

Güneş enerjisini elektrik enerjisine dönüştüren fotovoltaik (Photovoltaic, PV) evirici sistemlerin kullanımı son yıllarda artmıştır. Şebekeye bağlı PV evirici sistemlerde üretilen güç, anlık olarak şebekeye aktarılmaktadır ve herhangi bir depolama elemanına ihtiyaç duyulmamaktadır. Bu sayede hem depolama maliyetinden tasarruf edilmekte hem de daha verimli bir yapı oluşturulmaktadır (Arulkumar ve ark., 2016). PV evirici sistemler, PV modüllerde üretilen doğru akım (DC) gücünü, beslenecek şebekeye uygun alternatif akım (AC) güce dönüştürürler (Carrasco ve ark., 2006). Şebekeye bağlı PV evirici sistemlerinin verimliliğini etkileyen önemli bir etken de DC'den AC'ye dönüşümünün verimliliğidir (Boumaaraf ve ark., 2015). DC'den AC'ye güç dönüşümü ve şebeke ile senkronizasyonu, evirici devreleri kullanılarak yapılmaktadır. Güç dönüşümünde üç fazlı voltaj kaynaklı evirici (Voltage Source Inverter, VSI) devreleri yaygın olarak kullanılmaktadır. Birçok çalışmada, çıkışında pasif filtre kullanılan VSI eviriciler tercih edilmektedir (Hannan ve ark., 2010; Leon ve ark., 2016).

Güç elektroniğinde ve eviricilerde, matematiksel modelden bağımsız olarak kullanılabilen yaklaşımlar günümüzde artmıştır. Böylelikle, matematiksel modele ve kontrol parametresi ayarlamaya ihtiyaç duyulmadan eviriciler kontrol edilebilmektedir. Bu yaklaşımlardan en yaygın olarak kullanılan yöntem Yapay Sinir Ağları (YSA)'dır. İnsan beynini taklit eden YSA içerisindeki nöronlar istenilen kontrol çıkışını verecek şekilde eğitilmeye çalışılmaktadır. Bu amaçla, önce sistemin benzetimi yapılarak gerekli olan eğitim veri seti çevrim dışı olarak elde edilmektedir. (I. S. Mohamed ve ark., 2019). Matematiksel modeli karmaşık olan ve doğrusal olmayan ayrık zamanlı sistemlerin kontrolünde YSA kullanımı oldukça faydalıdır. Ayrıca YSA'lar olası hatalı girişlere karşıda toleransa sahiptir (Harashima ve ark., 1989; Shuzhi Sam Ge ve ark., 2008).

PV sistemlerin verimliliğini artırmak amacıyla farklı güç kademelerinde kullanılan çeşitli YSA çalışmaları mevcuttur. Mohamed ve arkadaşları, (2019)'da yaptıkları çalışmada üç fazlı şebeke bağlantılı bir DC-DC dönüştürücüsüne sahip bir PV sistem için adaptif bir PI kontrolcüsü önermişler. Bu kontrolcü DC bara voltajını, şebekeye enjekte edilen gücü ve harmoniklerin azaltılmasını denetlemektedir. Önerilen denetleyicide, PI kontrol parametreleri, öngörülü sinir ağı denetleyicisi (Predictive Neural Network Controller, PNNC) kullanılarak sürekli olarak ayarlanmaktadır. Sistem, MATLAB/Simulink ortamında modellenerek farklı çalışma koşulları için test edilmiş (A. A. S. Mohamed ve ark., 2019).

Şebeke bağlantılı PV sistemlerde güneş panelinin güç noktasının takibinde veya evirici kontrolünde de YSA'lar kullanılmaktadır. PV sistemlerinde kullanılan geleneksel Maksimum güç noktası takibi (Maximum Power Point Tracking, MPPT) yöntemleri, güç noktası çevresinde salınımlara neden olabilmektedir. Vora ve arkadaşları tarafından 2024 yılında gerçekleştirilen bir çalışmada Derin öğrenme ve takviyeli öğrenmenin entegrasyonu olan Derin Q-öğrenme yöntemi MATLAB/Simulink ortamında şebekeye bağlı bir PV sistem üzerinde uygulanmıştır. MPPT algoritması olarak tasarlanan bu kontrolcü ile DC-DC yükseltici devresi kontrol edilmiştir (Vora ve ark., 2024). Literatürde, MPPT fonksiyonunun yerine YSA öneren çeşitli çalışmalar mevcuttur (Babaie ve ark., 2020; Boumaaraf ve ark., 2015).

PV sistemlerde kullanılan eviricinin kontrolüne odaklanan bir başka çalışmada, MATLAB/Simulink ortamında tek fazlı iki aşamalı bir PV evirici sisteminde eviricinin kontrolü için YSA önerilmektedir (Bouaouaou ve ark., 2022; Rajab Al-Jaboury ve ark., 2024). Ayrıca üç fazlı PV sistemlerde evirici kontrolüne odaklanan çalışmalarda da evirici kontrolü için YSA öneren çalışmalar bulunmaktadır (Babaie ve ark., 2020; Singh ve ark., 2014).

Şebeke bağlantılı PV evirici sistemlerde kontrolcü olarak Model Öngörülü Kontrol (Model Predictive Control, MPC) kullanılan bazı çalışmalar mevcuttur (Bouaouaou ve ark., 2022; Cameron ve ark., 2020; Gopakumar ve Vijayakumari, 2017; Syed ve Raahemifar, 2015). MPC ile kontrol edilen evirici benzetiminden elde edilen veriler ile eğitilen YSA yapısına MPC tabanlı YSA denmektedir. MPC tabanlı YSA yapıları genellikle MPPT kontrolü için kullanılmaktadır (Khan ve ark., 2021).

Bu çalışmada ise diğer çalışmalardan farklı olarak bir öngörücü kullanılarak şebekenin faz açısı iki kontrol adımı öncesinden öngörülmüştür. Bu öngörü akım referansında kullanılarak donanım ve yazılım kaynaklı gecikmeler tolere edilmiştir. Daha sonra işlemcinin işlem yükünün azaltılması için oluşturulan kontrol yapısı tek bir YSA'ya dönüştürülmüş ve referans akım öngörülü bir YSA oluşturulmuştur. Bunun için ilk olarak Matlab/Simulink ortamında şebeke bağlantılı tek aşamalı iki seviyeli bir PV evirici sistemi oluşturulmuştur. Sistemde akım kontrolcüsü olarak, klasik PI akım kontrolcüsü ve tasarlanan PI tabanlı Referans Öngörülü YSA (PI-based Predictive Neural Network, PI-PNN) akım kontrolcüsü yöntemleri kullanılmıştır. Bu iki yöntemden elde edilen sonuçlar karşılaştırılmıştır. Tasarlanması amaçlanan PI-PNN akım kontrolcüsü yapısının eğitim verilerinin elde edilmesi amacı ile ilk olarak sinüzoidal bir sinyalin iki adım (100µs) sonrasını öngören başka bir YSA yapısı olan Referans Akım Öngörücü YSA (Reference Predictive Neural Network, RefPNN) yapı geliştirilmiştir. Daha sonra hazırlanan benzetimde elde MPPT çıkışında elde edilen referans evirici akımı önce bu RefPNN yapısına uygulanmıştır. RefPNN çıkışı olan öngörülen akım referansı PI akım kontrolcüsüne girilerek evirici kontrolü gerçekleştirilmiştir. Matlab/Simulink ortamında hazırlanan bu benzetim ile tasarlanması amaçlanan PI-PNN akım kontrolcüsü için gerekli eğitim verileri üretilmiştir. Tasarlanan PI-PNN akım kontrolcüsü, PV sisteminin kontrolünde test edilmiş ve bu yöntemin klasik PI yöntemine göre daha verimli çalıştığı görülmüştür. Ayrıca, elde edilen

öngörülü özelliğine sahip bu YSA yapısının sistemdeki değişikliklere daha iyi tepki ürettiği ve herhangi parametre ayarlanması gerekmeden uygulanabileceği tespit edilmiştir.

İkinci bölümünde üç fazlı şebeke bağlantılı PV sistem ve kontrol yapısı sunulmuştur. Üçüncü bölümde gerçekleştirilen benzetim çalışması ile önerilen YSA ve eğitimi detaylı bir şekilde anlatılmış. Ayrıca bu bölümde benzetim sonuçları verilerek karşılaştırılmıştır. Dördüncü bölümde benzetim ve deneysel sonuçlar karşılaştırılmalı olarak verilmiştir. Son bölümde ise elde edilen veriler karşılaştırılarak sunulmuştur.

2. ÜÇ FAZLI ŞEBEKE BAĞLANTILI FOTOVOLTAİK EVİRİCİLER

PV paneller güneş enerjisini DC elektrik enerjisine dönüştürmektedir (Vardar ve ark., 2018). PV paneller tarafından üretilen DC enerjinin, AC şebekeye aktarılması için DC enerjinin AC'ye dönüştürülmesi gerekmektedir. Bu dönüşüm için bir güç elektroniği devresi olan eviriciler kullanılmaktadır. PV sistemlerde eviricilerin iki ana görevi vardır. Bunlar PV panellerden maksimum gücün çekilmesi ve DC gücün AC güce dönüşümüdür. Güç dönüşümü yapılırken enerjinin şebekeye aktarılması için şebeke ile senkronizasyon sağlanması gerekmektedir. Bu sebeplerden dolayı şebeke bağlantılı PV sistemlerin en önemli parçalardan biri eviricilerdir (Blaabjerg ve ark., 2004; Hassaine ve ark., 2009; Jana ve ark., 2017). İki aşamalı PV sistemlerde, MPPT kısmının gerçekleştirildiği ilk aşama için bir DC-DC güç devresi kullanılırken, DC gücün AC güce dönüştürülerek şebekeye aktarıldığı ikinci aşama için ise evirici güç devresi kullanılmaktadır.

Tüm bu işlemler tek bir güç devresi kullanılarak gerçekleştirildiği durum için tek aşamalı terimi kullanılmaktadır. Endüstride en yaygın kullanılan evirici türlerinden biri iki seviyeli voltaj kaynaklı eviricilerdir (Two Level Voltage Source Inverter, 2L-VSI). Üç fazlı şebeke bağlantılı tek aşamalı 2L-VSI devre şeması Şekil 1'de verilmiştir. Yapıda her faz çıkışı için bir faz kolu ve her kolun pozitif (P) ve negatif (N) baralara olan bağlantılarını kontrol eden anahtarlar bulunmaktadır (Leon ve ark., 2016; Rivera ve ark., 2015).

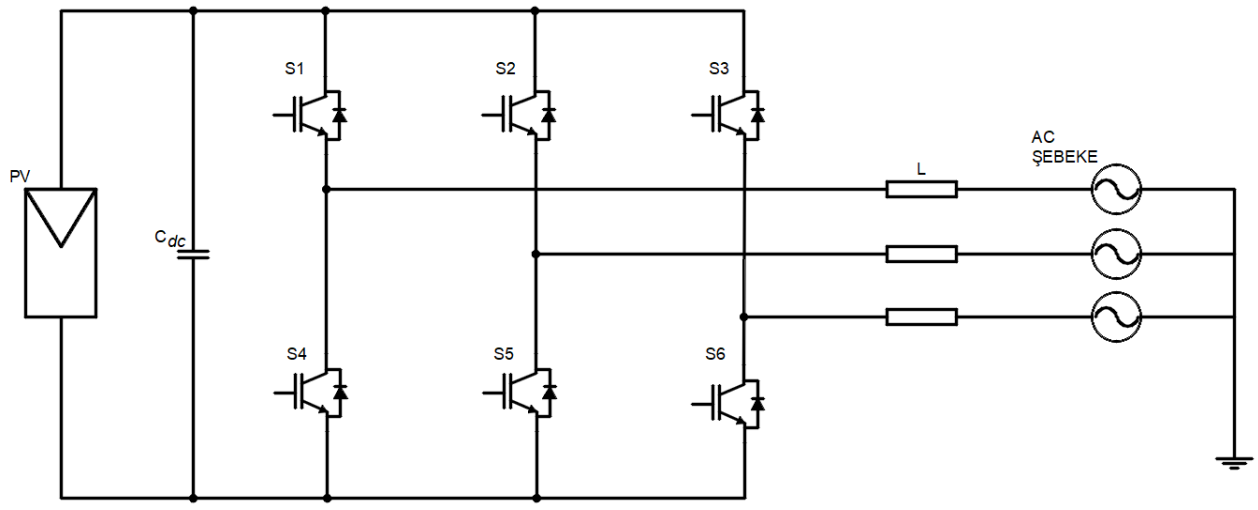

Şekil 1. Üç fazlı şebeke bağlantılı tek aşamalı PV evirici sistemi devre şeması

2L-VSI eviricilerde, invertörün 6 anahtarını (S1, S2, S3, S4, S5 ve S6) kontrol etmek için üç kontrol pozisyonu yeterlidir. Bu üç pozisyon Sa, Sb ve Sc ile temsil ediyorsa, bunların tümleyenleri da Sa', Sb' ve Sc' olarak tanımlanarak kullanılabilir.

$$S_a = \begin{cases} 1\,; & \mathrm{S1} = on \quad \text{ve} \quad \mathrm{S4} = off \\ 0\,; & \mathrm{S1} = off \quad \text{ve} \quad \mathrm{S4} = on \end{cases}$$

$$S_b = \begin{cases} 1\,; & \mathrm{S2} = on \quad \text{ve} \quad \mathrm{S5} = off \\ 0\,; & \mathrm{S2} = off \quad \text{ve} \quad \mathrm{S5} = on \end{cases}$$

$$S_c = \begin{cases} 1\,; & \mathrm{S3} = on \quad \text{ve} \quad \mathrm{S6} = off \\ 0\,; & \mathrm{S3} = off \quad \text{ve} \quad \mathrm{S6} = on \end{cases}$$

PV panellerin çıkışında üretilen DC gerilimin evirici girişine iletilmesi için genellikle bir DC bara hattı kullanılmaktadır. DC bara üzerine kondansatör (C_{dc}) konularak DC bara gerilimi dengelenir ve bu hattaki dalgalanmalar bastırılır. Evirici güç devresi ile DC bara hattı gerilimi ve evirici çıkış akımı kontrol edilir. Evirici çıkışında filtre kullanılarak evirici çıkış akımı filtrelenir ve şebekeye bağlanmadan önce sinüzoidal sinyale dönüştürülür. PV panellerden çekilen güç, güneş ışığı yoğunluğuna bağlı olarak değişmektedir. Ayrıca V-I karakteristik eğrileri lineer olmadığı için verdikleri güç, panellerden çekilen akıma göre de değişmektedir. Bu yüzden anlık olarak panellerden çekilecek maksimum güç değişebilmektedir. Panellerden en yüksek verimi almak için maksimum güç noktasının (Maximum Power Point, MPP) tespit edilerek panellerden en uygun akımın çekilmesi ve panellerin en uygun gerilim değerinde tutulması gerekmektedir. Bunun için geliştirilmiş çeşitli MPPT algoritmaları bulunmaktadır (Gupta ve Saxena, 2016; Selvan ve ark., 2016). Bu algoritmalar arasında en çok bilinen ve kullanım kolaylığı nedeniyle sıklıkla tercih edilen algoritmalardan biri hata-gözlem (Perturb and Observation-P&O) algoritmasıdır (Çınar ve ark., 2022). MPPT algoritması kullanılarak DC bara referans gerilimi üretilmektedir. Üretilen DC bara referans gerilimi ile DC bara gerilimi arasındaki hata değeri (e_{dc}) bir PI kontrolcüsü tarafından değerlendirilerek evirici referans akım değerini üretir. Sinüzoidal olamayan DC bara kontrolü için genellikle PI kontrolcüsü tercih edilmektedir.

Şebeke bağlantılı PV sistemlerin şebekeye entegrasyonu için Faz Kilitleme Döngüsü (Phase-Locked Loop, PLL) kullanılarak şebekenin faz açısı izlenir. Bu şebeke faz açısı kullanılarak birim sinüs sinyalleri üretilir. Birim sinüs sinyalleri ile DC bara kontrolcüsü (PI) çıkışında üretilen referans akım genlik çarpılarak evirici referans akımı elde edilir (Ciobotaru ve ark., 2006). Üç fazlı uygulamalarda PLL olarak sıklıkla Senkron Dönen Referans Çerçeve PLL (SRF-PLL) yöntemi kullanılmaktadır (Panigrahi ve ark., 2018; Yağan ve ark., 2018). Bu çalışmada PLL olarak SRF-PLL yöntemi tercih edilmiştir.

3. KLASİK VE YSA TABANLI AKIM KONTROLCÜLERİN BENZETİMİ

Matlab/Simulink ortamında oluşturulan şebeke bağlantılı tek aşamalı PV evirici sistemi benzetimi Şekil 2'de verilmiştir. Benzetimin örnekleme zamanı, güç katlarının fiziksel bir sisteme daha yakın olması için 0.5 µs olarak ayarlanmıştır. Ayrıca, kontrol sisteminin gerçek bir sistem ile benzer çalışma şartları altında tepkisini gözlemlemek için MPPT bloğunun örnekleme zamanı 50 µs ve diğer kontrol bloklarının örnekleme süresi 500 µs olarak ayarlanmıştır.

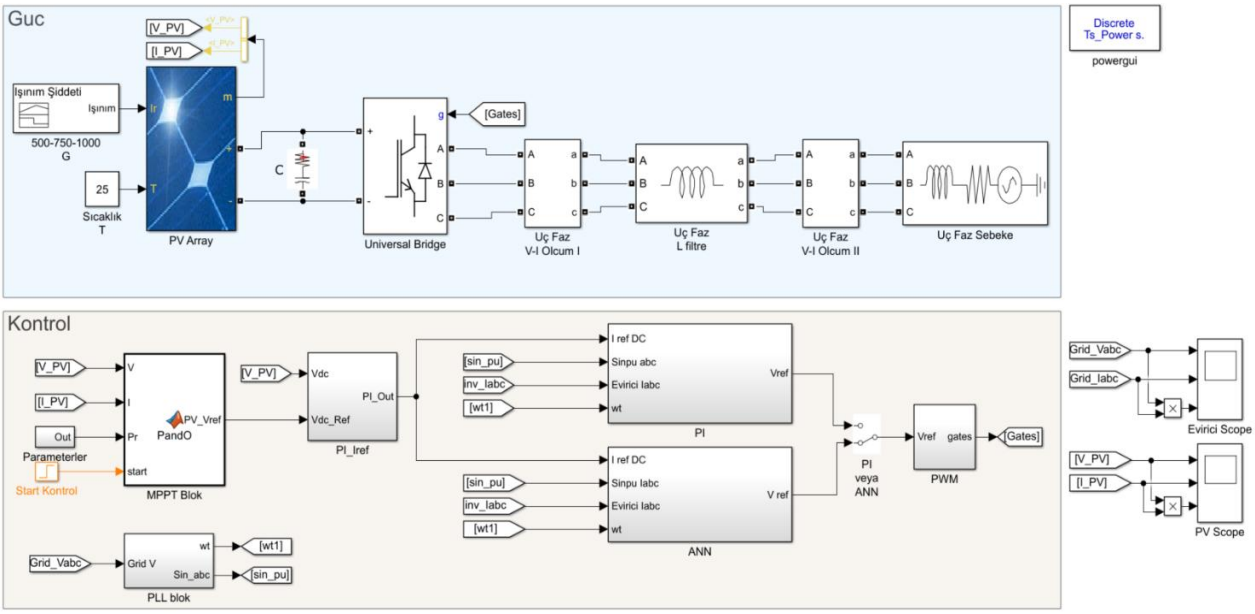

Şekil 2. Gerçekleştirilen üç fazlı şebeke bağlantılı tek aşamalı PV evirici Matlab benzetimi

Oluşturulan benzetimde güneş panelleri dizisi için Matlab/Simulink kütüphanesinde bulunan PV Array (PV Dizisi) bloğu kullanılmıştır. PV Dizi bloğu, tek bir kolda 13 tane seri bağlı SunPower SPR-305_WHT güneş panelinden oluşturulmuştur. Bu şekilde PV Dizi bloğu MPP noktasında 3968W maksimum güç üretmektedir. DC bara dalgalanmalarının azaltılması için DC baraya bir kondansatör eklenmiştir. Gerçek bir sistemde, başlangıç aşamasında PV panellerde ve kondansatörde gerilim olacağı için kondansatör başlangıç voltajı 750V olarak ayarlanmıştır. Evirici çıkışında L filtre kullanılarak şebeke bağlantısı bu filtre üzerinden gerçekleştirilmiştir. Şebeke bağlantılı PV evirici sistem benzetiminde kullanılan güç devrelerine ait parametreler Çizelge 1'de verilmiştir.

Çizelge 1. Şebeke bağlantılı PV evirici devre parametreleri

Devre	Değeri	Birimi
Paralel Dizi Sayısı	1	-
Dizi Başına Seri Bağlı Modül Sayısı	13	-
Panel Açık Devre Gerilimi, Voc	64.2	V
Panel Kısa Devre Akımı, Isc	5.96	A
Panel MPP Gerilimi, Vmp	54.7	V
Panel MPP Akımı, Imp	5.58	A
Toplam PV Gücü	3968	W
DC Bara Kondansatörü	330	µF
L Filtre	6	mH
Şebeke Gerilimi	220	V
Şebeke Frekansı	50	Hz

MPPT bloğu, bir Matlab fonksiyonu bloğu kullanılarak hata gözlem algoritmasının kodlanması ile oluşturulmuştur. Bu blok tarafından üretilen PV panel referans gerilim değeri, aynı zamanda evirici girişi için DC bara referans gerilim değeridir. MPPT bloğu tarafından üretilen DC bara referans gerilim değeri PI_Iref bloğuna uygulanmaktadır. PI_Iref bloğunun çıkışı ise eviricinin akım referans genlik değeridir. PLL bloğu kullanılarak PV sistem için gerekli olan şebeke faz açısı bilgisi ve bu faz açısı değeri kullanılarak oluşturulan 3 fazlı birim sinüs sinyalleri üretilmektedir. PI_Iref bloğunun

çıkışında üretilen bu akım genlik bilgisi, klasik PI kontrol yöntemli benzetim için PI alt bloğunda ve önerilen PI-PNN kontrol yöntemli benzetim için ANN alt bloğunda kullanılmaktadır.

PLL bloğu içerisinde Matlab/Simulink kütüphanesinde bulunan PLL(3ph) bloğu ile Matlab Function1 isimli fonksiyon bloğu kullanılmıştır. PLL(3ph) bloğu, şebeke faz açısını (*wt*) izlemektedir. PLL(3ph) bloğu ile bulunan faz açısı (wt), Matlab Function1 bloğuna girilerek 3 faz birim sinüs sinyalleri üretilmektedir. Benzetimde VSI yapısını oluşturmak için H-köprü yapısına sahip Universal Bridge bloğu kullanılmıştır. Blokta anahtarlama güç elemanı olarak diyotlu IGBT (Insulated Gate Bipolar Transistor) kullanılmıştır. Bu yapıda, 6 adet IGBT kullanılarak DC bara gerilimi AC gerilime dönüştürülmektedir. PWM bloğunda, kontrolcüler tarafından üretilen Vref bilgisi 20kHz'lik bir üçgen dalga ile karşılaştırılarak IGBT anahtarlama sinyalleri üretilmektedir. Benzetimde, PI bloğu ve ANN bloğu tarafından üretilen kontrol sinyallerinden hangisinin eviriciyi kontrol edeceği "PIveyaANN" isimli anahtar vasıtasıyla seçilmektedir. Böylece tek benzetimde herhangi farklılık olmadan iki kontrolcüden hangisinin kontrol edeceği değiştirilebilmektedir.

3.1 PI Akım Kontrolcüsü Kullanılan Benzetim

Matlab/Simulink ortamında oluşturulan PV evirici sisteminin kontrolünde yaygın olarak kullanılan yöntemlerden biri olan klasik PI akım kontrol yöntemi kullanılmıştır. Klasik PI kontrol yöntemi, doğrusal kontrolcüler sınıfında, uygulanması basit ve kullanımı kolay olan bir yöntemdir. Sinüzoidal referans takibinde PI kontrol yöntemi kullanıldığında, sistemde sabit durum hatası (steady-state error) oluşmakta ve küçük bozulmalara karşı zayıf tepki vermektedir. Bu yüzden PI kontrol yöntemi, eviricilerde kullanılırken genellikle abc-dq eksen dönüşümü yapılarak kullanılmaktadır (Ciobotaru ve ark., 2006). PI transfer fonksiyonu $G_{PI}(s)$ Eşitlik 1. de verilmiştir. Denklemde K_p oransal kazancı, K_i ise integratör kazancını temsil etmektedir.

$$G_{PI}(s) = K_p + \frac{K_i}{S} \tag{1}$$

Klasik PI akım kontrol yöntemi, benzetimde PI alt bloğu içerisinde modellenmiştir. Şekil 3'de yapısı verilen PI alt bloğunun dört adet girişi bulunmaktadır. Bunlar, eviriciden şebekeye aktarılan anlık gerçek akım bilgisi (*Evirici Iabc*), akım genlik referans bilgisi (*Iref*), PLL bloğu tarafından üretilen şebeke faz açısı (*wt*) ve faz açısı bilgisi kullanılarak üretilen birim sinüs sinyalleridir. (*Sinpu abc)*. Bu blokta, *Iref* ile Sinpu abc çarpılarak referans akım sinyali üretilmektedir. Elde edilen referans akım sinyali dq0 eksenine dönüştürülerek PI akım kontrolcüsü (PI CC) bloğuna girilmektedir. Yine bu bloğa aynı zamanda, evirici akımları da abc ekseninde dq0 eksenine dönüşümü yapılarak uygulanmaktadır.

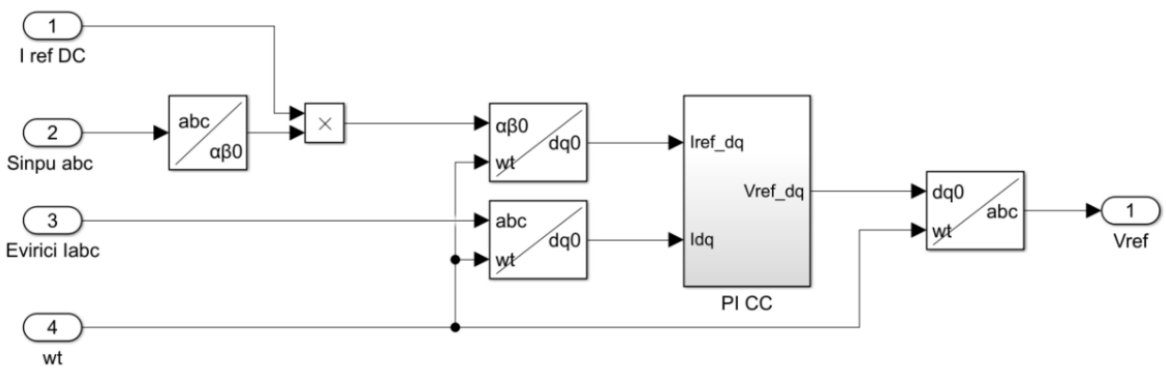

Şekil 3. Klasik PI akım kontrolcüsü benzetiminde kullanılan "PI" alt bloğu içyapısı

Şekil 4'te iç yapısı verilen PI CC bloğunda, d ve q eksenleri için iki adet klasik PI kontrolcüsü kullanılarak dq0 eksenlerinde kontrol çıkış sinyali (Vref_dq) üretilir. PI bloklarından ilki d eksen için kullanılmaktadır. "Discrete PI Controller1" bloğu girişine, Id akım bilgisi ile Iref_d akım referans bilgisinin farkı alınarak girilmektedir. Uygulamamızda Q eksen için referans girişine sıfır girilmiştir. Reaktif güç talebi olduğu durumda bu değer değiştirilebilir.

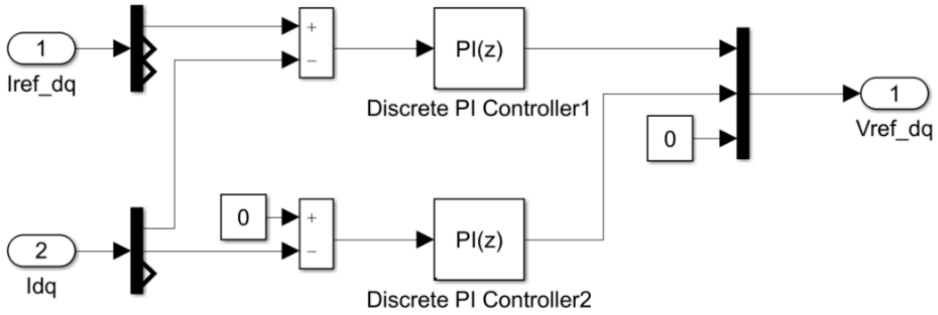

Şekil 4. "PI" alt bloğu içerisinde bulunan "PI CC" alt bloğunun içyapısı

PI CC alt bloğunun çıkışı olan dq0 eksenindeki referans gerilimler sonrasında abc eksenine döndürülerek PWM alt bloğuna uygulanmaktadır. Burada 20kHz'lik testere dişi sinyal ile karşılaştırılarak IGBT'ler için gerekli anahtarlama sinyalleri elde edilmektedir.

3.2 YSA Tabanlı Öngörülü Akım Kontrolcüsü Tasarımı ve Benzetimi

YSA'lar biyolojik sinir ağlarının çalışma prensibine benzetilerek geliştirilen, modern kontrol teknikleri arasında yerini almış bir yapay zeka modelleme tekniğidir. Geçmiş giriş-çıkış verilerini kullanarak, giriş-çıkış arasındaki ilişkileri öğrenme, bu ilişkileri modelleme ve optimize etme yeteneğine sahiptir. YSA'ların güvenirliliği farklı alanlarda yapılan çeşitli çalışmalarda uygulanmış ve kanıtlanmıştır. Çeşitli mimariler arasında ileri beslemeli YSA'lar öne çıkmaktadır. İleri beslemeli ağlar, katmanlar halinde statik bir yapıdadır (I. S. Mohamed ve ark., 2019; Rivera ve ark., 2015). Birden çok nöronun birlikte kullanılmasıyla YSA'lar oluşur. İleri beslemeli çok girişli tek nöronun yapısı Şekil 5'te verilmiştir.

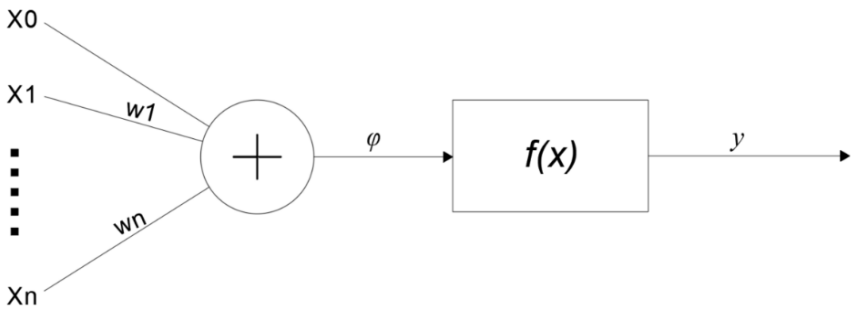

Şekil 5. Tek katmanlı tek nöronlu ileri beslemeli YSA yapısı

Burada; *y* nöron çıkışını, *f(x)* aktivasyon fonksiyonu, *φ* toplam çıkış sinyalini, w0 sapma (bias) w1'den wn'e kadar ağırlıklandırmalar ve X1'den Xn'e kadar girişleri ifade etmektedir.

Bu çalışmada öncelikle, YSA tabanlı öngörülü (PI-PNN) bir akım kontrolcüsü gerçekleştirebilmek ve bu ağın eğitim verilerinin elde edilebilmesi için ayrı bir YSA ağı tasarlanmıştır. Bu ağ ile sinüzoidal referans akımın, iki örnekleme adımı öncesinden (100µs) tahmin edilmesi amaçlanmıştır. Ağın eğitimi için birim sinüs dalgası kullanılmıştır. İki örnekleme adımı

([k+2]) sonrasına ait referans akım değerini tahmin edebilen referans akım öngörücü YSA (RefPNN) Matlab/Simulink ortamında tasarlanmıştır. Benzetimde iki adım sonrasının 100µs olması için, YSA bloğunun örnekleme zamanı 50µs olarak ayarlanmıştır. Tasarlanan ağının eğitilmesi için gerekli veriler bu benzetimden alınmıştır. Ağın girişi olarak, 50 Hz frekansında üretilen birim sinüs sinyalinin mevcut değeri ile beş geçmiş değeri kullanılmıştır. Ağın çıkışı ise mevcut örnekten iki örnekleme zamanı sonrasına ait veridir. Sinüzoidal giriş referansın farklı değerleri için (anlık zaman değeri kaydırılarak) yukarıdaki giriş ve çıkış eğitim verileri oluşturulmuş ve kaydedilmiştir. Ağ, Levenberg-Marquardt metodu ile eğitilmiştir. Eğitilen RefPNN, bir gizli katmanında 10 adet nöron bulunan ileri beslemeli bir YSA'dan oluşturulmuştur (Şekil 6). Gizli katmanda transfer fonksiyonu olarak hyperbolic tanjant sigmoid (tansig) fonksiyonu kullanılmıştır. Ağın çıkış katmanında ise bir adet nöron ve doğrusal aktivasyon fonksiyonu kullanılmıştır.

Tasarlanması amaçlanan PI-PNN akım kontrolcüsünün eğitim verilerini elde edilmesi için ikinci aşama, RefPNN ve klasik PI akım kontrolcüsünün birlikte simüle edilmesidir. Evirici kontrol yapısına öngörü özelliği katma amacı ile tasarlanan RefPNN yapısı sinüzoidal giriş sinyali alması gereksiniminden dolayı referans akımın girişi α-β eksenlerinde kullanılmış olup çıkışında üretilen öngörülmüş referans akımı PI akım kontrolcüsüne uygulanacağından, öncesinde dq0 eksenine dönüştürülmektedir. dq eksenlerine dönüşümü gerçekleştirilen öngörülü referans akım, PI kontrolcüsünün girişine uygulanmış ve böylelikle oluşturulan RefPNN ve PI akım kontrolcüsü içeren Matlab/Simulink benzetimi ile PI-PNN akım kontrolcüsünün eğitimi için gerekli eğitim seti verileri elde edilmiştir. Eğitim verileri için RefPNN ve PI kontrol algoritmalarının örnekleme adım aralığı 50µs olarak ayarlanmış ve her bir giriş-çıkış için 1200 adetlik veri dizisi alınmıştır.

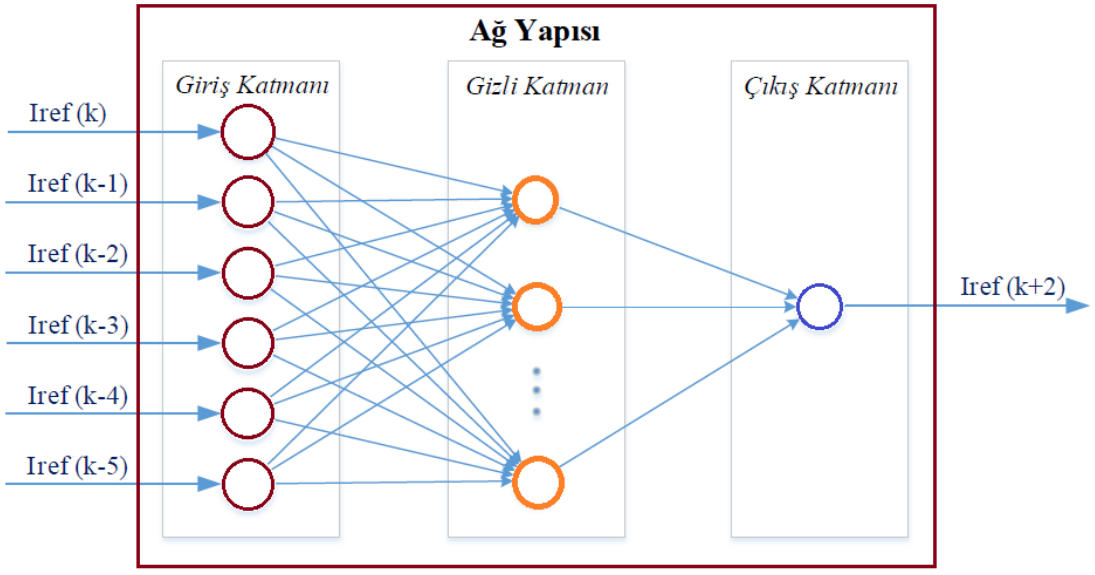

Şekil 6. İleri beslemeli RefPNN ağ yapısı

Son aşamada, bu veriler kullanılarak PI-PNN akım kontrolcüsünün tasarımı ve eğitimi gerçekleştirilmiştir. Tasarlanan PI-PNN ağı için girişler, dq0 ekseninde akım hataları (Id_err[k] ve Iq_err[k]), bir önceki akım hataları (Id_err[k-1] ve Iq_err[k-1]) ve PI CC'ın bir önceki çıkış (Vd_out[k-1] ve Vq_out[k-1]) verileridir. Ağ çıkışı için ise dq0 ekseninde PI CC çıkışı (Vd_out[k] ve Vq_out[k]) verileri kullanılmıştır. Elde edilen veriler ile 6 giriş, 2 çıkış ve 1 gizli katmana sahip dinamik bir ağ yapısı oluşturulmuştur. Şekil 7'de tasarlanan geri beslemeli ağ yapısı verilmiştir.

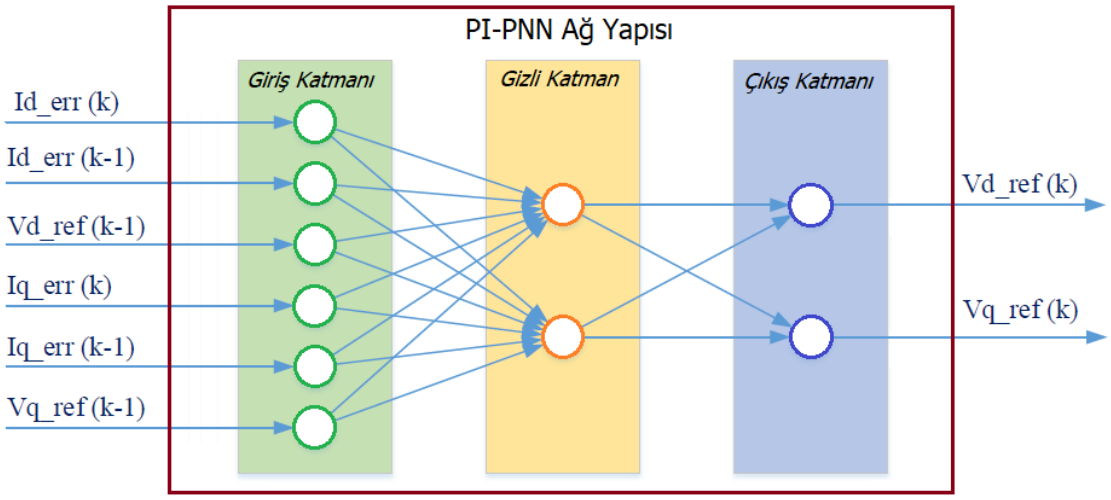

Şekil 7. Geri beslemeli PI-PNN akım kontrolcüsü ağ yapısı

Ağ yapısı oluşturulurken ağda minimum nöron kullanımı amaçlanmıştır ve gizli katmanda 2 adet nöron kullanılmıştır. Aktivasyon fonksiyonu olarak gizli katmanda tansig, çıkış katmanında ise lineer (pureline) fonksiyonu kullanılmıştır. Ağın eğitimi, Levenberg-Marquardt geri yayılım (backpropagation) yöntemi ile gerçekleştirilmiştir. Şekil 2'de verilen genel benzetimde görülen, tasarlanan PI-PNN'ün kullanıldığı durumdaki "ANN alt bloğu" içyapısı Şekil 8'de verilmiştir.

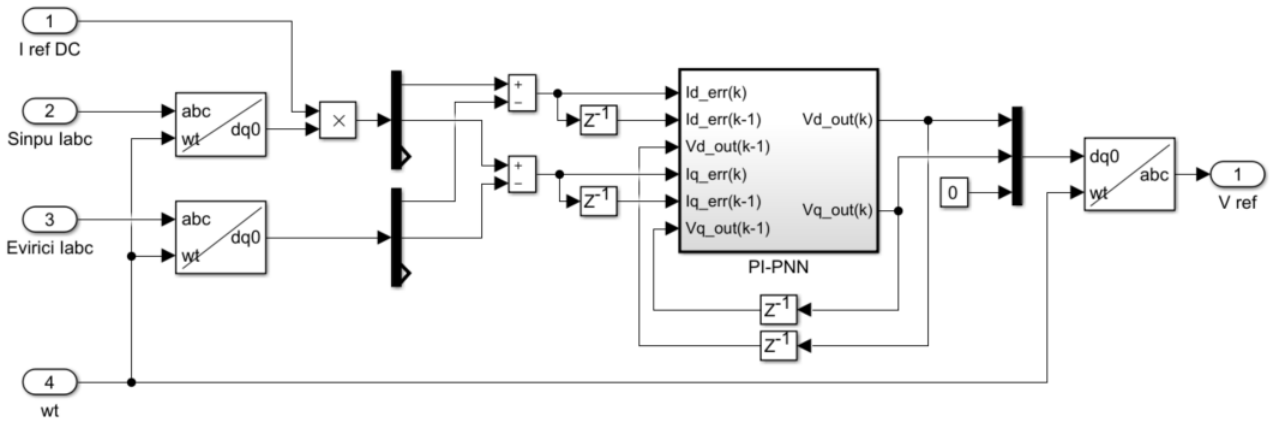

Şekil 8. PI-PNN akım kontrolcüsü benzetiminde kullanılan "ANN alt bloğu" içyapısı

İlk olarak blokta, sinüzoidal dalga olan birim sinüs (Sinpu Iabc) ile Evirici çıkış akımı (Evirici Iabc) dq0 eksenlerine dönüştürülmüştür. Bu dönüşüm için şebeke faz açısı kullanılmıştır. Birim sinüs ile DC akım referansı çarpılarak dq eksenlerinde referans akım genliği oluşturulmuştur. Daha sonra referans akımdan, evirici akımı çıkartılarak dq ekseninde akım hataları elde edilmiştir. Bu akım hatalarının bir önceki değeri de PI-PNN bloğuna girilmiştir. Blok çıkış değerlerinin (Vd_out ve Vq_out) bir öndeki değerleri de yine giriş için geri beslenmiştir. Son olarak çıkışta, dq0 eksenlerinde elde edilen referans gerilim abc eksenlerine dönüştürülerek blok çıkışına gönderilmiştir.

3.3 Benzetim Sonuçları ve Karşılaştırmalar

Bu bölümde, üç faz şebeke bağlantılı PV evirici sisteminin Matlab/Simulink ortamında gerçekleştirilen benzetim çalışması sonuçları verilmiştir. Önceki bölümlerde detayları sunulan klasik PI ve YSA tabanlı iki farklı akım kontrolcüsü kullanan sisteminin benzetim sonuçları bu bölümde

verilerek karşılaştırılmıştır. Her iki kontrol yöntemi de Şekil 2'de verilen tek bir benzetimde sırayla gerçekleştirilmiştir. Benzetimde, PV dizisi için güneş ışınım şiddeti 0-0.5s arası 500W/m^2, 0.5-1s arası 750W/m^2 ve 1-1.5s arası 1000W/m^2 olarak ayarlanmıştır. Grafiklerdeki güç değerleri, gerilim değeri ile akım değeri çarpılarak elde edilmiştir. Kondansatörün başlangıç anındaki voltaj değeri PV dizesinin çıkışında voltaj olacağı için 750V olarak ayarlanmıştır. PV dizesinin karakteristik akım-gerilim ve güç-akım grafiği Şekil 9'da verilmiştir.

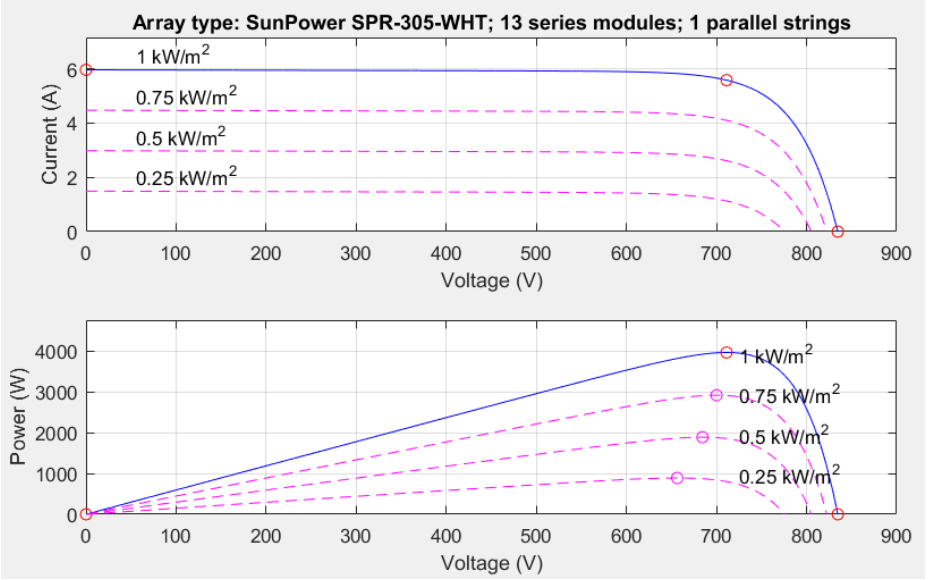

Şekil 9. PV panel dizesinin MPP noktalarına ait akım-gerilim ve güç-gerilim grafikleri

Grafikte MPP noktaları Matlab/simulink programı tarafından otomatik olarak işaretlenmiştir. Bu noktalar incelendiğinde panellere 1kW/m^2 ışınım şiddeti uygulandığında, panellerden çekilebilecek 3968W maksimum güç için panel gerilimi 711.1V olmalıdır. Panellere 750 W/m^2 ışınım şiddeti uygulandığında 2920W maksimum güç 700.1V'ta elde edilmektedir ve panellere 500 W/m^2 ışınım şiddeti uygulandığında panellerden 1890W'lık maksimum güç 684.4V'ta elde edilmektedir.

PI akım kontrolcüsü kullanılarak yapılan evirici sistem benzetimde, PV panel çıkışına ait gerilim, akım ve güç grafikleri ile evirici akım referansına ait grafik Şekil 10'da verilmiştir. Grafikte üstten alta doğru sırayla PV panellerde oluşan gerilim, panellerden çekilen akım, elde edilen güç ve evirici referans akımı verilmektedir. PV gerilim grafiği incelendiğinde, gerilimin kondansatör başlangıç değeri olan 750V'tan MPP noktası değeri 684.4V'a 0.094s'de ulaştığı görülmektedir. Işınım değişimlerinde ise sırasıyla 0.665'inci saniyede 700V'a ve 1.116'ncı saniyede 711V'a ulaşmaktadır. Güç grafiği incelendiğinde ise PV panellerden çekilen gücün maksimum güç değerine hızlı bir şekilde vardığı görülmektedir. Şekil 10'da en altta verilen akım referans grafiği MPPT bloğu çıkışında PI_Iref bloğu tarafından üretilen akım referansının grafiğidir. Bu grafik, klasik PI akım kontrolcüsü kullanımı esnasında PI kontrolcü için oluşan referans akım genlik grafiğidir.

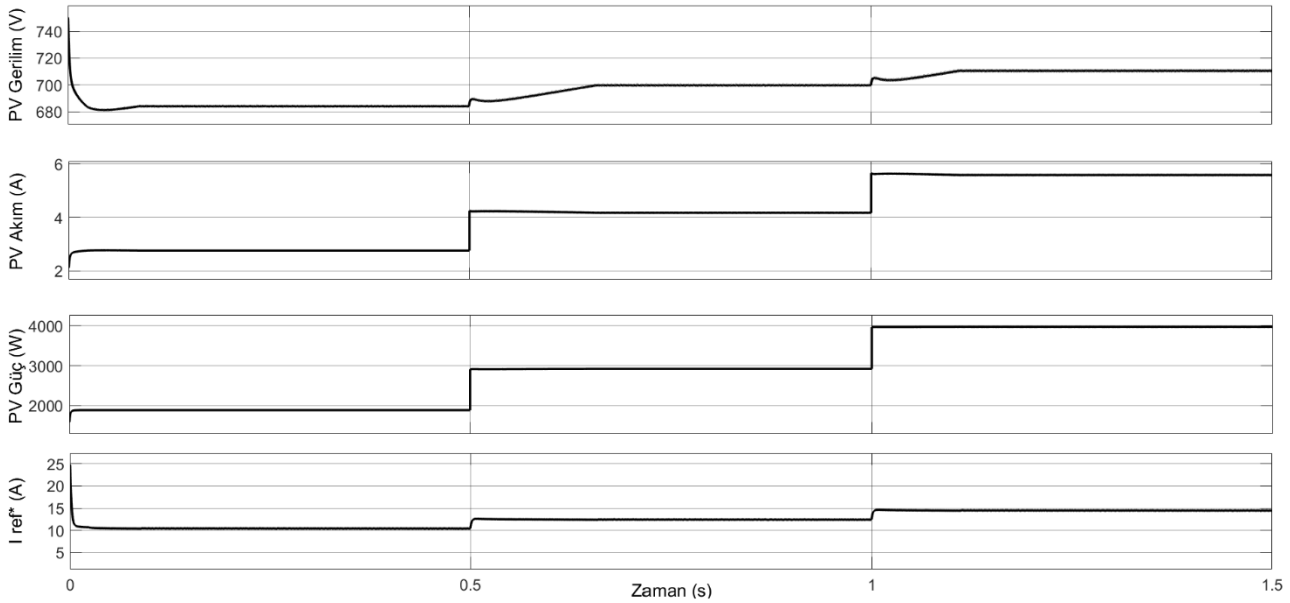

Şekil 10. Klasik PI kontrolcüsü kullanılan benzetimde PV panel çıkışına ait gerilim, akım, güç ve referans akım grafiği

PI-PNN akım kontrolcüsü kullanılarak yapılan PV evirici benzetimde, PV panel çıkışını ait gerilim, akım ve güç grafikleri ile evirici referans akım grafiği Şekil 11'de verilmiştir. Grafikte üstten alta doğru sırayla PV panellerin gerilimi, panellerden çekilen akım, üretilen çekilen güç ve evirici referans gerilimi verilmektedir. PV gerilim grafiği incelendiğinde, 750V gerilim başlangıç değerinden MPP noktası gerilim değeri 684.4V'a 0.061s'de ulaşmıştır. Işınım değişimlerinde ise sırasıyla 0.661'inci saniyede 700V'a ve 1.111'inci saniyede de 711V'a ulaştığı görülmektedir. Bu değerlere göre PV evirici sistemin hızı, PI-PNN kontrolcüsü kullanıldığında klasik PI kontrolcüsü kullanıldığına göre çok az daha hızlıdır. Güç grafiği incelendiğinde akım ve gerilim değişimlerinin birbirini dengeleyerek, PV panellerden maksimum gücün çok hızlı bir şekilde çekildiği görülmektedir. Şekil 11'de en altta evirici için MPPT bloğu çıkışında PI_Iref bloğu tarafından üretilen akım referansına ait grafik verilmiştir. Bu grafik, PI-PNN akım kontrolcüsü kullanımı esnasında oluşan referans akımın genlik grafiğidir.

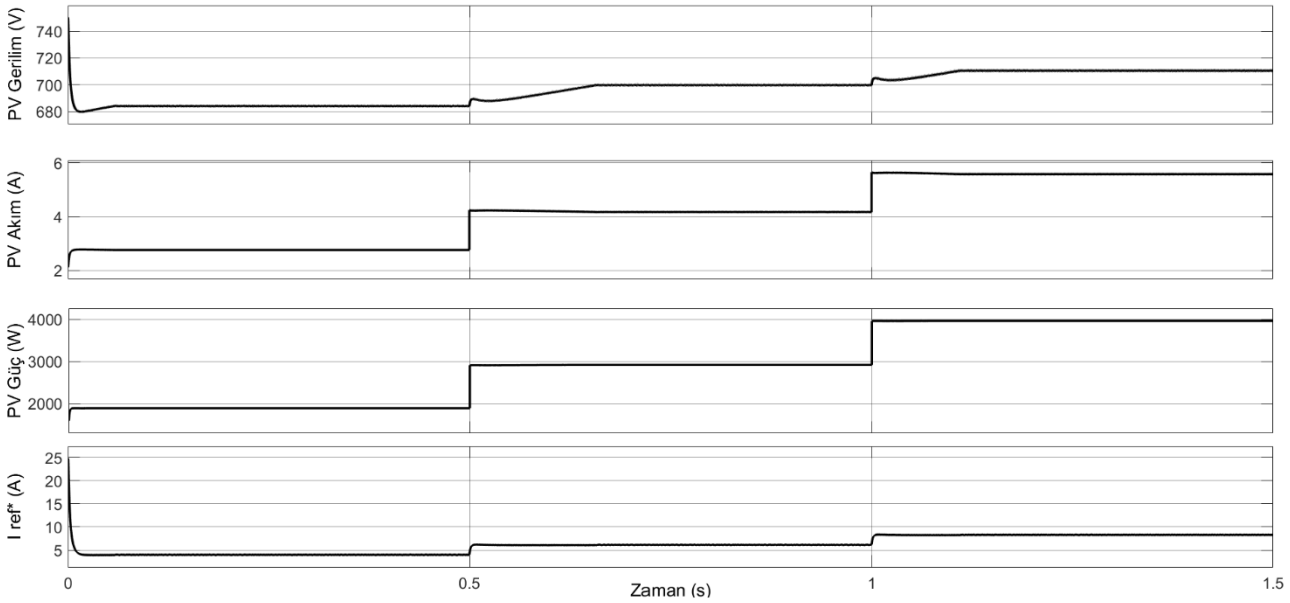

Şekil 11. PI-PNN kontrolcüsü kullanılan benzetimde PV panel çıkışına ait gerilim, akım, güç ve referans akım grafiği

Klasik PI akım kontrolcüsü ve önerilen PI-PNN akım kontrolcüsü yöntemlerinin uygulandığı PV evirici sisteminin benzetim grafikleri incelendiğinde, sonuçların genel olarak birbirine oldukça yakın olduğu fakat PI-PNN'ün değişimlere biraz daha hızlı tepki verdiği görülmektedir. Evirici akım grafiklerine göre sistemin ilk çalışmasında evirici çıkış akımının, PI-PNN'ün klasik PI yönteminden 30ms daha hızlı bir şekilde MPP değerine ulaştığı tespit edilmiştir. Bu değişim hızının farkı, PV gerilim grafiklerinde de fark edilmektedir. PI-PNN'ün daha hızlı ve stabil çalıştığı, akım referansının başlangıç ve ışınım değişim anlarındaki ölçülen tepkisi ile tespit edilmiştir. Farklı çevre koşullarında ki çalışma beceresi için farklı ışınım şiddeti değerleri kullanılarak test edilmiştir. PV panelleri etkileyen bir diğer çevre etkeni ise sıcaklıktır. Farklı sıcaklıklar için yapılan simülasyon testlerinde de önerilen YSA tabanlı kontrolcü aynı kontrol başarısını elde etmiştir.

4. BENZETİM VE DENEYSEL SONUÇLAR

Deneysel çalışmalar için tasarlanan üç fazlı 5 kVA'lik evirici güç kartında 7MBP50RJ120 1200V 50A IPM modül kullanılmıştır. Evirici çıkış akımlarının ölçümü LEM LA55-P hall sensörü kullanılarak gerçekleştirilmiştir. Kontrol kartının şebeke gerilimi ile izolasyonu için HCPL 7840 entegresi tercih seçilmiştir. Evirici kartını kontrol etmek için STM32F407 mikrodenetleyicisi kullanılırken, kaynak kodların derlenmesi ve yüklenmesi için MikroC for ARM programı kullanılmıştır. Gerçekleştirilen uygulamada, PV paneller yerine güç kartında DC gerilime dönüştürülen şebeke gerilimi kullanılmıştır ve evirici çıkışı şebeke yerine RL yüke bağlanmış. Böylece DC besleme gerilimi ve çekilen akım sabitlenerek gerekli testler yapılmıştır. DC besleme gerilimi 210V olarak ayarlanmıştır. Filtre olarak 3mH'lik bobin ve rezistif yük olarak 10Ω'luk direnç yük kullanılmıştır. Sabit yük ve sabit besleme geriliminde farklı akım referansları için evirici çıkış akımları üretilmiş ve evirici tepkisi kontrol edilmiştir. Deneysel çalışmalar için hazırlanan test düzeneğinin fotoğrafı Şekil 12'de verilmiştir.

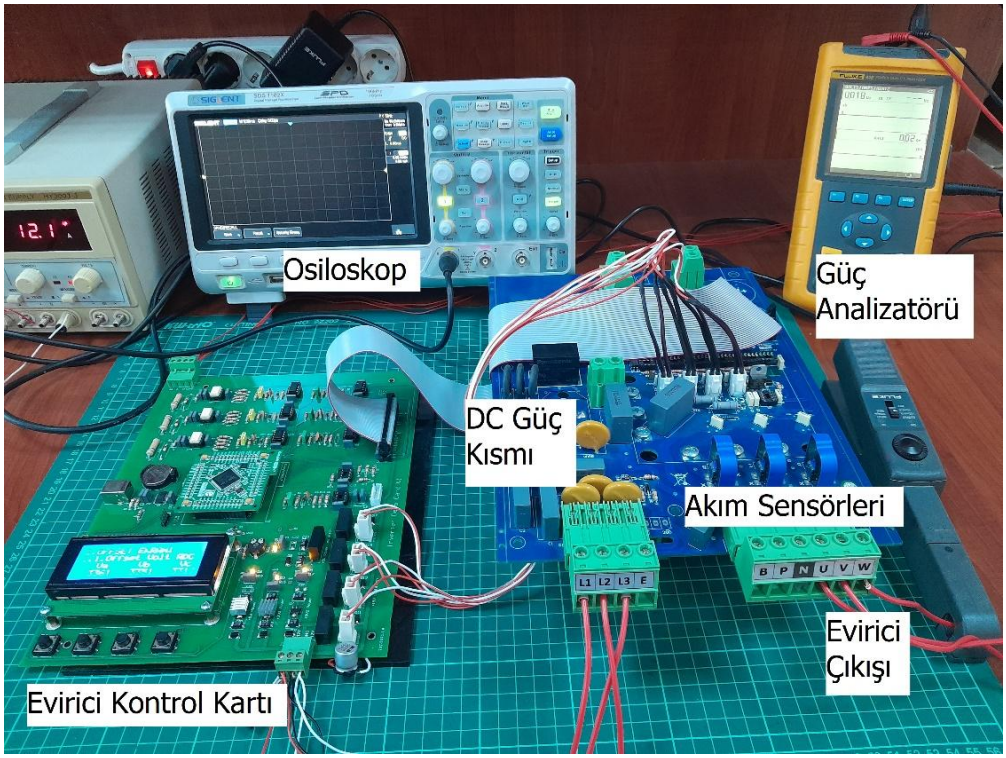

Şekil 12. Deneysel test düzeneği fotoğrafı

İlk olarak 2A ve 4A gibi düşük akım referans değerleri için akım evirici test edilmiştir. Daha sonra evirici referans akımları sırasıyla 2A, 5A ve 10A olarak ayarlanmıştır. Bu değerler, PV evirici sisteminde çekilecek akım değerlerini kapsayan değerlerdir. Osiloskop kullanılarak ölçülen evirici çıkış akım grafiği Şekil 13'te verilmiştir. Grafik incelendiğinde, referans akım değişimlerinin ve sürekli durumunun takibinin evirici tarafından başarılı bir şekilde gerçekleştirildiği görülmektedir.

Şekil 13. Deneysel test sonuçları evirici çıkış akım grafikleri a)2A-4A b)2A-5A-10A

Deneysel çalışmalarda, toplam harmonik bozulma (Total Harmonic Distortion-THD) ölçümleri FLUKE 43B güç kalitesi analizör cihazı kullanılarak gerçekleştirilmiştir. Yapılan ölçümler sonucunda, klasik PI akım kontrolcüsü yöntemi kullanılarak kontrol edilen evirici çıkış akımındaki THD %3.2 olurken, önerin YSA tabanlı öngörülü kontrolcü kullanılarak kontrol edilen evirici çıkış akımındaki THD değeri %2.4 olmuştur. Benzetim çalışmalarında, evirici çıkış akımlarında oluşan toplam harmonik bozulmaların görüldüğü FFT analiz ekranları Şekil 14'te verilmiştir. PV evirici benzetiminde analiz için 1000W/m^2 ışınım şiddeti ve ikinci 5 periyotluk zaman dilimi kullanılmıştır.

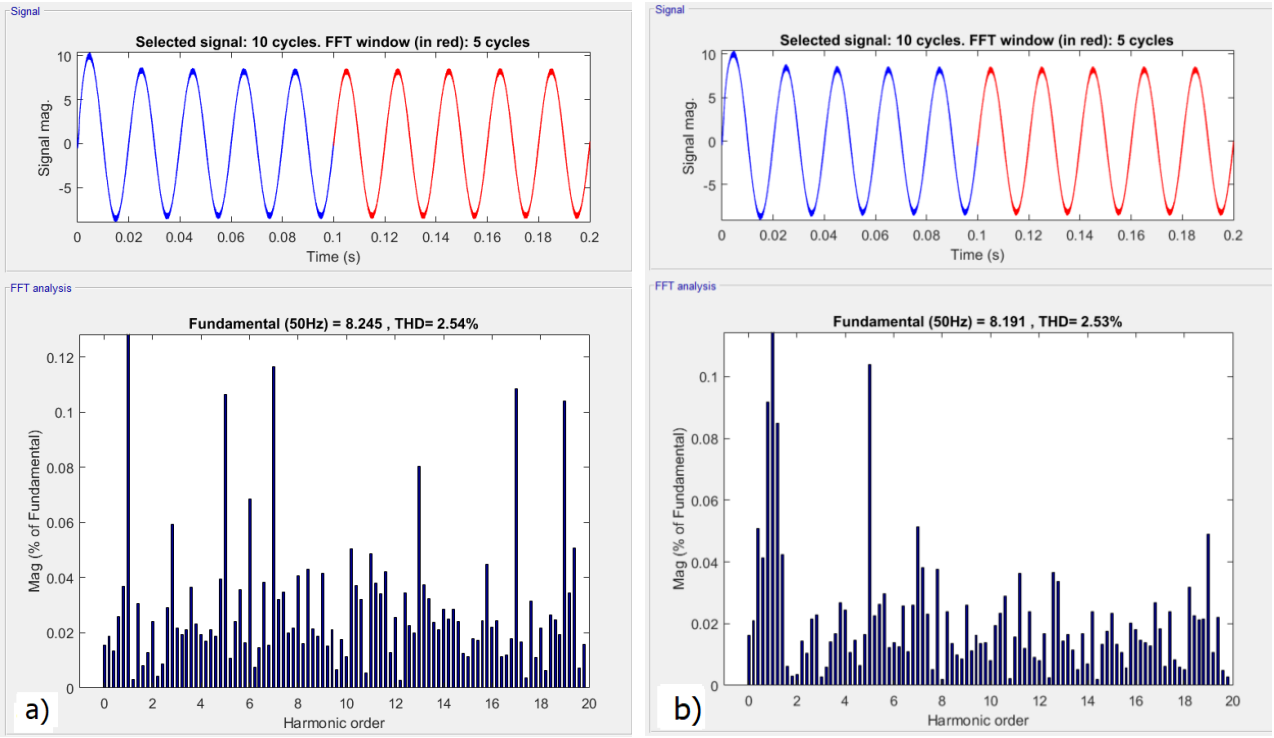

Şekil 14. Benzetim sonuçlarına göre evirici çıkış akımlarının FFT analizi; a) PI akım kontrolcüsü kullanıldığında, b) RefPNN ile birlikte PI akım kontrolcüsü kullanıldığında, c) PI-PNN akım kontrolcüsü kullanıldığında

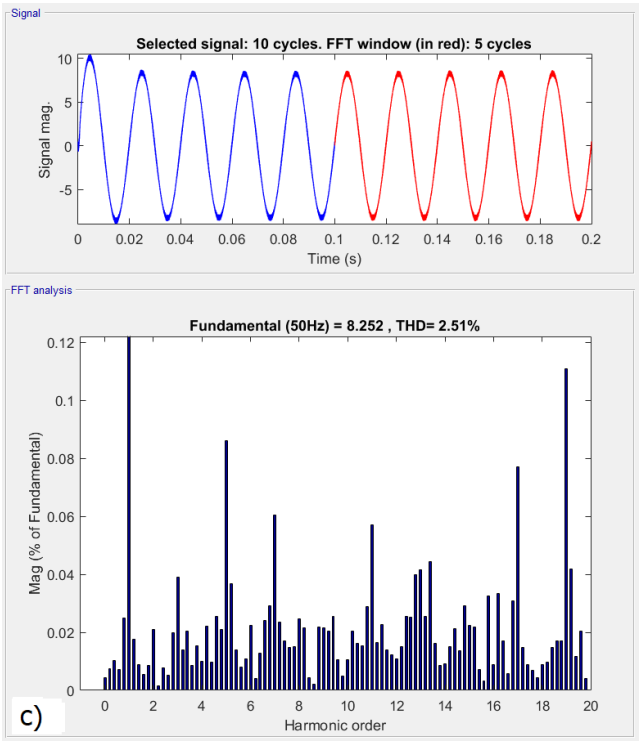

Şekil 14. Benzetim sonuçlarına göre evirici çıkış akımlarının FFT analizi; a) PI akım kontrolcüsü kullanıldığında, b) RefPNN ile birlikte PI akım kontrolcüsü kullanıldığında, c) PI-PNN akım kontrolcüsü kullanıldığında (devamı)

Benzetimde, klasik PI akım kontrolcüsü kullanılan yöntemde THD değeri %2.54 elde edilirken, RefPNN ve PI akım kontrolcüsü ile elde edilen THD değeri %2.53'tür. Önerilen YSA tabanlı PI-PNN akım kontrolcüsü kullanıldığında ise THD değeri %2.51 olmuştur. Hem benzetim hem de deneysel çalışmalarda, önerilen PI-PNN kontrolörü ile kontrol edilen evirici çıkış akımının, klasik PI kontrolörü ile kontrol edilen evirici çıkış akımına göre daha düşük harmonik bozulmalara sahip olduğu gözlemlenmiştir.

5. SONUÇ

Bu çalışmada, üç fazlı şebeke bağlantılı PV eviriciler için YSA tabanlı öngörülü akım kontrolcüsü tasarlanmıştır. Tasarlanan akım kontrolcüsü, referans akımın iki adım sonrasını öngörerek yazılım ve donanım kaynaklı gecikmelerin önüne geçmesi planlanmıştır. Bunun için ilk olarak benzetim ortamında, 2 adım sonrasını öngörebilen YSA tabanlı bir referans akım öngörücüsü oluşturulmuştur. Klasik PI akım kontrolcüsü kullanılarak, öngörülen referans akıma göre PV evirici sistemi kontrol edilmiştir. Daha sonra bu benzetim çalışmasından alınan veriler kullanılarak, önerilen YSA tabanlı öngörülü akım kontrolcüsü eğitilmiştir. Klasik PI ve önerilen PI-PNN olmak üzere iki farklı akım kontrolcüsü kullanılarak benzetim ve deneysel çalışmalar gerçekleştirilmiştir. Yapılan benzetim çalışmasında, farklı güneş ışınım değerleri kullanılarak PV eviricinin tepkisi gözlemlenmiştir. Her iki kontrol sistemiyle de değişen ışınım şiddetleri altında PV kaynağından şebekeye güç transferi maksimum güç noktasında ve düşük THD değerleriyle sağlanmıştır. Yapılan benzetim çalışması sonucunda her ne kadar YSA tabanı kontrolcünün performansının daha iyi olsa da sonuçların birbirine oldukça yakın olduğu gözlemlenmiştir.

Deneysel çalışmalara geçildiğinde ise elektriksel gürültünün ve fiziksel ortamda meydana gelen diğer bozucuların etkileriyle karşılaşılmaktadır. Bu tür ortamlarda yüksek tolerans kabiliyeti sayesinde YSA'nın ön plana çıktığı görülmektedir. Yapılan çalışmalardan elde edilen sonuçlar

karşılaştırıldığında, her iki yönteminde kullanılabilir olduğu ve önerilen öngörülü YSA'ın klasik PI kontrolcüsüne göre daha evirici akımında düşük harmonik bozulma değeri elde edildiği ve daha hızlı tepki süresine sahip olduğu tespit edilmiştir. Ayrıca, PI kontrol yönteminde kullanılacak parametrelerin ayarlanma zorunluluğu bulunurken, önerilen YSA tabanlı kontrol yönteminde herhangi bir parametre ayarı gerektirmemektedir. Sonuç olarak, önerilen YSA tabanlı akım kontrolcüsünün şebeke bağlantılı PV evirici sistemine başarılı bir şekilde uygulandığı ve harmonik bozulmaları azalttığı gözlemlenmiştir.

6. TEŞEKKÜR

Bu çalışma Süleyman YARIKKAYA'nın Doktora tezinden üretilmiştir.

7. ÇIKAR ÇATIŞMASI

Yazarlar, bilinen herhangi bir çıkar çatışması veya herhangi bir kurum/kuruluş ya da kişi ile ortak çıkar bulunmadığını onaylamaktadırlar.

8. YAZAR KATKISI

Bu çalışmada Kadir VARDAR çalışmanın kavramsal ve tasarım süreçlerinin belirlenmesi, çalışmanın kavramsal ve tasarım süreçlerinin yönetimi, veri analizi ve yorumlama, makale taslağının oluşturulması, fikirsel içeriğin eleştirel incelemesi, son onay ve tam sorumluluk konusunda, Süleyman YARIKKAYA çalışmanın kavramsal ve tasarım süreçlerinin yönetimi, verilerinin toplanması, veri analizi ve yorumlama, son onay ve tam sorumluluk konusunda katkı sağlamıştır.

9. KAYNAKLAR

Arulkumar K., Vijayakumar D., Palanisamy K., Recent advances and control techniques in grid connected PV system - A review. International Journal of Renewable Energy Research 6(3), 1037-1049, 2016. https://doi.org/10.20508/ijrer.v6i3.4075.g6886

Babaie M., Sharifzadeh M., Mehrasa M., Chouinard G., Al-Haddad K., PV Panels Maximum Power Point Tracking based on ANN in Three-Phase Packed E-Cell Inverter. 2020 IEEE International Conference on Industrial Technology (ICIT), 854-859, 2020. https://doi.org/10.1109/ICIT45562.2020.9067218

Blaabjerg F., Chen Z., Kjaer S. B., Power electronics as efficient interface in dispersed power generation systems. IEEE Transactions on Power Electronics 19(5), 1184-1194, 2004. https://doi.org/10.1109/TPEL.2004.833453

Bouaouaou H., Lalili D., Boudjerda N., Model predictive control and ANN-based MPPT for a multi-level grid-connected photovoltaic inverter. Electrical Engineering 104(3), 1229-1246, 2022. https://doi.org/10.1007/s00202-021-01355-w

Boumaaraf H., Talha A., Bouhali O., A three-phase NPC grid-connected inverter for photovoltaic applications using neural network MPPT. In Renewable and Sustainable Energy Reviews 49, 1171-1179, 2015. https://doi.org/10.1016/j.rser.2015.04.066

Cameron S., Ameen G., M. E., H., Aman O., Model Predictive Control of Grid Connected Solar PV Inverter. 2020 Australasian Universities Power Engineering Conference (AUPEC), 1-6, 2020.

Carrasco J. M., Franquelo L. G., Bialasiewicz J. T., Galvan E., PortilloGuisado R. C., Prats M. A. M., Leon J. I., Moreno-Alfonso N., Power-Electronic Systems for the Grid Integration of Renewable Energy Sources: A Survey. IEEE Transactions on Industrial Electronics 53(4), 1002-1016, 2006. https://doi.org/10.1109/TIE.2006.878356

Ciobotaru M., Teodorescu R., Blaabjerg F., Control of single-stage single-phase PV inverter. EPE Journal (European Power Electronics and Drives Journal) 16(3), 20-26, 2006. https://doi.org/10.1080/09398368.2006.11463624

Çınar S. M., Bakım S., Hocaoğlu F. O., Designing a novel MPPT algorithm based on the extraterrestrial irradiance for photovoltaic energy generation systems and testing under partial shade conditions. Journal of Computational Electronics 21(4), 841-851, 2022. https://doi.org/10.1007/s10825-022-01906-9

Ge S. S., Yang C., Lee T. H., Adaptive Predictive Control Using Neural Network for a Class of Pure-Feedback Systems in Discrete Time. IEEE Transactions on Neural Networks 19(9), 1599-1614, 2008. https://doi.org/10.1109/TNN.2008.2000446

Gopakumar A., Vijayakumari A., Model predictive current controller for grid connected PV inverter. 2017 International Conference on Circuit, Power and Computing Technologies (ICCPCT), 1–6, 2017. https://doi.org/10.1109/ICCPCT.2017.8074309

Hannan M. A., Abd Ghani Z., Mohamed A., An Enhanced Inverter Controller for PV Applications Using the dSPACE Platform. International Journal of Photoenergy 2010, 1–10, 2010. https://doi.org/10.1155/2010/457562

Harashima F., Demizu Y., Kondo S., Hashimoto H., Application of neural networks to power converter control. Conference Record- IAS Annual Meeting (IEEE Industry Applications Society) pt 1, 1086–1091, 1989. https://doi.org/10.1109/ias.1989.96777

Hassaine L., Olias E., Quintero J., Haddadi M., Digital power factor control and reactive power regulation for grid-connected photovoltaic inverter. Renewable Energy 34(1), 315-321, 2009. https://doi.org/10.1016/j.renene.2008.03.016

Jana J., Saha H., Das Bhattacharya K., A review of inverter topologies for single-phase grid-connected photovoltaic systems. Renewable and Sustainable Energy Reviews 72, 1256-1270, 2017. https://doi.org/10.1016/j.rser.2016.10.049

Khan H. S., Mohamed I. S., Kauhaniemi K., Liu L., Artificial Neural Network-Based Voltage Control of DC/DC Converter for DC Microgrid Applications. 2021 6th IEEE Workshop on the Electronic Grid (eGRID), 1-6, 2021. https://doi.org/10.1109/eGRID52793.2021.9662132

Leon J. I., Kouro S., Franquelo L. G., Rodriguez J., Wu B., The Essential Role and the Continuous Evolution of Modulation Techniques for Voltage-Source Inverters in the Past, Present, and Future Power Electronics. IEEE Transactions on Industrial Electronics 63(5), 2688-2701, 2016. https://doi.org/10.1109/TIE.2016.2519321

Mohamed A. A. S., Metwally H., El-Sayed A., Selem S. I., Predictive neural network based adaptive controller for grid-connected PV systems supplying pulse-load. Solar Energy 193(September), 139-147, 2019. https://doi.org/10.1016/j.solener.2019.09.018

Mohamed I. S., Rovetta S., Do T. D., Dragicevic T., Diab A. A. Z., A neural-network-based model predictive control of three-phase inverter with an output LC Filter. IEEE Access 7, 124737-124749, 2019. https://doi.org/10.1109/ACCESS.2019.2938220

Panigrahi R., Mishra S. K., Srivastava S. C., Grid Integration of Small-Scale Photovoltaic Systems-A Review. 2018 IEEE Industry Applications Society Annual Meeting (IAS), 1-8, 2018. https://doi.org/10.1109/IAS.2018.8544503

Rajab Al-Jaboury, O. N., Hamodat Z., Daoud R. W., Design of Power Control Circuit for Grid-Connected PV System-Based Neural Network. Journal of Robotics and Control (JRC) 5(3), 821-828, 2024. https://doi.org/10.18196/jrc.v5i3.20751

Rivera M., Morales F., Baier C., Munoz J., Tarisciotti L., Zanchetta P., Wheeler P., A modulated model predictive control scheme for a two-level voltage source inverter. 2015 IEEE International Conference on Industrial Technology (ICIT), 2224-2229, 2015. https://doi.org/10.1109/ICIT.2015.7125425

Selvan S., Nair P., Umayal U., A Review on Photo Voltaic MPPT Algorithms. International Journal of Electrical and Computer Engineering (IJECE) 6(2), 567, 2016. https://doi.org/10.11591/ijece.v6i2.9204

Singh K., Swathi P., Reddy M. U., Performance analysis of PV inverter in microgrid connected with PV system employing ANN control. 2014 International Conference on Green Computing Communication and Electrical Engineering (ICGCCEE), 1-6, 2014. https://doi.org/10.1109/ICGCCEE.2014.6922390

Syed I. M., Raahemifar K., Model Predictive Control of Three Phase Inverter for PV Systems. International Journal of Energy and Power Engineering 9(10), 1188-1193, 2015. https://doi.org/10.5281/zenodo.1109641

Vora K., Liu S., Dhulipati H., Deep Reinforcement Learning Based MPPT Control for Grid Connected PV System. 2024 IEEE 7th International Conference on Industrial Cyber-Physical Systems (ICPS), 1-5, 2024. https://doi.org/10.1109/ICPS59941.2024.10639977

Yağan Y. E., Vardar K., Ebeoğlu A., Investigation of MPPT Methods Used In PV Systems. IOSR Journal of Electrical and Electronics Engineering (IOSR-JEEE) 13(2), 84-95, 2018. https://doi.org/10.9790/1676-1302028495

JOURNAL of
MATERIALS and MECHATRONICS:A

e-ISSN 2717-8811
JournalMM, 2025, 6(1), 203-213
https://doi.org/10.55546/jmm.1663026

Araştırma Makalesi / Research Article

Precursor Molarity Dependent Morphological, Structural and Optical Properties of Hydrothermally Deposited Antimony Sulfide Thin Films

Fulya TURKOGLU*

* Iskenderun Technical University, Faculty of Engineering and Natural Sciences, Department of Metallurgical and Materials Engineering, Hatay, Türkiye,
ORCID ID: https://orcid.org/0000-0003-0378-8975, fulya.koseoglu@iste.edu.tr

Geliş/ Received: 21.03.2025; **Revize/Revised:** 15.04.2025 **Kabul / Accepted:** 12.05.2025

ABSTRACT: Antimony sulfide (Sb_2S_3) holds great promise as an absorber material for inorganic semiconductor photovoltaics. However, despite recent progress, the achieved efficiencies of Sb_2S_3 solar cells remain substantially below their theoretical potential. Optimizing the morphological, optical, and structural properties of Sb_2S_3 films is crucial for realizing its full potential. This research utilized hydrothermal deposition technique to deposit high-quality Sb_2S_3 thin films on indium tin oxide (ITO) coated glass substrates with varying antimony potassium tartrate ($C_8H_4K_2O_{12}Sb_2 \bullet xH_2O$) and sodium thiosulfate pentahydrate ($Na_2S_2O_3 \bullet 5H_2O$) concentrations. The films were characterized using X-ray diffraction (XRD), scanning electron microscopy (SEM), and UV-visible spectroscopy to evaluate their structural, morphological, and optical properties. Characterization results revealed a strong correlation between the concentrations of the reactants and the resulting film characteristics. Notably, controlled molarities of Sb and S sources in the precursor solution yielded Sb_2S_3 films with suitable band gap, compact surface, and (hk1) preferred orientation, all vital for efficient photovoltaics.

Keywords: Antimony sulfide, Hydrothermal deposition, Thin film solar cells

*Sorumlu yazar / Corresponding author: fulya.koseoglu@iste.edu.tr
Bu makaleye atıf yapmak için /To cite this article

Turkoglu, F. (2025). Precursor Molarity Dependent Morphological, Structural and Optical Properties of Hydrothermally Deposited Antimony Sulfide Thin Films. Journal of Materials and Mechatronics: A (JournalMM), 6(1), 203-213.

1. INTRODUCTION

Thin film solar cells have garnered significant interest due to their potential for flexibility and low environmental impact. While Cu (In, Ga) Se_2 (CIGS) and CdTe demonstrate exceptional power conversion efficiencies (PCEs) over 22% (Green et al., 2018; Wang et al., 2021), their commercial viability is hindered by the high cost of indium and gallium and the environmental concerns associated with cadmium. Cu_2ZnSn (S, Se)$_4$ (CZTSSe), composed of abundant and inexpensive elements, offers a promising alternative. However, its efficiency is hindered by high rates of charge carrier recombination, resulting in short carrier lifetimes and diffusion lengths (Kim et al., 2018; Turkoglu et al., 2019). With its non-toxic and abundant elements, suitable bandgap (~1.7 eV), and high absorption coefficient (~10^5 cm^{-1}), antimony sulfide (Sb_2S_3) has the potential to overcome the limitations of other materials and contributes to the development of cost-effective, high-performance thin-film solar cells (Kondrotas et al., 2018).

Currently, the highest efficiency attained by Sb_2S_3 solar cells is 8.2% (Deng et al., 2024). Despite this endeavor, these devices fall short of the theoretical maximum efficiency predicted by the Shockley-Queisser limit (Shockley and Queisser, 1961). To realize the complete potential of Sb_2S_3 solar cells, it is crucial to develop efficient and scalable deposition techniques, as it influences the material's morphology, structure, electrical properties, and defect density. To produce state-of-the-art Sb_2S_3 thin films, researchers utilize a range of physical and chemical deposition techniques, each with its own set of benefits and drawbacks (Ito et al., 2013; Shaji et al., 2017; Lee et al., 2020). Out of these, hydrothermal method has gained significant interest in depositing Sb_2S_3 thin films. This preference stems from the inherent advantages of hydrothermal deposition, such as low-cost, low-temperature processing, favorable film growth, precise control over film thickness and morphology, and high reproducibility (Liu et al., 2016; Tang et al., 2020; Chen and Chen, 2020; Jin et al., 2020). Moreover, Sb_2S_3 solar cells fabricated via hydrothermal deposition currently hold the record for the highest PCE (Deng et al., 2024).

The effectiveness of hydrothermal deposition relies heavily on the careful manipulation of temperature, deposition time, pressure, precursor molarity, and pH, which are crucial reaction parameters. These parameters, along with annealing conditions, directly influence final film properties, such as thickness, crystallinity, morphology, composition, grain size, and orientation (Zhao et al., 2009; Vavale et al., 2018). Therefore, optimizing these parameters is crucial for tailoring thin films with desired properties for specific applications. Optimization of hydrothermal deposition processes, specifically through doping (Myagmarsereejid et al., 2021), post-annealing treatment (Pawar et al., 2022), and surfactant additives (Zheng et al., 2022), is the primary focus of current studies. However, the role of precursor molarity in determining the film's microstructural and physical properties lacks a thorough investigation.

To leverage the inherent simplicity, cost-effectiveness, and scalability offered by this deposition process, this work aimed to investigate the hydrothermal synthesis of Sb_2S_3 thin films, focusing on optimizing the molarities of Sb (Antimony potassium tartrate) and S (sodium thiosulfate pentahydrate) sources to achieve optimal film properties. Ultimately, dense, highly crystalline Sb_2S_3 thin films with (hk1) preferred orientation were successfully synthesized on indium tin oxide (ITO) coated glass substrates. The findings of this research are expected to pave the way for the development of economically viable and efficient Sb_2S_3-based solar cells.

2. MATERIALS AND METHODS

Hydrothermal deposition was employed to produce Sb_2S_3 thin films on 26 mm x 76 mm SLG/ITO substrates with ITO thickness of 120 nm, purchased from Teknoma Technological Materials Industrial and Trading Inc. (https://teknoma.net/). Antimony potassium tartrate ($C_8H_4K_2O_{12}Sb_2 \bullet xH_2O$, 99%, Merck) and sodium thiosulfate pentahydrate ($Na_2S_2O_3 \bullet 5H_2O$, 99%, Merck) were used as Sb and S sources, respectively. 60 mL of aqueous solutions of $C_8H_4K_2O_{12}Sb_2 \bullet xH_2O$ and $Na_2S_2O_3 \bullet 5H_2O$ were prepared with different molarities. Solutions were stirred using a magnetic stirrer at 400 rpm until homogeneous mixtures were obtained and the pH of the solutions was measured using a pH meter. To optimize Sb and S source molarities, three precursor solutions were prepared with the compositions detailed in Table 1. The Sb_2S_3 thin films synthesized from these solutions were labeled AG-S1, AG-S2, and AG-S3. After that, solutions were poured into the Teflon tank (100 ml) of the autoclave. SLG/ITO substrates were placed in the hydrothermal reactor with the ITO side down and oriented at a 75° angle. The autoclave was then sealed, and Sb_2S_3 thin films were deposited on ITO via hydrothermal treatment at 135 °C for 7.5 hours. Following their formation, the Sb_2S_3 films were rinsed with deionized water and subsequently dried under ambient conditions. Finally, thermal annealing was conducted at 325 °C, employing a temperature ramp rate of 23 °C/min and a 15-minute dwell time, under an argon atmosphere. After annealing, samples AG-S1, AG-S2, and AG-S3 were designated as A-S1, A-S2, and A-S3.

Scanning electron microscopy (SEM) analysis was conducted using Thermo Fisher Scientific Apreo S LoVac SEM device to examine the morphology and determine stoichiometry of the Sb_2S_3 films. Surface topographies of the prepared films were visualized using Everhart-Thornley Detector (ETD) at 10 kX and 25 kX magnifications with 10 kV acceleration voltage and 10 spot size. To reveal elemental compositions of the films, Energy-Dispersive X-ray Spectroscopy (EDS) measurements were performed at 30 kV, 10 kX magnification, and 10 mm working distance. The thicknesses of the fabricated thin films were determined using side view SEM images at 50 kX magnifications. X-ray diffraction (XRD) was employed to analyze the crystal structure of the films. XRD measurements were conducted on a Malvern Panalytical EMPYREAN X-Ray diffractometer in Bragg-Brentano setup, using copper K-alpha radiation with the wavelength of 1.5406 angstroms. XRD data were collected for all samples across a 2θ range of 10°- 60°, using a step size of 0.0262° and a scan rate of 2 °/min. Band gaps of fabricated films were determined by analyzing their ultraviolet-visible (UV-VIS) transmission spectra within the 1100 to 500 nm range using Jasco/V-750 UV/VIS Spectrophotometer.

Table 1. The molarities of Sb and S sources in the precursor solutions employed for the synthesis of Sb_2S_3 thin films AG-S1, AG-S2, and AG-S3. The pH values of the respective precursor solutions

Sample Name	$C_8H_4K_2O_{12}Sb_2 \bullet xH_2O$ (mM)	$Na_2S_2O_3 \bullet 5H_2O$ (mM)	pH of the solution
AG-S1	30	150	5.82
AG-S2	20	160	5.85
AG-S3	20	120	5.80

3. RESULTS AND DISCUSSION

3.1 Scanning Electron Microscopy Analysis

Scanning electron microscopy (SEM) was used to examine the top-view and cross-sectional morphologies of the fabricated Sb_2S_3 thin films, with Figures 1a)-i) and 2a)-f) showing the respective

images of the as-grown and annealed films. While cross-sectional SEM images showed compact and continuous Sb_2S_3 films, the top-view images primarily revealed a collection of spherical particles both on as-deposited and annealed samples. The particles were closely packed together, forming a dense layer. However, depending on concentrations of reactants, hollow cone-like structures were also observed on the surface of some Sb_2S_3 films (Figures 1a)-f)), likely resulting from the growth mechanisms of the materials during hydrothermal synthesis. Because the films were fabricated under identical growth conditions, varying only the molarities of S and Sb sources, it is evident that concentrations of the reactants impact the morphology of the hydrothermally synthesized films (Vavale et al., 2018). The magnified SEM images presented in Figures 1c), f), and i) provided clear visual evidence of inter-particle voids formed between some large spherical particles on the surfaces of the films with high concentrations of S and Sb sources (A-S1 and A-S2), while the film having lower concentration of the reactants (A-S3) did not display these inter-particle voids. It's a very interesting point that hollow cone-like structures grew inside these inter-particle voids. The formation of these structures is likely driven by surface energy minimization. The Sb_2S_3 crystals within the void may grow in a way that minimizes their surface energy. The confined space within the void restricts the growth of the Sb_2S_3 crystals in certain directions. The hollow cone-like shape may represent a configuration that minimizes the overall surface energy of the crystals within the confined space. This can lead to anisotropic growth, where the crystals preferentially grow outwards from the void, forming the hollow cone-like structures. Decreasing the concentration of reactants yielded Sb_2S_3 thin films (A-S3) with a compact surface morphology and no observable morphological alterations. Thus, optimizing the concentration of precursors is crucial for achieving high-quality Sb_2S_3 films.

As determined by cross-sectional SEM, as-grown samples AG-S1, AG-S2, and AG-S3 exhibited film thicknesses of 1200 nm, 885 nm, and 835 nm with a precision 4%, respectively. Annealing resulted in film thickness reductions, yielding 1005 nm, 735 nm, and 728 nm with a precision 4% for the samples A-S1, A-S2, and A-S3, respectively. The observed reduction in thickness was attributed to the densification of the films during the annealing process. Specifically, annealing provides thermal energy, facilitating the rearrangement of atoms or grains into a more compact and denser configuration. Sample AG-S1, produced with a higher concentration of the Sb source, possessed a greater thickness and, therefore, a higher film deposition rate. Lower thicknesses of the AG-S2 and AG-S3 films confirmed the expected dependence of growth rate on concentration of the Sb source.

As evidenced by EDS analysis (Table 2), the S/Sb atomic ratios of both as-deposited and annealed films (ranging from 1.45 to 1.49) are in close alignment with the stoichiometric Sb_2S_3 composition of 1.5. Notably, the observation that these ratios remained nearly constant following annealing suggests the formation of a homogeneous Sb_2S_3 film exhibiting a uniform spatial distribution of Sb and S.

Table 2. Average atomic compositions of fabricated Sb_2S_3 thin films

Sample Name	[S] Atomic %	[Sb] Atomic %	S/Sb
AG-S1	59.11	40.89	1.45
AG-S2	59.51	40.49	1.47
AG-S3	59.34	40.66	1.46
A-S1	59.21	40.79	1.45
A-S2	59.52	40.48	1.47
A-S3	59.77	40.23	1.49

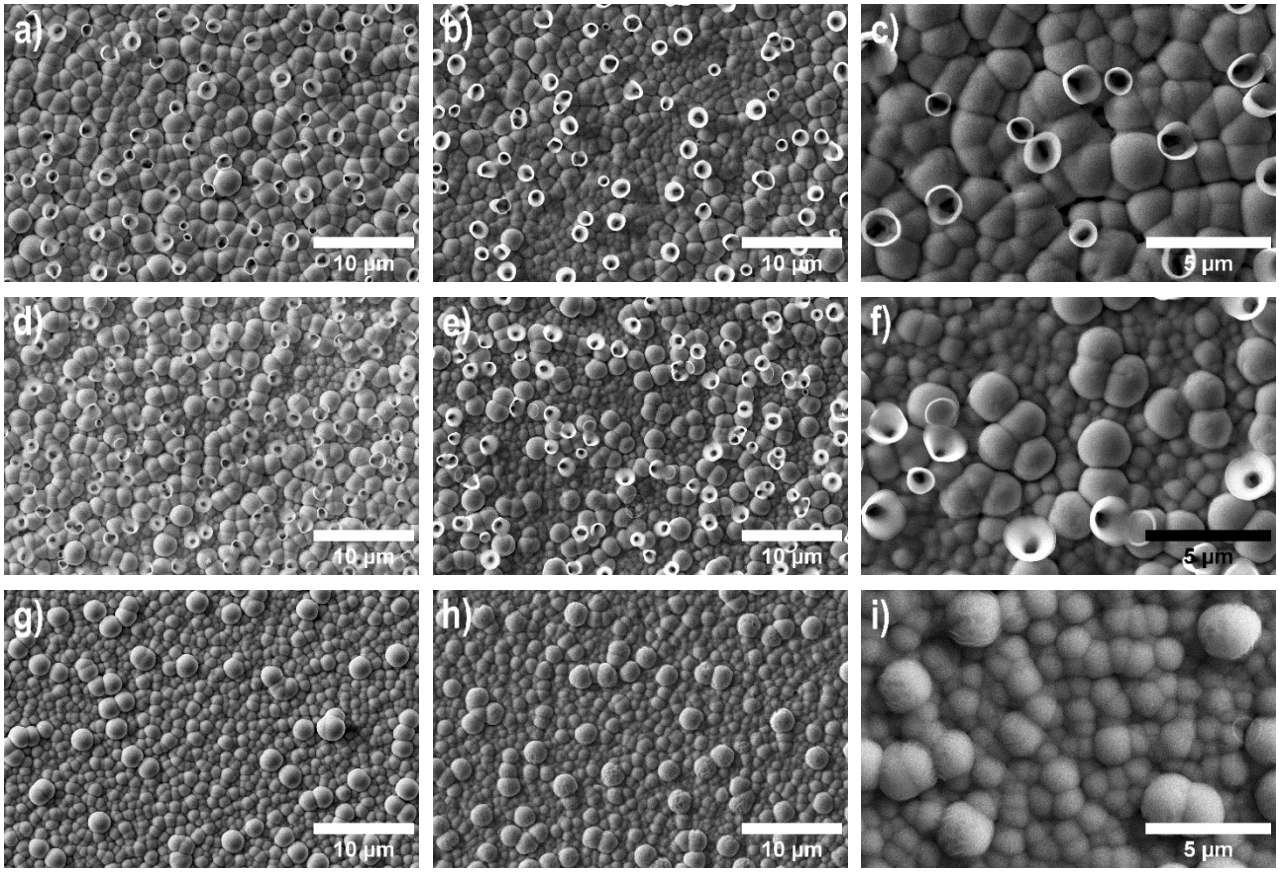

Figure 1. SEM images of as-grown a) AG-S1, d) AG-S2, g) AG-S3 and annealed b) A-S1, e) A-S2, h) A-S3 Sb_2S_3 thin films synthesized with varying concentrations of the S and Sb precursors. Magnified views of the annealed samples c) A-S1, f) A-S2, i) A-S3 are included for detailed analysis

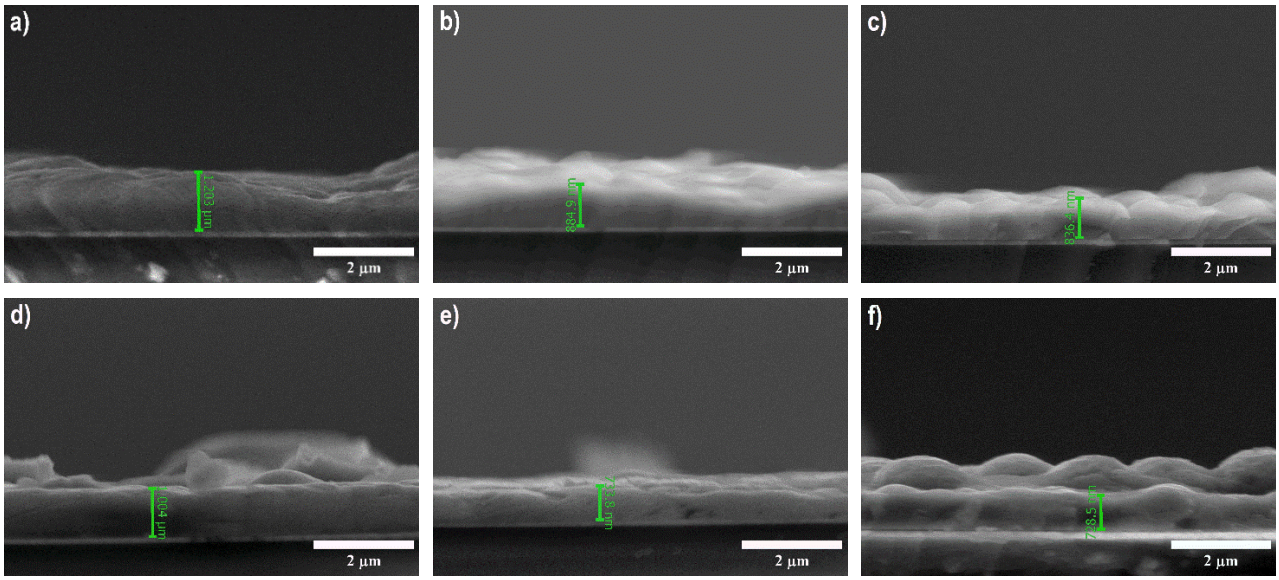

Figure 2. Cross-sectional SEM images of as-grown a) AG-S1, b) AG-S2, c) AG-S3, and annealed d) A-S1, e) A-S2 and f) A-S3 Sb_2S_3 thin films fabricated with varying concentrations of the S and Sb precursors

3.2 X-Ray Diffraction Analysis

Figure 3 shows the X-ray diffraction patterns of deposited Sb_2S_3 thin films. All films were found to be polycrystalline in nature. The XRD patterns provided confirmation of the orthorhombic Sb_2S_3 phase (JCPDS # 42-1393), with diffraction peaks observed at 2θ values of 17.546°, 29.249°,

25.005°, 32.379°and 33.413°, corresponding to the (120), (211), (310), (221), (301) crystallographic planes, respectively. The absence of impurity or secondary phase peaks, coupled with sharp diffraction peaks, confirmed the successful synthesis of highly crystalline Sb_2S_3 thin films. While the positions of the diffraction peaks remained unchanged despite variations in concentrations of reactants, their relative intensities changed significantly.

The crystallographic orientation of Sb_2S_3 thin films plays a crucial role in determining solar cell performance, as it impacts charge carrier transport mechanisms and the formation of beneficial grain boundaries. In photovoltaic applications, vertical orientation, characterized by the c-axis orientation perpendicular to the substrate, is considered advantageous for facilitating efficient charge carrier transport within the absorber layer (Tang et al., 2020; Cantas et al., 2023). It was observed that the preferential orientations of hydrothermally deposited Sb_2S_3 thin films are highly sensitive to the relative concentrations of Sb and S ions in the precursor's solution. Films synthesized with a higher Sb (A-S1) and S (A-S2) molarities exhibited a preferential orientation along the (310), whereas film synthesized with a lower Sb and S molarity (A-S3) showed a preference for the (211). Variations in preferential orientation may arise from alterations in ion adsorption and surface energy. Changing concentrations of the reactants may shift the balance of adsorbed ions, potentially favoring the growth of planes with lower surface energies in the new environment.

For quantitative analysis of the samples' preferred orientation, texture coefficients (TCs) of the diffraction peaks were determined based on the following equation and presented graphically in Figure 4.

$$TC_{(hkl)} = \frac{I_{(hkl)}}{I_{0(hkl)}} \Big/ \left(\frac{1}{N} \sum \frac{I_{(hkl)}}{I_{0(hkl)}} \right)$$

In this formula, $I_{(hkl)}$ represents the measured intensity of the (hkl) diffraction peak, $I_{0(hkl)}$ is the corresponding peak intensity from the reference pattern (JCPDS # 42-1393), and N is the total number of reflections considered. The TC value directly indicates the degree of preferred orientation of crystallites along the (hkl) plane within the film, with higher values denoting stronger orientation (Turkoglu et al., 2022). As demonstrated in Figure 4, the film with the highest Sb molarity in the precursor solution (A-S1) displayed the most pronounced (hk0) preferred orientation. It is postulated that the elevated Sb molarity in the solution, which accelerates the film deposition process, may promote a stronger (hk0) preferred orientation. A similar trend was reported in (Xie et al., 2022), where high Sb_2S_3 thin film deposition rates resulted in a stronger (hk0) preferred orientation. For films having equal Sb concentrations and similar thicknesses (A-S2 and A-S3), it is evident that a lower sulfur concentration enhances the (hk1) preferred orientation. A comparison of the texture coefficients (TC) for the (211) and (310) crystal planes (inset of Figure 4) also revealed that the film prepared with lower Sb and S molarities (A-S3) had the highest TC (211)/TC (310) ratio of 1.26. These results highlight that manipulating the concentration of the precursors enables the growth of tilted $(Sb_4S_6)_n$ ribbons and higher TC value for (hk1) planes.

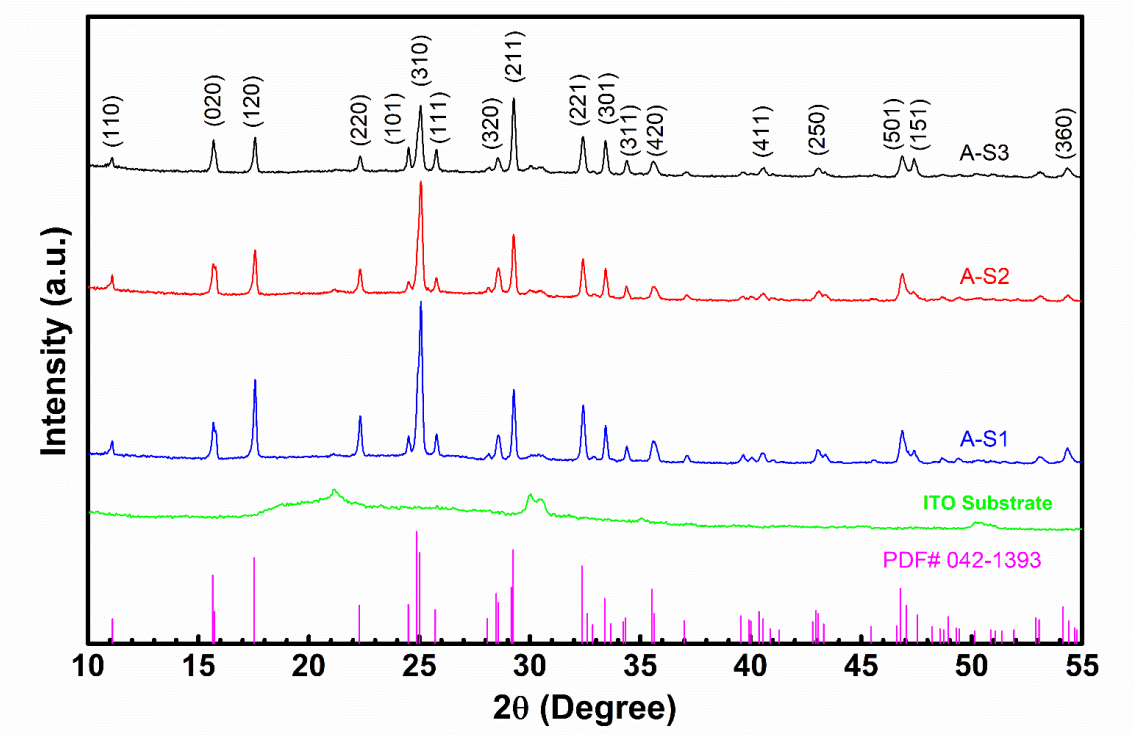

Figure 3. XRD spectra of Indium Tin Oxide (ITO) substrate and annealed Sb_2S_3 thin films (A-S1, A-S2 and A-S3) fabricated with varying concentrations of reactants

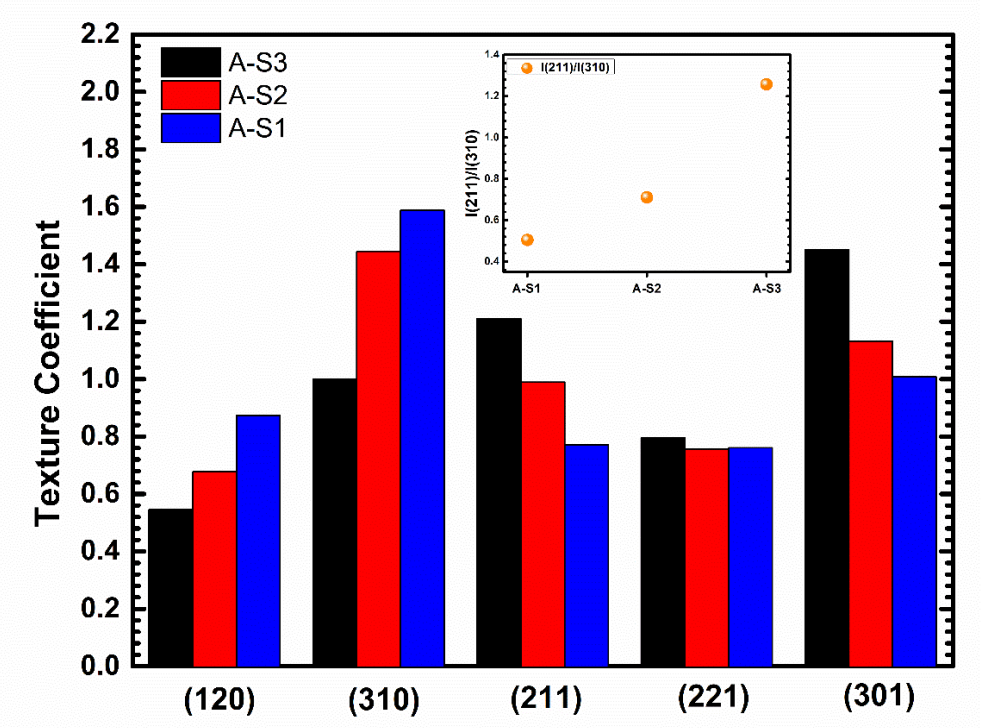

Figure 4. The texture coefficients (TC) of the diffraction patterns of the annealed Sb_2S_3 thin films (A-S1, A-S2 and A-S3). Inset graph: variation of the TC (211)/TC (310) ratio of the diffraction patterns

3.3 UV/VIS Spectrophotometer Analysis

The optical band gap energies of the Sb_2S_3 thin films were determined by analyzing their ultraviolet-visible (UV-VIS) transmission spectrum within the wavelength range of 500 to 1100 nm.

As shown in Figure 5, the observed very low transmission in both as-grown and annealed Sb_2S_3 thin films suggests that the fabricated films effectively absorb a significant portion of visible light (Chen and Chen, 2020). The transmission spectra showed a shift towards shorter wavelengths in as-grown Sb_2S_3 thin films, indicating wider band gaps compared to annealed films. The observed shift towards shorter wavelengths after annealing is likely due to improved crystallinity and a reduction in defects, leading to a change in the electronic band structure. Optical band gaps of the Sb_2S_3 thin films were determined using Tauc equation, $\alpha h\nu = A(h\nu - E_g)^{1/2}$, where α is the absorption coefficient, hν is the photon energy, A is a constant, and E_g is the optical band gap. The bandgaps of the films were obtained through extrapolation of the linear portions of the $(\alpha h\upsilon)^2$ versus (hυ) plots (Figure 6). As-grown films had optical band gaps of 2.13 eV (AG-S1), 2.08 eV (AG-S2), and 2.04 eV (AG-S3), while annealed films had band gaps of 1.67 eV (A-S1), 1.69 eV (A-S2), and 1.68 eV (A-S3). The optical band gap values obtained in this work are consistent with previously published results (Liu et al., 2016; Chen and Chen, 2020). In summary, optical characterization showed that the band gaps of the Sb_2S_3 films are not significantly affected by molarities of precursors, and films with suitable band gaps can be obtained via the hydrothermal method.

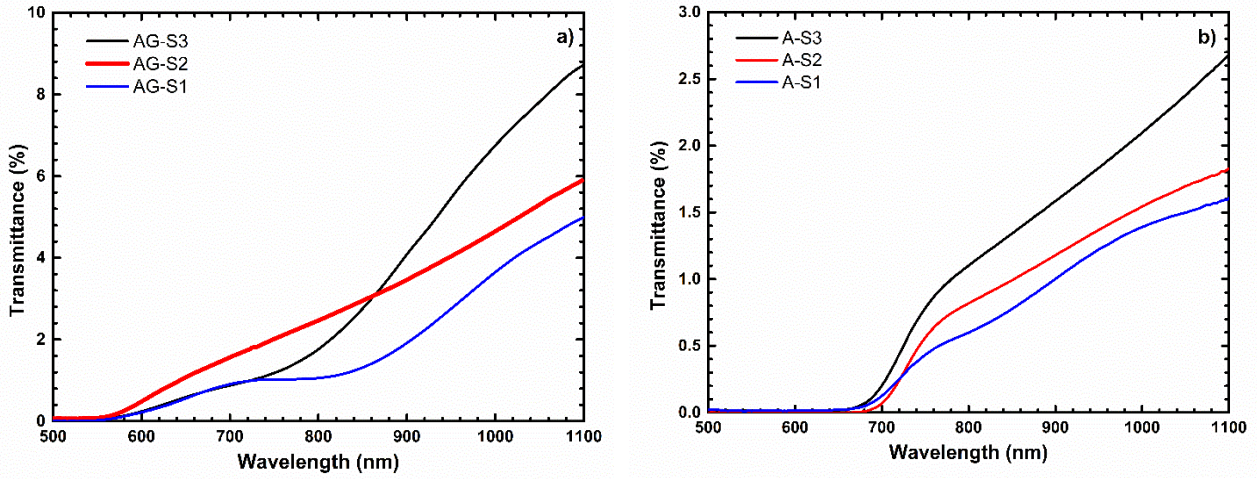

Figure 5. Transmission spectra of a) as-grown and b) annealed Sb_2S_3 thin films with varying concentrations of the reactants

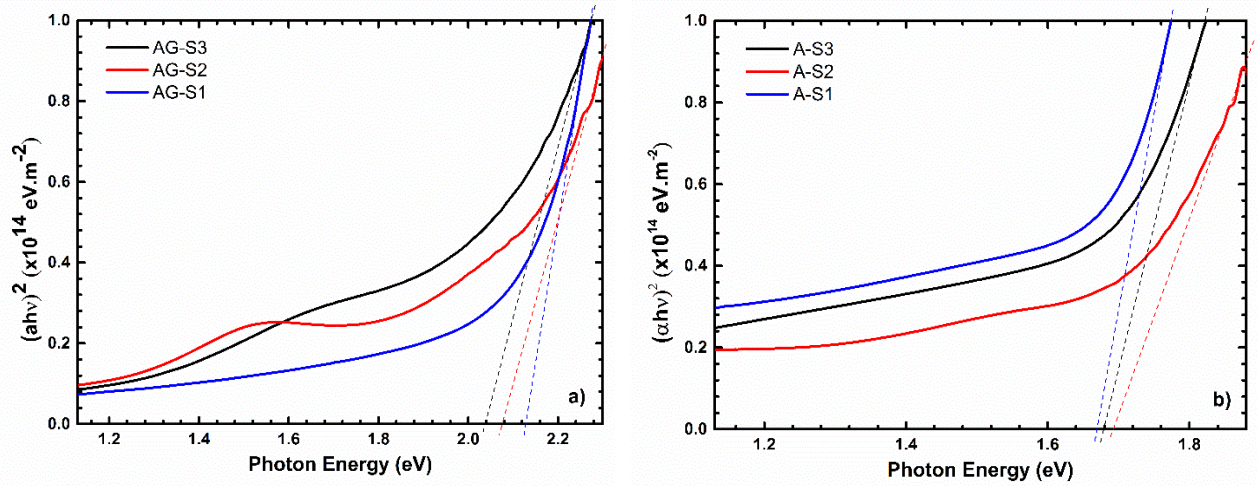

Figure 6. Optical band gap energy of a) as-grown and b) annealed Sb_2S_3 thin films with varying concentrations of the reactants

4. CONCLUSION

This study employed hydrothermal deposition to fabricate Sb_2S_3 thin films on ITO coated glass substrates. The influence of antimony potassium tartrate ($C_8H_4K_2O_{12}Sb_2 \cdot xH_2O$) and sodium thiosulfate pentahydrate ($Na_2S_2O_3 \cdot 5H_2O$) concentrations in the precursor solution was examined. Morphological, structural and optical properties of the films were investigated through SEM, XRD, and UV-visible spectroscopy. Top-view SEM images revealed a consistent presence of spherical particles on the surface of synthesized Sb_2S_3 samples, while cross-sectional SEM indicated continuous film formation. However, hollow cone-like structures were observed growing within inter-particle voids in samples A-S1 and A-S2, which were synthesized with higher S and Sb source concentrations. This was potentially due to surface energy minimization within the voids. Low reactant concentration yielded compact and uniform surface. The preferred orientation of Sb_2S_3 films was also found to be highly sensitive to concentrations of the reactants. It was observed that films synthesized with higher Sb and S concentrations displayed a preference for (hk0) orientation, whereas those synthesized with lower concentrations exhibited a preference for (hk1) orientation. Optical characterization showed that the band gaps of the films were not significantly affected by molarities of precursors, and films with suitable band gaps can be obtained via the hydrothermal method. The synthesis of Sb_2S_3 films with a suitable band gap, compact surface morphology, and (hk1) preferred crystallographic orientation was successfully accomplished utilizing a precursor solution containing 20 mM antimony potassium tartrate and 120 mM sodium thiosulfate pentahydrate. To summarize, the reactant concentration significantly influences Sb_2S_3 film properties, making careful control essential for achieving consistent and desired outcomes. It is expected that these findings hold promise for the development of efficient and cost-effective Sb_2S_3-based solar cells.

5. ACKNOWLEDGEMENTS

The author acknowledge the use of facilities provided by ISTE Center for Science and Technology Studies and Research (ISTE-CSTSR) for this research.

6. CONFLICT OF INTEREST

Author approves that to the best of their knowledge, there is not any conflict of interest or common interest with an institution/organization or a person that may affect the review process of the paper.

7. AUTHOR CONTRIBUTION

Fulya TURKOGLU has the full responsibility of the paper about determining the concept of the research, data collection, data analysis and interpretation of the results, preparation of the manuscript and critical analysis of the intellectual content with the final approval.

8. REFERENCES

Cantas A., Gundogan S. H., Turkoglu F., Koseoglu H., Aygun G., Ozyuzer L., Photovoltaic performance of magnetron sputtered antimony selenide thin film solar cells buffered by cadmium sulfide and cadmium sulfide/zinc sulfide, Thin Solid Films 784, 140070, 2023.

Chen Z., Chen G., The effect of absorber thickness on the planar Sb_2S_3 thin film solar cell: Trade-off between light absorption and charge separation, Solar Energy 201, 323-329, 2020.

Deng H., Feng X., Zhu Q., Liu Y., Wang G., Zhang C., Zheng Q., Wu J., Wang W., Cheng S., 8.2%-Efficiency hydrothermal Sb_2S_3 thin film solar cells by two-step RTP annealing strategy, Science China Materials 67(11), 3666-3674, 2024.

Green M. A., Hishikawa Y., Dunlop E. D., Levi D. H., Hohl-Ebinger J., Ho-Baillie A.W., Solar cell efficiency tables (version 52), Progress in Photovoltaics: Research and Applications 26(1), 3-12, 2018.

Ito S., Tsujimoto K., Nguyen D-C., Manabe K., Nishino H., Doping effects in Sb_2S_3 absorber for full-inorganic printed solar cells with 5.7% conversion efficiency, International Journal of Hydrogen Energy 38, 16749-16754, 2013.

Jin X., Fang Y., Salim T., Feng M., Hadke S., Leow S. W., Sum T. C., Wong L.H., In Situ Growth of [hk1]-Oriented Sb_2S_3 for Solution-Processed Planar Heterojunction Solar Cell with 6.4% Efficiency, Advanced Functional Materials 30, 2002887, 2020.

Kim S., Park J-S., Walsh A., Identification of killer defects in kesterite thin-film solar cells, ACS Energy Letters 3(2), 496-500, 2018.

Kondrotas R., Chen C., Tang J., Sb_2S_3 solar cells, Joule 2(5), 857-878, 2018.

Lee S-J., Sung S-J., Yang K-J., Kang J-K., Kim J. Y., Do Y. S., Kim D-H., Approach to Transparent Photovoltaics Based on Wide Band Gap Sb_2S_3 Absorber Layers and Optics-Based Device Optimization, ACS Applied Energy Materials 3, 12644-12651, 2020.

Liu M., Gong Y., Li Z., Dou M., Wang F., A green and facile hydrothermal approach for the synthesis of high-quality semi-conducting Sb_2S_3 thin films, Applied Surface Science 387, 790–795, 2016.

Myagmarsereejid P., Ingram M., Batmunkh M., Zhong Y.L., Doping strategies in Sb_2S_3 thin films for solar cells, Small 17(39), 2100241, 2021.

Pawar P. S., Nandi R., Neerugatti K. E., Cho J. Y., Heo J., Hydrothermal growth of Sb_2S_3 thin films on molybdenum for solar cell applications: Effect of post-deposition annealing, Journal of Alloys and Compounds 898, 162891, 2022.

Shaji S., Garcia L.V., Loredo S.L., Krishnan B., Aguilar Martinez J.A., Das Roy T.K., Avellaneda D.A., Antimony sulfide thin films prepared by laser assisted chemical bath deposition, Applied Surface Science 393, 369-376, 2017.

Shockley W., Queisser H.J., The Shockley-Queisser limit, Journal of Applied Physics 32(3), 510-519, 1961.

Tang R., Wang X., Lian W., Huang J., Wei Q., Huang M., Yin Y., Jiang C., Yang S., Xing G., Chen S., Zhu C., Hao X., Green M.A., Chen T., Hydrothermal deposition of antimony selenosulfide thin films enables solar cells with 10% efficiency, Nature Energy 5, 587-595, 2020.

Turkoglu F., Ekren M.E., Cantas A., Yakinci K., Gundogan H., Koseoglu H., Aygun G., Ozyuzer L., Structural and optical characteristics of antimony selenosulfide thin films prepared by two-step method, Journal of the Korean Physical Society 81 (3), 278-284, 2022.

Turkoglu F., Koseoglu H., Cantas A., Akca F.G., Meric E., Buldu D.G., Ozdemir M., Tarhan E., Ozyuzer L., Aygun G., Effect of defects and secondary phases in Cu_2ZnSnS_4 absorber material on the performance of Zn(O,S) buffered devices, Thin Solid Films 670, 6-16, 2019.

Vavale S.D., Pawar S.G., Deshmukh D.H., Deshmukh H.P., Hydrothermal method for Synthesis of different Nanostructure Metal Oxide thin film, International Journal of Innovative Knowledge Concepts 6(11), 126, 2018.

Wang D., Yang Y., Guo T., Xiong X., Xie Y., Li K., Li B., Ghali M., Effect of pulse bias voltages on performance of CdTe thin film solar cells prepared by pulsed laser deposition, Solar Energy 213, 118-125, 2021.

Xie Y., Li K., Li X., Gao F., Xiong X., Zeng G., Li B., Fabrication of Sb_2S_3 solar cells by close space sublimation and enhancing the efficiency via co-selenization, Materials Science in Semiconductor Processing 142, 106451, 2022.

Zhao X., Lee J.Y., Kim C-R., Heo J., Shin C.M., Leem J-Y., Sun X., Dependence of the properties of hydrothermally grown ZnO on precursor concentration, Physica E: Low-Dimensional Systems and Nanostructures 41(8), 1423-1426, 2009.

Zheng J., Liu C., Zhang L., Chen Y., Bao F., Liu J., Zhu H., Shen K., Mai Y., Enhanced hydrothermal heterogeneous deposition with surfactant additives for efficient Sb_2S_3 solar cells, Chemical Engineering Journal 446, 136474, 2022.

JOURNAL of
MATERIALS and MECHATRONICS:A

e-ISSN 2717-8811
JournalMM, 2025, 6(1), 214-225
https://doi.org/10.55546/jmm.1665380

Araştırma Makalesi / Research Article

Investigation of Hydrophobicity in Calcium Stearate-Epoxy Based Composite Materials

İsmail Sinan ATLI[1*], Hakan ÇİFTÇİ[2]

[1*] Afyon Kocatepe Üniversitesi, Teknoloji Fakültesi, Metalurji ve Malzeme Mühendisliği Bölümü, Afyonkarahisar Türkiye,
ORCID ID: https://orcid.org/0000-0002-5899-4082, sinanatli@aku.edu.tr
[2] Afyon Kocatepe Üniversitesi, Mühendislik Fakültesi, Maden Mühendisliği Bölümü, Afyonkarahisar Türkiye,
ORCID ID: https://orcid.org/0000-0001-7910-7350, hciftci@aku.edu.tr

Geliş/ Received: 25.03.2025**;** **Revize/Revised:** 18.04.2025 **Kabul / Accepted:** 13.05.2025

ABSTRACT: Hydrophobic surfaces are essential for enhancing the longevity and performance of products across various sectors, particularly in construction, automotive, electronics, and medicine. This characteristic minimizes maintenance expenses by establishing a natural barrier against pollution and corrosion, hence prolonging the lifespan of the materials. Moreover, implementing this technology provides novel methods for attaining energy efficiency and environmental sustainability objectives. This research introduced a composite material formulated with calcium stearate (CS) and epoxy, designed as a coating solution to enhance hydrophobic qualities on surfaces. This technique is intended to create a formulation that integrates the water-repellent characteristics of CS with the structural resilience of epoxy for application on various surfaces. The contact angle of the composite, derived from adding CS into epoxy at concentrations of 1%, 2%, 4%, 6%, 8%, and 10% by weight, was assessed against pure water. Neat epoxy has a hydrophilic structure with a contact angle of 70.5°, whereas the composite containing 8% CS demonstrates the highest hydrophobicity, with a contact angle of 117.5°. Furthermore, adding CS led to a decrease in Shore D hardness values.

Keywords: Composite, Calcium stearate, Hydrophobic, Hydrophilic, Contact angle

*Sorumlu yazar / Corresponding author: sinanatli@aku.edu.tr
Bu makaleye atıf yapmak için /To cite this article

Atlı, İ. S., Çiftçi, H. (2025). Investigation of Hydrophobicity in Calcium Stearate-Epoxy Based Composite Materials. Journal of Materials and Mechatronics: A (JournalMM), 6(1), 214-225.

1. INTRODUCTION

Today, due to their water resistance, corrosion resistance, and antifouling properties, hydrophobic coatings have become necessary and have a wide range of uses. Calcium stearate (CS) has found a place in many studies in this context due to its hydrophobic properties. CS is a water-insoluble metallic stearate salt formed by the combination of stearic acid and calcium ions. It is frequently used in industry as anti-wear, plastic stabilizer, water-repellent additive and surface coating additive (Wang et al., 2020; Li & Yao, 2011). In a study where it was used as a PVC additive due to its high thermal stability, it was stated that CS delayed thermal degradation and preserved the structural integrity of the polymers (Wang et al., 2020). In addition, it has been observed that when used in cement and concrete-based building materials, CS reduces the water absorption rate by reducing the number of pores in the structure and thus increases the resistance to external factors in the long term (Maryoto, 2017; Chen et al., 2022; Lv et al., 2022). However, its use in high-performance polymer matrices like epoxy, especially at the micro-scale level, remains limited and underexplored.

Due to its low surface energy, CS exhibits hydrophobic properties. When used as a coating, it increases the contact angle against water and, therefore, the water resistance. In a study, nano-sized CS-added coatings were prepared via a single-step dipping method, and contact angles of over 150° against water were obtained (Bai et al., 2023). In the same study, it was revealed that the mentioned coatings maintained their hydrophobicity for a long time (Bai et al., 2023). Superhydrophobic coatings containing CS have high resistance to thermal shock, organic solvents, and UV rays (Bai et al., 2023). It has been observed that the coated surfaces retain their hydrophobic properties even after 100 times of sandpaper abrasion and 300 times of tape peeling test. Therefore, it has been suggested that CS can be used in the production of low-cost and environmentally friendly water-repellent coatings (Bai et al., 2023). However, most literature focuses on nano-structured additives or chemical surface modifications to achieve hydrophobicity in epoxy systems. For example, Chen et al. (2024) showed that the contact angle increased from 60.43° to 114.66° by adding 0.89 wt% GO, significantly improving the corrosion resistance.

Ari (2025) evaluated epoxy composites filled with ignimbrite and pine waste and found that the contact angle increased up to 113.79°, while mechanical properties decreased with increasing filler content. These findings highlight the need for studies that optimize both hydrophobicity and mechanical integrity, particularly with industrially relevant micro-fillers like CS.

CS is applied with different methods to provide a hydrophobic surface for different materials. When added to concrete mixtures, it increases the material's service life by reducing the water absorption rate and chloride ion penetration (Chen et al., 2022). In the study, it was shown that the optimum ratio of CS used as an additive at different rates was 4% and that when used at this rate, it significantly reduced the water absorption rate (Chen et al., 2022). It has been suggested that when 3% CS is added to ultra-high molecular weight polyethylene (UHMWPE), the dry wear resistance of UHMWPE increases by 4 times, the friction coefficient decreases by 1.2 times, and therefore it can be used as a solid lubricant (Panin et al., 2015).

Epoxy resins are thermoset polymers used as matrix materials in protective coatings, structural adhesives, and composite materials due to their high mechanical strength, chemical resistance, and high adhesion properties (Xavier, J.R., 2020). Epoxy coatings are frequently used to protect metallic material surfaces from corrosion. Epoxy coatings modified with various metal oxide nanopowders greatly reduce water permeability and corrosion (Xavier et al., 2024). In addition, thin and porous coatings may increase the contact of the substrate material with the water environment and negatively

affect long-term durability. Therefore, different methods may need to be applied to increase the hydrophobic properties of epoxies (Xavier et al., 2024). In one study, fluorine-based additives, nanoparticles that increase surface roughness, and silicon-containing modifications were used to increase the water repellency of epoxy-based coatings (Chang et al., 2022). In another study, as a result of modification of ZIF-8 particles with DMBIM, the contact angle increased to 124.9°, and the hydrophobicity of the coating and thus the corrosion resistance in acidic, basic, and salty environments was significantly increased (Chen et al., 2025). In a study on epoxy composite coatings produced with clay modification, it was observed that water permeability was reduced, and therefore, the coatings maintained their long-term stability (Verma et al., 2024). Aparna et al. (2022) provide a comprehensive review of superhydrophobic epoxy nanocomposites, detailing how fabrication methods, surface roughness, and low-energy additives such as silica and carbon-based nanostructures contribute to water repellency. However, these methods often require complex chemistry and high costs. Doganci and Sevinc (2023) showed that epoxy coatings reinforced with stearic-acid-modified alumina nanoparticles reached contact angles over 150° and demonstrated superior corrosion resistance and surface roughness, especially on galvanized steel. This validates the relevance of roughness-enhancing micro-fillers for practical applications.

This study aimed to investigate the effects of different amounts of CS addition to increase the hydrophobic characteristics of epoxy surfaces. In the literature, it has been demonstrated that CS has water-repellent properties in concrete and cement structures, but its effect on epoxy surfaces has not been investigated sufficiently. Improving the hydrophobic properties of epoxy coatings can increase corrosion resistance and extend the service life of coatings by reducing water absorption. In this context, epoxy composites with CS additive were produced and their contact angle against water and hardness were analyzed. The results of this study will contribute to the development of low-cost, environmentally friendly, and high-performance hydrophobic surfaces. By evaluating CS content ranging from 1 to 10 wt%, this study provides one of the first systematic efforts to quantify the relationship between CS loading, hydrophobic response, and Shore D hardness in epoxy composites, thus offering practical guidelines for material design and application.

2. MATERIALS AND METHODS

2.1 Materials

Epoxy is used as the matrix material and reinforced with CS to increase its hydrophobic properties. MGS LR135/LH135 lamination epoxy set was provided by Dost Kimya Company/Türkiye. According to the information received from the supplier company, the mixing ratio of the resin LR135 and hardener LH135 is: 100:35 ±2 g, and has a working time of 30-45 minutes, depending on the ambient temperature. Its density is 1.1-1.23 g/cm^3, and its viscosity is 1000-1500 mPas.

Melos Inc./Türkiye provided the CS 3701 particles. The company claims that CS3701 is obtained from the reaction of stearic acid and lime: $2C_{17}H_{35}COOH + CaO \rightarrow (C_{17}H_{35}COO)\ 2Ca + H_2O$. The appearance of the powders is white powder, and the melting point is 150,0 ±2,0 °C.

2.2 Particle Size Distribution Measurements

Particle-size distributions of CS particles were determined using the dynamic light scattering (DLS) method by a Malvern Mastersizer 2000 instrument, shown in Fig. 1 (Malvern Panalytical Co., UK), equipped with a dry measuring apparatus. First, the vacuum and compressed air flow were started to clean the measuring system for about 2 minutes. Subsequently, an automatic background

reset was executed while the airflow persisted. The dry sample was thereafter filled in the sample section, and the sample feeding rate was augmented until the laser obscuration level attained 4-5%. Subsequently, automatic measurements commenced, and the average values were taken by conducting each analysis thrice.

Figure 1. Malvern Mastersizer 2000 particle size analyzer instrument

2.3 Sample Preparation

Flat surface composite samples were prepared to measure contact angle against water and Shore D hardness. Composite materials were produced with different CS additive ratios of 0%, 1%, 2%, 4%, 6%, 8%, and 10% by weight. First, the epoxy sample without additive was poured into the mold after mixing the resin and hardener components in a 100:35 ratio by weight with a mechanical mixer for 5 minutes. To prepare the CS-added samples, firstly, the powder CS particles in the determined ratios were mixed with the resin component for 10 minutes. Then the resin-powder mixture was mixed with the hardener for 5 minutes.

Composite samples were produced by pouring the epoxy mixtures into circular polyethylene molds with a diameter of 25 mm. To prevent any effects from the mold surface texture on subsequent measurements, the analyses were performed on the top surface of each composite, which was not in direct contact with the mold material. The curing was performed in two steps, based on manufacturer recommendations: initial curing at room temperature (approximately 23 ± 2 °C) for 24 hours, followed by post-curing at 80 °C for 30 minutes. During room temperature curing, the samples were isolated from environmental pollutants by placing them inside a closed desiccator. After curing processes, the sample surfaces were ground sequentially using sandpapers with grit sizes of 800, 1000, 1200, and 2000 and then polished with the 1 μm alumina solution. Before conducting measurements, samples were thoroughly cleaned using aqueous detergent, followed by rinsing with distilled water in an ultrasonic cleaner.

2.4 Surface Roughness (Ra) Measurements

The surface roughness (Ra) of the top surfaces has been assessed, where contact angles were measured on free surfaces not in touch with the mold, as surface roughness significantly influences the contact angle. The measurements were conducted using the Nanovea ST400 3D optical surface profilometer (AnMo Electronics Corporation, New Taipei City, Taiwan). The profilometer is shown in Fig. 2. The profilometer scanned the surface at a velocity of 5 mm/s throughout a 1 mm x 1 mm region, and the measurement data were evaluated via MountainsMap software. The mean of five measurements for each sample was recorded.

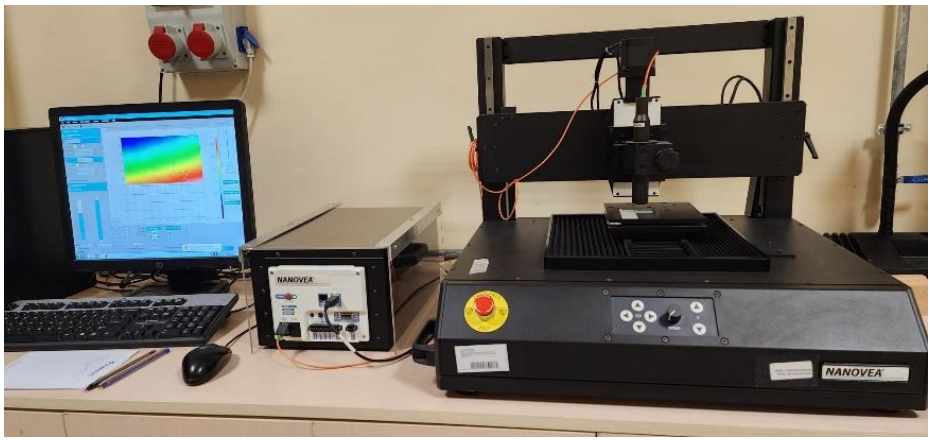

Figure 2. The 3D Optical profilometer device is used in surface roughness (Ra) measurements

2.5 Contact Angle Measurements

The wettability (or conversely, hydrophobicity) of the samples was determined by contact-angle (θ) measurements using the sessile drop method at room temperature by a One Attension theta optical goniometer (Biolin Scientific Co., Espoo, Finland). The device is shown in Fig. 3. Before initiating θ measurements, the surfaces of the samples were cleaned by washing with aqueous detergent. Then, it was rinsed with distilled water. Finally, the cleaned samples were left to dry in a vacuum oven at 60°C for 24 hours. Subsequently, the θ measurement was started by settling about 5 µL of distilled water onto the sample using a Hamilton injector. The value at the 2nd second after the water drop was released onto the sample surface was recorded. The θ measurements were taken from three different points on the surface of each sample, and the values closest to the average were recorded.

Figure 3. One Attension theta optical goniometer used for water drop contact angle measurement

2.6 Hardness Tests

5 hardness values were measured from the surface of each sample, and the average was recorded. In this study, Shore D hardness measurements were conducted using a Shore D durometer as per ASTM D2240, which is also commonly employed in polymeric and composite materials research due to its reliability, ease of use, and wide industrial acceptance (Dinesh et al., 2020; Ganapathy et al., 2021; James et al., 2020). Barcol hardness testing, while also could be preferred, is more commonly applied to composite materials with fiber reinforcement (Ceritbinmez et al., 2021; Ceritbinmez et al., 2022).

3. RESULTS AND DISCUSSION

3.1 Particle Size Analysis

The d_{10}, d_{50}, and d_{90} values (Fig. 3) show particle sizes, and 10%, 50%, and 90% of the sample amount are smaller than these particle sizes, respectively. For example, d_{90} of the CS sample means that 90% of the sample consists of particles with a size under 16.8 µm.

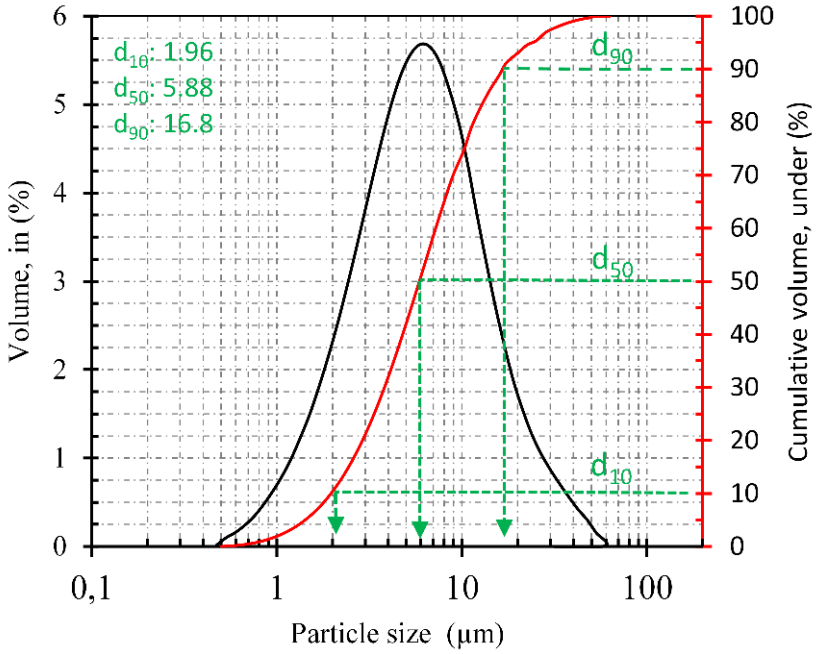

Figure 4. Particle size distribution analysis of CS particles

Figure 4 revealed that the CS powder sample consisted of very fine-sized particles. Namely, the particle size distribution varied uniformly between 0.5-60 µm, and the d_{90} value of the sample was determined as 16.8 µm. According to Figure 4, the particles constituting the CS powder were mostly concentrated around the 6 µm size. Thus, the average particle size of the sample can be expressed as approximately 6 µm. The d_{50} value of the sample, being 5.88 µm, is also an indication of this. In addition, the CS powder sample has a narrow size distribution at the medium scale, as can be seen from the low slope of the cumulative undersize curve. As a result, according to the particle size distribution data, it can be said that the CS sample can form topographically homogeneous dispersions with epoxy-like resins under appropriate conditions.

3.2 Hydrophobicity of Composites

The hydrophobic characteristics of epoxy were assessed by measuring the contact angles of the specimens produced with water, utilizing various ratios of CS additives (0%, 1%, 2%, 4%, 6%, 8%, and 10%). Due to its effect on contact angles, the surface roughness of the composites was measured and is shown in Table 1. Fig. 5 depicts the effect of different CS additions on contact angles. The contact angle of pure epoxy with water is shown in Fig. 5(b), and the angle of 70.5° indicates that it has a hydrophilic structure. Generally, surfaces with a contact angle below 90° are termed hydrophilic, while those above 90° are termed hydrophobic (Ma et al., 2007). Due to CS's low surface energy, it exhibits hydrophobic properties (Bai et al., 2023), and the contact angles have significantly increased with the addition of CS (Fig. 5). With a 1% CS addition, the contact angle increased to 104.7°, followed by small fluctuations in contact angles at 2%, 4%, and 6% (101.5°, 102.0°, and

107.9°, respectively). The maximum contact angle attained was 117.5° using 8% CS. Despite anticipating an increased contact angle with the addition of 10% CS, the contact angle marginally fell to 112.5°, likely due to agglomeration effects. The reduction in contact angle with a high CS content ratio may be related to pore formation resulting from the epoxy's inadequate wetting of CS particles with low surface energy in specific regions.

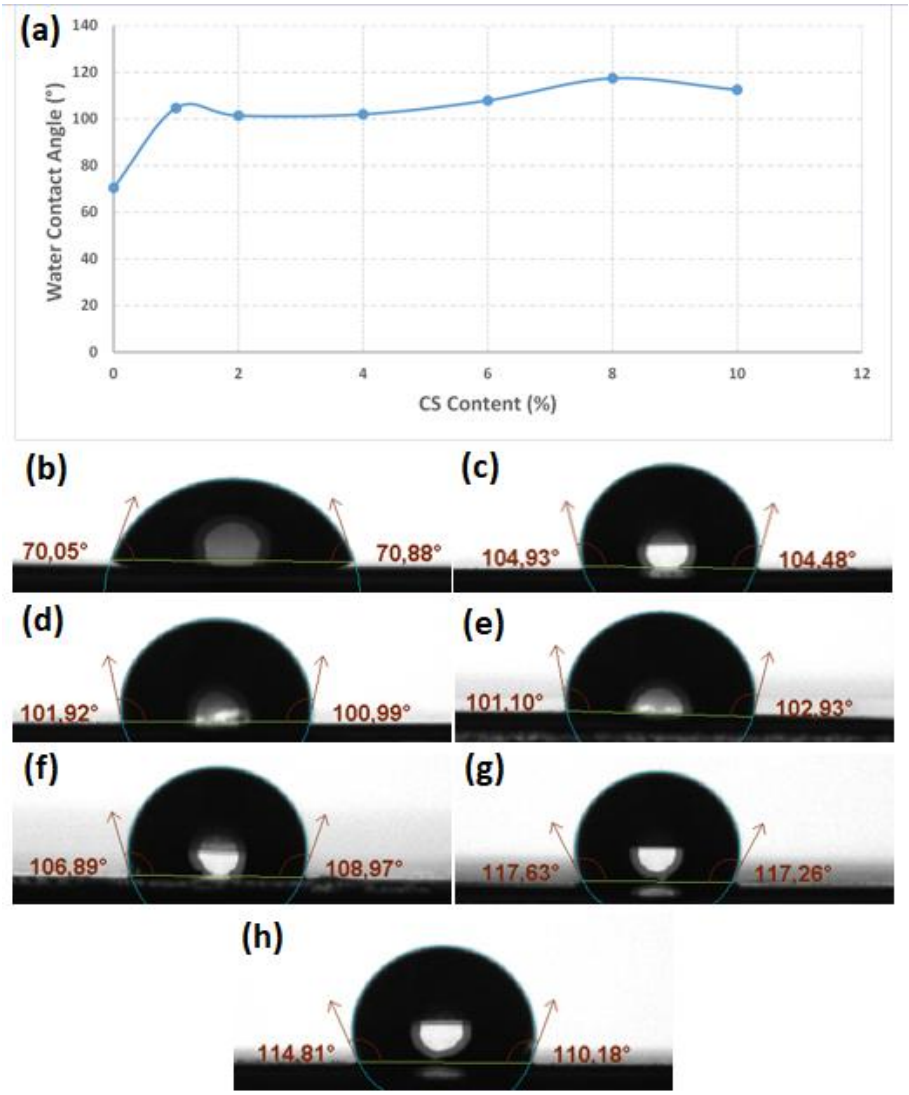

Figure 5. Contact angle measurement results against water (a) the graph illustrating the variation of contact angles with water with different CS ratios, and contact angles of specimens with (b) 0%, (c) 1%, (d) 2%, (e) 4%, (f) 6%, (g) 8% and (h) 10% CS additions

A study on coatings using CS nanoparticles found contact angles of 150° against water, indicating good mechanical durability and resistance to UV radiation, thermal shock, and organic solvents (Bai et al., 2023). Similarly, adding CS to cement and concrete lowers the amount of water that can penetrate structures and the amount of chloride ions that can get in (Chen et al., 2022; Lv et al., 2024).

It has been demonstrated in various studies that the hydrophobic properties of epoxy can be enhanced using different methods. It has been reported that the contact angle of epoxy surfaces modified with ZIF-8 and DMBIM increased to approximately 124.9°, and the corrosion resistance in harsh environments such as acid, alkali, and saline water was significantly improved (Chen et al.,

2025). Additionally, the use of nanoparticles such as clay-modified silico-graphitic carbon (Verma et al., 2024), graphitic carbon nitride, and manganese dioxide (Xavier et al., 2024) has improved the hydrophobicity and mechanical properties of epoxy surfaces.

3.3 Hardness of Composites

In order to observe the effect of CS additives on the mechanical properties of epoxy, Shore D hardness values of the samples were examined. While the hardness of neat epoxy is 89.5, the hardness of the composite with 1% CS additive is 89.6, and these two values are quite close. However, as can be seen in Fig. 6, the Shore D hardness values of the composites with 2% or more CS additives are visibly lower. Especially after adding 4% CS, the hardness value (approximately 70.9) significantly fell below the hardness value of pure epoxy. At the 6% and 8% ratios, the hardness decreased to approximately 61.3 and 63.7, respectively, while at the 10% ratio, it slightly increased again to approximately 69.4.

The general mechanical properties and hardness of epoxy resins are directly dependent on the type, amount, and distribution of fillers added to the polymer matrix (Pham & Marks, 2002). It is stated that if the filler materials show a homogeneous distribution within the polymer matrix, the mechanical properties will improve. However, the addition of high amounts of filler materials acts as a defect in the structure and negatively affects the mechanical properties (Zhou et al., 2008; Panin et al., 2015). CS is a material with low surface energy and may not have been wetted enough in some areas when mixed with epoxy. In this case, it is possible that the dry areas were trapped in the structure during the curing of the epoxy and caused the hardness to decrease by creating voids after full curing.

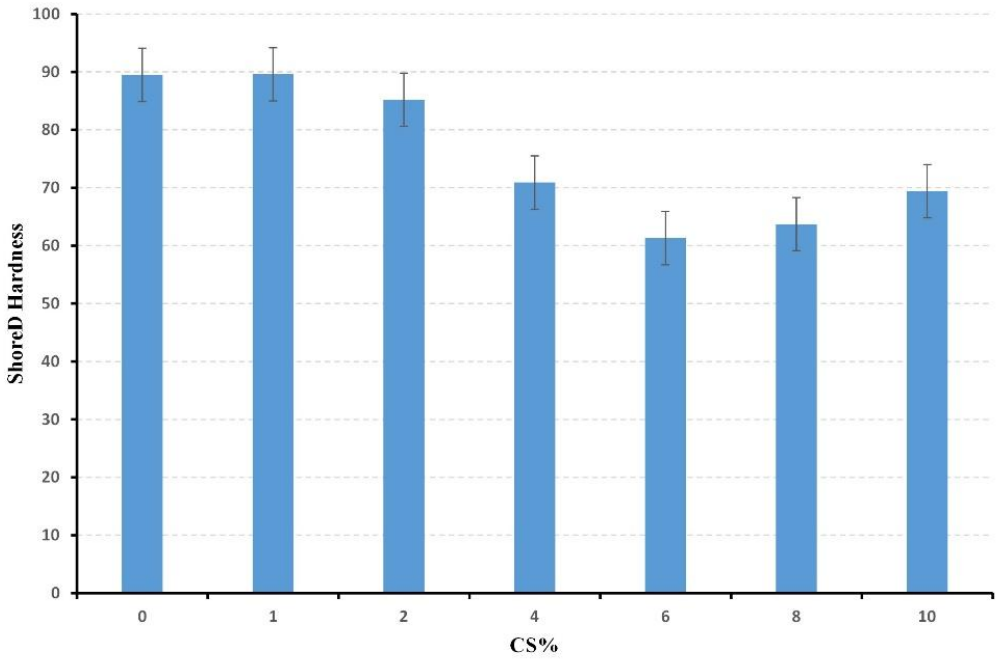

Figure 6. Shore D hardness values of neat epoxy and Epoxy-CS composites

Panin et al. (2015) state that the hardness values decrease with the high addition of CS to the UHMWPE matrix, and this situation is due to the soft structure of CS (Panin et al., 2015). The reduction in hardness with increased CS concentration aligns with findings reported by Zhou et al. (2008), who studied carbon nanotube-epoxy composites. They observed that particle agglomeration at higher filler ratios resulted in stress concentration points within the epoxy matrix, which facilitated

early crack initiation and subsequent mechanical failure. This perspective is additionally corroborated by prior research that highlights the essential function of filler dispersion in mechanical reinforcement. Onuegbu and Igwe (2011) examined polypropylene composites filled with snail shell powder and found that larger filler particle sizes, along with increased agglomeration, led to diminished hardness values due to decreased interfacial adhesion and stress transfer. Dinesh et al. (2020) similarly reported that jute fiber-epoxy composites reinforced with coarse rosewood dust demonstrated lower Shore D hardness than those with fine Padauk wood dust, a phenomenon attributed to inadequate dispersion and the creation of filler agglomerates that functioned as weak points within the matrix. These data validate the correlation identified in our study between filler agglomeration and diminished hardness, highlighting the necessity of attaining a uniform filler distribution to preserve the integrity of the composite structure.

Similarly, our results suggest that at elevated CS concentrations, agglomerated particles and associated void formation likely created structural heterogeneities within the epoxy matrix, thus leading to a noticeable decrease in hardness. The decreasing trend of hardness values in our study confirms this literature information. It is thought that the homogeneous distribution of particles is optimal in the sample with 1% addition, where the hardness is highest. However, with the increase in the CS ratio, the agglomeration of particles increases, leading to the formation of non-homogeneous regions within the matrix and a decrease in hardness. The slight increase in hardness at the 10% ratio may be the result of different structural changes caused by the higher filler content, but it is still quite low compared to the hardness of the sample containing 1% CS.

Table 1. Surface Roughness (Ra), Shore D Hardness, and Contact Angle Values of the Composite Samples

Sample	Ra	Shore D	Contact Angle (°)
0%	0.177	89.5	70.47
1%	0.166	89.6	104.7
2%	0.176	85.2	101.46
4%	0.178	70.9	102.01
6%	0.157	61.3	107.93
8%	0.195	63.7	117.45
10%	0.245	69.4	112.5

4. CONCLUSION

The findings of the hydrophobicity and hardness assessment of composites created by incorporating CS particles in varying proportions into epoxy resin are detailed below:

- The size range of CS particles used in the study is narrow, at around 6 μm. The homogeneous size distribution shows that CS particles are suitable for homogeneous dispersion in the epoxy matrix.
- Pure epoxy exhibited a hydrophilic property with a contact angle of approximately 70.5°. With the addition of CS, the water contact angles of epoxy composites increased significantly, and maximum hydrophobic properties were obtained (117.5° with 8% CS). However, a slight decrease in the contact angle (112.5°) was observed with the addition of CS at higher rates (10% CS), which is thought to be due to the agglomeration of particles and the pores formed in the epoxy matrix.

- Low rate (1%) CS additive did not create a visible difference in the hardness of the epoxy. However, when 2% and higher rates of CS were added, a significant decrease was experienced in the hardness values, especially at 6%, where hardness decreased to 61.3. This situation is attributed to the difficulty of the homogeneous distribution of CS particles in the matrix at high rates and the decrease in mechanical performance caused by agglomeration.

The results of this study reveal that calcium stearate additives should be kept at an optimum level in epoxy matrices. It is recommended to use CS at low rates, such as 1-2%, to increase both hydrophobic properties and preserve mechanical properties. The use of higher rates should be evaluated carefully, as they may have negative effects on mechanical properties

5. ACKNOWLEDGEMENTS

This study did not benefit from any support.

6. CONFLICT OF INTEREST

Authors approve that to the best of their knowledge, there is not any conflict of interest or common interest with an institution/organization or a person that may affect the review process of the paper.

7. AUTHOR CONTRIBUTION

İsmail Sinan ATLI contributed to determining the concept and/or design process of the research, managing the concept and/or design process, data collection, data analysis and interpretation of the results, preparation of the manuscript, critical analysis of the intellectual content, and final approval and full responsibility. Hakan ÇİFTÇİ contributed to data collection, data analysis and interpretation of the results, critical analysis of the intellectual content, and final approval and full responsibility.

8. REFERENCES

Aparna A., Sethulekshmi A.S., Saritha A., Joseph K., Recent advances in superhydrophobic epoxy based nanocomposite coatings and their applications. Progress in Organic Coatings 166, 106819, 2022.

Ari A.C., Mechanical and hydrophobic properties determination of epoxy/ignimbrite/pine waste composites. Polymer Composites, 1–14, 2025.

Bai H., Zhang L., Gu D., Calcium stearate nanoparticles as building blocks for mechanically durable superhydrophobic coatings. Materials Chemistry and Physics 294, 127040, 2023.

Ceritbinmez F., Yapici A., Kanca E., The effect of nanoparticle additive on surface milling in glass fiber reinforced composite structures. Polymers and Polymer Composites 29(9_suppl), S575–S585, 2021.

Ceritbinmez F., Özkan V., Saracoglu G., Yapici A., MWCNTs doped GFRPs drilling: crosscheck among holes obtained by alternative manufacturing methods. The International Journal of Advanced Manufacturing Technology 118(1), 33–41, 2022.

Chang J., He X., Yang Z., Bai X., Yuan C., Effects of chemical composition on the hydrophobicity and antifouling performance of epoxy-based self-stratifying nanocomposite coatings. Progress in Organic Coatings 167, 106827, 2022.

Chen H., Wang Z., Li J., Liu X., Li C., Li Y., Yu W., Liu L., Zhang Y., Lai Y., Cai W., Facile preparation of highly hydrophobic ZIF-8/DMBIM modified epoxy coatings with enhanced acid, alkali and marine corrosion resistance. Materials Today Chemistry 43, 102512, 2025.

Chen L., Ni X., Shen Y., Liu Z., Liu C., Experimental and simulation investigation on hydrophobicity and corrosion resistance of graphene oxide reinforced composite coating. Applied Surface Science 648, 159072, 2024.

Chen R., Liu J., Mu S., Chloride ion penetration resistance and microstructural modification of concrete with the addition of calcium stearate. Construction and Building Materials 321, 126188, 2022.

Dinesh S., Kumaran P., Mohanamurugan S., Vijay R., Singaravelu D.L., Vinod A., Bhat K.S., Influence of wood dust fillers on the mechanical, thermal, water absorption and biodegradation characteristics of jute fiber epoxy composites. Journal of Polymer Research 27, 1–13, 2020.

Doganci M.D., Sevinc H., Investigation of superhydrophobic and anticorrosive epoxy films with Al_2O_3 nanoparticles on different surfaces. ACS Omega 8(24), 21559–21570, 2023.

Ganapathy T., Sathiskumar R., Sanjay M.R., Senthamaraikannan P., Saravanakumar S.S., Parameswaranpillai J., Siengchin S., Effect of graphene powder on banyan aerial root fibers reinforced epoxy composites. Journal of Natural Fibers 18(7), 1029–1036, 2021.

Guangbao W., Shangsuo Y., Jijun X., Thermal degradation kinetics of calcium stearate-PVC composite. Results in Materials 8, 100123, 2020.

James D.J.D., Manoharan S., Saikrishnan G., Arjun S., Influence of bagasse/sisal fibre stacking sequence on the mechanical characteristics of hybrid-epoxy composites. Journal of Natural Fibers 17(10), 1497–1507, 2020.

Li S., Yao Y., Effect of thermal stabilizers composed of zinc barbiturate and calcium stearate for rigid poly(vinyl chloride). Polymer Degradation and Stability 96 (4), 637–641, 2011.

Lv Y., Luo Y., Song C., Jin W., Xiang T., Qiao M., Dang J., Bai W., Yang Z., Zhao J., Effect of calcium stearate hydrophobic agent on the performance of mortar and reinforcement corrosion in mortar with cracks. Construction and Building Materials 450, 138684, 2024.

Ma Y., Cao X., Feng X., Ma Y., Zou H., Fabrication of super-hydrophobic film from PMMA with intrinsic water contact angle below 90°. Polymer 48 (26), 7455–7460, 2007.

Maryoto A., Resistance of concrete with calcium stearate due to chloride attack tested by accelerated corrosion. Procedia Engineering 171, 511–516, 2017.

Onuegbu G.C., Igwe I.O., The effects of filler contents and particle sizes on the mechanical and end-use properties of snail shell powder filled polypropylene. Materials Sciences and Application 2, 811–817, 2011.

Panin C.V., Kornienko L.A., Suan T.N., Ivanova L.R., Poltaranin M.A., The effect of adding calcium stearate on wear-resistance of ultra-high molecular weight polyethylene. Procedia Engineering 113, 490–498, 2015.

Pham H.Q., Marks M.J., Epoxy Resins. Ullmann's Encyclopedia of Industrial Chemistry, Wiley-VCH Verlag GmbH & Co. KGaA, Weinheim, 2002.

Verma A., Tiwary C.S., Bhattacharya J., Enhancement of hydrophobic, resistive barrier and anticorrosion performance of epoxy coating with addition of clay-modified green silico-graphitic carbon. Carbon Trends 15, 100347, 2024.

Xavier J.R., Electrochemical, mechanical and adhesive properties of surface modified NiO-epoxy nanocomposite coatings on mild steel. Materials Science & Engineering B 260, 114639, 2020.

Xavier J.R., Bhaskar R., Subramanian S., Multifunctional graphitic carbon nitride manganese dioxide epoxy nanocomposite coating on steel for enhanced anticorrosion, flame retardant, mechanical, and hydrophobic properties. Journal of Industrial and Engineering Chemistry 134, 514–536, 2024.

Zhou Y., Pervin F., Lewis L., Jeelani S., Experimental study on the thermal and mechanical properties of multi-walled carbon nanotube-reinforced epoxy. Materials Science and Engineering A 452–453, 657–664, 2007.

JOURNAL of
MATERIALS and MECHATRONICS:A

e-ISSN 2717-8811
JournalMM, 2025, 6(1), 226-240
https://doi.org/10.55546/jmm.1669215

Araştırma Makalesi / Research Article

Fatigue Life Estimation of Welded Joints in Mobile Cranes with Ultra High Strength Steels Using the Structural Stress Method

Osman Bahadır ÖZDEN[1*], Barış GÖKÇE[2], Abdullah ERDEMİR[3]

[1*] MPG Machinery Production Group Co., Konya, Türkiye,
ORCID ID: https://orcid.org/0000-0003-1231-2936, bahadir.ozden@outlook.com
[2] Mechatronic Engineering Department, Necmettin Erbakan University, Konya, Türkiye,
ORCID ID: https://orcid.org/0000-0001-6141-7625, bgokce@erbakan.edu.tr
[3] MPG Machinery Production Group Co., Konya, Türkiye,
ORCID ID: https://orcid.org/0000-0002-7267-3111, aerdemir@mpg.com.tr

Geliş/ Received: 04.04.2025**;** **Revize/Revised:** 21.04.2025 **Kabul / Accepted:** 13.05.2025

ABSTRACT: In this study, static and dynamic finite element analysis (FEA) of a mobile crane design model were per-formed and stresses of welded joints were examined by the structural hot spot method. Especially in the welding of ultra-high strength steel (UHSS), choice of welding parameters affects mechanical properties. According to the FEA results, specimens containing different materials and welding parameters were prepared for investigated regions and an evaluation approach was proposed by performing destructive tests applied in this study. In this way, uncertainties in the production of welded joints are avoided by using destructive test results and FEA evaluations. As a result of the analysis, the hotspot value for maximum principal stress in critical regions of welded joints was found to be 527.54 MPa, and S960QL material was selected. As a result of these studies, UHSS materials were preferred and the minimum fatigue life estimate for welded joints was calculated as 13665 cycles and a mobile crane was produced.

Keywords: Fatigue life estimation, Finite element analysis, Mobile cranes, Ultra-high strength steels, Welded joints

*Sorumlu yazar / Corresponding author: bahadir.ozden@outlook.com
Bu makaleye atıf yapmak için /To cite this article

Özden, O. B., Gökçe, B., Erdemir, A. (2025). Fatigue Life Estimation of Welded Joints in Mobile Cranes with Ultra High Strength Steels Using the Structural Stress Method. Journal of Materials and Mechatronics: A (JournalMM), 6(1), 226-240.

1. INTRODUCTION

Mobile cranes are work machines used to carry heavy loads to the desired location. The ability to meet the desired function and the safe operation of the crane depend on the designs before manufacturing. Analytical calculations in large structures can take a long time to be calculated due to hyper-static situations, and therefore, more practical and accurate evaluations can be made by performing analyzes using the finite element analysis (FEA). While evaluating the safe operation of cranes, fatigue life in terms of general structure is as important as working under static loads (Lu et al., 2014). Especially in mobile cranes, more occupational accidents and loss of life can be experienced compared to other crane types (Al-Humaidi and Tan 2009, Im and Park 2020). Many studies have been conducted on the most important causes of these accidents and loss of life (Cheng and Teizer 2014, Shin 2015, Raviv et al., 2017, Sadeghi et al., 2021). As stated in many studies, the design, analysis and calculations of mobile cranes are important for manufacturers due to the high number of work accidents and the effects of crane manufacturers. For this reason, it is especially important to make correct fatigue life calculations of welded joints.

The use of high-strength steels with high yield strength can be preferred both for obtaining a more reliable structure and for obtaining lighter structures. With the development of material technology, steels up to 1500 MPa yield strength can be used (Esterl et al., 2019). Steels with very high yield strength, called ultra-high strength fine grained structural steels, can also provide sufficient material toughness (Berg and Stranghöner 2016). With the selection of ultra-high-strength materials, greater load carrying capacity can be achieved with smaller and lower weights. Currently, studies are ongoing to evaluate the fatigue life of welded joints in ultra-high strength steels such as S960 material and to develop IIW recommendations (Ahola et al., 2024, Ahola et al., 2025, Xu et al., 2025).

Generally, the structures with the lowest fatigue life are the welded joints. In welded joints, many parameters such as voltage, current, feed rate, shielding gas, filler wire, environment conditions and weld geometry can affect the microstructure of the heat affected zone (HAZ). These parameters also can affect the phase formed in that area with the weld cooling (Gáspár 2019, Moravec et al., 2019, Mičian et al., 2020). Therefore, the selected parameters can affect the safety of the structure under static and dynamic loads (Tsutsumi et al., 2022).

In this study, destructive tests were carried out for welded joints and the selected welding parameters and the mechanical properties of the material were determined for evaluation as a result of FEA. As a result of a mobile crane design, the welded joints with the lowest fatigue life were examined using the structural hotspot stress approach, under the scenario created by performing FEA. Suggestions have been made for the evaluation of welded connections, especially in complex structures. By evaluating the studies conducted in the literature, fatigue life estimations have been made according to the recommended FAT classes in critical regions in complex structures. In addition, hardness measurement tests have been carried out to emphasize the importance of the hardness of the HAZ regions in welded structures. Although similar methodologies exist, the integration of hotspot stress analysis and destructive validation in mobile crane structures using UHSS materials remains underrepresented in literature.

2. MATERIALS AND METHODS

2.1 Creating a Finite Element Model

Having too many parameters that can affect the life of the structure in welded joints can cause many uncertainties during the evaluation phase. While estimating fatigue life in welded joints according to IIW (Hobbacher 2016) and Eurocode 3 standards, it is assumed that appropriate selections are made for welding parameters, selections are made according to fatigue strength class (FAT) tables according to weld type, shape and shapes, and life cycles are calculated according to S-N curves (Berg and Stranghöner 2014, Fuštar et al., 2018, Pamuk and Durgutlu 2018, Akyıldız et al., 2021, Gök and Baltacı 2021). While evaluating the results of FEA, there are approaches such as nominal stress method, structural hotspot stress method, effective notch method (effective notch) and fracture mechanics method (Paris law) (Sonsino et al., 2012, Niemi et al., 2018). As shown in Figure 1, according to the complexity of the structure, the method chosen and the accuracy rate and effort vary.

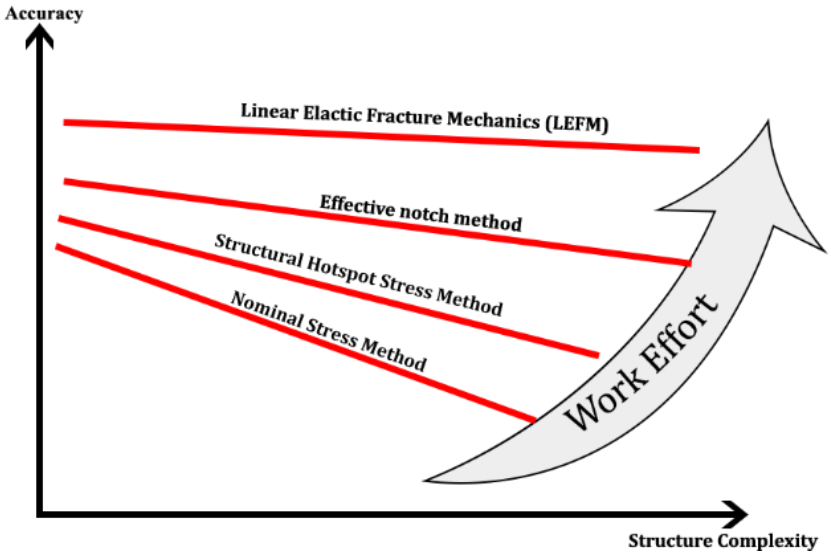

Figure 1. Accuracy-structure complexity according to fatigue evaluation approaches (Özden et al., 2022)

Solidworks, the computer-aided design software for the mobile crane, and Ansys, the FEA software, were used for the design and analysis processes. After all processes are completed, the production phase begins. Figure 2 shows the mobile crane, whose final design has been completed after analysis and improvements. In this study, the structures on the truck chassis were examined.

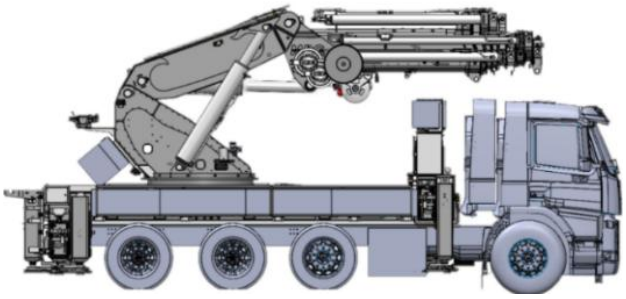

Figure 2. Mobile crane design

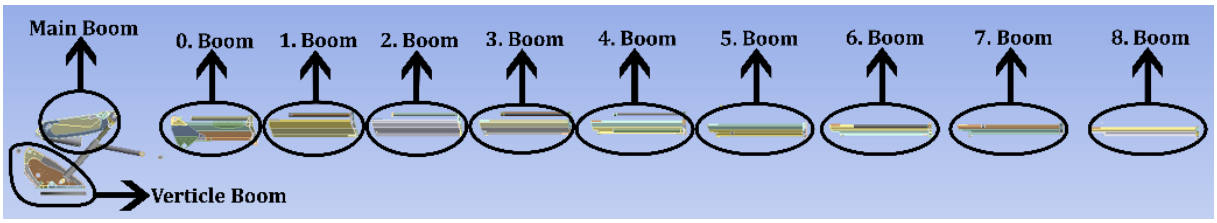

Figure 3. Analysis model classifications

For the analysis made for the upper group of the vehicle chassis, it is divided into groups as vertical boom, main boom and booms. Extension booms are classified as 1st, 2nd, 3rd..., 8th boom. With these classifications indicated in Figure 3, evaluations were made according to the results of the analysis.

Analyzes were made according to the specified scenarios and the results were evaluated according to the criteria described under the heading of design criteria in the DIN EN 1993-1-8 standard. For the stresses occurring in the weld seam, the static load and fatigue calculations according to the scenario applied depending on the static load were made according to IIW and EN 1993 standards.

In the finite element network of the analyzed model, 452775 elements and 689069 nodes were used. Quadratic mesh types are preferred in order not to cause shear locking and hexagonal mesh types are preferred in order to obtain more accurate results. While preparing the finite element mesh, the quality of the mesh structure was increased by making necessary corrections according to the skewness values. The skewness criteria refer to the deviation from the ideal element shape (equilateral triangle and square in 2 dimensions). The skewness quality value for the analyzed model is 0.25 on average and the skewness standard deviation value is 0.20. According to the element quality evaluation criterion, an average value of 0.85 was determined.

Since the model consists of more than one part, the contact definitions of the parts are made. Among these definitions, there are bonded and no separation contact definitions, and as stated in the introduction, they are linear contact definitions. In joint definitions, fixed, cylindrical, revolute joint properties are defined according to the degree of freedom. Flexible is defined instead of rigid in joint definitions and definitions closer to reality are obtained. All definitions are defined linearly and since the material properties are below the yield strength, they are defined linearly. As a scenario, analyses were performed in the horizontal position of the crane where maximum stresses occur. Other kinematic configurations were not examined because they were less stressed. Boundary conditions were defined from the feet in contact with the ground. If there are forces in the sliding direction, definitions were performed with remote displacement instead of fixed joint. In addition, joint definitions are used to model the behavior of the structure in various regions. Elastic properties of materials are considered important because linear analysis is performed in the analysis. While preparing the analysis model, sheet metal parts were converted into shell parts. Radius, chamfer, hole, tooth, wedge, etc., which will not be used as a reference in the analysis model, which has no effect on the analysis of sheet metal and solid parts. geometry has been removed from the model. Machine elements, hydraulic, electrical, electronic, etc., which will not be examined structurally. hardware has been removed from the model. The effects of the components that will affect the results of the analysis in terms of mass properties, although they will not be examined structurally, are included in the analysis with various definitions.

2.2 Criteria for Finite Element Analysis Results

For the designs made, the geometric and loading conditions specified for the scenarios and the analysis results were evaluated, and the regions with a safety factor above 1.5 were determined as

safe zones. Analyzes were made according to different scenarios and the results were evaluated according to the normal stress and shear stress criteria in the DIN EN 1993-1-8 standard. For unsafe areas, the design in that area has been improved and more efficient designs have been obtained for resistance to load. In Equation 1,2,3, the criteria for shear stress, normal stress and equivalent stress according to EN 1993-1-8 were evaluated as a result of FEA, and design or material changes were made.

$$f_{vw,d} \leq \frac{f_u / \sqrt{3}}{\beta_w \gamma_{m2}} \tag{1}$$

$$\sigma_1 \leq \frac{0.9 f_u}{\gamma_{m2}} \tag{2}$$

$$\sigma_{vonmises} \leq \frac{f_u}{\beta_w \gamma_{m2}} \tag{3}$$

While evaluating the structural stress method, stress values can be taken from 2 or 3 points and hotspot stresses can be determined (Hobbacher 2016). The hotspot stress is calculated with Equation 4 by taking the stress values from 2 points according to the maximum 0.5.t (thickness) fine mesh size value and applying extrapolation. In Equation 5, hotspot stress is calculated by quadratic extrapolation from 3 points. The calculated hotspot stress values are calculated by determining the FAT class, and the fatigue life (N) is calculated by finding the maximum and minimum hotspot stress difference ($\Delta\sigma$hs) with the formulation created according to the S-N curve in Equation 6.

$$\sigma_{hs} = 1.67\sigma_{0.4t} - 0.67\sigma_{1t} \tag{4}$$

$$\sigma_{hs} = 2.52\sigma_{0.4t} - 2.24\sigma_{0.9t} + 0.72\sigma_{1.4t} \tag{5}$$

$$\Delta\sigma_{hs}^{m} = N.C \tag{6}$$

2.3 Materials Used in Welded Joint Production

For welded joints, there are many factors that can affect the mechanical properties after processing during production and may cause discontinuity in the weld pool. Preheating, interpass temperature, shielding gas selection, voltage, current etc. These choices greatly affect the mechanical properties of the welded joint. Destructive tests should be performed in order to determine the mechanical properties according to the selection of these parameters. Finite element analysis results should be evaluated according to the mechanical properties of the structure to be produced, determined as a result of the tests.

S960QL and S690QL ultra high strength steels are preferred for base material and workpiece in welded joints. For the welding filler material, filler material-1 (FM-1) in S960QL steel and filler material-2 (FM-2) in S690QL steel was preferred. Destructive tests were performed to verify the parameters. The chemical compositions of the materials used are indicated in Table 1.

Table 1. Chemical compositions of used materials, wt %

	C	Si	Mn	Cr	Ni	Mo	Ceq
S960QL	0.17	0.22	1.24	0.2	0.06	0.599	0.54
S690QL	0.13	0.27	1.19	0.25	0.05	0.151	0.41
FM-1	0.081	0.8	1.75	0.41	2.22	0.533	
FM-2	0.089	0.53	1.54	0.26	1.23	0.24	

In order to determine the preheating values of the materials used in welded joints, Ceq (Carbon Equivalent) values were calculated according to the chemical composition values. Preheating value was preferred for t8/5 time, in which bainitic phase formation was preferred after welding. This process affects the hardness of the weld bead, the heat affected zone (HAZ) and the base material. Hardness and mechanical properties are checked for compliance with tests performed according to the selected welding parameters. At the end of the tests, it was concluded that it is suitable if the hardness values are less than 350 HV and the yield strength value is at least 960 MPa.

2.4 Proposed Method

In finite element analysis, the solution time of large and complex structures can take a very long time. While preparing the analysis model, geometries that will affect the results at a very low level and negatively affect the mesh structure should be removed. Depending on the number of nodes and elements of the network structure, solution time can take a long time. The use of shell modeling instead of solid modeling also affects the solution time, as it will cause great changes in the number of nodes and elements in the network structure. Therefore, in finite element analyzes of machines with large and complex structures such as mobile cranes, geometries that will affect the results should be simplified, and linear definitions should be preferred in shell modeling and material, connection, geometry settings.

Before performing the FEA of the structure, preference should be made for welded joints according to the 4 different approaches indicated in Figure 1. The most accurate results can be achieved with the linear elastic fracture mechanics approach, but it can take a very long time in large and complex structures. For large and complex structures such as mobile cranes, the structural hotspot stress approach may be preferred as in this study. In this way, works that may take a long time before production can be completed in a shorter time with the choices made.

The mechanical properties evaluated for the critical weld regions determined as a result of FEA and the welding parameter can change after production. It was recommended to prepare welded joint specimens according to the specified parameters, perform destructive tests, and evaluate them according to the determined mechanical properties, especially for FEA in the welding of ultra-high strength steels.

The studies in the literature for weld T joints, the study called ID Ped1 (Pedersen et al., 2010), the study called ID Gal2 and ID Gal1 (Galtier and Statnikov 2004), the study called ID Sta1 (Statnikov et al., 2004), and the IIW recommendation (Hobbacher 2016) results are shown in Figure 4. In these studies, the material of the welded joints was not taken as a basis and the results were shared in general. In addition, there are many studies that were developed by comparing according to IIW recommendations (Zhu et al., 2022, Fass et al., 2023, Baumgartner et al., 2024).

The studies in the literature for weld T joints, the study called ID Ped1 (Pedersen et al., 2010), the study called ID Gal2 and ID Gal1 (Galtier and Statnikov 2004), the study called ID Sta1 (Statnikov et al., 2004), and the IIW recommendation (Hobbacher 2016) results are shown in Figure 4. In these studies, the material of the welded joints was not taken as a basis and the results were shared in

general. In addition, there are many studies that were developed by comparing according to IIW recommendations (Zhu et al., 2022, Fass et al., 2023, Baumgartner et al., 2024).

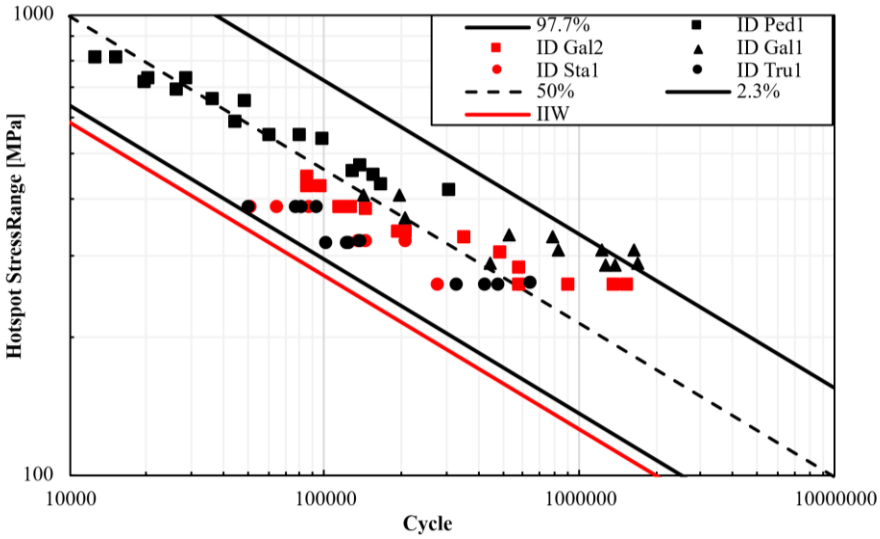

Figure 4. Hotspot stress method fatigue test results for T joints in the literature

63 test results were taken from the studies in the literature and curves were created according to 50%, 97.7% and 2.3% probability distributions as shown in Figure 4. FAT 109 was determined according to 97.7% probability distribution, FAT 265 was determined according to 2.3% probability distribution and FAT 170 was determined according to 50% probability distribution. Standard deviation was determined as 147.01 according to stress range values. Since FAT 109 class will obtain higher conversion values than FAT 100 class, which is one of the IIW recommendations, according to 97.7% probability distribution, FAT 100 or lower classes are recommended for more conservative results.

3. RESULTS AND DISCUSSION

FEA of the structure was carried out and critical points were examined. The most critical regions were evaluated from the extension booms, vertical boom and main boom groupings. They were named region under investigation (RUI), and critical areas were named RUI-1 in the vertical boom group, RUI-2 in the main boom group, and RUI-3,4,5 in the extension boom group. The analysis results of the general structure and these regions are shown in Figure 5.

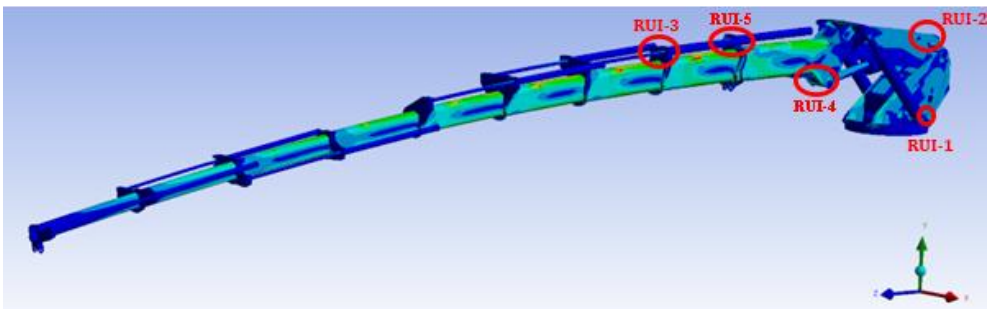

Figure 5. General structure analysis results and RUI regions

RUI regions and FAT classes were determined in detail and according to IIW. While making FAT classifications for the RUI-1 region, single-sided corner welding type was selected in the vertical boom group and FAT 90 class was selected according to the structural stress method. The same weld type is selected in the welded region in the RUI-2,3,4,5 regions. FAT 100 class was selected from the nominal stress structural stress method tables according to the double-sided beveled type called K butt weld. In Figure 6, the regions examined for FAT classifications are indicated with a red ellipse.

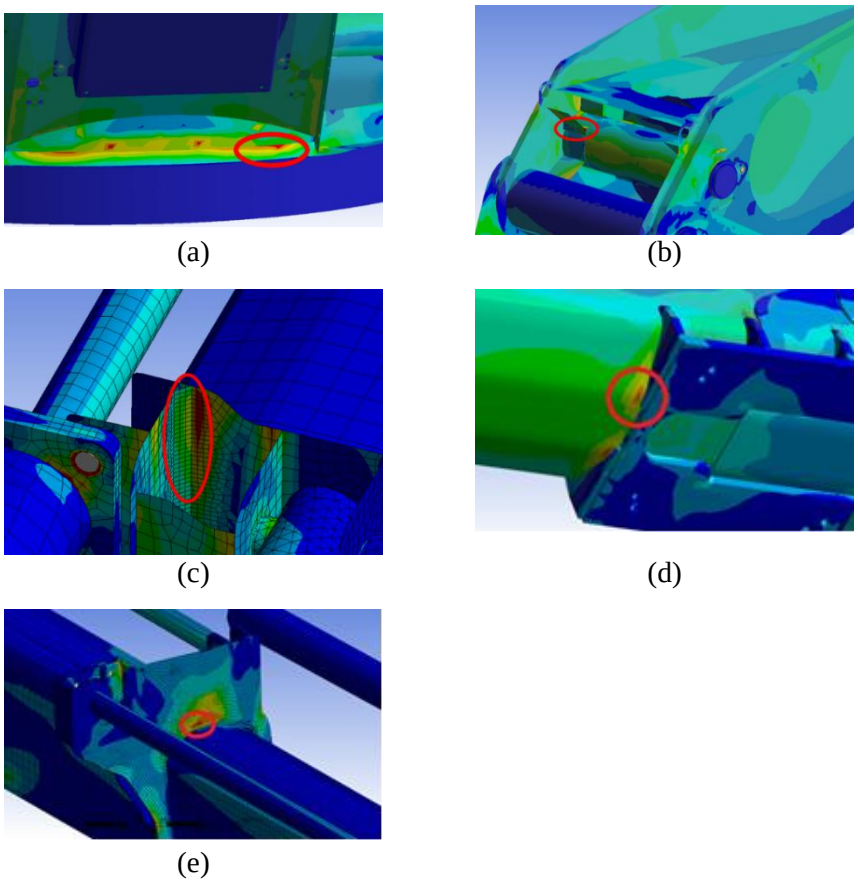

Figure 6. Analysis results for FAT classifications of welded joints (a) RUI-1, (b) RUI-2, (c) RUI-3, (d) RUI-4, (e) RUI-5

Stress values were taken up to 60 mm distance by taking the weld end of the examined critical welded joints as reference. The hotspot stresses of the regions were determined to estimate the fatigue life. Maximum principal, von-Misses and shear stress values are shown in Figure 7, and according to the results, the region with the highest maximum principal stress value is the RUI-3 region, and the hotspot stress was found to be 527.54 MPa. It can be seen that a horizontal graph is obtained in the RUI-2 region and the hotspot stress was found to be 246.28 MPa. The hotspot stress of the RUI-1 region was found to be 274.27 MPa. The hotspot stress of the RUI-4 region was found to be 250.43 MPa. The hotspot stress of the RUI-5 region was found to be 261.87 MPa.

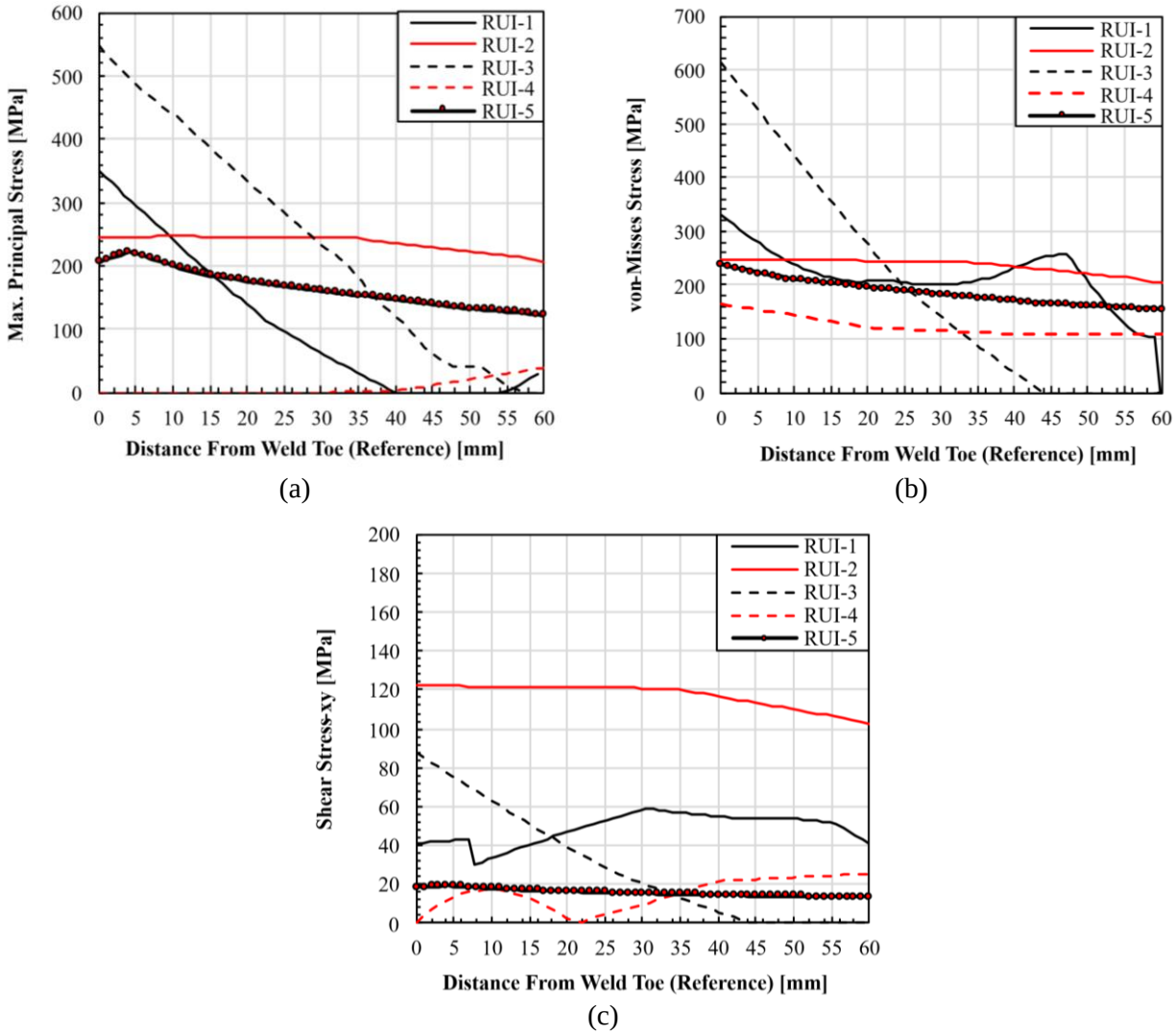

Figure 7. RUI regions stress results (a) Maximum principal stress (b) Equivalent (von-Misses) stress (c) Shear Stress

The hotspot stress values for the maximum principal stress determined by the structural stress method are used for fatigue life estimation. While estimating the fatigue life, the minimum stress is assumed to be 0 MPa and harmonic loads are assumed. In this case, the stress range is equal to the hotspot stress. In Figure 8, the S-N curve is drawn for the FAT classes determined according to the RUI regions. These FAT S-N curves have a probability accuracy of 97.7% relative to IIW. According to the results, 70877 cycles were found for the RUI-1 region, 97938 cycles for the RUI-2 region and 13665 cycles for the RUI-3 region, 251647 cycles for the RUI-4 region, 82954 cycles for the RUI-5 region. Since the results were above 10000 cycles, it was accepted in terms of fatigue life. In the production of RUI welded joint zones, for which fatigue life was estimated according to the results of FEA, the selected welding parameters can affect the mechanical properties of this zone.

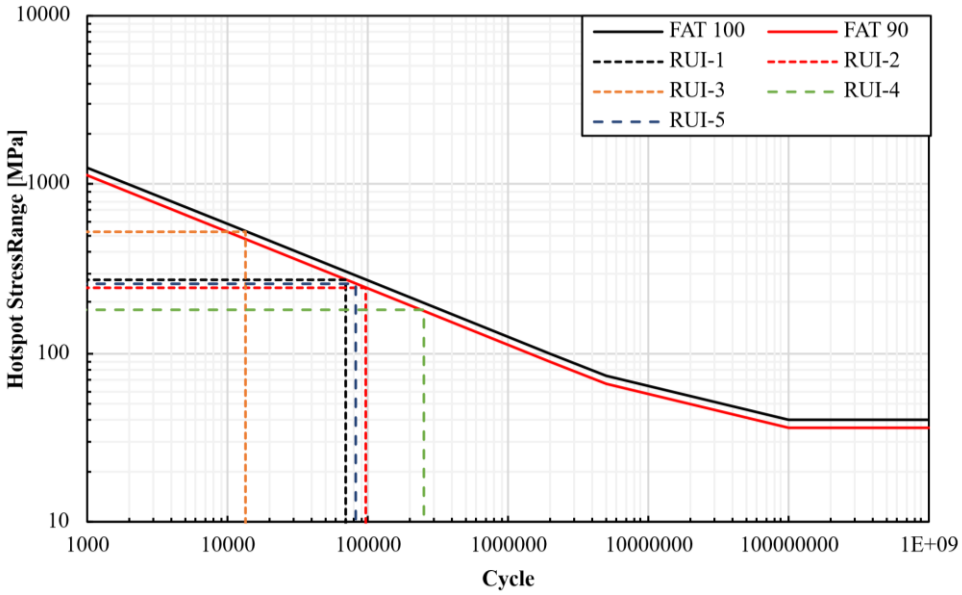

Figure 8. Fatigue life results according to S-N curves and hotspot stress range of RUI regions

Therefore, destructive tests were carried out according to the determined parameters in the critical welded joints examined by FEA and their mechanical properties were determined. In this study, welded joint design was carried out within the RUI-1,2,3,4,5 regions, specimens were prepared according to the parameters and destructive tests were carried out. S960QL, an ultra-high strength fine grain structural steel, was selected for RUI-1 zone materials and S690QL for RUI-2,3,4,5 zone materials. These selections were made according to the criteria that provide the safety criteria of EN 1993-1-8 for the equivalent stress values coming to that region. M21 (80% Ar + 20% CO_2) group shielding gas was selected with a flow rate of 12 lt/min for MAG welding in order to provide the penetration depth value and to protect it from the harmful effects of the atmosphere. For faults that may occur due to unforeseen reasons, ultrasonic, magnetic particle and penetration non-destructive tests (NDT) were performed after welding to prevent discontinuities that may occur in the weld seam. 1.2 mm filler material was used and welded according to 100 C° preheat and 200 C° interpass temperature. Table 2 specifies the welding parameters for the welded joint specimens prepared for destructive testing at the RUI sites.

Table 2. Chemical compositions of used materials, wt %

Specimen	I [A]	U [V]	V_{sp} [mm/s]	Heat Input [kJ/mm]
RUI-1–1. pass	250	26	5	1.04
RUI-1–2. and 3. pass	200	25	5	0.8
RUI-1–4. pass	200	25	5.83	0.69
RUI-2,3,4,5-1. pass	240	24	5.84	0.82
RUI-2,3,4,5-2. pass	240	24	5	0.96

Hardness measurements of base metal, HAZ and weld zones were made and evaluations were made. It was ensured that the hardness of 350 HV remained in all specimens. In Figure 9 weld seam design in images (a) and (b) for RUI-1, macro images in images (c) and (d) and ways for hardness measurement are indicated. In the RUI-2,3,4,5 regions, the base material and workpiece thicknesses are the same and are 10 mm. In Figure 9, weld seam design in images (e) and (f) of RUI-2,3,4,5 regions, macro images in images (g) and (h) and ways for hardness measurement are indicated.

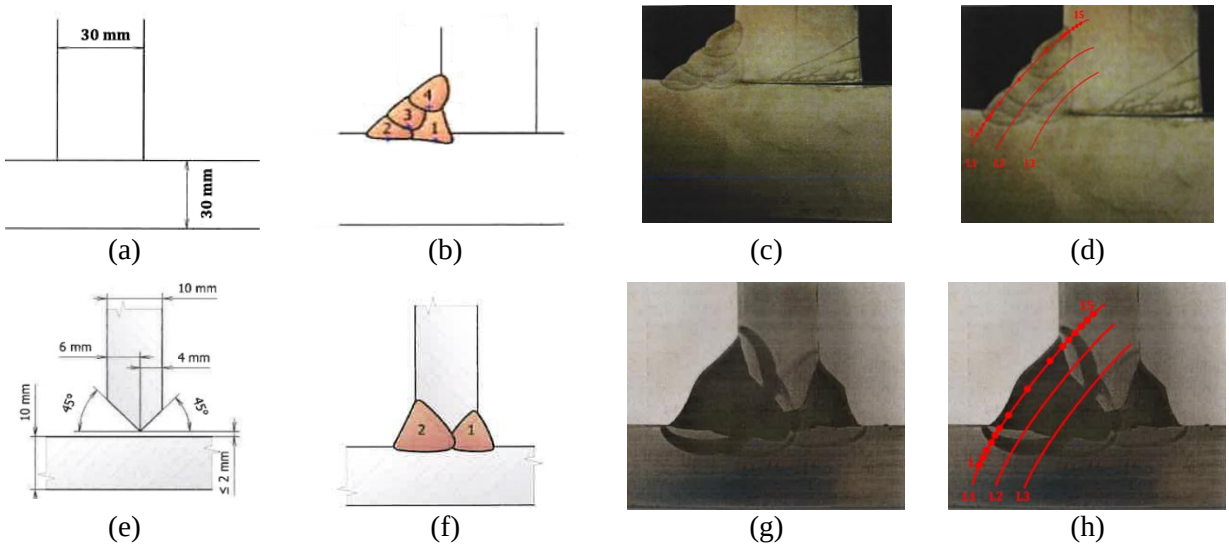

Figure 9. (a) RUI-1 base material and workpiece 30 mm, (b) RUI-1 weld seam number of passes, (c) RUI-1 weld seam macro view, (d) RUI-1 hardness measurement path, (e) RUI-2,3,4,5 base material and workpiece thicknesses, (f) RUI-2 and RUI-3 weld seam design, (g) RUI-2 and RUI-3 weld seam macro view, (h) RUI-2,3,4,5 path for hardness measurement

The hardness measurements taken from the base metal, HAZ and weld zones according to the paths in Figure 9 (d) and (h) are shown in Figure 10. The maximum hardness for RUI-1 was found to be 349 HV in the weld zone. In RUI-2,3,4,5, the maximum hardness was found to be 292 HV in the HAZ region. These hardness values realized in UHSS materials are found to be suitable because they are below 350 HV.

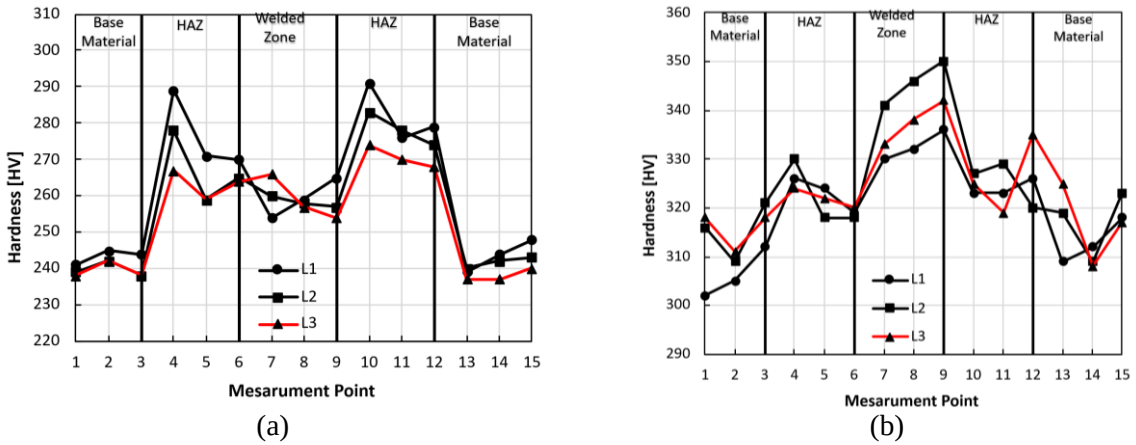

Figure 10. Hardness measurements for (a) RUI-1, (b) RUI-2,3,4,5 fatigue life results according to S-N curves and hotspot stress of RUI regions

Statistical results of hardness measurement tests performed for all critical regions are given in Table 3 and Table 4. While L1 measurement values were higher in RUI-1 tests, L1 measurement values were determined to be lower in other measurements. Standard deviations were determined to be 17.46 in RUI-1 measurements and 8.97 in L1 at the highest and 8.97 in other measurements. This situation was interpreted as being related to multiple passes and cooling times.

Table 3. RUI-1 statistical results

Measure	Mean	Standard Deviation	Variance	Minimum	Maximum	RMSE
L1	261.07	17.46	304.91	239.00	291.00	7.82
L2	257.13	15.41	237.54	238.00	283.00	5.88
L3	252.20	13.12	172.20	237.00	274.00	5.46

Table 4. RUI-2,3,4,5 statistical results

Measure	Mean	Standard Deviation	Variance	Minimum	Maximum	RMSE
L1	319.87	8.97	80.51	302.00	336.00	7.99
L2	324.53	11.81	139.41	309.00	350.00	5.85
L3	324.13	10.36	107.35	308.00	342.00	6.08

While evaluating the welded joint area in the FEA, the yield strengths were taken as 960 MPa for RUI-1 and 690 MPa for RUI-2,3,4,5. As a result of the destructive tests, the mechanical properties and yield strengths were found to be 1050 MPa for RUI-1 and 730 MPa for RUI-2,3,4,5. Tensile strengths were found to be 1080 MPa for RUI-1 and 800 MPa for RUI-2,3,4,5. According to the destructive test results, it was found to be more positive than the mechanical properties evaluated in the FEA, and the welding parameter selections were deemed appropriate for production. Weld seam design was made for the critical welded connection areas determined by FEA and it was found to be suitable for the production of mobile cranes as a result of destructive tests. As a result of the calculations, destructive tests and FEA evaluations, ultra-high strength steel was selected and the mobile crane machine was produced. With the calculations made according to IIW and EN 1993 in welding joints, it was concluded that the structure is safe. It is predicted the discontinuities that may occur in the weld seam due to such as cold cracks, porosity and slag inclusions will be detected by NDT tests and a smooth weld seam will be provided.

4. CONCLUSION

UHSS steels can provide high strength of the structure and reduce their weight by improving them with FEA of the structure in which they were used. Parameters such as voltage, current, preheating, interpass temperature and shielding gas determined in the welded joints of UHSS steels affect the mechanical properties after welding. Since there is no analytical formulation of the parameters, they are examined by experimental studies. In this study, after evaluating the FEA, destructive tests of the critical welded regions were carried out and their mechanical properties were checked. With this evaluation approach, the effects of welding parameters for production after the design process were determined.

In this study, UHSS steels were preferred in critical welded areas of the crane. The critical welded junction sites were investigated with FEA and were named as RUI-1, RUI-2, RUI-3, RUI-4, and RUI-5 as a result. RUI regions were investigated using the structural hotspot stress method approach. Static and dynamic FEA were performed and improvements were made to meet the safety criteria according to Equation 1, Equation 2 and Equation 3. Due to the high axial force and moment in the RUI-1 region, 30 mm thickness was selected and S960QL material was chosen. For RUI-2 and RUI-3 regions, evaluations were made by choosing S690QL steel. By determining the design that provides the safety, the hotspot stresses were calculated according to the maximum principal stress

values in the final design, 274.27 MPa for the RUI-1 region, 246.8 MPa for the RUI-2 region, and 527.54 MPa for the RUI-3 region, 250.43 MPa for the RUI-4 region, 261.87 MPa for the RUI-5 region. It was made according to the hotspot stresses in the S-N curves of the FAT class selected while estimating the fatigue life. According to IIW recommendations documents, FAT 90 class was chosen for RUI-1 and FAT 100 class was selected for RUI-2 and RUI-3. For dynamic stresses, the hotspot stress range was calculated by assuming harmonic loads and determining the minimum hotspot stress of 0 MPa.

Fatigue life was estimated according to the hotspot stress range in the S-N curves of the FAT classes and it was found 70877 cycles for RUI-1, 97938 cycles for RUI-2 and 13665 cycles for RUI-3, 251647 cycles for RUI-4, 82954 cycles for RUI-5. Since it was above 10000 cycle value, a mid-cycle structure was obtained and the design was considered suitable for FEA.

After the final design was evaluated, welding parameters were determined according to the weld seam designs and UHSS materials, and destructive tests were carried out with the prepared specimens. In the welding of UHSS materials, it has been observed that the mechanical properties of the post-production welded joints have improved as a result of the tests. Furthermore, it was decided that the selection of welding parameters was correct and the production of the mobile crane was carried out. In this study, especially if UHSS materials are used in the designed structures, FEA and destructive tests should be evaluated together, since the selected welding parameters affect the mechanical properties. Although similar methodologies exist, the integration of hotspot stress analysis and destructive validation in mobile crane structures using UHSS materials remains underrepresented in literature.

5. ACKNOWLEDGEMENTS

The authors gratefully acknowledge the support of “MPG Machinery Production Group Inc. Co.” in this study.

6. CONFLICT OF INTEREST

Authors approve that to the best of their knowledge, there is not any conflict of interest or common interest with an institution/organization or a person that may affect the review process of the paper.

7. AUTHOR CONTRIBUTION

Osman Bahadır ÖZDEN contributed to determining the concept and/or design process of the research, managing the concept and/or design process, data collection, data analysis and interpretation of the results, preparation of the manuscript, critical analysis of the intellectual content, and final approval and full responsibility. Barış GÖKÇE contributed to data analysis and interpretation of the results, critical analysis of the intellectual content. Abdullah ERDEMİR contributed to data analysis and interpretation of the results, critical analysis of the intellectual content.

8. REFERENCES

Ahola A., Leitner M., Grönlund K., Brunnhofer P., Buzzi C., Moshtaghi M., Björk T., Fatigue Assessment of as-Welded and Hfmi-Treated High-Strength Steel Joints under Variable Amplitude Loading Using Local Approaches. Welding in the World, 1-14, 2025.

Ahola A., Salerto S., Loisa T., Lipiäinen K., Björk, T., Fatigue Strength of Single-Sided Fillet Welds in Overlapping Ultra-High-Strength Steel Sheets. Welding in the World 68(5), 1225-1239, 2024.

Akyıldız U., Poyrazoğlu O., Demirel M. Y., Anodik Oksidasyonun Aa7050-T7451 Alaşımının Yorulma Performansına Etkisi. Politeknik Dergisi 26(1), 191-198, 2021.

Al-Humaidi H., Tan F. H., Mobile Crane Safe Operation Approach to Prevent Electrocution Using Fuzzy-Set Logic Models. Advances in Engineering Software 40(8), 686-696, 2009.

Baumgartner J., Hobbacher A., Levebvre F., Recent Update of the Iiw-Recommendations for Fatigue Assessment of Welded Joints and Components. Procedia Structural Integrity 57, 618-624, 2024.

Berg J., Stranghöner N., Application of Design Concepts at High Frequency Hammer Peened Welded Ultra High Strength Steels, IABSE Symposium: Engineering for Progress, Nature and People, Madrid, Spain, 3-5 September 2014,2014.

Berg J., Stranghöner N., Fatigue Behaviour of High Frequency Hammer Peened Ultra High Strength Steels. International Journal of Fatigue 82, 35-48, 2016.

Cheng T., Teizer J., Modeling Tower Crane Operator Visibility to Minimize the Risk of Limited Situational Awareness. Journal of Computing in Civil Engineering 28(3), 04014004, 2014.

Esterl R., Sonnleitner M., Weißensteiner I., Hartl K., Schnitzer R., Influence of Quenching Conditions on Texture and Mechanical Properties of Ultra-High-Strength Steels. Journal of materials science 54(19), 12875-12886, 2019.

Fass M., Hecht M., Baumgartner J., Bauer N., Evaluation of the Approach Based on the Maximum Principal Stress from the Iiw-Recommendation for Welded Joints under Proportional, Multiaxial Stress States. Welding in the World 67(10), 2323-2332, 2023.

Fuštar B., Lukačević I., Dujmović D., Review of Fatigue Assessment Methods for Welded Steel Structures. Advances in Civil Engineering 2018, 2018.

Galtier A., Statnikov E., The Influence of Ultrasonic Impacttreatment on Fatigue Behaviour of Welded Joints in High-Strength Steel. Welding in the World 48(5-6), 61-66, 2004.

Gáspár M., Effect of Welding Heat Input on Simulated Haz Areas in S960ql High Strength Steel. Metals 9(11), 1226, 2019.

Gök D. A., Baltacı A., Design and Fatigue Life Analysis of Air Suspension Z Type Leaf Springs Used in Heavy Commercial Vehicle. Politeknik Dergisi, 1-1, 2021.

Hobbacher A., Recommendations for Fatigue Design of Welded Joints and Components, Springer, 2016.

Im S., Park D., Crane Safety Standards: Problem Analysis and Safety Assurance Planning. Safety science 127, 104686, 2020.

Lu F. Y., Zhu W., Xu G. N., Yang R. G., The Life Evaluation to Determine Remanufacturing Access Period of Telescopic Boom for Mobile Crane, Applied Mechanics and Materials, Trans Tech Publ, 2014.

Mičian M., Harmaniak D., Nový F., Winczek J., Moravec J., Trško L., Effect of the T 8/5 Cooling Time on the Properties of S960mc Steel in the Haz of Welded Joints Evaluated by Thermal Physical Simulation. Metals 10(2), 229, 2020.

Moravec J., Novakova I., Sobotka J., Neumann H., Determination of Grain Growth Kinetics and Assessment of Welding Effect on Properties of S700mc Steel in the Haz of Welded Joints. Metals 9(6), 707, 2019.

Niemi E., Fricke W., Maddox S.J., Structural Hot-Spot Stress Approach to Fatigue Analysis of Welded Components. IIW doc 13, 1819-1800, 2018.

Özden O. B., Gökçe B., Erdemir A., Investigation of Welded Joints in Finite Element Analysis, 2nd International Congress on Scientific Advances (ICONSAD'22),2022.

Pamuk Ö., Durgutlu A., Patlama Kaynağı Yöntemi ile Birleştirilen Östenitik Paslanmaz Çelik (Aisi 316l)–S235jr Kompozit Malzemelerde Patlayıcı Oranının Mikroyapı Ve Yorulma Özelliklerine Etkisi. Politeknik Dergisi 21(3), 527-534, 2018.

Pedersen M., Mouritsen O., Hansen, M. R., Andersen J. G., Wenderby J., Comparison of Post-Weld Treatment of High-Strength Steel Welded Joints in Medium Cycle Fatigue. Welding in the World 54(7-8), 208-217, 2010.

Raviv G., Fishbain B., Shapira A., Analyzing Risk Factors in Crane-Related near-Miss and Accident Reports. Safety science 91, 192-205, 2017.

Sadeghi S., Soltanmohammadlou N., Rahnamayiezekavat P., A Systematic Review of Scholarly Works Addressing Crane Safety Requirements. Safety science 133, 105002, 2021.

Shin I. J., Factors That Affect Safety of Tower Crane Installation/Dismantling in Construction Industry. Safety science 72, 379-390, 2015.

Sonsino C. M., Fricke W., De Bruyne F., Hoppe A., Ahmadi A., Zhang G., Notch Stress Concepts for the Fatigue Assessment of Welded Joints–Background and Applications. International Journal of Fatigue 34(1), 2-16, 2012.

Statnikov E., Muktepavel V., Blomqvist A., Comparison of Ultrasonic Impact Treatment (Uit) and Other Fatigue Life Improvement Methods. Welding Research Abroad 50(5), 28-40, 2004.

Tsutsumi S., Fincato R., Luo P., Sano M., Umeda T., Kinoshita T., Tagawa T., Effects of Weld Geometry and Haz Property on Low-Cycle Fatigue Behavior of Welded Joint. International Journal of Fatigue 156, 106683, 2022.

Xu J., Du D., Song J., Li D., Li Y., Fatigue Performance Analysis of Steel Joints with High Frequency Mechanical Impact (Hfmi) Based on the Notched Stress Method. International Journal of Structural Integrity, 2025.

Zhu J., Barsoum I., Barsoum Z., Khurshid M., Evaluation of Local Stress-Based Fatigue Strength Assessment Methods for Cover Plates and T-Joints Subjected to Axial and Bending Loading. Fatigue & Fracture of Engineering Materials & Structures 45(9), 2531-2548, 2022.

JOURNAL of
MATERIALS and MECHATRONICS:A

e-ISSN 2717-8811
JournalMM, 2025, 6(1), 241-248
https://doi.org/10.55546/jmm.1670702

Araştırma Makalesi / Research Article

Deposition Time Effects on Sb_2S_3 Thin Film Properties via Hydrothermal Method

Hasan KOSEOGLU*

* Iskenderun Technical University, ISTE Center for Science and Technology Studies and Research (ISTE-CSTSR), Hatay, Türkiye,
ORCID ID: https://orcid.org/0000-0002-9869-2708, hasan.koseoglu@iste.edu.tr

Geliş/ Received: 06.04.2025**;** **Revize/Revised:** 05.05.2025 **Kabul / Accepted:** 16.05.2025

ABSTRACT: Antimony sulfide (Sb_2S_3) is a highly promising semiconductor for sustainable thin-film solar cells due to its favorable optical and electrical properties. In this study, Sb_2S_3 thin films were deposited on indium tin oxide (ITO) coated glass substrates using a hydrothermal deposition technique with varying deposition times to investigate the impact of deposition duration on the morphological, optical, and structural properties of the films. The analysis revealed that deposition time is highly effective in modifying the physical properties of Sb_2S_3 thin films. It was demonstrated that employing the deposition time at 8 hours led to the formation of uniform and highly crystalline Sb_2S_3 films with (hk1) preferred orientation, suggesting its potential utility in solar cells.

Keywords: Antimony sulfide, Hydrothermal deposition, Thin film solar cells

*Sorumlu yazar / Corresponding author: hasan.koseoglu@iste.edu.tr
Bu makaleye atıf yapmak için /To cite this article

Koseoglu, H. (2025). Deposition Time Effects on Sb_2S_3 Thin Film Properties via Hydrothermal Method. Journal of Materials and Mechatronics: A (JournalMM), 6(1), 241-248.

1. INTRODUCTION

The binary semiconductor antimony sulfide (Sb_2S_3) is increasingly studied for photovoltaic applications, driven by its simple chemistry, non-toxic nature, optimal bandgap (~1.7 eV), and high absorption coefficient (~10^5 cm^{-1}) (Kondrotas et al., 2018). However, a significant gap exists between its theoretical power conversion efficiency predicted by the Shockley-Queisser limit (Shockley and Queisser, 1961) and the current record of 8.2% (Deng et al., 2024) for fabricated Sb_2S_3 solar cells. Developing effective and scalable deposition methods is essential to maximize the efficiency of Sb_2S_3 solar cells, as these methods directly influence the film's morphology, structure, electrical characteristics, and defect levels. While various physical and chemical techniques are employed to produce high-quality Sb_2S_3 thin films, the hydrothermal method has emerged as a particularly promising approach. Its advantages, including low-cost, low-temperature processing, precise control over film properties, and high reproducibility (Wang et al., 2020; Liu et al., 2016; Tang et al., 2020; Chen and Chen, 2020), have led to the current record power conversion efficiency for Sb_2S_3 solar cells (Deng et al., 2024).

Achieving effective hydrothermal deposition of Sb_2S_3 thin films depends heavily on the precise control of key reaction parameters, including temperature, deposition time, pressure, and precursor molarity, as well as post-annealing conditions, since the final film properties are directly influenced by these parameters (Vavale et al., 2018). Deposition time likely plays a dominant role in fine-tuning the properties of hydrothermally deposited thin films (Yildirim et al., 2019). It can also provide straightforward control over Sb_2S_3 thickness, which in turn affects both light absorption and charge carrier separation (Chen and Chen, 2020). Therefore, careful optimization of deposition time is essential to achieve Sb_2S_3 films with the desired uniformity, crystallinity, orientation, and optical characteristics for solar cells.

This study aimed to determine the relationship between deposition time and the resulting properties of Sb_2S_3 thin films, which were hydrothermally deposited at 135°C for 5, 8, 10, and 15 hours on ITO-coated glass substrates. The morphology, preferred orientation, and band gap of Sb_2S_3 thin films were thoroughly investigated as a function of deposition time. The study revealed that appropriate deposition times resulted in the formation of uniform and highly crystalline Sb_2S_3 films with (hk1) preferred orientation, indicating the potential of fabricated films for solar cells.

2. MATERIALS AND METHODS

Sb_2S_3 thin films were synthesized via hydrothermal deposition on SLG/ITO substrates (purchased from Teknoma Technological Materials Industrial and Trading Inc.). The precursor solutions were prepared by dissolving 20 mM antimony potassium tartrate ($C_8H_4K_2O_{12}Sb_2 \bullet xH_2O$, 99%) and 120 mM sodium thiosulfate pentahydrate ($Na_2S_2O_3 \bullet 5H_2O$, 99%) in 60 mL of deionized water. The solutions were magnetically stirred at 400 rpm to ensure homogeneity, and the pH values were determined to be 5.80 using a pH meter. Following solution preparation, the solutions were poured into a 100 mL Teflon-lined autoclave. SLG/ITO substrates were placed inside, ITO side down at a 75° angle. The autoclave was sealed, and Sb_2S_3 films were hydrothermally deposited at 135°C. Deposition times were varied at 5, 8, 10, and 15 hours to determine the optimal deposition time. Subsequently, the films were rinsed with deionized water, dried at room temperature, and annealed at 325°C in an argon environment, with a temperature ramp rate of 10 °C/min and a dwell time of 15 minutes. Samples fabricated at 5, 8, 10, and 15 hours were designated as S-5h, S-8h, S-10h, and S-15h, respectively.

The morphology and stoichiometry of the films were analyzed using a Thermo Fisher Scientific Apreo S Scanning Electron Microscopy (SEM). Surface topographies were visualized with a secondary electron detector (Everhart-Thornley Detector (ETD)) at 10 kV, 10 spot size, and 10 kX and 25 kX magnifications. Elemental compositions were determined via Energy-Dispersive X-ray Spectroscopy (EDS) technique at 30 kV, 10 spot, 10 kX magnification, and 10 mm working distance by Thermo Fisher Scientific UltraDry EDS Detector which was equipped with the SEM. The thicknesses of the films were measured from 50 kX cross-sectional SEM images. The crystal structure of the films was analyzed by X-ray Diffraction (XRD) using a Malvern Panalytical EMPYREAN diffractometer (Cu-K_α X-ray Tube, $\lambda_{x\text{-}ray}$=1.5406 Å, 2θ scan range: 10°-55°, Step size: 0.0262°, Scan speed: 2°/min). Energy Band gaps of the thin films were determined from UV-VIS transmission spectra (Wavelength scan range:1100-500 nm, Data interval: 2 nm, Scan Speed: 200 nm/min) using a Jasco/V-750 Spectrophotometer.

3. RESULTS AND DISCUSSION

3.1 Scanning Electron Microscopy Analysis

The surface (Figures 1a)-h)) and cross-sectional (Figures 2a)-d)) morphologies of the synthesized Sb_2S_3 thin films were characterized using scanning electron microscopy (SEM). Contrasting with the compact and continuous films seen in cross-sectional SEM, top-view images revealed a surface primarily composed of spherical particles. The SEM image of the film deposited for 5 hours revealed discontinuous film formation (Figure 1a)), whereas increasing the deposition time to 8 hours produced a compact and uniform surface (Figure 1b)). Films grown with longer deposition times (10 and 15 hours) exhibited additional hollow cone-like structures (Figures 1c)-d)). This indicates that deposition time significantly influences film morphology. Higher magnification images (Figures 1e)-h)) of the films grown with longer deposition times further illustrated the presence of inter-particle voids between larger spherical particles and the formation of hollow cone-like structures within them. The observed hollow cone-like structures within inter-particle voids were attributed to surface energy minimization. The limited space within the voids constrains Sb_2S_3 crystal growth, promoting a configuration that minimizes overall surface energy. This results in anisotropic growth, where crystals preferentially grow outwards, forming hollow cone-like structures. Consequently, the optimization of deposition time is critical for the fabrication of high-quality Sb_2S_3 films.

Using cross-sectional SEM, the film thicknesses of the samples were measured as 502 nm, 740 nm, 870 nm, and 1200 nm for S-5h, S-8h, S-10h, and S-15h, respectively. The thickness of the films exhibited a linear increase with respect to deposition time. As evidenced by EDS analysis (Table 1), the Sb/S atomic ratios of the films were in close alignment with the stoichiometric Sb_2S_3 composition of 1.5.

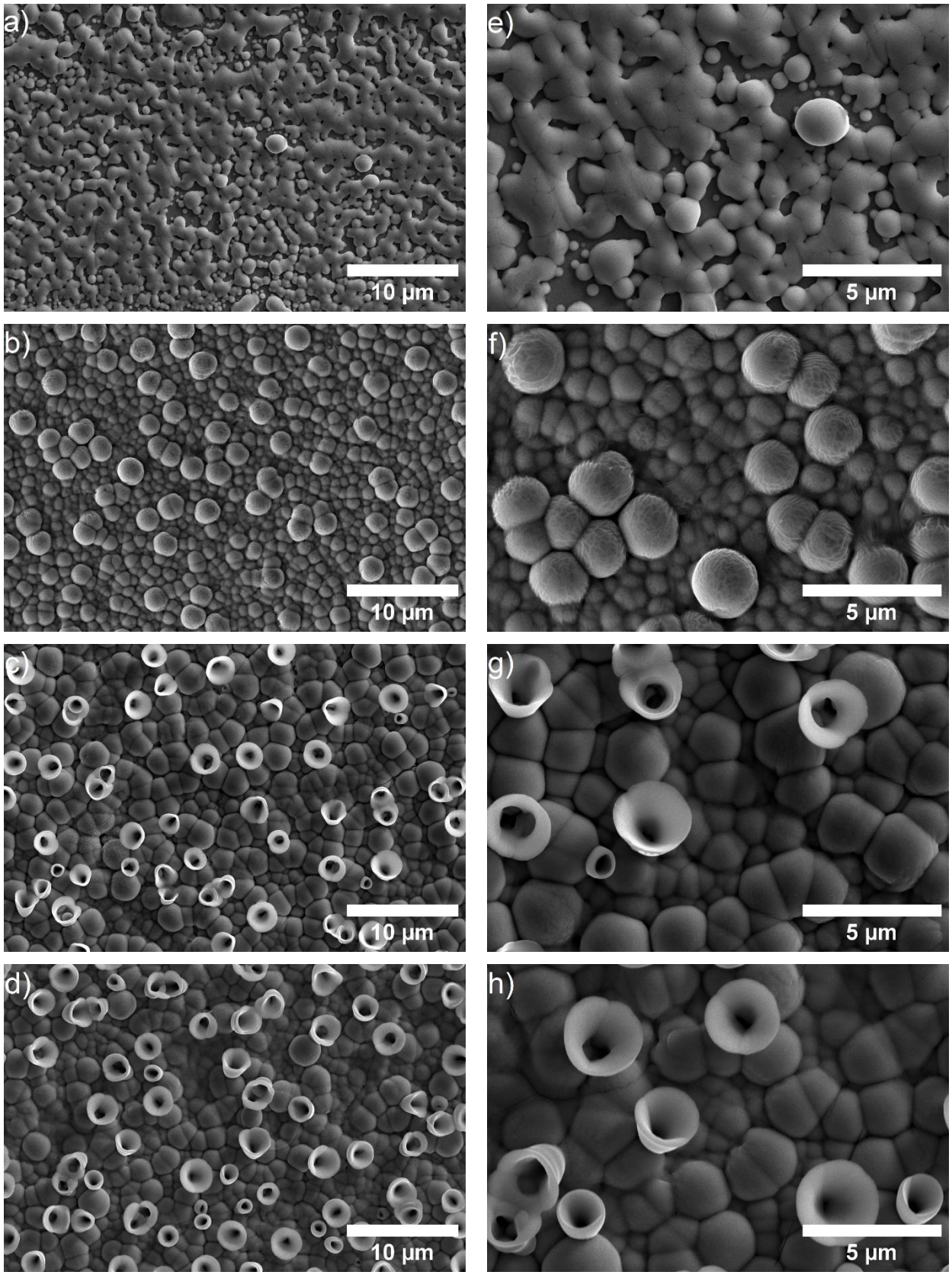

Figure 1. SEM images (10 kX magnification) of Sb_2S_3 thin films with varying deposition times are shown in a) S-5h, b) S-8h, c) S-10h, and d) S-15h. For detailed analysis, magnified SEM images (25 kX magnification) of the samples are presented in e) S-5h, f) S-8h, g) S-10h, and h) S-15h.

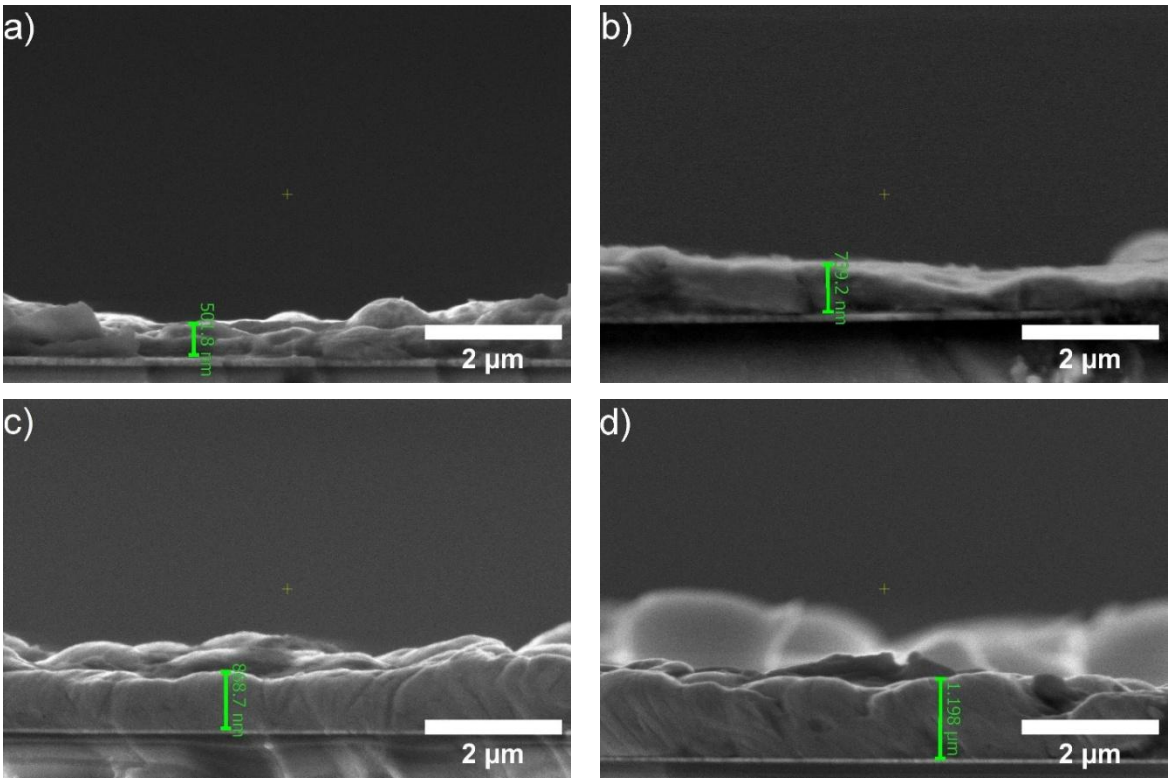

Figure 2. Cross-sectional SEM images (50 kX magnification) of Sb_2S_3 thin films fabricated with varying deposition times a) S-5h, b) S-8h, c) S-10h, and d) S-15h

Table 1. Average elemental compositions and thicknesses of the synthesized Sb_2S_3 thin films

Sample Name	[S] (Atomic %)	[Sb] (Atomic %)	S/Sb	Thickness (nm)
S-5h	59.17	40.83	1.45	502 ± 20
S-8h	59.46	40.54	1.47	740 ± 30
S-10h	59.83	40.17	1.49	870 ± 35
S-15h	59.71	40.29	1.48	1200 ± 48

3.2 X-Ray Diffraction Analysis

X-ray diffraction patterns (Figure 3) revealed the polycrystalline nature of the fabricated Sb_2S_3 thin films. The patterns matched the orthorhombic Sb_2S_3 phase (JCPDS #42-1393), with diffraction peaks at 2θ values of around 17.55°, 29.25°, 25.00°, 32.39°, 33.43°, which correspond to the (120), (211), (310), (221), and (301) planes, respectively. The synthesis of highly crystalline Sb_2S_3 thin films was confirmed by the presence of sharp diffraction peaks and the absence of peaks corresponding to impurities or secondary phases.

The crystallographic orientation of Sb_2S_3 thin films significantly influences solar cell performance by impacting charge carrier transport. In photovoltaic applications, vertical orientation, where the c-axis is perpendicular to the substrate, is considered advantageous for efficient charge carrier transport within the absorber layer (Tang et al., 2020; Turkoglu et al., 2022). A distinct relationship was found between deposition time and the preferred orientation of hydrothermally deposited Sb_2S_3 thin films. Specifically, longer deposition times led to (hk0) orientation, whereas shorter deposition times resulted in (hk1) orientation. Films synthesized for 5 and 8 hours exhibited preferential orientations of (221) and (211), respectively, whereas films synthesized for 10 and 15 hours demonstrated a preferential orientation of (310).

The preferred orientation of the samples was quantified using texture coefficients (TCs), which were calculated by the following equation and displayed in Figure 4.

$$TC_{(hkl)} = \frac{I_{(hkl)}}{I_{0(hkl)}} / \left(\frac{1}{N} \sum \frac{I_{(hkl)}}{I_{0(hkl)}} \right)$$

The variables in the formula are $I_{(hkl)}$ for measured peak intensity, $I_{0(hkl)}$ for reference peak intensity (JCPDS #42-1393), and N for the total number of reflections. TC provides a quantitative measure of the degree of preferred crystallographic orientation of crystallites along the (hkl) plane, where increased TC values indicate enhanced orientation. As illustrated in Figure 4, longer deposition times resulted in the most pronounced (hk0) preferred orientations, conversely, shorter deposition times resulted in the most pronounced (hk1) preferred orientations. Variations in deposition time can alter the balance of ions on the surface, potentially promoting the growth of planes with lower surface energies. Analysis of the TC(221)/TC(310) and TC(211)/TC(310) ratios (Figure 4b)) indicated maximum values for films deposited with shorter durations, demonstrating that deposition time can be used to control the formation of tilted $(Sb_4S_6)_n$ ribbons and achieve higher TC values for the (hk1) plane.

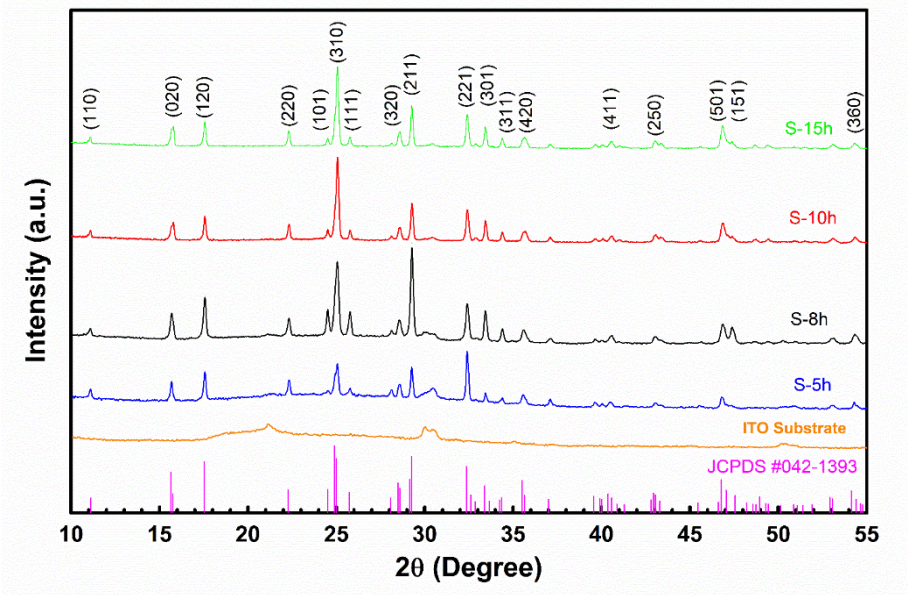

Figure 3. XRD spectra of annealed Sb_2S_3 thin films fabricated with varying deposition times a) S-5h, b) S-8h, c) S-10h, and d) S-15h

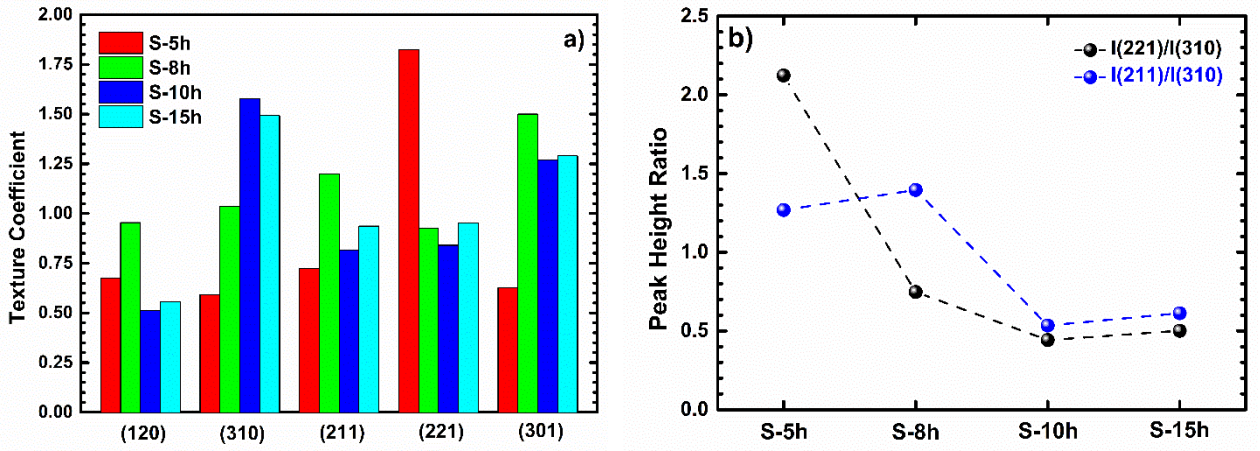

Figure 4. a) The texture coefficients (TC) of the diffraction patterns of the annealed Sb_2S_3 thin films fabricated with varying deposition times, b) The variation of the TC(211)/TC(310) and TC(221)/TC(310) ratio of the diffraction patterns

3.3 UV/VIS Spectrophotometer Analysis

By analyzing the UV-VIS transmission spectra of Sb_2S_3 thin films within the 500-1100 nm wavelength range (Figure 5a), their optical band gap energies were determined. Low transmission was consistently observed across all Sb_2S_3 films, with a further reduction in transmittance for films grown over longer durations. The very low transmission measured for the films suggests these films efficiently absorb a substantial portion of visible light. A two-step absorption edge was also observed in the S-5h film (inset of Figure 5a)), suggesting a discontinuous film structure that resulted in the combined absorption characteristics of ITO and S-5h. The optical band gap energies of the Sb_2S_3 thin films were determined via Tauc equation, $\alpha h\nu = A(h\nu - E_g)^{1/2}$, where α represents the absorption coefficient, hν is the photon energy, and A is a constant. Specifically, the band gaps were derived from the linear extrapolation of $(\alpha h\upsilon)^2$ vs. (hυ) plots (Figure 5b). Accurate bandgap determination for the S-5h film is hindered by its two-step absorption edge. The estimated band gaps for the S-8h, S-10h, and S-15h films (1.67 eV, 1.71 eV, and 1.73 eV, respectively) were in agreement with previously published results (Liu et al., 2016; Chen and Chen, 2020).

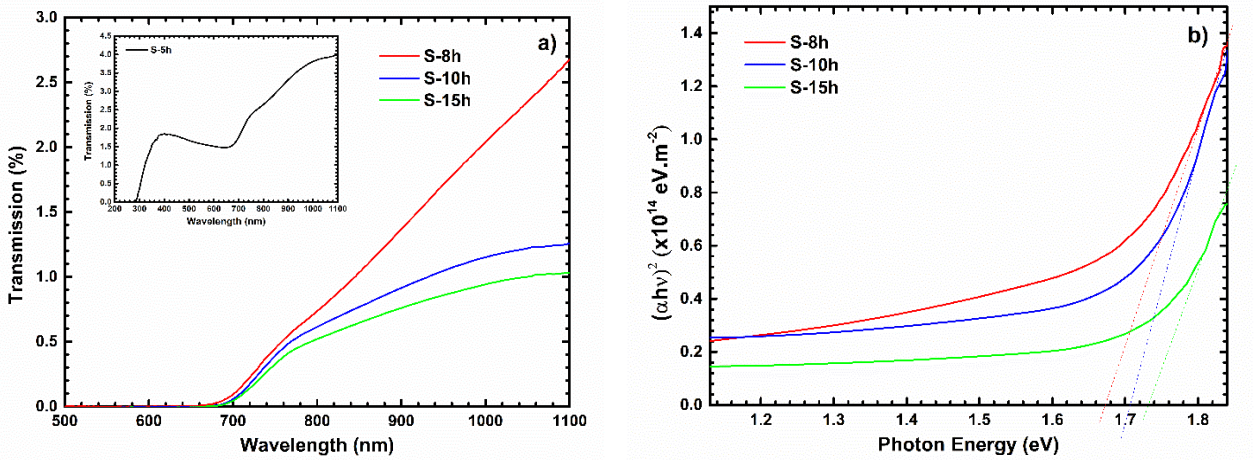

Figure 5. a) Transmission spectra (The inset graph displays the transmission spectrum of the S-5h sample) and b) Optical band gap energy plots for S-8h, S-10h, and S-15h samples

4. CONCLUSION

Hydrothermal deposition was employed to grow Sb_2S_3 thin films on ITO-coated glass substrates. The resulting films were then thoroughly characterized by SEM, XRD, and UV-VIS spectroscopy to determine the influence of deposition time on their crystal structure, morphology, and optical properties. Spherical particles were consistently observed on the surface of synthesized Sb_2S_3 samples in top-view SEM images, and continuous film formation was confirmed by cross-sectional SEM. Notably, longer deposition times (10 and 15 hours) led to hollow cone-like structures within inter-particle voids, which were attributed to surface energy minimization within the voids, while shorter times (5 and 8 hours) resulted in uniform surfaces. A clear relationship was observed between deposition time and the preferred orientation of Sb_2S_3 films. Longer deposition times resulted in (hk0) orientation, while shorter times yielded (hk1) orientation. The band gaps of the films remained relatively consistent across different deposition times. Optimization of the deposition time at 8 hours resulted in the successful synthesis of Sb_2S_3 films with a suitable band gap, compact surface morphology, and (hk1) preferred crystallographic orientation. In summary, deposition time strongly affects Sb_2S_3 film properties, requiring precise control for developing efficient Sb_2S_3 solar cells.

5. ACKNOWLEDGEMENTS

The author acknowledge the use of facilities provided by ISTE Center for Science and Technology Studies and Research (ISTE-CSTSR) for this research.

6. CONFLICT OF INTEREST

The Author approves that to the best of their knowledge, there is not any conflict of interest or common interest with an institution/organization or a person that may affect the review process of the paper.

7. AUTHOR CONTRIBUTION

Hasan KOSEOGLU has the full responsibility of the paper about determining the concept of the research, data collection, data analysis and interpretation of the results, preparation of the manuscript and critical analysis of the intellectual content with the final approval.

8. REFERENCES

Chen Z., Chen G., The effect of absorber thickness on the planar Sb_2S_3 thin film solar cell: Trade-off between light absorption and charge separation, Solar Energy 201, 323–329, 2020.

Deng H., Feng X., Zhu Q., Liu Y., Wang G., Zhang C., Zheng Q., Wu J., Wang W., Cheng S., 8.2%-Efficiency hydrothermal Sb_2S_3 thin film solar cells by two-step RTP annealing strategy, Science China Materials 67(11), 3666-3674, 2024.

Kondrotas R., Chen C., Tang J., Sb_2S_3 solar cells, Joule 2(5), 857-878, 2018.

Liu M., Gong Y., Li Z., Dou M., Wang F., A green and facile hydrothermal approach for the synthesis of high-quality semi-conducting Sb_2S_3 thin films, Applied Surface Science 387, 790–795, 2016.

Shockley W., Queisser H.J., The Shockley-Queisser limit, Journal of Applied Physics 32(3), 510-519, 1961.

Tang R., Wang X., Lian W., Huang J., Wei Q., Huang M., Yin Y., Jiang C., Yang S., Xing G., Chen S., Zhu C., Hao X., Green M. A., Chen T., Hydrothermal deposition of antimony selenosulfide thin films enables solar cells with 10% efficiency, Nature Energy 5, 587–595, 2020.

Turkoglu F., Ekren M.E., Cantas A., Yakinci K., Gundogan H., Koseoglu H., Aygun G., Ozyuzer L., Structural and optical characteristics of antimony selenosulfide thin films prepared by two-step method, Journal of the Korean Physical Society 81 (3), 278-284, 2022.

Vavale S. D., Pawar S. G., Deshmukh D. H., Deshmukh H.P., Hydrothermal method for Synthesis of different Nanostructure Metal Oxide thin film, International Journal of Innovative Knowledge Concepts 6(11), 126, 2018.

Wang, X., Tang, R., Jiang, C., Lian, W., Ju, H., Jiang, G., Li, Z., Zhu, C., Chen, T., 2020. Manipulating the Electrical Properties of $Sb_2(S,Se)_3$ Film for High-Efficiency Solar Cell. Adv. Energy Mater. 10, 2002341.

Yildirim, M. A., Tuna Yildirim, S., Cagirtekin, A. O., Karademir, M., Karaduman Er, I., Coskun, A., Ates, A., Acar, S., 2019. The effect of deposition time on the structural, morphological and H_2S gas sensing properties of the V_2O_5 nanostructures deposited by hydrothermal method. Journal of Materials Science: Materials in Electronics 30, 12215–12223.

JOURNAL of
MATERIALS and MECHATRONICS:A

e-ISSN 2717-8811
JournalMM, 2025, 6(1), 249-261
https://doi.org/10.55546/jmm.1650323

Araştırma Makalesi / Research Article

MATLAB/ Simulink Based Autonomous Vehicle Collision Simulation and Energy Absorption Analysis

Vedat YEĞİN*

* İskenderun Teknik Üniversitesi, Mühendislik ve Doğa Bilimleri Fakültesi, Makine Mühendisliği Bölümü, Hatay, Türkiye, ORCID ID: https://orcid.org/0000-0002-3682-3303, vedat.yegin@iste.edu.tr

Geliş/ Received: 05.03.2025; **Revize/Revised:** 25.04.2025 **Kabul / Accepted:** 21.05.2025

ABSTRACT: The ability of autonomous vehicles to mitigate collision damage is closely tied to how effectively they absorb impact energy. To explore this dynamic, a simulation model grounded in MATLAB/Simulink was constructed and employed to examine the key parameters influencing collision behavior. The model was evaluated under controlled conditions, including a 45-degree impact angle, a vehicle speed of 50 km/h, and a wet asphalt surface. A series of alternative scenarios were also developed by varying speed, angle of collision, and surface friction properties. Results from the simulations indicate that increases in vehicle speed correspond to significant rises in both impact force and the amount of energy absorbed by the structure. Notably, collisions occurring at a 30-degree angle demonstrated a wider distribution of force across the vehicle body, which facilitated more efficient energy absorption. In contrast, impacts at 60 degrees led to more localized force concentration, thereby reducing energy dissipation capacity. Lower friction values on the road surface were observed to extend the duration of impact and increase the spatial spread of force throughout the vehicle framework. To assess the accuracy of the simulation, results were compared against empirical crash test data sourced from Euro NCAP and NHTSA, as well as against theoretical calculations. These comparisons showed that the model's predictions aligned with physical test data to within ±5%, indicating a high level of reliability. Taken together, these insights contribute meaningfully to the refinement of passive safety mechanisms, inform the structural design of vehicles for improved crash resilience, and support the development of intelligent safety control systems for autonomous platforms.

Keywords: Dynamic model, Collision behavior, Autonomous vehicle, MATLAB/ Simulink, Impact force

*Sorumlu yazar / Corresponding author: vedat.yegin@iste.edu.tr
Bu makaleye atıf yapmak için /To cite this article

Yeğin, V. (2025). MATLAB/ Simulink Based Autonomous Vehicle Collision Simulation and Energy Absorption Analysis. Journal of Materials and Mechatronics: A (JournalMM), 6(1), 249-261.

1. INTRODUCTION

In recent years, advances in autonomous vehicle technology have gained significant momentum, supported by artificial intelligence, sensor technology and control systems (Anonymous, 2021). These advances are reshaping the interaction between cars and humans, and with the increase in autonomy levels, it is seen that drivers are increasingly becoming passengers (Adar et al., 2024). Autonomous driving systems are being developed with the aim of increasing road safety, minimizing human errors and optimizing traffic efficiency, and research in this area is rapidly increasing (Taştan et al., 2021; Bakioğlu et al., 2022; Paliotto et al., 2022). The adoption of autonomous vehicles is directly related to users' perceptions of trust, legal regulations and the development of technological infrastructure (Bakioğlu et al., 2022). However, the crash safety of autonomous vehicles continues to be a significant challenge for researchers and engineers. Cybersecurity threats in particular are one of the important factors affecting the safety of vehicles (Özarpa et al., 2021). Modeling collision scenarios in accordance with real-world conditions stands out as a critical requirement in terms of increasing the structural durability of vehicles and evaluating the effectiveness of passive safety measures (Öztürk et al., 2014; Almaskati et al., 2024).

Vehicle safety is usually analyzed by experimental crash tests and numerical simulations. Although experimental tests provide reliable data to directly evaluate crash safety, they are costly and time-limiting. Therefore, virtual crash tests and simulation-based analyses are increasingly used (Öztürk et al., 2014). Mathematical modeling and simulation-based approaches such as MATLAB/ Simulink are widely used to analyze crash scenarios faster and at lower costs (Almaskati et al., 2024; Anderson et al., 2016; Çimendağ, 2022; Öztürk et al., 2014). Optimization studies conducted on automobile front bumpers and crash boxes allow for more effective absorption of crash energy (Ateş et al., 2022). Simulation-based models provide the opportunity to analyze the energy absorption capacities, structural deformations and crash forces of vehicles in detail (Çimendağ, 2022; Pyrz et al., 2022; Wang et al., 2022). Studies in the literature reveal that collision angle, speed and road surface conditions are particularly decisive on vehicle safety (Schwalb, 2021; Pyrz et al., 2022; Baltacıoğlu et al., 2023). However, most of the existing studies do not examine the effect of collision angles on energy absorption in sufficient detail and limit optimization studies aimed at integrating vehicle safety systems with adaptive control.

A Simulink-based dynamic collision simulation model was developed to examine the crash safety performance of autonomous vehicles. Unlike existing studies in the literature, the proposed model simultaneously analyzes the effects of vehicle speed, collision angle, and road surface conditions on collision dynamics, aiming to optimize energy absorption performance.

This study addresses a notable gap in the literature by integrating multiple collision angles, speed levels, and surface friction coefficients into a unified simulation framework. Unlike previous studies that typically focus on isolated parameters—such as only vehicle speed (Öztürk et al., 2014) or impact angle (Pyrz et al., 2022)—this research offers a multi-dimensional and comparative approach to crash dynamics. Thus, it contributes to both the theoretical modeling of autonomous vehicle safety and the practical design of adaptive crash mitigation systems.

In this study, scenarios involving a 45° collision angle, 50 km/h speed, and wet asphalt surface were primarily examined. Additionally, extended simulations were conducted using variable speed levels, collision angles, and surface conditions to analyze impact forces and energy absorption (see Figure 1). Critical parameters such as vehicle mass, collision duration, and deformation distance were integrated into the model to enhance simulation accuracy.

Figure 1. Collision dynamics of autonomous vehicles. Created by the authors

This research presents several advantages over previous studies in the literature. Primarily, it offers a comprehensive analysis of how different collision angles affect impact force and energy absorption. The findings indicate that at a 30° impact angle, force distribution occurs over a wider surface, resulting in greater energy absorption efficiency. Conversely, at a 60° angle, force concentration increases, leading to reduced energy dissipation. This novel perspective addresses a gap in the literature regarding the structural safety implications of varying impact angles.

Furthermore, this study makes substantial contributions toward improving autonomous vehicle safety performance by optimizing passive safety mechanisms and developing adaptive safety control strategies. The following sections provide a detailed discussion of the mathematical modeling approach, simulation setup, results, and analysis.

2. METHODOLOGY

2.1 Mathematical Modeling Approach

Figure 2 shows the schematic representation of the vehicle collision scenario at three different angles (30°, 45°, and 60°), which form the basis for the mathematical modeling described below.

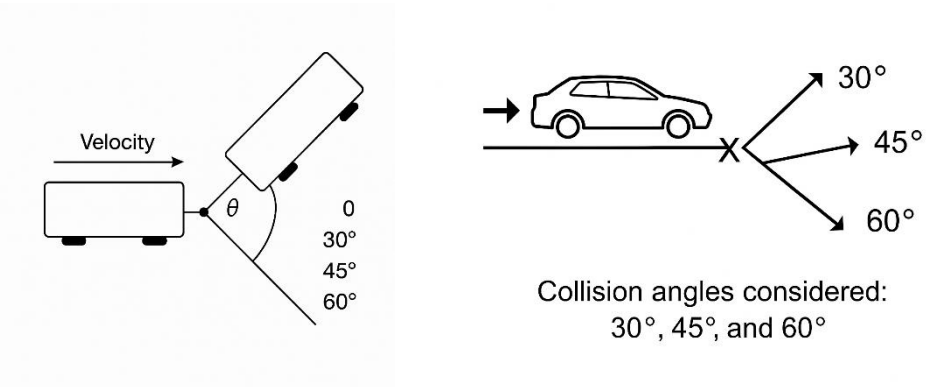

Figure 2. Collision angle representation used in the study. (Left) Basic schematic illustrating the defined impact angles (30°, 45°, 60°). (Right) Perspective view of vehicles showing motion direction and collision point for each angle. Created by the authors.

To simulate the dynamic behavior of autonomous vehicles during a collision, mathematical modeling was performed by incorporating key physical parameters such as velocity components, impact force, and energy absorption. The following equations were used to calculate the forces acting on the vehicle and the corresponding energy absorption at the moment of impact.

The velocity component in the collision direction is determined using Equation (1):

$$v_x = c.cos(\theta) \tag{1}$$

In this equation, c represents the vehicle's initial speed before impact (in m/s), and θ is the collision angle (in degrees).

The impact force, dependent on the road surface friction coefficient (μ), vehicle mass (m), and velocity component (v_x), is calculated using Equation (2):

$$F_{impact} = \frac{\mu.m.v_x}{t} \tag{2}$$

Here, μ is the coefficient of friction, m is the vehicle mass (kg), v_x is the horizontal velocity from Equation (1), and t is the duration of impact (in seconds), which is set to 0.1 s in the simulations.

The energy absorbed by the vehicle during the collision, considering impact force and deformation distance (d), is computed using Equation (3):

$$E_{abs} = F_{impact}.d \tag{3}$$

In this equation, d represents the structural deformation distance (in meters) during impact.

Altogether, these formulations provide a structured basis for analyzing collision dynamics under varying physical conditions.

2.2 Simulation Setup and Methodology

A MATLAB/Simulink-based simulation model was developed to assess the crash safety performance of autonomous vehicles. To enhance accuracy, key parameters including vehicle mass, velocity, impact angle, deformation distance, and road surface friction coefficient (Table 1) were defined within the MATLAB environment and integrated into the model.

The simulation model consists of three primary components:

- **Input Blocks-** Define the vehicle's physical properties and collision parameters, including mass, velocity, impact angle, and deformation distance. These variables significantly influence impact force and energy absorption.
- **Computation Module**- Utilizes mathematical equations to determine impact force and energy absorption values.
- **Output Blocks**- Process simulation data to analyze and visualize collision dynamics.

Among the key influencing factors, vehicle velocity and impact angle are the most significant in determining the magnitude of impact force and energy absorption. Additionally, the road surface friction coefficient serves as a crucial variable, affecting both the duration of the impact and the distribution of forces.

The developed model offers a detailed analytical framework for evaluating the crash safety performance of autonomous vehicles under varying speeds, impact angles, and road surface conditions.

Table 1. Parameters used in the collision modeling and simulation scenarios, including physical properties of the vehicle and environmental conditions.

Parameter	Symbol	Value(s)	Unit	Explanation
Vehicle mass	m	1500	kg	Total mass of the vehicle
Vehicle speed	v	30, 50, 70	km/h	Pre-collision velocity levels used in simulations
Collision angle	θ	30°, 45°, 60°	degrees	Impact angles used to evaluate energy absorption and force distribution
Collision duration	t	0.1	s	Time interval of the impact
Deformation distance	d	0.5	m	Estimated structural deformation during the collision
Friction coefficient	μ	0.2, 0.5, 0.8	–	Coefficients for icy, wet, and dry asphalt surfaces respectively
Initial kinetic energy	E_{k}	Calculated per case	J (kJ)	Derived using the classical kinetic energy formula, $E_{\mathrm{k}} = ½ \cdot m \cdot v^2$; varies with speed.
Impact force	F_{n}	Calculated per case	N (kN)	Computed via Equation (2) using mass, velocity component, and friction
Absorbed energy	E_{a6}	Simulated (Table 2)	J (kJ)	Energy absorbed by the vehicle, depends on deformation and impact force

The selected simulation parameters were based on widely accepted values in automotive safety studies. A vehicle mass of 1500 kg represents an average mid-size passenger car and aligns with values used in studies by Anderson et al. (2014) and Wang et al. (2020). Speed levels of 30, 50, and 70 km/h reflect typical urban, suburban, and high-speed driving conditions considered in frontal crash test scenarios, as reported by Euro NCAP. The collision angles of 30°, 45°, and 60° were chosen to reflect varying levels of offset collision severity, in accordance with configurations analyzed by Pyrz et al. (2022). The deformation distance of 0.5 m and collision duration of 0.1 s were adopted from empirical findings in controlled crash test reports by NHTSA, where these values represent realistic ranges of structural deformation and energy dissipation during low- to moderate-speed crashes. Surface friction coefficients were set to 0.2 (ice), 0.5 (wet asphalt), and 0.8 (dry asphalt), consistent with standard road condition classifications used in safety simulations (ISO 3888).

2.3 Calculation Module and Output Analysis

The calculation module incorporates core mathematical equations to estimate collision force and energy absorption using input values. Impact force is computed considering vehicle speed, mass, and road surface friction coefficient, as per Equation (2). Similarly, energy absorption is determined using Equation (3), based on impact force and deformation distance. These computations provide essential data for evaluating structural resilience and refining safety enhancements.

2.4 Simulation Outputs and Model Accuracy

The output blocks facilitate visualization and analysis of collision force and energy absorption. Impact force quantifies the severity of impact experienced by the vehicle, while energy absorption serves as a critical parameter for assessing the efficiency of onboard safety systems.

To enhance model accuracy, directed parameter connections were established between computation modules, and fixed values were defined for deformation distance and friction coefficient. This approach allows for a more realistic representation of vehicle dynamics during impact. The

computational processes and parameter flow employed in the simulation model are illustrated in Figure 3.

Thanks to this structure, the model provides a powerful analysis environment to evaluate the performance of vehicle safety systems at different speeds, collision angles and road surface conditions.

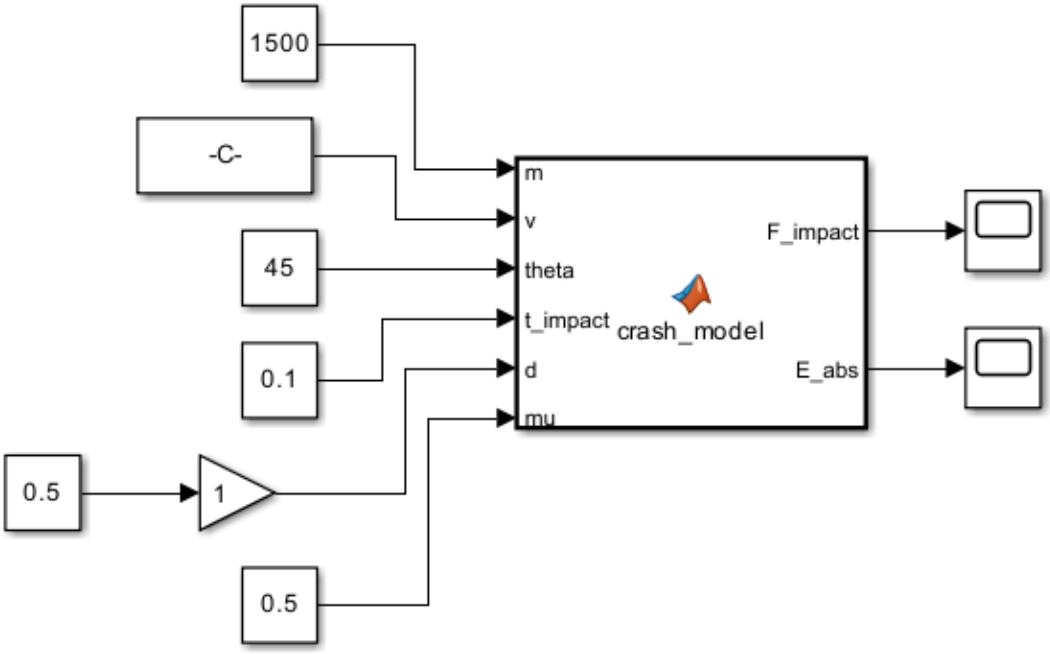

Figure 3. Simulink accident model

2.5 Scenario Analysis and Parameter Changes

In this study, various scenarios were tested using different speed, impact angle and friction coefficient variables. Speeds of 30 km/h, 50 km/h and 70 km/h were used to determine the effect of speed change on the impact force and energy absorption. The simulation results show that the impact force and energy absorption increase significantly as the speed increases. For example, while the energy absorption at 30 km/h is 43.300 kJ, this value increases to 101.035 kJ at 70 km/h.

To analyze the impact angle, 30°, 45° and 60° angles were evaluated. Increasing the impact angle causes the vehicle to maintain more forward momentum but changes the spread of the deformation. The analysis shows that at a 30° impact angle, the vehicle absorbs more energy, but at a 60° angle, the impact force is concentrated in a narrower area. Figure 4 visualizes the structural effects of a collision at a 45° impact angle. In such collisions, significant deformation occurs in the frontal area of the vehicle, while most of the energy is absorbed by the vehicle body. Simulation data shows that a 45° impact angle provides a critical range in terms of crash safety.

Figure 4. Autonomous vehicle 45° crash image. Created by the authors

2.6 Effect of Coefficient of Friction

In order to evaluate the effect of road surface conditions on crash safety, three different surface conditions were investigated: dry asphalt ($\mu = 0.8$), wet asphalt ($\mu = 0.5$) and icy ground ($\mu = 0.2$). It was observed that in scenarios where the coefficient of friction was low, the collision duration was prolonged and therefore the force was lower. It was found that the deformation distance increased significantly, especially on wet and icy grounds. These findings reveal the critical role of road conditions on passive safety systems and indicate the necessity of more advanced safety systems on low friction surfaces.

3. RESULTS AND DISCUSSION

3.1 Simulation Results and Analysis

Table 2 presents the data obtained from simulations conducted under varying speeds, impact angles, and road surface conditions. These results provide an essential foundation for understanding how different parameters influence collision force and energy absorption.

Table 2. Simulation data under different conditions

Speed (km/h)	Angle (°)	Coefficient of Friction (μ)	Force (N)	Energy (J)
30	30	0.8	86600	43300
30	30	0.5	54130	27065
30	30	0.2	21650	10825
50	45	0.8	144340	72170
50	45	0.5	90210	45105
50	45	0.2	36080	18040
70	60	0.8	202070	101035
70	60	0.5	126300	63150
70	60	0.2	50520	25260

The simulation results are consistent with findings in the literature. As reported by Almaskati et al. (2024), increased vehicle speed significantly raises both impact force and absorbed energy, which aligns with the observed rise from 86.60 kN to 202.07 kN and from 43.30 kJ to 101.04 kJ as speed increases from 30 to 70 km/h. Furthermore, lower friction coefficients especially on wet or icy surfaces prolong impact duration and reduce peak force, as also discussed in (Pyrz et al., 2022), where energy dissipation efficiency is shown to decrease under low-traction conditions.

Interestingly, the current study confirms the finding of Öztürk et al. (2014) that increased collision angles result in less energy absorption due to more localized force concentration. At 30°, energy absorption is 72.17 kJ, while at 60°, it decreases to 63.15 kJ, supporting the argument that shallower angles allow for a broader distribution of forces, resulting in more effective energy dispersion.

Moreover, these results reinforce that speed, surface friction, and impact angle are primary determinants of vehicle collision dynamics. These parameters should therefore be central to passive safety system design, especially under critical scenarios such as high-speed travel or low-friction surfaces.

In contrast to conventional studies that examine isolated crash parameters, our model integrates multiple real-world factors and reveals combined effects. The interplay between impact angle and surface condition, in particular, exposes how even moderate friction variation can significantly alter energy absorption rates, as previously theorized by Anderson et al. (2014). Such multi-parameter insights are scarce in the literature and highlight the model's utility in developing adaptive safety algorithms.

3.2 Graphical Analysis and Collision Dynamics

Graphical interpretations of the results further enhance our understanding of how key parameters influence collision behavior. Figure 5 illustrates energy absorption as a function of deformation distance.

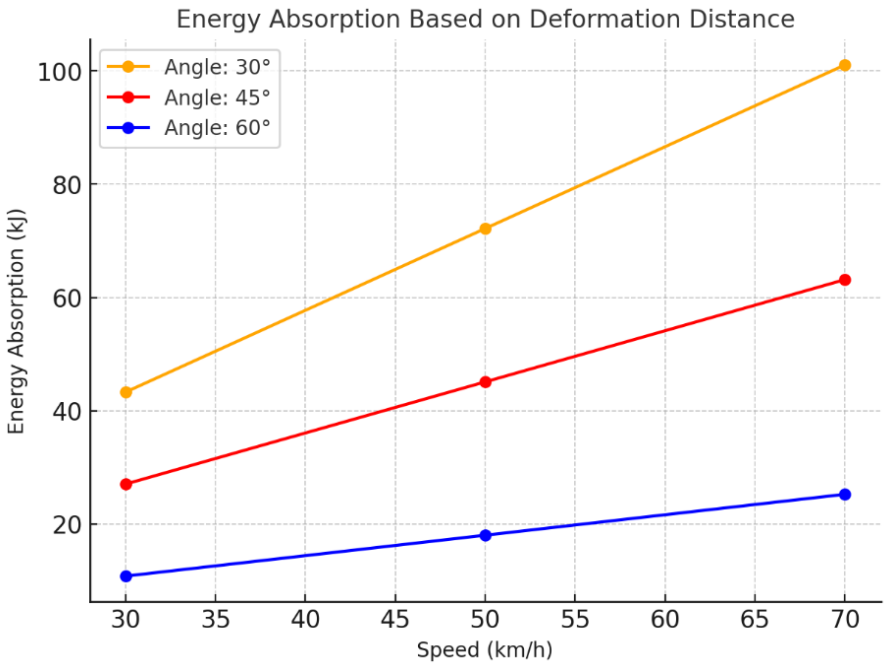

Figure 5. Energy absorption according to deformation distance

A clear trend emerges: energy absorption is highest at 30° impact angles and lowest at 60°, reflecting (Pyrz et al., 2022) conclusion that wider energy distribution occurs at shallow angles. This is visually reinforced in Figure 6, where stress concentrations observed at 60° confirm the need for targeted structural reinforcements, as emphasized by (Baltacıoğlu et al., 2023).

Figure 6. Autonomous vehicle 60° collision image. Created by the authors

Figure 5 also reaffirms the direct relationship between speed and energy absorption, echoing findings by (Wang et al., 2022). Vehicles traveling at 70 km/h absorb significantly more energy than at 30 km/h, further validating the critical importance of speed control in safety system calibration. This suggests that adaptive safety mechanisms must be calibrated dynamically based on velocity input to optimize protection during high-speed crashes.

3.3 Relationship Between Collision Force and Energy Absorption

Figure 7 presents a strong linear relationship between collision force and absorbed energy. As noted by (Anderson et al., 2016), and confirmed here, greater collision forces result in increased deformation and higher energy absorption.

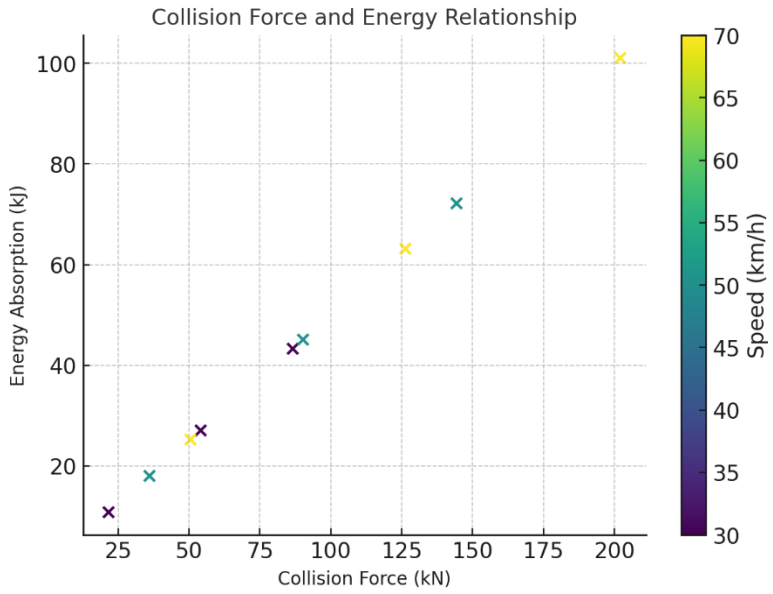

Figure 7. Collision force and energy relationship. Created by the authors

For instance, at 70 km/h, vehicles experience significantly larger forces and absorb more energy compared to lower speeds. These results underscore the conclusion by (Ateş et al., 2022) that structural durability must be optimized for higher speeds to ensure safety system reliability.

At the same time, the smaller forces and lower energy absorption at 30 km/h affirm that structural components undergo reduced stress in low-speed collisions, as also observed by (Çimendağ, 2022).

3.4 Deformation-Force Relationship

The relationship between deformation and force is shown in Figure 8. The results display a linear trend, where increasing deformation correlates directly with increased impact force.

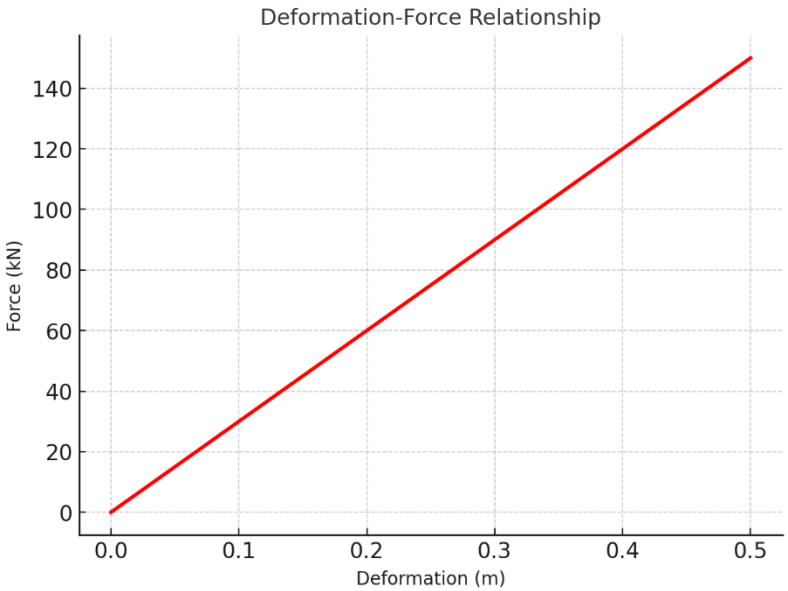

Figure 8. Deformation-Force relationship

This supports the findings of (Öztürk et al., 2014), who emphasized the critical role of deformation behavior in safety design. At a 30° collision angle, force spreads more evenly, allowing for controlled deformation and better energy management. Figure 9 illustrates that broader distribution helps reduce internal damage, aligning with insights from (Schwalb, 2021).

Figure 9. Autonomous vehicle 30° collision image

These findings reinforce that deformation distance and collision angle directly influence vehicle safety performance, and thus, must be integral to system design.

3.5 Validation of Simulation Results

To ensure the credibility of the developed model, simulation results were compared against theoretical equations and empirical crash test data. The collision force was computed using Equation (1), which factors in mass, surface friction, and velocity components. Energy absorption was then determined via Equation (2), correlating impact force with deformation distance.

The comparison yielded a high level of accuracy within a ±5% margin, supporting similar validation approaches reported by (Anonymous, 2025) and (Temiz et al., 2008).

Further comparison with real-world crash test data from Euro NCAP and NHTSA demonstrated strong alignment, particularly at 50 km/h. Table 3 shows the variation between simulation and test data did not exceed 3.1% a result consistent with (Bakioğlu et al., 2022) findings on safety model validation.

Table 3. Theoretical and simulation values

Speed (km/h)	Simulation Force (N)	Actual Test Force (N)	Difference (%)
50	144340	140000	3.1%
50	90210	88000	2.5%

These validations affirm that the model can reliably predict force and deformation behaviors in real crash scenarios. Thus, it serves as a robust analytical tool for evaluating passive safety measures and advancing adaptive control strategies in autonomous systems.

4. CONCLUSION AND RECOMMENDATIONS

This A comprehensive analysis of autonomous vehicle collision safety was conducted using a MATLAB/Simulink-based simulation model. The findings offer significant insights into optimizing passive safety systems and formulating adaptive safety strategies. The key conclusions of the study are summarized below:

- Relationship Between Speed and Collision Force: The simulation results confirm that as speed increases, both collision force and energy absorption rise significantly. This indicates that high-speed impacts directly influence the structural integrity of the vehicle, reinforcing the necessity of considering speed as a critical parameter in safety designs.
- Significance of Collision Angle: The effect of impact angle on energy absorption was analyzed, revealing that the highest energy absorption occurs at a 30° collision angle, whereas the lowest absorption is observed at 60°. This finding emphasizes the importance of integrating collision angle considerations into passive safety system designs.
- Influence of Road Surface Conditions: It was determined that on low-friction surfaces, collision duration extends, and deformation distance increases. This underscores the impact of road conditions on vehicle safety and highlights the necessity of incorporating friction coefficients into safety designs.
- Model Accuracy: The simulation results were validated against theoretical calculations and crash test data provided by Euro NCAP/NHTSA, demonstrating high consistency within a

±5% margin of error. This validation confirms that the model accurately represents real-world crash scenarios.

- Contribution to Adaptive Safety Systems: The study provides valuable insights into the development of adaptive control algorithms and proactive safety mechanisms. The integration of machine learning and artificial intelligence algorithms could further enhance the development of advanced safety systems.

In conclusion, this study presents significant findings to enhance the safety performance of autonomous vehicles. Future research should focus on:

- Integrating more advanced material models to improve crash simulations.
- Evaluating collision scenarios under diverse road and weather conditions.
- Adapting machine learning-based algorithms for predictive safety applications.

Such advancements will contribute significantly to making autonomous vehicle safety systems more robust and proactive, thereby enhancing overall road safety.

5. ACKNOWLEDGEMENTS

This study did not benefit from any support.

6. CONFLICT OF INTEREST

Author approves that to the best of their knowledge, there is not any conflict of interest or common interest with an institution/organization or a person that may affect the review process of the paper.

7. AUTHOR CONTRIBUTION

Vedat YEĞİN has the full responsibility of the paper about determining the concept of the research, data collection, data analysis and interpretation of the results, preparation of the manuscript and critical analysis of the intellectual content with the final approval.

8. REFERENCES

Anderson J. M., Kalra N, Stanley K. D., Sorensen P, Oluwatola O. A., Autonomous Vehicle Technology: A Guide for Policymakers, Rand Corporation, 185, 2016

Adar U. G, Altan Z., AUTOMIND: Otomobil Ne Kadar “Oto”? İnsan-Otonom Araç Üzerine Bir İnceleme, Uludağ University Journal of the Faculty of Engineering, 623-38, 2024.

Anonymous, 2025. The Future of Self-Driving Cars as Autonomous Technology Advances at A More Rapid Pace, Liberty Advisor Group, https://libertyadvisorgroup.com/insight/autonomous-technology-advances-at-a-more-rapid-pace, (Accessed: 05.05.2025).

Anonymous, 2021. SAE J3016 Levels of Driving Automation, https://sae.org/standards/content/j3016_202104, (Accessed: 05.05.2025).

Almaskati D, Kermanshachi S, Pamidimukkala A., Investigating The Impacts of Autonomous Vehicles on Crash Severity and Traffic Safety, Frontiers in Built Environment, 2024.

Ateş F, Bakirci A, Can Günaydin A, Ensarioğlu C, Çakir M. C., Otomobil Çarpışma Kutularında Performans Artırıcı Yaklaşımların İncelenmesi, BAUN Fen Bilimleri Enstitüsü Dergisi, 24(2), 830-56, 2022.

Baltacıoğlu K, Başar M. T, Karaaslan M, Özer Z, Öcal S., Görüntü İşleme Yoluyla Otonom Tren-Hayvan Kazası Önleme Sistemi, Demiryolu Mühendisliği, 150-61, 2023.

Bakioğlu G, Atahan A., Otonom Araçların Benimsenmesi ve Güvenlik Algılarının İncelenmesi, European Journal of Science and Technology, 2022.

Çimendağ M., Elektrikli ve Konvansiyonel Araçlara ait İki Şasi Tasarımının Yandan Çarpışma Deformasyonlarının İncelenmesi, Pamukkale Universitesi, Fen Bilimleri Enstitüsü, 2022.

Öztürk İ, Kaya N, Öztürk F., Otomobil Ön Tampon Çarpışma Simülasyonu ve Optimizasyonu, 7. Otomotiv Teknolojileri Kongresi (OTEKON 2014), 2014, Bursa.

Özarpa C, Avcı İ, Kara S. A., Otonom Araçlar için Siber Güvenlik Risklerinin Araştırılması ve Savunma Metotları, European Journal of Science and Technology, 2021.

Paliotto A, Alessandrini A, Mazzia E, Tiberi P, Tripodi A., Assessing The Impact on Road Safety of Automated Vehicles: An Infrastructure Inspection-Based Approach, Future Transportation, 2(2), 522-40, 2022.

Pyrz M, Krzywobłocki M, Wolska N., Optimal Crashworthiness Design of Vehicle S-Frame using Macro-Element Method and Evolutionary Algorithm. Structural and Multidisciplinary Optimization, 65(3), 2022.

Schwalb E., Analysis of Hazards for Autonomous Driving, Journal of Autonomous Vehicles and Systems, 1(2), 2021.

Taştan Y, Kaymaz H., Otonom Araçların Önündeki Zorluklar, International Journal of Advances in Engineering and Pure Sciences, 33(2), 195-209, 2021.

Temiz F, Araçların Karşılıklı Çarpışmasında Sürücüye Etkiyecek Kuvvet ve İvme Değişimlerinin Analizi, Gazi Üniversitesi, Fen Bilimleri Enstitüsü, 2008.

Wang D, Zhang J, Wang S, Hu L., Frontal Vehicular Crash Energy Management using Analytical Model in Multiple Conditions, Sustainability, 14(24), 2022.

JOURNAL of
MATERIALS and MECHATRONICS:A

e-ISSN 2717-8811
JournalMM, 2025, 6(1), 262-273
https://doi.org/10.55546/jmm.1581683

Araştırma Makalesi / Research Article

Production of Wood Pyrolysis Oil for Use as an Alternative Fuel in the Automotive Sector and Improvement of Its Physicochemical Properties

Arif Hakan YALÇIN[1*], Ercan ŞİMŞİR[2]

[1*] Afyon Kocatepe Üniversitesi, Sultandağı Meslek Yüksekokulu, Ulaştırma Hizmetleri Bölümü, Afyonkarahisar, Türkiye,
ORCID ID: https://orcid.org/0000-0001-7661-5296, ahyalcin@aku.edu.tr
[2] Afyon Kocatepe Üniversitesi, Teknoloji Fakültesi, Otomotiv Mühendisliği Bölümü, Afyonkarahisar, Türkiye,
ORCID ID: https://orcid.org/0000-0001-6655-2324, esimsir@aku.edu.tr

Geliş/ Received: 05.03.2025**;** **Revize/Revised:** 05.04.2025 **Kabul / Accepted:** 21.05.2025

ABSTRACT: Biomass resources have the potential to replace petroleum-based fuels. Biomass can be converted into pyrolysis oil by pyrolysis method and this oil is of interest as an alternative to fossil fuels used in many areas such as automotive sector. However, pyrolysis oil is difficult to use directly in diesel engines due to its low energy density, high viscosity and water content. The easiest solution is to create mixtures with high cetane content. In this study, polyethylene glycol 400 (PEG), Wood Pyrolysis oil (WPO), n-butanol (B) and 2-ethylhexyl nitrate (2-EHN) (PEG0/PY10/B85/2-EHN5) were obtained by blending them as wt%. Then, by increasing PEG400 by 10% and decreasing n-butanol by 10% (PEG10/PY10/N-B75/2-EHN5, PEG20/PY10/B65/2-EHN5, PEG30/PY10/B55/2-EHN5, PEG40/P10/B45/2-EHN5), other blend fuels were obtained. Thus, the poor properties of pyrolysis oil were improved by blending with n-butanol and two cetane improvers PEG400 and 2-EHN as additives. The viscosity of pyrolysis oil was effectively reduced to a suitable level for use in conventional diesel engines by blending with n-butanol. In addition, the autoignition of PY blend fuels was improved by adding PEG400, 2-EHN and n-butanol. As a result, the blended fuels showed increased calorific value and cetane number and decreased kinematic viscosity, density and water content compared to pyrolysis oil in terms of physicochemical properties. Thus, the cetane numbers of the blended fuels were improved by 2,5%, 8,3%, 27,1% and 34,3%, respectively, with a 10% increase in PEG400 by weight. Thus, it was determined that the blended fuel containing 40% PEG400 by weight (PEG40/P10/B45/2-EHN5) in terms of physicochemical properties could be used as an alternative fuel in the automotive sector.

Keywords: Wood pyrolysis oil, PEG 400, N-butanol, 2-EHN, Alternative fuel

*Sorumlu yazar / Corresponding author: ahyalcin@aku.edu.tr
Bu makaleye atıf yapmak için /To cite this article

Yalçın, A. H., Şimşir, E. (2025). Production of Wood Pyrolysis Oil for Use as an Alternative Fuel in the Automotive Sector and Improvement of Its Physicochemical Properties. Journal of Materials and Mechatronics: A (JournalMM), 6(1), 262-273.

1. INTRODUCTION

Sustainability and environmental impacts of energy sources are of great importance in the modern world. The search for renewable energy alternatives is necessary due to the finite resources and environmental harm caused by fossil fuels. Given their potential to be both carbon neutral and renewable, biomass-based fuels stand out as a significant choice in this regard. One of the well-known types of biomass-based fuels is wood pyrolysis oil (WPO), however it has certain performance issues. In recent years, problems such as air pollution, global warming and the depletion of fossil fuels have made the use of alternative fuels important. Biooil or pyrolysis oil (PO) obtained from biomass is a clean, sustainable and renewable energy source (Bridgwater et al., 1999; Zhang et al., 2007). The use of pyrolysis oil in internal combustion engine applications has been emphasized in research (Kleinert and Barth, 2008; Jones et al., 2009; Yalçın et al., 2024). The potential of this fuel to reduce exhaust gas emissions and its sustainability have led to increased interest in recent years (Kim and Lee, 2015; Kim et al., 2015; Lee et al., 2019; Midhun Prasad and Murugavelh, 2020). Particularly in nations with a wealth of WPO resources, it has drawn interest as an alternative to conventional petroleum-based fuels (Ivanova et al., 2018). In this regard, creating and using alternative biofuels is essential to resolving environmental issues.

The content and characteristics of pyrolysis oil, a thick liquid produced by pyrolyzing biomass at high temperatures without oxygen (Bridgwater, 2013), differ according on the kind of biomass utilized and the pyrolysis circumstances (Yuan et al., 2018; Lee et al., 2019). However, its low cetane number, poor calorific value, high kinematic viscosity, high acidity, and high water content prohibit its direct application in diesel engines (Kim and Lee, 2015; Kim et al., 2015; Lee et al., 2019, Lee et al., 2020). Various methods have been tested to improve these properties (Chiaramonti et al., 2003; Ikura et al., 2003; Xiaoxiang and Ellis, 2009; Huang et al., 2012; Lu et al., 2012; Alcala and Bridgwater, 2013; Lee et al., 2013, Lee et al., 2019, Lee et al., 2020; Kim et al., 2015; Lin et al., 2016), the most effective approach is to physically enhance the fuel properties by blending pyrolysis oil with hydrocarbon fuels (Ikura et al., 2003; Honnery et al., 2008; Murugan et al., 2009; Doğan et al., 2012; Huang et al., 2012; Lu et al., 2012; Lee et al., 2013, Lee et al., 2020; Martínez et al., 2014; Karagoz, 2020).

The use of WPO in diesel engines is limited by technical difficulties such as low cetane number and high viscosity. Low cetane number delays the ignition process of the fuel and negatively affects engine performance, while high viscosity reduces atomization and combustion efficiency. These problems prevent the efficient use of WPO in engines. In this context, the potential of various cetane improvers and additives to improve performance is gaining importance. Additionally, some researchers are studying the possibility of wood-based biofuels becoming the primary fuel for diesel engines (Solantausta et al., 1993; Beld et al., 2013; Beld et al., 2018; Chiaramonti et al., 2003).

Due to polarity and density differences, pyrolysis oil creates miscibility problems with conventional hydrocarbon fuels and phase separation occurs in a short time (Kim and Lee, 2015; Lin et al., 2016; Lee et al., 2019, Lee et al., 2020). To overcome this situation, additives are needed for the pyrolysis oil to be successfully mixed with conventional fuels and burned in engines. According to Alcala and Bridgwater, using organic solvents such as alcohol increases miscibility and allows the formation of stable mixtures; in this context, the type and amount of alcohol used are critical. When n-butanol and PEG400 are mixed with pyrolysis oil, it provides the widest homogeneous stable mixture (Alcala and Bridgwater, 2013) and has a better autoignition property (Nguyen and Honnery, 2008). Therefore, n-butanol was selected as the blend component to blend WPO with PEG 400.

PEG400 and 2-EHN, used as cetane improvers, aim to improve engine performance by increasing the cetane number of WPO. PEG400 stands out as an economical and chemically stable option, while 2-EHN is known as a more costly but effective cetane improver. Both components can optimize the combustion properties of WPO.

N-butanol is another significant additive. By raising the cetane number, N-butanol increases combustion efficiency and lowers the high viscosity of WPO. Furthermore, n-butanol's ability to suppress polymerization improves the fuel's chemical stability, reducing wear and engine clogging issues. These characteristics facilitate the more effective use of fuels derived from biomass in diesel engines. N-butanol can lower the viscosity of the blended fuel since its viscosity of 2.2 mm^2/s is comparable to the kinematic viscosity of 2.7 mm^2/s for diesel fuel (Lee et al., 2020). Furthermore, by dissolving the solid particles in the pyrolysis oil, it can prevent the sticky polymers created by the polymerization of tar, enhancing the pyrolysis oil's engine performance and fuel qualities (Jin et al., 2011; Alcala and Bridgwater, 2013; Kim and Lee, 2015). In this context, our study aimed to improve the performance properties of the fuel mixture by using n-butanol as an additive.

Our study assessed the impact of PEG 400, 2-EHN, and n-butanol on the physicochemical characteristics of WPO-based fuel performance. It was examined how the engine's ideal fuel properties could be raised and how the combinations of the components made by varying their ratios enhanced the fuel's qualities. Kinematic viscosity, density, water content, cetane number, lower heating value (LHV), and major components were used to characterize the chosen samples (Alcala and Bridgwater, 2013; Chong and Bridgwater, 2017; Lee et al., 2020). In order to compensate for the unfavorable physicochemical characteristics of the pyrolysis oil, stable homogenous mixtures between WPO were formed with the addition of n-butanol, PEG400, and 2-EHN. In addition, the cetane number and calorific values of the blended fuels were improved by the addition of PEG400 and 2-EHN. The results offered strategies to enable wider applications of biomass-based fuels and reduce their environmental impact.

2. MATERIALS AND METHODS

The biomass waste wood sawdust to be used in the studies was supplied from a private company operating in Afyonkarahisar province, as shown in Figure 1. In the study, wood sawdust weighed as 100 gr on a precision scale was subjected to the pyrolysis process in order to subject the raw material to the pyrolysis process homogeneously.

Figure 1. Wood dust

WPO was converted to vapor by thermal decomposition in an oxygen-free environment and cooled to liquid form. The resulting pyrolysis oil is a dark brown liquid. In addition, gases containing flammable components, called pyrolytic gases, are separated from the reactor, while solid coal residues are formed at the end of the process. The pyrolysis process is shown schematically in Figure 2.

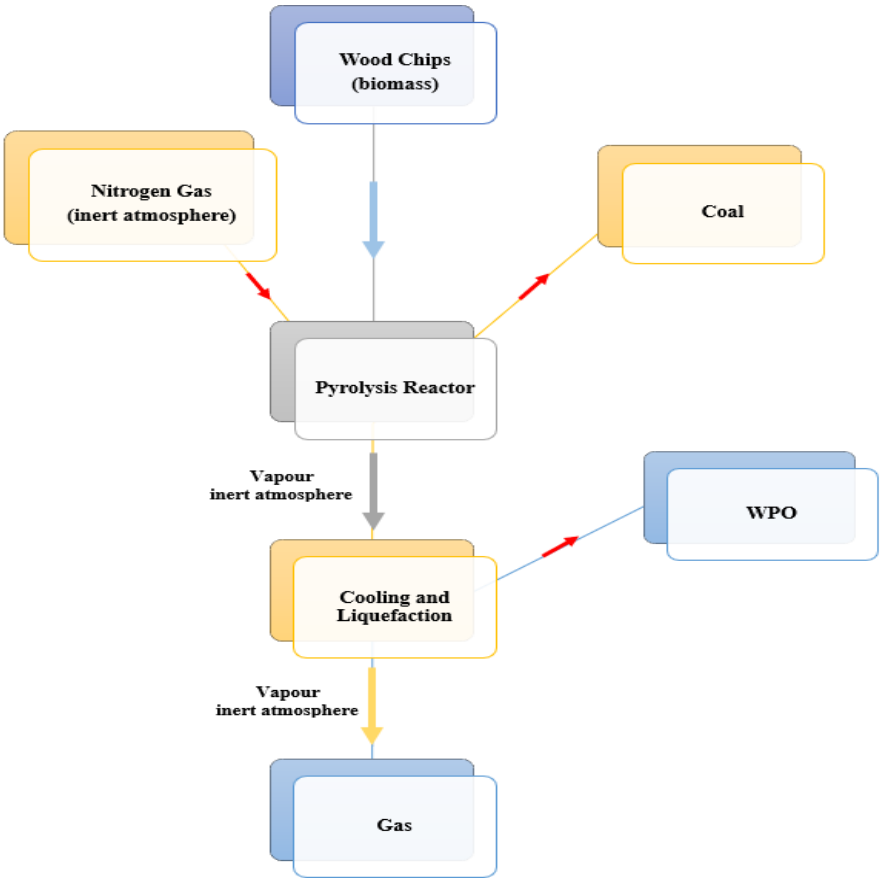

Figure 2. WPO production scheme

Optimization studies to obtain the optimum level of wood sawdust oil obtained by subjecting it to the pyrolysis process were carried out in the existing pyrolysis reactor in the Automotive Engineering Biofuel Laboratory of Afyon Kocatepe University, Faculty of Technology (Figure 3).

The pyrolysis reactor used in this study has a laboratory type, vertically placed, 0.5 liter stainless steel tank. The reactor system is equipped with a temperature sensor containing a K-type thermocouple that can operate stably at high temperatures, a PID-controlled digital panel that provides automatic temperature control (0–800°C operating range), a heating system with programmable ramp function, and leak-proof gaskets and connection devices to create a vacuum/nitrogen environment. High purity (≥99.99%) nitrogen gas was used to provide an inert atmosphere, and the gas flow rate was adjusted to 0.5 L/min with the help of a regulator and a gas flow meter. The glass condenser in the condensation system ensures the separation of liquid products, and the cooling circuit operates according to the principle of continuous circulation with tap water. The phase separation funnel used in the separation process of the obtained pyrolytic liquid allows the separation of liquid phases according to their density differences. Filtration was carried out with Whatman No.1 filter paper to remove solid particles. A rotary evaporator was used for solvent (dichloromethane) removal. The evaporator device operates at a rotation speed of 200 rpm, with the

support of a 50°C hot water bath and a vacuum pump, and purifies the pyrolytic oil by evaporating the dichloromethane. The presence of water in the fuel is an undesirable situation as it negatively affects combustion. Therefore, the pyrolytic liquid product was first subjected to phase separation in the separating funnel to separate the water phase and the pyrolytic oil + dichloromethane phase. Afterwards, during the evaporation process carried out with the rotary evaporator operating in a 50°C hot water bath under vacuum in order to remove dichloromethane, a small amount of volatile water was also removed from the system.

Optimization studies were carried out for each parameter under fixed conditions with three repetitive experiments in accordance with the pyrolysis parameters specified in the Table 1. All parameters except the parameter whose optimum value was desired were kept constant; after determining the optimum value, this value was fixed and the same method was followed for the other parameters. In the first study, the fixed parameter values were determined as: temperature 450°C, gas flow rate 1L/min, pyrolysis time 15 minutes and the heating rate (10 and 20°C/min) was optimized as a variable. The liquid product obtained at the end of the experiments was analyzed by the phase separation method; water and pyrolytic oil amounts were measured, the solid product was determined from the residue remaining in the reactor and the gas product amount was calculated by mass difference. After determining the optimum conditions, pyrolytic oil production was continued under these conditions.

Table 1. Pyrolysis conditions and process parameters

Process parameters	**Pyrolysis conditions**
Flow rate of propellant nitrogen gas	(0, 0.5 and 1) L/min.
Reactor internal temperatures	(300, 350, 400, 450, 500 and 550) ℃.
Reactor internal temperature increase rate	(10 and 20) ℃/min.
Pyrolysis time	(0, 15, 30, 45 and 60) min.

Figure 3. Pyrolysis reactor

The maximum pyrolysis oil yield was obtained at 500 °C reactor temperature, 0.5 L/min nitrogen gas flow rate and 10 °C/min heating rate. Under these optimum conditions, total product yields were determined as 23.4% pyrolysis oil, 35.3% aqueous phase, 25.9% biochar and 15.4% gas. The yields are shown in Figure 4.

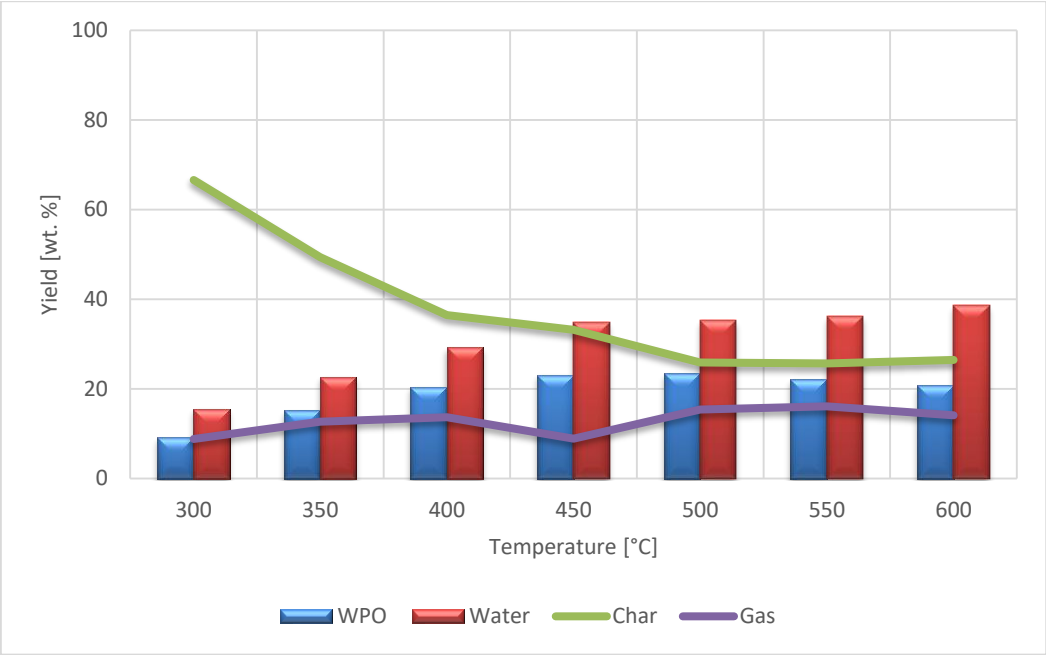

Figure 4. WPO yield change graph depending on temperature

The physicochemical properties of WPO were determined in an external laboratory and the results are presented in Table 2. The kinematic viscosity of PY at 40 °C is 8.9 mm²/s, which is approximately 3.2 times higher than that of conventional diesel; high viscosity may negatively affect engine performance (Alptekin and Canakci, 2008; Maroa and Inambao, 2019). In addition, the density of PO was determined as 1100 kg/m³, which makes miscibility difficult (Lin et al., 2016).

Table 2. Compositions and fuel properties of WPO, PEG400, 2-EHN, N-butanol and Diesel

	WPO	**PEG400**	**2-ehn**	**N-butanol**	**Diesel**
Kinematic viscosity (mm^2/s) at 40°C (TS 1451 EN ISO 3104)	8.9	4.5	1.8	2.2	2.7
LHV (MJ/kg) (ASTM D 240 / TS 1740)	20.1	23.6	28.5	33.1	42.9
Water content (%) (TS 6147 EN ISO 12937)	1.1	0.3	<0.1	-	-
C (wt %) (ASTM D 5373)	40.2	52.2	54.9	64.8	86.1
H (wt %) (ASTM D 5373)	11.3	9.2	9.7	13.6	13.9
O (wt %) (ASTM D 5373)	49.3	38.6	27.4	21.6	-
Density (kg/m^3) (ASTM D 4052)	1100	1126	963	810	822
Cetane number (TS 10317 EN ISO 5165)	-	-	-	15.9	52
Flash point (°C) (ASTM D 93)	98	-	76.1	35	55

The low heating value (LHV) of PO is approximately 20.1 MJ/kg, which is 2.1 times lower than that of conventional diesel, indicating that the energy density of PO is lower than that of diesel. The water content of PO is due to the feedstock and pyrolysis reactions (Alcala and Bridgwater, 2013;

Chong and Bridgwater, 2017). High water content makes PO unstable and separates into oily-aqueous phases (Lee et al., 2020). Water both reduces the heating value and reduces the viscosity (Hossain et al., 2016). In addition, the presence of water can cause ignition delay and corrosion problems in injectors (Oasmaa et al., 2015). The water content in WPO obtained by keeping the evaporation time long is around 1.1%, and at this level, it can provide long-term stability without causing corrosion problems.

In this study, the fuel mixtures required for the improvement of physicochemical fuel properties and the conduction of experimental studies for the usability of pyrolysis oil as an alternative fuel were prepared using a similar methodology to (Kim et al., 2015). Briefly, the mixtures were prepared at room temperature by following a simple procedure at varying weight percentages. Pyrolysis oil, PEG400, n-butanol and 2-EHN were used in the mixture fuel content to obtain blended fuels. The weight percentages given in Table 2 were used while preparing the obtained blended fuels.

Table 3. Weight% contents of blended fuels

Mixed Fuels	PEG400	N-butanol	WPO	2-EHN
Fuel 1 (PEG0/PY10/NB85/2-EHN5)	%0	%85	%10	%5
Fuel 2 (PEG10/PY10/NB75/2-EHN5)	%10	%75	%10	%5
Fuel 3 (PEG20/PY10/NB65/2-EHN5)	%20	%65	%10	%5
Fuel 4 (PEG30/PY10/NB55/2-EHN5)	%30	%55	%10	%5
Fuel 5 (PEG40/PY10/NB45/2-EHN5)	%40	%45	%10	%5

Then, the pyrolysis oil fuel mixtures given in Table 3 were characterized in terms of physicochemical properties. The physicochemical properties of the pyrolysis oil and homogeneous mixtures were analyzed in a nationally accredited laboratory by following standard methods (ASTM / EN ISO), which is an indicator of the suitability of the mixtures for use in CI engines, and measured as shown in Table 4.

Table 4. PEG 400, PH, NB and 2-EHN blend components and fuel properties

Mixed Fuels	Kinematic viscosity (mm^2/s) 40°C	LHV (MJ/kg)	Water content (%)	Intensity (kg/m^3)	Cetane number	C	H	O
Fuel 1	2,9	31,6	2,51	847	27,7	61,8	13,2	24,6
Fuel 2	3,1	30,6	2,54	878	28,4	60,6	12,7	26,3
Fuel 3	3,3	29,7	2,57	910	30	59,3	12,3	28,0
Fuel 4	3,5	28,7	2,60	941	35,2	58,1	11,9	29,7
Fuel 5	3,8	27,8	2,63	973	37,2	56,8	11,4	31,4
Diesel	2,7	42,9	-	822	52	86,1	13,9	-

3. RESULTS AND DISCUSSION

Many studies have been conducted on the conversion of bio-oils into more stable fuels by physical, catalytic or chemical methods (Bridgwater, 2012). The aim of this study is to investigate the usability of WPO as an alternative fuel in internal combustion engines. There is not enough research on the usability of the mixtures obtained by blending PO obtained from wood sawdust with PEG400, n-butanol and 2-EHN as fuel. Therefore, our study aims to fill this gap.

Although there are many studies in the literature on the production of fuel by pyrolysis of wood chips, the majority of the studies on the usability of these fuels in internal combustion engines have focused on diesel and biodiesel (wood chip pyrolysis oil) mixtures. The fuel mixtures used in this

study (combinations of PEG400, wood pyrolysis oil, n-butanol and 2-ethylhexyl nitrate) address a very current and innovative topic within the scope of alternative and environmentally friendly fuel research. Although there are various studies on each of these components in the literature review, studies using these four components together are quite limited. In this respect, the presented study provides an original contribution to the literature. In addition, systematically changing the ratios of these four components (especially increasing the PEG400 ratio and decreasing the n-butanol ratio) aims to provide a new parameter analysis and provide a different perspective on the subject.

The combustion properties of pyrolysis oil blends may be limited by high acidic content and uneven combustion. PEG400, 2-EHN and b-butanol can increase combustion efficiency and improve the combustion properties of pyrolysis oil. Optimizing the mixture ratios can improve combustion performance (Bridgwater, 2012).

WPO cannot be used directly in diesel engines due to its insufficient properties such as high kinematic viscosity and low LHV; therefore, blending PY with diesel offers a solution to improve fuel properties (Lee et al., 2020). However, WPO is known to be incompatible with other additives directly, so an organic solvent such as n-butanol is required (Alcala and Bridgwater, 2013). N-butanol increases the calorific value by reducing the viscosity and acidity of the blends (Yalçın and Mutlu, 2022).

The effect of cetane number on combustion in diesel engines is important, therefore PEG400 and 2-EHN were added to the blends as cetane enhancers to increase cetane numbers (Kim et al., 2015). As seen in Table 4, it was observed that there was an increase in the cetane numbers and oxygen amounts of the blended fuels due to the increase in PEG400 as a weight percent in the blended fuels.

As seen in Table 4, the density and kinematic viscosity of blended fuels containing 10 wt% WPO are close to diesel, but an increase is observed when compared to the increase in PEG400; kinematic viscosity was measured between 2.9-3.8 mm^2/s. Blended fuels show increased calorific values compared to the original WPO. As the PEG400 content increases, the density and kinematic viscosity increase, while the calorific values decrease, which leads to longer injection times and combustion delay (Kim et al., 2015). In addition, blended fuels carry a water content of 2.51-2.63% compared to WPO, and the water content increases as the PEG400 ratio increases (See Table 4). In general, the n-butanol ratio decreases with the increase in the PEG400 ratio, and this reduces the calorific values of blended fuels. The increase in the presence of n-butanol improved the stability of the mixtures, reduced density differences and increased their calorific values.

In Europe, the minimum cetane number is ≥51, and in the USA it is ≥40 (Lapuerta et al. 2009). As the PEG400 content increases, the cetane number increases, which does not improve adverse conditions such as ignition delay and incomplete combustion. To increase the cetane number, PEG400 was added to the blended fuels in 10% weight increments and a fixed 5% 2-EHN, thus increasing the cetane numbers to the range of 27.7-37.2.

The cetane numbers of the blended fuels were improved with PEG400, 2-EHN and n-butanol. Since the cetane number of the fuels containing 40% PEG400 by weight approaches the optimum value compared to diesel, it may be suitable for diesel engine applications. In the present study, by selecting appropriate WPO-mixable additives for WPO blended fuels in a diesel engine, fuel properties such as viscosity and autoignition of WPO blended fuels were improved. As a result, physicochemically improved blended fuels that can be tested in CI engines were obtained. In the future, diesel engine performance and exhaust emissions of these fuels can be compared with pure diesel.

In the study conducted in line with the above-mentioned analyses, it was concluded that the inadequate fuel properties of PO could be improved in terms of physicochemical fuel properties by applying modifications based on the determination of its fuel properties and that it could be used as an alternative fuel in a diesel engine.

4. CONCLUSION

This A WPO was obtained by pyrolysis from wood sawdust. The optimum conditions for maximum 23.4% yield are 10 °C/min heating, 500 °C reactor temperature and 0.5 L/min N2 flow rate. However, the density of WPO is 1100 kg/m³ and its kinematic viscosity is 8.9 mm²/s, which is higher than diesel, which can cause engine deposits and engine problems such as fuel pump and injector wear. WPO, which has a low calorific value, has a low water content of 1.1%. The low water content increases the stability of the fuel, reduces ignition delay and abrasiveness, and can increase the viscosity of the fuel. Due to this situation, modification is required for Po in terms of physicochemical properties.

To improve the fuel properties of PY, it was mixed with PEG400, 2-EHN and n-butanol. To obtain stable mixtures due to polarity, n-butanol was used as a co-solvent. In this way, WPO, PEG400 and 2-EHN were mixed homogeneously.

The increasing n-butanol due to the proportional decrease of PEG400 decreased the kinematic viscosity of the blended fuels and increased the calorific value. The negative properties of PO were reduced by the addition of PEG400, 2-EHN and n-butanol, and the cetane numbers reached the minimum specification of diesel. Thus, the blended fuels can be considered as a potential biofuel source in CI engine applications.

In this study, blended fuels based on n-butanol, PEG 400, 2-EHN and WPO were evaluated as potential alternatives to conventional diesel fuel. It was found that the autoignition properties of blended fuels could be improved with two cetane improvers, PEG400 and 2-EHN. PEG 400, 2-EHN and n-butanol are effective tools to improve the performance of biomass-based fuels. The cetane improving properties of PEG 400 and 2-EHN, the viscosity reducing and polymerization inhibiting abilities of n-butanol enable biomass-based fuels such as WPO to be used more efficiently in diesel engines. The use of these components in appropriate proportions can increase fuel performance and provide a wider range of applications for biomass-based fuels. In addition, determining the effects of blended fuels on long-term performance, combustion characteristics and exhaust emissions in diesel engines is important for the integration of these fuels into practical applications. In addition, comparative evaluation of alternative cetane improvers other than PEG400 and 2-EHN and viscosity modifiers other than n-butanol can contribute to further improvement of fuel properties. Studies to be carried out in this direction will support biomass-based fuels to become a competitive alternative to diesel fuel in terms of sustainability and environmental compatibility.

5. ACKNOWLEDGEMENTS

This study was supported by Afyon Kocatepe University Scientific Research Projects Coordination Unit with Project number of 22.KARİYER.06.

6. CONFLICT OF INTEREST

Authors approve that to the best of their knowledge, there is not any conflict of interest or common interest with an institution/organization or a person that may affect the review process of the paper.

7. AUTHOR CONTRIBUTION

Arif Hakan YALÇIN contributed to determining the concept and/or design process of the research, data analysis and interpretation of the results, critical analysis of the intellectual content, and final approval and full responsibility. Ercan ŞİMŞİR contributed to managing the concept and/or design process, data collection, preparation of the manuscript, and final approval and full responsibility.

8. REFERENCES

Alcala A., Bridgwater A. V., Upgrading Fast Pyrolysis Liquids: Blends of Biodiesel and Pyrolysis Oil, Fuel 109, 417–426, 2013.

Alptekin E., Canakci M., Determination of The Density and The Viscosities of Biodiesel–Diesel Fuel Blends, Renewable Energy 33 (12), 2623–2630, 2008.

Bridgwater A., Fast Pyrolysis of Biomass for The Production of Liquids, Biomass Combustion Science, Technology and Engineering 130–171, 2013.

Bridgwater A. V., Review of Fast Pyrolysis of Biomass and Product Upgrading, Biomass and Bioenergy 38, 68–94, 2012.

Bridgwater A. V., Meier D., Radlein D., An Overview of Fast Pyrolysis of Biomass, Organic Geochemistry 30 (12), 1479–1493, 1999.

Chiaramonti D., Bonini M., Fratini E., Tondi G., Gartner K., Bridgwater A. V., Grimm H. P., Soldaini I., Webster A., Baglioni P., Development of Emulsions from Biomass Pyrolysis Liquid and Diesel and Their Use in Engines—Part 1 : Emulsion Production, Biomass and Bioenergy 25 (1), 85–99, 2003.

Chong K. J., Bridgwater A. V., Fast Pyrolysis Oil Fuel Blend for Marine Vessels, Environmental Progress & Sustainable Energy 36 (3), 677–684, 2017.

Doğan O., Elik M. B., Özdalyan B., The Effect of Tire Derived Fuel/Diesel Fuel Blends Utilization on Diesel Engine Performance and Emissions, Fuel 95, 340–346, 2012.

Honnery D., Ghojel J., Stamatov V., Performance of a DI Diesel Engine Fuelled by Blends of Diesel and Kiln-Produced Pyroligneous Tar, Biomass and Bioenergy 32 (4), 358–365, 2008.

Hossain A. K., Serrano C., Brammer J. B., Omran A., Ahmed F., Smith D. I., Davies P.A., Combustion of Fuel Blends Containing Digestate Pyrolysis Oil in A Multi-Cylinder Compression Ignition Engine, Fuel 171, 18–28, 2016.

Huang Y., Han X., Shang S., Wang L., Performance And Emissions of A Direct-İnjection Diesel Engine Operating on Emulsions of Corn Stalk Bio-Oil in Diesel 226 (8), 1119–1129, 2012.

Ikura M., Stanciulescu M., Hogan E., Emulsification of Pyrolysis Derived Bio-Oil in Diesel Fuel, Biomass and Bioenergy 24 (3), 221–232, 2003.

Ivanova N. N., Khomich L. M., Perova I. B., Eller K. I., Sour Cherry Juice Nutritional Profile, Voprosy pitaniia 87 (4), 78–86, 2018.

Jin C., Yao M., Liu H., Lee C. F. F., Ji J., Progress in The Production and Application of N-Butanol as a Biofuel, Renewable and Sustainable Energy Reviews 15 (8), 4080–4106, 2011.

Jones S. B., Valkenburt C., Walton C. W., Elliott D. C., Holladay J. E., Stevens D. J., Kinchin C., Czernik S., Production of Gasoline and Diesel from Biomass via Fast Pyrolysis, Hydrotreating and Hydrocracking, A Design Case 2009.

Karagöz M., Investigation of Performance and Emission Characteristics of an CI Engine Fuelled With Diesel – Waste Tire Oil – Butanol Blends, Fuel 282, 118872, 2020.

Kim T. Y., Lee S. H., Combustion and Emission Characteristics of Wood Pyrolysis Oil-Butanol Blended Fuels in a DI Diesel Engine, International Journal of Automotive Technology 16 (6), 903–912, 2015.

Kim T. Y., Lee S., Kang K., Performance and Emission Characteristics of A High-Compression-Ratio Diesel Engine Fueled With Wood Pyrolysis Oil-Butanol Blended Fuels, Energy 93, 2241–2250, 2015.

Kleinert M., Barth T., Motor Fuels From Biomass Pyrolysis, Chemical Engineering and Technology 31 (5), 773–781, 2008.

Lapuerta M., Rodríguez-Fernández J., de Mora E. F., Correlation For The Estimation of The Cetane Number of Biodiesel Fuels and Implications on The Iodine Number, Energy Policy 37 (11), 4337–4344, 2009.

Lee S., Kim T., Kang K., Performance and Emission Characteristics of A Diesel Engine Operated With Wood Pyrolysis Oil, Proceedings of The Institution of Mechanical Engineers, Part D: Journal of Automobile Engineering 228 (2), 180–189, 2013.

Lee S., Choi Y., Kang K., Application of Blended Fuel Containing Coffee Ground Pyrolysis Oil in A Diesel Generator, Fuel 256, 115998, 2019.

Lee S., Woo S. H., Kim Y., Choi Y., Kang K., Combustion and Emission Characteristics of A Diesel-Powered Generator Running With N-Butanol/Coffee Ground Pyrolysis Oil/Diesel Blended Fuel, Energy 206, 118201, 2020.

Lin B. J., Chen W. H., Budzianowski W. M., Hsieh C. T., Lin P. H., Emulsification Analysis of Bio-Oil and Diesel Under Various Combinations of Emulsifiers, Applied Energy 178, 746–757, 2016.

Lu Q., Zhang Z. B., Liao H. T., Yang X. C., Dong C. Q., Lubrication Properties of Bio-Oil and Its Emulsions with Diesel Oil, Energies 5 (3), 741–751, 2012.

Maroa S., Inambao F., The Effect of Cetane Number and Oxygen Content in The Performance and Emissions Characteristics of A Diesel Engine Using Biodiesel Blends, Journal of Energy in Southern Africa 30 (2), 1–13, 2019.

Martínez J. D., Ramos Á., Armas O., Murillo R., García T., Potential for Using A Tire Pyrolysis Liquid-Diesel Fuel Blend in A Light Duty Engine Under Transient Operation, Applied Energy 130, 437–446, 2014.

Midhun Prasad K., Murugavelh S., Experimental Investigation and Kinetics of Tomato Peel Pyrolysis: Performance, Combustion and Emission Characteristics of Bio-Oil Blends in Diesel Engine, Journal of Cleaner Production 254, 120115, 2020.

Murugan S., Ramaswamy M. C., Nagarajan G., Assessment of Pyrolysis Oil as An Energy Source for Diesel Engines, Fuel Processing Technology 90 (1), 67–74, 2009.

Nguyen D., Honnery D., Combustion of Bio-Oil Ethanol Blends at Elevated Pressure, Fuel 87 (2), 232–243, 2008.

Oasmaa A., Van De Beld B., Saari P., Elliott D. C., Solantausta Y., Norms, Standards, and Legislation for Fast Pyrolysis Bio-oils from Lignocellulosic Biomass, Energy and Fuels 29 (4), 2471–2484, 2015.

Solantausta Y., Nylund N. O., Westerholm M., Koljonen T., Oasmaa A., Wood-pyrolysis oil as fuel in a diesel-power plant, Bioresource Technology 46(1-2), 177-188, 1993.

Van de Beld B., Holle E., Florijn J., The use of pyrolysis oil and pyrolysis oil derived fuels in diesel engines for CHP applications, Applied energy 102, 190-197, 2013.

Van de Beld B., Holle E., Florijn J., The use of a fast pyrolysis oil Ethanol blend in diesel engines for chp applications, Biomass and bioenergy 110, 114-122, 2018.

Xiaoxiang J., Ellis N., Upgrading Bio-oil Through Emulsification with Biodiesel: Mixture Production, Energy and Fuels 24 (2), 1358–1364, 2009.

Yalçın A.H., Mutlu İ., Atık Vişne Çekirdeği Pirolitik Yağın Dizel Motorlarda Alternatif Yakıt Olarak Kullanılabilirliği, Afyon Kocatepe Üniversitesi Fen ve Mühendislik Bilimleri Dergisi 22 (4), 963–971, 2022.

Yalçın A. H., Mutlu İ., Şimşir E., Akbulut F., Emiroğlu A. O., Şen M., Keskin A., The impact of mixed fuels containing pyrolysis oil, diesel, n-butanol and 2-EHN on emissions and performance of diesel engine, CT&F-Ciencia, Tecnología y Futuro 14 (2), 59-66, 2024.

Yuan X., Ding X., Leng L., Li H., Shao J., Qian Y., Huang H., Chen X., Zeng G., Applications of Bio-Oil-Based Emulsions in A DI Diesel Engine: The Effects of Bio-Oil Compositions on Engine Performance and Emissions, Energy 154, 110–118, 2018.

Zhang Q., Chang J., Wang T., Xu Y., Review of Biomass Pyrolysis Oil Properties and Upgrading Research, Energy Conversion and Management 48 (1), 87–92, 2007.

JOURNAL of
MATERIALS and MECHATRONICS:A

e-ISSN 2717-8811
JournalMM, 2025, 6(1), 274-290
https://doi.org/10.55546/jmm.1675925

Araştırma Makalesi / Research Article

Development of Electronically Controlled Dual-Component Continuous Powder Feeder to Build Functional Graded Materials with Additive Manufacturing Process

Mehmet ERMURAT[1*], Serhat ZIBA[2]

[1*] Kahramanmaras Sutcu Imam University, Faculty of Engineering and Architecture, Department of Mechanical Engineering, Kahramanmaras, Türkiye,
ORCID ID: https://orcid.org/0000-0002-5661-2108, ermurat@ksu.edu.tr
Lutuf Mensucat A.Ş. Kahramanmaraş, Türkiye,
ORCID ID: https://orcid.org/0000-0002-9709-6285, serhatziba4605@hotmail.com

Geliş/ Received: 14.04.2025**;** **Revize/Revised:** 05.05.2025 **Kabul / Accepted:** 23.05.2025

ABSTRACT: Directed Energy Deposition methods allow parts to be produced in functional grades with different compositions across distinct regions. For this, there is a need for a powder feeder that allows multiple components to be fed into the process area simultaneously and in an integrated manner. In this study, a dual-component powder feeder was designed and manufactured. This electronically controlled powder feeder can feed two different powder materials at different flow rates at the same time. The performance of the powder feeder was tested with Ti6Al4V (flow rates of 5, 10, and 15 g/min), Zirconium (13, 20, and 30 g/min), and Inconel 625 (20, 50, and 75 g/min) powder materials. Following the calibration process, the minimum deviations were observed as 2.9% for Ti6Al4V at 15 g/min, 11.5% for Zirconium at 30 g/min, and 6.5% for Inconel 625 at 75 g/min. Conversely, the maximum deviations were recorded as 12.3% for Ti6Al4V at 10 g/min, 28.8% for Zirconium at 20 g/min, and 18.4% for Inconel 625 at 20 g/min. Overall, the lowest deviations occurred at the higher end of the examined flow rate range.

Keywords: Dual component powder feeder design, Direct energy deposition, Functionally graded material

*Sorumlu yazar / Corresponding author: ermurat@ksu.edu.tr
Bu makaleye atıf yapmak için /To cite this article

Ermurat, E., Ziba, S. (2025). Development of Electronically Controlled Dual-Component Continuous Powder Feeder to Build Functional Graded Materials with Additive Manufacturing Process. Journal of Materials and Mechatronics: A (JournalMM), 6(1), 274-290.

1. INTRODUCTION

In additive manufacturing methods used for fabricating components from metallic materials, sintering or melting can be performed using laser-based or electron beam energy sources. These methods are applicable not only to steel but also to lightweight materials such as titanium and its alloys, which possess high strength, wear resistance, and fatigue life—properties that make them suitable for the aerospace industry. Owing to their exceptional attributes, including high specific strength and excellent resistance to corrosion and oxidation, titanium and its alloys are increasingly utilized in the aerospace, marine, chemical, and biomedical industries (Wang and Liu, 2002; Courant et al., 1999; Altus and Konstantino, 2001; Zhu et al., 2014; Bruni et al., 2005; Ganesh et al., 2014; Wang et al., 2013; Weng et al., 2014).

Achieving the desired microstructure (e.g., grain size and morphology) and mechanical properties (e.g., strength, hardness, residual stress) in materials processed via additive manufacturing remains a significant challenge. It is well-established in the literature that complex metallurgical phenomena occur during the process, influenced by both material characteristics and processing parameters. Key factors such as powder characteristics (e.g., chemical composition, particle shape, particle size and distribution, flowability) and process parameters (e.g., laser type, spot size, laser power, scanning speed, and powder layer thickness) govern these phenomena (Gu et al., 2012; Santos et al., 2006).

Directed Energy Deposition (DED)—also known as Laser Metal Deposition (LMD), Direct Metal Deposition, or Laser Direct Manufacturing—is an additive manufacturing technique in which metal parts are fabricated in three dimensions. Unlike laser sintering or melting, in DED the powder is not pre-deposited but is instead delivered simultaneously and coaxially with the laser beam into the processing zone, enabling the layer-by-layer construction of components (Figure 1) (Mahamood et al., 2013). The powder feeding system includes a specially designed mechanism that transfers powder into the gas stream via a nozzle. A high-energy laser beam, focused through a lens, is directed along the Z-axis to the part, which is centered within the nozzle assembly. The vertical movement of the lens and powder nozzle enables control over the focal height of both the laser and powder. To form the desired geometries at each cross-section, the workpiece is moved in the X-Y plane by a computer-controlled system, while successive layers are deposited to create the final 3D object. Advanced DED systems—featuring multi-axis deposition, multiple powder feeders, and closed-loop control systems—facilitate the fabrication, coating, and repair of complex geometries with dimensional precision and reliable material integrity (Mazumder, 1995; Mazumder, 2010).

Recent advances have increasingly focused on the production of Functionally Graded Materials (FGMs), which provide a compositionally graded interface rather than an abrupt material transition, thereby improving bonding between the coating and substrate and reducing residual stresses (Weng et al., 2014; Dai et al., 1997; Fu and Bathchelor, 1998; Gu et al., 2012). Some studies have explored laser-melted graded coatings. For instance, Pei et al. (2002) successfully fabricated SiC/Ti-6Al-4V FGMs using laser melt injection. Developing a straightforward approach for multilayer coating via laser deposition is therefore imperative. A device with multiple, independently controlled powder feeding channels and precise flow control could significantly advance the field of multilayer FGM production (Weng et al., 2014).

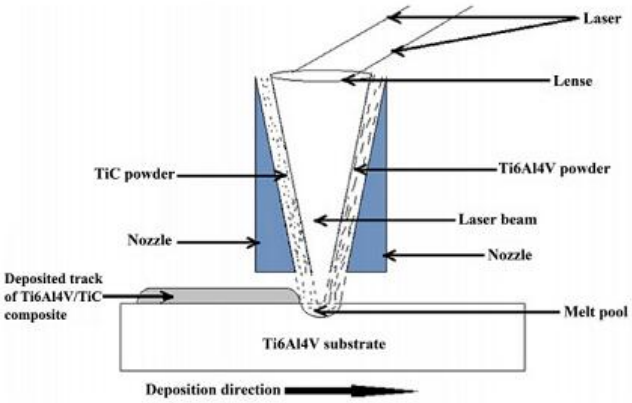

Figure 1. Directed Energy Deposition process (Mahamood RM vd. 2013)

Beyond the general capabilities of additive manufacturing, the continuous and simultaneous delivery of powder into the processing zone via the DED method enables the creation of components with spatially varying compositions.

Recent literature includes various studies on multi-material part fabrication using different additive manufacturing methods. Some employ powder bed fusion, while others utilize LMD techniques. Although many investigations focus on flat-shaped specimens, others explore the production of complex geometries. These studies generally adopt a layer-based approach, wherein material transitions occur between successive layers. They often involve the fabrication and characterization—such as microstructural analysis and mechanical testing—of metal-metal or metal-ceramic composite components (Wei et al., 2018; Wei et al., 2019; Lin and Yue, 2005; Lin et al., 2006; Li et al., 2018; Xu et al., 2015; Zhang et al., 2016; Hofmann et al., 2014).

The ability to produce point-based FGMs is a unique capability of the DED process—one not achievable through other existing additive manufacturing techniques. Realizing this functionality requires a multi-component powder feeder capable of automatically and proportionally controlling the delivery of different powder materials through independently regulated channels.

Powder control systems play a critical role in ensuring consistent and accurate delivery of powder materials by regulating key parameters such as powder quantity, flow rate, bulk density, and the ratio of mixed components. These systems are essential for maintaining process stability, material homogeneity, and overall product quality, particularly in precision-sensitive applications like additive manufacturing and pharmaceutical production. Numerous powder feeder designs exist. Screw feeders—featuring single or multiple screws—are among the most widely adopted, accommodating various powder types and sizes, and are suitable for both continuous and intermittent feeding (Engisch and Muzzio, 2015; Li et al., 2020; Blackshields and Crean, 2017; Janssen et al., 2022). In contrast, the screw-brush feeder integrates a screw for bulk transport with a rotating brush that enhances flowability and prevents bridging and aggregation, making it especially suitable for fine or easily clumping powders (Barati et al., 2015). Vibratory feeders, on the other hand, use oscillatory motion to transport and dose fragile, irregular, and cohesive powders (Singh and Chandravanshi, 2022; Wang et al., 2018).

Pump feeders operate on a simple volumetric principle, either via a cylinder-piston system that controls piston speed or via a paddle wheel system that regulates rotational speed (Besenhard et al., 2017; Mendez et al., 2012). Similarly, slide feeders are intermittent volumetric feeders that use gravity-assisted mechanisms with adjustable slides or gates to control flow—offering simplicity and reliability for handling free-flowing powders (Pohorely et al., 2004).

Fluidized feeders represent a class of systems that aerate the powder bed to achieve a fluid-like state, enhancing flowability and enabling uniform dosing. This method is particularly effective for ultrafine or cohesive powders that typically challenge conventional feeding mechanisms (Wen and Simons, 1959; Annamalai et al., 1992; Suri and Horio, 2009; Özdemir, 2009; Hou, 2024). Each type of feeder presents unique operational characteristics; the optimal choice depends on powder properties, required feed accuracy, and the specific application.

In DED additive manufacturing and cladding applications—where continuous powder feeding is essential—fluidized powder feeder types offer particularly suitable solutions due to their stable delivery characteristics. Another approach combines vibration and carrier gas flow to regulate powder delivery through gravity via an orifice. A schematic representation of such a powder feeder, presented in earlier work, is shown in Figure 2 (Ermurat, 2009), where a similar design was employed. The powder flow rate is regulated by adjusting the opening of a valve at the feeder outlet.

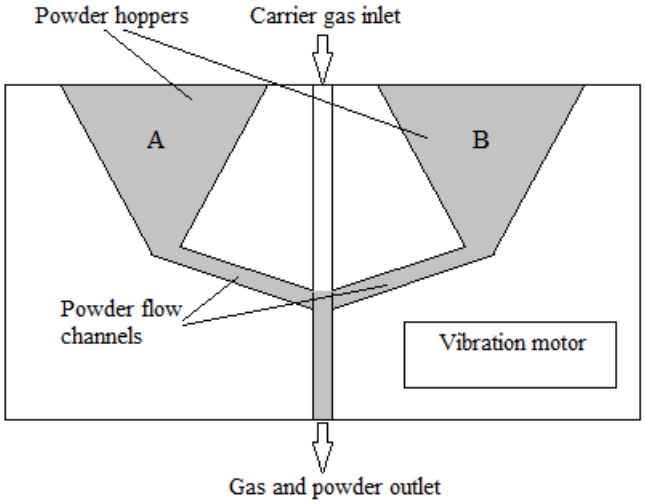

Figure 2. Schematic of Dual Component Powder Feeder (Ermurat M, 2009)

The powder feeder developed for laser metal deposition applications is capable of delivering both metallic and ceramic powders. In applications involving ceramic coatings on steel substrates, the ratio of ceramic to metallic powders varies across layers. As the deposition progresses, the ceramic content increases, culminating in a final layer composed entirely of ceramic material. This compositional gradient ensures stronger and more homogeneous bonding between the coating and substrate. Accordingly, a dual-component powder feeder is essential to achieve such gradation.

As a critical component of laser metal deposition systems, the powder feeder must fulfill specific functional requirements. The system offers an adjustable powder flow rate, a controllable carrier gas flow rate, and the ability to deliver two distinct powder types at specified ratios—with all adjustments performed manually.

In addition to its dual-component design, the powder feeder must incorporate automated control to enable efficient FGM fabrication. Although mechanical adjustment of powder flow is possible, it poses challenges in terms of precision and responsiveness. In contrast, computer-controlled systems allow more accurate and rapid regulation.

Despite the growing number of studies on multi-material additive manufacturing and functionally graded components, there remains a significant gap in the development of compact, low-cost, and semi-automated dual-component powder feeding systems specifically tailored for DED applications. Existing feeders are often either overly sophisticated and cost-prohibitive or lack the

precision and flexibility needed for real-time compositional gradation. Furthermore, most systems rely on manual adjustment mechanisms, which compromise repeatability and limit point-wise material gradient control. Therefore, a versatile and accessible powder feeding system capable of accurate, simultaneous regulation of multiple powder streams is urgently needed to support the fabrication of complex FGM structures.

In response to this gap, the present study developed and implemented a dual-component, semi-automated powder feeder using the Arduino programming platform.

2. MATERIALS AND METHODS

The operating principle of the dual-component powder feeder is based on the opening of valves located beneath the powder hoppers, allowing powders to flow—assisted by vibration—into a powder transport channel. Within this channel, the powder is accelerated by a carrier gas and expelled through distribution channels at the bottom of the feeder. The valve shaft is cylindrically shaped and operates via a rotational motion driven by a stepper motor, which adjusts the opening by aligning a slit on the adjustment shaft.

The valve mechanism designed in this study adjusts the powder flow by altering the cross-sectional area of the opening as the adjustment shaft rotates. The valve shaft with some dimensions and attached O-rings is depicted in Figure 3.

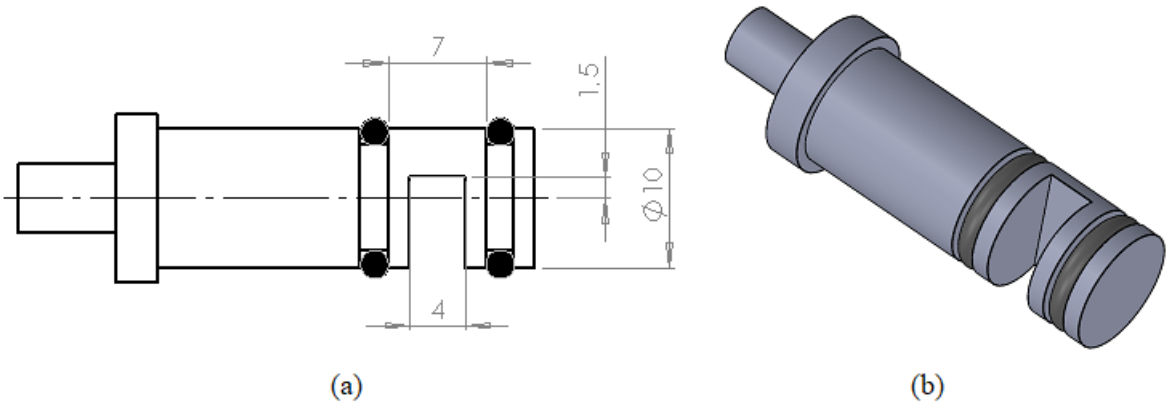

Figure 3. Valve Shaft a) front view with some dimensions b) perspective of 3D model

In Figure 4, the valve shaft is shown connected to the stepper motor via a coupling, allowing rotation. Figure 4 also presents a cross-sectional view of how the shaft is mounted on the feeder body, which is a revised version of the previous design (Figure 2), now equipped with a stepper motor to control powder flow.

When the valve adjustment shaft is aligned parallel to the feeder body channel, the valve is considered fully open, as depicted in the figure. Rotation of the adjustment shaft regulates the amount of powder being dispensed. A completely closed position corresponds to a 0% valve opening.

The vibration motor, carrier gas inlet, and valve adjustment motor are mounted on the aluminum body of the powder feeder. The internal powder flow channel follows the direction of gravity, and the mass flow rate is regulated via the valve.

Vibration is a crucial parameter in powder flow, as it reduces inter-particle friction and facilitates smoother movement. The vibration motor, mounted horizontally, employs an eccentric

mass that shifts its center of gravity during rotation, thereby producing vibrational motion. The horizontal alignment of the motor enhances vertical particle movement, promoting better flowability.

The opening and closing of the stepper motors that drive the valve shaft, carrier gas, and vibration motor are all controlled automatically using the Arduino programming platform.

Due to the typically low quantities of powder fed into these systems, maintaining precise control over the feed rate is imperative for achieving reliable material deposition and process stability. Therefore, the control system must be capable of performing calculations based on user-input mass flow rates. The stepper motor is controlled via the Arduino platform.

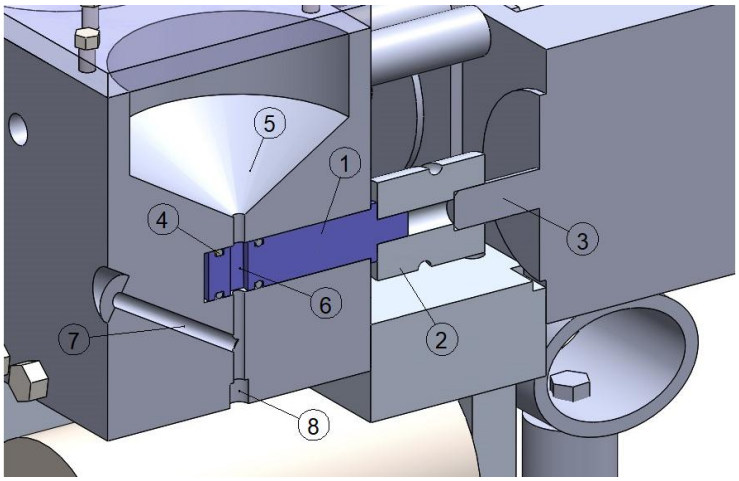

1. Valve shaft
2. Coupling
3. Stepper motor shaft
4. O-ring
5. Powder hopper
6. Shaft opening channel
7. Carrier gas channel
8. Powder feeding channel

Figure 4. Valve adjusting shaft assembly

A photograph of the fully assembled powder feeder is shown in Figure 5.

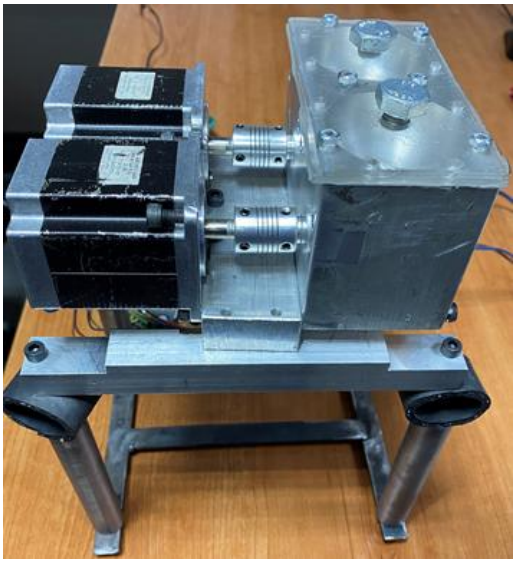

Figure 5. Dual Component Powder Feeder

To ensure rapid and accurate adjustment of powder mass flow rates, manual measurements are incorporated into an automated control system. The Arduino platform is used to perform the necessary calculations and adjustments. The control schematic of the designed powder feeder is illustrated in Figure 6, and the corresponding algorithm is provided in Figure 7.

As indicated in the flowchart of Figure 7, calibration must first be performed to determine the flow rate corresponding to specific valve shaft angles. Measurements are required at 25%, 50%, 75%,

and 100% valve openings. A function must then be established to relate the valve opening to the flow rate, allowing for intermediate values to be interpolated and matched with appropriate stepper motor angles. Since the powder feeding channel is a cylindrical hole, each valve opening corresponds to a variable circular cross-sectional area. Therefore, a third-degree polynomial function has been employed to accurately model the relationship. Given the availability of four data points, this function provides a suitable fit for precise calibration, yielding a coefficient of determination of one, which denotes a perfect fit to the data and ensures an accurate representation of the relationship between flow rate and valve opening.

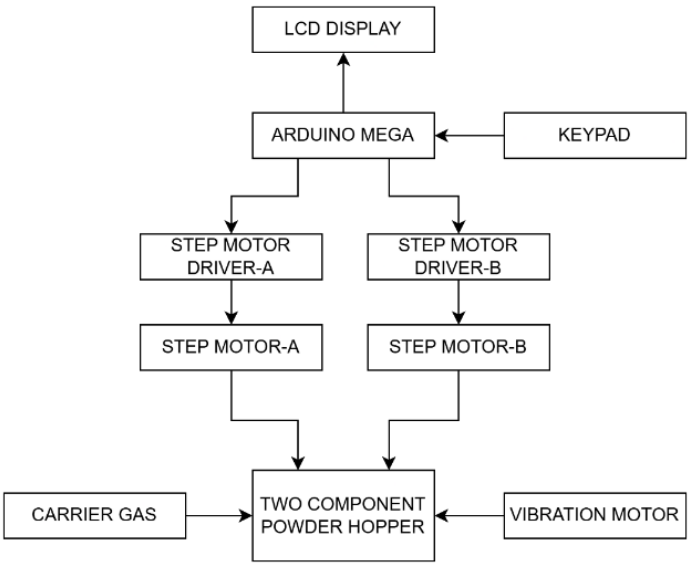

Figure 6. The powder feeder control schematic

Interpolation refers to the mathematical process of estimating unknown intermediate values of a continuous function based on a finite set of known data points. The objective is to construct a function *f(x)* that passes through these known points and can reliably predict values at locations where data is not explicitly available. This process is critical in numerical analysis and engineering applications, particularly when experimental or computational constraints prevent the acquisition of continuous data.

Various interpolation techniques are employed depending on the nature and distribution of the data points. When the known data points are not equally spaced, methods such as Lagrange interpolation or Newton's divided difference are commonly used (Burden and Faires, 2011). For equally spaced data, finite difference methods such as Newton-Gregory forward or backward interpolation are more efficient. The chosen interpolation model—whether polynomial, spline-based, or piecewise—directly affects the accuracy and smoothness of the estimated function.

In the context of additive manufacturing or mechatronic systems, interpolation functions are often utilized to calibrate or model relationships between system inputs (e.g., valve opening angles) and outputs (e.g., powder flow rates), especially when real-time sensor measurements are not feasible.

Due to the potential variation in initial valve opening positions with each run and the cylindrical cross-sectional area of the powder feeding channel, the resulting calibration data points are not uniformly spaced.

Consequently, Lagrange interpolation is employed in this study to construct a fitting polynomial that accurately represents the nonlinear relationship between the valve opening and the powder flow

rate. By using a Lagrange interpolation polynomial, the model does not require equally spaced data points, thereby accommodating the inherent variability in the valve's initial positioning and ensuring reliable performance of the control algorithm.

If a parabolic interpolation in the form of $f(x) = a + a\,x + a\,x^2$ is to be performed using Lagrange polynomials based on data points such as (*x0,f0*), (*x1,f1*) and (*x2,f2*), the coordinates of these points are substituted into Equation 1 to construct a system of equations.

$$\begin{aligned} f_0 &= a_0 + a_1 x_0 + a_2 {x_0}^2 \\ f_1 &= a_0 + a_1 x_1 + a_2 {x_1}^2 \\ f_2 &= a_0 + a_1 x_2 + a_2 {x_2}^2 \end{aligned} \tag{1}$$

The coefficients of the resulting polynomial *f(x)* are then obtained by solving this system and are presented in Equation 2.

$$\begin{aligned} a_0 &= \frac{f_0(x_1 {x_2}^2 - x_2 {x_1}^2) + f_1(x_2 {x_0}^2 - x_0 {x_2}^2) + f_2(x_0 {x_1}^2 - x_1 {x_0}^2)}{(x_0 - x_1)(x_0 - x_2)(x_2 - x_1)} \\ a_1 &= \frac{f_0({x_1}^2 - {x_2}^2) + f_1({x_2}^2 - {x_0}^2) + f_2({x_0}^2 - {x_1}^2)}{(x_0 - x_1)(x_0 - x_2)(x_2 - x_1)} \\ a_2 &= \frac{f_0(x_2 - x_0) + f_1(x_0 - x_2) + f_2(x_1 - x_0)}{(x_0 - x_1)(x_0 - x_2)(x_2 - x_1)} \end{aligned} \tag{2}$$

In this case, the parabolic equation is rearranged for *f0*, *f1*, and *f2*, as shown in Equation 3.

$$f(x) = L_0 f_0 + L_1 f_1 + L_2 f_2 \tag{3}$$

The magnitudes of *Li* here are given by Equation 4, and these magnitudes are referred to as Lagrange polynomials (Yükselen, 2008).

$$L_k = \frac{(x - x_0)(x - x_1) \dots (x - x_{k-1})(x - x_{k+1}) \dots (x - x_n)}{(x_k - x_0)(x_k - x_1) \dots (x_k - x_{k-1})(x_k - x_{k+1}) \dots (x_k - x_n)} = \prod_{\substack{j=0 \\ j \neq k}}^{n} \frac{x - x_j}{x_k - x_j} \tag{4}$$

Consequently, curve fitting was performed using a third-degree polynomial function, $f(x)=a+ax+ax^2+ax^3$, which offers greater accuracy than lower-degree polynomials.

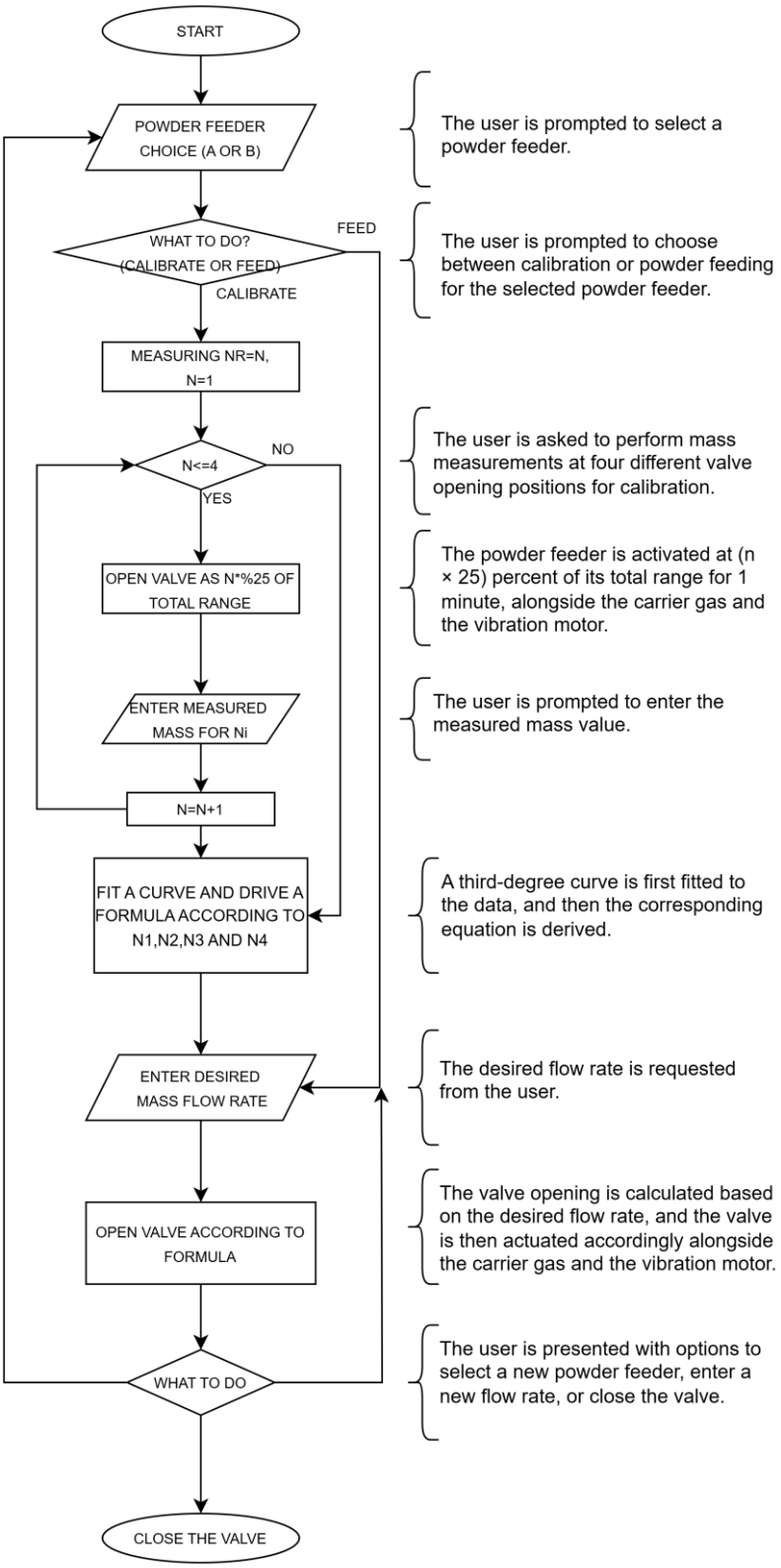

Figure 7. Algorithm of the powder feeder working

An Arduino code was developed in accordance with the algorithm illustrated in Figure 7. This implementation utilizes user-defined flow rate values corresponding to known valve opening ratios to perform polynomial regression, thereby generating a mathematical function. The resulting function enables precise calculation of the required valve opening to achieve any desired flow rate, and based

on this calculation, the stepper motors are adjusted to the appropriate position, rotating the valve shaft accordingly.

All experiments conducted during both the calibration and feeding stages were repeated three times, and the average values were used for all calculations. In both stages, the valve shaft was kept open for a predetermined time interval, during which the discharged powder was collected in a clean container and weighed using a precision balance. The corresponding mass flow rates were then calculated using the standard mass flow rate equation.

Following the completion of the calibration process, three target mass flow rates were defined for each material. Based on the calibration data, the powder feeder was adjusted to determine the appropriate valve opening corresponding to each target. During each feeding test, the powder delivered over the set time interval was collected and measured, and the resulting flow rates were calculated accordingly.

3. RESULTS AND DISCUSSION

In DED processes, the precise and continuous delivery of multiple powder materials is essential for the successful fabrication of FGMs. Since metallic and ceramic powders often differ significantly in terms of density, particle morphology, and flow behavior, a conventional single-channel feeding system is usually insufficient to ensure accurate dosing and homogeneous mixing during deposition. Therefore, a dual-component powder feeding system was developed in this study to enable the simultaneous and adjustable delivery of two distinct powders. This system was designed to support the controlled production of gradient structures by providing independent flow regulation for each powder stream. In addition, the integration of a predictive control model allowed the system to calculate appropriate valve positions based on target flow rates and material-specific characteristics. The following section evaluates the calibration procedure and feeding accuracy of this system under various operating conditions.

The calibration process was conducted using different powder materials, followed by assessments of whether the actual feeding rates matched the predicted values generated by the developed model. The results obtained from these evaluations are discussed in detail.

The powder materials used and their key properties are summarized in Table 1.

Table 1. Powder materials and their some properties

Powder Material	Particle size (μm)	Particle shape
Ti6Al4V	+109 -154	Spherical
Zirkonyum	+75 -154	Irregular
Inconel 625	+90 -154	Spherical

The microscope images of the powder materials, with their sizes and shapes specified in Table 1, are presented in Figure 8.

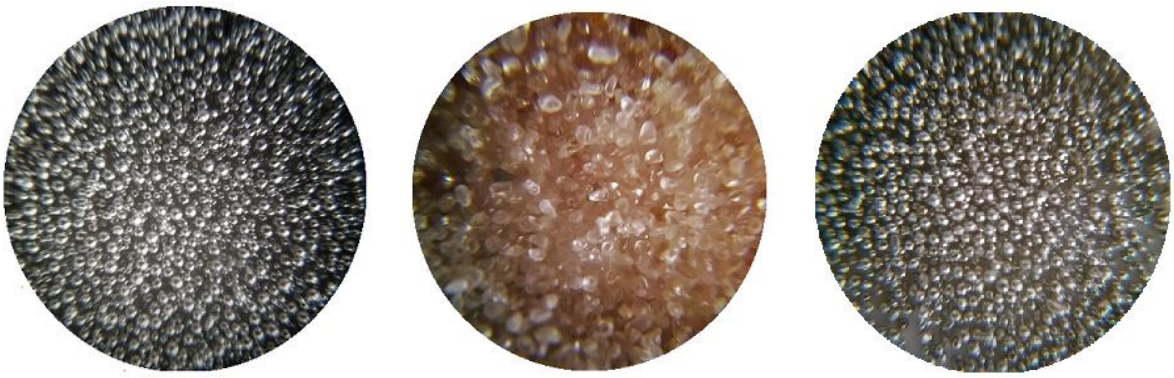

Ti6Al4V (+109-154µm) Zirconium (+75-154µm) Inconel 625 (+90-154µm)

Figure 8. Microscope images of the powder materials

Initially, calibration experiments were carried out for each powder type. Subsequently, three intermediate feed rate values were selected, and the powder feeder was commanded to calculate and adjust the valve opening angle accordingly. The amount of powder dispensed over a fixed time interval was measured, and the resulting mass flow rates were calculated. All measurements during both the calibration and the feeding phases were repeated three times for each setting, and the average values were used for analysis. In both cases, the valve was kept open for a predefined duration, during which the dispensed powder was collected in a container and weighed using a precision balance. The mass flow rate was then calculated using the standard mass flow formula. These calculations were automated via the Arduino-based control system.

Table 2 presents the average mass values obtained during calibration corresponding to valve openings of 25%, 50%, 75%, and 100% of the full opening for three powder materials.

Table 2. The average of the measurement results obtained during the calibration of the powder materials

Valve Opening	Powder flow rate (g/m)		
(%)	Ti6Al4V	Zirconium	Inconel 625
25	1,68	9,06	6,18
50	8,46	17,61	54,06
75	13,56	26,55	68,28
100	19,74	36,69	91,44

Following this, feeding was conducted at various intermediate target values, and the corresponding measurements were recorded. Table 3 presents the target values, the mean of three measurements for each case, and the relative errors for each powder material.

Table 3. Feeding results of the powder materials at the target and measured values and the resulting relative error rates

Ti6Al4V			Zirconium			Inconel 625		
Target Flowrate (g/min)	Measured Flowrate (g/min)	Rel. Error (%)	Target Flowrate (g/min)	Measured Flowrate (g/min)	Rel. Error (%)	Target Flowrate (g/min)	Measured Flowrate (g/min)	Rel. Error (%)
5	4.51	-9.8	13	11.22	-13.7	20	23.68	18.4
10	11.23	12.3	20	25.76	28.8	50	54.06	8.1
15	14.56	-2.9	30	26.55	-11.5	75	70.13	-6.5

Although the regression model demonstrates a perfect fit with the calibration dataset ($R^2 = 1$), noticeable discrepancies were observed between the predicted and actual powder feed rates during operation.

These results collectively highlight the influence of particle size, shape, and target flow rates on the precision of the feeding system, underscoring the need for material-specific calibration strategies in powder-based manufacturing processes. These deviations are primarily attributed to the inherent complexity and dynamic behavior of powder flow systems, rather than deficiencies in the mathematical model itself.

Among the tested powders, Ti6Al4V powder exhibited the lowest relative error across all target flow rates, followed by Inconel 625 powder, while Zirconium showed the highest deviations. As summarized in Table 1, Ti6Al4V and Inconel 625 exhibit spherical morphology, which is known to promote stable and predictable flow. Furthermore, Ti6Al4V powder possesses the narrowest size distribution among them. In contrast, Zirconium has angular, irregularly shaped particles with a somewhat broader size distribution, likely contributing to increased flow variability and feeding errors.

These results support the widely acknowledged view that particle shape and size distribution significantly influence flow behavior in powder feeders. Spherical particles, due to their reduced interlocking and lower surface area-to-volume ratio, generally experience less resistance during flow and are less susceptible to arching and bridging phenomena. This characteristic facilitates smoother transport through constricted geometries such as valves and funnels, leading to more consistent delivery rates—an observation consistent with the superior performance of Ti6Al4V.

On the other hand, irregular particles, like those of Zirconium, tend to interlock and form unstable flow patterns, particularly at lower feed rates. Irregular particles not only cause interlocking among themselves, but also induce flow disturbances due to the interaction between the particle and the flow path, especially around sharp features such as the valve shaft. This behavior aligns with the findings of Barati et al. (2015), where significant fluctuations in mass flow rate were observed due to powder cohesion and particle-wall interactions.

Wang et al. (2018) and Besenhard et al. (2017) also have shown that fine and cohesive powders are particularly prone to erratic flow due to agglomeration, inter-particle adhesion, and arching effects, which reduce flow reproducibility even under seemingly controlled conditions. Besenhard et al. (2017) also concluded that flow fluctuations are more likely at low feed rates due to the high surface-to-volume ratio. Similar to these findings, lower flow fluctuations were observed at higher target flow rates for each powder in this study, as presented in Table 3.

Studies by Pohorely et al. (2004) and Annamalai et al. (1992) underscore that low-rate feeding systems are particularly sensitive to small disturbances in powder behavior, especially under micro-feeding regimes. These physical phenomena introduce nonlinearities and disturbances that are not captured by regression models trained on static datasets.

These insights underscore the importance of integrating material-specific considerations into the design and calibration of powder feeding systems. For instance, in applications involving powders with poor flowability—like Zirconium—strategies such as vibrational agitation, assisted gas flow, and optimized flow channel geometry should be precisely tuned to stabilize the feed. This is supported by Mendez et al. (2012), who showed that feed frame geometry and dynamic interactions between powder and wall surfaces can drastically affect feed uniformity.

Therefore, while the regression model provides an idealized estimation of the valve position required to achieve a target flow rate, real-time deviations stem predominantly from transient flow

instabilities, batch-to-batch material variability, and mechanical limitations of the feeder hardware—all of which are well-documented challenges in the field of powder technology (Blackshields and Crean, 2017; Engisch and Muzzio, 2015; Janssen et al., 2022).

In summary, the deviations observed in Table 3 are not merely the result of mechanical limitations but reflect the complex interplay between powder shape, size, cohesion, and the chosen feeding method. These findings highlight the need for adaptive and material-aware control strategies in dual-channel powder feeders, particularly when dealing with non-spherical or fine-grained powders.

The dual-channel powder feeder developed in this study provides a robust and adaptable foundation for the implementation of FGM strategies via DED, particularly in high-performance components such as compressor disks and turbine blades. These components must withstand extreme thermal loads, high rotational speeds, and severe wear conditions—especially in the case of compressor disks, where both fatigue and surface degradation due to abrasion pose significant operational risks (Aschenbruck J et al.,2014). The ability to precisely regulate and independently deliver different powder materials enables tailored material gradients, which significantly enhance resistance to mechanical and thermal stresses. This flexibility, combined with the automatic control of variable feed rates for dual powder materials, makes such a powder feeder particularly valuable for the production of performance-critical components—especially in defense, aerospace, and energy sectors—through FGM strategies implemented via DED additive manufacturing (Nazir A et al., 2023).

4. CONCLUSION

This study introduced a novel dual-component powder feeding system designed to enable independent flow control for each powder line in DED applications. The system integrates a calibration-based predictive model that determines the appropriate valve position for a target flow rate based on the feeding characteristics of each powder type. The proposed method was validated through a series of calibration and controlled feeding experiments using Ti6Al4V, Inconel 625, and Zirconium materials. Based on the results obtained, the following conclusions can be drawn:

- Each material was fed at selected target flow rates, and the achieved values were compared against predicted outputs to evaluate the system’s accuracy.
- The minimum relative deviations were observed as 2.9% for Ti6Al4V at a flow rate of 15 g/min, 11.5% for Zirconium at 30 g/min, and 6.5% for Inconel 625 at 75 g/min. Conversely, the maximum deviations were recorded as 12.3% for Ti6Al4V at 10 g/min, 28.8% for Zirconium at 20 g/min, and 18.4% for Inconel 625 at 20 g/min. In general, lower deviations were observed at higher flow rates.
- Ti6Al4V powder exhibited the lowest relative error across all target flow rates due to its spherical morphology and narrow size distribution. Conversely, Zirconium powder exhibited the highest relative error, primarily due to its irregular morphology and broader particle size distribution.
- The mass flow behavior of powders was fundamentally governed by material-specific physical properties, especially density and particle morphology, under gravity-driven feeding conditions. For instance, Inconel 625, with its substantially higher density, exhibited the highest mass flow rate among all tested powders. This aligns with the literature emphasizing

the dominant influence of gravitational forces in free-flow feeding systems (Engisch and Muzzio, 2015; Annamalai et al., 1992).

- Despite the irregular morphology of Zirconium powder—which is commonly associated with poor flowability—the presence of finer particles in its distribution appeared to enhance its flow behavior. As a result, Zirconium outperformed Ti6Al4V in terms of mass flow rate under comparable conditions, underscoring the compensatory role of particle size over shape (Barati Dalenjan et al., 2015; Janssen et al., 2022).
- The favorable flow performance of Inconel 625 was further enhanced by its spherical particle shape, which minimized inter-particle friction and supported a more streamlined flow through the valve opening. Additionally, its relatively narrow particle size distribution enabled higher volumetric fill and more uniform movement through the feeder system, consistent with findings in Besenhard et al. (2017) and Wang et al. (2018).
- Polynomial regression modeling enabled precise calibration of the relationship between valve opening and powder mass flow rate. The calibration curve, established via third-order polynomial interpolation based on four data points, exhibited a perfect fit ($R^2 = 1.000$). However, deviations observed in actual feed performance, particularly at lower valve openings, indicate that such models alone may not capture all dynamic effects present in real-time operations—especially in the presence of complex powder behaviors. This aligns with prior studies emphasizing that while modeling provides a foundational understanding, physical phenomena such as particle bridging, vibration-induced segregation, or refill-induced disturbances can significantly affect feeding stability (Li et al., 2020; Blackshields and Crean, 2017).
- The most pronounced deviation from predicted feed rates was observed with Zirconium, which also exhibited the largest variation across repeated measurements. This instability is attributable to its irregular particle shape and broader size distribution, which likely caused erratic flow, frequent clogging, and intermittent surges. Such behaviors are consistent with the challenges of feeding cohesive or irregularly shaped powders highlighted in Wang et al. (2018) and Pohorely et al. (2004).
- A general trend of reduced error and improved consistency was observed at higher valve openings for all powder types. This observation suggests that increased aperture reduces the relative influence of particle morphology and enhances bulk flow stability—findings that are in agreement with the work of Singh and Chandravanshi (2022), who demonstrated the positive correlation between opening size and feed uniformity in vibratory feeder systems.

In conclusion, this study confirms that the dual-channel powder feeder system is capable of delivering accurate and consistent powder flow for a variety of materials. Nevertheless, for powders with challenging flow characteristics—such as Zirconium—enhanced control strategies, including real-time feedback or active vibration mechanisms, may be necessary to mitigate fluctuations. These findings highlight the critical interplay between powder physical characteristics and mechanical feeding design, reinforcing the need for integrated approaches that combine predictive modeling with process-aware engineering solutions in future developments.

5. ACKNOWLEDGEMENTS

This study was supported by the Scientific Research Projects Unit (BAP) of Kahramanmaraş Sütçü İmam University under the project number 2019/6-12 YLS.

6. CONFLICT OF INTEREST

Authors approve that to the best of their knowledge, there is not any conflict of interest or common interest with an institution/organization or a person that may affect the review process of the paper.

7. AUTHOR CONTRIBUTION

Mehmet ERMURAT contributed to determining the concept and/or design process of the research, managing the concept and/or design process, data collection, data analysis and interpretation of the results, preparation of the manuscript, critical analysis of the intellectual content, and final approval and full responsibility. Serhat ZIBA contributed to determining the concept and/or design process of the research, data collection, data analysis and interpretation of the results, preparation of the manuscript, and final approval and full responsibility.

8. REFERENCES

Altus E., Konstantino E., Optimum laser surface treatment of fatigue damaged Ti–6Al–4V alloy. Materials Science and Engineering: A 302(1), 100–105, 2001.

Annamalai K., Ruiz M., Vo N., Anand V., Locally fluidizing feeder for powder transport. Powder Technology 73, 181–190, 1992. https://doi.org/10.1016/0032-5910(92)80079-C

Aschenbruck J, Adamczuk R, Seume J. R., Recent Progress in Turbine Blade and Compressor Blisk Regeneration, Procedia CIRP 22, 256-262, 2014. https://doi.org/10.1016/j.procir.2014.07.016.

Barati Dalenjan M., Jamshidi E., Ale Ebrahim H., A screw-brush feeding system for uniform fine zinc oxide powder feeding and obtaining a homogeneous gas-particle flow. Advanced Powder Technology 26, 303–308, 2015. https://doi.org/10.1016/j.apt.2014.10.010

Besenhard M. O., Fathollahi S., Siegmann E., Slama E., Faulhammer E., Khinast J. G., Micro-feeding and dosing of powders via a small-scale powder pump. International Journal of Pharmaceutics 519(1-2), 314–322, 2017. https://doi.org/10.1016/j.ijpharm.2016.12.029

Blackshields C. A., Crean A. M., Continuous powder feeding for pharmaceutical solid dosage form manufacture: a short review. Pharmaceutical Development and Technology 23(6), 554–560, 2017. https://doi.org/10.1080/10837450.2017.1339197

Bruni S., Martinesi M., Stio M., Treves C., Bacci T., Borgioli F., Effects of surface treatment of Ti–6Al–4V titanium alloy on biocompatibility in cultured human umbilical vein endothelial cells. Acta Biomater 1(2), 223–234, 2005.

Burden R. L., Faires, J. D., Numerical Analysis. 9th Edition, Brookscole, Boston, 259-253, 2011.

Courant B., Hantzpergue J. J., Benayoun S., Surface treatment of titanium by laser irradiation to improve resistance to dry-sliding friction. Wear 236, 39–46, 1999.

Dai Z. D., Pan S. C., Wang M., Yang S. R., Zhang X. S., Xue Q. J., Improving the fretting wear resistance of titanium alloy by laser beam quenching, Wear 213(1-2), 135–139, 1997.

Engisch W. E., Muzzio F. J., Feedrate deviations caused by hopper refill of loss-inweight feeders. Powder Technology 283, 389–400, 2015.

Ermurat M., Lazerli Doğrudan Metal Parça İmalatı Sisteminin Geliştirilmesi, Üretilen Parça Özelliklerinin İncelenmesi ve Sistem Optimizasyon, Kocaeli Üniveritesi Fen Bilimleri Enstitüsü, Doktora Tezi (Basılmış), 2009.

Fu Y. Q., Batchelor A. W., Laser nitriding of pure titanium with Ni, Cr for improved wear performance, Wear 214, 83–90, 1998.

Ganesh B. K. C., Sha W., Ramanaiah N., Krishnaiah A., Effect of shotpeening on sliding wear and tensile behavior of titanium implant alloys. Materials & Design, 56, 480–486, 2014.

Gu D. D., Meiners W., Wissenbach K., Poprawe R., Laser additive manufacturing of metallic components: materials, processes and mechanisms. International Materials Reviews, 57(3), 133-164, 2012.

Hofmann D. C., Kolodziejska J., Roberts S., Otis R., Dillon R. P., Suh J. O., Liu Z-K., Borgonia, J. P., Compositionally graded metals: A new frontier of additive manufacturing, Journal of Materials Research, 29(17), 1899-1910, 2014.

Hou P. C. H., Development of a Micro-Feeder for Cohesive Pharmaceutical Powders, PhD.Thesis, Strathclyde Institute of Pharmacy and Biomedical Sciences University of Strathclyde, Glasgow, UK, 2024,

Janssen P. H. M., Kulkarni S. S., Torrecillas C. M., Tegel F., Weinekötter R., Meir B., Dickhoff, B. H. J., Effect of batch-to-batch variation of spray dried lactose on the performance of feeders. Powder Technology. 409, 117776, 2022. https://doi.org/10.1016/J.POWTEC.2022.117776

Li J., Cheng X., Liu D., Zhang S. Q., Li Z., He B., Wang H. M. Phase evolution of a heat-treatable aluminium alloy during laser additive manufacturing. Materials Letters 214, 56-59, 2018.

Li T., Scicolone J. V., Sanchez E., Muzzio F. J., Identifying a Loss-in-Weight Feeder Design Space Based on Performance and Material Properties. Journal of Pharmaceutical Innovation 15, 482–495, 2020.

Lin X., Yue T. M., Yang H. O., Huang W. D., Microstructure and phase evolution in laser rapid forming of a functionally graded Ti-Rene88DT alloy. Acta Materialia 54(7), 1901-1915, 2006.

Lin X., Yue T. M., Phase formation and microstructure evolution in laser rapid forming of graded ss316L/Rene88DT alloy. Materials Science and Engineering: A 402, 294-306, 2005.

Mahamood R. M., Akinlabi E. T., Shukla M., Pityana S., Scanning velocity influence on microstructure, microhardness and wear resistance performance of laser deposited Ti6Al4V/TiC composite. Materials & Design 50, 656–666, 2013.

Mazumder J., Voelkel D. D., Method and apparatus for noncontact surface contour measurement. US patent no. 5446549, 1995.

Mazumder J., Morgan D., Skszek T. W., Lowney M., Direct metal deposition apparatus utilizing rapid-response diode laser source. US patent no. 7765022, 2010.

Mendez R., Velazquez C., Muzzio F. J., Effect of feed frame design and operating parameters on powder attrition, particle breakage, and powder properties, Powder Technology, 229, 253-260, 2012. ISSN 0032-5910

Nazir A, Gokcekaya O, Masum Billah K. M, Ertugrul O, Jiang J, Sun J, Hussain S, Multi-material additive manufacturing: A systematic review of design, properties, applications, challenges, and 3D printing of materials and cellular metamaterials, Materials & Design 226, 111661, 2023. ISSN 0264-1275, https://doi.org/10.1016/j.matdes.2023.111661.

Özdemir A. C., Lens'te 3 Farklı Tozu Aynı Katmana Yığma Kafası Tasarımı, Gebze Yüksek Teknoloji Enstitüsü, Mühendislik ve Fen Bilimleri Enstitüsü, Yüksek Lisans Tezi (Basılı), 2009

Pei Y. T., Ocelik V., De Hosson J. T. M., SiCp/Ti6Al4V functionally graded materials produced by laser melt injection. Acta Materialia 50(8), 2035–2051, 2002.

Pohořelý M., Svoboda K., Hartman M., Feeding small quantities of particulate solids. Powder Technology 142, 1–6, 2004. https://doi.org/10.1016/j.powtec.2004.03.005

Santos E. C., Shiomi M., Osakada K., Laoui T., Rapid manufacturing of metal components by laser forming. International Journal of Machine Tools and Manufacture 46(12-13), 1459–1468, 2006.

Singh C., Chandravanshi M. L., Dynamic analysis and performance assessment of a vibratory feeder for different motor positions on trough. Mechanics Based Design of Structures and Machines 51(11), 6453-6470, 2022. https://doi.org/10.1080/15397734.2022.2047720

Suri A., Horio M., A novel cartridge type powder feeder, Powder Technology,189(3), 497-507, 2009.

Wang H. M., Liu Y. F., Microstructure and wear resistance of laser clad Ti5Si3/NiTi2 intermetallic composite coating on titanium alloy, Materials Science and Engineering: A 338(1-2), 126–132, 2002.

Wang Q., Zhang P. Z., Wei D. B., Chen X. H., Wang R. N., Wang H. Y., Microstructure and sliding wear behavior of pure titanium surface modified by double-glow plasma surface alloying with Nb, Materials & Design, 52, 265–73, 2013.

Wang H., Wu L., Zhang T., Chen R., Zhang L., Continuous micro-feeding of fine cohesive powders actuated by pulse inertia force and acoustic radiation force in ultrasonic standing wave field. International Journal of Pharmaceutics. 545, 153–162, 2018. https://doi.org/10.1016/j.ijpharm.2018.05.006

Wei C., Li L., Zhang X., Chueh Y. H. 3D Printing of multiple metallic materials via modified selective laser melting. CIRP Annals-Manufacturing Tech, 67, 245-248, 2018.

Wei C., Sun Z., Chen Q., Liu Z., Li L., Additive Manufacturing of Horizontal and 3D Functionally Graded 316L/Cu10Sn Components via Multiple Material Selective Laser Melting. Journal of Manufacturing Science and Engineering 141(8) 081014, 2019.

Wen C. Y., Simons H. P., Flow characteristics in horizontal fluidized solids transport. AIChE Journal, 5(2), 263–267, 1959. https://doi.org/https://doi.org/10.1002/aic.690050225

Weng F., Chen C., Yu H., Research status of laser cladding on titanium and its alloys: A review. Materials and Design, 58, 412–425, 2014.

Xu W., Brandt M., Sun S., Elambasseril J., Liu Q., Latham K., Qian M., Additive manufacturing of strong and ductile Ti-6Al-4V by selective laser melting via in site martensite decomposition. Acta Materialia 85, 74-84, 2015.

Yükselen M. A, HM504 Uygulamalı Sayısal Yöntemler Ders Notları, 2008.

Zhang Y. Z., Liu Y. T., Zhao X. H., Tang Y. J., The interface microstructure and tensile properties of direct energy deposited TC11/Ti2AlNb dual alloy. Materials and Design 110, 571-580, 2016.

Zhu Y. Y., Liu D., Tian X. J., Tang H. B., Wang H. M., Characterization of microstructure and mechanical properties of laser melting deposited Ti–6.5Al–3.5Mo–1.5Zr–0.3Si titanium alloy. Materials & Design, 56, 445–453, 2014.

JOURNAL of
MATERIALS and MECHATRONICS:A

e-ISSN 2717-8811
JournalMM, 2025, 6(1), 291-300
https://doi.org/10.55546/jmm.1661268

Araştırma Makalesi / Research Article

Görev Döngüsünün (Duty Cycle) Plazma Nitrürleme Üzerindeki Etkisi

Şükrü ÜLKER*

[1*] Afyon Kocatepe Üniversitesi, Teknoloji Fakültesi, Makine Mühendisliği Bölümü, Afyonkarahisar, Türkiye,
ORCID ID: https://orcid.org/0000-0002-2561-3044, ulker@aku.edu.tr

Geliş/ Received: 20.03.2025; **Revize/Revised:** 12.04.2025 **Kabul / Accepted:** 23.05.2025

ÖZET: Makine parçalarının mikro yapısını iyileştirmek, aşınmaya karşı dayanıklılığını artırmak, korozyona karşı direnç kazandırmak ve yorulma ömrünü uzatmak için farklı yüzey sertleştirme yöntemleri uygulanmaktadır. Plazma nitrürleme işlemi, elde edilen sertleşmiş tabakaların hassas bir şekilde kontrol edilebilmesi ve diğer sertleştirme tekniklerine kıyasla sunduğu çeşitli avantajlar sayesinde endüstride geniş çapta kullanılmaktadır. Bu araştırmada AISI 5115 çeliğine %50 H_2+%50 N_2 gaz karışımı ortamında 500 ºC sıcaklıkta 5 saat süreyle DC plazma nitrürleme, %75 ve %50 görev döngüsü ile darbeli (puls) plazma nitrürleme işlemi uygulanmıştır. Plazma nitrürlenmiş numunelerin faz özellikleri XRD ve optik mikroskop ile incelenmiştir. Mikrosertlik ölçümleri ile yüzey sertlikleri belirlenmiştir. Metalografik incelemeler sonucunda beyaz tabakanın oluştuğu, görev döngüsünün azalmasıyla tabaka kalınlığının azaldığı görülmüştür. X-ışınları incelemeleri sonucunda DC plazma nitrürleme ile Fe_3N, Fe_4N fazlarının oluştuğu %50 görev döngüsü ile yapılan çalışmada ise bu fazlara ek olarak yüzeyde α-Fe ve Fe_3O_4 fazları görülmüştür. Mikrosertlik incelemeleri sonucunda yüzey sertliğinde işleme bağlı olarak yaklaşık 3-5 kat artış olduğu tespit edilmiştir.

Anahtar Kelimeler: 5115 çeliği, Plazma nitrürleme, Görev döngüsü, Mikrosertlik

*Sorumlu yazar / Corresponding author: ulker@aku.edu.tr
Bu makaleye atıf yapmak için /To cite this article

Ülker, Ş. (2025). Görev Döngüsünün (Duty Cycle) Plazma Nitrürleme Üzerindeki Etkisi. Journal of Materials and Mechatronics: A (JournalMM), 6(1), 291-300.

The Influence of Duty Cycle on Plasma Nitriding

ABSTRACT: Different surface hardening methods are applied to improve the microstructure of machine parts, increase wear resistance, provide resistance to corrosion and extend fatigue life. Plasma nitriding process is widely used in the industry due to the precise control of the hardened layers obtained and the various advantages it offers compared to other hardening techniques. In this research, DC plasma nitriding and pulsed plasma nitriding with 75% and 50% duty cycles were applied to AISI 5115 steel in a 50% H_2+50% N_2 gas mixture environment at 500 ºC for 5 hours. The phase properties of plasma nitrided samples were examined by XRD and optical microscope. Surface hardness was determined by microhardness measurements. As a result of metallographic examinations, it was observed that a white layer was formed and the layer thickness decreased with the decrease in duty cycle. As a result of X-ray examinations, Fe_3N, Fe_4N phases were formed with DC plasma nitriding and in the study carried out with 50% duty cycle, α-Fe and Fe_3O_4 phases were observed on the surface in addition to these phases. As a result of microhardness examinations, it was determined that there was an increase of approximately 3-5 times in surface hardness depending on the process.

Keywords: AISI 5115 Steel, Plasma nitriding, Duty cycle, Microhardness

1. GİRİŞ

AISI 5115 (16MnCr5) çeliği, sementasyon işlemiyle yüzeyi sertleştirilebilen, değişken ve darbeli zorlamalara karşı dayanıklı, alaşımlı bir yapı çeliğidir. Bu özelliği sayesinde dişli çarklar, aktarma organları vb. parçaların imalatında tercih edilir (Cai ve ark., 2021).

Plazma nitrürleme çeşitli plazma difüzyon işlemleri arasında yaygın olarak kullanılan yüzey işlemleri arasındadır. Plazma nitrürleme teknolojisi, azot gazı ortamında plazma deşarjı yoluyla azot iyonlarını metale nüfuz eder ve yayar. Yüzeyde nitrürlenmiş bir tabaka oluşturur. Bu nitrürlenmiş tabaka mükemmel sertlik, aşınma direnci ve korozyon direnci gösterir (Chong ve Kim, 2017). Plazma nitrürlemenin bir sonucu olarak çeliğin yüzeyinde beyaz tabaka ve difüzyon tabakası olarak bilinen yapılar oluşur. Beyaz tabaka en dıştaki tabaka olup tek fazlı (γ′-Fe_4N veya ε-$Fe_{2-3}N$) veya çok fazlı (γ′-Fe_4N+ε-$Fe_{2-3}N$) olabilir (Ohtsu ve ark., 2021; Shen ve Wang, 2019; Esfahani, 2007).

Uygulamaya bağlı olarak, DC deşarjları, darbeli DC deşarjları, RF deşarjları ve mikrodalga deşarjları dahil olmak üzere çeşitli güç kaynakları plazma üretebilir (Anders, 2004; Conrads ve Schmidt, 2000). Nitrürleme sistemi genellikle DC güç kaynakları tarafından çalıştırılır (Conrads ve Schmidt, 2000). Ancak, puls frekansı veya puls görev döngüsü değiştirilerek nitrürleme performansı üzerinde ek kontrol sağlaması nedeniyle puls DC deşarjları tercih edilir (Alves ve ark., 1999; Sharma ve ark., 2006). Darbeli DC glow deşarjlarında, iyon bombardımanı ile saçılma, aktif puls sırasında (bir pulsun açık süresi $T_{açık}$) etkiliyken, plazmanın aktif türleri tüm döngü boyunca korunur ($T = T_{açık} + T_{kapalı}$) (Cooke ve ark., 2004). Bu nedenle, puls görev döngüsünün ($T_{açık}$ /($T_{açık} + T_{kapalı}$) plazma parametreleri ve nitrürleme performansının etkisini incelemek önemlidir (Fenili ve ark., 2017).

Puls plazma nitrürleme, puls süresi ve görev döngüsünün hassas ayarlanabilirliği sayesinde parçaların yüzeyinde dengeli bir sıcaklık dağılımı sağlayarak, aşırı ısınma riskini ortadan kaldırır ve yüksek plazma gücünün güvenle kullanılmasını mümkün kılar (Huchel, 1995). Yüksek plazma

gücünün kullanımı nitrürleme zamanını kısaltır (Leskovsĕk, 1995). Bunun yanında puls güç kaynağı arkı önlemeye yardımcı olur (Podgornik ve Vizintin, 2003; Naem ve ark., 2016).

Birkaç çalışmada, geleneksel bir plazma nitrürleme sisteminde çeşitli altlık malzeme üzerinde darbeli görev döngüsünün etkisi incelenmiştir. Bunlar arasında Menthe ve ark. (2000) farklı N_2 – H_2 gaz karışımları ve işlem süreleri ile darbeli-DC plazma kullanılarak 375-475 ° C sıcaklık aralığında AISI 304L çeliği üzerinde plazma nitrürleme gerçekleştirmişlerdir. Alves ve ark. (1999) AISI 409 çeliğini plazma nitrürleyerek darbe genişliği $t_{açık}$'ın nitrürlenmiş tabaka üzerindeki etkisini incelemişlerdir. Taherkhani ve Mahboubi (2013) nitrürlenmiş H13 çeliği üzerinde görev döngüsü (%40–%80) ve frekans (8–10 kHz) etkisini incelemişlerdir. Díaz-Guillén ve ark. (2009) darbeli (puls) plazma nitrürleme işleminde, AISI 4340 düşük alaşımlı çeliğin yüzey özellikleri üzerinde görev döngüsünün (%10 – %80 $t_{açık}$ aralığı uygulayarak) yüzey sertliği, işlem derinliği, bileşik bölge genişliği ve kristalin faz bileşimi üzerindeki etkisini incelemişlerdir. Díaz-Guillén ve ark. (2015) plazma nitrürlenmiş AISI 316L çeliğinin yüzey karakteristiklerine darbe zamanı değişiminin sertlik, kristalin fazlar ve elektrokimyasal korozyon duyarlılığı üzerindeki etkisini incelemişlerdir. Durisic ve ark. (2006) C45 çeliğini puls plazma nitrürlemede görev döngüsü etkisini araştırmışlardır. Luo ve ark. (2017) puls plazma nitrürlenmiş östenitik paslanmaz çeliğinin aşınma davranışlarını incelemişlerdir. Yasir ve ark. (2024) AISI 321 paslanmaz çeliğini %10-%60 arasındaki görev döngülerinde plazma nitrürlemişlerdir. Cieslik ve ark. (2011), DIN 16MnCr5 çeliği için plazma nitrürleme işlem süreci üzerine bir çalışma yürütmüştür. Azot (N_2) ve Hidrojenin (H_2) farklı gaz bileşimlerini kullanarak ek bir difüzyon aşamasının, bileşik tabaka kalınlığı ve sertlik profili üzerindeki etkisini araştırmışlardır.

AISI 5115 çeliğinin mekanik ve tribolojik özelliklerini belirlemek amacıyla nitrürleme ve borlama gibi yöntemler kullanılarak farklı çalışmalar yapılmış olmasına rağmen, literatürde farklı görev döngülerinde nitrürlemenin malzeme yüzeyine etkisi üzerine çalışmaya rastlanılmamıştır. Bu çalışmada AISI 5115 çeliği 500 ºC sıcaklıkta, 5 saat işlem süresinde, %50 N_2-%50 H_2 karışımında DC plazma ve %75, %50 görev döngüsü oranlarıyla plazma nitrürlenerek mikroyapısal özellikleri üzerindeki etkisi incelenmiştir. Nitrürlenen numunelerin mikroyapı, yüzey pürüzlülüğü, sertlik ve XRD analizleri yapılmıştır.

2. MATERYAL VE YÖNTEM

Bu çalışmada altlık malzeme olarak kullanılan AISI 5115 çeliğinin kimyasal bileşimi Çizelge 1'de görülmektedir.

Çizelge 1. AISI 5115 Çeliğinin Kimyasal Bileşimi, %

C	Mn	Cr	Si	P	S	Fe
0.14-0.19	1-1.3	0.8-1.1	0.15-0.4	0.02-0.035	0.02-0.035	Kalan

24 mm çapındaki AISI 5115 çeliği 1 metre boyunda kesilmiş halde temin edilmiştir. Çelikler 25'er cm aralıklarla hidrolik testere ile kesilerek 900^0C sıcaklıkta 45 dakika süreyle tam tavlama işlemine tabi tutulmuştur. Daha sonra çeliğin çapı torna ile 20 mm ye düşürülerek 10 mm kalınlığında kesilmiştir. Sonrasında numuneler metalografik olarak parlatılmıştır.

Numuneler alkolle temizlendikten sonra katot üzerine yerleştirilmiş ve haznenin kapağı kapatıldıktan sonra havası $8.4x10^{-2}$ mbar basınca boşaltılmıştır. Nitrürleme işlemine geçilmeden önce numuneler 5 mbar basınç altında 30 dakika H_2 gazı ile saçılma işlemine tutulmuştur. Plazma

nitrürleme işlemi DC, %75 ve %50 görev döngüsü uygulayarak 500 ºC sıcaklıkta, 5 mbar vakum basıncında %50 H_2-% 50 N_2 gaz karışımında ve 5 saat süreyle gerçekleştirilmiştir. Deney süresince sıcaklık, numuneye temas halinde olan bir termokupl ile ölçülmüştür. İstenilen sıcaklığa ulaşınca nitrürleme süresi başlatılmıştır. Plazma nitrürlenen numuneler üzerinde XRD analizi, mikrosertlik ve metalografi yüzey pürüzlülüğü incelemeleri yapılmıştır. Nitrürlenmiş numunelerin sertlikleri malzeme yüzeyinden, Vickers ucuyla 50 gr yük altında 10 saniye süre ile ölçülmüştür. Yüzey pürüzlülüğü ölçümleri Taylor-Hobson Rugosimeter Surtronic 25 marka cihaz ile gerçekleştirilmiştir. Nitrürlenmiş yüzeylerdeki mevcut fazların analizi Shimadzu XRD–6000 cihazında CuK_α (λ = 1,5418 Å) radyasyonu kullanılarak gerçekleştirilmiştir.

3. BULGULAR VE TARTIŞMA

3.1 Nitrür Tabakasının Karakterizasyonu

Şekil 1'de DC plazma nitrürlenen AISI 5115 çeliğinin iç yapı fotoğrafı görülmektedir. Numunelerin dış yüzeyinde ortalama 5 µm kalınlığında beyaz tabaka oluşmuştur. Numune üzerinde oluşan tabaka düzgün bir şekilde yayılmıştır. Cieslik ve ark. (2011) %30 N_2-%70 H_2 gaz karışımında 5 saat plazma nitrürleme sorasında 1.5 µm kalınlığında beyaz tabaka oluştuğunu tespit etmişlerdir.

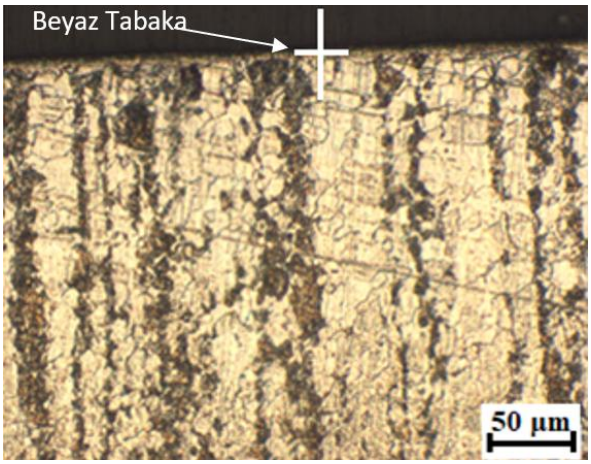

Şekil 1. Nitrürlenmiş AISI 5115 çeliğinin optik mikroskopta görünümü

Şekil 2'de %75 görev döngüsü ile plazma nitrürleme sonrası mikroyapı fotoğrafı görülmektedir. Beyaz tabaka kalınlığı ortalama 4 µm olarak tespit edilmiştir.

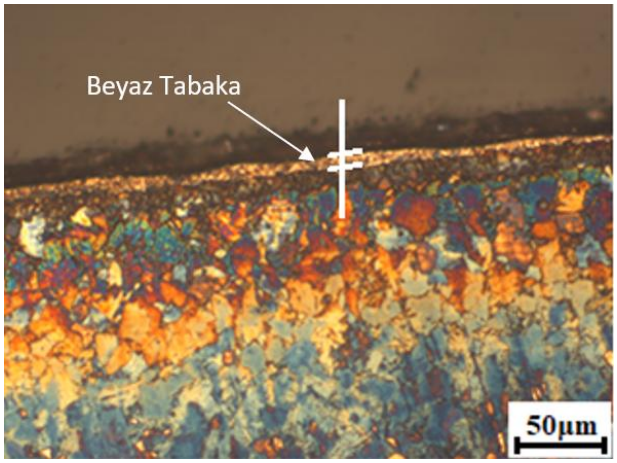

Şekil 2. %75 görev döngüsü ile plazma nitrürlenmiş AISI 5115 çeliğinin optik mikroskopta görünümü

Şekil 3'te %50 görev döngüsü ile plazma nitrürleme sonrası mikroyapı fotoğrafı görülmektedir. Beyaz tabaka kalınlığı ortalama 2.5 µm olarak tespit edilmiştir.

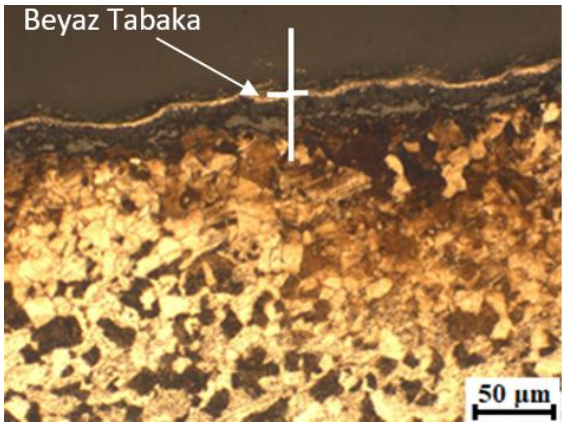

Şekil 3 %50 görev döngüsü ile plazma nitrürlenmiş AISI 5115 çeliğinin optik mikroskopta görünümü

Beyaz tabaka nispeten yüksek bir sertliğe sahip olmasına rağmen, iç gerilimler onu kırılgan hale getirir. Bu katman belirli uygulamalarda kayma aşınmasını ve yorulma direncini korumak için en aza indirilir. Buna karşılık, beyaz tabaka malzemeye aşınma ve yuvarlanma sürtünmesine karşı iyi fiziksel özellikler sağlar (Çelik ve Karadeniz, 1996), bu da daha sonra homojen ve daha kalın bir beyaz tabakanın istendiği anlamına gelir. Beyaz tabakanın plazma nitrürlenmiş sert kaplama sonrası işlemde üstün kayma aşınması özelliklerine yol açan ara sert bir katman olarak hareket ettiği bulunmuştur (Podgornik ve ark., 2001). Bu nedenle, tabakanın kalınlığı malzemenin kullanımına göre belirlenmelidir ve sonuçlardan görev döngüsünün bir beyaz tabaka kontrol yöntemi olarak kabul edilebileceği çıkarılabilir (Díaz-Guillén ve ark., 2009).

Şekil 4'te plazma nitrürlenmiş çeliğin beyaz tabaka kalınlığı ile yüzey pürüzlülüğü grafiği birlikte verilmiştir. Görev döngüsünün artmasıyla beyaz tabaka kalınlığının arttığı görülmüştür (Taherkhani ve Mahboubi, 2013). En yüksek beyaz tabaka DC plazma ile elde edilmiştir (Arul Mozhi Varman ve Huchel, 2017). Tabaka kalınlığının azalmasıyla birlikte yüzey pürüzlülük değerleri de düşmüştür. Benzer bir çalışmada da Taktak ve ark. (2014) %75 görev döngüsü ile yaptıkları çalışmada da beyaz tabaka kalınlığının azaldığını tespit etmişlerdir. Görev döngüsü oranının artmasıyla birlikte yüzey pürüzlülük değerleri de artmıştır (Jeong ve ark., 2000). Plazma nitrürlenmiş numunenin yüzey pürüzlülüğü Ra değeri 0.38, %75 görev döngüsü ile plazma nitrürleme sonucu Ra değeri 0.3, %50 görev döngüsü ile plazma nitrürleme sonucu Ra 0.24 olarak tespit edilmiştir.

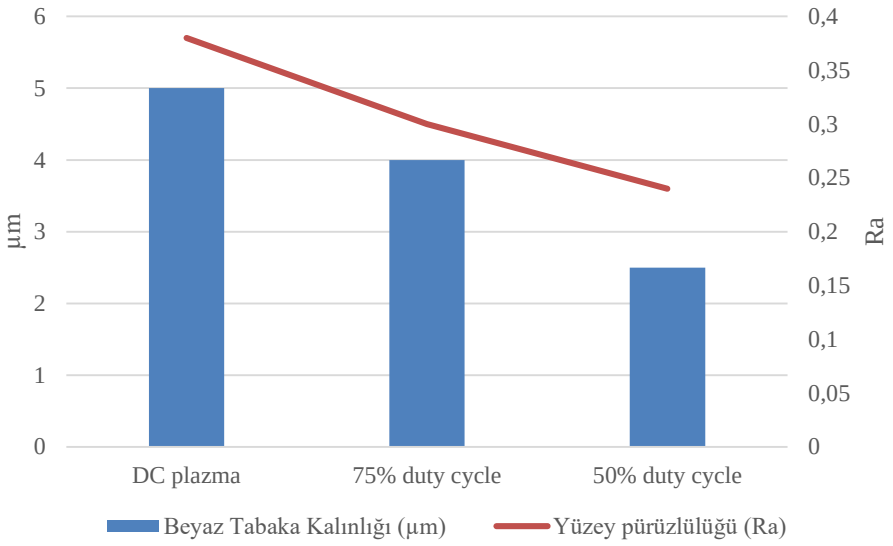

Şekil 4. Plazma nitrürlenmiş çeliğin beyaz tabaka kalınlığı ve yüzey pürüzlülüğü grafiği

Şekil 5'te DC plazma nitrürleme işlemine tabi tutulmuş çeliğin XRD analizi görülmektedir. Tabaka ağırlıklı olarak Fe_3N (Ref.No: 86-0232 (29.964, 41.215, 43.705, 57.515, 69.234, 76.857, 85.558)) ve Fe_4N (Ref.No: 86-0231(41.223, 47.969, 70.180, 84.767, 89.508)) fazlarından oluşmaktadır (Espinoza ve ark., 2024; Esfahani ve ark., 2007). Bu durum literatürle de uyumludur. Esfahani ve ark. (2007) 5115 çeliğini 550 °C'de 5 saat boyunca %80 N_2 +%20 H_2 gaz karışımlarında DC plazma nitrürlemiş ve yapısında Fe_3N ve Fe_4N fazlarının oluştuğunu tespit etmişlerdir. Arul Mozhi Varman ve Huchel (2017) 4340 çeliğini puls plazma nitürleme sonucunda Fe_3N, Fe_4N ve Cr_2N fazlarını tespit etmişlerdir.

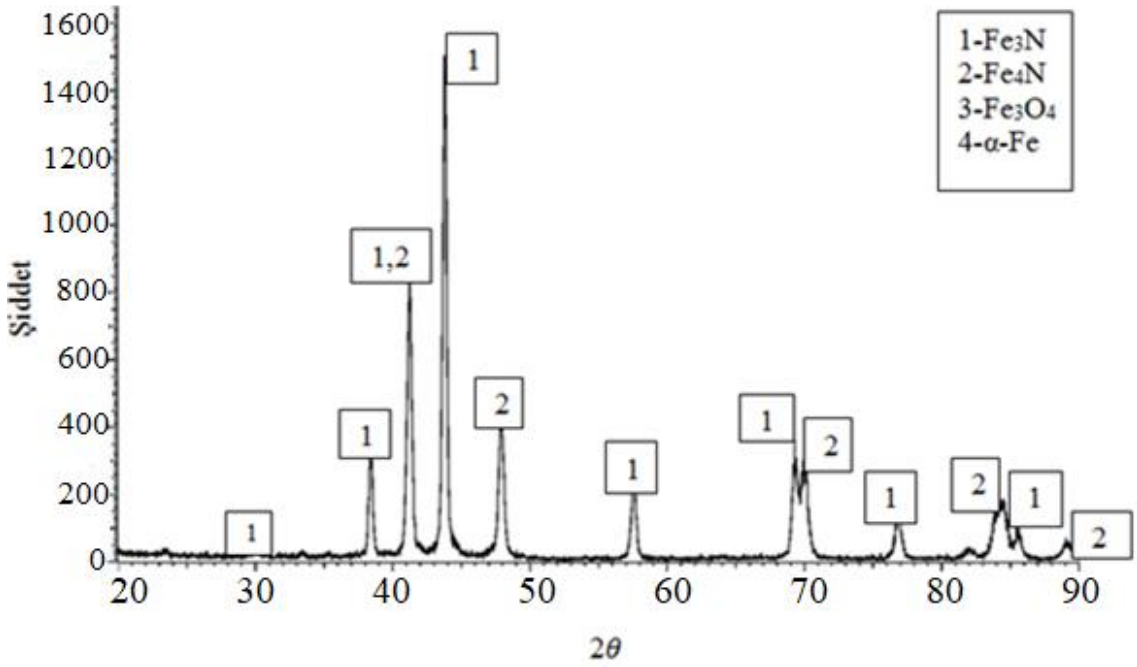

Şekil 5. DC plazma nitrürleme işlemine tabi tutulmuş çeliğin XRD analizi sonucu

Şekil 6'da %50 görev döngüsü ile plazma nitrürleme işlemine tabi tutulmuş çeliğin XRD analizi sonucu görülmektedir. Fe_4N (Ref. No: 86-0231(23.454, 41.223, 47.969, 70.180, 84.767, 89.508), Fe_3N (Ref.No: 86-0232 (29.964, 38.293, 41.215, 43.705)), Fe_3N (Ref.No:020389 (82,242)), Fe_3O_4

(Ref.No: 85-1436 (35.443, 56.964)) fazları tespit edilmiştir. En şiddetli fazın Fe_4N olduğu ve az da olsa Fe_3O_4 oluştuğu tespit edilmiştir. Fernando ve ark. (2019) AISI 8620 çeliğini puls plazma nitrürlemişler ve yüzeyde Fe_3N ve Fe_4N fazlarının yanında Fe_3O_4 ve Fe_2O_3 fazlarını da görmüşlerdir. Cieslik ve ark. (2011) 16MnCr5 çeliğini farklı süre ve gaz karışımlarında plazma nitrürlemişler ve tabakanın Fe ve Fe_4N fazlarından oluştuğunu gaz karışım oranının artmasıyla birlikte Fe_4N oranının daha fazla görüldüğünü tespit etmişlerdir. Díaz-Guillén ve ark. (2009) 4340 çeliğini puls plazma nitrürleyerek görev döngüsünün etkisini inceledikleri çalışmada tek fazlı Fe_4N den oluşan tabaka tespit etmişlerdir. Naem ve ark. (2023) orta karbonlu çeliği %15 ile %75 görev döngüsü arasında katot kafesi içinde plazma nitrürleme yaparak oluşan tabakada Fe_3N ve Fe_4N fazlarını tespit etmişlerdir.

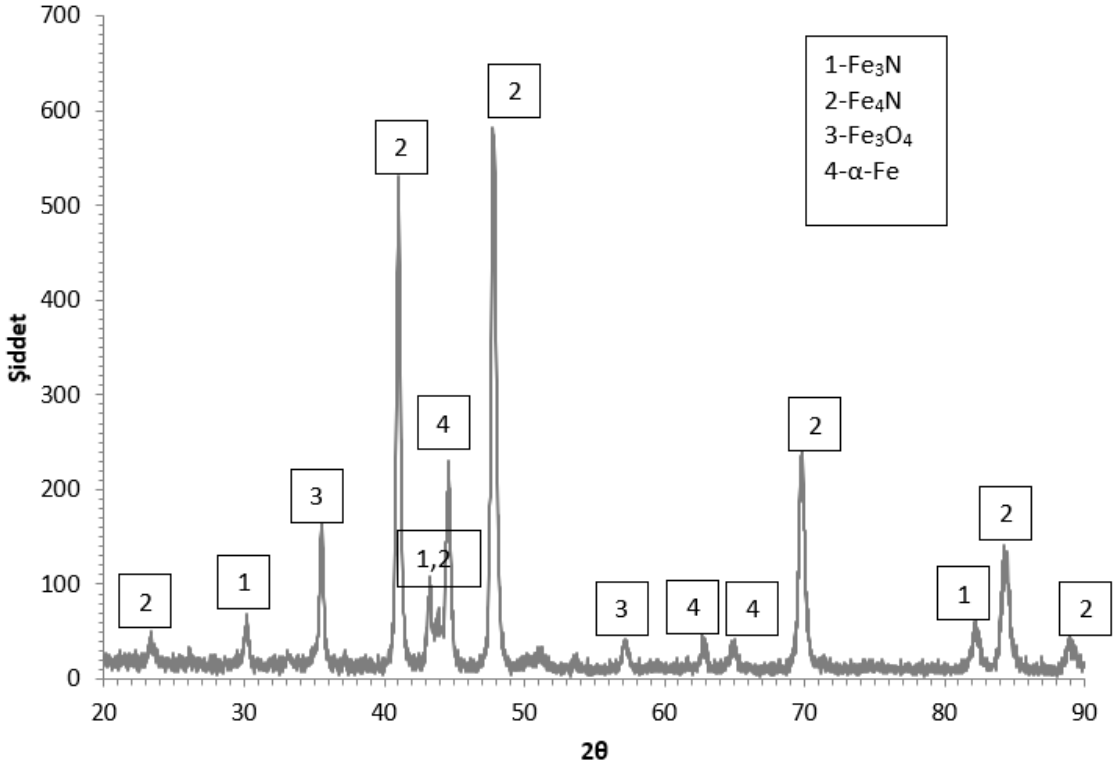

Şekil 6. %50 görev döngüsü ile plazma nitrürlenmiş çeliğin XRD analizi sonucu

Şekil 7'de plazma nitrürlenmiş numunelerin yüzeyden itibaren sertlik değerleri verilmiştir. Görev döngüsü değerinin artmasıyla yüzey sertlik değerlerinin arttığı görülmüştür (Taherkhani ve Mahboubi, 2013). En yüksek yüzey sertliği DC plazma nitrürleme sonucunda elde edilmiştir (Arul Mozhi Varman ve Huchel, 2017). Plazma nitrürlenmiş numunenin yüzey sertliği 755 $HV_{0.05}$, %75 görev döngüsü ile plazma nitrürleme sonucu yüzey sertliği 630 $HV_{0.05}$, %50 görev döngüsü ile plazma nitrürleme sonucu yüzey sertliği 540 $HV_{0.05}$ tespit edilmiştir. DC plazma nitürlemede sertliğin daha yüksek olmasının sebebi oluşan Fe_3N fazından kaynaklı olduğu düşünülmektedir (Naeem ve ark., 2023). Malzemenin işlem görmeden önceki sertliği 160 $HV_{0.05}$ iken plazma nitrürleme sonrasında sertlik değerlerinde yaklaşık 3-5 kat aralığında artış sağlanmıştır. Difüzyon derinliği olarak altlık malzeme sertliğinin %10 fazlası kabul edildiğinde (Sirin ve ark., 2008) beyaz tabakanın haricinde yaklaşık 65 µm lik bir difüzyon derinliği elde edilmiştir. Sabit sıcaklıkta tüm numunelerde aynı difüzyon derinliği görülmüştür (Díaz-Guillén ve ark., 2009).

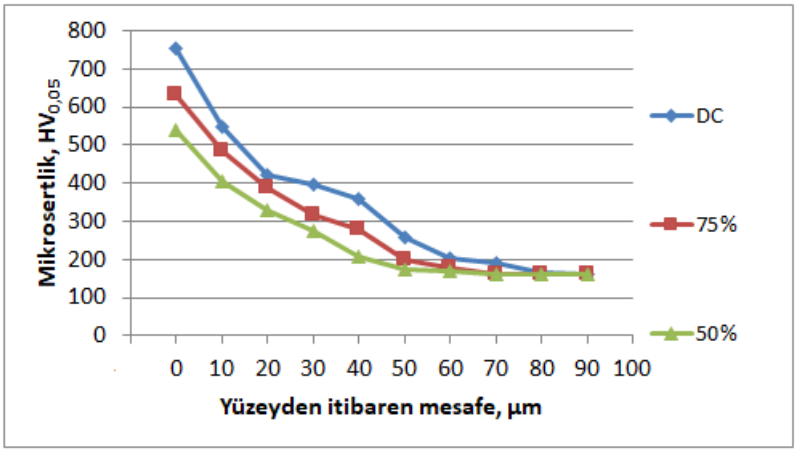

Şekil 7. Plazma nitrürlenmiş numunelerin yüzeyden itibaren mikrosertlik değerleri

4. SONUÇ

Deneysel 5115 çeliği 500 ºC sıcaklıkta, 5 saat işlem süresinde, %50 N_2-%50 H_2 karışımında DC plazma, %75 ve %50 görev döngüsü oranlarıyla plazma nitrürleyerek;

- Metalografik incelemeler sonucunda DC, %75 ve %50 görev döngüsü ile beyaz tabakanın oluştuğu, sırasıyla tabaka kalınlıkları 5 µm, 4 µm, 2.5 µm olarak belirlenmiştir.
- X-ışınları incelemeleri sonucunda DC plazma nitrürleme ile Fe_3N, Fe_4N fazlarının oluştuğu %50 görev döngüsü ile yapılan çalışmada ise bu fazlara ek olarak yüzeyde α-Fe ve Fe_2O_3 fazları görülmüştür.
- Plazma nitrürlenmiş numunenin yüzey sertliği 755 $HV_{0.05}$, %75 Görev döngüsü ile plazma nitrürleme sonucu 630 $HV_{0.05}$, %50 Görev döngüsü ile plazma nitrürleme sonucu 540 $HV_{0.05}$ olarak tespit edilmiştir.
- Plazma nitrürlenmiş numunenin yüzey pürüzlülüğü Ra değeri 0.38, %75 görev döngüsü ile plazma nitrürleme sonucu Ra değeri 0.3, %50 görev döngüsü ile plazma nitrürleme sonucu Ra 0.24 olarak tespit edilmiştir.

5. TEŞEKKÜR

Bu çalışma Afyon Kocatepe Üniversitesi Bilimsel Araştırma Projeleri Koordinasyon Birimi tarafından 13.FEN. BİL.45 nolu proje kapsamında desteklenmiştir.

6. ÇIKAR ÇATIŞMASI

Yazar, bilinen herhangi bir çıkar çatışması veya herhangi bir kurum/kuruluş ya da kişi ile ortak çıkar bulunmadığını onaylamaktadırlar.

7. YAZAR KATKISI

Şükrü ÜLKER, çalışmanın kavramsal ve/veya tasarım süreçlerinin belirlenmesi ve yönetilmesi, verilerin toplanması, verilerin analizi ve sonuçların yorumlanması, makalenin hazırlanması ve fikirsel içeriğin eleştirel incelenmesi ve son onay konusunda tam sorumluluğa sahiptir.

8. KAYNAKLAR

Alves C., Rodrigues J., Martinelli A., The Effect of Pulse Width on the Microstructure of DC-Plasma-Nitrided Layers. Surface and Coatings Technology 122, 112-117, 1999.

Anders A., Fundamentals of Pulsed Plasmas for Materials Processing. Surface and Coatings Technology 183, 301–311, 2004.

Arul Mozhi Varman J. P., Huchel U., Effect of Pulse Repetition Time on Surface Properties of Pulsed Plasma Nitrided AISI 4340 Steel. Indian Journal of Science and Technology 10 (38), 1-8, 2017.

Cai S., Sun J., He Q., Shi T., Wang D., Si J., Yang J., Li F., Xie K., Li M., 16MnCr5 Gear Shaft Fracture Caused by Inclusions and Heat Treatment Process. Engineering Failure Analysis 126, 105458, 1-9, 2021.

Cieslik J., Jacquet P., Tlili B., Mulin H., Decrease of Compound Layer Thickness Obtained in Plasma Nitriding of Alloyed Steels by Diffusion Stage. Journal of Materials Science and Engineering A, 1, 974-980, 2011.

Chong S O, Kim S J., Corrosion Characteristics of 16Cr-10Ni-2Mo Stainless Steel with Plasma Ion Nitriding Temperatures by Galvanostatic Experiment. Journal of Surface Science and Engineering 50 (2), 91–97, 2017.

Conrads H., Schmidt M., Plasma Generation and Plasma Sources. Plasma Sources Science and Technology 9, 441, 2000.

Cooke K. E., Hamsphire J., Southall W., Teer D. G., The Industrial Application of Pulsed DC Bias Power Supplies in Closed Field Unbalanced Magnetron Sputter Ion Plating. Surface Engineering 20(3), 189-195, 2004.

Çelik A., Karadeniz S., Investigation of Compound Layer Formed During Ion Nitriding of AISI 4140 Steel. Surface and Coatings Technology 80, 283-286, 1996.

Díaz-Guillén J. C., Campa-Castilla A., Pérez-Aguilar S. I., Granda-Gutiérrez E. E., Garza-Gómez A., Candelas-Ramírez J., Méndez-Méndez R., Effect of Duty Cycle on Surface Properties of AISI 4340 Using a Pulsed Plasma Nitriding Process. Superficies y Vacío 22(1) 1-4, 2009.

Díaz-Guillén J, Vargas-Gutiérrez G, Granda-Gutiérrez E, González M, Díaz-Guillén J, Alvarez-Contreras L, Effects of Pulse Length on Low Frequency Plasma Nitrided 316L Steels. Surface Engineering 31 (8), 2015.

Durisic Z., Kunosic A., Trifunovic J., Influence of Process Parameters in Pulse Plasma Nitriding of Plain Carbon Steel. Surface Engineering, 22(2), 147-152, 2006.

Esfahani A., Sohi M. H., Rassizadehghani J, Mahboubi F., Effect of Treating Atmosphere in Plasma Post-Oxidation of Nitrocarburized AISI 5115 Steel. Vacuum 82(3), 346-351, 2007.

Espinoza R. C., Vera M., Wettlaufer M., Kerl M., Barth S., Garibaldi P.M., Díaz Guillen J.C., García H. M. H., Arroyo R. M., Ortega J. A., Study on the Tribological Properties of DIN 16MnCr5 Steel after Duplex Gas-Nitriding and Pack Boriding. Materials 17(13), 3057, 2024.

Fenili C. P., Souzab F.S., Marina G., Probst S. M. H., Binder C., Klein A. N., Corrosion Resistance of Low-Carbon Steel Modified by Plasma Nitriding and Diamond-Like Carbon. Diamond & Related Materials 80, 153-161, 2017.

Huchel U., Crummenauer J., Stramke S., Dressler S., Pulsed Plasma Nitriding and Combined Processes, Proceedings of the 5th World Seminar on Heat Treatment and Surface Engineering, Iran, 329–335, 1995.

Jeong G. H., Hwang M. S., Jeon B. Y., Kim M. H., Lee C., Effects Of The Duty Factor on The Surface Characteristics of The Plasma Nitrided And Diamond – Like Carbon Coated High Speed Steel. Surface and Coatings Technology 124, 222–227, 2000.

Leskovsěk V., Pulse Plasma Ionitriding. Vakuumist 15(2), 4-10, 1995.

Luo Q., Oluwafemi O., Kitchen M., Yang S., Tribological Properties and Wear Mechanisms of DC Pulse Plasma Nitrided Austenitic Stainless Steel in Dry Reciprocating Sliding Tests. Wear 376-377, 1640-1651, 2017.

Menthe E., Bulak A., Olfe J., Zimmermann A., Rie K. T., Improvement of the Mechanical Properties of Austenitic Stainless Steel after Plasma Nitriding. Surface and Coatings Technology 133-134, 259-263, 2000.

Naeem M., Waqas M., Jan I., Zaka-ul-Islam M., Díaz-Guillén J. C., Rehman N. U., Shafiq M., Zakaullah M., Influence of Pulsed Power Supply Parameters on Active Screen Plasma Nitriding. Surface and Coatings Technology 300, 67-77, 2016.

Naeem M., Qadeer M., Mujahid Z. İ., Rehman N.U., Díaz-Guill´en J. C., Sousa R. R. M., Shafiq M., Time-Resolved Plasma Diagnostics of Cathodic Cage Plasma Nitriding System with Variable Pulsed Duty Cycle and Surface Modification of Plain Carbon Steel. Surface & Coatings Technology 464, 129542, 2023.

Ohtsu N., Miura K., Hirano M., Kodama K., Investigation of Admixed Gas Effect on Plasma Nitriding of AISI 316L Austenitic Stainless Steel. Vacuum 193,110545, 2021.

Podgornik B., Vizintin J., Wear Resistance of Plasma and Pulse Plasma Nitrided Gears. Gear Technology 20, 33-37, 2003.

Podgornik B., Vižintin J., Wänstrand O., Larsson M., Hogmark S., Ronkainen H., Holmberg K. Tribological Properties of Plasma Nitrided and Hard Coated AISI 4140 Steel, Wear 249, 254-259, 2001.

Sharma M., Saikia B., Phukan A., Ganguli B., Plasma Nitriding of Austenitic Stainless Steel in N_2 and N_2–H_2 Dc Pulsed Discharge. Surface and Coatings Technology 201, 2407-2413, 2006.

Shen H., Wang L., Influence of Temperature and Duration on The Nitriding Behavior of 40Cr Low Alloy Steel in Mixture of NH_3 and N_2. Surface and Coatings Technology, 378: 124953, 2019.

Sirin S. Y., Sirin K., Kaluc E., Effect of the Ion Nitriding Surface Hardening Process on Fatigue Behavior of AISI 4340 Steel. Materials Characterization 59, 351-358, 2008.

Taherkhani K., Mahboubi F., Investigation Nitride Layers and Properties Surfaces on Pulsed Plasma Nitrided Hot Working Steel AISI H13. Iranian Journal of Materials Science & Engineering 10(2), 29-36, 2013.

Taktak S., Gunes I., Ulker S., Effect of Pulse Plasma Nitriding on Tribological Properties of AISI 52100 and 440C Steels. International Journal of Surface Science and Engineering, 8(1), 39, 2014.

Yasir H R M., Naeem M., Abrar M., Mahmood S., Enhancement of Hardness and Tribological Properties of AISI 321 by Cathodic Cage Plasma Nitriding at Various Pulsed Duty Cycle. Journal of Alloys and Compounds 1002, 175280, 2024.